Poly(ionic liquid)s for Magnetic, Ionic, and Electrical Stimuli-Responsive Applications

A dissertation submitted in partial fulfillment
of the requirements for the degree of
Doctor of Philosophy in Engineering, with a concentration in Chemical Engineering

by

Kayla Ann Foley
University of Oklahoma
Bachelor of Science in Chemical Engineering, 2016
University of Oklahoma
Master of Science in Chemical Engineering, 2017

August 2023
University of Arkansas

This dissertation is approved for recommendation to the Graduate Council.

Keisha B. Walters, Ph.D.
Dissertation Director

Daniel Glatzhofer, Ph.D.
Committee Member

Tammy Lutz-Rechtin, Ph.D.
Committee Member

Karthik Nayani, Ph.D.
Committee Member

Wan Shou, Ph.D.
Committee Member

Abstract

Poly(ionic liquid)s (PILs) are a fascinating subclass of strong polyelectrolytes formed from polymerizable ionic liquids. As a result of their unique properties and counterion exchangeability, PILs can exhibit conformation structure or material property changes in response to external stimuli such as changes in pH/ionic environment, magnetic fields, and electric potentials. In Chapter 1, a comprehensive review of PILs design as well as their stimuli-responsive behavior is provided. Additional motivation for each dissertation chapter is also discussed.

In Chapter 2, magnetically responsive PILs (MPILs) are developed from complexing paramagnetic salts with a random PIL copolymer containing a metal-coordinating co-monomer, acrylamide. A systematic spectroscopic investigation (FTIR, UV-Vis, Raman, XPS) was performed to analyze the influence of the acrylamide comonomer on the paramagnetic transition metal complex and its binding to the polymers. A preliminary investigation into its room temperature magnetic properties through AC susceptometry and magnetic attraction to handheld magnets is also provided.

In Chapter 3, self-assembly of these random copolymers is induced through complexation with the surfactant sodium dodecyl sulfate to form magnetically responsive polyelectrolyte-surfactant micellular solutions and films. Micellular self-assembly is examined as a function of surfactant concentration through DLS and ZP measurements for both a cobalt-based MPIL and the corresponding non-magnetic PIL copolymer. Cryogenic transmission electron microscopy and FTIR characterizations provide additional insight into the self-assemble structure. Applied magnetic stimuli responsive is investigated of both the solution structures and drop-cast films, with and without the presence of weak (~0.6 T) magnetic fields, through optical microscopy, AFM, and GISAXS.

Chapter 4 completes the investigation of select MPIL copolymers and their polyelectrolyte-surfactant complexes through a thorough vibrating sample magnetometry study as a function of magnetic field strength and temperature. Additional FTIR, DLS, ZP, SEM, and DSC characterizations provide insight into the observed magnetic behavior.

In Chapter 5, an all-polyelectrolyte block copolymer comprised of a poly(ionic liquid) block and a weak tertiary amine polyelectrolyte block is synthesized and characterized through a Cu(0) mediated atom transfer radical polymerization. NMR and FTIR spectroscopies confirm the synthesis and provide insight into intermolecular interactions, specifically electrostatics and hydrogen bonding, of the novel block copolymer in dry and solution states. DLS measurements indicate the block copolymer exhibits an expanded network like structure in pure dimethyl sulfoxide solution that collapses on addition to potassium nitrate (KNO_3) salt, demonstrating salt responsive behavior. Self-assembly of the block copolymer as a drop-cast film was analyzed with a new technique to PIL systems, namely, a hybrid AFM-IR characterization. The films exhibited different morphology depending on film thickness.

Chapter 6 examines the electrical stimuli responsive nature of the block copolymer and its corresponding homopolymer in ionic electro active polymer actuator composites. Ionic liquid was combined with the homo- and block copolymer PILs to decrease glass transition temperature and increase ion conductivity. Key parameters for ionic actuation were investigated, including glass transition temperature (DSC), thermal stability (TGA), ion conductivity (EIS), chemical interactions (FTIR), Young's modulus (AFM force curves), film morphology (AFM), and actuation behavior to small, applied voltage.

Acknowledgments

First and foremost, I would like to thank my advisor Dr. Keisha B. Walters for her guidance, patience, mentorship, encouragement, and for always believing in me even when I found it hard to believe in myself. I have grown significantly as both a person and a young scientist under her mentorship during the last 5 years, and I would certainly not be the person I am today had I never met her.

I would like to thank my previous masters' thesis advisor, Dr. R. L. Shambaugh, for his friendship, encouragement, our many walking-discussions, and for introducing me to research and polymers, which ultimately led me to pursue this PhD.

I would like to thank both my previous OU committee members (Dr. Lance Lobban Dr. Steven Crossley, Dr. Shambaugh), my current UA committee members (Dr. Wan Shou, Dr. Karthik Nayani, Dr. Tammy Lutz-Rechtin), and Dr. Daniel Glatzhofer who was willing to serve on both my OU and UA committees. Thank you for your advice and support through this academic journey.

I would like to thank all of the members of my lab group—OU PolySEL, UA PolyNEL, and briefly, SNaP—for your encouragement, support, and camaraderie: Collin Britten, Brandon Abbott, Austin Castorino, Onyinyechi Igwe, Yokly Leng, David Chem, Olufemi Ogunjimi, Yousef Fathisola, Dr. Muhammad Nazrul Islam, and Dr. Fatema Tarannum. A special thank you to the undergrad researchers that have worked with me on various projects over the years: Stephen Cockmon, Amber Veach, An Tran, Noa Raimond, Lucas Condes, Natalie Berryman, August Limvaree, Sushil Dhev Munian, Kaylee Huckaby, and Emily Grace Long.

A special thank you to Dr. Tammy Lutz-Rechtin, Dearl D. Peachee, and James K. Cole who helped me get my research up and running again at UA and for their continued support. Thank you

to Sarah Bonner, Emily Ebbing, Terri Colliver, and Madena McGinnis for helping me with all things administrative.

A special thank you to Dr. Dale Huber (CINT/ Sandia National Labs), Dr. Jean Luc-Brousseau (Anton Paar), Dr. Javen Weston (University of Tulsa), Dr. Cassandra Phillips (Bruker), Dr. I-Wei Chu (I2AT), Dr. Andy Madden (OU Microscopy), Dr. Preston Larson (OU Microscopy), Dr. Julian Sabisch (OU Microscopy), Dr. Mourad Benamara (NANO Materials Characterization), and Dr. Susan Nimmo (OU NMR) for their collaboration, support in my research, and teaching me various characterization techniques over the years.

Finally, a huge thanks to my friends and family. Without your love and support, I am not sure I would have made it through this PhD. Thank you.

Dedication

This work is dedicated to the memory of my paternal and maternal grandfathers.

John William Foley—January 24, 1942 - December 26, 2015

William (Bill) Stuebe—January 21, 1941 - May 21, 2022

Contents

List of Published Papers

Publications from Ph.D. Dissertation Efforts

First Author

1. **Kayla Foley**, Keisha B. Walters. "Development of Nano- and Micro- Fluids Using Magnetic Poly(ionic liquid)-Surfactant Complexes for Stimuli Response." Proceedings of the ASME 2022 Fluids Engineering Division Summer Meeting. Volume 2: Multiphase Flow (MFTC); Computational Fluid Dynamics (CFDTC); Micro and Nano Fluid Dynamics (MNFDTC). Toronto, Canada. August 3-5, 2022. V002T06A006. In Print. ASME. https://doi.org/10.1115/FEDSM2022-87758. This text is used in Chapter 3.
2. **Kayla Foley**, Lucas Condes, Keisha B. Walters. Influence of metal-coordinating comonomers on the coordination structure and binding in magnetic poly(ionic liquid)s. [Accepted July 9th, 2023. ID ME-ART-05-2023-000076, Pre-publication] Journal: *RSC Molecular Systems Design and Engineering.* This text is used in Chapter 2.

Submitted and Under Review or In Revision

First Author

1. **Kayla Foley**, Keisha B. Walters. Solution and film self-assembly behavior of a block copolymer comprised of a poly(ionic liquid) and a stimuli-responsive weak polyelectrolyte. [Submitted June 6th, 2023. ID ao-2023-039894, In Revision] Journal: *ACS Omega.* This text is used in Chapter 5.

In Preparation

1. **Kayla Foley**, Iwei Chu, Keisha B. Walters. Evaluation of novel poly(ionic liquid) block copolymer and homopolymer as electroactive polymer actuators. [In Preparation]. This text is used in Chapter 6.

2. **Kayla Foley,** Charles P. Easterling, Dale L. Huber. Keisha B. Walters. Magnetometry studies of magnetic poly(ionic liquids) using surfactant complexation to direct self-assembly and increase the effective moment. [In Preparation]. This text is used in Chapter 4.

Chapter 1: Introduction

1.1. Poly(ionic liquid)s for Stimuli Response: An Overview of PIL Design and Objectives

Stimuli responsive or "smart" polymers are fascinating materials due to their ability to change their conformation and even material properties in response to environmental factors (e.g., pH, temperature)[1, 2] or applied external stimuli (e.g., magnetic field, electrical field)[3]. Poly(ionic liquids), or PILs, are a polymer class that is capable of stimuli response through non-covalent interactions[4, 5]. PILs are comprised from monomers formed from ionic liquids (IL)—organic salts with melting points generally below 100 °C[6]—forming a strong polyelectrolyte with permanently charged groups immobilized on pendant groups or along the polymer backbone and mobile exchangeable counterions. PILs combine the diverse functionality of ionic liquids with the processability and mechanical integrity of polymeric systems. In particular, PILs exhibit relatively high ion conductivity, wide electrical chemical windows, high thermal stability, antibacterial properties, and a variety of other favorable properties which are tunable through polymer design and counterion exchange[7-10]. As a result, they have rapidly found growing interest in a variety of fields including catalysis, sensors, energy materials, separations, biomedical applications, nanomaterials, and composites[7, 9-14]. In terms of stimuli response applications, PILs have demonstrated responsive behavior to salt[15-17], pH[18, 19], temperature[20-22], redox reactions[11, 23], CO_2 sorption[24, 25], magnetic fields[26], and applied electrical voltages[27, 28]. The particular responsive behavior displayed is a function of the chemical decomposition and supramolecular properties.

PIL material property targeting can be achieved through the polymer design including the careful selection of the polymer backbone type, immobilized ILM ion, and counterion (Figure 1.1). Polymerization can be achieved before or after counterion exchange through most polymerization techniques including conventional radical polymerization and controlled "living" radical

polymerizations (e.g., ATRP, RAFT, NMP) which are often used for the synthesis of block copolymer (BCP) systems[7, 9, 13]. Alternatively, IL units can also be added post-polymerization through other chemical grafting methods, typically using a quaternization reaction or Menshutkin reaction of amines or phosphoniums with alkyl halide groups[7, 13]. The most common polymeric backbones for PILs are vinyl, styrenic, and acrylate based (Figure 1.1c), although others such as norbornene[29], thiophene[30], and amides[31], have also been utilized. Also, PILs have often been copolymerized with neutral comonomers (e.g., polystyrene, polymethyl methacrylate) [32] or other stimuli responsive materials (e.g., poly(n-isopropylacrylamide)[21, 22, 33]) to add microstructural design components and/or and functionality.

The majority of cationic PILs have fixed imidazolium, triazolium, pyridinium, ammonium, phosphonium, or pyrrolidinium type groups whereas anionic PILs are mainly composed from sulfonate, carboxylate, or phosphonate units (Figure 1.1a). PIL properties can be modified through covalent alteration of the immobilized ion. For instance, quaternation of imidazolium with ether chains or carboxylate functionalities—as opposed to the typical alkyl chain—can give the PIL additional zwitterionic behavior[34] or adhesive properties[35].

Counterion selection is based on the desired end properties of the polymer (Figure 1.1b). The initial/original counterion can be exchanged through a metathesis reaction with inorganic salts, ionic surfactants, polyelectrolytes, or other ionic materials (Figure 1.1d). This is a very important aspect of PILs, as the material properties are strongly dependent on the selected counterion. For instance, exchanging the counterion can change the solubility of PILs in both polar and organic solvents, allowing for tunable hydrophobicity and hydrophilicity[36]. The glass transition temperature (T_g) can be lowered and ion conductivity increased with weakly coordinating fluorinated anions through plasticizing effects, whereas smaller coordinating halide counterions

typically produce PILs with higher glass transition temperatures and poorer electrochemical performance[13]. Anionic pH sensitive dyes can be noncovalently bound to PIL films making pH responsive plastic colorimetric sensors[19]. Redox active polymers can be synthesized by exchanging counterions with redox active ions such as anthraquinone-2-sulfonate[11]. As with free ionic liquids, the number of cation-anion "pairs" possible in PILs are vast, giving a large toolbox for intelligent polymer design and applications simply through a non-covalent counterion exchange.

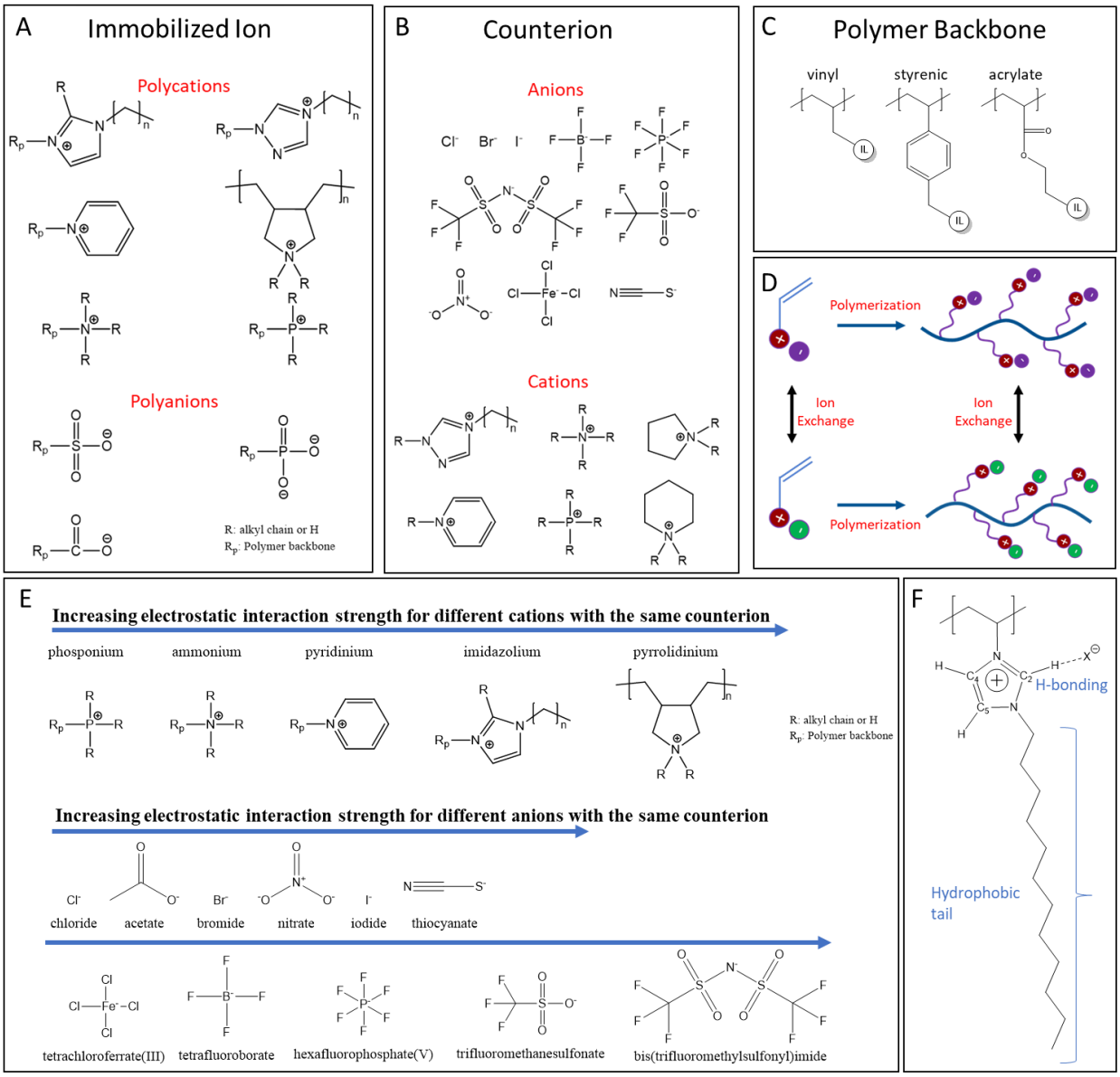

Figure 1.1 PIL (poly(ionic liquid)) Toolbox: The primary PIL design parameters include selection of (a) immobilized ions, (b) electrostatically bound counterions, and (c) polymer backbone. (d) PIL properties may be readily tuned through a simple ion exchange either in the monomeric or polymeric forms without resorting to covalent chemistry. (e) The general trends for electrostatic interaction strength for different cations and anions as determined by both computational and experimental studies of ionic liquids and polyelectrolytes[37-41]. Generally, the strength of electrostatic interaction in cations is largely determined by charge localization/stabilization (i.e., aromatic ring vs localized charge on N atom) and charge shielding from cations. Anion interaction strength depends on hydration, charge delocalization, size, valency, and generally follows the Hofmeister series[41-43]. (f) In addition to electrostatics, PIL interactions between cations-anions and the surrounding chemical environment are also mediated by other supramolecular interactions, including hydrophobic and hydrogen bonding (H-bonding).

Although less explored in PIL materials compared to their IL counterparts, the use of multiple cations or anions within a single PIL system presents the opportunity to even further expand the vast pool of possible PILs and their applications. Ionic liquid mixtures containing multiple cations and anions yield intermediate properties compared to their individual behavior, allowing specific material design for properties such as solubility, viscosity, thermal properties, and even magnetic character[44-46]. The use of covalently attached di- and tri-cationic ionic liquids has become a growing subclass of ionic liquids as they provide an additional structural design parameter for tuning IL properties[45, 47]. In PIL systems, the use of multiple ions has mainly been limited to counterion mixtures. The ratio of different counterions in the system can lead to significant changes in polymer chain dynamics, structure, hydrogen bonding abilities, and hydrophobic interactions. This leads to fine tuning of properties such as self-healing[29], glass transition temperature[29], gas diffusivities[48], micellar self-assembly[15], and noncovalent specific crosslinking interactions[49]. A few systems have also immobilized multiple cations on the polymer backbone; however, these have predominately been limited to block copolymer imidazolium type polycations with different modifications to the pendant alkyl chains for each block[50-53]. Further exploration of multi-cation PIL copolymers with different cation types offers the potential for expanding PIL design through differences in the supramolecular interaction abilities of the immobilized cations (e.g., hydrogen bonding, hydrophobic) and their interaction strength with different counterions (Figure e, f). The use of weak cationic polyelectrolytes, such as tertiary amines, instead of strong cationic PIL groups will also imbue the polymer with pH stimuli-responsive behavior, where the overall charge density of the polymer can be controlled through environmental pH.

Task specific counterions may also be utilized to induce PIL property changes in response to environmental stimuli, including magnetic fields and applied electric potential. Magnetically

responsive PILs (or MPILs) are formed when paramagnetic transition metal ionic complexes are electrostatically bound to the polymer. These MPILs have been shown to respond to magnetic fields as powders, processed films, or particles in solution[26, 54] and have found application in a variety of fields including magnetic separations[55], catalysis[26], and nanoparticle synthesis[56]. MPIL magnetic properties and responsiveness are largely dependent on metal content and the polymer and chemistry and architecture. As the ideas for MPIL application expand, the complexity of MPIL design will continue to increase—or vice versa. This supports the need for more investigation of stimuli responsive behavior, structure-property material relationships, and nano- and micro-scale assembly behavior in PIL and PIL-based multicomponent systems (e.g., copolymers, blends, composites).

PILs also respond to electrical stimuli. As polyelectrolytes, PILs are inherently responsive to electrical fields through ionic conductivity of the mobile counterion and the overall charged state of the polymeric material. However, PILs with fluorinated counterions (e.g., $[(CF_3SO_2)_2N^-]$, $[BF_4]^-$, $[CF_3SO_3]^-$) are generally preferable for electrical response due to their favorable electrochemical properties including wide electrochemical windows, low glass transition temperatures, and high ion conductivity. As such, these strong polyelectrolytes have found significant interest for electrochemical applications such as solid-state batteries, sensors, electrowetting, and wearable electronics[27, 57, 58]. In the last decade, PILs have begun to be explored as novel electrolytes in electromechanical actuators for soft robotics and sensor applications[59, 60]. However, there is significant room for further investigation and development of new PIL actuators systems, particularly for non-ambient environments.

In this dissertation, the focus is on developing poly(ionic liquid) materials with different stimuli responsive behavior with particular focus on three specific stimuli: (i) magnetic, (ii) salt, and (iii)

electrical. In particular, the aims for the magnetically responsive PILs were (1) investigating the relationship between chemical, structural, and magnetic properties of novel multicomponent MPIL systems and (2) evaluating their magnetic stimuli response behavior in self-assembled systems; these MPIL studies are discussed in Chapters 2-4 (CH 2-4). In order to investigate multi-cationic PILs, an all-polyelectrolyte block copolymer comprising a strong cationic PIL block and a weak cationic tertiary amine block was synthesized. Preliminary examination of the all-polyelectrolyte PIL block copolymer's self-assembly behavior in response to salt in solution and the bulk is investigated (CH 5). PIL electrical stimuli response was explored through the synthesis and characterization of novel PIL and PIL-IL composites, known as ionogels, with the end application goal of developing PIL-based electromechanical actuator systems or similar electrochemical devices such as flexible electronics or sensors (CH 6).

In addition to the introductions provided in each chapter, this chapter (CH 1) will serve to provide motivation and context for the studies included in this dissertation. First, an overview of the MPIL field related to magnetic property enhancement and applied magnetic stimuli response is provided in section 1.2. In section 1.3, a summary of PIL salt responsive behavior and self-assembly in PILs blocked with both neutral and other polyelectrolytes is provided. An introduction to electroactive actuators and the use of PIL ionogels as electroactive polymer actuator (EPA) electrolytes is provided in section 1.4.

1.2. Magnetic PILs

1.2.1. Overview and Magnetic Properties of MPILs

The first reported magnetic ionic liquid (MIL) commonly cited was 1-butyl-3-methylimidazolium tetrachloroferrate ($C_4C_1Im[FeCl_4]^-$) by Hayashi et al. in 2006, which exhibited paramagnetic behavior as it could be visually attracted to a handheld magnet and had a measured

magnetic mass susceptibility (measure of attraction to a magnetic field) of ~41.9 x 10^{-6} emu/g[61]. In 2011, Döbbelin et al. developed magnetic poly(ionic liquid)s from polyvinylimidazolium and poly(diallyl dimethyl ammonium) polycations and $FeCl_3$ and $FeBr_3$ salts[26]. The MPILs were formed through coordination of the polycation Cl^- counterion with the metal halide salts, forming anionic transition metal complexes (e.g., $[FeCl_4]^-$, $[Fe_2Cl_7]^-$, $[FeBrCl_3]^-$, $[FeBr_3Cl]^-$) that were electrostatically bonded to the polymers (Figure 1.2b). These MPILs were found to be paramagnetic at room temperature with susceptibilities between ~24-52 x 10^{-6} emu/g depending on the MPIL type, metal concentration, and the transition metal complex type. While the work of Döbbelin et al. (2011) is generally considered to be the first case of magnetic poly(ionic liquid)s, it should be noted that an earlier 2008 work by Yang et al. developed random and block copolymers from poly[2-(1-butylimidazolium-3-yl) ethyl methacrylate tetrafluoroborate], a covalent metal-coordinating polymer poly[N-2-thiazolylmethacrylamide], and complexed $NiSO_4$ and $NdCl_3$ salts which also displayed magnetic properties[62].

Since 2011, approximately 23 papers have been published on magnetic poly(ionic liquid)s, which is classified in this work as PIL materials containing paramagnetic transition metal salts and does not include PILs blended or grafted with iron oxide or metal nanoparticles. Table 1.1 summarizes these publications, with application and magnetic property information included. In the past decade, the primary focus has been synthesis of new MPIL systems, magnetic property characterization, and demonstration of magnetic stimuli responsive behavior through attraction to relatively weak magnets (< 2 T). In simpler MPIL systems, such as homopolymers, the magnetic behavior is generally found to be paramagnetic with the magnetic mass susceptibilities values largely dependent on weight percentage of metal content in the polymer system and the transition metal type complexed[26, 56, 63, 64]. However, as the MPIL field continues to develop, more complex

multi-component systems have been developed including block copolymers, blends, composites, and homopolymers with modified pendant groups. These more complex multi-component systems have often reported cases where the paramagnetic susceptibility is enhanced[65, 66] or other forms of magnetic coupling behaviors are displayed, such as ferromagnetic[62, 67-71], antiferromagnetic[71], and superparamagnetic[68, 72, 73].

For instance, Bonnefond et al. developed magnetic latexes from the copolymerization of an MPIL with butyl acrylate and methyl methacrylate copolymers that exhibited weak antiferromagnetic interactions with reported Neel temperatures between 1.4 and 6.7 K for metal halide salts for Fe^{3+}, Co^{2+}, and Mn^{2+} [63]. Carrasco and coauthors formed thermoset MPILs with weak ferromagnetic properties from a partially quaternized pyridine MPIL and acrylate block copolymers blended with epoxy that exhibited nanophase separated spherical morphology[74]. MPILs containing long pendant alkyl chains or grafted brush topography has exhibited increased paramagnetic susceptibility values believed to be due to restricted motion and increased packing of the transition metal salts in lamellar-like structures[65, 66]. In a series of recent articles, Ren et al. has successfully enhanced the magnetic coupling interactions in MPILs by decreasing the distance between Fe^{3+}-Fe^{3+} centers to ~ 4 Å using π-π stacking linker groups incorporated between the polymer backbone and pendant magnetic ionic liquid group[68, 70, 71]. In a similar work, Cui et al. developed imidazolium $[FeCl_4]^-$-based random copolymers with a pendant pyrene group on the comonomer. Superparamagnetic behavior was reported for this MPIL copolymer with $[FeCl_4]^-$ anions that acted as quenchers for the fluorescent pyrene-based comonomer[75]. In many of the above cases, MPIL structure and morphology was found to be important for enhancing magnetic coupling interactions of the transition metal species in the polymer system.

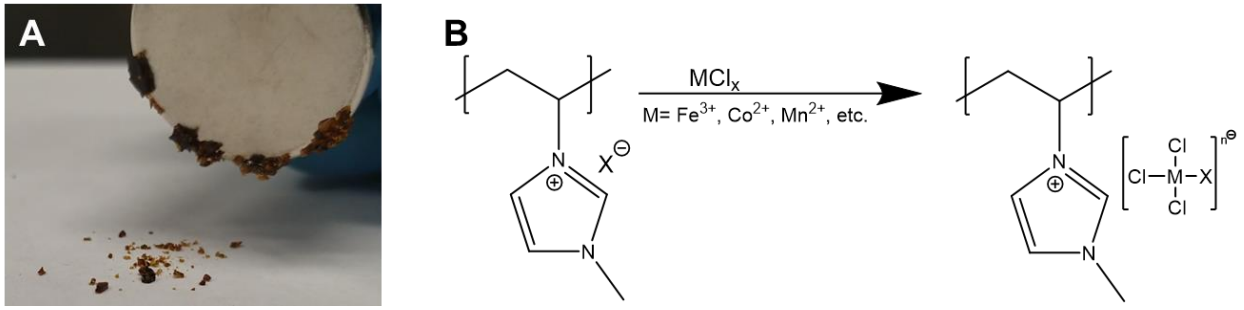

Figure 1.2 (a) Video frame capture of one of a quaternary ammonium-based MPIL copolymers discussed in CH 2 showing magnetic attraction to a 0.62 T neodymium magnet. (b) General synthesis scheme for an imidazolium-based MPIL homopolymer through coordination of transition metal salts with the original counterion (X^-), typically a halide (e.g., Cl^-, Br^-, I^-). The resulting electrostatically bound paramagnetic anion provides the magnetic responsive property to the PIL.

Table 1.1 Summarization of the MPIL literature displaying primary application and magnetic properties.

Ref.	Main Application or Study	Polymer System	Metal Component	Reported Magnetism	Study Type	Magnetic Susceptibility ($x10^{-6}$ emu/g) or other magnetic property
Yang et al. 2008[62]	Magnetic property study	random copolymer of N-2-thiazolylmethacrylamide and 2-(1-butylimidazolium-3-yl) ethyl methacrylate tetrafluoroborate	$NdCl_3$,	diamagnetic to ferromagnetic transition at 292 K	MVT 4-300 K at 30 kOe; MVH at 4K	1.09 emu/g saturation magnetization
			$NiSO_4$	NR		1.73 emu/g saturation magnetization
			$NdCl_3/NiSO_4$	ferromagnetic (θ_{CW} = 12 K)		12.16 saturation magnetization
		block copolymer of N-2-thiazolylmethacrylamide and 2-(1-butylimidazolium-3-yl) ethyl methacrylate tetrafluoroborate	$NdCl_3$,	ferromagnetic (θ_{CW} = 175 K)	MVT 4-300 K at 30kOe; MVH at 4K	1.42 emu/g saturation magnetization
			$NiSO_4$	paramagnetic with antiferromagnetic interactions (θ_{CW} = -15 K)		9.08 emu/g saturation magnetization
			$NdCl_3/NiSO_4$	antiferromagnetic (θ_{CW}= -28 K)		11.88 emu/g saturation magnetization
Döbbelin et al. 2011[26]	Lewis Acid catalysis	polyvinylimidazolium	$[FeCl_4]^-$, $[Fe_2Cl_7]^-$, $[FeBr_3Cl]^-$, $[FeBrCl_3]^-$	paramagnetic	MVH at 300 K	24.1-51.5 depending on metal content
		poly(diallyl dimethylammonium)	$[FeCl_4]^-$	paramagnetic	MVH at 300 K	29.3-35.3 depending on metal content

Table 1.1 Cont.

Ref.	Main Application or Study	Polymer System	Metal Component	Reported Magnetism	Study Type	Magnetic Susceptibility ($x10^{-6}$ emu/g) or other magnetic property
Cui et al. 2012[72]	Fluorescence and magnetic stimuli response	copolymer of vinylimidazole, vinylimidazolium, and methacrylate with pendant pyrene groups	$[FeCl_4]^-$	superparamagnetic with antiferromagnetic interactions (θ_{CW}= -36.7 K)	MVH at 5 and 300 K; MVT 2 to 300 K at 100 Oe	9.2-19.1
Carrasco et al. 2013[67]	Epoxy thermosets	Vinylpyridinium type diblock copolymer with methyl methacrylate and unquaternized vinypyridine	$[Fe_3Br_{10}]^-$	soft ferromagnet	MVH at 300 K	coercive field 72 Oe; 1.04 x 10^{-2} emu/g magnetic saturation
		Vinylpyridinium type diblock copolymer with methyl methacrylate and unquaternized vinypyridine/Epoxy Blend	$[Fe_3Br_{10}]^-$	soft ferromagnet	MVH at 300 K	coercive field 83 Oe; 1.68x 10^{-3} emu/g magnetic saturation
Rahamn et al. 2013[76]	Liquid beads and magnetic response	poly(1,3-bis(1-pentenyl)-2-methylimidazolium crosslinked with polyethylene glycol diacrylate	$FeCl_3$ or $DyCl_3$	assumed paramagnetic	NR	NR
Sahiner et al. 2014[77]	Template for metal nanoparticle synthesis	crosslinked poly[(3-acrylamidopropyl)-trimethylammonium] crosslinked with N,N-methylenebisacrylamide	$[CoCl_4]^{2-}$, $[CuCl_4]^{2-}$, $[NiCl_4]^{2-}$, $[FeCl_4]^-$	paramagnetic	AC susceptibility balance at 300 K	1.88
Yu et al. 2015[78]	Magnetic property study	linear or branched polyethyleneimine quaternized to varying degrees	$[FeCl_4]^-$	paramagnetic	MVH at 300 K	10.7-41.6 depending on metal content

Table 1.1 Cont.

Ref.	Main Application or Study	Polymer System	Metal Component	Reported Magnetism	Study Type	Magnetic Susceptibility ($x10^{-6}$ emu/g) or other magnetic property
Yu et al. 2016[54]	Magnetic property study	norbornene-type block copolymers with pendant quaternary ammonium on ethyl pendant chain	$[FeCl_4]^-$	paramagnetic with ferromagnetic interactions (θ_{CW}= 4.8K)	MVH at 300K; MVT 2-300 K at 10 kOe	23.7
Hazell et al. 2016[79]	Magnetic directed separations for water treatment	poly(diallyl dimethylammonium)	$[FeCl_4]^-$	assumed paramagnetic	NR	NR
Bonnefond et al. 2016[63]	Magnetic latexes	polyvinylimidazolium random copolymers with butyl acrylate and methyl methacrylate	$[FeBrCl_3]^-$, $[CoBrCl_2]^-$, $[MnBrCl_2]^-$	paramagnetic with antiferromagnetic interactions	MVT 2-300 K at 1000 Oe	μ_{eff} [μ_B] per metal complex: 5.6 (Fe^{3+}), 4.2 (Co^{2+}), 5.9 (Mn^{2+})
Alard et al. 2017[80]	Multi-stimuli response	Quaternized poly[2-(dimethylamino)ethyl methacrylate] copolymers	$FeCl_3X$, X= Cl-, Br-, I-	paramagnetic	MVH at 300K	μ_{eff} [μ_B] per based on polymer and metal combined molecular weight: 14.7-61.2
Ohara et al. 2017[64]	Living RAFT polymerization	poly[3-(methylacrylamido)propyltrimethylammonium chloride)]	$[FeCl_4]^-$	paramagnetism	MVH at 300 K	31.9
Sun et al. 2017[81]	Template for metal nanoparticle synthesis	1,2,4-triazolium PIL poly(4-hexyl-1-vinyl-1,2,4-triazolium iodide)	Pd, Ag, Pt, Au, Ru, Rh, Ni, Co nitrates, chlorides, and acetates	NR	NR	NR
Lu et al. 2018[82]	Antimicrobial Agents	poly(diallyl dimethylammonium)	$[FeCl_4]^-$	assumed paramagnetic	NR	NR

Table 1.1 Cont.

Ref.	Main Application or Study	Polymer System	Metal Component	Reported Magnetism	Study Type	Magnetic Susceptibility (x10^{-6} emu/g) or other magnetic property
Zhang et al. 2018[83]	Self assembly and magnetic property study	vinylpyridinium	$[FeCl_4]^-$	paramagnetic	MVH at 300K	9.12
		block copolymer polystyrene and post-quaternized vinylpyridinium	$[FeCl_4]^-$	paramagnetic	MVH at 300K	12.7
		block copolymer of polyhedral oligomeric silsequioxanes, polystyrene, post-quaternized vinylpyridinium	$[FeCl_4]^-$	paramagnetic	MVH at 300K	27.5 after self-assembly; 15.4 after de-assembly
Xia et al. 2018[65]	Magnetic property study	imidazolium modified norbornene polymer with varying alkyl chain length on imidazolium ring	$[FeCl_4]^-$	paramagnetic	MVH at 300K	25.5-30.9 for C_2 to C_6 alkyl chain length
Yu et al. 2018[73]	Self assembly and magnetic property study	norbornene-type block copolymers with pendant quaternary ammonium on dodecyl pendant chain	$[FeCl_4]^-$	superparamagnetic	MVH at 300 K	sigmoidal MVH response
Xia et al. 2019[66]	Self assembly and magnetic property study	polyvinylpyridinium grafted on polyhedral oligomeric silsequioxanes	$[FeCl_4]^-$	paramagnetic	MVH at 300K	16-39 depending on DP; 15.8-41.0 after self assembly depending on DP
Yu et al. 2019[71]	Structure and magnetic property study	norborene-type imidazolium	$[FeCl_4]^-$	paramagnetic with weak antiferromagnetic interactions (θ_{CW}= -5 K)	MVH at 100-380K; MVT 2-300 K at 10 kOe	linear MVH response without saturation
		norborene-type imidazolium with biphenol linker	$[FeCl_4]^-$	superparamagnetic with ferromagnetic interactions (θ_{CW}= 25 K)	MVH at 100-380K; MVT 2-300 K at 10 kOe	S-shape MVH response with hysteresis. Coercive force 24 Oe; 3.57 x 10^{-3} emu/g remanence

Ref.	Main Application or Study	Polymer System	Metal Component	Reported Magnetism	Study Type	Magnetic Susceptibility (x10^{-6} emu/g) or other magnetic property
Malecha et al. 2020[84]	Living ROMP polymerization	norborene-type block copolymers with pendant alkyl chain or imidazolium	$[FeCl_4]^-$	paramagnetism	MVH at 300 K	25.8-27.6
Yu et al. 2021[70]	Molecular magnet development and fluorescence properties	norborene-type imidazolium with pyrene linker	$[FeCl_4]^-$	ferromagnetic (θ_{CW}= ca. 75 K)	MVH at 50-380K; MVT 2-300 K at 10 kOe	ZFC-FC bifurcation at 175 K
Li et al. 2022[69]	Molecular magnet development and self assembly	quaternized poly[2-(dimethylamino)ethyl methacrylate] grafted on polynorborene based polymer bottle-brush	$[FeCl_4]^-$	paramagnetic with ferromagnetic transition at 2.6 K	MVH at 2 and 50 K; MVT 2-40 K at 100 Oe	ZFC-FC bifurcation at 2.6 K
Ji et al. 2023[68]	Molecular magnet development and self assembly	norborene-type imidazolium with terphenyl linker	$[FeCl_4]^-$	superparamagnetic to ferromagnetic transition	MVH at 2, 5, and 50 K; MVT 2-40 K at 1 kOe	ZFC-FC bifurcation at 36 K; coercivity 135 Oe and 0.005 emu/g remanence

MVH: magnetization study as a function of magnetic field strength; MVT: magnetization study as a function of temperature, usually as zero-field cooling(ZFC)/field cooling(FC) curves; θ_{CW} is the Weiss constant determined after fitting MVT data to the Curie Weiss law; μ_{eff}: the effective magnetic moment in units of Bohr magnetron, μ_B. See appendix C for more information on the Curie Weiss Law, effective magnetic moment, and ZFC-FC studies.

Though significantly less explored, coordination effects from co-materials may also influence magnetic behavior due to changes in the transition metal coordination complex, particularly in systems containing amine, amide, carbonyl, or thiol functionalities. In the work of Yang et al., the copolymers displayed either antiferromagnetic interactions or ferromagnetic behavior which was believed to be due to a combination of block copolymer structure and changes in coordination interactions of the Nd^{3+} and Ni^{2+} metal cations with the thiazolylmethacrylamide comonomer and PIL methyl methacrylate backbone[62]. While not investigated as an MPIL, Sun et al. verified the presence of carbene formation and coordination with transition metal salts in poly(vinyltriazolium)-based PILs[81]. In water treatment magnetic separations application, a poly(diallyldimethyl ammonium tetrachloroferrate) MPIL dissolved in water did not exhibit magnetic response; however, upon complexation with carboxyl-functionalized graphene oxide, the combined complex became magnetically responsive[79]. Several of the MPIL systems described above and in Table 1.1 also contain varying degrees of un-quaternized imidazole, pyridine, and amine functionalities capable of metal coordinating interactions[67, 72, 78, 80], though no investigation was done to examine coordination effects on the transition metal complexes or its binding to the polymer.

Currently, the effects of coordinating co-materials in MPIL systems and their impact on the transition metal complex structure, binding to the MPIL polymer, and the resulting magnetic properties are not well understood. *More investigation into multi-component MPIL materials containing co-materials capable of metal ion coordination is needed to inform design parameters for the development of novel MPIL systems, improve their magnetic properties, and expand MPIL applications into new fields.* It was hypothesized that metal coordinating comonomers will influence how the paramagnetic species complex is formed and interacts with the polymer. In

Chapter 2 of this dissertation, an MPIL random copolymer with a metal-coordinating acrylamide comonomer is complexed with different concentrations and types of transition metal halide salts. An in-depth spectroscopic study is performed to analyze the influence of the acrylamide comonomer on the transition metal complexes and its binding to the polymer. An initial evaluation of its magnetic properties is also provided through AC magnetic susceptibility measurements at room temperature. In Chapter 4, the magnetic properties of these MPIL copolymers are further examined as a function of both magnetic field strength and temperature through vibrating sample magnetometry (VSM). *These studies inform the relationships between magnetic properties and polymer chemistry and will help direct the future development of magnetically responsive nanomaterials, such as self-assembled MPIL block copolymers or MPIL composites with non-magnetic nanomaterials (e.g., silica particles, graphene, etc.) for applications in organic magnets, magnetic separations, stimuli-response, and more.*

1.2.2. Applied Stimuli Response in MPILs and similar MIL and Magnetic Surfactant (Mag-Surf) Systems

MPILs have found application in many applications including Lewis-Acid catalysis[26], antibacterial agents[82], metal nanoparticle synthesis templates[77, 81], fluorescence quenchers[70, 72], polymer latexes[63], liquid beads[76], thermosets[67], materials with multiple stimuli response[80], and magnetic separations for water treatment[79]. However, only one MPIL article has applied the magnetic stimuli response to an application beyond simple attraction to a magnetic field. In particular, Hazell et al. complexed poly(diallyldimethyl ammonium $[FeCl_4]^-$) and utilized the polymer as a flocculating agent to magnetically separate graphene oxide and graphene oxide complexes with antibiotic tetracycline and gold nanoparticles from water[79]. On the small molecule side, magnetic ionic liquids (MILs) and magnetic surfactants (Mag Surf) have demonstrated more

applications in applied magnetic stimuli response. In particular, MILs have been utilized for liquid-liquid extractions and subsequent magnetic separation[85, 86]. In a series of papers, Brown and Eastoe et al. utilized magnetic surfactants and magnetic fields from handheld magnets to induce changes in pendant drop surface tension[87-90] and for directed motion of proteins and DNA[91, 92]. McCoy et al. complexed ammonium- and imidazolium-based iron halide surfactants to graphene oxide sheets for magnetic separation from aqueous solution[93]. Several mag-surfs have also been used to magnetically influence self-assembly of DNA and phospholipid vesicular structures[94, 95].

MPILs similarly have the potential to be employed in more applied magnetic stimuli-responsive applications, such as magnetic manipulations or directed nanomaterial assembly, as they have similar or even better magnetic susceptibilities compared to their small molecule MIL and mag-surf counterparts. Currently, no studies to the author's knowledge have investigated the use of MPILs for magnetically directing self-assembly of nanostructures either in solution or the bulk. Magnetic fields have been used previously to direct self-assembly of diamagnetic block copolymers into aligned films through differences in diamagnetic susceptibility of each domain[96, 97]. However, these diamagnetic polymers typically require a significant difference in the diamagnetic susceptibility of each block to induce magnetic alignment, and large magnetic fields produced from superconducting magnets are typically required to induce the magnetic alignment. Utilizing paramagnetic MPILs in multicomponent self-assembled structures, could lead to magnetically driven alignments under weaker magnetic fields provided by neodymium permanent magnets. *Studying the magnetic stimuli response in MPIL nanostructures will help develop new applications for MPILs in magnetically driven delivery, magnetic manipulation, and nano assembly fields.*

In Chapter 3 of this dissertation, a surfactant is used to induce micellar self-assembly in the random MPIL copolymers developed in Chapter 2, forming magnetically responsive polyelectrolyte-surfactant complexes. The influence of the paramagnetic species on the micellar self-assembling behavior is examined as a function of surfactant concentration. Applied magnetic stimuli responsive is examined through a study of magnetic manipulation of the nanostructures in solution and using a magnetic field to direct self-assembly of the nanostructures into dried thin films. Chapter 4 also examines the influence of self-assembly on the magnetic properties of the MPIL-surfactant complexes through similar VSM studies as performed on the MPIL copolymers.

1.3. Salt-Responsive Self-Assembly of PILs and All-polyelectrolyte PIL Systems

Poly(ionic liquid)s block copolymerized with neutral polymer blocks self-assemble into a variety of hierarchical micellular structures in solution including worm-like micelles, core-shell spheres, vesicles, and cubosomes[98-101]. In addition to the same design parameters that control the morphology of all-neutral block copolymers (e.g., polymer block size, compatibility with solvent and with co-blocks, annealing conditions, concentration, additives) [102], PIL self-assembly is also highly dependent on their counterions due to their strong polyelectrolyte nature. This is largely attributed to changes in localized solubility of the PIL chain upon ion exchange from more hydrophilic anions (e.g., Cl^-, NO_3^-) to more hydrophobic anions (e.g., BF_4^-, PF_6^-, Tf_2N^-). For instance, in a series of poly(methacrylic acid) or poly(acrylamide) block copolymers with poly(alkylimidazolium propyl methacryliamido bromide) developed by Vijayakrishna et al., ion exchange of the Br^- anion with Tf_2N^- converted the double hydrophilic block copolymers to amphiphilic core-shell micellular structures and vesicles[99, 100] . In pyridinium-based random and block copolymers with polystyrene, ion exchange from Br^- to I^-, SCN^- , and PF_6^- anions lead to different micellular structures including spherical micelles, wormlike particles, networks, and

vesicles depending on ion type and concentration[103, 104]. This salt responsive behavior can also induce self-assembly behavior in PIL homo- and random copolymers through partial ion exchanges from halide to hydrophobic PF_6^- and Tf_2N^- anions, with self-assembled structure dependent on the extent of ion exchange[15, 16, 105]. These examples demonstrate the salt responsive nature of PILs and their influence on polymeric structure through a simple non-covalent ion exchange as well as the fine-tuning abilities of counterion mixtures.

As mentioned earlier, the use of multiple types of ions on the polymer backbone may also provide an additional tool in PIL design, including in block copolymers. However, the exploration of self-assembly in all-PIL block copolymer is significantly less explored compared to PILs blocked with neutral polymers. Primarily, all-PIL block copolymers have consisted of polyvinylimidazolium based polymer blocks with different pendant groups on the imidazolium ring[50-52] or spacer chain between the polymer backbone and imidazolium group[53]. In their first work, Cordella et al. developed poly(vinylalkyl imidazolium) block copolymers with ethyl and methyl groups and a mixture of Br^- and Tf_2N^- anions. While self-assembly of this block copolymer was not examined, emulsion stabilization behavior was observed in water- ethyl acetate mixtures, which was attributed more towards to the solubility effects induced by the counterions rather than the imidazolium alkyl chain length[51]. Later, Cordella et al. produced amphiphilic poly(vinylalkyl imidazolium bromide) block copolymers with ethyl and octyl alkyl chains through polymerization induced self-assembly (PISA) [50]. These block copolymers produced spherical or rice-like shaped morphologies depending on the degree of polymerization of the poly(vinyloctyl imidazolium bromide) block. Similar spherical morphologies were also produced for poly(vinylalkyl imidazolium bromide) with fluorinated or glycol groups pendant groups on the imidazolium ring[52]. Depoorter et al., proposed the limitation to producing morphologies other than spherical in these

works was due to low incompatibility of the modified imidazolium blocks[53]. In their work, Depoorter et al. instead altered the alkyl chain length between the polymer backbone and pendant imidazolium group for the two imidazolium-based blocks, which allowed for the production of rods and vesicles in addition to spheres due to reduced compatibility between the two blocks. There is still significant room for further investigation into synthesis and self-assembly behavior of other types of all-PIL block copolymers, particularly for PILs containing differ types of immobilized cations beyond only imidazolium. Further, no studies to the author's knowledge have examined the self-assembly behavior of all-PILs in the bulk phase.

Similarly, there are also only a few efforts involving the synthesis and self-assembly of PILs blocked with weak polyelectrolytes. He, Matyjaszewski, and coauthors synthesized a poly[acrylic acid-*block*-vinylbenzyl butyl imidazolium bis(trifluoromethanesulfonyl)imide] block copolymer and examined its solution assembly in water-THF mixtures as a function of solvent ratio, pH, polymer concentration, and ionic strength[98]. They produced different micellar structures including spheres, (multi)lamella, and cubosomes. As described above, Vijayakrishna et al. produced [poly(methacrylic acid)-*block*-alkylimidazolium propyl methacryliamido bromide] copolymers with core-shell and vesicular structure dependent on Br^- and Tf_2N^- ion exchange[99, 100]. However, they did not examine the influence of pH on the assembly behavior. On the cationic side, a poly[1-[2-acryloylethyl]-3-methylimidazolium bromide] PIL block copolymer with polyvinypyridine was synthesized through PISA, producing spheres, networks, and vesicles depending on solids content and degree of polymerization of the polyvinypyridine block[106]. After synthesis, they crosslinked the nanoobjects and exposed them to acidic conditions below the pKa of polyvinylpyridine, producing all-charged nanostructures.

Utilizing weak polyelectrolytes over other PILs are perhaps of even more interest as the weak polyelectrolyte blocks exhibit pH responsive behavior and can be easily converted to a strong PIL block through a post-polymerization quaternization reaction and ion exchange. In Chapter 5, an all-polyelectrolyte block copolymer consisting of an imidazolium-based PIL and a tertiary amine weak polyelectrolyte was synthesized through a living radical polymerization. A preliminary investigation into the block copolymer's solution salt responsive behavior and resulting self-assembled structure behavior is examined. The morphology of the all-polyelectrolyte PIL in a dry state is also examined with a hybrid atomic force microscopy and IR technique—a new characterization method for PILs.

1.4. PILs for Ionic Electroactive Actuators

As strong polyelectrolytes, PILs are single-ion conductive materials, with ion conductivities typically between 10^{-10} to 10^{-5} S/cm in a dry state[107-111]. Similar to ionic liquids, they also exhibit excellent thermal stability (>300 °C) and wide electrochemical windows while also exhibiting the mechanical integrity of polymers. As such, they have been largely evaluated as solid polymer electrolytes for electrochemical applications such as solid-state batteries, sensors, flexible electronics, fuel cells, and, recently, soft ionic actuators.

Ionic polymer metal composite (IPMC) actuators are polyelectrolyte-metal composites that can produce an electromechanical response to an applied voltage. Typically, they are composed of an ionic electroactive polymer (iEAP) film sandwiched between two metal electrodes (e.g., Au, Pt) and clamped at one end to a DC or AC power supply (Figure 1.3). The composite film produces a bending motion as a result of ion migration and subsequent swelling at the polymer-electrolyte interface under an applied voltage, typically < 10 V. There are two main categories of IEAPS, hydrogel and ionogel.

Hydrogel IPMCs are typically composed of an anionic polyelectrolyte, such as Nafion, and hydrated in an aqueous salt solution. Small cations (e.g., Li^+, Ca^{2+}) coordinated with water clusters migrate to the negatively charge electrode, causing swelling at that electrode and contraction at the opposite electrode (Figure 1.3a) [112] . Hydrogel IPMCs can generally operate under relatively low applied voltages (<10 V) compared to other actuator systems such as dielectric elastomers and piezoelectric polymers[76, 113, 114]. As a hydrated system, they are also able to actuate within aqueous environments[114-116]. However, hydrogels IPMCs suffer from several disadvantages. When operated in air environments, vacuum, or higher temperatures, water evaporation results in dehydration of the polyelectrolyte layer, preventing long-term operation life or operation in more extreme environments such as aeronautical and space[117, 118] . Further, at higher voltages, water electrolysis occurs, resulting in the production of hydrogen and oxygen gas bubbles within the polymer layer. This can lead to rapid drying of the polymer layer as well as adsorption of H_2(g) and O_2(g) gases at the noble metal electrodes and alteration of the electrochemical behavior of the actuator[119].

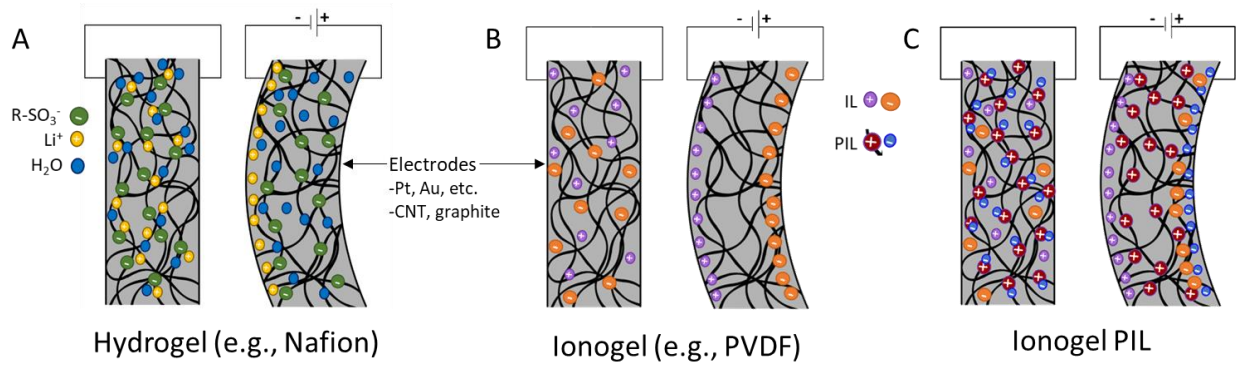

Figure 1.3 Illustration of IPMC actuators consisting of a polyelectrolyte layer between two electrode layers where the polyelectrolyte may be a (a) hydrogel, (b) ionogel, and (c) PIL-based ionogel.

In more recent years, ionogel based iEAP layers have been evaluated for actuation performance as they address some of these issues. Ionogels are ionic liquid-polymer composite materials that

exhibit high ion conductivity (~10^{-3} to 10^{-2} S/cm) and improved thermal and electrical stability properties due to the free ionic liquid within the polymer layer. The electromechanical actuation behavior in ionogel- based IPMCs is a result of both the ionic liquid free cations and anions migrating towards and swelling at oppositely charged electrodes (Figure 1.3b). In this case, the resulting bending motion is dependent on the extent of swelling at each side of the film which in turn is a function of cation and anion size and mobility. [118, 120] The most commonly studied ionogel iEAP layers are Nafion and PVDF polymers combined with imidazolium-based ionic liquids. As ILs have wide electrochemical windows (>7 V) and are practically nonvolatile at most operating temperatures and pressures, they overcome the operational limitations of hydrogel-based actuators. However, depending on the polymer and ionic liquid selection, these materials can face IL leakage and compatibility issues which limits their overall operational life[57, 121].

PILs have also been recently evaluated as polyelectrolyte layers for ionic actuator applications. They are ideal polymer matrices for ionogels-based polyelectrolytes due to their high compatibility with ionic liquids, resulting in gels with minimal IL leakage at higher weight percentages and longer periods of electrochemical operational stability[57]. However, the study of PIL-based ionic actuators is still actively emerging with a few actuator studies involving dry[122, 123], hydrogel[124], and ionogel[59, 60, 125, 126] PILs systems.

PILs themselves are inherently conductive (~10^{-7}-10^{-5} S/cm dry) without hydration or swelling with ILs, and they have shown some limited actuation ability in a dry state[122, 123]. In this case, the actuation behavior is a result of counterion migration to the opposite electrode (Figure 1.3c). Hydrogel and ionogels PIL systems with higher ionic conductivities (10^{-4}-10^{-2} S/cm) due to plasticization of the polyelectrolyte layer and higher unrestricted ion mobility, resulting in suitable actuation ability on the millimeter-scale. In the ionogel systems, the free ionic liquid ions provide

the main contribution to the polyelectrolyte layer ion conductivity, which can be enhanced when confined to microphase separated ion channels similar to the behavior of hydrated Nafion[112]. Several groups have developed triblock copolymer PILs to increase the storage modulus of the overall polyelectrolyte layer with stiffer polymer blocks while maintaining reasonable ionic conductivity with microphase separated conductive channels[59, 60, 125, 126]. However, most of these studies were mainly limited to PIL ABA triblock copolymers or penta-block copolymers with polystyrene A-blocks. *More investigation into PIL block copolymer systems is needed to expand and improve PIL performance as IEAPs and to provide preliminary data for actuator performance in more extreme environments, such as aeronautical and space applications.*

In Chapter 6, the block copolymer synthesized and characterized in Chapter 5 and is corresponding homopolymer are combined with ionic liquid to form ionogels and evaluated for their thermal, electrochemical, and actuation performance Important polymer actuator design parameters was examined, including glass transition temperature (T_g), elastic modulus, polymer-ionogel structure, and ion conductivity. Appendix F also provides preliminary data for examining several reinforcing materials to improve mechanical properties in PIL-based ionogels.

1.5. References

(1) Eyiler, E.; Walters, K. B. Magnetic iron oxide nanoparticles grafted with poly(itaconic acid)-block-poly(N-isopropylacrylamide). *Colloids and Surfaces A: Physicochemical and Engineering Aspects* **2014**, *444*, 321-325. DOI: https://doi.org/10.1016/j.colsurfa.2013.12.070.

(2) Ding, S.; Shen, Y.; Walters, K. B.; Chen, J.; Jin, Y. pH Responsive Behavior of Fe3O4@PDEA-PEGMA Core-Shell Hybrid Magnetic Nanoparticles. *International Journal of Polymeric Materials and Polymeric Biomaterials* **2014**, *63* (10), 487-492. DOI: 10.1080/00914037.2013.854219.

(3) Manouras, T.; Vamvakaki, M. Field responsive materials: photo-, electro-, magnetic- and ultrasound-sensitive polymers. *Polymer Chemistry* **2017**, *8* (1), 74-96, 10.1039/C6PY01455K. DOI: 10.1039/C6PY01455K.

(4) Banerjee, P.; Anas, M.; Jana, S.; Mandal, T. K. Recent developments in stimuli-responsive poly(ionic liquid)s. *Journal of Polymer Research* **2020**, *27* (7), 177. DOI: 10.1007/s10965-020-02091-8.

(5) Kausar, A. Research Progress in Frontiers of Poly(Ionic Liquid)s: A Review. *Polymer-Plastics Technology and Engineering* **2017**, *56* (17), 1823-1838. DOI: 10.1080/03602559.2017.1289410.

(6) Zhigang Lei, B. C., Yoon-Mo Koo, and Douglas R. MacFarlane. Introduction: Ionic Liquids. *Chemical Reviews* **2017**, *117* (10), 6633-6635. DOI: 10.1021/acs.chemrev.7b00246.

(7) Mecerreyes, D. Polymeric ionic liquids: Broadening the properties and applications of polyelectrolytes. *Prog. Polym. Sci.* **2011**, *36* (12), 1629-1648, 10.1016/j.progpolymsci.2011.05.007. DOI: 10.1016/j.progpolymsci.2011.05.007.

(8) Qian, W.; Texter, J.; Yan, F. Frontiers in poly(ionic liquid)s: synthesis and applications. *Chem. Soc. Rev.* **2017**, *46* (4), 1124-1159, 10.1039/C6CS00620E. DOI: 10.1039/C6CS00620E.

(9) Yuan, J.; Antonietti, M. Poly(ionic liquid)s: Polymers expanding classical property profiles. *Polymer* **2011**, *52* (7), 1469-1482, 10.1016/j.polymer.2011.01.043. DOI: 10.1016/j.polymer.2011.01.043.

(10) Yuan, J.; Mecerreyes, D.; Antonietti, M. Poly(ionic liquid)s: An update. *Prog. Polym. Sci.* **2013**, *38* (7), 1009-1036, 10.1016/j.progpolymsci.2013.04.002. DOI: 10.1016/j.progpolymsci.2013.04.002.

(11) Hernandez, G.; Isik, M.; Mantione, D.; Pendashteh, A.; Navalpotro, P.; Shanmukaraj, D.; Marcilla, R.; Mecerreyes, D. Redox-active poly(ionic liquid)s as active materials for energy storage applications. *J. Mater. Chem. A* **2017**, *5* (31), 16231-16240, 10.1039/C6TA10056B. DOI: 10.1039/C6TA10056B.

(12) Munoz-Bonilla, A.; Fernandez-Garcia, M. Poly(ionic liquid)s as antimicrobial materials. *Eur. Polym. J.* **2018**, *105*, 135-149, 10.1016/j.eurpolymj.2018.05.027. DOI: 10.1016/j.eurpolymj.2018.05.027.

(13) Qian, W.; Yan, F.; Texter, J. Frontiers in poly(ionic liquid)s: syntheses and applications. *Chem Soc Rev* **2017**, *46* (4), 1124-1159.

(14) Zhang, S.-Y.; Zhuang, Q.; Zhang, M.; Wang, H.; Gao, Z.; Sun, J.-K.; Yuan, J. Poly(ionic liquid) composites. *Chem. Soc. Rev.* **2020**, *49* (6), 1726-1755, 10.1039/c8cs00938d. DOI: 10.1039/c8cs00938d.

(15) Guo, J.; Zhou, Y.; Qiu, L.; Yuan, C.; Yan, F. Self-assembly of amphiphilic random co-poly(ionic liquid)s: the effect of anions, molecular weight, and molecular weight distribution. *Polym. Chem.* **2013**, *4* (14), 4004-4009, 10.1039/c3py00460k. DOI: 10.1039/c3py00460k.

(16) Isik, M.; Fernandes, A. M.; Vijayakrishna, K.; Paulis, M.; Mecerreyes, D. Preparation of poly(ionic liquid) nanoparticles and their novel application as flocculants for water purification. *Polym. Chem.* **2016**, *7* (8), 1668-1674, 10.1039/C5PY02001H. DOI: 10.1039/C5PY02001H.

(17) Wu, B.; Zhang, W.; Gao, N.; Zhou, M.; Liang, Y.; Wang, Y.; Li, F.; Li, G. Poly (ionic liquid)-Based Breath Figure Films: A New Kind of Honeycomb Porous Films with Great Extendable Capability. *Scientific Reports* **2017**, *7* (1), 13973. DOI: 10.1038/s41598-017-14563-x.

(18) Matini, T.; Francini, N.; Battocchio, A.; Spain, S. G.; Mantovani, G.; Vicent, M. J.; Sanchis, J.; Gallon, E.; Mastrotto, F.; Salmaso, S.; et al. Synthesis and characterization of variable conformation pH responsive block co-polymers for nucleic acid delivery and targeted cell entry. *Polymer Chemistry* **2014**, *5* (5), 1626-1636, 10.1039/C3PY00744H. DOI: 10.1039/C3PY00744H.

(19) Guo, J.; Qiu, L.; Deng, Z.; Yan, F. Plastic reusable pH indicator strips: preparation via anion-exchange of poly(ionic liquids) with anionic dyes. *Polym. Chem.* **2013**, *4* (5), 1309-1312, 10.1039/c2py21076b. DOI: 10.1039/c2py21076b.

(20) Seno, K.-I.; Kanaoka, S.; Aoshima, S. Synthesis and LCST-type phase separation behavior in organic solvents of poly(vinyl ethers) with pendant imidazolium or pyridinium salts. *Journal of Polymer Science Part A: Polymer Chemistry* **2008**, *46* (17), 5724-5733, https://doi.org/10.1002/pola.22881. DOI: https://doi.org/10.1002/pola.22881 (acccessed 2023/06/05).

(21) Karjalainen, E.; Aseyev, V.; Tenhu, H. Counterion-Induced UCST for Polycations. *Macromolecules (Washington, DC, U. S.)* **2014**, *47* (21), 7581-7587, 10.1021/ma501924r. DOI: 10.1021/ma501924r.

(22) Karjalainen, E.; Suvarli, N.; Tenhu, H. Thermoresponsive behavior of poly[trialkyl-(4-vinylbenzyl)ammonium] based polyelectrolytes in aqueous salt solutions. *Polymer Chemistry* **2020**, *11* (36), 5870-5883, 10.1039/D0PY00917B. DOI: 10.1039/D0PY00917B.

(23) Yuan, C.; Guo, J.; Tan, M.; Guo, M.; Qiu, L.; Yan, F. Multistimuli Responsive and Electroactive Supramolecular Gels Based on Ionic Liquid Gemini Guest. *ACS Macro Letters* **2014**, *3* (3), 271-275. DOI: 10.1021/mz500113n.

(24) Bara, J. E.; Lessmann, S.; Gabriel, C. J.; Hatakeyama, E. S.; Noble, R. D.; Gin, D. L. Synthesis and Performance of Polymerizable Room-Temperature Ionic Liquids as Gas Separation Membranes. *Industrial & Engineering Chemistry Research* **2007**, *46* (16), 5397-5404. DOI: 10.1021/ie0704492.

(25) Zhang, J.; Xu, D.; Guo, J.; Sun, Z.; Qian, W.; Zhang, Y.; Yan, F. CO2 Responsive Imidazolium-Type Poly(Ionic Liquid) Gels. *Macromolecular Rapid Communications* **2016**, *37* (14), 1194-1199, https://doi.org/10.1002/marc.201600069. DOI: https://doi.org/10.1002/marc.201600069 (acccessed 2023/06/05).

(26) Dobbelin, M.; Jovanovski, V.; Llarena, I.; Marfil, L. J. C.; Cabanero, G.; Rodriguez, J.; Mecerreyes, D. Synthesis of paramagnetic polymers using ionic liquid chemistry. *Polym. Chem.* **2011**, *2* (6), 1275-1278, 10.1039/c1py00044f. DOI: 10.1039/c1py00044f.

(27) Ricks-Laskoski, H. L.; Snow, A. W. Synthesis and Electric Field Actuation of an Ionic Liquid Polymer. *Journal of the American Chemical Society* **2006**, *128* (38), 12402-12403. DOI: 10.1021/ja064264i.

(28) Zhao, Z.; Zhang, G.; Yin, Y.; Dong, C.; Liu, Y. D. The electric field responses of inorganic ionogels and poly(ionic liquid)s. *Molecules* **2020**, *25* (19), 4547, 10.3390/molecules25194547. DOI: 10.3390/molecules25194547.

(29) Cui, J.; Nie, F.-M.; Yang, J.-X.; Pan, L.; Ma, Z.; Li, Y.-S. Novel imidazolium-based poly(ionic liquid)s with different counterions for self-healing. *J. Mater. Chem. A* **2017**, *5* (48), 25220-25229, 10.1039/C7TA06793C. DOI: 10.1039/C7TA06793C.

(30) Pipertzis, A.; Mühlinghaus, M.; Mezger, M.; Scherf, U.; Floudas, G. Polymerized Ionic Liquids with Polythiophene Backbones: Self-Assembly, Thermal Properties, and Ion Conduction. *Macromolecules* **2018**, *51* (16), 6440-6450. DOI: 10.1021/acs.macromol.8b01201.

(31) O'Harra, K. E.; Noll, D. M.; Kammakakam, I.; DeVriese, E. M.; Solis, G.; Jackson, E. M.; Bara, J. E. Designing Imidazolium Poly(amide-amide) and Poly(amide-imide) Ionenes and Their Interactions with Mono- and Tris(imidazolium) Ionic Liquids. In *Polymers*, 2020; Vol. 12.

(32) Meek, K. M.; Elabd, Y. A. Polymerized ionic liquid block copolymers for electrochemical energy. *Journal of Materials Chemistry A* **2015**, *3* (48), 24187-24194, 10.1039/C5TA07170D. DOI: 10.1039/C5TA07170D.

(33) Wang, Z.; Lai, H.; Wu, P. Influence of PIL segment on solution properties of poly(N-isopropylacrylamide)-*b*-poly(ionic liquid) copolymer: micelles, thermal phase behavior and microdynamics. *Soft Matter* **2012**, *8* (46), 11644-11653, 10.1039/C2SM26172C. DOI: 10.1039/C2SM26172C.

(34) Biswas, Y.; Mandal, T. K. Structural Variation in Homopolymers Bearing Zwitterionic and Ionic Liquid Pendants for Achieving Tunable Multi-Stimuli Responsiveness and Hierarchical Nanoaggregates. *Macromolecules* **2017**, *50* (24), 9807-9820. DOI: 10.1021/acs.macromol.7b02106.

(35) Zhang, J.; Chen, Z.; Zhang, Y.; Dong, S.; Chen, Y.; Zhang, S. Poly(ionic liquid)s Containing Alkoxy Chains and Bis(trifluoromethanesulfonyl)imide Anions as Highly Adhesive Materials. *Advanced Materials* **2021**, *33* (30), 2100962, https://doi.org/10.1002/adma.202100962. DOI: https://doi.org/10.1002/adma.202100962 (acccessed 2023/06/05).

(36) Marcilla, R.; Blazquez, J. A.; Rodriguez, J.; Pomposo, J. A.; Mecerreyes, D. Tuning the solubility of polymerized ionic liquids by simple anion-exchange reactions. *J. Polym. Sci., Part A: Polym. Chem.* **2003**, *42* (1), 208-212, 10.1002/pola.11015. DOI: 10.1002/pola.11015.

(37) Cremer, T.; Kolbeck, C.; Lovelock, K. R. J.; Paape, N.; Woelfel, R.; Schulz, P. S.; Wasserscheid, P.; Weber, H.; Thar, J.; Kirchner, B.; et al. Towards a Molecular Understanding of Cation-Anion Interactions-Probing the Electronic Structure of Imidazolium Ionic Liquids by NMR Spectroscopy, X-ray Photoelectron Spectroscopy and Theoretical Calculations. *Chem. - Eur. J.* **2010**, *16* (30), 9018-9033, S9018/9011-S9018/9017, 10.1002/chem.201001032. DOI: 10.1002/chem.201001032.

(38) Fernandes, A. M.; Rocha, M. A. A.; Freire, M. G.; Marrucho, I. M.; Coutinho, J. A. P.; Santos, L. M. N. B. F. Evaluation of cation-anion interaction strength in ionic liquids. *J. Phys. Chem. B* **2011**, *115* (14), 4033-4041, 10.1021/jp201084x. DOI: 10.1021/jp201084x.

(39) Fumino, K.; Wittler, K.; Ludwig, R. The Anion Dependence of the Interaction Strength between Ions in Imidazolium-Based Ionic Liquids Probed by Far-Infrared Spectroscopy. *J. Phys. Chem. B* **2012**, *116* (31), 9507-9511, 10.1021/jp306173t. DOI: 10.1021/jp306173t.

(40) Matsuno, R.; Kokubo, Y.; Kumagai, S.; Takamatsu, S.; Hashimoto, K.; Takahara, A. Molecular Design and Characterization of Ionic Monomers with Varying Ion Pair Interaction Energies. *Macromolecules (Washington, DC, U. S.)* **2020**, *53* (5), 1629-1637, 10.1021/acs.macromol.9b02731. DOI: 10.1021/acs.macromol.9b02731.

(41) Naert, P.; Rabaey, K.; Stevens, C. V. Ionic liquid ion exchange: exclusion from strong interactions condemns cations to the most weakly interacting anions and dictates reaction equilibrium. *Green Chem.* **2018**, *20* (18), 4277-4286, 10.1039/C8GC01869C. DOI: 10.1039/C8GC01869C.

(42) Liu, G. Tuning the Properties of Charged Polymers at the Solid/Liquid Interface with Ions. *Langmuir* **2019**, *35* (9), 3232-3247, 10.1021/acs.langmuir.8b01158. DOI: 10.1021/acs.langmuir.8b01158.

(43) Zhang, Y.; Cremer, P. S. Interactions between macromolecules and ions: the Hofmeister series. *Curr. Opin. Chem. Biol.* **2006**, *10* (6), 658-663, 10.1016/j.cbpa.2006.09.020. DOI: 10.1016/j.cbpa.2006.09.020.

(44) Niedermeyer, H.; Hallett, J. P.; Villar-Garcia, I. J.; Hunt, P. A.; Welton, T. Mixtures of ionic liquids. *Chemical Society Reviews* **2012**, *41* (23), 7780-7802, 10.1039/C2CS35177C. DOI: 10.1039/C2CS35177C.

(45) Chang, J.-C.; Ho, W.-Y.; Sun, I. W.; Tung, Y.-L.; Tsui, M.-C.; Wu, T.-Y.; Liang, S.-S. Synthesis and characterization of dicationic ionic liquids that contain both hydrophilic and hydrophobic anions. *Tetrahedron* **2010**, *66* (32), 6150-6155. DOI: https://doi.org/10.1016/j.tet.2010.05.105.

(46) Nacham, O.; Clark, K. D.; Yu, H.; Anderson, J. L. Synthetic Strategies for Tailoring the Physicochemical and Magnetic Properties of Hydrophobic Magnetic Ionic Liquids. *Chemistry of Materials* **2015**, *27* (3), 923-931. DOI: 10.1021/cm504202v.

(47) Masri, A. N.; Mi, A. M.; Leveque, J.-M. A review on dicationic ionic liquids: Classification and application. *Ind. Eng. Manag* **2016**, *5*, 197-204.

(48) Tome, L. C.; Aboudzadeh, M. A.; Rebelo, L. P. N.; Freire, C. S. R.; Mecerreyes, D.; Marrucho, I. M. Polymeric ionic liquids with mixtures of counter-anions: a new straightforward strategy for designing pyrrolidinium-based CO2 separation membranes. *J. Mater. Chem. A* **2013**, *1* (35), 10403-10411, 10.1039/c3ta12174g. DOI: 10.1039/c3ta12174g.

(49) Ren, Y.; Guo, J.; Liu, Z.; Sun, Z.; Wu, Y.; Liu, L.; Yan, F. Ionic liquid-based click-ionogels. *Sci Adv* **2019**, *5* (8), eaax0648.

(50) Cordella, D.; Debuigne, A.; Jerome, C.; Kochovski, Z.; Taton, D.; Detrembleur, C. One-Pot Synthesis of Double Poly(Ionic Liquid) Block Copolymers by Cobalt-Mediated Radical Polymerization-Induced Self-Assembly (CMR-PISA) in Water. *Macromol. Rapid Commun.* **2016**, *37* (14), 1181-1187, 10.1002/marc.201600039. DOI: 10.1002/marc.201600039.

(51) Cordella, D.; Kermagoret, A.; Debuigne, A.; Jerome, C.; Mecerreyes, D.; Isik, M.; Taton, D.; Detrembleur, C. All Poly(ionic liquid)-Based Block Copolymers by Sequential Controlled Radical Copolymerization of Vinylimidazolium Monomers. *Macromolecules (Washington, DC, U. S.)* **2015**, *48* (15), 5230-5243, 10.1021/acs.macromol.5b01013. DOI: 10.1021/acs.macromol.5b01013.

(52) Cordella, D.; Ouhib, F.; Aqil, A.; Defize, T.; Jerome, C.; Serghei, A.; Drockenmuller, E.; Aissou, K.; Taton, D.; Detrembleur, C. Fluorinated Poly(ionic liquid) Diblock Copolymers Obtained by Cobalt-Mediated Radical Polymerization-Induced Self-Assembly. *ACS Macro Lett.* **2017**, *6* (2), 121-126, 10.1021/acsmacrolett.6b00899. DOI: 10.1021/acsmacrolett.6b00899.

(53) Depoorter, J.; Yan, X.; Zhang, B.; Sudre, G.; Charlot, A.; Fleury, E.; Bernard, J. All poly(ionic liquid) block copolymer nanoparticles from antagonistic isomeric macromolecular blocks via aqueous RAFT polymerization-induced self-assembly. *Polymer Chemistry* **2021**, *12* (1), 82-91, 10.1039/D0PY00698J. DOI: 10.1039/D0PY00698J.

(54) Yu, X.; Mu, C.; Dai, D.; Yuan, X.; Zhang, K.; Ren, L. Well-Defined Magnetic Responsive Polymers Containing Ammonium FeCl4 from ROMP. *Macromolecular Chemistry and Physics* **2016**, *217* (24), 2700-2707. DOI: https://doi.org/10.1002/macp.201600435.

(55) Hazell, G.; Hinojosa-Navarro, M.; McCoy, T. M.; Tabor, R. F.; Eastoe, J. Responsive materials based on magnetic polyelectrolytes and graphene oxide for water clean-up. *Journal of Colloid and Interface Science* **2016**, *464*, 285-290. DOI: https://doi.org/10.1016/j.jcis.2015.11.029.

(56) Sahiner, N.; Demir, S.; Yildiz, S. Magnetic colloidal polymeric ionic liquid synthesis and use in hydrogen production. *Colloids and Surfaces A: Physicochemical and Engineering Aspects* **2014**, *449*, 87-95. DOI: https://doi.org/10.1016/j.colsurfa.2014.02.046.

(57) Eshetu, G. G.; Mecerreyes, D.; Forsyth, M.; Zhang, H.; Armand, M. Polymeric ionic liquids for lithium-based rechargeable batteries. *Mol. Syst. Des. Eng.* **2019**, *4* (2), 294-309, 10.1039/c8me00103k. DOI: 10.1039/c8me00103k.

(58) Wang, Z.; Si, Y.; Zhao, C.; Yu, D.; Wang, W.; Sun, G. Flexible and Washable Poly(Ionic Liquid) Nanofibrous Membrane with Moisture Proof Pressure Sensing for Real-Life Wearable Electronics. *ACS Applied Materials & Interfaces* **2019**, *11* (30), 27200-27209. DOI: 10.1021/acsami.9b07786.

(59) Green, M. D.; Wang, D.; Hemp, S. T.; Choi, J.-H.; Winey, K. I.; Heflin, J. R.; Long, T. E. Synthesis of imidazolium ABA triblock copolymers for electromechanical transducers. *Polymer* **2012**, *53* (17), 3677-3686. DOI: https://doi.org/10.1016/j.polymer.2012.06.023.

(60) Jangu, C.; Wang, J.-H. H.; Wang, D.; Sharick, S.; Heflin, J. R.; Winey, K. I.; Colby, R. H.; Long, T. E. Well-Defined Imidazolium ABA Triblock Copolymers as Ionic-Liquid-Containing

Electroactive Membranes. *Macromolecular Chemistry and Physics* **2014**, *215* (13), 1319-1331, https://doi.org/10.1002/macp.201400121. DOI: https://doi.org/10.1002/macp.201400121 (acccessed 2022/08/10).

(61) Hayashi, S.; Saha, S.; Hamaguchi, H. A new class of magnetic fluids: bmim[FeCl/sub 4/] and nbmim[FeCl/sub 4/] ionic liquids. *IEEE Transactions on Magnetics* **2006**, *42* (1), 12-14. DOI: 10.1109/TMAG.2005.854875.

(62) Yang, J.; Sun, W.; Lin, W.; Shen, Z. Synthesis and magnetic properties of comb-like copolymeric complexes based on thiazole ring and ionic liquid. *Journal of Polymer Science Part A: Polymer Chemistry* **2008**, *46* (15), 5123-5132. DOI: https://doi.org/10.1002/pola.22840.

(63) Bonnefond, A.; Ibarra, M.; Mecerreyes, D.; Leiza, J. R. Adding magnetic ionic liquid monomers to the emulsion polymerization tool-box: Towards polymer latexes and coatings with new properties. *J. Polym. Sci., Part A: Polym. Chem.* **2016**, *54* (8), 1145-1152, 10.1002/pola.27953. DOI: 10.1002/pola.27953.

(64) Ohara, Y.; Kawata, Y.; Hyde, A.; Phan, C.; Takeda, R.; Takemura, Y.; Yusa, S.-i. Preparation of a Magnetic-responsive Polycation with a Tetrachloroferrate Anion. *Chemistry Letters* **2017**, *46* (10), 1473-1475. DOI: 10.1246/cl.170621 (acccessed 2021/11/07).

(65) Xia, Z.; Yu, X.; Dai, D.; Yuan, X.; Ren, L. Magnetic monomers and polymers based on alkyl-imidazolium FeCl4: The effect of alkyl chain length. *Polymer* **2018**, *157*, 32-37. DOI: https://doi.org/10.1016/j.polymer.2018.10.015.

(66) Xia, Z.; Yu, X.; Zhang, T.; Yuan, X.; Ren, L. Inorganic/organic hybrid magnetic polymers based on POSS and pyridinium FeCl4: the effect of self-assembly. *Polymer Chemistry* **2019**, *10* (33), 4604-4610, 10.1039/C9PY00807A. DOI: 10.1039/C9PY00807A.

(67) Carrasco, P. M.; Tzounis, L.; Mompean, F. J.; Strati, K.; Georgopanos, P.; Garcia-Hernandez, M.; Stamm, M.; Cabanero, G.; Odriozola, I.; Avgeropoulos, A.; et al. Thermoset Magnetic Materials Based on Poly(ionic liquid)s Block Copolymers. *Macromolecules (Washington, DC, U. S.)* **2013**, *46* (5), 1860-1867, 10.1021/ma302261c. DOI: 10.1021/ma302261c.

(68) Ji, S.; Yuan, X.; Guo, Q.; Ren, L. Self-assembly induced ferromagnetic interaction in magnetic polymers with terphenyl linkers. *Polymer Chemistry* **2023**, *14* (18), 2238-2245, 10.1039/D3PY00186E. DOI: 10.1039/D3PY00186E.

(69) Li, J.; Ji, S.; Yu, X.; Yuan, X.; Zhang, K.; Ren, L. Magnetic Poly(ionic liquid)s: Bottlebrush versus Linear Structures. *Macromolecules* **2022**, *55* (6), 2067-2074. DOI: 10.1021/acs.macromol.1c02457.

(70) Yu, X.; Xia, Z.; Zhao, T.; Yuan, X.; Ren, L. Pyrene-Enhanced Ferromagnetic Interaction in a FeCl4−-Based Poly(ionic liquid)s Organic Magnet. *Macromolecules* **2021**, *54* (9), 4227-4235. DOI: 10.1021/acs.macromol.1c00213.

(71) Yu, X.; Yuan, X.; Zhao, Y.; Ren, L. From Paramagnetic to Superparamagnetic Ionic Liquid/Poly(ionic liquid): The Effect of π–π Stacking Interaction. *ACS Macro Letters* **2019**, *8* (11), 1504-1510. DOI: 10.1021/acsmacrolett.9b00714.

(72) Cui, J.; Yang, S.; Zhang, J.; Zhao, S.; Yan, Y. A novel poly[(N-vinylimidazole)-co-(1-pyrenylmethyl methacrylate)] ferric complex with fluorescence and superparamagnetism. *RSC Adv.* **2012**, *2* (32), 12224-12230, 10.1039/c2ra22395c. DOI: 10.1039/c2ra22395c.

(73) Yu, X.; Yuan, X.; Xia, Z.; Ren, L. Self-assembly of magnetic poly(ionic liquid)s and ionic liquids in aqueous solution. *Polym. Chem.* **2018**, *9* (41), 5116-5122, 10.1039/c8py01254g. DOI: 10.1039/c8py01254g.

(74) Carrasco, P. M.; Tzounis, L.; Mompean, F. J.; Strati, K.; Georgopanos, P.; Garcia-Hernandez, M.; Stamm, M.; Cabañero, G.; Odriozola, I.; Avgeropoulos, A.; et al. Thermoset Magnetic Materials Based on Poly(ionic liquid)s Block Copolymers. *Macromolecules* **2013**, *46* (5), 1860-1867. DOI: 10.1021/ma302261c.

(75) Cui, J.; Yang, S.; Zhang, J.; Zhao, S.; Yan, Y. A novel poly[(N-vinylimidazole)-co-(1-pyrenylmethyl methacrylate)] ferric complex with fluorescence and superparamagnetism. *RSC Advances* **2012**, *2* (32), 12224-12230, 10.1039/C2RA22395C. DOI: 10.1039/C2RA22395C.

(76) Rahman, M. H.; Werth, H.; Goldman, A.; Hida, Y.; Diesner, C.; Lane, L.; Menezes, P. L. Recent Progress on Electroactive Polymers: Synthesis, Properties and Applications. *Ceramics* **2021**, *4* (3), 516-541. DOI: 10.3390/ceramics4030038.

(77) Sahiner, N.; Demir, S.; Yildiz, S. Magnetic colloidal polymeric ionic liquid synthesis and use in hydrogen production. *Colloids Surf., A* **2014**, *449*, 87-95, 10.1016/j.colsurfa.2014.02.046. DOI: 10.1016/j.colsurfa.2014.02.046.

(78) Yu, X.; Yuan, X.; Zhao, Y.; Ren, L. Synthesis of paramagnetic polymers based on polyethyleneimine (PEI). *RSC Advances* **2015**, *5* (112), 92207-92211, 10.1039/C5RA18175E. DOI: 10.1039/C5RA18175E.

(79) Hazell, G.; Hinojosa-Navarro, M.; McCoy, T. M.; Tabor, R. F.; Eastoe, J. Responsive materials based on magnetic polyelectrolytes and graphene oxide for water clean-up. *J. Colloid Interface Sci.* **2016**, *464*, 285-290, 10.1016/j.jcis.2015.11.029. DOI: 10.1016/j.jcis.2015.11.029.

(80) Chikh Alard, I.; Soubhye, J.; Berger, G.; Gelbcke, M.; Spassov, S.; Amighi, K.; Goole, J.; Meyer, F. Triple-stimuli responsive polymers with fine tuneable magnetic responses. *Polym. Chem.* **2017**, *8* (16), 2450-2456, 10.1039/C7PY00218A. DOI: 10.1039/C7PY00218A.

(81) Sun, J.-K.; Kochovski, Z.; Zhang, W.-Y.; Kirmse, H.; Lu, Y.; Antonietti, M.; Yuan, J. General Synthetic Route toward Highly Dispersed Metal Clusters Enabled by Poly(ionic liquid)s. *Journal of the American Chemical Society* **2017**, *139* (26), 8971-8976. DOI: 10.1021/jacs.7b03357.

(82) de la Fuente-Nunez, C.; Brown, P.; Torres, M. D. T.; Cao, J.; Lu, T. K. Magnetic Surfactant Ionic Liquids and Polymers With Tetrahaloferrate (III) Anions as Antimicrobial Agents With Low

Cytotoxicity. *Colloid and Interface Science Communications* **2018**, *22*, 11-13. DOI: https://doi.org/10.1016/j.colcom.2017.11.002.

(83) Zhang, T.; Yu, X.; Yuan, X.; Zhao, Y.; Ren, L. Tadpole-shaped magnetic block copolymer: Self-assembly induced increase of magnetic susceptibility. *Polymer* **2018**, *135*, 9-15. DOI: https://doi.org/10.1016/j.polymer.2017.12.009.

(84) Malecha, J. J.; Biller, J. R.; Lama, B.; Gin, D. L. System for Living ROMP of a Paramagnetic FeCl4–-Based Ionic Liquid Monomer: Direct Synthesis of Magnetically Responsive Block Copolymers. *ACS Macro Letters* **2020**, *9* (1), 140-145. DOI: 10.1021/acsmacrolett.9b00902.

(85) Clark, K. D.; Nacham, O.; Purslow, J. A.; Pierson, S. A.; Anderson, J. L. Magnetic ionic liquids in analytical chemistry: A review. *Anal. Chim. Acta* **2016**, *934*, 9-21, 10.1016/j.aca.2016.06.011. DOI: 10.1016/j.aca.2016.06.011.

(86) Joseph, A.; Zyla, G.; Thomas, V. I.; Nair, P. R.; Padmanabhan, A. S.; Mathew, S. Paramagnetic ionic liquids for advanced applications: A review. *J. Mol. Liq.* **2016**, *218*, 319-331, 10.1016/j.molliq.2016.02.086. DOI: 10.1016/j.molliq.2016.02.086.

(87) Abbott, B. S., Karimi, L. & Walters, K.B. Synthesis and Stability of Ligand-Modified Iron Oxide Nanoparticles *[In Preparation]* **2022**.

(88) Brown, P.; Bushmelev, A.; Butts, C. P.; Eloi, J.-C.; Grillo, I.; Baker, P. J.; Schmidt, A. M.; Eastoe, J. Properties of New Magnetic Surfactants. *Langmuir* **2013**, *29* (10), 3246-3251. DOI: 10.1021/la400113r.

(89) Brown, P.; Butts, C. P.; Cheng, J.; Eastoe, J.; Russell, C. A.; Smith, G. N. Magnetic emulsions with responsive surfactants. *Soft Matter* **2012**, *8* (29), 7545-7546, 10.1039/C2SM26077H. DOI: 10.1039/C2SM26077H.

(90) Brown, P.; Bushmelev, A.; Butts, C. P.; Cheng, J.; Eastoe, J.; Grillo, I.; Heenan, R. K.; Schmidt, A. M. Magnetic Control over Liquid Surface Properties with Responsive Surfactants. *Angewandte Chemie International Edition* **2012**, *51* (10), 2414-2416, https://doi.org/10.1002/anie.201108010. DOI: https://doi.org/10.1002/anie.201108010 (acccessed 2023/06/05).

(91) Brown, P.; Bromberg, L.; Rial-Hermida, M. I.; Wasbrough, M.; Hatton, T. A.; Alvarez-Lorenzo, C. Magnetic Surfactants and Polymers with Gadolinium Counterions for Protein Separations. *Langmuir* **2016**, *32* (3), 699-705. DOI: 10.1021/acs.langmuir.5b04146.

(92) Brown, P.; Khan, A. M.; Armstrong, J. P. K.; Perriman, A. W.; Butts, C. P.; Eastoe, J. Magnetizing DNA and Proteins Using Responsive Surfactants. *Advanced Materials* **2012**, *24* (46), 6244-6247, https://doi.org/10.1002/adma.201202685. DOI: https://doi.org/10.1002/adma.201202685 (acccessed 2023/06/05).

(93) McCoy, T. M.; Brown, P.; Eastoe, J.; Tabor, R. F. Noncovalent Magnetic Control and Reversible Recovery of Graphene Oxide Using Iron Oxide and Magnetic Surfactants. *ACS Appl. Mater. Interfaces* **2015**, *7* (3), 2124-2133, 10.1021/am508565d. DOI: 10.1021/am508565d.

(94) Beck, P.; Liebi, M.; Kohlbrecher, J.; Ishikawa, T.; Ruegger, H.; Zepik, H.; Fischer, P.; Walde, P.; Windhab, E. Magnetic Field Alignable Domains in Phospholipid Vesicle Membranes Containing Lanthanides. *J. Phys. Chem. B* **2010**, *114* (1), 174-186, 10.1021/jp907442e. DOI: 10.1021/jp907442e.

(95) Xu, L.; Feng, L.; Hao, J.; Dong, S. Controlling the Capture and Release of DNA with a Dual-Responsive Cationic Surfactant. *ACS Appl. Mater. Interfaces* **2015**, *7* (16), 8876-8885, 10.1021/acsami.5b01514. DOI: 10.1021/acsami.5b01514.

(96) Hu, H.; Gopinadhan, M.; Osuji, C. O. Directed self-assembly of block copolymers: a tutorial review of strategies for enabling nanotechnology with soft matter. *Soft Matter* **2014**, *10* (22), 3867-3889, 10.1039/c3sm52607k. DOI: 10.1039/c3sm52607k.

(97) Majewski, P. W.; Gopinadhan, M.; Osuji, C. O. Magnetic field alignment of block copolymers and polymer nanocomposites: Scalable microstructure control in functional soft materials. *J. Polym. Sci., Part B: Polym. Phys.* **2012**, *50* (1), 2-8, 10.1002/polb.22382. DOI: 10.1002/polb.22382.

(98) He, H.; Rahimi, K.; Zhong, M.; Mourran, A.; Luebke, D. R.; Nulwala, H. B.; Moller, M.; Matyjaszewski, K. Cubosomes from hierarchical self-assembly of poly(ionic liquid) block copolymers. *Nat. Commun.* **2017**, *8*, 14057pp., 10.1038/ncomms14057. DOI: 10.1038/ncomms14057.

(99) Vijayakrishna, K.; Jewrajka, S. K.; Ruiz, A.; Marcilla, R.; Pomposo, J. A.; Mecerreyes, D.; Taton, D.; Gnanou, Y. Synthesis by RAFT and Ionic Responsiveness of Double Hydrophilic Block Copolymers Based on Ionic Liquid Monomer Units. *Macromolecules (Washington, DC, U. S.)* **2008**, *41* (17), 6299-6308, 10.1021/ma800677h. DOI: 10.1021/ma800677h.

(100) Vijayakrishna, K.; Mecerreyes, D.; Gnanou, Y.; Taton, D. Polymeric vesicles and micelles obtained by self-assembly of ionic liquid-based block copolymers triggered by anion or solvent exchange. *Macromolecules (Washington, DC, U. S.)* **2009**, *42* (14), 5167-5174, 10.1021/ma900549k. DOI: 10.1021/ma900549k.

(101) Yang, Y.; Zheng, J.; Man, S.; Sun, X.; An, Z. Synthesis of poly(ionic liquid)-based nano-objects with morphological transitions via RAFT polymerization-induced self-assembly in ethanol. *Polym. Chem.* **2018**, *9* (7), 824-827, 10.1039/C8PY00040A. DOI: 10.1039/C8PY00040A.

(102) Mai, Y.; Eisenberg, A. Self-assembly of block copolymers. *Chemical Society Reviews* **2012**, *41* (18), 5969-5985, 10.1039/C2CS35115C. DOI: 10.1039/C2CS35115C.

(103) Luo, H.; Tang, Q.; Zhong, J.; Lei, Z.; Zhou, J.; Tong, Z. Interplay of Solvation and Size Effects Induced by the Counterions in Ionic Block Copolymers on the Basis of Hofmeister Series. *Macromol. Chem. Phys.* **2019**, *220* (4), n/a, 10.1002/macp.201800508. DOI: 10.1002/macp.201800508.

(104) Zhong, J.; Luo, H.; Tang, Q.; Lei, Z.; Tong, Z. Counterion-Mediated Self-Assembly of Ion-Containing Block Copolymers on the Basis of the Hofmeister Series. *Macromol. Chem. Phys.* **2019**, *220* (5), n/a, 10.1002/macp.201800554. DOI: 10.1002/macp.201800554.

(105) Chavan, S. N.; Lee, H.-i. Random ionic polymers: Salt-triggered reversible vesicular self-assembly in water. *European Polymer Journal* **2023**, *193*, 112114. DOI: https://doi.org/10.1016/j.eurpolymj.2023.112114.

(106) Zhang, B.; Yan, X.; Alcouffe, P.; Charlot, A.; Fleury, E.; Bernard, J. Aqueous RAFT Polymerization of Imidazolium-Type Ionic Liquid Monomers: En Route to Poly(ionic liquid)-Based Nanoparticles through RAFT Polymerization-Induced Self-Assembly. *ACS Macro Letters* **2015**, *4* (9), 1008-1011. DOI: 10.1021/acsmacrolett.5b00534.

(107) Weber, R. L.; Ye, Y.; Schmitt, A. L.; Banik, S. M.; Elabd, Y. A.; Mahanthappa, M. K. Effect of Nanoscale Morphology on the Conductivity of Polymerized Ionic Liquid Block Copolymers. *Macromolecules* **2011**, *44* (14), 5727-5735. DOI: 10.1021/ma201067h.

(108) Li, S.; Zhang, Z.; Yang, K.; Yang, L. Polymeric Ionic Liquid-poly(ethylene glycol) Composite Polymer Electrolytes for High-Temperature Lithium-Ion Batteries. *ChemElectroChem* **2018**, *5* (2), 328-334, https://doi.org/10.1002/celc.201700984. DOI: https://doi.org/10.1002/celc.201700984 (acccessed 2023/06/13).

(109) Fan, F.; Wang, W.; Holt, A. P.; Feng, H.; Uhrig, D.; Lu, X.; Hong, T.; Wang, Y.; Kang, N.-G.; Mays, J.; et al. Effect of Molecular Weight on the Ion Transport Mechanism in Polymerized Ionic Liquids. *Macromolecules* **2016**, *49* (12), 4557-4570. DOI: 10.1021/acs.macromol.6b00714.

(110) Choi, U. H.; Lee, M.; Wang, S.; Liu, W.; Winey, K. I.; Gibson, H. W.; Colby, R. H. Ionic Conduction and Dielectric Response of Poly(imidazolium acrylate) Ionomers. *Macromolecules* **2012**, *45* (9), 3974-3985. DOI: 10.1021/ma202784e.

(111) Biswas, Y.; Banerjee, P.; Mandal, T. K. From Polymerizable Ionic Liquids to Poly(ionic liquid)s: Structure-Dependent Thermal, Crystalline, Conductivity, and Solution Thermoresponsive Behaviors. *Macromolecules* **2019**, *52* (3), 945-958. DOI: 10.1021/acs.macromol.8b02351.

(112) White, B. T.; Long, T. E. Advances in Polymeric Materials for Electromechanical Devices. *Macromolecular Rapid Communications* **2019**, *40* (1), 1800521, https://doi.org/10.1002/marc.201800521. DOI: https://doi.org/10.1002/marc.201800521 (acccessed 2022/08/10).

(113) Akle, B. J.; Bennett, M. D.; Leo, D. J. High-strain ionomeric–ionic liquid electroactive actuators. *Sensors and Actuators A: Physical* **2006**, *126* (1), 173-181. DOI: https://doi.org/10.1016/j.sna.2005.09.006.

(114) Martins, P.; Correia, D. M.; Correia, V.; Lanceros-Mendez, S. Polymer-based actuators: back to the future. *Physical Chemistry Chemical Physics* **2020**, *22* (27), 15163-15182, 10.1039/D0CP02436H. DOI: 10.1039/D0CP02436H.

(115) Pugal, D.; Kim, K. J.; Aabloo, A. An explicit physics-based model of ionic polymer-metal composite actuators. *Journal of Applied Physics* **2011**, *110* (8), 084904. DOI: 10.1063/1.3650903 (acccessed 2022/08/10).

(116) Shen, Q.; Palmre, V.; Stalbaum, T.; Kim, K. J. A comprehensive physics-based model encompassing variable surface resistance and underlying physics of ionic polymer-metal composite actuators. *Journal of Applied Physics* **2015**, *118* (12), 124904. DOI: 10.1063/1.4931912 (acccessed 2022/08/10).

(117) Bashir, M.; Rajendran, P. A review on electroactive polymers development for aerospace applications. *Journal of Intelligent Material Systems and Structures* **2018**, *29* (19), 3681-3695. DOI: 10.1177/1045389X18798951 (acccessed 2022/10/12).

(118) Dong, Y.; Yeung, K.-W.; Tang, C.-Y.; Law, W.-C.; Tsui, G. C.-P.; Xie, X. Development of ionic liquid-based electroactive polymer composites using nanotechnology. *Nanotechnology Reviews* **2021**, *10* (1), 99-116. DOI: doi:10.1515/ntrev-2021-0009.

(119) Edgar, H.; Zane, Z.; Andres, P.; Urmas, J.; Alvo, A. Some electrochemical aspects of aqueous ionic polymer-composite actuators. In *Proc.SPIE*, 2016; Vol. 9798, p 979815. DOI: 10.1117/12.2219031.

(120) Correia, D. M.; Fernandes, L. C.; Martins, P. M.; García-Astrain, C.; Costa, C. M.; Reguera, J.; Lanceros-Méndez, S. Ionic Liquid–Polymer Composites: A New Platform for Multifunctional Applications. *Advanced Functional Materials* **2020**, *30* (24), 1909736, https://doi.org/10.1002/adfm.201909736. DOI: https://doi.org/10.1002/adfm.201909736 (acccessed 2022/08/10).

(121) Alashkar, A.; Al-Othman, A.; Tawalbeh, M.; Qasim, M. A Critical Review on the Use of Ionic Liquids in Proton Exchange Membrane Fuel Cells. *Membranes* **2022**, *12* (2), 178.

(122) Frederic, B. R.; Cedric, P.; Giao, T. M. N.; Sofia, M. M.; Eric, D.; Alexander, S. S.; Frederic, V. All-solid state ionic actuators based on polymeric ionic liquids and electronic conducting polymers. In *Proc.SPIE*, 2018; Vol. 10594, p 105941H. DOI: 10.1117/12.2300774.

(123) Kokubo, H.; Sano, R.; Murai, K.; Ishii, S.; Watanabe, M. Ionic polymer actuators using poly(ionic liquid) electrolytes. *European Polymer Journal* **2018**, *106*, 266-272. DOI: https://doi.org/10.1016/j.eurpolymj.2018.07.026.

(124) Kanaan, A. F.; Piedade, A. P.; de Sousa, H. C.; Dias, A. M. A. Effect of mold assemblies-induced interfaces in the mechanical actuation of electro-responsive ionic liquid-based polycationic hydrogels. *Applied Materials Today* **2020**, *20*, 100711. DOI: https://doi.org/10.1016/j.apmt.2020.100711.

(125) Jangu, C.; Wang, J.-H. H.; Wang, D.; Fahs, G.; Heflin, J. R.; Moore, R. B.; Colby, R. H.; Long, T. E. Imidazole-containing triblock copolymers with a synergy of ether and imidazolium sites. *Journal of Materials Chemistry C* **2015**, *3* (16), 3891-3901, 10.1039/C5TC00169B. DOI: 10.1039/C5TC00169B.

(126) Margaretta, E.; Fahs, G. B.; Inglefield, D. L.; Jangu, C.; Wang, D.; Heflin, J. R.; Moore, R. B.; Long, T. E. Imidazolium-Containing ABA Triblock Copolymers as Electroactive Devices. *ACS Applied Materials & Interfaces* **2016**, *8* (2), 1280-1288. DOI: 10.1021/acsami.5b09965.

Chapter 2: Influence of metal-coordinating comonomers on the coordination structure and binding in magnetic poly(ionic liquid)s

* This chapter is adapted from the submitted journal article: Kayla Foley., Lucas Condes, Keisha B. Walters. "Influence of metal-coordinating comonomers on the coordination structure and binding in magnetic poly(ionic liquid)s," Submitted and under review April 2023, *Molecular Systems Design and Engineering (RSC)*

Abstract

A poly(ionic liquid) (PIL), poly(acrylamide-*co*-diallyl dimethylammonium chloride), was systematically complexed with Co^{2+}, Fe^{3+}, and Co^{2+}/Fe^{3+} (mixed) at different molar equivalencies to form a series of magnetic PILs (MPILs). These novel MPILs were utilized to examine molecular structure and binding between the polymer and metal species using comprehensive spectroscopic studies in both dry and liquid states. FTIR, X-ray photoelectron, UV-Vis, and Raman spectroscopies showed evidence of metal coordination of both the iron and cobalt chloride species with the acrylamide comonomer. Using AC susceptibility measurements, the MPILs were found to have magnetic properties within the range of typical MPIL homopolymers with magnetic mass susceptibilities dependent on metal cation type and concentration. This work demonstrates MPILs can be tuned using the metal ion species and concentration to increase the magnetic mass susceptibility and alter metal-ion coordination structure and binding with the PIL copolymer. Further, the coordination structure of the transition metal halide complex was determined to be dependent on metal halide concentration in the polymer for the iron-based system, and it was shown that both metal cations (Fe^{3+} and Co^{2+}) bond not only electrostatically with the PIL monomer but also predominantly with the acrylamide comonomer. In particular, metal-oxygen and metal-nitrogen bonding was observed with the amide group present in the acrylamide.

Understanding and controlling the coordination structure and binding in PILs is significant as these materials allow for the formability and flexibility advantages of polymers to be combined with properties atypical for polymers, such as high ion conductivity, electrical and thermal stability, antibacterial properties, and magnetic responsiveness in the case of MPILs.

2.1. Introduction

Poly(ionic liquid)s, or PILs, are composed of polymerized ionic liquid monomers that form strong polyelectrolytes with permanent charge groups on the polymer pendant groups and exchangeable counterions. PILs exhibit high ion conductivity, electrical and thermal stability, antibacterial properties, and a variety of other favorable properties which are tunable through counterion exchange[1-3]. Task-specific counterions may also be introduced to impart PILs with stimuli responsive properties to environmental conditions such as pH[4], light[5], electric potential[6], and magnetic fields[7].

Magnetic poly(ionic liquid)s (MPILs) are an emerging class of PILs with ionically bound paramagnetic counterions, frequently metal halides (i.e., $[FeCl_4]^-$, $[CoCl_4]^{2-}$), that imbue the polymers with magnetic responsiveness. Instead of a counterion exchange, MPILs are typically synthesized through coordination interactions between PIL halide counterions and added transition metal salts that electrostatically bind to the polyelectrolyte. Dobbelin et al. developed some of the first paramagnetic MPILs by complexing $FeCl_3$ or $FeBr_3$ salts with poly(vinyl alkyl imidazolium chloride) and poly(diallyl dimethylammonium chloride) type PILs to form MPILs with high spin paramagnetic iron complexes ($[FeCl_4]^-$, $[FeBr_3Cl]^-$, $[FeBr_4]^-$, $[Fe_2Cl_7]^-$, $[Fe_3Cl_{10}]^{1-}$)[7]. These MPILs could be processed into powders or films and showed comparable or higher magnetic susceptibilities than their non-polymerized, small molecule counterparts, magnetic ionic liquid (MILs) [8-10] and magnetic surfactant (Mag-surf) [11, 12] complexes.

In the past decade, the MPIL field has expanded to a variety of applications including catalysis[7], organic templates and metal ion sources for *in situ* metal nanoparticles synthesis[13], magnetic separations[14, 15], antibacterial materials[16], optical and fluorescent quantum dots for biological labeling, and molecular magnet development[17, 18]. In many of these systems, MPILs have been incorporated into multicomponent systems, such as copolymers and composites. For instance, Bonnefond et al. developed magnetic latexes from the copolymerization of an MPIL with butyl acrylate and methyl methacrylate copolymers[19]. Thermoset MPILs with weak ferromagnetic properties were formed by Carrasco et al. from a partially quaternized pyridine MPIL and acrylate block copolymers blended with epoxy. Cui et al. developed imidazolium-based superparamagnetic MPIL copolymers with $FeCl_4^-$ anions that acted as quenchers for the fluorescent pyrene comonomer[20]. MPILs and MILs have been used to form composites with carboxyl-functionalized graphene oxide, as well as other nanoparticles, which were magnetically separatable from aqueous solution[15, 21].

The co-materials in these multicomponent systems often contain functional groups (e.g., carboxylic acids, amides, amines, thiols) capable of interacting or coordinating with transition metal complexes which may in turn influence the magnetic properties of those complexes or how they are integrated into the MPIL system. However, very few have examined how the transition metal halide complex interacts with the polymer in multicomponent MPIL systems. While it was not a traditional MPIL, it is noteworthy to mention the work of Yang et al. where metal ion coordination (in this case, Ni^{2+} and Nd^{3+}) in a imidazolium BF_4^- based PIL copolymerized with N-2-thiazolylmethacrylamide greatly influenced the magnetic behavior and properties of the polymer depending on metal cation type, random or block copolymerization, and coordination structure

with the thiazole ring[22]. Similar coordination behavior is expected for traditional MPILs with metal-coordinating comonomers or co-materials in multicomponent systems.

This work provides an in-depth analysis into the metal ion coordination structure and binding interactions in magnetically responsive multi-component PIL systems, an effort that, to the authors' knowledge, has not been previously presented in the literature. After systematic complexation of a PIL copolymer with different metal salts at different molar equivalencies, molecular structure and binding were characterized through a comprehensive spectroscopic study. In particular, poly(acrylamide-*co*-diallyl dimethylammonium chloride), a PIL copolymer with a quaternary ammonium PIL group and a comonomer capable of metal coordinating interactions, was selected as the halide PIL for this study, and this PIL was complexed with Co^{2+} and Fe^{3+} metal halide salts to form the MPIL copolymers. After synthesis, the chemical properties and molecular interactions of these copolymers were studied in both the liquid and dry states as a function of metal salt concentration and cation type using FTIR, X-ray photoelectron, UV-Vis, and Raman spectroscopies. The magnetic properties of these MPIL copolymers were evaluated using AC susceptibility measurements. As magnetically responsive PIL functional materials show tremendous promise for technological innovation and novel applications, it is critical to understand how transition metal ions interact in MPIL multicomponent systems and subsequently impact the properties of these unique materials.

2.2. Materials and Experimental Methods

2.2.1. Materials

A 10 wt% solution of poly(acrylamide-*co*-diallyldimethylammonium chloride) ([Pam-*co*-PDADMA][Cl^-]) in water was purchased from Sigma Aldrich. The copolymer contained 55% acrylamide (Pam) and 45% diallyldimethylammonium chloride (DADMA[Cl^-]) by weight.

$CoCl_2$•$6H_2O$ was purchased from Sigma Aldrich, and $FeCl_3$·$6H_2O$ was purchased from Alfa Aesar. All materials were used as received.

2.2.2. Synthesis of Magnetic Copolymers

Magnetic copolymers were synthesized through complexation of the metal halide in aqueous solution with the copolymer. In a typical synthesis, 10 ml of the 10 wt% [Pam-*co*-PDADMA][Cl^-] copolymer solution was added to a round bottom flask and further diluted with 5 mL of Millipore water. Aqueous solutions of $FeCl_3$ ·$6H_2O$, $CoCl_2$·H_2O, or ratioed mixtures of iron and cobalt chlorides were prepared in various concentrations to yield magnetic copolymers with 1 (3.09 mmol), 2 (6.19 mmol), or 3 (9.28 mmol) equivalents of the metal halide anions with respect to the PDADMA group. The metal halide solutions were then added dropwise to the copolymer solution under stirring. (Note gelling was observed after addition of 3-5 drops of $FeCl_3$·$6H_2O$ solution, but the gel structure collapsed with continued addition of the metal halide solutions). For the cases where significant gelling occurred, the system was further diluted with water until completely solubilized. All solutions were stirred overnight at room temperature. The water was evaporated from the system, and the magnetic MPIL polymer product was placed in a vacuum oven (~ 45 °C) for further drying before characterization.

2.2.3. Spectroscopic Characterizations

Attenuated total reflection (ATR) FTIR spectra of dried polymer were collected using a ThermoFisher Scientific Nicolet iS50R spectrometer with 4 cm^{-1} resolution and a minimum of 64 scans over the 4000-400 cm^{-1} spectral range. Raman spectroscopy was performed on a Renishaw inVia Raman microscope with a 785 nm red laser at a 1% power setting and 30-second scans for the 1200-200 cm^{-1} spectral range. Samples were prepared by drop casting thin films from aqueous solution onto microscope slides.

Physical Electronics PHI VersaProbe 5000 station X-ray photoelectron spectrophotometer (XPS) was used to obtain XPS spectra of dry polymer films. A monochromated 25.0W Al 1486.6eV source was used for data collection. Survey scans and high-resolution scans were obtained at pass energies of 117.40 eV and 23.5 eV, respectively. Samples were prepared by drop casting MPIL aqueous solutions onto gold-coated silicon wafers. The peak maximum in the C1s spectra was pinned to 285 eV, corresponding to the aliphatic C-C/C-H C1s band, used to provide for charge correction. All data were analyzed using CasaXPS (Version 2.3.23PR1.0) software. The C1s, N1s, O1s, and Cl2p high-resolution spectra were fit using Shirley backgrounds and Gaussian-Lorentzian mixed line shapes, typical for polymers[23]; the experimental error for all high-resolution spectra was ±0.2 eV. The Fe 2p and Co 2p high-resolution spectra were fit using asymmetrical line shapes typical for transition metals[24, 25]. To avoid collecting photoelectrons from excess unbound metal chloride salts, the 3 eq samples were not examined with XPS.

Solution samples were analyzed with a double beam Shimadzu UV-2450 ultraviolet-visible (UV-Vis) spectrophotometer. UV-Vis spectra were collected for each sample at room temperature at a scan rate of 500 nanometers per minute over a 190-750 nm spectral range with a 0.5 nm sampling interval and 2.0 nm slit width. All samples were measured in UV grade fused silica cuvettes with a path length of 10 mm (International Crystal Laboratories). UV-Vis absorption spectra of solid films coated on microscope slides were also obtained with a Shimadzu Biospec 1601 spectrophotometer over 800-190 nm spectral range and a 1 nm sampling interval.

2.2.4. Magnetic Characterizations

Magnetic mass susceptibilities were obtained with a Kappabridge MFK1 magnetic AC susceptibility meter. Solid sample flakes were added to 4 mL quartz cuvettes. The instrument was operated at a field strength of 450 A/m and at an AC field frequency of 976 Hz. The magnetic

susceptibility reported is an average of 10 measurements. The diamagnetic contribution of the quartz cuvette was subtracted from the volume susceptibility and then normalized by mass, yielding the magnetic mass susceptibilities. A similar procedure was followed for liquid samples where 4 mL of copolymer solution was added to a quartz cuvette. The mass susceptibility measured from a cuvette filled with 4 mL of Millipore water was used to subtract the diamagnetic contributions from the water. Two back-to-back 0.5 T neodymium magnets with a 1-inch diameter and 0.75-inch thickness were used to examine the magnetic response of the copolymers. The combined magnetic field of the two magnets was calculated to be ~0.6 T at the magnet surface.

2.3. Results and Discussion

Paramagnetic poly(ionic liquid) copolymers were synthesized by complexing $FeCl_3$, $CoCl_2$ or a ratioed mixture of the iron and cobalt metal halide salts with [Pam-*co*-PDADMA][Cl-] in aqueous solution to form the corresponding magnetic copolymer complexes [Pam-*co*-PDADMA][Fe^{3+}] and [Pam-*co*-PDADMA][Co^{2+}] (Figure 2.1). During synthesis, the metal halide salts solutions were slowly added dropwise in concentrations to provide 1, 2, or 3 mole equivalents of the metal halide with respect to the DADMA monomer unit. During the synthesis, gelation initially occurred upon addition of the first ~3-5 drops for the Fe^{3+} samples, likely due to the formation of metal coordination bonds between acrylamide units. The gel structure collapsed with continued metal halide solution addition. Following complexation and removal of the solvent, magnetic PIL copolymers were obtained. Similar copolymer systems with a 1:1 mole ratio of mixed $FeCl_3$ and $CoCl_2$ salts were also prepared to form the [Pam-*co*-PDADMA][Mixed Fe^{3+}/Co^{2+}] series. For example, [Pam-*co*-PDADMA][Mixed Fe^{3+}/Co^{2+} 1eq] consists of 0.5 mol equivalents of $CoCl_2$ and 0.5 mol equivalents of $FeCl_3$ for a total of 1 mole equivalent of metal salts added to the copolymer with respect to the PDADMA monomer unit. In total, nine magnetic

copolymers were prepared with various metal types and concentrations. As observed in other MPIL systems, these copolymers displayed different colors based on the metal species and concentration as seen in Figure 2.2a. The [Pam-*co*-PADAMA][Cl^-] copolymer with no added metal content was a light pink color. The iron copolymers, [Pam-*co*-PADAMA][Fe^{3+}], were colored dark brown (1eq), light brown (2eq), and orange-brown (3eq). All equivalents of the cobalt copolymer series, [Pam-*co*-PADAMA][Co^{2+}], were a dark blue color. The [Pam-*co*-PADAMA][Mixed Fe^{3+}/Co^{2+}] copolymers were green (1eq), dark green (2eq), and green-brown (3eq). In general, the color of MPILs, and other metal-ion polymer complexes, can vary significantly depending on metal complex coordination structure (e.g., $[FeCl_4]^-$ vs $[FeCl_3Br]^-$), metal ion concentration, and the ligand or polymer chemical composition. Dobbelin et al. reported a yellow color for the poly(diallyl dimethylammonium $[FeCl_4]^-$) homopolymer and light brown for poly(vinyl butylimidazolium $[FeCl_4]^-$) homopolymer; the latter darkened upon formation of the $[Fe_2Cl_7]^-$ and $[Fe_3Cl_{10}]^-$ complexes[7]. The iron copolymers in this work start with a dark brown color at the lowest iron concentration, which lightens to a light-brown color for the [Pam-*co*-PDADMA][Fe^{3+} 2eq] copolymer and darkens again upon increase of iron content. The cobalt series copolymers display a darker blue color than the typical light blue colors reported for the MPILs poly(3-acrylamidopropyl)-trimethylammonium $[CoCl_4]^-$) [13] and poly(viny dodecyl imidazolium $[CoCl_3Br]^-$) [19]. The green color of the mixed metals series derives from the combination of blue and yellow of the cobalt and iron systems, indicating the ability to tune polymer color by combining different metal salts. These color differences in the MPIL copolymers, particularly in those containing iron chloride salts, provide qualitative evidence of changes in metal-polymer complexation at different mole equivalencies. This observation was corroborated by corresponding changes in solubility.

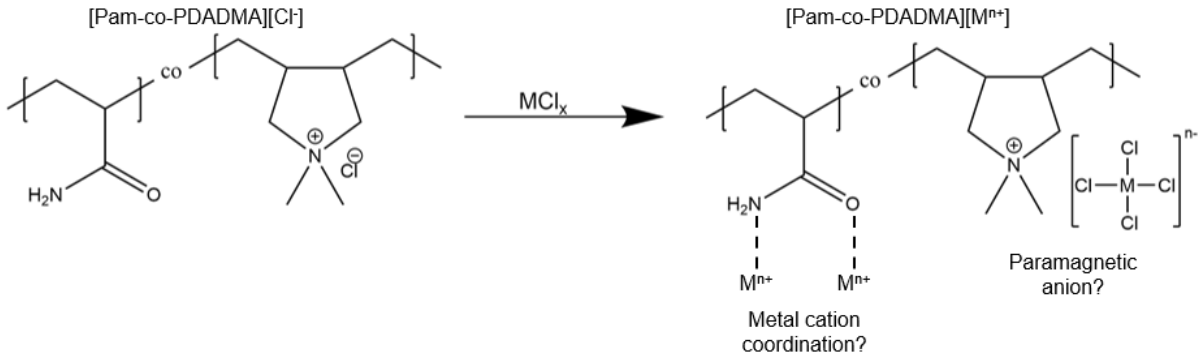

Figure 2.1 Complexation of [Pam-*co*-PDADMA][Cl^-] with metal halide salts to form magnetic [Pam-*co*-PDADMA][M^{n+}]. MCl_x refers to the metal halide salts $FeCl_3$ or $CoCl_2$. MCl_x^{n-} denotes either $[FeCl_4]^-$ or $[CoCl_4]^{2-}$ anionic complexes. M^{n+} refers to Fe^{3+} or Co^{2+} metal cations.

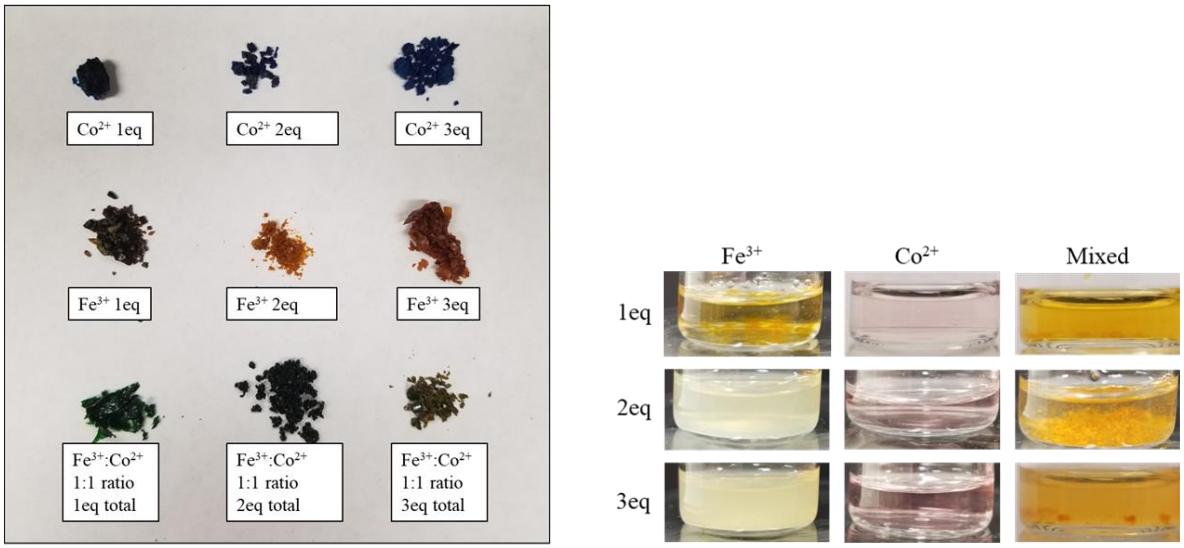

Figure 2.2 (A) Dried magnetic copolymers flakes displaying blue (cobalt), orange-brown (iron), and green (mixed) colors based on metal ion type and concentration. (B) Aqueous solutions at 7 mg/mL of the magnetic copolymers. The [Pam-*co*-PDADMA][Co^{2+}] MPIL copolymers showed complete solubility at all equivalencies, while the [Pam-*co*-PDADMA][Fe^{3+}] and [Pam-*co*-PDADMA][Mixed Fe^{3+}/Co^{2+}] MPIL copolymers showed limited solubility and some gelation and suspension behaviors.

Solubilities of the magnetic poly(ionic liquid) copolymers were examined in water (Figure 2.2b). The neat (unmodified) Cl^- based copolymer, [Pam-*co*-PDADMA][Cl^-], was completely

soluble in water at room temperature. Upon complexation with the cobalt metal halide salts, the copolymers (at all equivalents) were found to be completely soluble in water, and all resulted in pink solutions. In contrast, [Pam-*co*-PDADMA][Fe^{3+}] and [Pam-*co*-PDADMA][Mixed Fe^{3+}/Co^{2+}] copolymer series were both found to display only partial solubility. The [Pam-*co*-PDADMA][Fe^{3+} 1eq] sample appeared to form some orange-brown hydrogel-like structures, while higher equivalents resulted in only pale-yellow suspensions that were stable for 2-3 hours. The [Pam-*co*-PADAMA][Mixed Fe^{3+}/Co^{2+}] copolymer series displayed the formation of large particulates for all equivalents when placed in water. Hazell et al. produced PDADMA homopolymers complexed with iron halide salts that were completely soluble in water[15]. This suggests here that the iron halide salts interact with the acrylamide units of the copolymer in solution during synthesis, forming coordinating crosslinked regions in the polymer, resulting in precipitation or gelation. Differences in the solubilities obtained for the iron based MPIL copolymers containing a metal coordinating comonomer compared to other similar homopolymer systems further suggest that polymer-metal ion binding are occurring at least partially through metal-ion coordination rather than purely electrostatic interactions in aqueous solution and possibly during the complexation reaction.

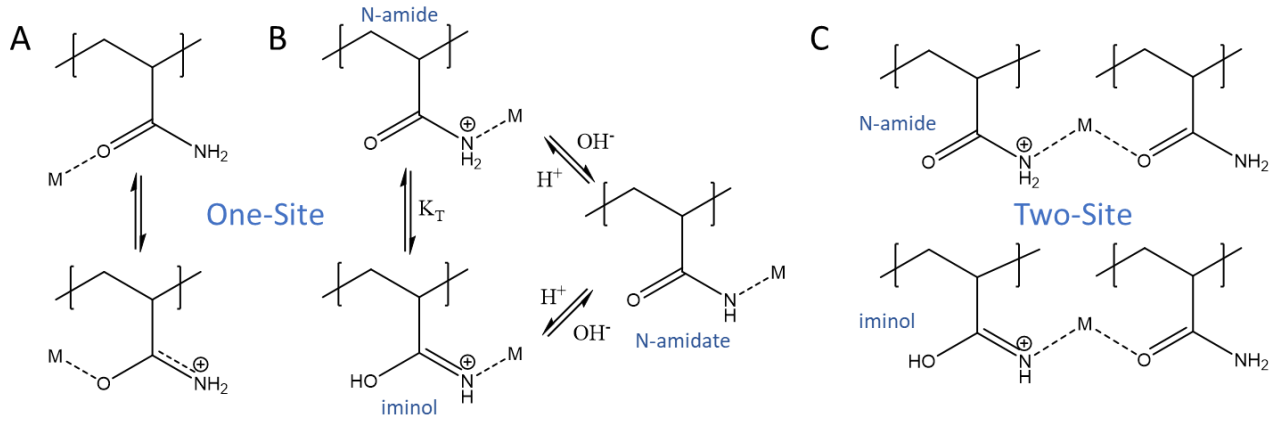

Figure 2.3 Possible transition metal ion binding sites for single-site (a) O-binding and its resonance structure, (b) N-binding, and (c) two-site O- and N-binding cases. (b) is adapted from Grima et al.[26]

Multiple spectroscopic methods were used to study the chemical interactions and structure of the copolymers and transition metal complexes in both the dry and solution state. MPILs are formed through electrostatic binding with paramagnetic ion complexes, typically through tetrahedral transition metal halide anions ($[FeCl_4]^-$, $[CoCl_4]^{2-}$, etc.). However, the comonomer, acrylamide, is capable of forming metal coordination bonds through interaction with the carbonyl oxygen atom (O-binding) or the amide nitrogen atom (N-binding) [26, 27] as shown in Figure 2.3. Acrylamide predominately binds with metal ions through the more basic carbonyl site, though N-binding is also possible depending on the acidity or hardness of the metal cation and the availability of adjacent anchoring chelation sites to stabilize the N-binding complex[26-29]. Monomeric acrylamide coordinated with metal chloride salts has been found to form mainly 6-coordinated structures (e.g., $[Co(AAm)_4Cl_2]$, $[Fe(AAm)_4Cl_2]$, $[Ni(AAm)_4Cl_2]$) or associated cation-anion pair complexes (e.g., $[Co(AAm)_6]^{2+}[CoCl_4]^{2-}$)[26, 30], though steric constraints imposed by the polymeric backbone mainly alter these structures in the MPIL copolymers. As coordination with acrylamide may influence the formation of the transition metal complex in the MPIL copolymers, the coordination structure of the transition metal species was first examined using Raman and UV-vis

spectroscopies. Characterization using FTIR and XPS spectroscopies was then performed to investigate the interactions between the transition metal species and the MPIL copolymers. Raman microscopy is typically performed on MPILs to confirm the formation of the tetrahedral anionic complex (i.e., $[FeCl_4]^-$ or $[CoCl_4]^{2-}$).

Figure 2.4 shows the Raman spectra for the MPIL copolymer films in the dry state. The Fe-Cl str 334 cm^{-1} peak, typically considered characteristic for the $[FeCl_4]^-$ and $FeCl_3$ species, was observed in the [Pam-*co*-PDADMA][Fe^{3+}] samples[7, 14]. For the solid samples, the $[FeCl_4]^-$ can form $[Fe_2Cl_7^-]$ dimers as the metal halide concentration increases, resulting in Raman peaks at 315 and 420 cm^{-1} [7, 31]. Here, this bridging complex peak was observed at ~314 cm^{-1} for the [Pam-*co*-PDADMA][Fe^{3+} 2eq] and [Pam-*co*-PDADMA][Fe^{3+} 3eq] samples. The broad absorbance observed between 250 and 500 cm^{-1} prevents the observation of a distinct 420 cm^{-1} peak. In the cobalt-based samples, there is an intense broad peak from 250 to 500 cm^{-1} with a maximum at ~358 cm^{-1} that is not observed for the [Pam-*co*-PDADMA][Cl^-] MPIL spectra. This broad peak is likely composed of multiple peaks related to metal species complexes—including the characteristic tetrahedral cobalt halide complex peak expected at 270 cm^{-1} [32-34]. Specifically, this broad peak at low wavenumbers is likely due to metal bonding with oxygen and/or nitrogen (M-O or M-N). Freire et al. reported a broad band centered at ~313 cm^{-1} for Cu-O bonding in formamide Cu^{2+} coordination complexes[35]. Other examples of M-O and M-N stretching modes have been reported in the 600-200 cm^{-1} region[35-39]. Therefore, the presence of this band is expected to be due to metal cation coordination with the acrylamide unit. Due to the intensity of the band in the cobalt and mixed series, it is possible that the tetrahedral $[CoCl_4]^{2-}$ and $[FeCl_4]^-$ complex modes are overlapping in this region. Yu et al. observed similar broad peak behavior in this region for small degrees of quaternization in polyethyleneimine polymers complexed with the $[FeCl_4]^-$

anions[40], where the majority of the amine groups have lone electron pairs available for coordination bonding.

The broad peak absorbance observed with Raman in all the MPIL copolymer samples indicates the presence of the acrylamide-metal species coordination. Further, while evidence is observed for the presence of Fe-Cl bonds and the possible presence of the [$FeCl_4^-$] and [$Fe_2Cl_7^-$] for MPIL copolymers, particularly at higher iron halide mole equivalencies, the formation of the [$CoCl_4^-$] structure is less clear. UV-vis spectroscopy was therefore used to provide additional insight into the [$FeCl_4$]$^-$ and [$CoCl_4$]$^{2-}$ complexes.

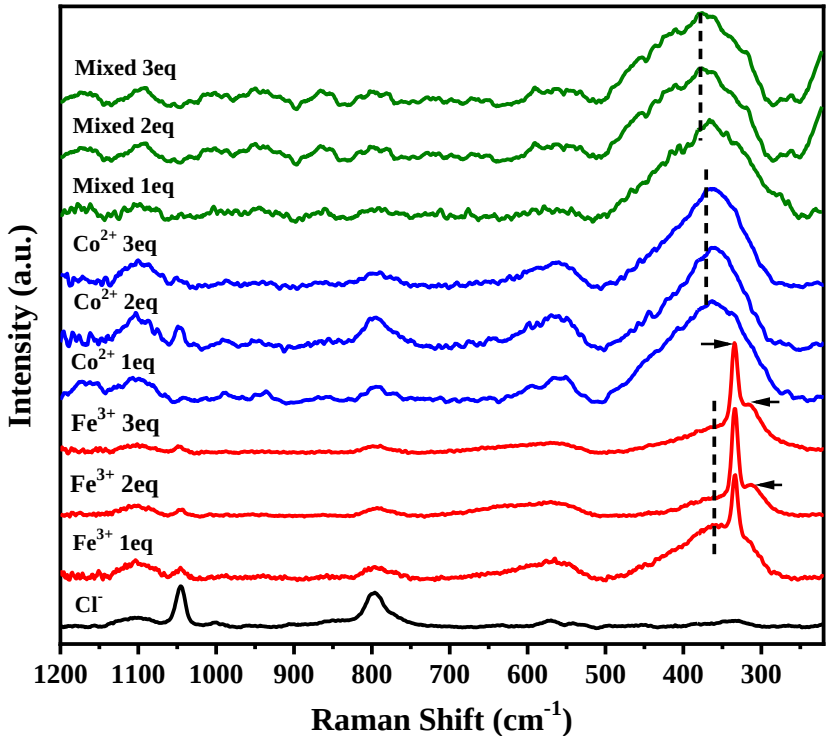

Figure 2.4 Raman spectra of the MPIL copolymers from 1200 to 220 cm^{-1} are shown for [Pam-*co*-PDADMA][Cl^-] (black), [Pam-*co*-PDADMA][Fe^{3+}] (red), [Pam-*co*-PDADMA][Co^{2+}] (blue), and [Pam-*co*-PDADMA][Mixed Fe^{3+}/Co^{2+}] (green) at each mole equivalence. The solid arrows indicate the intense Fe-Cl stretch peak at 334 cm^{-1} for the $FeCl_3$ or [$FeCl_4$]$^-$ species and the 315 cm^{-1} shoulder characteristic of the [Fe_2Cl_7]$^-$ bridging complex. Dashed lines mark the peak center for the broad band assigned to coordination of the metal cation with oxygen or nitrogen groups (i.e., M-O or M-N) in acrylamide.

UV-vis spectroscopy of the solid MPIL copolymer films was performed to provide further insight into the metal species coordination structure, and the results are displayed in Figure 2.5a-c. A second derivative analysis was performed to aid in peak assignments and are shown in Figure 2.5d-f. The [Pam-*co*-PDADMA][Cl^-] copolymer (Figure 2.5a,d, black line) had a major peak absorbance at 282 nm that can be attributed to the acrylamide carbonyl band as the quaternary ammonium group does not contain a chromophore.

In the visible region, three main bands are observed at ca. 628, 665, and 692 nm with two minor peaks at ~610 and 640 nm for both the cobalt and mixed series films. The tetrahedral geometry of cobalt complexes typically display d-d transition bands at ~625 nm and 665 nm while an octahedral coordination complex is designated by a band at ~525 nm[41, 42]. The absence of the ~525 nm band in the films indicates that the cobalt species only have a tetrahedral structure in these film samples. These three main bands and the general shape of the spectra are in close agreement with the ~630, ~665, and ~690 nm reported for the [$CoCl_4]^{2-}$ [43-46]. This UV-vis data confirms the presence of the paramagnetic $[CoCl_4]^{2-}$ anion in the MPIL films for all equivalents examined. However, other tetrahedral coordination structures (e.g., $[CoCl_2L_2]$, $[CoCl_3L]^-$, $[CoL_4]^{2+}[Cl]_2^-$, where L is acrylamide ligand) cannot be dismissed. Similar absorbances in the 600-700 nm range have been previously assigned to tetrahedral coordination of $CoCl_2$ with other ligands such as nitrate and diethyl sulfoxide[46-48]. The similarity of the UV-vis spectra in the 500-800 nm range for all [Pam-*co*-PDADMA][Co^{2+}] and [Pam-*co*-PDADMA][Mixed Fe^{3+}/Co^{2+}] copolymers indicates that the cobalt complex structure forms similarly for all mole equivalences.

In the UV region, bands at ~248 nm and 286 nm are also observed in the cobalt series films. These peaks are attributed to the acrylamide carbonyl and are slightly shifted compared to the [Pam-*co*-PDADMA][Cl^-] copolymer, possibly indicating metal ion coordination with the amide

group. In the iron and mixed series films, the first broad peak centered at ~270 nm can be deconstructed into 2-3 bands in the 240-300 nm range (ca. 250, 270, and 286 nm) by second derivative analysis. These bands are similarly assigned to acrylamide carbonyl modes interacting with Fe^{3+} species. These results are in agreement with similar work reported by Sowwan and Dweik et al. for metal coordinated polyacrylamide with bands at 276 nm and 285 nm for Cu^{2+} and Ni^{2+} complexes, respectively[49, 50].

The $[FeCl_4]^-$ complex characteristically shows intense absorbances at ca. 250, 315, and 360 nm[51-54]. These peaks are evident in the 2 and 3 eq [Pam-*co*-PDADMA][Fe^{3+}] and [Pam-*co*-PDADMA][Mixed Fe^{3+}/Co^{2+}] series films, but not in the 1 eq sample, which corroborates the Raman results for 2 and 3 eq [Pam-*co*-PDADMA][Fe^{3+}]. Second derivative analysis of the second broad band centered at ~370 nm in the [Pam-*co*-PDADMA][Fe^{3+} 1eq] sample shows a set of three peaks at 327, 354, and 395 nm, which are tentatively assigned to $FeCl_3$ complexation with the acrylamide unit. While identification of the specific $FeCl_3$-acrylamide coordination complex structures is beyond the scope of this work, these results demonstrate that changes in coordination structure occur as a function of concentration of iron chloride salts. At low concentrations there is first coordination of $FeCl_3$ with acrylamide units of the polymer followed by formation of $[FeCl_4]^-$ and $[Fe_2Cl_7]^-$ anions, which bind electrostatically with the quaternary ammonium PIL units, at higher metal salt concentrations as acrylamide binding sites have become occupied. Compared to the Co^{2+} cation, the trivalent nature of the Fe^{3+} cation likely leads to more rapid occupation of the acrylamide binding sites as metal halide concentration increases. Overall, it was observed that the acrylamide monomer unit influences the transition metal complex coordination structure in the dry iron-containing MPIL copolymer samples as metal content is increased. The findings are significant as they demonstrate that comonomer-metal coordination is occurring in these multi-

component MPIL materials and provide additional understanding of the role of the metal species and concentration in this binding.

UV-vis spectroscopy of the copolymer solutions indicates significant hydration of the metal complexes for all systems (Figure 2.6). Hydration of the Co^{2+} ions was evidenced by the presence of two peaks at ~465 and 510 nm typical of the octahedral Co aqueous species[45] as will be discussed further in the magnetic properties discussion below. The iron and mixed series showed broad absorbances between 300-500 nm, which are attributed to various $Fe(OH)_x$ and $FeCl_3$ aq. species[53, 55] and resemble spectra of the $FeCl_3$ and $CoCl_2$ salt-only solutions (Supplemental Info, Figure A.1). The acrylamide carbonyl is indicated by two peaks at ~216 and ~250 nm in [Pam-*co*-PDADMA][Cl^-]. These peaks do not shift appreciably in the cobalt series films, indicating little interaction of the metal cation with the amide group in solution. Unfortunately, the iron species absorbances dominated in the iron and mixed copolymer solutions and the acrylamide carbonyl peaks could not be identified. However, it may be inferred from the gelation and solubility behavior exhibited by the [Pam-*co*-PDADMA][Fe^{3+}] systems, partial coordination between the metal ions and the acrylamide units is taking place in the aqueous suspensions.

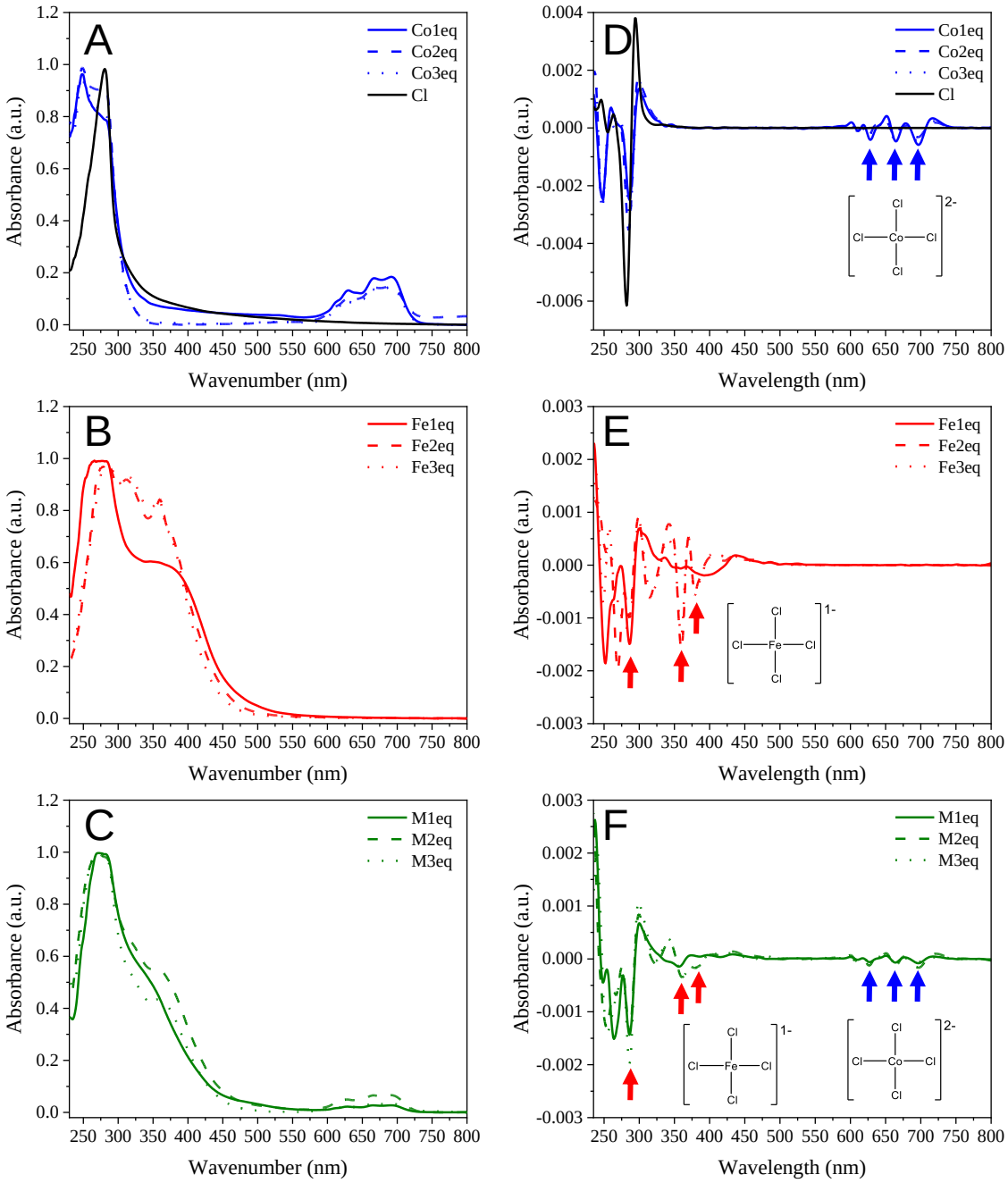

Figure 2.5 UV-vis spectra and their second derivatives of the solid MPIL films are displayed in (a and d, blue) [Pam-*co*-PDADMA][Co^{2+}], (b and e, red) [Pam-*co*-PDADMA][Fe^{3+}], and (c and f, green) [Pam-*co*-PDADMA][Mixed Fe^{3+}/Co^{2+}]. UV-vis spectra and second derivative plots for the base copolymer [Pam-*co*-PDADMA][Cl^-] are also shown (a and d, black). Characteristic $[CoCl_4]^{2-}$ and $[FeCl_4]^-$ peaks are indicated by blue and red arrows, respectively, in the second derivative plots. The tetrahedral structure of the cobalt species is confirmed by the presence of the 628, 665, and 692 nm peaks (blue arrows). Characteristic $[FeCl_4]^-$ complex is also confirmed for the 2 and 3 eq [Pam-*co*-PDADMA][Fe^{3+}] and [Pam-*co*-PDADMA][Mixed Fe^{3+}/Co^{2+}] copolymers (red arrows).

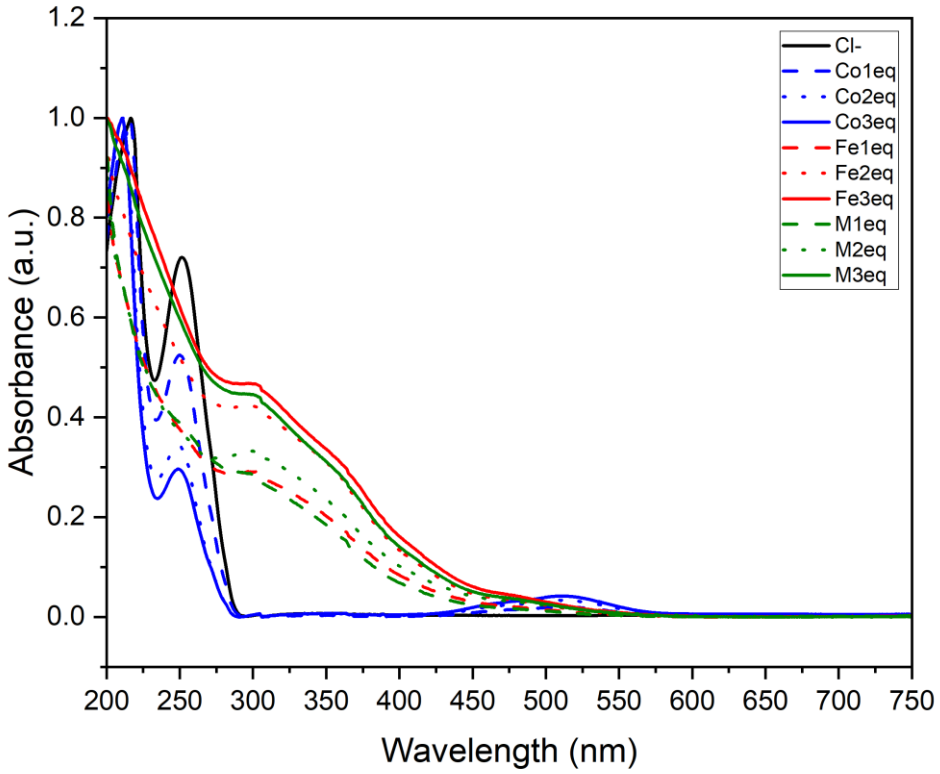

Figure 2.6 UV-vis spectra of the copolymer solutions shows the predominate presence of hydrated $Co(OH)_6$ and $Fe(OH)_x$ in aqueous solutions as indicated by the series of absorbances between 300-500 nm in the [Pam-*co*-PDADMA[Fe^{3+}] and [Pam-*co*-PDADMA][Mixed Fe^{3+}/Co^{2+}] copolymers and by the characteristic octahedral cobalt species peaks at 465 nm and 510 nm in the [Pam-*co*-PDADMA][Co^{2+}] copolymers.

Fe^{3+} coordination in solution of the [Pam-*co*-PDADMA][Fe^{3+}] copolymers during the synthesis influences the final iron coordination structure in the dry state as seen in the UV-vis spectra of the dry films. Conversely, the dissociation of the hydrated Co^{2+} species in solution and the similarity of the dry film UV-vis spectra observed for the [Pam-*co*-PDADMA][Co^{2+}] and [Pam-*co*-PDADMA][Mixed Fe^{3+}/Co^{2+}] copolymers at all molar equivalences suggests that acrylamide coordination with Co^{2+} species in solution does not play a significant role in the final cobalt species coordination structure.

ATR-FTIR spectroscopy was performed to examine binding interactions between the transition metal complexes and the MPIL copolymers. The unmodified commercial copolymer PIL-Cl^- copolymer displayed the characteristic amide I (C=O str) and amide II (NH_2 wag) bands at 1662 cm^{-1} and 1615 cm^{-1}, respectively (Figure 2.7 a and b, black trace). The amide III (C-N str and NH bending) modes are typically characterized by several bands in the 1430-1200 cm^{-1} region[56, 57]. Here, the band at ~1417 cm^{-1} is assigned to the amide III (C-N str) mode, though there are several weaker bands in the 1400-1200 cm^{-1} region which may also contribute to the NH bending modes. The corresponding symmetrical primary amide N-H stretching mode is seen at ~3200 cm^{-1}. The asymmetrical N-H stretch is overlapping with the broad peak at 3370 cm^{-1} assigned to hydrogen bonding of the Cl^- ion with the polymer and molecularly absorbed water. The peak at 1489 cm^{-1} is due to the bending modes of the quaternary ammonium methyl groups[58-61].

Figure 2.7 and Table A.1 show the absorbance shifts of the copolymers after metal complexation. Above 3000 cm^{-1}, a slight decrease in frequency to ~3190-3196 cm^{-1} in the symmetrical N-H stretch is observed (Figure 2.7 a). A defined band at ~3330-3335 cm^{-1} emerges and is tentatively assigned to the N-H asymmetrical stretching mode. The decrease in the N-H stretching modes seen here is an indication of increased interactions of the amide hydrogen atoms in the intermolecular or intramolecular environment of the copolymers upon metal complexation, though not necessarily an indication of metal coordination[57]. However, due to significant overlap with the hydrated metal complex -OH stretches, assignments and peak shifts in this region must be interpreted with caution. The spectra for the pure hexahydrate metals show peaks (Supplemental Info, Figure A.2) at 3522, 3383, and 3163cm^{-1} for $CoCl_2 \bullet 6H_2O$ and 3526, 3386, 3217, 3005 cm^{-1} for $FeCl_3 \bullet 6H_2O$. These modes are clearly observed in the spectra for the 3 eq metal complexed

copolymers. For copolymers with lower metal content, these peaks are not clearly defined, though broadening is observed in the region.

All copolymer samples showed significant downshifts in both the amide I and amide II bands, indicating metal ion interactions with the polyacrylamide units (Figure 2.7 b). The cobalt series showed the smallest shifts with 6 to 14 cm^{-1} and 11 to 18 cm^{-1} downshifts for the amide C=O str and NH_2 wagging modes, respectively. The [Pam-*co*-PDADMA][Fe^{3+}] series showed the greatest decreases, shifting downwards ~12 to 19 cm^{-1} for the amide I band and 41-50 cm^{-1} for the amide II band. The C=O bands for the [Pam-*co*-PDADMA][Mixed Fe^{3+}/Co^{2+}] series showed intermediate downshifts to ~1653, 1650, and 1642 cm^{-1} for the 1 eq, 2 eq, and 3 eq samples, respectively. Assignment of the amide II band was more difficult for the [Pam-*co*-PDADMA][Mixed Fe^{3+}/Co^{2+}] series due to a complex overlapping of bands in the amide II region. Peak deconvolution was performed for the [Pam-*co*-PDADMA][Mixed Fe^{3+}/Co^{2+} (1eq)] copolymer, yielding three fitted peaks at 1657, 1607, and 1572 cm^{-1} (Supplement Figure A.3). The first peak is attributed to the amide carbonyl band, as determined above. The peaks at 1607 and 1572 cm^{-1} are attributed to the NH_2 wagging mode due to cobalt and iron coordination interactions, respectively. Peak fittings for the [Pam-*co*-PDADMA][Mixed Fe^{3+}/Co^{2+} 2eq] and [Pam-*co*-PDADMA][Mixed Fe^{3+}/Co^{2+} 3eq] samples are shown in Supplemental Info, Fig. S4 and Fig. S5. For the samples with 3 eq equivalents of metal content, another band emerges at approximately 1618 cm^{-1} for the cobalt and 1608 cm^{-1} for the iron samples. These bands are attributed to the M-OH bending of uncoordinated metal halide salt in the copolymer. The ~1417 cm^{-1} amide III band did not shift appreciably upon metal complexation, though several of the modes in the 1400-1200 cm^{-1} region displayed small shifts to higher wavenumbers.

Metal ion coordination with amides is typically indicated by shifts in the amide I and amide II bands[57, 62]. Similar redshifts were observed by Halevi et al. upon Ni^{2+} ion complexation with a poly(acrylamide) homopolymer[62], which were attributed to O-binding interactions. N-bonding of acrylamide may also occur depending on the stability of the ligand complex and cation acidity with possible acrylamide N-bonding modes of N-amide, N-amidate, and iminol groups as shown in Figure 2.3. Deprotonation of the amide group results in the formation of either an n-amidate or an iminol group characterized by the absence or decrease in intensity of the amide II band[28, 29, 63]. As the amide II band and N-H stretches are present in the MPIL copolymers, it is unlikely significant amide tautomerization to iminol or deprotonation to n-amidate has occurred. Decreases in the C=O frequencies potentially indicate O-binding interactions with both the Fe^{3+} and Co^{2+}. Monodentate O-binding of amides results in a decrease in the amide I frequency but an increase in the amide II frequency due to weakening of the C=O bond and subsequent stiffening of the C-N bond in the amide group due to resonance[38, 57, 64, 65]. However, both the amide I and amide II bands display shifts to lower wavenumbers in all cases, indicating binding with both the oxygen (Figure 2.3a) and nitrogen (Figure 2.3b) of the amide groups. It is clear coordination between the transition metal complex and the polymer acrylamide unit is evidenced for both the Fe^{3+} and Co^{2+} halide species at all equivalences with possible bonding at both the acrylamide oxygen and nitrogen atoms.

It should be noted that if hydrolysis of the amide group occurred with metal complexation, it would result in the formation of either carboxylic acids, denoted by a C=O str in the 1740-1700 cm^{-1} region, or carboxylate groups, characterized by a C=O asymmetrical str mode between 1695-1540 cm^{-1} and a symmetrical stretching mode between 1440-1335 cm^{-1} [38]. No modes are observed above 1700 cm^{-1}, excluding carboxylic acid formation. Further, no new bands emerge in the 1440-

1335 cm^{-1} region suggesting no carboxylate groups are formed either. Therefore, there is no evidence of hydrolysis of the acrylamide group occurring upon the addition of metal salts.

The quaternary ammonium methyl group bending mode at 1489 cm^{-1} disappears in the metal systems, but an increase in the peak intensity at ~1465 cm^{-1} was observed. This suggests the peak downshifts and overlaps with the polymer backbone CH_2/CH_3 bending modes. However, due to this overlap, electrostatic interaction between the transition metal complexes and quaternary ammonium group cannot be confirmed. As many of the C-N infrared modes for the PDADMA group overlap with the acrylamide modes, XPS spectroscopy was performed to better understand the metal halide interactions with the polymer.

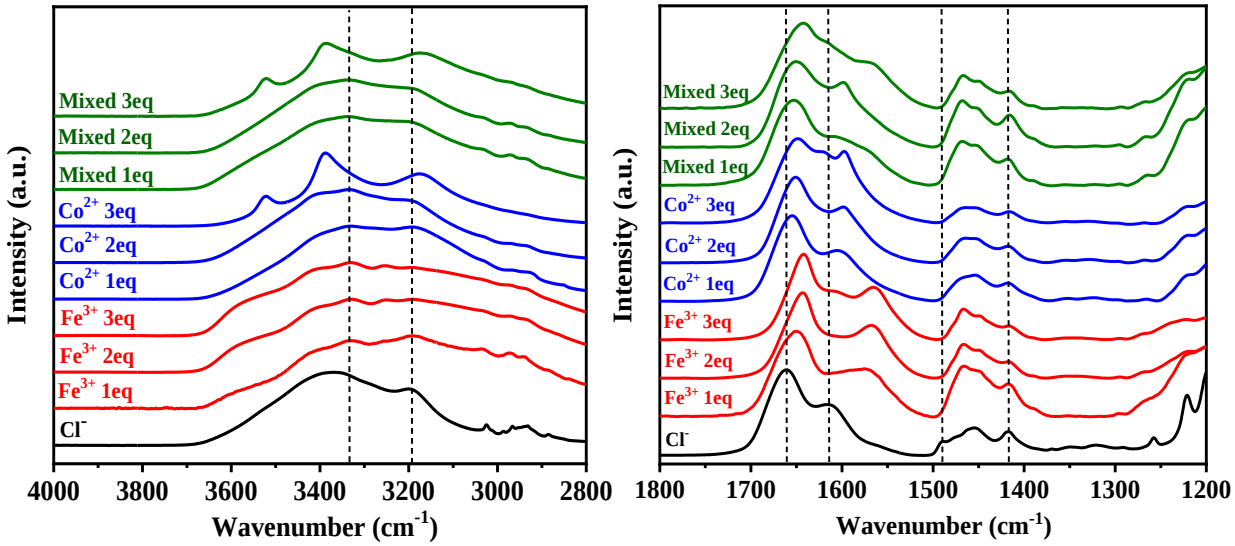

Figure 2.7 ATR-FTIR spectra of the MPIL copolymers from (A) 4000-2800 cm^{-1} and (B) 1800-1350 cm^{-1}. At higher wavenumbers (A) the black dashed lines show the general location for the N-H asymmetrical and symmetrical stretches. In (B) the black dashed lines show the peak centers for the [Pam-*co*-PDADMA][Cl^-] copolymer amide I (C=O str), amide II (NH_2 wag), the PDADMA methyl bending mode, and the amide III (CN str) (left to right). Significant shifts to lower wavenumbers are observed for both the amide I and amide II bands for each of the metal-copolymers, indicating transition metal species coordination with acrylamide unit, likely through both O- and N- bonding. Greater downshifts are observed for the [Pam-*co*-PDADMA][Fe^{3+}] series compared to the [Pam-*co*-PDADMA][Co^{2+}] and [Pam-*co*-PDADMA][Mixed Fe^{3+}/Co^{2+}].

XPS studies were carried out to provide further understanding of the polymer-metal salt binding. Figure 2.8 displays representative nitrogen, oxygen, carbon, and chloride high resolution spectra for the [Pam-*co*-PDADMA][Cl^-] sample, and Table A.2 and Table A.3 in the supplemental information summarize the XPS data for all of the copolymer samples. [Pam-*co*-PDADMA][Cl^-] showed the N1s peaks for the quaternary ammonium nitrogen at 402.4 eV and the acrylamide peak at 399.6 eV, which is in good agreement with the literature[66, 67]. Three peaks in the C1s spectra—285.0 eV, 286.1 eV, and 287.7 eV—are attributed to the aliphatic C-C/C-H bonds, quaternary ammonium ring C-N bonds, and the acrylamide carbonyl bond[23, 66]. The Cl 2p spectrum shows two chemical species as indicated by two sets of $2p^{3/2}$ and $2p^{½}$ peaks with binding energy separations of 1.6 eV. The major chemical species has a Cl $2p^{3/2}$ peak at 198.8 eV which is attributed to the chloride anion of the quaternary ammonium group. This value is approximately 2 eV higher than that seen for the poly(diallyl dimethyl ammonium chloride) homopolymer (~196.9 eV) and pyrrolidinium based ionic liquids[68, 69], which is likely due to the hydrogen bonding interactions with the acrylamide units. This is supported by the slightly lower binding energy for the Pam-NH_2 N1s peak (399.6 eV) compared to 399.9 eV reported by Chen et al. in pure polyacrylamide[66]. The minor component Cl $2p^{3/2}$ peak at 197.6 eV is assigned to residual NaCl salt in the source polymer. The main peak in the O1s spectrum at 531.3 eV is attributed to the acrylamide carbonyl band. The peaks at 536.1eV and 538.0 eV are likely the Na KLL auger peaks. A small amount of sodium was observed in the survey spectra (Supplemental Figure A.6), likely due to residual salt in the polymer stock solution. The 532.5 eV peak was assigned to either molecularly absorbed water, which is typically observed from 532-533 eV[62, 70, 71], or partially exchanged -OH anions[69].

Adding the transition metal salts resulted in significant changes in several of the high-resolution spectra shown in Figure 2.8. An initial examination of the N1s spectra (Figure 2.8 a) still shows two peaks for the PDADMA quaternary ammonium at higher binding energies and the Pam-NH_2 nitrogen group at lower energies. Interestingly, a change in the area ratio of the (Pam-NH_2 / PDADMA) N1s peak is observed for all the metal complexed copolymers with the exception of the [Pam-*co*-PDADMA][Co^{2+} 1eq] sample. As significant hydrolysis was eliminated in the FTIR analysis, the N1s spectra were refitted to include a metal coordinated Pam-$H_2N^+\cdots$M peak to account for the area ratio change and maintain the monomer balance of Pam and PDADMA in the copolymer. The resulting three peaks (ca. 402.5, 402.1, and ~400 eV) were assigned to PDADMA quaternary ammonium peak, the Pam-$H_2N^+\cdots$M, and Pam-NH_2 peaks.

The PDADMA N1s peak shows slight increases in binding energy (~0.1-0.2 eV) depending on metal type and mole equivalent. For instance, the quaternary ammonium N1s peak increases from 402.4 eV in the [Pam-*co*-PDADMA][Cl^-] sample to 402.4 and 402.6 eV for the [Pam-*co*-PDADMA][Co^{2+}] 1 eq and 2 eq samples, respectively (Table A.2). Both the [Pam-*co*-PDADMA][Fe^{3+}] 1 and 2 eq samples had a N1s binding energy of 402.5 eV. Similar binding energy increases have been seen in pyrrolidinium, imidazolium, and ammonium ionic liquids for different counterions [67, 72, 73]. Counterion size, basicity, and coordinating ability influences the counterion's ability to transfer charge to the nitrogen cation, resulting in different binding energies for the quaternary ammonium nitrogen for different counterions. Generally, quaternary ammonium N 1s binding energy increases with different counterions in the order of $Cl^- < I^- \sim [CoCl_4]^{2-} < [BF_4]^- < [PF_6]^- < [Tf_2N]^- \sim [FeCl_4]^-$ [73, 74]. However, these shifts are within the instrument resolution (±0.2 eV), so while an overall trend is evidenced, increases with specific metal cation type cannot be discerned here. Further, the small ~0.1-0.2 eV binding energy shifts observed here are lower than

those observed in other MIL systems. For example, Taylor et al. observed an increase of binding energy from 401.7 eV in an imidazolium based ionic liquid to 402.2 eV (Δ=0.5 eV) and 401.9 eV (Δ=0.2 eV) on addition of $FeCl_3$ and $CoCl_2$ salts, respectively[74]. This suggests that the electrostatic environment of the PIL quaternary ammonium does not change significantly upon addition of the transition metal salts and that the main binding mechanism between the MPIL copolymers and the metals species is not due to electrostatic interactions with the PIL monomer unit.

Conversely, binding energy increases of ~0.2-0.6 eV were observed for the original Pam-NH_2 N1s peak (399.6 eV), with larger increases observed for the copolymers as a function of higher metal content (Table A.2). This peak is associated with the O-bonding case (Figure 2.8 A) where the metal cation coordinates with the carbonyl oxygen and the resonance shift results in a withdraw of electron density from the NH_2 group. In the [Pam-*co*-PDADMA][Fe^{3+}] copolymers, this peak is at 399.8 and 400.0 eV for 1 and 2 molar equivalences, respectively (Table A.2). Binding energies of 400.0 and 400.2 eV were observed for this peak in [Pam-*co*-PDADMA][Co^{2+} 1eq] and [Pam-*co*-PDADMA][Co^{2+} 2eq] copolymers. The [Pam-*co*-PDADMA][Mixed 1eq] copolymer had a similar binding energy (399.8 eV) as the [Pam-*co*-PDADMA] [Fe^{3+} 1eq] copolymer.

The peak that emerges at ~402 eV in several of the metal copolymer spectra is attributed to direct coordination of the metal cation with the acrylamide nitrogen Pam-$H_2N^+\cdots M$ (Figure 2.8 a). Zhang et al. assigned similar O- and N-bonded N1s peaks for $CaCl_2$ coordinated polyacrylamide hydrogels[75]. The associated Pam C=O C1s (Figure 2.8 C) and O1s peak (Figure 2.8 b) also shift to higher binding energies between 288.1-288.8 eV and 531.9-532.3 eV respectively upon metals addition. These shifts agree well with binding energy increases observed in the literature for metal coordinated polyacrylamide[15, 75]. In the iron and mixed samples, an additional small peak at ~530 eV emerges, which is typically associated with lattice metal-oxide bonds (Fe-O) [71]. In other $FeCl_3$

based material systems, a similar peak at ~530 eV has been attributed to the formation of FeClO due to storage of materials in ambient air conditions[76, 77]. Small amounts of Na were still observed in the survey spectra for several of the metal copolymers (Supplemental Figure A.7-Figure A.11), the peak at ~536 eV is assigned to the Na KLL Auger peaks. A peak between 532.3 and 533.6 eV was observed at varying intensities in the metal copolymer O1s spectra and was assigned to absorbed water or hydroxyl groups[62, 69-71]. The XPS findings corroborate the FTIR spectroscopy results and show that the transition metal complexes predominately bind to the polymer by coordination interactions with the acrylamide unit through both oxygen and nitrogen bonding rather than by purely electrostatic binding with the quaternary ammonium group.

High resolution spectra for Fe 2p and Co 2p were also collected (Figure 2.9 a,b). High-spin coordination structures are characterized by observed spin-orbit splitting into $2p^{3/2}$ and $2p^{1/2}$ peaks for transition metals and are typically accompanied by shake-up satellite peaks[25, 74, 78]. In all samples, these $2p^{3/2}$ and $2p^{1/2}$ multiplet splitting peaks and satellite peaks were observed in both the Fe 2p and Co 2p high resolution spectra. This indicates that the MPIL copolymers contain metal species with paramagnetic high spin-states as expected for magnetically responsive MPILs.

As high-resolution spectra for metals are often highly complex, component fitting was not attempted for the Fe 2p and Co 2p spectra. Rather, the peak maximums were taken to be the binding energy values for the predominate metal species (Table A.3). The intense Fe $2p^{3/2}$ peak is located at 710.9 eV, 711.4 eV, and 710.9 eV for the [Pam-*co*-PDADMA] [Fe^{3+} 1eq], [Pam-*co*-PDADMA] [Fe^{3+} 2eq], and [Pam-*co*-PDADMA] [Mixed Fe^{3+}/Co^{2+}1eq] samples, respectively. The [Pam-*co*-PDADMA][Fe^{3+} 2eq] Fe $2p^{3/2}$ binding energy is similar to those reported for $FeCl_3$ salt (711.5-712.0 eV) [25], imidazolium-based $FeCl_4^-$ ionic liquid (711.9 eV) [74], and quaternary tetraethylammonium $FeCl_4^-$ salt (711.2 eV) [79]. A similar trend is observed in the corresponding Cl

2p spectra where the main Cl $2p^{3/2}$ peak was found to be at 198.4 eV, 198.7 eV, and 198.4 eV for the [Pam-*co*-PDADMA] [Fe^{3+} 1eq], [Pam-*co*-PDADMA] [Fe^{3+} 2eq], and [Pam-*co*-PDADMA] [Mixed Fe^{3+}/Co^{2+} 1eq] samples, respectively. The lower Fe $2p^{3/2}$ binding energy of the [Pam-*co*-PDADMA] [Fe^{3+} (1eq)] and [Pam-*co*-PDADMA][Mixed Fe^{3+}/Co^{2+} 1eq] samples paired with corresponding lower Cl 2p binding energies indicate that overall the iron halide complex species are more electron rich than the [Pam-*co*-PDADMA][Fe^{3+} 2eq] sample (Figure 2.8 d, Table A.3). This may be due to a change in the charge distribution across the metal cation and Cl atom as electron density is gained from acrylamide coordination, which is also supported by the binding energy increases for the acrylamide O1s and N1s peaks and the downward shift in wavenumbers for the amide modes in the FTIR spectroscopy results. Further, the presence of the shake-up satellite peaks in the [Pam-*co*-PDADMA][Fe^{3+} 1eq] sample also suggests that the iron-acrylamide coordinated species are also in a paramagnetic high spin-state. In the [Pam-*co*-PDADMA][Fe^{3+} 2eq] sample, the Cl^- concentration is higher from the increased concentration of metal halide, allowing for the formation of the $[FeCl_4]^-$ anion as suggested in the UV-vis film results. For the iron and mixed cases, the Cl 2p spectra could not be adequately fit with one chemical state and maintain the 1.6 eV spin-orbit coupling splitting[80]. An additional minor Cl $2p^{3/2}$ peak was also fitted at ~200 eV in the iron and mixed copolymer samples, which is attributed to the $[Fe_2Cl_7]^-$ bridging complex as noted in the Raman results [81, 82].

The Co $2p^{3/2}$ and Cl $2p^{3/2}$ peaks for the [Pam-*co*-PDADMA][Co^{2+} 1eq], [Pam-*co*-PDADMA][Co^{2+} 2eq], and [Pam-*co*-PDADMA][Mixed Fe^{3+}/Co^{2+} 1eq] samples were located at 781.6 eV, 781.9 eV, and 781.3 eV and 198.4 eV, 198.8 eV, and 198.4 eV, respectively. These Co $2p^{3/2}$ binding energies are bounded by those reported for $CoCl_2$ salt (782.1 eV) [83] and the 780.6 eV reported for an imidazolium-based $[CoCl_4]^{2-}$ ionic liquid[74]. As was seen for the iron samples,

similar lower binding energies in the 1 eq samples compared to the 2 eq sample are also noted for the Co $2p^{3/2}$ and Cl $2p^{3/2}$ peaks, indicating a more electron rich coordination environment for the Co^{2+} cation at lower metal mole equivalents in the polymer. This may also be related to changes in tetrahedral speciation from acrylamide coordinated Co^{2+} (e.g., $[CoCl_2L_2]$, $[CoCl_3L]^-$, or $[CoL_4]^{2+}[CoCl_4]^{2-}$, where L is acrylamide ligand) to the formation of predominantly $[CoCl_4]^{2-}$ anions at higher Cl^- concentrations.

Magnetic studies were conducted on these [Pam-*co*-PDADMA][Fe^{3+}], [Pam-*co*-PDADMA][Co^{2+}], and [Pam-*co*-PDADMA][Mixed Fe^{3+}/Co^{2+}] magnetic PIL copolymers. Samples were examined both in the dry (solid) state and as solutions (Co^{2+} copolymers) or suspensions (Fe^{3+} and Fe/Co-mixed copolymers). Table 2.1 and Figure 2.10a show the magnetic mass susceptibilities for the dry polymer samples. Magnetic susceptibility, χ_m, is a measure of the paramagnetic copolymer's strength of attraction to a magnetic field. The magnetic mass susceptibilities increased linearly with increasing metal ion content in the MPILs copolymers. The iron copolymer series displayed mass susceptibilities that were consistently higher than those for the cobalt and Fe^{3+}/Co^{2+}-mixed copolymers, at a given metal halide equivalency. The dry [Pam-*co*-PDADMA][Fe^{3+}] samples showed magnetic susceptibilities that increased from ~25 x 10^{-6} to 44 x 10^{-6} emu/g as the metal equivalency was increased from 1 to 3. These values correspond well with the 29.3 x 10^{-6} and 35.3 x 10^{-6} emu/g values obtained by Dobbelin et al. for similar diallyl dimethylammonium-based PIL homopolymers containing $FeCl_4^-$ and $Fe_2Cl_7^-$ counterions, respectively[7]. The cobalt series displayed the lowest mass susceptibilities from this study, with values of 17.5 x 10^{-6}, 29.4 x 10^{-6}, and 34 x 10^{-6} emu/g, for the 1, 2, and 3 equivalent samples, respectively. The[Pam-*co*-PDADMA][Mixed Fe^{3+}/Co^{2+}] series showed apparent mixing rule behavior, with intermediate magnetic susceptibility values between those of iron and cobalt

(ranging from 22 x 10^{-6} to 36.2 x 10^{-6} emu/g). The dry copolymers were also responsive to a 0.62 T magnetic field produced by neodymium magnets, as shown for the [Pam-*co*-DADMA][Co^{2+} 2eq] sample in the insert of Figure 2.10a and Supplemental Info Video V2. Similar responses were seen for all other samples (Supplemental Videos V1-V9).

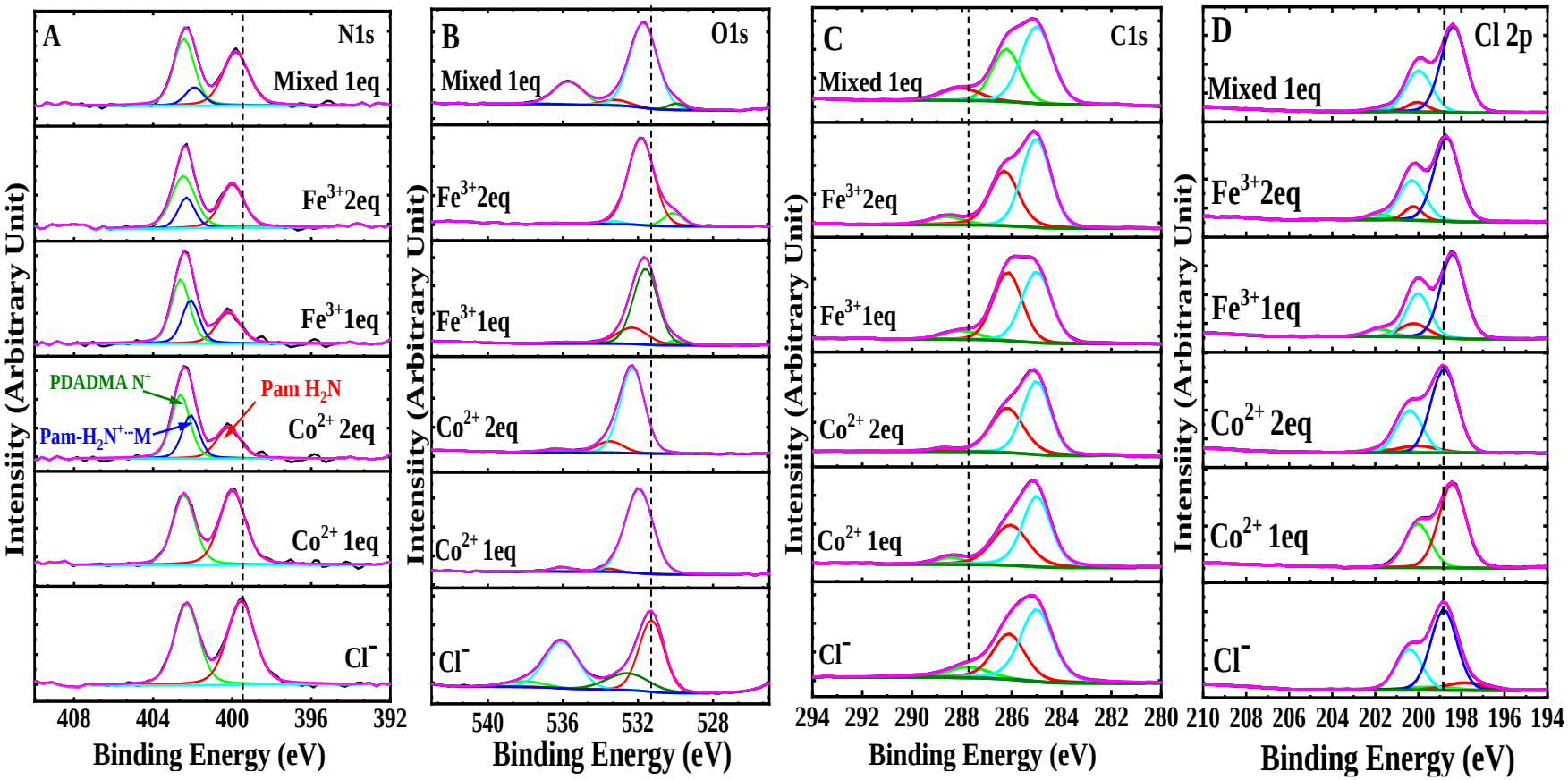

Figure 2.8 High resolution XPS spectra of the MPIL copolymers were collected in the (a) N1s, (b) O1s, (c) C1s, and (d) Cl 2p spectral ranges. The bottom red trace shows the spectra for the original non-magnetic [Pam-*co*-PDADMA][Cl^-] copolymer. The dotted black lines show the shifts of the peaks in the MPIL copolymers for the 1 eq and 2 eq with respect to the [Pam-*co*-PDADMA][Cl^-] copolymer as discussed in the text. Where appropriate, the N1s spectra was fitted with three peaks for the PDADMA quaternary ammonium, O-bonded Pam-NH_2, and the N-bonded Pam-H_2N···M groups. These peaks are marked for the [Pam-*co*-PDADMA][Co^{2+} 2eq] sample in (a). While slight shifts are observed in the N1s spectra for the PDADMA quaternary ammonium, the greater shifts observed for the O-bonded Pam-NH_2 and the emergence of the N-bonded Pam-H_2N···M band suggests greater interaction of the transition metal complexes with the acrylamide group compared to the PIL quaternary ammonium.

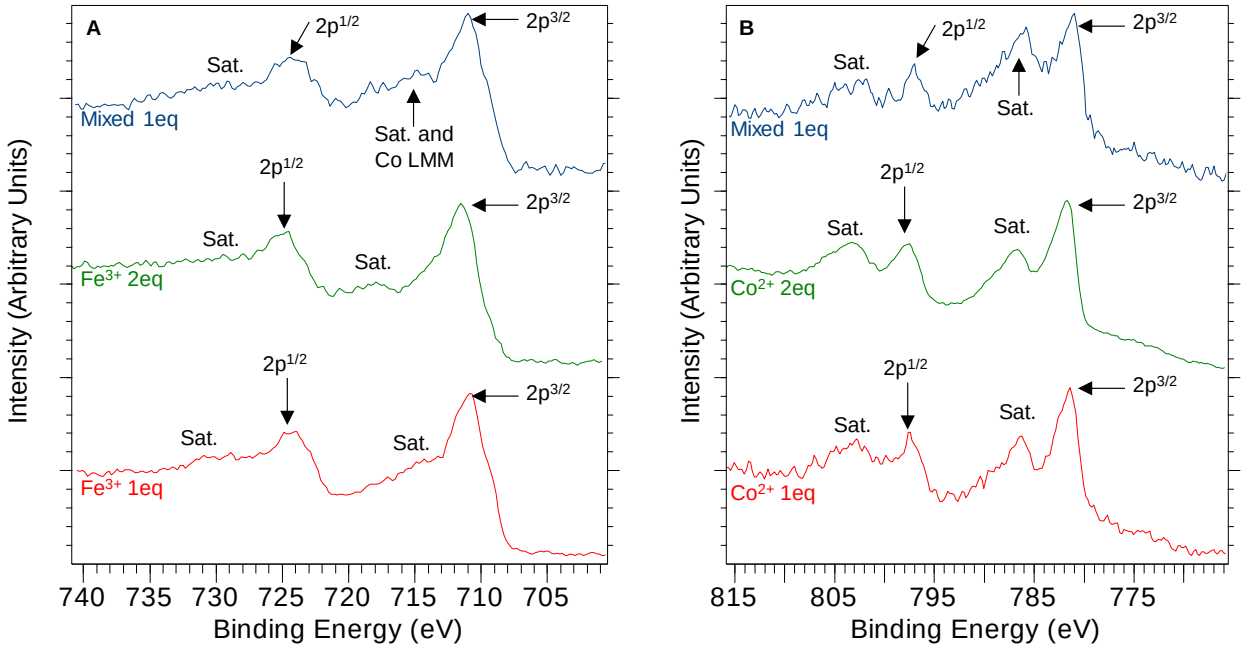

Figure 2.9 XPS high resolution (a) Fe 2p and (b) Co 2p spectra show the 2p splitting and satalite peaks characteristic of the paramagnetic high spin iron and cobalt species in [Pam-*co*-PDADMA][Co^{2+}], [Pam-*co*-PDADMA][Fe^{3+}], and [Pam-*co*-PDADMA][Mixed Fe^{3+}/Co^{2+}] MPIL copolymers.

Table 2.1 Magnetic mass susceptibilities and metal halide weight percentages for the MPIL copolymers in dry and aqueous solution (0.7 wt/vol%) sample states are shown. χ_m generally increased with increasing wt% for all transition metal types and the mixed system, though this increase was greater in the dry polymers than in the wet state. Generally, the [Pam-*co*-PDADMA][Fe^{3+}] MPIL copolymers had the highest χ_m for the same mole equivalence and physical state followed by [Pam-*co*-PDADMA][Mixed Fe^{3+}/Co^{2+}] and [Pam-*co*-PDADMA][Co^{2+}].

Sample	Metal Halide wt% [a]	Dry Sample χ_m (x10^{-6} emu g^{-1})	Polymer Solution or Suspension χ_m (x10^{-6} emu g^{-1})
[Pam-*co*-PDADMA][Fe^{3+} 1eq]	42.9%	24.73 (± 0.03)	23.5 (± 0.6)
[Pam-*co*-PDADMA][Fe^{3+} 2eq]	60.1%	37.22 (± 0.04)	27.9 (± 0.5)
[Pam-*co*-PDADMA][Fe^{3+} 3eq]	69.3%	43.95 (± 0.05)	35.9 (± 0.9)
[Pam-*co*-PDADMA][Co^{2+} 1eq]	39.8%	17.53 (± 0.03)	20.8 (± 0.9)
[Pam-*co*-PDADMA][Co^{2+} 2eq]	57.0%	29.37 (± 0.03)	21.6 (± 0.2)
[Pam-*co*-PDADMA][Co^{2+} 3eq]	66.5%	33.58 (± 0.04)	23.3 (± 0.3)
[Pam-*co*-PDADMA][Mixed Fe^{3+}/Co^{2+} 1eq]	41.4%	21.99 (± 0.02)	24.1 (± 0.4)
[Pam-*co*-PDADMA][Mixed Fe^{3+}/Co^{2+} 2eq]	58.6%	30.39 (± 0.06)	30.9 (± 0.7)
[Pam-*co*-PDADMA][Mixed Fe^{3+}/Co^{2+} 3eq]	68.0%	36.17 (± 0.03)	35.0 (± 0.5)

(a) calculated based on added metal salt

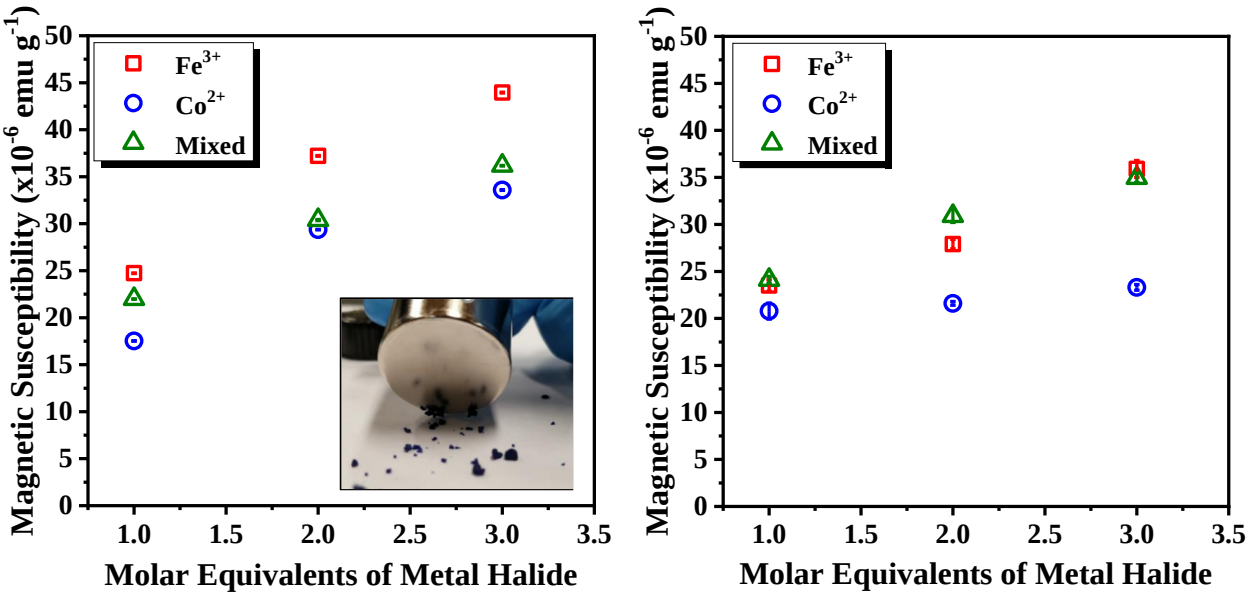

Figure 2.10 Magnetic mass susceptibilities of (A) the dry MPIL copolymers and (B) the aqueous solution (~7 mg/ml) as a function of molar equivalents of the metal halide(s). In both cases, χ_m correspondingly increased with increasing metal content, though the χ_m for the dry polymers were ~1-10x10^{-6} emu/g higher than the MPIL copolymers in solution or suspension. The standard deviations in χ_m for the solid samples was on the order of 0.02-0.06 x 10^{-6} emu/g while the standard deviations for the liquid samples were slightly higher at 0.2-0.9 x 10^{-6} emu/g. [Pam-*co*-PDADMA][Fe^{3+}] copolymers generally had the highest χ_m followed by the [Pam-*co*-PDADMA][Mixed Fe^{3+}/Co^{2+}] and the [Pam-*co*-PDADMA][Co^{2+}] MPIL copolymers. The insert in (A) shows the dried [Pam-*co*-PDADMA][Co^{2+} 2eq] copolymer attracted to a 0.62 T magnet in the video frame capture of Supplemental Info Video V2. All other dry MPIL copolymers also demonstrated magnetic responsiveness (see Supplemental Info Videos V1-V9).

MPIL systems have generally been found to exhibit magnetic susceptibilities ranging between 10 x 10^{-6} to 60 x 10^{-6} emu/g depending on the metal complex concentration, the type of transition metals, and the diamagnetic contributions of the organic polymer chemistries[7, 14, 84]. MPIL systems with higher concentrations of the high spin paramagnetic MCl_4^{n-} species (where M = Fe^{3+}, Co^{2+}, etc.) have demonstrated higher susceptibilities[7, 14] as was observed here for the MPIL copolymers with higher metal mole equivalencies. MPILs and MILs containing Co^{2+} counterions generally have lower magnetic susceptibilities than Fe^{3+} based systems [19, 85] as was also observed here. The paramagnetism of a material is dependent on the total orbital and spin angular moment of unpaired

electrons in the complex under an applied magnetic field. For the tetrahedral anions $[MCl_4]^{n-}$, the higher magnetic mass susceptibilities of $[FeCl_4]^-$ species compared to $[CoCl_4^{2-}]$ species is due to the higher electron spin state of the $[FeCl_4^-]$ (5/2 spin) compared to the $[CoCl_4]^{2-}$ anion (3/2 spin). However, for different coordinating ligands, the geometry and distortion of the coordination complex, the ligand field strength (i.e., spectrochemical series), and the oxidation state of the transition metal ion may significantly influence the spin state and the net orbital angular momentum of unpaired electrons in the complex[86, 87]. Therefore, the formation of metal-ion complexes coordinated with the acrylamide comonomer and different concentrations of this complex compared to the high spin $[FeCl_4]^-$ and $[CoCl_4]^{2-}$ complexes may potentially influence the overall magnetic susceptibility of each MPIL copolymer. Due to instrument limitations, a full temperature study of magnetic susceptibility could not be performed to confirm paramagnetic behavior. However, assuming the MPILs are paramagnetic at room temperature with negligible magnetic correlations, the effective magnetic moment can be estimated by $\mu_{eff} = \sqrt{8\chi T}$ where χ is the molar susceptibility and T is the temperature 298 K[88]. The μ_{eff} per mole of $FeCl_3$ was found to be 4.72 , 4.89, and 4.95 μ_B (Bohr magnetron) for the [Pam-*co*-PDADMA][Fe^{3+} 1eq], [Pam-*co*-PDADMA][Fe^{3+} 2eq], and [Pam-*co*-PDADMA][Fe^{3+} 3eq], respectively. These effective magnetic moments are lower than the expected 5.9 μ_B for high spin Fe^{3+} (5/2 spin) and similar moments observed for single component MILs and MPILs containing $[FeCl_4]^-$ counterions[9, 19, 88]. The cobalt-based MPIL copolymers had effective magnetic moments of 3.69, 3.99, and 3.95 μ_B per mole of $CoCl_2$ with increasing cobalt halide concentration. These values are in closer agreement with the expected high spin Co^{2+} (3/2) spin of 3.88 μ_B though still lower than effective moments typically observed for $[CoCl_4]^{2-}$ based systems (4.2-5.2 μ_B) [19, 88, 89]. These results suggest that the metal ion-acrylamide coordination does contribute to a reduction in the overall effective magnetic

moment, and that coordination effects from comonomers or co-materials should be carefully considered in future design of multi-component MPIL systems. The authors are currently conducting further magnetometry studies as a function of metal chloride concentration, magnetic field strength, and temperature to verify paramagnetic behavior of these MPIL copolymers and evaluate the presence of magnetic correlations.

The magnetic properties of the solution samples were also examined. Fully solvated polymer solutions, such as the [Pam-*co*-PDADMA][Co^{2+}] series samples, did not respond to the neodymium magnet. This lack of magnetic response for the MPIL is due to some degree of dissociation of the magnetic metal complexes from the polymer and hydration of the Co^{2+} ion into a cationic $[Co(H_2O)_6]^{2+}$ coordination complex as indicated by the pink color of these solutions (Figure 2.2 b) [90]. Precipitants from the partially insoluble iron and mixed series samples did visually respond to the magnet in water (Supplemental Video V10), which has been observed for other MPIL particles in nonsolvents[40, 91, 92] or MPILs complexed to insoluble particles[15]. In similar small molecule MIL and Mag-surf systems, this magnetic response in an aqueous environment is predominately attributed to confining the paramagnetic ions into a hydrophobic domain (e.g. immiscible MILs or hydrophobic surfactant cores) or the Stern layer of an insoluble particle[21, 93, 94]. Here, the observed magnetic responses for the [Pam-*co*-PDADMA][Fe^{3+}] and [Pam-*co*-PDADMA][Mixed Fe^{3+}/Co^{2+}] series MPILs are due to the confinement of the paramagnetic iron species within the insoluble polymer precipitants.

Magnetic mass susceptibilities of the copolymer solutions and suspensions were also measured (Figure 2.10 b). Generally, the susceptibilities of the MPILs in solution were approximately 1 to 10 x 10^{-6} emu/g lower in an aqueous environment than their dry counterparts, likely due to dissociation of some of the paramagnetic species into the aqueous phase. Both the [Pam-*co*-

PDADMA][Fe^{3+}] and [Pam-*co*-PDADMA][Mixed Fe^{3+}/Co^{2+}] copolymer series showed a linear increase in magnetic susceptibilities with metals content while the cobalt series did not significantly increase. These magnetic susceptibility data match the qualitative visual magnet responses. As stated before, the iron species in the [Pam-*co*-PDADMA][Fe^{3+}] and [Pam-*co*-PDADMA][Mixed Fe^{3+}/Co^{2+}] MPIL copolymers is being retained in the insoluble polymeric precipitants while the Co^{2+} species dissociate, at least in part, from the polymer and hydrate in solution. Interestingly, the [Pam-*co*-PDADMA][Co^{2+} 1eq] samples showed a slight increase to 20.8 x 10^{-6} emu/g in the liquid state from 17.5 x 10^{-6} emu/g in the dry state. One possible interpretation would be that, as the Co^{2+} species are dissociating from the polymer, the measured susceptibility for this sample is predominately from the high spin $[Co(H_2O)_6]^{2+}$ species without the added diamagnetic contribution of the [Pam-*co*-PDADMA][Cl^-] copolymer. However, even though the concentration of the cobalt species increases in the 2 and 3 eq cases, the ions are dispersed in the liquid phase and do not interact or contribute to long-range ordering in solution. Whereas the iron species confined in the polymer matrix do interact allowing for long-range ordering at higher equivalents. These results indicate that the acrylamide metal coordinating comonomer also plays a role in the MPIL copolymer magnetic behavior in solutions or suspensions.

2.4. Conclusions

Poly(acrylamide-*co*-diallyl dimethylammonium chloride) is a poly(ionic liquid) (PIL) copolymer containing quaternary ammonium IL groups and comonomer groups capable of metal coordinating interactions. Complexation with Co^{2+} and Fe^{3+} metal halide salts was utilized to form magnetic PIL (MPIL) copolymers. The impact of metal salt cation type and concentration were examined. Color and solubility results showed metal-polymer complexation was occurring, but the

complexation was changing as a function of metal type and molar equivalency. To verify the metal species-polymer binding interactions and the metal complex structure, the MPIL samples were examined with multiple spectroscopic methods.

Binding interactions for these unique MPIL polymers were characterized in both the liquid and dry states using multiple molecular absorption spectroscopic techniques. Raman and UV-vs spectroscopy results confirmed the formation of the $[FeCl_4]^-$ and $[CoCl_4]^{2-}$ species in the dry MPIL copolymer particularly through the presence of the Fe-Cl str 314 cm^{-1} Raman mode and UV-vis 250, 315, and 360 nm absorbances for the $FeCl_4^-$ anion and the ~630, ~665, and ~690 nm UV-vis absorbances for $[CoCl_4]^{2-}$. However, these spectroscopies also indicated the presence of metal cation-acrylamide coordination species as well through a broad Raman band between 600-200 cm^{-1} typical for M-O and M-N stretching modes for both iron and cobalt-based MPILs. UV-vis further showed a change in the Fe^{3+} species coordination structure with increasing iron concentration from 1 to 2 mole equivalences, indicating the iron coordinates first with acrylamide before forming the anionic $[FeCl_4]^-$ and $[Fe_2Cl_7]^-$ species denoted by characteristic peaks at ca. 250, 315, and 360 nm. UV-vis results of the MPILs in aqueous solution indicate the formation of octahedral Co^{2+} species through the emergences of the peaks at 465 and 510 nm and various $Fe(OH)_x$ and $FeCl_3$ aq. species with broad absorbances between 300-500 nm. FTIR results confirm metal-acrylamide coordination for both metal cations through both O- and N-bonding with the amide group as indicated by significant downshifts in both the amide I (C=O str) and amide II (NH_2 wag) IR modes. Downshifts were found to be greater for the [Pam-*co*-PDADMA][Fe^{+3}] copolymer (12-19 cm^{-1} amide I, 41-50 cm^{-1} amide II) compared to the [Pam-*co*-PDADMA][Co^{2+}] copolymers (6-14 cm^{-1} amide I, 11-18 cm^{-1} amide II) with intermediate behavior for the [Pam-*co*-PDADMA][Mixed Fe^{3+}/Co^{2+}] copolymer system. While downshifts in the quaternary ammonium methyl bending

modes were also observed, XPS spectroscopy results indicated only small increases in binding energy (~0.1-0.2 eV) for the corresponding ammonium N1s peak. Large increases in binding energy for the O-bonding Pam-NH_2 N1s peak and the emergence of the N-bonding Pam-$H_2N^+\cdots M$ N1s reveal that the main binding mechanism between the copolymer and metal species is through acrylamide coordination.

Magnetic properties of the MPIL copolymers were confirmed using AC susceptibility measurements and showed magnetic mass susceptibilities comparable to other MPIL homopolymer and copolymer systems (~17 to 44 x 10^{-6} emu/g) in the dry state and were visually responsive to a 0.6 T magnet. While the cobalt-based MPILs were completely soluble in water and displayed no visual magnetic response, the partially insoluble iron-based MPILs were visually responsive to magnetic field and displayed magnetic mass susceptibilities between 23.5 and 35.9 x 10^{-6} emu/g. Here, coordination with the acrylamide unit is believed to account for the partial insolubility and resulting magnetic response in aqueous based systems.

This work describes the first synthesis of [Pam-*co*-PDADMA][Fe^{3+}] and [Pam-*co*-PDADMA][Co^{2+}] MPIL copolymers reported in the literature. In addition, the authors are not aware of MPILs being characterized using XPS prior to this study. Most importantly this study demonstrated not only binding between the metal in the counterion and the amide group of the acrylamide monomer group, but it provided insight into the coordination structures of the transition metal halide complexes. Understanding transition metal ions interactions in MPIL systems will guide the design and selection criteria for other magnetically responsive PIL functional materials, particularly in multicomponent systems.

Acknowledgements

We would like to thank Andrew Rodriguez and Dr. Megan Madden (University of Oklahoma) for their aid in Raman data collection, as well as Dr. Matt Hamilton and Dr. Richard D. Elmore (University of Oklahoma) for their aid in the magnetic mass susceptibility measurements.

2.5. References

(1) A. Munoz-Bonilla and M. Fernandez-Garcia, *Eur. Polym. J.*, 2018, **105**, 135-149.

(2) W. Qian, J. Texter and F. Yan, *Chem. Soc. Rev.*, 2017, **46**, 1124-1159.

(3) J. Yuan, D. Mecerreyes and M. Antonietti, *Prog. Polym. Sci.*, 2013, **38**, 1009-1036.

(4) J. Guo, L. Qiu, Z. Deng and F. Yan, *Polymer Chemistry*, 2013, **4**, 1309-1312.

(5) J. Yang, H. Wang, J. Wang, X. Guo and X. Pei, *Langmuir*, 2016, **32**, 66-72.

(6) H. L. Ricks-Laskoski and A. W. Snow, *Journal of the American Chemical Society*, 2006, **128**, 12402-12403.

(7) M. Dobbelin, V. Jovanovski, I. Llarena, L. J. C. Marfil, G. Cabanero, J. Rodriguez and D. Mecerreyes, *Polym. Chem.*, 2011, **2**, 1275-1278.

(8) K. D. Clark, O. Nacham, J. A. Purslow, S. A. Pierson and J. L. Anderson, *Analytica Chimica Acta*, 2016, **934**, 9-21.

(9) S. Hayashi, S. Saha and H. Hamaguchi, *IEEE Transactions on Magnetics*, 2006, **42**, 12-14.

(10) A. Joseph, G. Żyła, V. I. Thomas, P. R. Nair, A. S. Padmanabhan and S. Mathew, *Journal of Molecular Liquids*, 2016, **218**, 319-331.

(11) P. Brown, T. Alan Hatton and J. Eastoe, *Current Opinion in Colloid & Interface Science*, 2015, **20**, 140-150.

(12) L. Wang, S. Dong and J. Hao, *Current Opinion in Colloid & Interface Science*, 2018, **35**, 81-90.

(13) N. Sahiner, S. Demir and S. Yildiz, *Colloids and Surfaces A: Physicochemical and Engineering Aspects*, 2014, **449**, 87-95.

(14) I. Chikh Alard, J. Soubhye, G. Berger, M. Gelbcke, S. Spassov, K. Amighi, J. Goole and F. Meyer, *Polym. Chem.*, 2017, **8**, 2450-2456.

(15) G. Hazell, M. Hinojosa-Navarro, T. M. McCoy, R. F. Tabor and J. Eastoe, *Journal of Colloid and Interface Science*, 2016, **464**, 285-290.

(16) C. de la Fuente-Nunez, P. Brown, M. D. T. Torres, J. Cao and T. K. Lu, *Colloid and Interface Science Communications*, 2018, **22**, 11-13.

(17) X. Yu, Z. Xia, T. Zhao, X. Yuan and L. Ren, *Macromolecules*, 2021, **54**, 4227-4235.

(18) X. Yu, X. Yuan, Y. Zhao and L. Ren, *ACS Macro Letters*, 2019, **8**, 1504-1510.

(19) A. Bonnefond, M. Ibarra, D. Mecerreyes and J. R. Leiza, *J. Polym. Sci., Part A: Polym. Chem.*, 2016, **54**, 1145-1152.

(20) J. Cui, S. Yang, J. Zhang, S. Zhao and Y. Yan, *RSC Advances*, 2012, **2**, 12224-12230.

(21) T. M. McCoy, P. Brown, J. Eastoe and R. F. Tabor, *ACS Applied Materials & Interfaces*, 2015, **7**, 2124-2133.

(22) J. Yang, W. Sun, W. Lin and Z. Shen, *Journal of Polymer Science Part A: Polymer Chemistry*, 2008, **46**, 5123-5132.

(23) C. D. Easton, C. Kinnear, S. L. McArthur and T. R. Gengenbach, *Journal of Vacuum Science & Technology A*, 2020, **38**, 023207.

(24) M. C. Biesinger, B. P. Payne, A. P. Grosvenor, L. W. M. Lau, A. R. Gerson and R. S. C. Smart, *Applied Surface Science*, 2011, **257**, 2717-2730.

(25) A. P. Grosvenor, B. A. Kobe, M. C. Biesinger and N. S. McIntyre, *Surface and Interface Analysis*, 2004, **36**, 1564-1574.

(26) K. B. Girma, V. Lorenz, S. Blaurock and F. T. Edelmann, *Coordination Chemistry Reviews*, 2005, **249**, 1283-1293.

(27) H. Sigel and R. B. Martin, *Chemical Reviews*, 1982, **82**, 385-426.

(28) R. C. Dunbar, J. Martens, G. Berden and J. Oomens, *International Journal of Mass Spectrometry*, 2018, **429**, 198-205.

29. R. C. Dunbar, N. C. Polfer, G. Berden and J. Oomens, *International Journal of Mass Spectrometry*, 2012, **330-332**, 71-77.

30. K. B. Girma, V. Lorenz, S. Blaurock and F. T. Edelmann, *Zeitschrift für anorganische und allgemeine Chemie*, 2005, **631**, 2763-2769.

(31) T. Bäcker, O. Breunig, M. Valldor, K. Merz, V. Vasylyeva and A.-V. Mudring, *Crystal Growth & Design*, 2011, **11**, 2564-2571.

(32) K. Nakamoto, in *Handbook of Vibrational Spectroscopy*, 2001, DOI: https://doi.org/10.1002/0470027320.s4104.

(33) R. P. Rathore, S. S. Khatri and T. Chakraborty, *J. Raman Spectrosc.*, 1987, **18**, 429-434.

(34) A. Wesełucha-Birczyńska and C. Paluszkiewicz, *Journal of Molecular Structure*, 2002, **614**, 339-343.

(35) A. I. Freire and W. A. Alves, *Vibrational Spectroscopy*, 2014, **73**, 73-78.

(36) S. H. J. De Beukeleer and H. O. Desseyn, *Spectrochimica Acta Part A: Molecular Spectroscopy*, 1994, **50**, 2291-2309.

(37) K. Murata and D. E. Irish, *Spectrochim. Acta, Part A*, 1988, **44A**, 739-743.

(38) G. Socrates, *Infrared and Raman Characteristic Group Frequencies Tables and Charts*, John Wiley & Sons, LTD, Baffins Lane, Chichester, West Sussex PO19 1UD, England, 3rd edn., 2001.

(39) S. K. Sharma, *The Journal of Chemical Physics*, 1974, **60**, 1368-1375.

(40) X. Yu, X. Yuan, Y. Zhao and L. Ren, *RSC Advances*, 2015, **5**, 92207-92211.

(41) R. Ma, Z. Liu, K. Takada, K. Fukuda, Y. Ebina, Y. Bando and T. Sasaki, *Inorganic Chemistry*, 2006, **45**, 3964-3969.

(42) V. Sivo, G. D'Abrosca, L. Russo, R. Iacovino, P. V. Pedone, R. Fattorusso, C. Isernia and G. Malgieri, *Bioinorganic Chemistry and Applications*, 2017, **2017**, 1527247.

(43) J. Bjerrum, A. S. Halonin, L. H. Skibsted, A. F. Andresen, J. T. Southern, K. R. Edlund, M. Eliasen, C. Herskind, T. Laursen and P. M. Pedersen, *Acta Chemica Scandinavica*, 1975, **6**, 326-332.

(44) S. Chaouachi, S. Elleuch, B. Hamdi and R. Zouari, *Journal of Molecular Structure*, 2016, **1125**, 149-161.

(45) H. Ma, C. Wan and A. H. Zewail, *Proceedings of the National Academy of Sciences*, 2008, **105**, 12754-12757.

(46) M. B. Vraneš, S. M. Papović and S. B. Gadžurić, *Journal of Solution Chemistry*, 2019, **48**, 1364-1377.

(47) N. Banić, M. Vraneš, B. Abramović, J. Csanádi and S. Gadžurić, *Dalton Transactions*, 2014, **43**, 15515-15525.

(48) S. A. Markarian, H. H. Ghazoyan, H. R. Sargsyan and G. A. Shahinyan, *Journal of Solution Chemistry*, 2019, **48**, 1378-1392.

(49) H. Dweik, W. Sultan, M. Sowwan and S. Makharza, *International Journal of Polymeric Materials and Polymeric Biomaterials*, 2008, **57**, 228-244.

(50) M. Sowwan, *International Journal of the Physical Sciences*, 2011, **6**.

(51) H. Aoshima, K. Satoh, T. Umemura and M. Kamigaito, *Polymer Chemistry*, 2013, **4**, 3554-3562.

(52) G. A. Gamlen and D. O. Jordan, *Journal of the Chemical Society (Resumed)*, 1953, DOI: 10.1039/JR9530001435, 1435-1443.

(53) W. Liu, B. Etschmann, J. Brugger, L. Spiccia, G. Foran and B. McInnes, *Chemical Geology*, 2006, **231**, 326-349.

(54) M. Torras, C. Moya, G. A. Pasquevich and A. Roig, *Microchimica Acta*, 2020, **187**, 488.

(55) C. Loures, Alcantara, M., Filho, H., Teixeira, A., Silva, F., Paiva, T., Samananmud, G., *International Review of Chemical Engineering (IRECHE)*, 2013, **5**, 102-120.

(56) A. Barth, *Biochimica et Biophysica Acta (BBA) - Bioenergetics*, 2007, **1767**, 1073-1101.

(57) K. B. Girma, V. Lorenz, S. Blaurock and F. T. Edelmann, *Zeitschrift für anorganische und allgemeine Chemie*, 2005, **631**, 1843-1848.

(58) S. J. Kim, S. G. Yoon, I. Y. Kim and S. I. Kim, *Journal of Applied Polymer Science*, 2004, **91**, 2876-2880.

(59) E. Pigorsch, *Starch - Stärke*, 2009, **61**, 129-138.

(60) Y. Shin, W. H. Cheung, T. T. M. Ho, K. E. Bremmell and D. A. Beattie, *Physical Chemistry Chemical Physics*, 2014, **16**, 22409-22417.

(61) J. Zhang, J. Qiao, G. Jiang, L. Liu and Y. Liu, *Journal of Power Sources*, 2013, **240**, 359-367.

(62) O. Halevi, J. Chen, G. Thangavel, S. A. Morris, T. Ben Uliel, Y. R. Tischler, P. S. Lee and S. Magdassi, *RSC Advances*, 2020, **10**, 14812-14817.

(63) B. M. Marsh, J. Zhou and E. Garand, *RSC Advances*, 2015, **5**, 1790-1795.

(64) K. B. Girma, V. Lorenz, S. Blaurock and F. T. Edelmann, *Zeitschrift für anorganische und allgemeine Chemie*, 2005, **631**, 1419-1422.

(65) T. F. Zafiropoulos, S. P. Perlepes, P. V. Ioannou, J. M. Tsangaris and A. G. Galinos, *Zeitschrift für Naturforschung B*, 1981, **36**, 87-93.

(66) S. Chen and H. Tanaka, *Journal of Wood Science*, 1998, **44**, 303-309.

(67) S. Men, K. R. J. Lovelock and P. Licence, *Physical Chemistry Chemical Physics*, 2011, **13**, 15244-15255.

(68) R. K. Blundell and P. Licence, *Chemical Communications*, 2014, **50**, 12080-12083.

(69) R. L. McLaren, G. R. Owen and D. J. Morgan, *Results in Surfaces and Interfaces*, 2022, **6**, 100032.

(70) E. Desimoni and B. Brunetti, *Chemosensors*, 2015, **3**, 70-117.

(71) Y. J. Kim and C. R. Park, *Inorganic Chemistry*, 2002, **41**, 6211-6216.

(72) R. K. Blundell and P. Licence, *Physical Chemistry Chemical Physics*, 2014, **16**, 15278-15288.

(73) T. Cremer, C. Kolbeck, K. R. J. Lovelock, N. Paape, R. Wölfel, P. S. Schulz, P. Wasserscheid, H. Weber, J. Thar, B. Kirchner, F. Maier and H.-P. Steinrück, *Chemistry – A European Journal*, 2010, **16**, 9018-9033.

(74) A. W. Taylor, S. Men, C. J. Clarke and P. Licence, *RSC Advances*, 2013, **3**, 9436-9445.

(75) H. Zhang, Z. Liu, J. Mai, N. Wang, H. Liu, J. Zhong and X. Mai, *Advanced Science*, 2021, **8**, 2100320.

(76) C. Madrona, M. Vila, F. E. Oropeza, V. A. de la Peña O'Shea and J. J. Vilatela, *Carbon*, 2021, **173**, 311-321.

(77) Y. Wang, H. Zhang, Y. Zhu, Z. Dai, H. Bao, Y. Wei and W. Cai, *Advanced Materials Interfaces*, 2016, **3**, 1500801.

(78) T. Ivanova, A. Naumkin, A. Sidorov, I. Eremenko and M. Kiskin, *Journal of Electron Spectroscopy and Related Phenomena*, 2007, **156-158**, 200-203.

(79) M. V. Russo, G. Polzonetti, A. Furlani, A. Bearzotti, I. Fratoddi and P. Altamura, *Journal of Vacuum Science & Technology A*, 1998, **16**, 35-44.

(80) J. F. Moulder and J. Chastain, *Handbook of X-ray Photoelectron Spectroscopy: A Reference Book of Standard Spectra for Identification and Interpretation of XPS Data*, Physical Electronics Division, Perkin-Elmer Corporation, 1992.

(81) N. Calisi, S. Martinuzzi, A. Giaccherini, C. S. Pomelli, L. Guazzelli and S. Caporali, *Journal of Electron Spectroscopy and Related Phenomena*, 2021, **247**, 147034.

(82) M. D. Nguyen, L. V. Nguyen, E. H. Jeon, J. H. Kim, M. Cheong, H. S. Kim and J. S. Lee, *Journal of Catalysis*, 2008, **258**, 5-13.

(83) D. G. Brown and U. Weser, *Zeitschrift für Naturforschung B*, 1979, **34**, 1468-1470.

(84) J. J. Malecha, J. R. Biller, B. Lama and D. L. Gin, *ACS Macro Letters*, 2020, **9**, 140-145.

(85) R. E. Del Sesto, T. M. McCleskey, A. K. Burrell, G. A. Baker, J. D. Thompson, B. L. Scott, J. S. Wilkes and P. Williams, *Chemical Communications*, 2008, DOI: 10.1039/B711189D, 447-449.

(86) S. Blundell, *Magnetism in Condensed Matter*, Oxford University Press, Oxford University Press Inc., New York, 2001.

(87) M. W. Duward Shriver, Tina Overton, Jonathan Rourke, Fraser Armstrong, *Inorganic Chemistry*, Oxford University Press, Great Britain Sixth edn., 2014.

(88) S. Mugiraneza and A. M. Hallas, *Communications Physics*, 2022, **5**, 95.

(89) P. Brown, C. P. Butts, J. Eastoe, S. Glatzel, I. Grillo, S. H. Hall, S. Rogers and K. Trickett, *Soft Matter*, 2012, **8**, 11609-11612.

(90) A. Fortenberry, D. Reed, A. Smith and P. Scovazzo, *Langmuir*, 2019, **35**, 11843-11849.

(91) Y. Ohara, Y. Kawata, A. Hyde, C. Phan, R. Takeda, Y. Takemura and S.-i. Yusa, *Chemistry Letters*, 2017, **46**, 1473-1475.

(92) T. Zhang, X. Yu, X. Yuan, Y. Zhao and L. Ren, *Polymer*, 2018, **135**, 9-15.

(93) P. Beck, M. Liebi, J. Kohlbrecher, T. Ishikawa, H. Rüegger, H. Zepik, P. Fischer, P. Walde and E. Windhab, *The Journal of Physical Chemistry B*, 2010, **114**, 174-186.

(94) O. Nacham, K. D. Clark, H. Yu and J. L. Anderson, *Chemistry of Materials*, 2015, **27**, 923-931.

Chapter 3: Development of Nano- and Micro- Fluids Using Magnetic Poly(ionic liquid)-Surfactant Complexes for Stimuli Response

* This chapter is adapted from a published conference paper: Foley, K, & Walters, KB. "Development of Nano- and Micro-Fluids Using Magnetic Poly(Ionic Liquid)-Surfactant Complexes for Stimuli Response." *Proceedings of the ASME 2022 Fluids Engineering Division Summer Meeting. Volume 2: Multiphase Flow (MFTC); Computational Fluid Dynamics (CFDTC); Micro and Nano Fluid Dynamics (MNFDTC)*. Toronto, Ontario, Canada. August 3–5, 2022. V002T06A006. ASME. https://doi.org/10.1115/FEDSM2022-87758

Abstract

Poly(ionic liquid) (PILs) are a rapidly growing subclass of polyelectrolyte which combines the diverse functionality of ionic liquids with the mechanical integrity, processability, and macromolecular design of polymeric systems. PIL properties are highly dependent on their counterion, which can be easily exchanged to tailor their material properties. Incorporation of metal halide counterions ($[FeCl_4]^-$, $[CoCl_4]^{2-}$, etc.) into the PIL structure results in magnetically responsive metal-salt composites known as magnetic-PILs (MPILs). MPILs are predominately formed through electrostatic binding with anionic metal complexes typically resulting in paramagnetic properties at room temperature. The engineering properties and the ability to effectively apply these materials—is dependent on not only the chemical structure, but the nanostructure, co-materials, self-assembly, and stability in situ. In this study, a PIL copolymer, poly[acrylamide-*co*-diallyl dimethylammonium chloride], containing a quaternary ammonium PIL group and a comonomer capable of metal coordinating interactions, was combined with sodium dodecyl sulfate surfactant and cobalt (II) chloride salts to form magnetic polyelectrolyte-surfactant complexes. The self-assembly of these complexes was studied as a function of surfactant

concentration through DLS, Zeta potential, and TEM characterizations. The magnetic properties were examined using AC susceptibility. The impact of the metal ion(s) and magnetic field on nanostructure alignment and film formation were also investigated through optical microscopy, GISAXS, and AFM imaging. Results were compared to well-defined ferrofluids as a comparative benchmark.

3.1. Introduction

Poly(ionic liquid)s, or PILs, are a type of strong polyelectrolyte composed of a polymeric backbone with ionic liquid species in each repeat unit. Like their ionic liquid counterparts, PILs display a variety of favorable properties, such as high ion conductivity [1, 2], adhesive behavior [3], high stability in thermal and electrical environments [4, 5], tunable solubility [6], and more. PIL characteristics are easily tunable through a simple counterion exchange or complexation, making these polymers a unique and tailorable material for a variety of applications.

Recently, metal-containing PILs also known as magnetic PILs (MPILs), have emerged as an interesting class of stimuli-responsive polymers. MPILs are typically formed through complexation of metal salts (e.g., $FeCl_3$, $CoCl_2$) with PIL counterions to form paramagnetic counterions (e.g., $[FeCl_4]^-$, $[CoCl_4]^{2-}$). Like their magnetic ionic liquid (MIL) [7, 8] and magnetic surfactant (Mag-Surf) [9, 10] small-molecule counterparts, they can respond to relatively weak magnetic fields (< 2 T). However, due to the macromolecular nature of PILs, these materials typically show greater effective magnetic moments than MILs or Mag-surfs, being able to complex to greater amounts of paramagnetic metal [11]. These intrinsically magnetic polymers can be processed into a variety of materials including powders, films [12], copolymers [11, 13], composites [14-16], and nanomaterials [17].

Recently, magnetic surfactants have been used to aid in the nano-assembly of soft materials and magnetically manipulate or align nanomaterials in solutions in the presence of a magnetic field. Xu et al. successfully compacted elongated surfactant-DNA complexes into spherical particles under the influence of a 0.25 T field utilizing cationic surfactants with a $[FeCl_3Br]^-$ counterion [18]. Polarz et al. magnetically aligned tactoidal structures composed of surfactants coordinated with paramagnetic Dy^{3+} cations in water [19]. Beck et al. developed phospholipid-based vesicles chelated with paramagnetic lanthanides that could orient in magnetic fields after temperature-induced partial solid domain formation occurred in the vesicle [20]. McCoy et al. complexed ammonium- and imidazolium-based iron halide surfactants to graphene oxide sheets for magnetic separation from aqueous solution. Later, they achieved similar graphene oxide separation with a cationic MPIL and used the complexed material for gold nanoparticle and antibiotic magnetic separations [14].

While MPILs show similar potential for magnetically induced nanomaterial assembly or alignment, most MPIL studies have only focused on synthesis and investigation of general magnetic properties through magnetometry or visual attraction to a magnet. No studies to our knowledge have examined the magnetic response of MPIL nanomaterial in micellar solutions, nor at the effect of magnetic fields on the magnetic alignment of MPIL solution nanostructures or films.

In our recent work [21], we investigated the interactions of paramagnetic salt in a PIL copolymer containing acrylamide comonomers and their magnetic properties. Specifically, we studied the metal-polymer interactions and magnetic behavior of poly[acrylamide]-*co*-poly[diallyl dimethyl ammonium chloride] random copolymers complexed with $FeCl_3$ and $CoCl_2$ metal salts. These

systems showed magnetic susceptibilities ranging from 17 to 45 $x10^{-6}$ emu/g and were visually attracted to a 0.7 T neodymium magnet in the dry state or in the form of precipitants in solution.

Herein, we induce self-assembly of this copolymer MPIL by introducing the anionic surfactant, sodium dodecyl sulfate, to aqueous solutions of cobalt complexed poly[acrylamide-*co*-diallyl dimethyl ammonium chloride] copolymers. We perform a thorough examination of their complex formation in aqueous solution through particle sizing (DLS and TEM) and surface charge characterization techniques (ZP) and compare their behavior to metal-free PIL complexation. The magnetic properties are evaluated both in the dry and solution states through AC magnetic susceptibility measurements and optical microscopy in the presence of a magnetic field. These results are compared to magnetic iron oxide nanoparticles (MNPs) developed by our group [22-25]. We also examined the effect of magnetic field on polymer-surfactant film formation.

This study will guide the development of novel nano and micro-fluids in the examination of fluid behavior and characteristics at the nano- to micro-scales. In particular, the work will aid in the study of fluid control and structuring under non-contact forces, such as magnetic (studied here), ionic, or electrical fields. The ability to structure fluids over both short and long ranges through external stimuli have shown considerable interest in recent years, such as magnetically controlled fluid structuring or dielectrophoresis nano assembly [26-31]. As intrinsically ionic materials, ILs and PILs show good potential as dielectric materials for electrorheological and electric stimuli response [4, 32]. In addition to paramagnetism, including transition metals in these systems will incorporate favorable properties for potential applications in self-healing, optical properties, reversible coordination, and catalysis, and more [13, 33-36].

3.2. Materials and methods

3.2.1. Materials

A 10 wt% poly[acrylamide-*co*-diallyl dimethylammonium chloride] solution in water was used which was 55% acrylamide by weight—with a weight average molecular weight of 277,307 g/mol and a polydispersity index of 1.94 as measured by aqueous GPC. The acrylamide and ammonium monomer units will be defined as DADMA and Am, respectively. $CoCl_2*6H_2O$ (CAS 7646-79-9) and $FeCl_3*6H_2O$ (CAS 7705-08-0) were purchased from Sigma Aldrich. Sodium dodecyl sulfate (99% purity, CAS 151-21-3) was purchased from Sigma Aldrich and recrystallized in ethanol before use.

3.2.2. Synthesis of magnetic poly(ionic liquid) copolymers

Magnetic poly(ionic liquid) copolymers were synthesized as reported previously [21]. Figure 3.1 shows the synthesis of the MPIL copolymer and subsequent complexation with surfactant. In brief, an aqueous solution of cobalt (II) chloride was added dropwise to an aqueous solution of copolymer under stirring. The solution was allowed to stir overnight. The water was allowed to evaporate, and the resulting dark blue polymer material was dried in a vacuum oven overnight to remove residual water. The final MPIL had 1 equivalent (3.09 mmol) of added $CoCl_2$ relative to the DADMA unit.

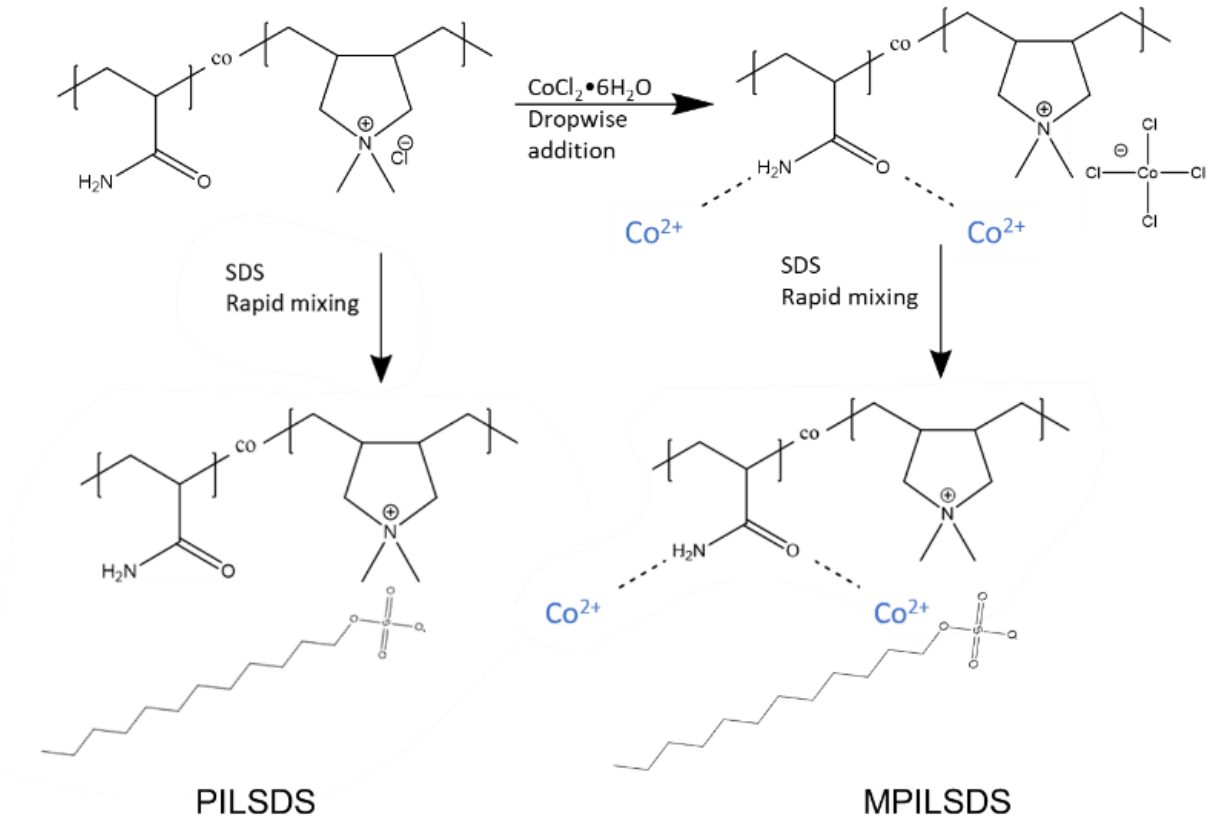

Figure 3.1 Chemical Structure and Synthesis of MPILs, and complexation with Surfactant to form PILSDS and MPILSDS Complex solutions.

3.2.3. Formation of magnetic polymer-surfactant complexes

Aqueous solutions of 2 mg/mL PIL copolymer, MPIL copolymer, and SDS solutions of varying concentration were prepared separately. 2 ml of copolymer solution was added to a test tube with a magnetic stirrer. While under stirring at 900 rpm, 2 ml of SDS solution was rapidly added to the test tube and allowed to stir for approximately 10 sec. Immediate clouding or bluing of the solution could be observed for certain surfactant concentrations. All solutions were allowed to age for 2 days before characterization. The final polymer-surfactant complex solutions (PILSDS or MPILSDS) had a polymer concentration of 1 mg/mL (2.7 mM based on the DADMA monomer unit and 7.74 mM based on the Am monomer unit) and surfactant concentrations between 3 and

16 mM. With respect to the PDADMA unit, there was 2.7 mM cobalt chloride in the polymer-surfactant system.

3.2.4. MPIL film formation

Silicon wafers were prepared by sonication in isopropyl alcohol solution for 10 minutes three times. They were then dried with filtered N_2(g) and cleaned with a UV-Ozone cleaner for 5 minutes. The wafers were then treated with piranha solution (70/30 v/v of 30% H_2O_2 and 95%w/w H_2SO_4) for at least 30 minutes. Wafers were then rinsed 3 times in filtered Millipore water before storing in a sealed container of Millipore water before use. Wafers were dried with filtered N_2(g) after removal from water storage immediately before sample preparation. 20 μL of MPILSDS-7mM was deposited on the wafer and left to dry in the fume hood. For wafers dried in the presence of a magnetic field, the wafer was placed between two 0.7 T neodymium magnets held 1 cm apart.

3.2.5. Characterizations

An AC magnetic susceptibility meter (Kappabridge MFK1) was used to determine the MPIL and MPILSDS magnetic susceptibilities. The magnetic field strength was 450 A/m and the AC field frequency was 976 Hz. The diamagnetic contributions of the sample holder were subtracted from the volume susceptibility and then normalized for mass. Attenuated total reflection Fourier infrared spectroscopy (ATR-FTIR) spectroscopy was performed on a Nicolet IS50R spectrometer (ThermoFisher Scientific) with 4 cm^{-1} resolution and a minimum of 64 scans over the spectral range of 4000-400 cm^{-1}. Dynamic light scattering (DLS) and zeta potential (ZP) was performed on a Nanobrook Omni particle analyzer (Brookhaven Instruments) using a 640 nm laser at 90° angle. Hydrodynamic diameters were determined using non-negative least squares (NNLS) model. ZP measurements were analyzed with the Smoluchowski model. Cryo-TEM imaging were performed on a JEOL 2010F field emission transmission electron microscope. 10-20 μL of the

MPILSDS solution was applied to plasma treated Lacey carbon TEM grids before it was blotted for 2 seconds and plunged into liquid ethane with a cryo-plunger. Images were analyzed with ImageJ software. Particle diameter averages are reported with a 95% confidence interval. A Nikon Eclipse LV100D equipped with a Lumenera XInfinity1 digital camera was used to obtain bright and darkfield images of the MPILSDS films. Grazing Incidence Small Angle X-ray Scattering (GI-SAXS) scattering patterns of MPILSDS films were obtained with the SAXSPoint2.0 (Anton Paar). X-rays with a wavelength of 0.154 nm were produced from a $Cu^{k}\alpha$ source. The wafers were placed at sample to detector distance of 155.8 mm and measured with an incident angle greater than the critical angle of the polymer-surfactant film (~0.16°). Here, the MPILSDS films were formed on 1 x 1 cm glass microscope slides. One sample was similarly dried in the presence of a magnetic field as described above. For randomly oriented lamellae. AFM microscopy was also performed on these films with a Dimension Icon (Bruker) system in PeakForce Tapping modes using silicon cantilever tips with a reflective backside aluminum coating.

3.3. Results and Discussion

Nanoparticle assembly in random copolymers, including polyelectrolytes, can be induced by adding surfactants to the system to form polyelectrolyte-surfactant complexes (PE-surf), which form unique nanostructures including spherical particles, worm-like micelles, pearl-and-necklace, and vesicles (Figure 3.2) [37, 38]. The structure of the formed complexes depends on several factors including, polyelectrolyte charge density, polymer and surfactant chemical structure and concentration, co-salts and additives, and ionic strength [37, 39, 40]. In a typical PE-surf system, surfactant begins binding at binding sites on the polymer through electrostatic or attractive interactions, resulting in partial collapse of the polymer chains from an extended conformation to a coiled state. As the surfactant concentration increases, surfactant will start to bind cooperatively

with the polymer, interacting with neighboring already bound surfactant, until a critical aggregation concentration is reached where the polymer-surfactant system begins to form micelle-like structures. Eventually, the surfactant binds with all the charged monomer units, resulting in charge neutralization of the polymer and the formation of precipitants and ordered structures. At excess surfactant concentrations, the precipitants become stabilized and eventually resolubilize.

In this case, the anionic surfactant sodium dodecyl sulfate (SDS) was used to induce assembly of the polycationic PIL and MPIL copolymers in water. Figure 3.3a and Figure 3.3b shows the hydrodynamic diameters (D_H) by volume for the formed complexes for both the PIL and MPIL copolymer as a function of surfactant concentration. In general, two different size populations were formed for most SDS concentrations. The hydrodynamic diameter of the PIL without added surfactant or cobalt salt was ~43 nm. The MPIL copolymer showed two populations with diameters of approximately ~29 nm and ~58 nm.

For the PILSDS complexes, turbid white solutions of unstable particles were formed in the 1-4 mM SDS concentrations range, which had settled to the bottom of the vial during the aging period. We were able to redisperse the complexes formed with the 1 mM, which remained stable long enough to perform DLS measurements.

These concentrations showed D_H values between 0.5-1.3 μm. Precipitants formed from 1.9 mM and 3.6 mM SDS concentrations could not be redispersed. All other SDS concentrations formed transparent solutions with particle sizes between 20 and 50 nm, indicating solubilization of the polymer. No stable PILSDS complex nanostructures were observed in the SDS concentration range measured.

The MPILSDS system also formed unstable turbid complexes at surfactant concentrations below 4 mM SDS. However, at concentrations between 4 mM and 7 mM, stable MPILSDS

complexes were formed, displaying mildly white clouding or bluing. These stable complexes ranged in D_H from 100 to 500 nm, and generally decreased with increasing surfactant concentration. At concentrations greater than 8 mM, the solutions became transparent, with D_H values similar to the polymer-only solutions, indicating re-solubilization of the polymer and surfactant.

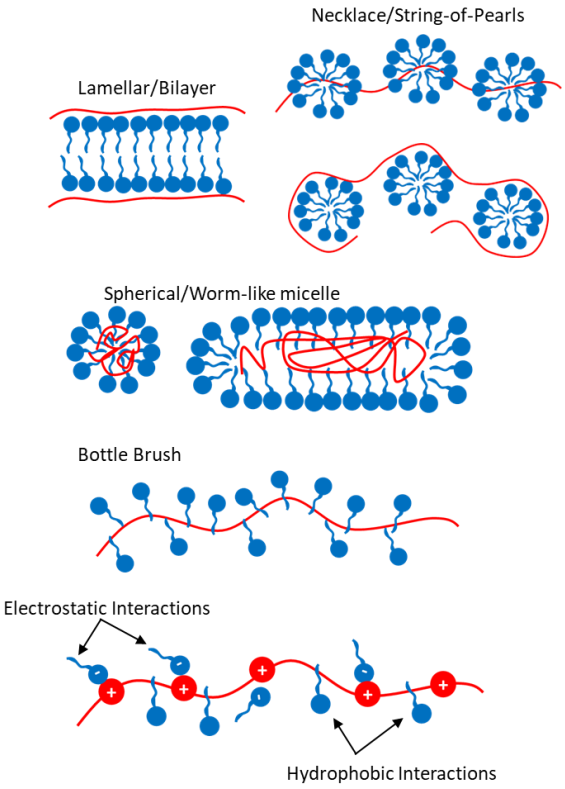

Figure 3.2 Examples of various polyelectrolyte-Surfactant complexes. Reproduced from Khan et al. [37]

Polyelectrolyte-surfactant binding is highly dependent on the electrostatic interactions between the components in addition to hydrophobic interactions. ZP measurements (Figure 3.3c) were taken to determine the overall surface charge of the formed complexes and provide insight to complex formation. The zeta potentials for the polymers PIL and MPIL with no surfactant were

14.2 mV and 20.6 mV respectively. The higher zeta potential of the MPIL copolymer indicates a higher positive surface charge of the polymer material, likely due to partial coordination of the added Co^{2+} cations to the acrylamide unit, indicating an increase in surface charge density.

Between 1-4 mM SDS concentration, where unstable complexes were formed, the zeta potential of redispersed complexes was 0.38 to -6.84 mV, indicating near charge neutrality of the particle surfaces. As anionic surfactant concentration increased, the surface charge became more negative, imparting stability to the complexes. This stability is attributed to adsorption of the hydrophobic surfactant alkyl chain with the neutralized complex surface and interaction of the anionic head group with the water phase, leading to a negative surface charge [41, 42]. The PILSDS complexes rapidly became more negative starting at 7 mM concentration, while the MPILSDS system showed a more gradual decline in surface charge. This behavior is attributed to the higher charge density of the MPIL copolymer, providing more electrostatic binding sites for the anionic surfactant, thereby accumulating less free sulfate groups on the complex surface. The lower surface charge also allows for the stabilization of MPILSDS complexes without resolubilizing the polymer and surfactant in the 4 mM to 7 mM SDS concentration range. Overall, these general trends in particle diameter and zeta potential for both the PILSDS and MPILSDS systems match similar work for other poly(diallyl dimethyl ammonium chloride) and sodium dodecyl sulfate complexes [40, 41].

The morphology of the particles *in situ* was investigated with cryo-TEM imaging of the 6.5 mM [SDS] MPILSDS complexes (Figure 3.4). The particles were generally spherical or oblong in shape with a disperse distribution of particle diameters ranging from ~30 to 290 nm with an average particle diameter of ~100 (±16) nm. The corresponding DLS data showed a higher hydrodynamic diameter of 185 (±19) nm. DLS is highly sensitive to small populations of large

particles as scattering intensity correlates to particle radius to the sixth power [43], explaining the disparity with the diameters measured by TEM. There were also a few instances of worm-like micelle formation (Figure 3.4d), but the dominate morphology are the spherical particles.

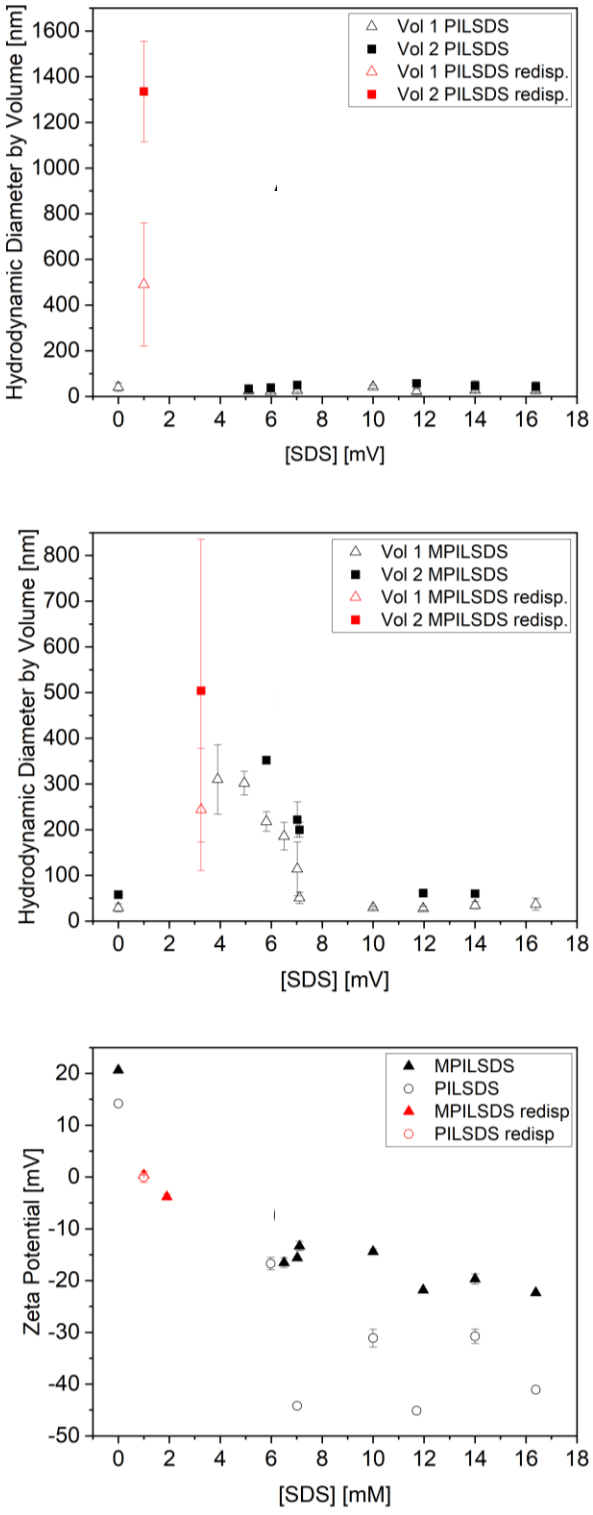

Figure 3.3 DLS hydrodynamic diameters, DH, of (A) PILSDS and (B) MPILSDS complexes and their (C) ZP are shown as a function of SDS concentration. Red and black symbols indicate unstable and Stable complexes, respectively.

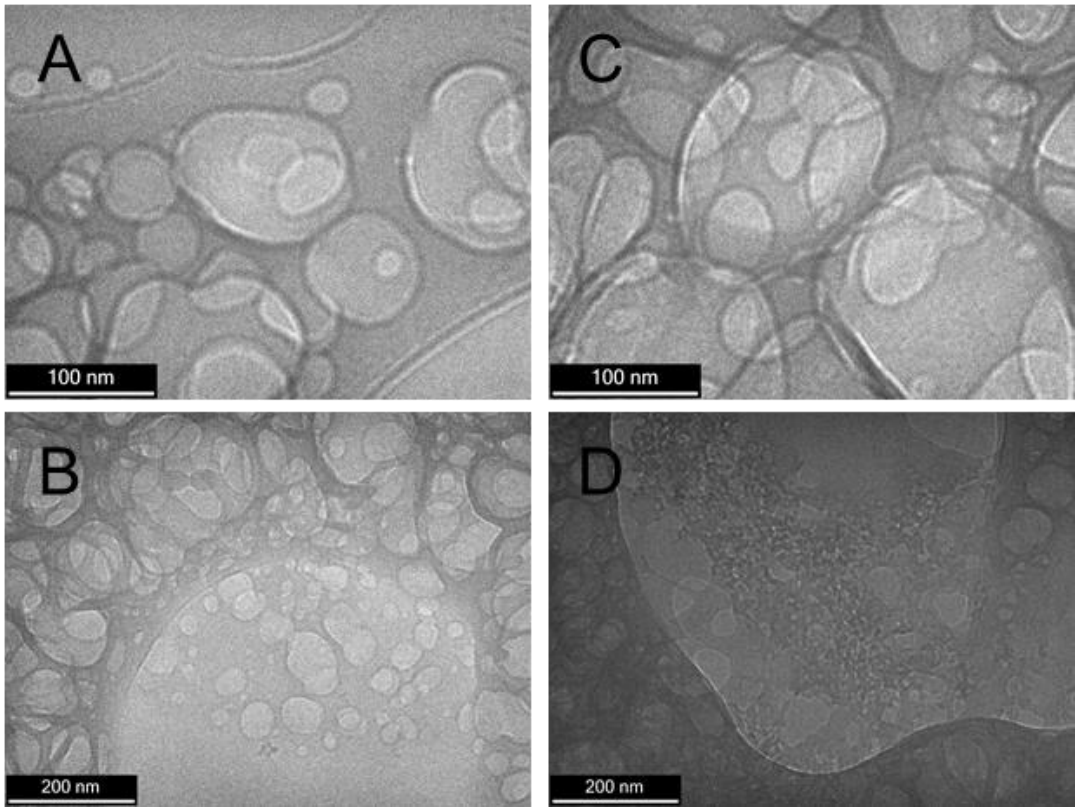

Figure 3.4 Cryo-TEM images of MPILSDS complexes at 6.5 mM concentration. Spherical or oblong particles are seen adhering to the TEM grid (a and c) and in the ice phase (b). A few instances of worm-like micelles (d) were also observed.

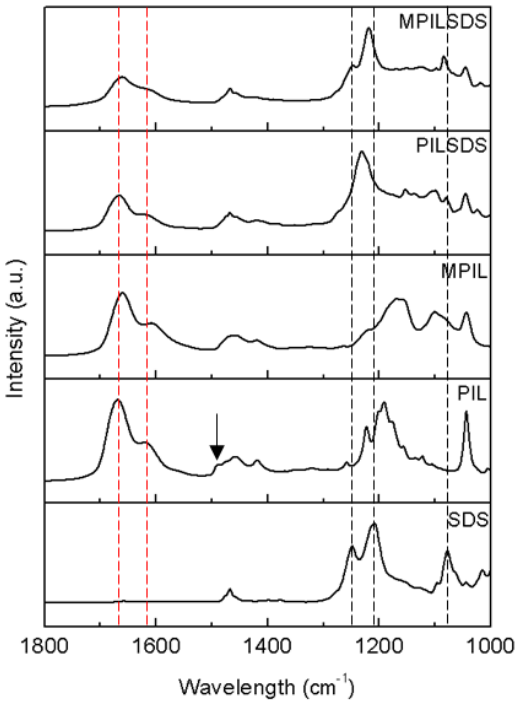

Figure 3.5 ATR-FTIR spectra of SDS, PIL, PILSDS, and MPILSDS in the range of 1800-1000 cm^{-1}. Dotted red and black lines show the shifts in the amide and SO4 modes, respectively, upon complexation with polymer and coordination with Co^{2+}. The black arrow points to the ammonium methyl bending mode.

Figure 3.5 and Table 3.1 shows the FTIR spectra for bands for the polymer and polymer-surfactant systems. As reported previously [21], the PIL copolymer exhibits bands at 1669 cm^{-1}, 1618 cm^{-1}, and 1490 cm^{-1}, which are assigned to the Amide I C=O stretch, Amide II NH_2 wag, and the CH_3 bending of the quaternary ammonium methyl groups respectively [44]. Upon addition of cobalt chloride salts, both amide bands in the MPIL copolymer downshift to 1660 cm^{-1} and 1606 cm^{-1}, indicating coordination of the cobalt salts with the acrylamide units [45, 46]. The 1490 cm^{-1} CH_3 bending mode for the methyl groups on the PDADMA unit disappears after metal complexation, possibly due to a downshift and overlap of the mode with the polymer backbone CH_2 bending modes.

FTIR spectra of the dried polymer-surfactant complexes indicates successful addition of the SDS as seen in the emergence of the SDS alkyl chain CH_2 and CH_3 stretching modes in the 2956-2850 cm^{-1} region and the CH_2 and CH_3 bending modes at 1467 cm^{-1} and 1378 cm^{-1}, respectively.

Shifts of the polymer amide and methyl ammonium bands and the surfactant sulfate SO_4 stretching modes in the MPILSDS and PILSDS systems also indicate successful complexation between the polymer and surfactant. The intense doublet at 1248 cm^{-1} and 1209 cm^{-1} in the native SDS is attributed to the SO_4 asymmetric stretch and the band at 1077 cm^{-1} to the SO_4 symmetric stretch [47, 48]. These bands show interesting shifts upon complexation with the PIL and MPIL copolymers as displayed in Table 1. Shifts and doublet splitting in the SO_4 stretching modes are an indication of change of dipole moment on the surfactant head group, which is influenced by metal ion coordination and electrostatic interactions with organic counterions [49-51]. Here, a definite difference in behavior of the surfactant in the PILSDS and MPILSDS systems suggests that the cobalt ions play a role in the SDS binding to the polymer. In the MPILSDS sample, the wavenumber of the C=O Amide I band (~1660 cm^{-1}) did not change with SDS to the MPIL, while the NH_2 wagging Amide II band showed an ~8 cm^{-1} upshift. This result implies that the Co^{2+} cations remain coordinated with the polyacrylamide through O-bonding while a change in the intermolecular or intramolecular environment of the NH_2 group occurs [46, 52]. In both cases for the PILSDS and MPILSDS systems, the methyl group on the ammonium polycation (at ~1490 cm^{-1} in the PIL), disappears, likely due to a downshift and overlap with other CH_2/CH_3 bending modes in the 1480 to 1440 cm^{-1} region upon SDS binding, indicating electrostatic binding of SDS to the PIL ammonium groups is also occurring.

Table 3.1 ATR-FTIR Wavenumber (cm^{-1}) of the major polymer and surfactant functional groups.

Assignment	SDS	PIL	MPIL	PILSDS	MPILSDS
Pam					
C=O amide I	**N/A**	**1669**	**1660**	**1666**	**1660**
NH_2 amide II	**N/A**	**1618**	**1606**	**1618**	**1614**
PDADMA					
(N^+)-CH_3 bending	N/A	1490	--	--	--
SDS					
CH_3 asym str	2956	--	--	2956	2956
CH_2 asym str	2917	--	--	2917	2917
CH_3 sym str	2872	--	--	2873	2873
CH_2 sym str	2850	--	--	2850	2850
CH_2 bending	1467	--	--	1467	1467
CH_3 i. ph. bend	1378	--	--	1378	1378
SO_4 asym str	**1248**	**--**	**--**	**1230**	**1247**
SO_4 asym Str	**1209**	**--**	**--**	**1220**	**1218**
SO_4 sym Str	**1077**	**--**	**--**	**1080**	**1084**

Table 3.2 AC Magnetic mass susceptibilities, χ_m (emu/g) for the MPIL and MPILSDS complexes. Comparative iron oxide nanoparticle samples are also included [22, 23].

Sample	χ_m, Dry	χ_m, Wet
MPIL	17.53 (±0.03) x 10^{-6}	20.78 (±0.85) x 10^{-6}
MPILSDS 7mM	7.04 (±1.48) x 10^{-6}	2.94 (±1.20) x 10^{-6}
MPILSDS 5mM	8.77 (±2.47) x 10^{-6}	2.13 (±0.75) x 10^{-6}
MNP-bare	4.64 (±0.06) x 10^{-2}	29.40 (±0.13) x 10^{-2}
MNP-citric acid	6.22 (±0.005) x 10^{-2}	56.95 (±0.07) x 10^{-2}

Based on the above results, the MPILSDS complexes are formed through a combination of SDS electrostatic binding to the ammonium monomer unit and coordination with Co^{2+} sites chelated to the acrylamide monomer. The MPILSDS spherical particles likely consist of a

hydrophobic core composed of the surfactant alkyl tail and a polymer shell with the Co^{2+} ions located at the polymer-surfactant interface. Stabilized complexes likely have an extra surface layer of surfactant hydrophobically binding with the polymer backbone to provide a negative surface charge.

We examined the intrinsic magnetic properties of the MPILSDS complexes through AC magnetic mass susceptibility measurements. The magnetic susceptibility, χ_m, describes the extent of material magnetization in a magnetic field. Generally, paramagnetic materials display small positive values in the range of 10^{-3} to 10^{-5} emu/g[53]. Table 2 shows the measured χ_m for the MPIL copolymer as previously reported [21], MPILSDS complexes at 5 mM and 7 mM SDS concentrations, and select iron oxide nanoparticles produced by our group in dry and wet states. The MPIL copolymer had a χ_m of 17.53 (±0.03) x 10^{-6} emu/g in the dry state and 20.78 (±0.85) x10^{-6} emu/g in solution, which is comparable to other paramagnetic MPILs [12, 54]. The dry MPILSDS susceptibilities were considerably lower at ~7 to 8 x 10^{-6} emu/g in the dry state and ~2 x 10^{-6} emu/g in the wet state, though they are still on par with similar cobalt-based MPILs [34]. The magnetic properties of MPILs are dependent on several factors including the weight percentage of the paramagnetic component (Co^{2+} complex) and distance between the transition metal ion centers [12, 15, 55]. Here the weight percentage of the paramagnetic Co^{2+} ions is reduced, and the concentration of diamagnetic content is increased upon addition of SDS compared to the original MPIL, leading to lower magnetic susceptibilities. These susceptibilities are significantly weaker compared to iron oxide nanoparticles produced by our group which have shown magnetic mass susceptibilities on the order of ~ x10^{-2} emu/g. Nonetheless, both the MPIL and MPILSDS dry powders could be attracted to a neodymium magnet with at 0.7 T surface field strength.

We tested the MPLSDS complexes and the MNP nanoparticles for their magnetic response in solution. Under optical microscopy, the polymer grafted MNPs in water can be seen assembling into aligned structures oriented in the direction of the magnetic field (Figure 3.6a). MPILSDS complexes formed from a 5 mM SDS concentration were similarly exposed to the magnet. Unfortunately, no visual alignment, magnetic orientation, or deviation from Brownian motion (Figure 3.6b) could be definitively discerned.

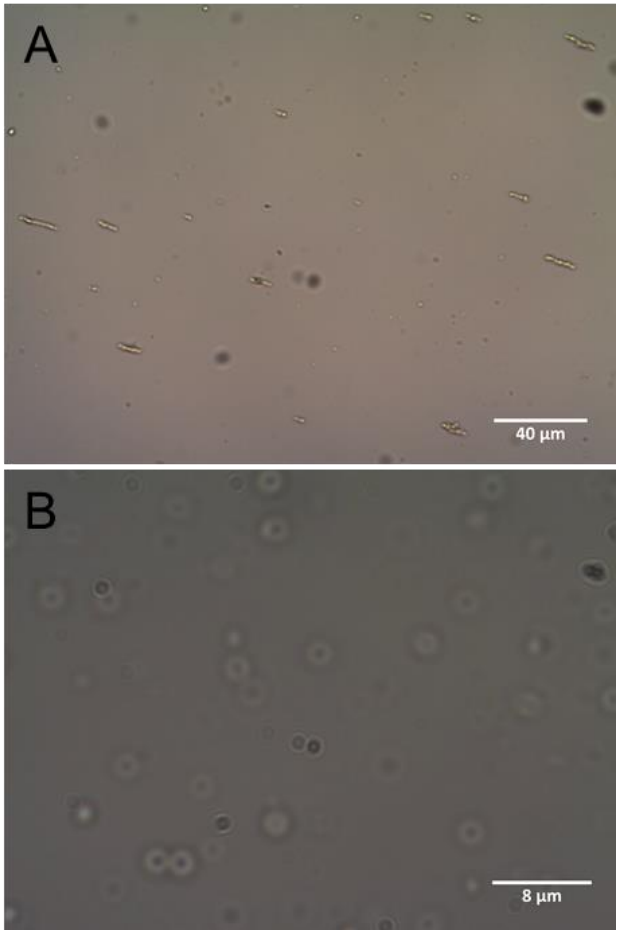

Figure 3.6 Optical microscopy video frames of (a) polymer-grafted MNPs and (b) MPILSDS complexes in the presence of a 0.7 T neodymium magnet.

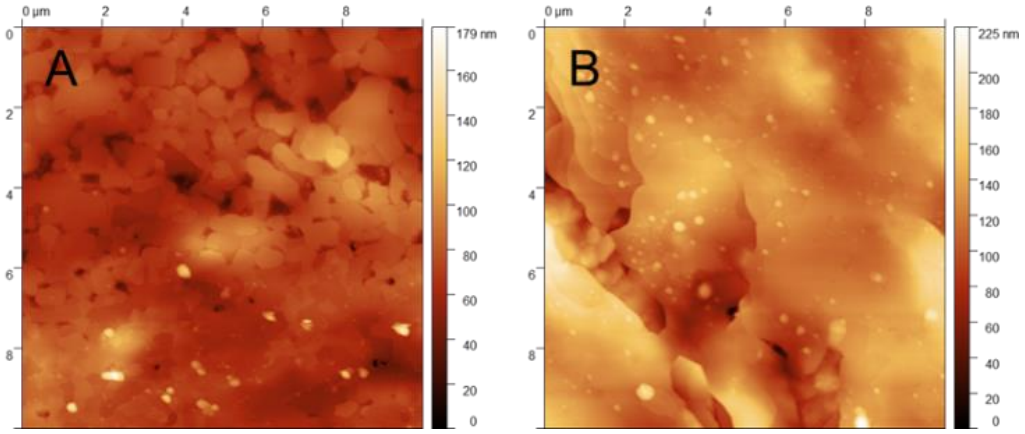

Figure 3.7 AFM Images of MPILSDS 7 mM films drop casted on SiO_2 substrates both (a) without and (b) with the presence of a magnetic field.

For this system, the face of the magnet was ~ 1.8 cm away from the microscope objective center. Magnetic field strength decays rapidly as you move away from the magnet surface. It is possible that the strength of the magnetic field was too weak to result in a noticeable magnetic response for the complex structures. Alternatively, the Co^{2+} ions may be partially dissociated from the complex in solution or hydrated within the MPILSDS complex. For most Mag-surf systems that demonstrate a magnetic response in solution, the magnetic ions are either (1) concentrated in a hydrophobic or phase separated domain that is stabilized by a surrounding hydrophilic domain, or (2) the magnetic ions are located in the Stern layer of the micelle or nanomaterial surface. Beck et al. ascribed the ability of the phospholipid-based vesicles to align in a magnetic field to concentration of the Dy^{+} ions in a solid domain formed in vesicle walls after temperature-induced demixing and reformation [20]. Zhao et al. attributed the magnetic manipulation of colloidal worm-like micelles to binding of the $FeCl_3Br^{-}$ anions in the Stern layer and partial migration into the micellar core [56]. Similarly, the magnetic manipulation and separation of graphene oxide complexed with Mag-Surf [57] and MPILs [14] has been attributed to associated paramagnetic counterions at the polymer-graphene oxide interface.

We also examined the effect of magnetic fields on the dry film assembly of MPILSDS complexes. Here, we drop-cast MPILSDS complexes formed from 7 mM SDS concentration on SiO_2-based substrates both with and without a magnetic field. In this case, the substrate was placed in between two 0.7 T magnets held 1 cm apart such that the center of the wafer was 0.5 cm from the magnet face. Figure 3.7 shows AFM images of the films. Films formed without a magnetic field show particles laying relatively flat on the substrate (Figure 3.7a), while the films formed with a magnetic field form more cohesive layers parallel to the substrate (Figure 3.7b).

GISAXS measurements were also taken of the drop casted films formed both without (Figure 3.8a) and with (Figure 3.8b) a magnetic field present. For films formed without a magnetic field, double diffraction arc-like features with high intensity spots located along $q_x=0$ are observed parallel to the q_x axis. These features are typical of randomly oriented lamellae with preferential orientation parallel to the substrate [58]. In comparison, the films formed in the presence of a magnetic field displayed two flatter diffraction spots, indicating increased orientation of the lamellae parallel to the substrate [58, 59].

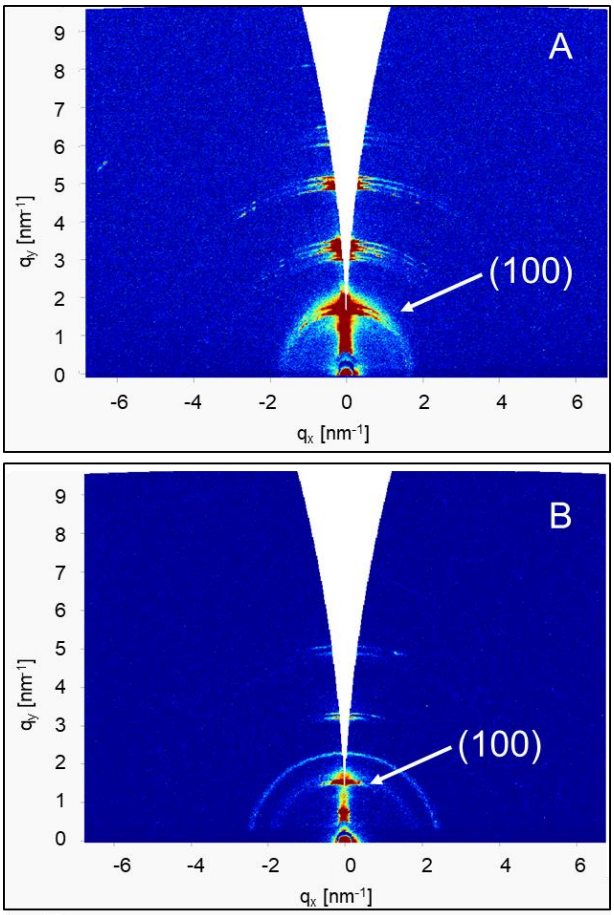

Figure 3.8 GI-SAXS spectra of MPILSDS 7mM films drop casted (a) without the presence of a magnetic field and (b) with the presence of a magnetic field.

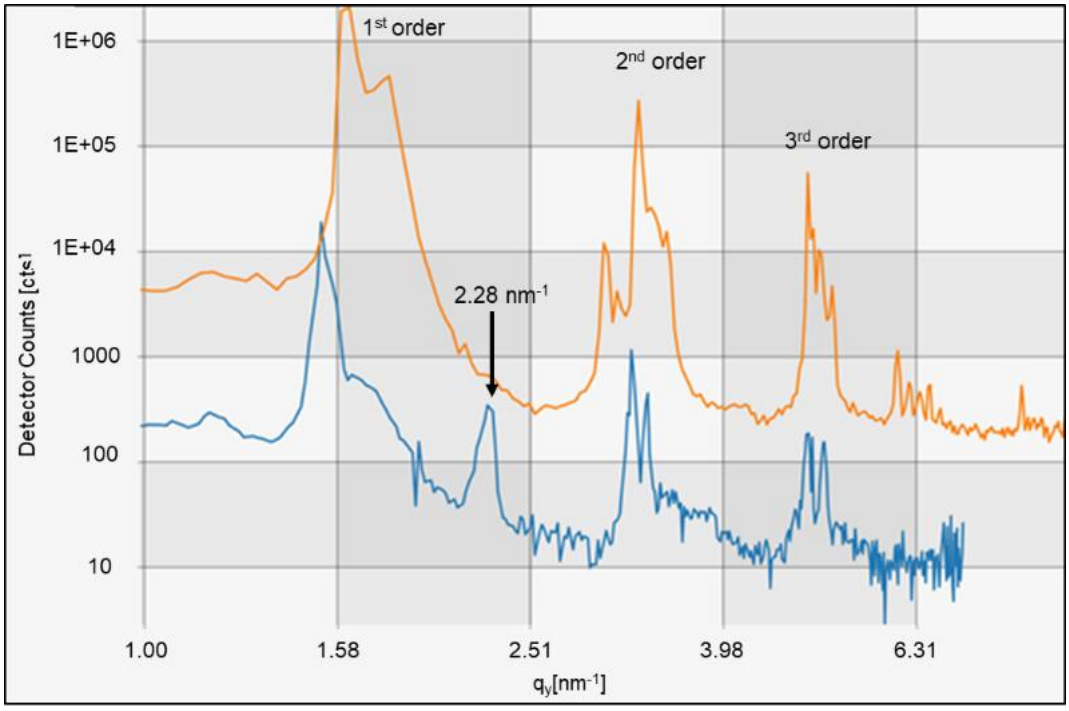

Figure 3.9 GI-SAXS vertical line cuts of the 2D scattering patterns produced from MPILSDS 7mM films drop casted (orange) without the presence of a magnetic field and (blue) with the presence of a magnetic field.

In both systems, the double diffraction arcs or lines are a result of direct diffraction from the incident beam and diffraction from the beam reflected off the substrate [59, 60]. This results in two diffraction lines: an upper branch ("+", reflection) and a lower branch ("-", direct). Their positions are given by:

$$\textbf{EQ 3-1: } q_y = \frac{2\pi}{\lambda}\left(\sin(\alpha_i) + \sqrt{\sin^2\alpha_m + \left[\left(\frac{m\lambda}{D_{lam}}\right) \pm \sqrt{\sin^2(\alpha_i) - \sin^2(\alpha_m)}\right]^2}\right)$$

where α_i and α_m are the X-ray beam incident angle and critical angle of the polymer-surfactant material, λ is the X-ray beam wavelength, m is the order of reflection, and D_{lam} is the thickness of the parallel lamellae layer. Vertical 1D line cuts taken perpendicular to the q_x axis are shown in Figure 3.9. For the films formed without a magnet field, the lower and upper 1st order branch (denoted 100 in Figure 3.8) diffraction arcs are at $q_y^- = 1.61$ nm^{-1} and $q_y^+ = 1.80$ nm^{-1}, respectively,

which correlates to a D_{lam} of 4.03 nm. The D_{lam} thickness of the film formed with a magnetic field was found to increase to 4.37 nm where q_y^- = 1.52 nm^{-1} and q_y^+ =1.65 nm^{-1}. The 3.4 Å increase in lamellae layer thickness and the increase in parallel orientation likely indicates surfactant alkyl chain straightening to an all-trans confirmation. These results demonstrate potential of magnetically influenced ordering in films containing paramagnetic components, as demonstrated by the increased ordering of lamellae parallel to the substrate and the change in lamellae layer thickness.

A single sharp ring pattern unique to the magnetically processed film also emerges at q_y = 2.28 nm^{-1} (measured at q_x =0 nm^{-1}) and q_x = 2.38 nm^{-1} (measured at q_y=0 nm^{-1}). Ring structures indicate isotropic orientation of lamellae with well-defined periodic ordering [61]. The lattice spacing, d, is calculated by:

$$\textbf{EQ 3-2}: d_i = \frac{2\pi}{q_i}$$

where *i* denotes either the x or y direction of the scattering pattern. The lattice spacing derived from this ring scattering pattern is estimated to be between 2.54 nm (d_x) and 2.76 nm (d_y) and is tentatively ascribed to MPILSDS layers oriented randomly with respect to the substrate. The broad diffuse halo feature centered at q_x = ~1.7 nm^{-1} corresponds to a repeating structure ~3.7 nm in size, which is the size of an SDS micelle [62]. The addition of these features also demonstrates the magnetic field influence on the MPILSDS film assembly.

Overall, we have investigated the formation and magnetic properties of magnetic poly(ionic liquid)-surfactant complexes through a number of characterizations. Particle sizing and morphology were examined through DLS and TEM techniques. Zeta potential surface charge measurements and FTIR spectroscopy provided insight into the polymer-surfactant complex formation. AC magnetic susceptibility measurements displayed paramagnetic character of the

MPILSDS complexes. While magnetic alignment of MPILSDS complexes in the solution were not observed under optical microscopy, we achieved magnetic alignment in drop-cast films of the magnetic complexes as analyzed through AFM and GISAXS. This work provides insight into the development of stimuli-responsive nano- and micro-scale structures fluids under the influence of non-contact force fields, namely, magnetic. In future work, we will examine the engineering properties and assembly of these materials in ionic and electric fields.

3.4. Conclusion

Magnetic poly(ionic liquid)-surfactant complexes were successfully developed, displaying spherical or oblong morphology and stability in solution under specific surfactant concentrations. The added Co^{2+} ions played a significant role in the development of stable complexes and polymer-surfactant binding. The complexes developed likely form hydrophobic surfactant cores and MPIL shells with the Co^{2+} coordinating at the surfactant-polymer interface. These complexes display paramagnetic susceptibilities. While magnetic alignment of MPILs in solution was not achieved, we were able to successfully utilize a magnetic field to achieve well-defined lamellae oriented parallel to the substrate. This work provides guidance in the development of nano- and micro-scale fluidic structures with stimuli-response to non-contact force fields.

Acknowledgements

We would like to thank Marta Sanchez, Matthew Hamilton, and Dr. Richard Elmore in the Geology department at the University of Oklahoma for conducting AC magnetic susceptibility measurements. We would also like to thank Dr. Jean-Luc Brousseau and Anton Paar for the time and assistance in collecting GISAXS data on their SAXSPoint2.0 system.

3.5. References

(1) Meek, K. M.; Elabd, Y. A. Correction: Polymerized ionic liquid block copolymers for electrochemical energy. *J. Mater. Chem. A* **2015**, *3* (48), 24568, 10.1039/C5TA90249E. DOI: 10.1039/C5TA90249E.

(2) Eshetu, G. G.; Mecerreyes, D.; Forsyth, M.; Zhang, H.; Armand, M. Polymeric ionic liquids for lithium-based rechargeable batteries. *Mol. Syst. Des. Eng.* **2019**, *4* (2), 294-309, 10.1039/c8me00103k. DOI: 10.1039/c8me00103k.

(3) Zhang, J.; Chen, Z.; Zhang, Y.; Dong, S.; Chen, Y.; Zhang, S. Poly(ionic liquid)s Containing Alkoxy Chains and Bis(trifluoromethanesulfonyl)imide Anions as Highly Adhesive Materials. *Advanced Materials* **2021**, *33* (30), 2100962, https://doi.org/10.1002/adma.202100962. DOI: https://doi.org/10.1002/adma.202100962 (acccessed 2022/02/13).

(4) Zhao, Z.; Zhang, G.; Yin, Y.; Dong, C.; Liu, Y. D. The electric field responses of inorganic ionogels and poly(ionic liquid)s. *Molecules* **2020**, *25* (19), 4547, 10.3390/molecules25194547. DOI: 10.3390/molecules25194547.

(5) Qian, W.; Texter, J.; Yan, F. Frontiers in poly(ionic liquid)s: synthesis and applications. *Chem. Soc. Rev.* **2017**, *46* (4), 1124-1159, 10.1039/C6CS00620E. DOI: 10.1039/C6CS00620E.

(6) Marcilla, R.; Blazquez, J. A.; Rodriguez, J.; Pomposo, J. A.; Mecerreyes, D. Tuning the solubility of polymerized ionic liquids by simple anion-exchange reactions. *J. Polym. Sci., Part A: Polym. Chem.* **2003**, *42* (1), 208-212, 10.1002/pola.11015. DOI: 10.1002/pola.11015.

(7) Clark, K. D.; Nacham, O.; Purslow, J. A.; Pierson, S. A.; Anderson, J. L. Magnetic ionic liquids in analytical chemistry: A review. *Anal. Chim. Acta* **2016**, *934*, 9-21, 10.1016/j.aca.2016.06.011. DOI: 10.1016/j.aca.2016.06.011.

(8) Joseph, A.; Zyla, G.; Thomas, V. I.; Nair, P. R.; Padmanabhan, A. S.; Mathew, S. Paramagnetic ionic liquids for advanced applications: A review. *J. Mol. Liq.* **2016**, *218*, 319-331, 10.1016/j.molliq.2016.02.086. DOI: 10.1016/j.molliq.2016.02.086.

(9) Wang, L.; Dong, S.; Hao, J. Recent progress of magnetic surfactants: Self-assembly, properties and functions. *Curr. Opin. Colloid Interface Sci.* **2018**, *35*, 81-90, 10.1016/j.cocis.2018.01.014. DOI: 10.1016/j.cocis.2018.01.014.

(10) Brown, P.; Alan Hatton, T.; Eastoe, J. Magnetic surfactants. *Curr. Opin. Colloid Interface Sci.* **2015**, *20* (3), 140-150, 10.1016/j.cocis.2015.08.002. DOI: 10.1016/j.cocis.2015.08.002.

(11) Chikh Alard, I.; Soubhye, J.; Berger, G.; Gelbcke, M.; Spassov, S.; Amighi, K.; Goole, J.; Meyer, F. Triple-stimuli responsive polymers with fine tuneable magnetic responses. *Polym. Chem.* **2017**, *8* (16), 2450-2456, 10.1039/C7PY00218A. DOI: 10.1039/C7PY00218A.

(12) Dobbelin, M.; Jovanovski, V.; Llarena, I.; Marfil, L. J. C.; Cabanero, G.; Rodriguez, J.; Mecerreyes, D. Synthesis of paramagnetic polymers using ionic liquid chemistry. *Polym. Chem.* **2011**, *2* (6), 1275-1278. DOI: 10.1039/c1py00044f.

(13) Cui, J.; Yang, S.; Zhang, J.; Zhao, S.; Yan, Y. A novel poly[(N-vinylimidazole)-co-(1-pyrenylmethyl methacrylate)] ferric complex with fluorescence and superparamagnetism. *RSC Adv.* **2012**, *2* (32), 12224-12230, 10.1039/c2ra22395c. DOI: 10.1039/c2ra22395c.

(14) Hazell, G.; Hinojosa-Navarro, M.; McCoy, T. M.; Tabor, R. F.; Eastoe, J. Responsive materials based on magnetic polyelectrolytes and graphene oxide for water clean-up. *J. Colloid Interface Sci.* **2016**, *464*, 285-290, 10.1016/j.jcis.2015.11.029. DOI: 10.1016/j.jcis.2015.11.029.

(15) Carrasco, P. M.; Tzounis, L.; Mompean, F. J.; Strati, K.; Georgopanos, P.; Garcia-Hernandez, M.; Stamm, M.; Cabanero, G.; Odriozola, I.; Avgeropoulos, A.; et al. Thermoset Magnetic Materials Based on Poly(ionic liquid)s Block Copolymers. *Macromolecules (Washington, DC, U. S.)* **2013**, *46* (5), 1860-1867, 10.1021/ma302261c. DOI: 10.1021/ma302261c.

(16) Zhang, S.-Y.; Zhuang, Q.; Zhang, M.; Wang, H.; Gao, Z.; Sun, J.-K.; Yuan, J. Poly(ionic liquid) composites. *Chem. Soc. Rev.* **2020**, *49* (6), 1726-1755, 10.1039/c8cs00938d. DOI: 10.1039/c8cs00938d.

(17) Yu, X.; Yuan, X.; Xia, Z.; Ren, L. Self-assembly of magnetic poly(ionic liquid)s and ionic liquids in aqueous solution. *Polym. Chem.* **2018**, *9* (41), 5116-5122, 10.1039/c8py01254g. DOI: 10.1039/c8py01254g.

(18) Xu, L.; Feng, L.; Hao, J.; Dong, S. Controlling the Capture and Release of DNA with a Dual-Responsive Cationic Surfactant. *ACS Appl. Mater. Interfaces* **2015**, *7* (16), 8876-8885, 10.1021/acsami.5b01514. DOI: 10.1021/acsami.5b01514.

(19) Polarz, S.; Baehrle, C.; Landsmann, S.; Klaiber, A. Panoscopic Structures by Hierarchical Cascade Self-Assembly of Inorganic Surfactants with Magnetic Heads Containing Dysprosium Ions. *Angew. Chem., Int. Ed.* **2013**, *52* (51), 13665-13670, 10.1002/anie.201303565. DOI: 10.1002/anie.201303565.

(20) Beck, P.; Liebi, M.; Kohlbrecher, J.; Ishikawa, T.; Ruegger, H.; Zepik, H.; Fischer, P.; Walde, P.; Windhab, E. Magnetic Field Alignable Domains in Phospholipid Vesicle Membranes Containing Lanthanides. *J. Phys. Chem. B* **2010**, *114* (1), 174-186, 10.1021/jp907442e. DOI: 10.1021/jp907442e.

(21) Foley, K. W., Keisha; Condes, Lucas. Chemical and Magnetic Properties of Metal-ion Poly(ionic liquid) Copolymers. Unpublished ed.; Arkansas, U. o., Ed.

(22) Abbott, B. S., Karimi, L. & Walters, K.B. Synthesis and Stability of Ligand-Modified Iron Oxide Nanoparticles *[In Preparation]* **2022**.

(23) Abbott, B. S., Condes, L. & Walters, K.B. . Optimizing Heavy Metal Adsorption Capacity for Various Iron Oxide-based Nanoadsorbents. . *[In Preparation]* **2022**.

(24) Theurer, J., Ajabe, O., Osorio, J., Elgaddafi, R., Ahmed, R., Walters, K.B. & Abbott, B. . Removal of Residual Oil from Produced Water Using Magnetic Nanoparticles. *SPE J.* **2020**, *25* (05), 2482-2495. DOI: 10.2118/199466-PA. .

(25) Vasquez, E. S., Prehn, E.M. & Walters, K.B. Assessing magnetic iron oxide nanoparticle properties under different thermal treatments, Journal of Thermal Analysis and Calorimetry. **2021**, *143*, 35-46. DOI: 10.1007/s10973-019-09195-4.

(26) Bornhoeft, L. R.; Castillo, A. C.; Smalley, P. R.; Kittrell, C.; James, D. K.; Brinson, B. E.; Rybolt, T. R.; Johnson, B. R.; Cherukuri, T. K.; Cherukuri, P. Teslaphoresis of Carbon Nanotubes. *ACS Nano* **2016**, *10* (4), 4873-4881. DOI: 10.1021/acsnano.6b02313.

(27) Park, B. J.; Fang, F. F.; Choi, H. J. Magnetorheology: materials and application. *Soft Matter* **2010**, *6* (21), 5246-5253, 10.1039/C0SM00014K. DOI: 10.1039/C0SM00014K.

(28) Morillas, J. R.; de Vicente, J. Magnetorheology: a review. *Soft Matter* **2020**, *16* (42), 9614-9642, 10.1039/D0SM01082K. DOI: 10.1039/D0SM01082K.

(29) Monroe, J. G.; Kumari, S.; Fairley, J. D.; Walters, K. B.; Berg, M. J.; Thompson, S. M. On the energy harvesting and heat transfer ability of a ferro-nanofluid oscillating heat pipe. *International Journal of Heat and Mass Transfer* **2019**, *132*, 162-171. DOI: https://doi.org/10.1016/j.ijheatmasstransfer.2018.11.096.

(30) Monroe, J. G.; Vasquez, E. S.; Aspin, Z. S.; Walters, K. B.; Berg, M. J.; Thompson, S. M. Electromagnetic induction by ferrofluid in an oscillating heat pipe. *Applied Physics Letters* **2015**, *106* (26), 263901. DOI: 10.1063/1.4923400 (acccessed 2022/02/16).

(31) Seol, M.-L.; Jeon, S.-B.; Han, J.-W.; Choi, Y.-K. Ferrofluid-based triboelectric-electromagnetic hybrid generator for sensitive and sustainable vibration energy harvesting. *Nano Energy* **2017**, *31*, 233-238. DOI: https://doi.org/10.1016/j.nanoen.2016.11.038.

(32) Zhao, Q.; Sun, J.; Chen, S.; Zhou, Q. Properties of a poly(acrylamide-co-diallyl dimethyl ammonium chloride) hydrogel synthesized in a water-ionic liquid binary system. *J. Appl. Polym. Sci.* **2010**, *115* (5), 2940-2945, 10.1002/app.31368. DOI: 10.1002/app.31368.

(33) Das, S.; Martin, P.; Vasilyev, G.; Nandi, R.; Amdursky, N.; Zussman, E. Processable, Ion-Conducting Hydrogel for Flexible Electronic Devices with Self-Healing Capability. *Macromolecules* **2020**, *53* (24), 11130-11141. DOI: 10.1021/acs.macromol.0c02060.

(34) Sahiner, N.; Demir, S.; Yildiz, S. Magnetic colloidal polymeric ionic liquid synthesis and use in hydrogen production. *Colloids Surf., A* **2014**, *449*, 87-95, 10.1016/j.colsurfa.2014.02.046. DOI: 10.1016/j.colsurfa.2014.02.046.

(35) Wei, Z.; Duan, H.; Weng, G.; He, J. Metals in polymers: hybridization enables new functions. *Journal of Materials Chemistry C* **2020**, *8* (45), 15956-15980, 10.1039/D0TC03810E. DOI: 10.1039/D0TC03810E.

(36) Zhang, X.; Vidavsky, Y.; Aharonovich, S.; Yang, S. J.; Buche, M. R.; Diesendruck, C. E.; Silberstein, M. N. Bridging experiments and theory: isolating the effects of metal–ligand interactions on viscoelasticity of reversible polymer networks. *Soft Matter* **2020**, *16* (37), 8591-8601, 10.1039/D0SM01115K. DOI: 10.1039/D0SM01115K.

(37) Khan, N.; Brettmann, B. Intermolecular interactions in polyelectrolyte and surfactant complexes in solution. *Polymers (Basel, Switz.)* **2019**, *11* (1), 51/51. DOI: 10.3390/polym11010051.

(38) Ober, C. K.; Wegner, G. Polyelectrolyte-surfactant complexes in the solid state. Facile building blocks for self-organizing materials. *Adv. Mater. (Weinheim, Ger.)* **1997**, *9* (1), 17-31, 10.1002/adma.19970090104. DOI: 10.1002/adma.19970090104.

(39) Gradzielski, M.; Hoffmann, I. Polyelectrolyte-surfactant complexes (PESCs) composed of oppositely charged components. *Curr. Opin. Colloid Interface Sci.* **2018**, *35*, 124-141, 10.1016/j.cocis.2018.01.017. DOI: 10.1016/j.cocis.2018.01.017.

(40) Nizri, G.; Magdassi, S.; Schmidt, J.; Cohen, Y.; Talmon, Y. Microstructural Characterization of Micro- and Nanoparticles Formed by Polymer-Surfactant Interactions. *Langmuir* **2004**, *20* (11), 4380-4385, 10.1021/la0364441. DOI: 10.1021/la0364441.

(41) Abraham, A.; Campbell, R. A.; Varga, I. New Method to Predict the Surface Tension of Complex Synthetic and Biological Polyelectrolyte/Surfactant Mixtures. *Langmuir* **2013**, *29* (37), 11554-11559. DOI: 10.1021/la402525w.

(42) Nizri, G.; Lagerge, S.; Kamyshny, A.; Major, D. T.; Magdassi, S. Polymer-surfactant interactions: Binding mechanism of sodium dodecyl sulfate to poly(diallyldimethylammonium chloride). *J. Colloid Interface Sci.* **2008**, *320* (1), 74-81, 10.1016/j.jcis.2008.01.016. DOI: 10.1016/j.jcis.2008.01.016.

(43) Stetefeld, J.; McKenna, S. A.; Patel, T. R. Dynamic light scattering: a practical guide and applications in biomedical sciences. *Biophysical Reviews* **2016**, *8* (4), 409-427. DOI: 10.1007/s12551-016-0218-6.

(44) Murugan, R.; Mohan, S.; Bigotto, A. FTIR and polarized Raman spectra of acrylamide and polyacrylamide. *J. Korean Phys. Soc.* **1998**, *32* (4), 505-512.

(45) Halevi, O.; Chen, J.; Thangavel, G.; Morris, S. A.; Ben Uliel, T.; Tischler, Y. R.; Lee, P. S.; Magdassi, S. Synthesis through 3D printing: formation of 3D coordination polymers. *RSC Adv.* **2020**, *10* (25), 14812-14817, 10.1039/d0ra01887b. DOI: 10.1039/d0ra01887b.

(46) Girma, K. B.; Lorenz, V.; Blaurock, S.; Edelmann, F. T. Coordination chemistry of acrylamide. 4. Crystal structures and IR spectroscopic properties of acrylamide complexes with CoII, NiII, and ZnII nitrates. *Z. Anorg. Allg. Chem.* **2005**, *631* (10), 1843-1848, 10.1002/zaac.200500210. DOI: 10.1002/zaac.200500210.

(47) Prosser, A. J.; Franses, E. I. Infrared Reflection Absorption Spectroscopy (IRRAS) of Aqueous Nonsurfactant Salts, Ionic Surfactants, and Mixed Ionic Surfactants. *Langmuir* **2002**, *18* (24), 9234-9242. DOI: 10.1021/la020568g.

(48) Larkin, P. Chapter 8 - Illustrated IR and Raman Spectra Demonstrating Important Functional Groups. In *Infrared and Raman Spectroscopy*, Larkin, P. Ed.; Elsevier, 2011; pp 135-176.

(49) Pereira, R. F. P.; Valente, A. J. M.; Burrows, H. D.; de Zea Bermudez, V.; Carvalho, R. A.; Castro, R. A. E. Structural characterization of solid trivalent metal dodecyl sulfates: from aqueous solution to lamellar superstructures. *RSC Adv.* **2013**, *3* (5), 1420-1433. DOI: 10.1039/c2ra21906a.

(50) Viana, R. B.; da Silva, A. B. F.; Pimentel, A. S. Infrared spectroscopy of anionic, cationic, and zwitterionic surfactants. *Adv. Phys. Chem.* **2012**. DOI: 10.1155/2012/903272.

(51) Scheuing, D. R.; Weers, J. G. A Fourier transform infrared spectroscopic study of dodecyltrimethylammonium chloride/sodium dodecyl sulfate surfactant mixtures. *Langmuir* **1990**, *6* (3), 665-671, 10.1021/la00093a023. DOI: 10.1021/la00093a023.

(52) Girma, K. B.; Lorenz, V.; Blaurock, S.; Edelmann, F. T. Coordination chemistry of acrylamide. *Coord. Chem. Rev.* **2005**, *249* (11-12), 1283-1293, 10.1016/j.ccr.2005.01.028. DOI: 10.1016/j.ccr.2005.01.028.

(53) Jiles, D. *Introduction to Magnetism and Magnetic Materials*; CRC Press., 2015. DOI: https://doi.org/10.1201/b18948.

(54) Bonnefond, A.; Ibarra, M.; Mecerreyes, D.; Leiza, J. R. Adding magnetic ionic liquid monomers to the emulsion polymerization tool-box: Towards polymer latexes and coatings with new properties. *J. Polym. Sci., Part A: Polym. Chem.* **2016**, *54* (8), 1145-1152, 10.1002/pola.27953. DOI: 10.1002/pola.27953.

(55) Yu, X.; Yuan, X.; Zhao, Y.; Ren, L. From Paramagnetic to Superparamagnetic Ionic Liquid/Poly(ionic liquid): The Effect of π–π Stacking Interaction. *ACS Macro Letters* **2019**, *8* (11), 1504-1510. DOI: 10.1021/acsmacrolett.9b00714.

(56) Zhao, W.; Dong, S.; Hao, J. Colloidal Wormlike Micelles with Highly Ferromagnetic Properties. *Langmuir* **2015**, *31* (41), 11243-11248, 10.1021/acs.langmuir.5b03148. DOI: 10.1021/acs.langmuir.5b03148.

(57) McCoy, T. M.; Brown, P.; Eastoe, J.; Tabor, R. F. Noncovalent Magnetic Control and Reversible Recovery of Graphene Oxide Using Iron Oxide and Magnetic Surfactants. *ACS Appl. Mater. Interfaces* **2015**, *7* (3), 2124-2133, 10.1021/am508565d. DOI: 10.1021/am508565d.

(58) Piccinini, E.; Tuninetti, J. S.; Irigoyen Otamendi, J.; Moya, S. E.; Ceolin, M.; Battaglini, F.; Azzaroni, O. Surfactants as mesogenic agents in layer-by-layer assembled polyelectrolyte/surfactant multilayers: nanoarchitectured "soft" thin films displaying a tailored mesostructure. *Phys. Chem. Chem. Phys.* **2018**, *20* (14), 9298-9308, 10.1039/C7CP08203G. DOI: 10.1039/C7CP08203G.

(59) Di, Z.; Posselt, D.; Smilgies, D.-M.; Li, R.; Rauscher, M.; Potemkin, I. I.; Papadakis, C. M. Stepwise Swelling of a Thin Film of Lamellae-Forming Poly(styrene-*b*-butadiene) in Cyclohexane Vapor. *Macromolecules (Washington, DC, U. S.)* **2012**, *45* (12), 5185-5195, 10.1021/ma3004136. DOI: 10.1021/ma3004136.

(60) Busch, P.; Posselt, D.; Smilgies, D. M.; Rauscher, M.; Papadakis, C. M. Inner Structure of Thin Films of Lamellar Poly(styrene-*b*-butadiene) Diblock Copolymers As Revealed by Grazing-

Incidence Small-Angle Scattering. *Macromolecules* **2007**, *40* (3), 630-640, 10.1021/ma061695c. DOI: 10.1021/ma061695c.

(61) Mahmood, A.; Wang, J.-L. A Review of Grazing Incidence Small- and Wide-Angle X-Ray Scattering Techniques for Exploring the Film Morphology of Organic Solar Cells. *Solar RRL* **2020**, *4* (10), 2000337, https://doi.org/10.1002/solr.202000337. DOI: https://doi.org/10.1002/solr.202000337 (acccessed 2022/05/17).

(62) Molero, M.; Andreu, R.; González, D.; Calvente, J. J.; López-Pérez, G. An Isotropic Model for Micellar Systems: Application to Sodium Dodecyl Sulfate Solutions. *Langmuir* **2001**, *17* (2), 314-322. DOI: 10.1021/la0010267.

Chapter 4: Magnetometry Studies of Magnetic Poly(ionic liquids) Using Surfactant Complexation to Direct Self Assembly and Increase the Effective Moment

***** This chapter is written in preparation for journal submission: Kayla Foley[1], Charles P. Easterling[2], Dale Huber[2], Keisha B. Walters[1]. "Magnetometry Studies of Poly(ionic liquid)s Using Surfactant Complexation to Direct Self Assembly and Increase the Effective Moment."

[1] Ralph E. Martin Department of Chemical Engineering, University of Arkansas, Fayetteville, AR 72701, USA

[2] Center for Integrated Nanotechnologies, Sandia National Laboratories, Albuquerque, NM 87123, USA

Abstract

Poly[acrylamide-*co*-diallyl dimethyl ammonium chloride] was complexed with Fe^{3+}, Co^{2+}, and Cu^{2+} chloride salts at 1 and 2 mole equivalencies to form a series of magnetic poly(ionic liquid) (MPIL) copolymers. MPIL polyelectrolyte-surfactant complexes (MPILSDS) were formed by binding sodium dodecyl sulfate with select Co^{2+} and Fe^{3+} MPIL copolymers. Magnetometry studies of the MPIL copolymers and MPILSDS complexes were conducted as a function of magnetic field strength and temperature (50 to 300 K) using a vibrating sample magnetometer (VSM) and revealed paramagnetic behavior for the MPIL copolymers with antiferromagnetic or ferromagnetic interactions that are dependent on the metal type and concentration. The MPILSDS complexes exhibited a small hysteresis loop in their magnetization response, suggesting non-paramagnetic behavior. Zero Field Cooling-Field Cooling (ZFC-FC) studies of the MPILSDS complexes suggest strong antiferromagnetic interactions are occurring. The effective magnetic moments of the MPILSDS complexes were larger than for the corresponding MPIL copolymers, indicating the self-assembled structures play a role in enhancing magnetic coupling interactions.

FTIR spectroscopy studies confirmed metal coordination and surfactant binding interactions in the MPIL copolymers and MPILSDS complexes. In the multi-component MPILSDS system, metal cation coordination was observed between the acrylamide units in the polymer and sulfate group in the surfactant. The micellular solution and freeze-dried structures of the MPILSDS complexes were also characterized with dynamic light scattering, zeta potential, dynamic scanning calorimetry, and scanning electron microscopy. FTIR shifts for the acrylamide and sulfate groups indicated that freeze drying influences the coordination structure of the metal species. This study provides insight into the magnetic behavior of multicomponent MPILs, specifically MPIL random copolymers and MPIL-surfactant complexes, showing the influence of group coordination and self-assembled structure. These findings will aid the design and guide the application of progressively more complex magnetically responsive MPIL systems.

4.1. Introduction

In the past decade, magnetic poly(ionic liquid)s (MPILs) have emerged as an exciting subclass of stimuli-responsive polymerized ionic liquids that contain magnetically responsive transition metal salts. They are typically formed through electrostatic binding of transition metal complexes (e.g., $[FeCl_4]^-$, $[CoCl_4]^{2-}$) to the permanently charged ionic liquid pendant groups along the polymer backbone. Similar to their small molecule counterparts such as magnetic ionic liquids (MILs) [1, 2] and magnetic surfactants (mag-surf) [3, 4], MPILs can be attracted by a handheld magnets with weak fields (≤ 2 T/ 20 kOe) and typically exhibit room temperature paramagnetic behavior, but MPILs also possess favorable mechanical properties and polymer processability due to their macromolecular structure. Due to the metal salt inclusions, MPILs have found applications in a variety of fields including catalysis[5, 6], magnetically induced separations[7], antimicrobial materials[8],

templates for nanoparticle synthesis[6, 9], magnetic stimuli response[5, 10-13], and initial forays into MPIL macromolecular magnet development[14-17].

Most MPILs studied to date display paramagnetic behavior with magnetic mass susceptibilities ranging from ~10 x10^{-6} emu/g to 60 x10^{-6} emu/g depending on transition metal type and content[5, 10, 12, 18-21]. Although rarely reported for MPILs, effective magnetic moments per metal complex are typically near the expected spin only values for the corresponding transition metal for Fe^{3+} (4.4-5.6 μ_B) and Co^{2+} (4.2 μ_B) [17, 22] . Their small molecule magnetic ionic liquid (MIL) and magnetic surfactant (Mag-Surf) counterparts, whose effective moments are more often reported, also generally have effective moments consistent with the spin only values for Fe^{3+} (5.2-5.6 μ_B) [22-29] and Co^{2+} (~4.2-4.5 μ_B) [24, 30].

Efforts to improve the magnetic properties of MPILs and to expand their application in magnetic stimuli response and molecular magnet development have generally involved the formation of multicomponent materials. MPIL systems that have displayed enhanced paramagnetic susceptibility or magnetism other than paramagnetic—including antiferromagnetic [22], ferromagnetic [16, 31], and superparamagnetic [17, 32]—have mainly consisted of multicomponent materials such as blends, copolymers, or homopolymers modified with functional groups. Self-assembled block copolymers or blends containing microphase separated regions aid in nanoconfinement and enhanced coupling of magnetic groups[21, 33, 34]. MPILs with long alkyl chains or pendant polymer chains similarly restrict movement of the magnetic groups, leading to increased coupling and improved susceptibilities[15, 18, 19]. In a series of MPILs containing π-π stacking functionalities, Ren et al. was able to decrease the Fe^{3+}-Fe^{3+} coupling distance to ~4 Å and resultantly increase ferromagnetic correlations[14, 16]. Cui et al. reported superparamagnetic behavior in a MPIL copolymer containing pendant pyrene groups[35]. Though reported less often,

metal ion-coordination with non-PIL co-materials in MPIL systems have also been shown to influence magnetic transitions as a function of temperature[34]. In many of these multi-component systems, the co-materials and modified structures contain functional groups capable of metal ion coordination, such as N, O, or S atoms, which can alter the coordination structure of the paramagnetic complex and consequently the magnetic behavior of the multicomponent MPIL systems. Examining the magnetic behavior and properties multi-component MPIL systems is necessary to further the design of MPIL systems and expand their application.

In prior studies by the authors, multicomponent MPILs were investigated for metal coordination effects and self-assembled structures. The coordination structure and binding of Fe^{3+} and Co^{2+} halide salts with a metal coordinating MPIL random copolymer, poly[acrylamide-*co*-diallyl dimethyl ammonium chloride], was thoroughly examined[36]. Using a suite of spectroscopic characterizations, it was found that the metal cations were bound to the copolymer through both acrylamide coordination and electrostatic interactions with the PIL monomer. The complex coordination structure of the metal species was also found to be dependent on metal type and concentration. These results demonstrated the influence of coordinating co-materials on MPIL synthesis and metal structure of the magnetically responsive species. The authors also examined the influence of Co^{2+} on solution self-assembly behavior for a MPIL copolymer complexed with surfactant, forming polyelectrolyte-surfactant micellular structures[37]. The micellular solution structures were found to be non-responsive to a static ~0.62 T (6.2 kOe) magnetic field produced form a handheld neodymium magnet, likely due to either too weak of a magnetic field or possible hydration and dissociation of the Co^{2+} species from the micellular structures. However, a similar static magnetic field was successfully utilized to induce alignment in drop-cast films and self-

assembly behavior for the MPIL-surfactant complexes, demonstrating an application of magnetic stimuli response for these MPIL-surfactant systems.

This work significantly expands the scope of investigation into multicomponent MPILs through a detailed magnetometry study of MPIL random copolymers along with their respective self-assembled polyelectrolyte-surfactant complexes. Specifically, poly[acrylamide-*co*-diallyl dimethyl ammonium chloride] was complexed with Fe^{3+}, Co^{2+}, and Cu^{2+} chloride salts at 1 and 2 mole equivalencies relative to the PIL monomer group to form the MPIL copolymers. MPIL polyelectrolyte-surfactant complexes (MPILSDS) were formed from binding a surfactant, sodium dodecyl sulfate, with select Co^{2+} and Fe^{3+} MPIL copolymers. Magnetic behavior of the MPIL copolymers and MPILSDS complexes was measured as a function of magnetic field strength and temperature between 50 and 300 K with vibrating sample magnetometry (VSM). FTIR spectroscopy was performed to characterize metal coordination and surfactant binding interactions in the MPIL copolymers and MPILSDS complexes. MPILSDS complex micelles in solution—along with freeze-dried structures—were observed with dynamic light scattering, zeta potential, and scanning electron microscopy. Differential scanning calorimetry studies of the MPIL copolymer and MPILSDS complexes provided insight into physical and magnetic thermal transitions.

4.2. Materials and Experimental Methods

4.2.1. Materials

A 10 wt% solution of poly(acrylamide-*co*-diallyldimethylammonium chloride) ([Pam-*co*-PDADMA][Cl^-]) in water was purchased from Sigma Aldrich. The copolymer contained 55% acrylamide (Pam) and 45% diallyldimethylammonium chloride (DADMA[Cl^-]) by weight. $CoCl_2$*$6H_2O$ and sodium dodecyl sulfate (99% purity, CAS 151-21-3) was purchased from Sigma

Aldrich. $FeCl_3 \cdot 6H_2O$ was purchased from Alfa Aesar. $CuCl_2$ was purchased from Carolina. All materials were used as received.

4.2.2. Synthesis of Magnetic Copolymers

Magnetic copolymers were synthesized through a complexation reaction with metal chloride salts (Fe^{3+}, Co^{2+}, or Cu^{2+}) in aqueous solution as described in the authors' previous work[36]. In a typical synthesis, aqueous solutions of either $FeCl_3 \cdot 6H_2O$, $CoCl_2 \cdot H_2O$, or $CuCl_2$ were added dropwise to an aqueous solution of ~1.1 g [Pam-*co*-PDADMA][Cl^-] copolymer in 10 ml of water in a round bottom flask. The metal halide species were added at either 1 or 2 mole equivalents with respect to the PDADMA group in the MPIL copolymer. All solutions were stirred for ~6 hours at room temperature before evaporating the water from the system. MPILs were further dried in a vacuum oven at (~45 °C) before characterizations. To ensure no contamination from paramagnetic species, no metal-based spatulas or stirrers were used during synthesis. The synthesized copolymers are denoted as [Pam-*co*-PDADMA][M^{n+} Xeq] throughout the remaining text where M^{n+} and X refer to Co^{2+}, Fe^{3+}, or Cu^{2+} metal cations and 1, 2, or 3 mol equivalents, respectively.

4.2.3. Synthesis of Magnetic Copolymer-Surfactant Complexes

Polyelectrolyte-surfactant micellar complexes were formed by complexing MPIL copolymers with sodium dodecyl sulfate (SDS) surfactant as described previously[37]. Briefly, aqueous solutions of the each MPIL copolymer (2 mg/mL) and SDS (either 10 mM or 14 mM concentrations) were prepared separately. Under rapid stirring (900 rpm), a given SDS solution was added to one of the aqueous MPIL copolymer solutions and the mixture was allowed to stir for approximately 10 seconds. Immediate clouding or precipitation was observed upon stirring, confirming the formation of the polyelectrolyte-surfactant complexes. The final concentration of the

polyelectrolyte-surfactant solution was 1 mg/mL MPIL copolymer and a surfactant concentration of either 5 or 7 mM. Only the [Pam-*co*-PDADMA][Co^{2+} 1eq] and [Pam-*co*-PDADMA][Fe^{3+} 1eq] copolymers were used for the MPILSDS complex formation. For this work, a portion of each micellar solution was freeze dried prior to spectroscopic or magnetic characterizations in an attempt to preserve the self-assembled structure of the complexes.

4.2.4. Chemical and Thermal Characterizations

Attenuated total reflection (ATR) FTIR spectra of dried polymer were collected using a PerkinElmer Frontier FTIR spectrophotometer (Waltham, MA, USA) with 4 cm^{-1} resolution and a minimum of 32 scans over the 4000-550 cm^{-1} spectral range. Differential scanning calorimetry (DSC) was performed using a Netzsch Jupiter STA 449 F1 thermal analyzer for select samples between 20 °C (293 K) and -150 °C (123 K). In a typical DSC experiment, the sample was first cooled to -150 °C using LN2 at 10 °C/min under He (50 mL/min) and held at -150 °C for 1 minute. The samples were then heated to 20 °C at a rate of 10 °C/min. Only the heating curves were analyzed for thermal transitions.

4.2.5. Magnetic Characterizations

A Quantum Design PPMS VersaLab 1300-001 vibrating sample magnetometer (VSM) was used to perform magnetic measurements. The magnetic copolymer powders were packed into polycarbonate pill capsules as sample holders. A piece of Kapton tape was used to affix the capsules to the instrument sample insertion tool. Kapton has been reported to have a small moment of ~10^{-6} emu[38], which is lower than the range of moments measured in this work (10^{-5} to 10^{-3} emu). To ensure minimal measured response from the Kapton tape, a piece of tape was affixed symmetrically along the axis of motion on the capsule with 1 cm of tape above and below the capsule, creating a uniform background field. Two sets of experiments were performed on the

copolymers including measuring magnetic moment with respect to magnetic field strength and also as a function of temperature. For the field strength sweeps, the magnetic moment was measured between ±30 kOe at selected temperatures of 50, 100, 150, 200, 250, and 300 K. Magnetization curves of the non-magnetic copolymer, [Pam-*co*-PDADMA][Cl-], and sodium dodecyl sulfate surfactant were collected at 300 K and their results are provided in the supplemental information (Figure C.15). Transitions in the magnetization curve as a function of temperature were measured through Zero Field Cooling/Field Cooling (ZFC-FC) curves at a field strength of 100 Oe. In particular, a sample capsule was first cooled to 50 °C under zero magnetic field. Magnetization measurements were then collected as the sample was heated to 300 °C at a heating rate of (5 ° C/min) under an applied magnetic field of 100 Oe for the ZFC curve. The sample was then cooled to 50 °C at the same heating rate and magnetic field settings to obtain the FC curve.

4.2.6. Processing of Magnetization Data

Magnetic moment data was normalized by sample mass and plotted as a function of magnetic field strength. In most cases, the magnetic mass susceptibility was determined from the slope of a linearly fitted line over the full data set. In the cases where saturation was clearly observed, only the linear center section of the magnetization curve was fitted, typically at low field strengths (± 10 kOe). ZFC-FC measured moments were converted to molar susceptibility, based either on only metal content or on the full MPIL copolymer molecular weight (see supplement for details). The molar susceptibility was then plotted as 1/χ-T. Typically, 1/χ-T plot is fitted to the Curie-Weiss law

$$\textbf{EQ 4-1}\ \chi = \frac{C}{T-\theta_{CW}}$$

over the higher temperature region where the plot is visually linear. However, all MPIL copolymers exhibited a $1/\chi$ response with a slight positive curvature resulting in difficulties in determining at which temperature the visual deviation from linearity began (see supplemental information Figure C.1). This curvature is attributed to a temperature independent contribution to the measured susceptibility and can be accounted for through a modified form of the Curie-Weiss as described by Mugiraneza et. al. [39]:

$$\textbf{EQ 4-2}\ \chi = \frac{C}{T-\theta_{CW}} + \chi_o$$

where χ is molar susceptibility, C is the material dependent Curie constant, T is the temperature in Kelvin, θ_{CW} is the Curie-Weiss temperature, and χ_o is a temperature independent susceptibility contribution. Several other groups have also used a modified Curie-Weiss law[40-42]. For all MPIL copolymers, the χ_0 was found to be a small positive value between 0.001 and 0.002 emu/mol. As the χ_0 values are positive, this indicates that the temperature independent contribution to susceptibility is not primarily due to the diamagnetic polymer backbone. However, these values are slightly above the upper limit for χ_0 values expected for Pauli paramagnetism (~10^{-4} to 10^{-5} emu/mol) [39] for metal species. The specific physical phenomenon for the χ_0 contribution is not apparent. Although it would likely not be strictly temperature independent, we do note that a small paramagnetic moment (~10^{-4} emu) was observed in one of the runs for the [Pam-*co*-PDADMA][Cl^-] copolymer (Figure C.15) which may contribute to χ_0. A comparison of the fittings to Curie-Weiss's law and the modified Curie-Weiss's law can be found in the supplemental information. The effective moment was then calculated by

$$\textbf{EQ 4-3}\ \mu_{eff} = \sqrt{8C}\mu_B$$

where C is the calculated Curie constant and μ_B is the Bohr magnetron. Assuming paramagnetic behavior with minimal magnetic correlations, the effective magnetic moment can also be estimated

at specific temperatures using (EQ 4-4) where the temperature, T, is in Kelvin and the mole susceptibility, χ, is in emu mol^{-1} Oe^{-1}:

$$\textbf{EQ 4-4}\ \mu_{eff} = \sqrt{8\chi T}$$

4.3. Results and Discussion

4.3.1. Chemical and Structural Characterization

A series of magnetically responsive poly(ionic liquid) copolymers were prepared by complexing Co^{2+}, Fe^{3+}, and Cu^{2+} chloride salts with the copolymer [Pam-*co*-PDADMA][Cl^-] at 1 and 2 mol equivalents relative to the DADMA monomer unit. The resulting MPIL copolymer powders were dark blue, yellow-brown, and yellow-green powders for the [Pam-*co*-PDADMA[Co^{2+}], [Pam-*co*-PDADMA[Fe^{3+}], and [Pam-*co*-PDADMA[Cu^{2+}], respectively (Figure 4.1). In order to induce self-assembled structure into the random copolymers, the [Pam-*co*-PDADMA[Co^{2+} 1eq] and [Pam-*co*-PDADMA[Fe^{3+} 1eq] copolymers were also complexed with the surfactant sodium dodecyl sulfate to produce polyelectrolyte-surfactant complexes (MPILSDS M^{n+} X mM where M^{n+} is either Fe^{3+} or Co^{2+} and X is 5 or 7 mM SDS concentration) (Figure 4.1). Polyelectrolyte-surfactant complexes can form a variety of micellar structures from spherical particles to worm like micelles and vesicular structures depending on surfactant concentration and salt additives[43, 44]. The MPILSDS Co^{2+} complexes were previously found to have spherical or oblong morphology through cryogenic electron microscopy imaging[37].

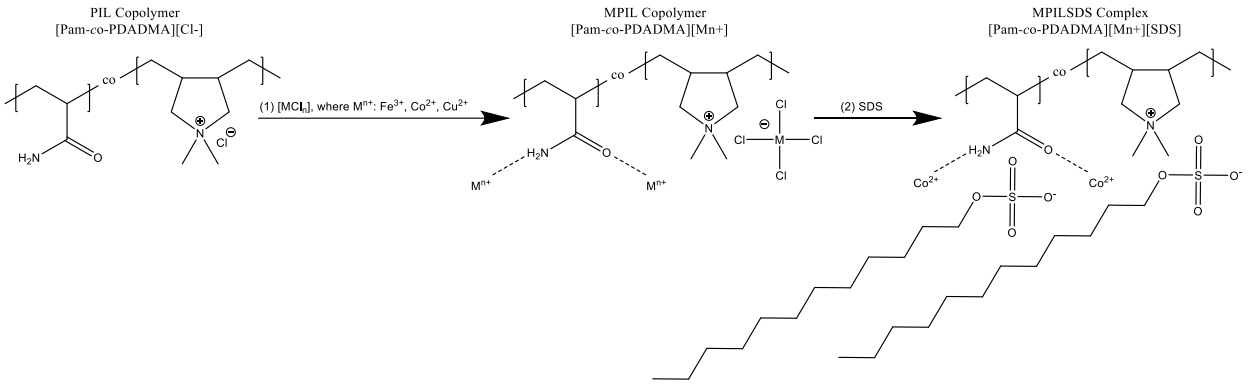

Figure 4.1 Schematic of the formation of the MPIL copolymers and MPILSDS polyelectrolyte surfactant complexes. In step (1), [Pam-*co*-PDADMA[Cl^-] is complexed with $FeCl_3$, $CoCl_2$, or $CuCl_2$ salts forming a combination of metal chloride anionic complexes and acrylamide coordinated complexes depending on metal halide concentration. In step (2), SDS surfactant is complexed with the [Pam-*co*-PDADMA][Co^{2+} 1eq] and [Pam-*co*-PDADMA][Fe^{3+} 1eq] copolymers to form the MPILSDS Co^{2+} and MPILSDS Fe^{3+} complexes.

As seen previously, the [Pam-*co*-PDADMA][Co^{2+} 1eq] solution produced a cloudy white color immediately after SDS addition indicating the formation of the complexes. Particle diameters measured through light scattering and zeta potential data for the complexes produced from 5 and 7 mM SDS concentrations are shown in Figure 4.2 and Table C.2. The complexes produced from [Pam-*co*-PDADMA][Co^{2+} 1eq] combined with 5 and 7 mM SDS concentrations have particle diameters of 409.2 nm (± 148.1 nm) and 402.9 nm (± 145.7 nm) and zeta potentials of -9.0 ± 0.2 mV and -23.2 mV (±0.7 mV), respectively, that correspond well to previous measurements[37]. In this work, [Pam-co-PDADMA[Fe^{3+}] was also complexed with SDS at 5 and 7 mM. However, only the 5 mM SDS solution produced stable complex particles while the 7mM sample resulted in immediate precipitation of the MPIL copolymer. The MPILSDS Fe^{3+} 5mM complexes had a hydrodynamic diameter of ~233 nm (±65 nm). Conversely to the MPILSDS Co^{2+} based complexes, the MPILSDS Fe^{3+} 5mM complex had a positive zeta potential of ~11 mV. Cationic polyelectrolytes binding with anionic surfactant typically exhibit a positive zeta potential until charge neutrality is reached at the critical aggregation concentration[43, 45-48]. The smaller

hydrodynamic diameter and the positive zeta potential of the MPILSDS Fe^{3+} 5mM complex suggests that the use of Fe^{3+} rather than Co^{2+} shifts the critical aggregation concentration to higher SDS concentrations. A DLS and ZP study as a function of surfactant concentration for the MPILSDS Fe^{3+} complex system could provide further insight into this behavior. Further, a broader study on the impact of iron versus cobalt, surfactant concentration, and even surfactant type could help provide general guidance on the parameters responsible in polyelectrolyte-surfactant complex formation.

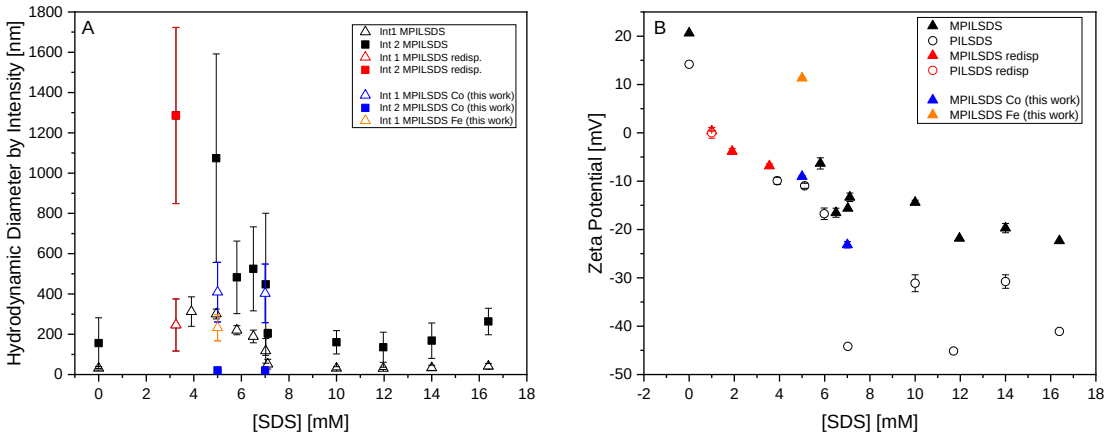

Figure 4.2 (a) Dynamic light scattering measurements showing intensity-based hydrodynamic diameters and (b) zeta potential for the MPILSDS Co^{2+} and MPILSDS Fe^{3+} complexes as a function of SDS concentration. Blue and orange markers are for the MPILSDS Co^{2+} and MPILSDS Fe^{3+} complexes that are later freeze dried and analyzed for magnetic properties in this work. Red markers indicate unstable complexes that were redispersed into solution prior to DLS/ZP analysis.

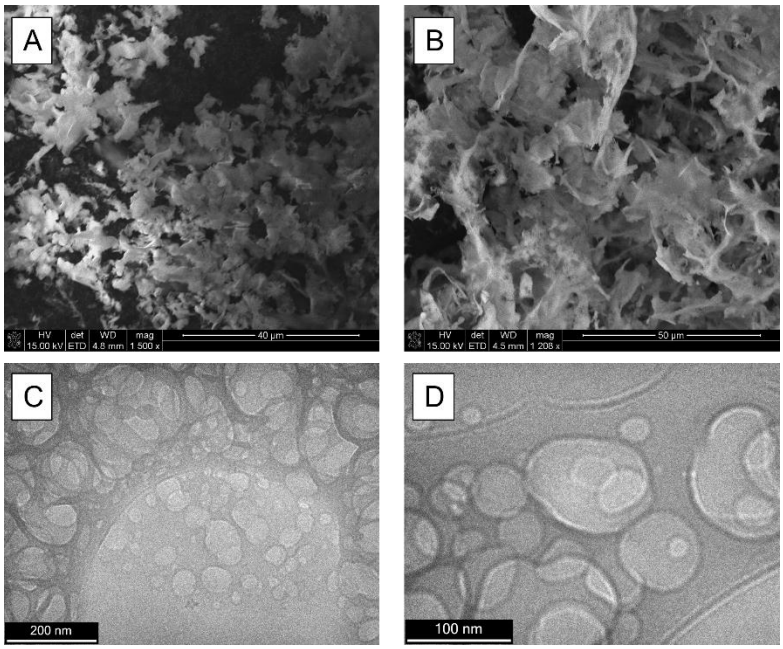

Figure 4.3 SEM images of the MPILSDS complexes freeze dried from aqueous solution containing (a) 7 mM SDS and (b) 5 mM SDS. The flake-like structure of the dried complexes differs from the spherical particle morphology (c and d) observed previously in cryo-TEM images of a 6.5 mM MPILSDS Co^{2+} complex[37], indicating a structural change upon freeze drying.

In an effort to preserve the self-assembled MPILSDS complex structure, the complexes were freeze dried before further characterizations. The resulting light and fluffy powders were a light blue and yellow color for the MPILSDS Co^{2+} and MPILSDS Fe^{3+} complexes, respectively. SEM images (Figure 4.3 a and b) of the freeze dried MPILSDS-Co^{2+} complexes exhibited a more flaky-like morphology compared to the air-dried powders obtained previously and is different from the solution spherical particle morphology observed through cryo-TEM (Figure 4.3 c and d). The supplemental information also provides dark field microscopy images of the MIPILSDS Co^{2+} freeze dried flakes and air-dried powders (Figure C.21). As no self-assembled structure was expected for the random copolymers without added surfactant, the MPIL copolymers were air dried, forming solid films that were then ground into coarse powders before analysis (Figure C.22-

Figure C.23). The MPIL Co^{2+} copolymers formed brittle particles, while the MPIL Fe^{3+} copolymers formed softer particles.

ATR-FTIR spectroscopy was performed to observe metal coordination interactions in the MPIL copolymers and the MPILSDS complexes. Table 4.1 summarizes key vibrational modes observed in the ATR-FTIR spectra of the MPIL copolymers (Figure 4.4a) and the MPILSDS complexes (Figure 4.4b). In our previous work, the transition metal salts were found to bind with the copolymer through coordination with the acrylamide monomer at both the carbonyl oxygen and amide nitrogen as evidenced by downshifts in both the amide I (C=O str) and amide II (NH_2 wag) bands compared to uncoordinated [Pam-*co*-PDADMA][Cl^-][36]. These shifts in the amide IR modes are a result of changes in the amide resonance structure upon metal cation coordination at the carbonyl oxygen or the amide nitrogen groups[49]. In addition to observed peak maxima wavenumbers, relative band shifts are also reported. The [Pam-*co*-PDADMA][Co^{2+}] and [Pam-*co*-PDADMA][Fe^{3+}] copolymers exhibit downshifts consistent with previously reported work[36]. [Pam-*co*-PDADMA][Co^{2+}] showed downshifts of 8 cm^{-1} for the amide I band and 16-18 cm^{-1} downshifts for the amide II band. Again, the [Pam-*co*-PDADMA][Fe^{3+}] copolymers showed larger wavenumber decreases of 13-18 cm^{-1} (amide I, C=O str) and 43-50 cm^{-1} (amide II, NH_2 wag) in comparison to the cobalt-based copolymers. The [Pam-*co*-PDADMA][Cu^{2+}] copolymers displayed intermediate downshifts compared to the iron- and cobalt-based copolymers with downshifts of 11-14 cm^{-1} (amide I, C=O str) and 22-29 cm^{-1} (amide II, NH_2 wag), indicating similar coordination of Cu^{2+} at both O- and N-bonding sites of the acrylamide comonomer. The extent of downshifts in the amide I (C=O str) and amide II (NH_2 wag) bands provides an indication of strength of both the O-bonded (Pam) and N-bonded metal-acrylamide interactions[50, 51]. This

would suggest the Cu^{2+} binds to the acrylamide with moderate strength compared to the weaker Co^{2+} binding and stronger Fe^{3+} binding.

All MPILSDS complexes indicated successful polymer-surfactant complexation through the emergence of several peaks related to SDS including a set of peaks attributed to the SO_4 asymmetric str (~1253 and ~1217 cm^{-1} in native SDS), SO_4 symmetrical str (1075 cm^{-1} in native SDS), and an increase in intensity of the methylene bending modes (~1468 cm^{-1}). In all MPILSDS complexes, slight decreases in the asymmetric SO_4^- str doublet peaks and increases in the SO_4^- symmetrical peak compared to native SDS were observed (shifts summarized in Table 4.1). These shifts differ from the authors' previous work on the MPILSDS complexes where increases of ~9 cm^{-1} and ~7 cm^{-1} were observed for the SO_4^- asymmetrical and symmetrical bands, respectively[37]. These SO_4^- str modes are particularly sensitive to shifts in the sulfate head group dipole moment which may result from changes in metal ion coordination or electrostatic interactions[52-54]. Pereira et al. observed similar downshifts in the asymmetrical SO_4^- band on complexation with different metal cations, with greater downshifts observed for stronger electrostatic interactions between the specific metal cations and sulfate group[52]. It may then be inferred that the metal cations are complexing with the SDS sulfate group more strongly in the MPILSDS complexes prepared here compared to the previous work[37]. Analysis of the methylene CH_2 asym (~2919-2920 cm^{-1}) and sym str (~2850-2852 cm^{-1}) (Figure C.17) and CH_2 bending modes (~1468 cm^{-1}) (Figure C.18) reveal modes consistent with partial ordering in the surfactant alkyl chain with a large portion of chains in an all-*trans* conformation[52, 54]. Similar IR modes were also observed for MPILSDS complexes air dried (Figure C.19-Figure C.20).

In the MPILSDS Co^{2+}-based complexes, both the amide I (C=O str) and amide II (NH_2 wag) modes exhibited upshifts in wavenumber to 1664 cm^{-1} and ~1610 cm^{-1}, respectively, compared to

1652 cm^{-1} and ~1599 cm^{-1} in the [Pam-*co*-PDADMA][Co^{2+} 1eq] copolymer. These ~12cm^{-1} (amide I) and ~11cm^{-1} (amide II) upshifts are greater than the shifts observed previously[37], where no shift was observed for the amide I band and a 8 cm^{-1} shift was observed for the amide II band. Further, the amide I band for the MPILSDS Co^{2+} complexes is at a greater wavenumber compared to the 1660 cm^{-1} of the uncoordinated [Pam-*co*-PDADMA][Cl^-]. This would suggest some loss of coordination of the Co^{2+} with acrylamide through the carbonyl group, which is corroborated by the increase of Co^{2+} binding with the surfactant sulfate group as noted above. Changes in the MPILSDS Co^{2+} coordination environment observed in this work compared to the authors' previous work is likely attributed structural changes in the polyelectrolyte-surfactant complex as a result of freeze drying the structures as opposed to air drying.

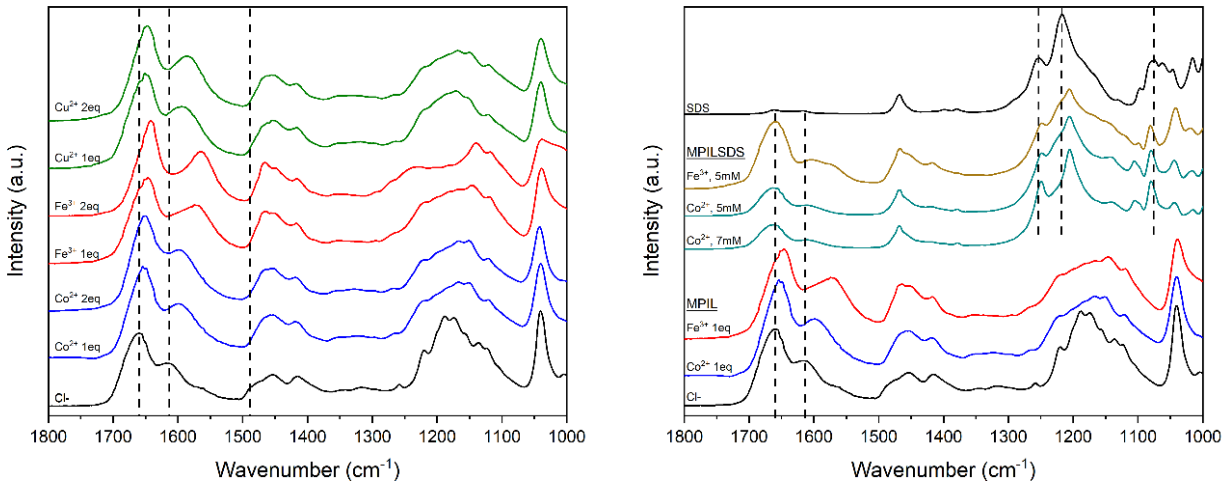

Figure 4.4 ATR-FTIR spectra for the MPIL copolymers (a) and MPILSDS complexes (b). In (a) the dashed lines mark from left to right the amide I (C=O str), amide II (NH_2 wag), and quaternary ammonium methyl bending (N^+-CH_3) modes for the [Pam-*co*-PDADMA][Cl^-] copolymer. In (b) the dashed lines mark from left to right the amide I (C=O str), amide II (NH_2 wag), and several of the SDS SO_4^- asymmetrical and symmetrical stretching modes.

Table 4.1 ATR-FTIR key modes in the MPIL copolymers and MPILSDS complexes including the acrylamide amide I (C=O str) and amide II (NH_2 wag) modes, the SDS SO_4^- asymmetric and symmetric stretching modes, and the quaternary ammonium methyl bending (N^+)-CH_3 modes.

	Pam				SDS					
	Amide I (C=O str)		**Amide II (NH_2 wag)**		**SO_4 asym str**		**SO_4 asym str**		**SO_4 sym str**	
Sample	**Position (cm^{-1})**	**Shift[a] (cm^{-1})**	**Position (cm^{-1})**	**Shift[a] (cm^{-1})**	**Position (cm^{-1})**	**Shift[b] (cm^{-1})**	**Position (cm^{-1})**	**Shift[b] (cm^{-1})**	**Position (cm^{-1})**	**Shift[b] (cm^{-1})**
[Pam-co-PDADMA]										
[Cl^-]	1660		1615		--	--	--	--	--	--
[Co^{2+} 1eq]	1652	8	1599	16	--	--	--	--	--	--
[Co^{2+} 2eq]	1652	8	1597	18	--	--	--	--	--	--
[Fe^{3+} 1eq]	1647	13	1572	43	--	--	--	--	--	--
[Fe^{3+} 2eq]	1642	18	1565	50	--	--	--	--	--	--
[Cu^{2+} 1eq]	1649	11	1593	22	--	--	--	--	--	--
[Cu^{2+} 2eq]	1646	14	1586	29	--	--	--	--	--	--
MPILSDS										
Co^{2+} 5mM SDS	1664	12[c]	1610	11[c]	1250	3	1206	12	1080	-5
Co^{2+} 7mM SDS	1664	12[c]	1608	9[c]	1250	3	1205	13	1080	-5
Fe^{3+} 5mM SDS	1659	12[d]	1604,1576	32, 4[d]	1248	5	1206	12	1081	-6
SDS	--	--	--	--	1253		1218		1075	

(a) peak shifts relative to [Pam-co-PDADMA][Cl-]; (b) peak shifts relative to SDS; (c) peak shift relative to [Pam-co-PDADMA][Co^{2+} 1eq]; (d) peak shift relative to [Pam-co-PDADMA][Fe^{3+} 1eq].

The MPILSDS-Fe^{3+} complex also shows an increase in the amide I band from 1647 cm^{-1} in [Pam-*co*-PDADMA][Fe^{3+} 1eq] to 1659 cm^{-1} in the polymer-surfactant complex. However, two

amide II (NH_2 wag) bands are also observed at 1604 cm^{-1} and 1576 cm^{-1} indicating two different Fe^{3+}-acrylamide binding interactions are occurring after complexation with surfactant. The later peak is close to the absorbance seen in the [Pam-*co*-PDADMA][Fe^{3+} 1eq] copolymer (1576 cm^{-1}) while the former peak shows similar increases as the MPILSDS Co^{2+} complexes. This is likely indicative of a mixture of Fe^{3+}-acrylamide coordinated groups and uncoordinated acrylamide groups in the copolymer.

4.3.2. Magnetometry

4.3.2.1. Magnetic Behavior of the MPIL Copolymers, [Pam-*co*-PDADMA][M^{n+} X eq]

Magnetic properties of the [Pam-*co*-PDADMA][Co^{2+}],[Pam-*co*-PDADMA][Fe^{3+}], and [Pam-*co*-PDADMA][Cu^{2+}] copolymers were first investigated with DC magnetic moment measurements as a function of magnetic field strength between ± 30 kOe with vibrating sample magnetometer (VSM). Figure 4.5a and b display the magnetization curves for the MPIL copolymers at 300 K and 50 K. At magnetic field strengths below ~ ±1500 Oe, a linear response was observed in the magnetic moment for all MPIL copolymers at 300K followed by slight curvature response above ±1500 Oe that did not saturate up to ±30 kOe. This behavior was most prominently observed in the [Pam-*co*-PDADMA][Fe^{3+} 2eq] copolymer (Figure 4.5a insert, solid red circles). Similar magnetization responses observed by Wyrzykowski et al. for quaternary ammonium FeCl4 MILs was attributed to paramagnetism with weak antiferromagnetic behaviors, while Yu et al. attributed the curvature without saturation to paramagnetism in imidazolium $FeCl_4^-$ based MPILs with a norbornene backbone[17, 28]. All copolymers at 50 K-250 K showed linear responses with no curvature with increasing magnetic field strength, indicating paramagnetic behavior (Figure 4.5b, Figure C.9-Figure C.14 150-250K). The magnetic mass susceptibilities were determined through a linear regression of the magnetic field response curves and are

displayed in Table 4.2. The magnetic susceptibilities at 300 K for the [Pam-*co*-PDADMA][Fe^{3+}] and [Pam-*co*-PDADMA][Co^{2+}] copolymers ranged between ~18.9-38.9 x 10^{-6} emu/g and ~19.0 to 24.5 x 10^{-6} emu/g, respectively, with increasing susceptibility for increasing mole equivalence of complexed metal halide. These DC susceptibilities and their increase with increasing metal content compare well to the authors' previous AC susceptibility measurements[36] and they fall within the range of typical magnetic mass susceptibilities (~10 to 60 x 10^{-6} emu/g) for iron and cobalt based-MPILs[5, 10, 11, 18, 19]. In comparison, the [Pam-*co*-PDADMA][Cu^{2+}] susceptibilities were significantly lower compared to the [Pam-*co*-PDADMA][Fe^{3+}] and [Pam-*co*-PDADMA][Co^{2+}] copolymers with values of ~2.86 x10^{-6} emu/g (1eq) and 4.05 x10^{-6} emu/g (2eq) at 300K. The lower susceptibilities are expected for Cu^{2+} based copolymers due to the lower spin state (S=1/2, μ_{eff} 1.73 μ_B) compared to Fe^{3+} (S=5/2, μ_{eff} = 5.92 μ_B) and Co^{2+} (S=3/2, μ_{eff} = 3.86 μ_B) [39, 55].

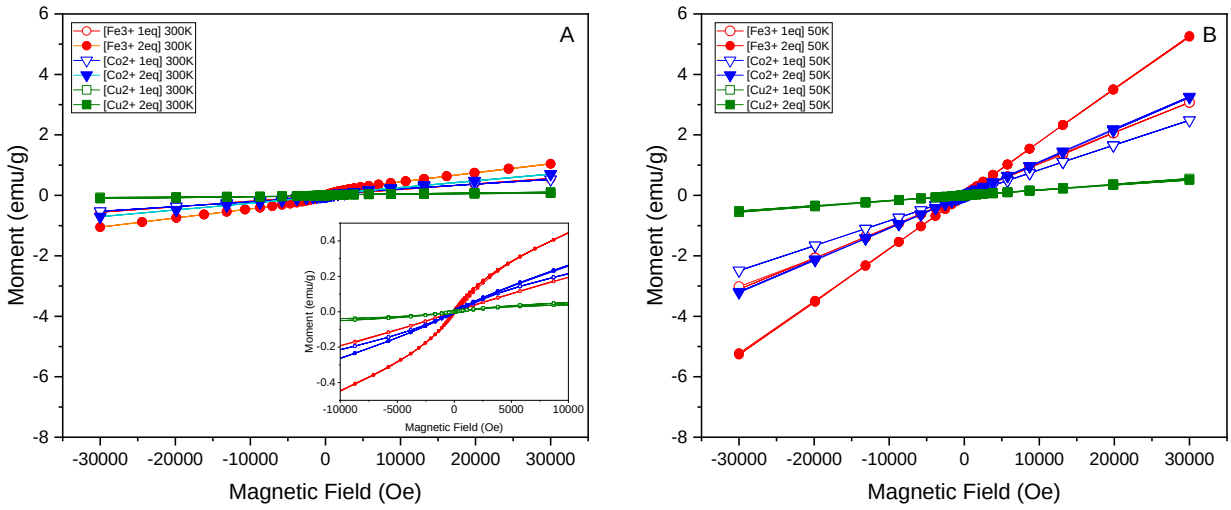

Figure 4.5 Magnetic field response for the MPIL copolymers at (a) 300 K and (b) 50 K. The insert in (a) shows the sinusoidal response of the MPIL copolymers, particularly [Pam-*co*-PDADMA][Fe^{3+} 2eq] (solid red circles), at ±10 kOe.

Substantially larger susceptibilities were obtained at 50 K for the MPIL copolymers, which were 4 to 5 times greater than the susceptibilities measured at 300 K. Figure C.24a shows the

increase in these susceptibilities with decreasing temperature between 300 and 50 K. The trends observed compare well to an expected paramagnetic response with increasing temperature[39, 56].

ZFC-FC curves were also performed for the MPIL copolymers to investigate magnetic thermal transitions occurring as a function of temperature at 100 Oe field strength. The ZFC-FC curves for the [Pam-*co*-PDADMA][Fe^{3+}] and [Pam-*co*-PDADMA][Co^{2+}] MPIL copolymers exhibited no significant hysteresis and displayed a typical paramagnetic response with a steeper decrease in magnetic moment from 50 to ~150 K followed by a more gradual decrease in moment up to 300 K (Figure C.8 a-c). The corresponding χT-T curves for the [Pam-*co*-PDADMA][Co^{2+}] copolymers show a gradual decrease in χT with decreasing temperature suggesting antiferromagnetic coupling interactions are occurring. The difference in the 300 K and 50 K χT value was 1.09 $x10^{-3}$ and 1.91$x10^{-3}$ emu K g^{-1} Oe^{-1} for 1eq and, 2eq respectively. The [Pam-*co*-PDADMA][Fe^{3+}] copolymers also appeared to display a decrease in χT, but to a lesser extent with χT^{300K}-χT^{50K} of 8.52$x10^{-4}$ (1eq) and 1.25$x10^{-3}$ emu K g^{-1} Oe^{-1} (2eq). Typically for antiferromagnetic ordering, a gradual decrease in χT followed by a sharp decrease in χT is observed with a corresponding maximum point in the moment response at the Neel temperature. In most MIL systems[23, 26, 28, 29], MPIL systems[22], and similar small molecule organic complexes containing $[FeCl_4]^-$ [25] reporting antiferromagnetic behavior, this sharp decrease in χT and the maximum point in χ occurs in the 1-10 K range, which is below the 50K minimum temperature for the current instrumentation and is likely why a sharp χT decrease is not observed here. Conversely, [Pam-*co*-PDADMA][Cu^{2+} 1eq] and [Pam-*co*-PDADMA][Cu^{2+} 2eq] copolymers exhibited a reasonably constant response over the 50 to 300 K temperature range, indicating paramagnetic behavior. Although a small splitting in the ZFC and FC curves between ~88 and ~145 K was observed, the extent of splitting was within the instrumental noise level.

Table 4.2 VSM magnetometry data summary for the MPIL copolymers and MPILSDS complexes.

	[Pam-*co*-PDADMA][MCl_n]						**MPILSDS**		
Sample	[Fe^{3+} 1eq]	[Fe^{3+} 2eq]	[Co^{2+} 1eq]	[Co^{2+} 2eq]	[Cu^{2+} 1eq]	[Cu^{2+} 2eq]	Co^{2+}-7mM	Co^{2+}-5mM	Fe^{3+}-5mM
Metal Content wt%	43.0%	60.1%	39.8%	57.0%	27.20%	42.80%	17.9%	21.3%	23.4%
χ x10^{-6} (emu/g) at 300K									
AC	24.73 (± 0.03)	37.22 (± 0.04)	17.53 (± 0.03)	29.37 (± 0.03)	--	--	7.04 (± 1.48)	8.77 (± 2.47)	--
VSM	18.85 (± 0.04)	38.90 (± 0.30)	19.00 (± 0.16)	24.45 (± 0.12)	2.86 (± 0.06)	4.05 (± 0.06)	19.60 (± 0.17)	24.36 (± 0.23)	36.10 (± 0.41)
χ x10^{-6} (emu/g) at 50K									
VSM (50 K)	104.00 (± 0.12)	176.00 (± 0.08)	83.40 (± 0.05)	108.00 (±0.10)	18.40 (± 0.01)	17.10 (± 0.01)	31.95 (± 0.08)	38.95 (± 0.13)	49.58 (± 0.14)
$\mu_{eff}=\sqrt{8\chi T}$ (μ_B) at 300 K									
per [MCl_n]	4.58	4.93	4.00	4.02	1.99	1.53	5.10	5.42	7.18
$\mu_{eff}=\sqrt{8\chi T}$ (μ_B) at 50 K									
per [MCl_n]	4.03	4.60	3.75	3.59	1.71	1.50	3.08	3.18	4.02
$\mu_{eff}=\sqrt{8C}$ (μ_B)									
per polymer	94.24	145.16	90.05	114.23	34.68	37.66	--	--	--
per [MCl_n]	4.02	4.57	3.69	3.47	1.74	1.34	--	--	--
Modified Curie-Weiss Law Fitting Results									
Θ_{CW} [K]	2.14	-2.19	-10.88	-7.83	10.97	10.97	--	--	--
χ_0 (emu/mol)	0.0019	0.0015	0.0012	0.0018	0.0004	0.0002	--	--	--
Int. Type	FM	AFM	AFM	AFM	FM	FM	--	--	--
Adj. R^2	0.99937	0.99983	0.99995	0.99983	0.99295	0.99906	--	--	--

Conversion to mole susceptibility per [MCl_n] and application of the modified Curie Weiss law (EQ 4-2) allowed for determining the Curie Weiss parameters. Figure C.2-Figure C.7 display the $1/\chi$-T responses and the non-linear regression fitting of the modified Curie Weiss law (EQ 4-2), and the resulting Weiss constant, θ_{CW}, and temperature independent susceptibility contribution, χ_o, are provided in Table 4.2. The [Pam-*co*-PDADMA][Co^{2+}] copolymers had Weiss constants of θ_{CW} = -10.88 K (1eq) and θ_{CW} = -7.83 K (2eq) confirming the presence of antiferromagnetic coupling interactions. Weak ferromagnetic coupling interactions were indicated by a Weiss constant of θ_{CW} = 2.14 K for [Pam-*co*-PDADMA][Fe^{3+} 1eq] while weak antiferromagnetic interactions were noted for [Pam-*co*-PDADMA][Fe^{3+} 2eq] with θ_{CW} = -2.19 K. In the vast majority of MIL literature, MILs containing $[FeCl_4]^-$ and $[CoCl_4]^{2-}$ were found to be paramagnetic with antiferromagnetic coupling interactions (typically θ_{CW} ~-0.5 to -13 K) that gained long-range antiferromagnetic ordering at temperatures below 10 K[23-26, 28, 29]. The [Pam-*co*-PDADMA][Co^{2+}] (at both 1 and 2eq) copolymers and [Pam-*co*-PDADMA][Fe^{3+} 2eq] copolymers, which were previously found to contain tetrahedral structured Co^{2+} and $[FeCl_4]^-$/$[Fe_2Cl_7]^-$ anions respectively[36], compare well to the MIL reported magnetic behavior. No definitive evidence of $[FeCl_4]^-$ formation was previously found in the [Pam-*co*-PDADMA][Fe^{3+} 1eq], rather the coordination structure was attributed to various acrylamide-$FeCl_3$ complexes[36]. The weak ferromagnetic coupling interactions, as indicated by a Weiss constant of θ_{cw} = 2.14 K, suggest the acrylamide coordination at lower metal halide addition influences the overall magnetic behavior of the copolymer, which becomes more antiferromagnetic with increasing addition of $[FeCl_4]^-$ and $[Fe_2Cl_7]^-$ species. However, further analysis of the magnetic behavior in the <50 K region will be needed to confirm ferromagnetic or antiferromagnetic behavior. Interestingly, the [Pam-*co*-PDADMA][Cu^{2+}] copolymers both had a θ_{CW} ~11 K, indicating ferromagnetic coupling interactions.

The effective magnetic moments per [MCl_n] shown in Table 4.2 were calculated based on both the fitted Curie constant through equation EQ 4-3 and at 300 K and 50 K through EQ 4-4 as often reported. For the purposes of this discussion, the moments calculated with EQ 4-3 are used. [Pam-*co*-PDADMA][Fe^{3+} 1eq] and [Pam-*co*-PDADMA][Fe^{3+} 2eq] had effective magnetic moments of 4.02 and 4.57 μ_B, which are lower than the expected spin only for high spin Fe^{3+} (S=5/2, ~5.92 μ_B) but still higher than low spin Fe^{3+} (S=1/2, ~1.73 μ_B) [39]. Most MIL and MPILs containing $[FeCl_4]^-$ anions are reported to have higher effective magnetic moments between 5.2-6.2 μ_B [22-29]. However, a few modified magnetic ionic liquids and metal organic coordination complexes have obtained similar effective magnetic moments. For instance, Nacham et al. developed a magnetic ionic liquid cation modified with carboxylate groups which had lower effective magnetic moments between ~3.5 and 4.7 μ_B [57]. They attributed the reduced magnetic moment to Fe^{3+} chelation with the carboxylate groups. Other Fe^{3+} coordination structures with various organic ligands (e.g, porphyrins, phosphine, salicylaldehyde) also having magnetic moments between ~3.8 and 4.3 μ_B were attributed to having an intermediate S= 3/2 (~3.87 μ_B) spin state or a mixture of low spin (S=1/2, ~1.73 μ_B) and high spin (S=5/2, ~5.92 μ_B) [58-62]. It is likely that the coordination of Fe^{3+} with acrylamide is resulting in similar behavior for the MPIL copolymers, although further studies involving electron paramagnetic resonance (EPR) or Mössbauer spectroscopies would be needed to determine the specific spin states of the [Pam-*co*-PDADMA][Fe^{3+}] copolymers. It should be noted that the magnetic moment for the [Pam-*co*-PDADMA][Fe^{3+} 2eq] sample is higher compared to the 1eq sample likely due to the presence of high spin $[FeCl_4]^-$ and $[Fe_2Cl_7]^-$ species that were confirmed by Raman and UV-vis spectroscopies previously[36]. This lends credence to the effective magnetic moment of the [Pam-*co*-PDADMA][Fe^{3+}] copolymers being a result of mixed S=1/2 and S=5/2 spin states as a result of mixed coordination complex species.

[Pam-*co*-PDADMA][Co^{2+} 1eq] and [Pam-*co*-PDADMA][Co^{2+} 2eq] copolymers had effective magnetic moments of 3.69 and 3.47 μ_B, respectively. These effective moments are also slightly lower than the expected high spin S=3/2 (3.88 μB, 4.3-5.2 observed) but higher than the expected low spin values (S=1/2 1.73 μ_B; 1.7-1.9 obs.) [39]. Although significantly fewer than their iron-based counterparts, MILs and MPILs containing $[CoCl_4]^-$ anions are typically reported to have effective magnetic moments values of ~4.2 to 4.5 μ_B[22, 24, 30]. The lower moments observed in the [Pam-*co*-PDADMA][Co^{2+}] may also be related to orbital contributions to the magnetic moment from acrylamide coordination[55]. Previous UV-vis spectroscopy measurements indicated the Co^{2+} was in a tetrahedral state, although Raman and FTIR spectroscopies suggested the presence of various tetrahedral acrylamide-Co^{2+} species (e.g., $[CoCl_2L_2]$, $[CoCl_3L]^-$) in addition to $[CoCl_4]^{2-}$ [36]. It is also possible there are multiple Co^{2+} species with different spin states, as was suggested above for the MPIL Fe^{3+} copolymer. Again, further EPR or Mössbauer spectroscopies would be needed to confirm the spin states present. [Pam-*co*-PDADMA][Cu^{2+}] copolymers had effective magnetic moments of 1.74 (1eq) and 1.34 (2eq) μ_B, which were in closer agreement with the with the expected spin only moment (S=1/2, 1.73 μ_B).

4.3.2.2. Magnetic Behavior of MPILSDS M^{n+} Polyelectrolyte-Surfactant Complexes.

Magnetic field dependences of the MPILSDS polyelectrolyte-surfactant complexes are shown in Figure 4.6 for 300 K (a and c) and 50 K (b and d). A more definite sigmoidal shape was observed for the MPILSDS complexes compared to the MPIL copolymers. Linear regression of the linear portion of the field response at low magnetic field strength (~ ± 2500 Oe) produced magnetic mass susceptibilities of 19.60, 24.36, and 36.10 $x10^{-6}$ emu/g for the MPILSDS Co^{2+} 7mM, MPILSDS Co^{2+} 5mM, and MPILSDS Fe^{3+} 5mM complexes at 300 K. Interestingly, these susceptibilities for the MPILSD Co^{2+} complexes were approximately 3x greater than that of the AC susceptibilities

measured for the air-dried complexes in prior work[37]. This result may be due to changes in metal coordination or structure due to the freeze-drying processes, and further structural studies (e.g., XRD, WAXS/SAXS) would be needed. The susceptibilities at 50 K were only ~ 1.5 times greater compared to 300 K with values of 31.95, 38.95, and 49.58 x 10^{-6} emu/g for MPILSDS Co^{2+} 7mM, MPILSDS Co^{2+} 5mM, and MPILSDS Fe^{3+} 5mM, respectively.

Possible small hysteresis curves were observed in both the MPILSDS Co^{2+} and MPILSDS Fe^{3+} samples, which were not present in the MPIL copolymers without surfactant. The coercive field values were 14.3, 14.7 and 13.1 Oe at 300 K and 20.0, 15.4, and 14.4 at 50 K for the MPILSDS Co^{2+} 7 mM, MPILSDS Co^{2+} 5 mM, and MPILSDS Fe^{3+} 7 mM complexes, respectively. The corresponding remanence values were 3.7 x10^{-4}, 5.4x10^{-7}, and 7.3 x10^{-4} emu/g at 300 K and 4.7x10^{-4}, 6.4x10^{-4}, and 1.1x10^{-3} emu/g at 50 K for the MPILSDS Co^{2+} 7 mM, MPILSDS Co^{2+} 5 mM, and MPILSDS Fe^{3+} 7 mM complexes, respectively. The presence of both the coercive fields and remanence in the magnetic field studies, especially in comparison to the MPIL copolymers without surfactant, would suggest magnetic behavior other than paramagnetic occurring for the MPILSDS complexes. Several MPIL systems have also reported similar behavior. Carrasco et al. developed an epoxy blended MPIL block copolymer that displayed weak ferromagnetic behavior as determined by the presence of coercive fields ~72-89 Oe and remanence 1.4-9.4x10^{-4} emu/g.[33] Although it should be noted the author did not perform ZFC-FC studies to verify the ferromagnetic behavior indicated by the hysteresis. Similarly, Yu et al. observed a 24 Oe coercive field and 3.6x10^{-3} emu/g remanence for a norbornene-type PIL with an imidazolium $[FeCl_4]^-$ magnetic group and biphenyl linker group. [17] They attributed the behavior of the MPIL to superparamagnetic properties and ferromagnetic interactions as determined through both magnetic field and temperature studies. Ni^{2+} and Nd^{3+} containing PIL block copolymers developed by Yang et al. had

coercive fields of ~20 Oe and remanence on the order of 10^{-3} to 10^{-4} emu/g.[34] In comparison, the coercive field values determined in this work are slightly lower than those observed by these authors, although the determined remanence values are consistent with the literature. In order to examine potential physical explanations for the hysteresis, ZFC-FC curves were also measured for the MPILSDS complexes.

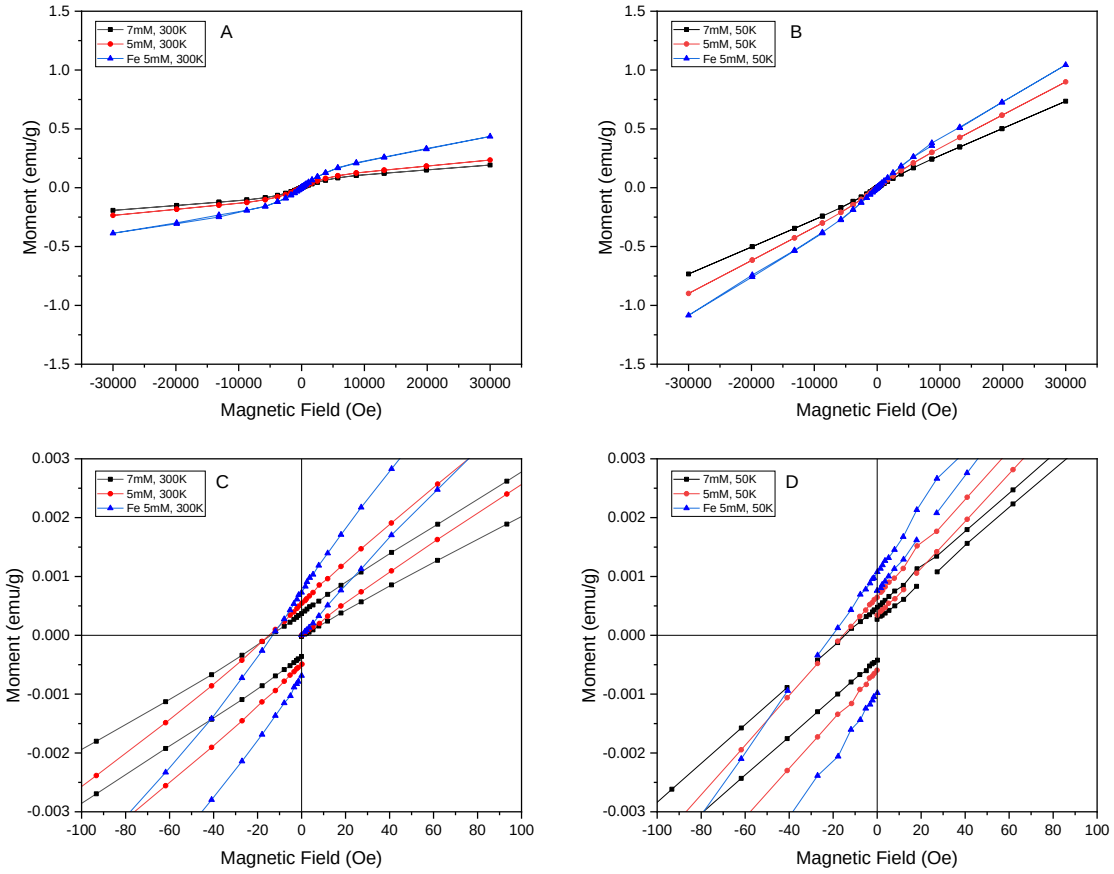

Figure 4.6 Magnetic moment as a function of magnetic field strength for the MPILSDS complexes at (a) 300 K and (b) 50 K. The magnetic moment response at low field strength (± 500 Oe) shows larger hysteresis curves at (c) 300 K compared to (d) 50 K.

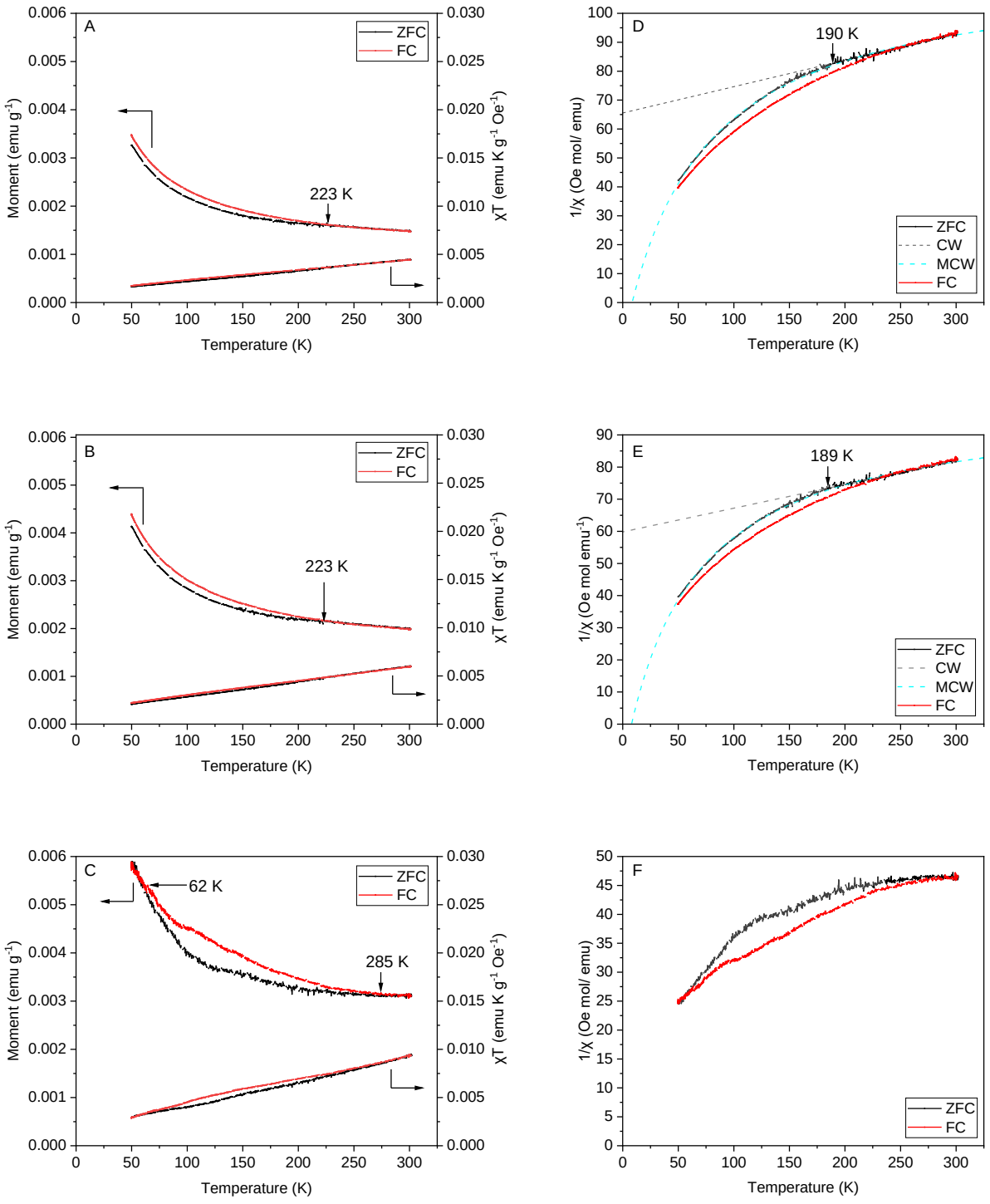

Figure 4.7 ZFC-FC temperature dependence of the magnetic moment, χT-T, and 1/χ-T responses for the MPILSDS complexes: MPILSDS Co^{2+}-7mM (a and d), MPILSDS Co^{2+} 5mM (b and e), and MPILSDS Fe^{3+} 5mM (c and f). In the 1/χ-T plots (d-e), Curie Weiss's law (CW, EQ 1, grey dash line) and the modified Curie Weiss's law (MC, EQ 2, blue dash line) were applied. For the MPILSDS Co^{2+} 7 mM complex (d), the CW fitting results in C= 10.99 emu K mol^{-1} , θ_{CW} = -720 K, and μ_{eff} = 9.377 μ_B. The MCW fitting results in C= 0.65 emu K mol^{-1}, θ_{CW} = 8.54, χ_o = 0.009 emu/mol, and μ_{eff} =2.29 μ_B. For the MPILSDS Co^{2+} 5 mM complex (e), the CW fitting results in C= 13.54 emu K mol^{-1} , θ_{CW} = -810 K, and μ_{eff} =10.41 μ_B. MCW fitting results in C = 0.67 emu K mol^{-1}, θ_{CW} =8.01, χ_o = 0.01 emu/mol, and μ_{eff} = 2.31 μ_B. CW and MCW fittings were not attempted for the MPILSDS Fe^{3+} 5 mM complex.

ZFC-FC moment and χT-T responses of the MPILSDS complexes as a function of temperature are shown in Figure 4.7 (a-c). A small bifurcation in the measured moment (Figure 4.7 a and b) was observed for the MPILSDS Co^{2+} complexes that started at ~ 223 K in both the 7 mM and 5 mM complex samples. A significant hysteresis was observed for the MPILSDS Fe^{3+} complex, starting at ~ 275 K and ending at 62 K with the largest deviation in moment at ~100 K (Figure 4.7c). Slightly larger χT^{300} -χT^{50} decreases (~2.85x10^{-3} emu K g^{-1} Oe^{-1} MPILSDS Co^{2+} 7 mM; 3.86x10^{-3} emu K g^{-1} Oe^{-1} MPILSDS Co^{2+} 5 mM; 6.56 x 10^{-3} emu K g^{-1} Oe^{-1} MPILSDS Fe^{3+} 5 mM) were observed for the MPILSDS complexes compared to the MPIL copolymers without surfactant, suggesting stronger antiferromagnetic interactions occurring in the MPILSDS complexes.

After converting the moment to mole susceptibility per [MCl_n], the 1/χ-T responses were determined and are shown in Figure 4.7(d-f). In the case of the MPILSDS Co^{2+} complexes, a linear region in the ZFC curve was observed between 300 K and ~190 K followed by a more rapid decrease between ~190 K and 50 K. This steeper decrease occurred at higher temperatures (~230-240 K) in the FC curve. As a clear deviation from linearity was observed, the first attempt to fit the ZFC 1/χ response to Curie Weiss law (EQ 4-1) was done over the 300-190 K range. The resulting Weiss constants were θ_{cw} ca. -720 K and -809 K for the MPILSDS Co^{2+} 7mM and MPILSDS Co^{2+} 5mM complexes, respectively. These Weiss constants suggest strong antiferromagnetic correlations are occurring in the MPILSDS Co^{2+} complexes in contrast to the MPIL copolymers, although the Neel temperature was not observed in the moment thermal responses down to 50 K. For comparative purposes, the 1/χ-T response was also fitted to the modified Curie Weiss law (EQ 4-2) over the full temperature range as done by Mugiraneza et. al. [39], which predicts an almost hyperbolic-like curve with an intercept temperature of ~8 K (blue

dashed line in Figure 4.7 d and e). Recalculation of the effective magnetic moments based on the modified Curie Weiss law fittings and EQ 4-3 yields moments of ~2.3 μ_B for the MPILSDS Co^{2+} complexes, which are closer to those predicted for low spin Co^{2+} (S=1/2, 1.73 μ_B). The decrease in magnetic moment would be consistent with antiferromagnetic behavior. Alternatively, a change in spin state may also occur with decreasing temperature. However, further temperature studies between 2 and 50 K are necessary to confirm this observation as well as determine the start of either long-range antiferromagnetic ordering or changes in spin state. EPR or Mössbauer experiments at temperatures within the 2-50 K range would also provide further clarification of the structure spin state.

Application of either the Curie Weiss law or the modified Curie Weiss law was not attempted for the MPILSDS Fe^{3+} 5mM complexes due to the irregular shape of the $1/\chi$-T response. However, it shows a gradual decrease in $1/\chi$-T response from 300-190 K followed by a more rapid decrease down to 50 K, also suggesting antiferromagnetic behavior. A bump in the $1/\chi$-T response at ~140 K in the ZFC data and at ~104 K in the FC curve is noted, although the physical basis for the response is currently uncertain. Additional magnetometry studies and EPR or Mössbauer experiments over the 2-50 K temperature range could provide additional information on the unique magnetic behavior of this system.

4.3.3. DSC

In order to aid analysis of the ZFC-FC responses, DSC was performed to examine thermal transitions due to physical changes in the MPIL copolymers and MPILSDS complexes in the 110-300 K temperature range (Figure 4.8). The large exothermal dip and endothermal peaks below 175 K in all samples are related to baseline correction artifacts as similar transitions were observed in all samples as well as in an adamantane thermal control sample (trace provided in the supplemental

information, Figure C.16). Note there is very limited DSC data reported in the literature for thermal transitions in the 300 to 110 K range for the polymer, surfactant, and metal chloride salts used in this study. The DSC trace for the non-magnetic base copolymer [Pam-*co*-PDADMA][Cl^-] showed no thermal transitions between 300 and 110 K. This is not unexpected as the reported glass transition temperature for a similar poly(acrylamide-*co*-diallyl dimethyl ammonium chloride) copolymer is well above room temperature (~170 °C) [63]. No clear thermal transitions were observed in the [Pam-*co*-PDADMA][Co^{2+}] and [Pam-*co*-PDADMA][Fe^{3+} 2eq] copolymers, although [Pam-*co*-PDADMA][Fe^{3+} 1eq] showed a possible endothermic peak at ~163 K (-110 °C) which, if not an artifact, would be likely related to a solid-solid phase transition. However, no corresponding transition in the ZFC-FC curves was observed at this temperature in the χT-T response for [Pam-*co*-PDADMA][Fe^{3+} 1eq] (Figure C.8c). Nor was the peak observed in the MPILSDS Fe^{3+} 5mM complex DSC trace.

The neat SDS trace exhibits two endothermic peaks located at ca. 229 K (-44 °C) and 290 K (17 °C). The latter peak is present in all the MPILSDS complex samples; this peak has been previously observed, though not identified, at ~18 °C in sodium dodecyl sulfate[52]. This transition is tentatively ascribed to a solid-solid phase transition, likely related to the surfactant alkyl chain structure. This peak was present at 290 K (17 °C) in the MPILSDS Co^{2+} complexes and slightly lower at 289 K (15 °C) in the MPILSDS Fe^{3+} complex. The former peak was not identified in any of the MPILSDS complexes, although the MPILSDS Co^{2+} 7 mM sample may exhibit a similar thermal transition at a higher temperature as seen by the small endothermic peak at ~270 K (-3 °C). Although given the temperature of this transition, it is possible the peak is related to melting of trace water.

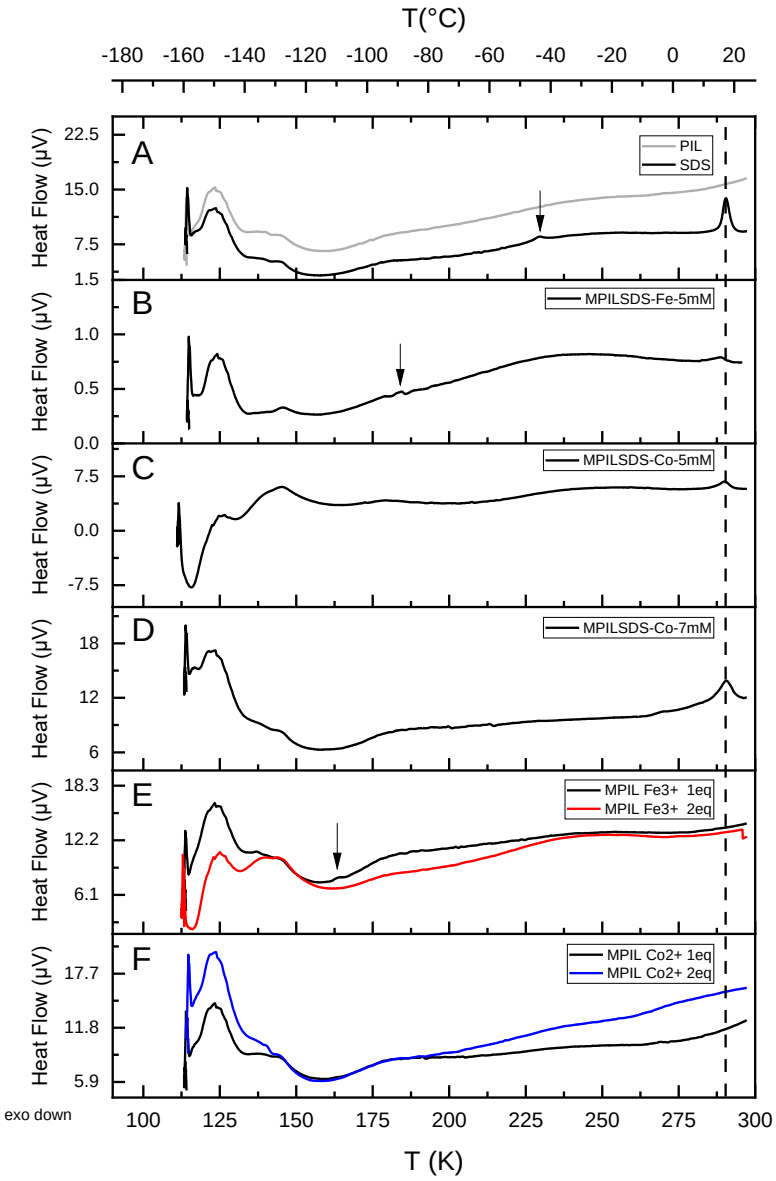

Figure 4.8 DSC traces between 110 and 300 K (-160 and 20 °C) for (a) the neat SDS (black) and [Pam-*co*-PDADMA][Cl^-] PIL controls, (b) MPILSDS Fe^{3+} 5mM, (c) MPILSDS Co^{2+} 5 mM, (d) MPILSDS Co^{2+} 7 mM, (e) [Pam-co-PDADMA][Fe^{3+} 1 and 2eq] MPIL copolymers, and (f) [Pam-co-PDADMA][Fe^{3+} 1 and 2eq] MPIL copolymers.

The magnetic response of the MPIL and MPILSDS systems do not appear to be due to their thermal properties. Thermal transitions observed in the DSC analysis do not align well with either the observed bifurcation in the ZFC-FC moment curves or the rapid decrease in the $1/\chi$-T response starting at ~190 K in the MPILSDS Co^{2+} complexes. Similarly, the DSC-determined thermal transitions do not correspond to the start of the hysteresis observed in the MPILSDS Fe^{3+} complex. These results show the magnetic behavior observed as a function of temperature is not a result of physical changes occurring in the MPIL copolymers or MPILSDS complexes. Therefore, the thermal transitions observed in the ZFC-FC experiments result from magnetic interaction changes with decreasing temperature.

4.3.4. Comparison of Magnetic Behavior Between MPIL Copolymers and the MPILSDS Complexes

While the magnetic mass susceptibilities of the MPILSDS complexes are lower than the MPIL copolymers due to lower overall weight percentages of metal content, the effective magnetic moments per $[MCl_n]$ were higher in the MPILSDS complexes as seen in Figure 4.9. As the magnetic behavior and Curie Weiss fittings for the MPILSDS complexes are currently uncertain, the effective magnetic moment for the MPIL copolymers and MPILSDS complexes were estimated with EQ 4-4 at 300 K where paramagnetic behavior with the least amount of influence from magnetic correlations is expected for both systems. The MPILSDS Co^{2+} 7 mM and 5 mM complexes show effective moments of 5.10 and 5.42 μ_B, respectively, which is greater than the 4.00 μ_B moment calculated for [Pam-*co*-PDADMA][Co^{2+} 1eq]. Both values are more consistent with typically observed moments for high spin Co^{2+} (4.3-5.2 μB) [39] compared to the Curie constant calculated moment, although the MPILSDS Co^{2+} moment falls on the higher end of the range. The MPILSDS Fe^{3+} 5mM complex also exhibits a higher effective moment of 7.18 μ_B compared to the

4.58 μ_B effective moment for [Pam-*co*-PDADMA][Fe^{3+} 1eq]. MPILSDS Fe^{3+} 5 mM effective moment is both higher than the expected spin only value for high spin Fe^{3+} (S=5/2, 5.92 μ_B) and typical experimentally observed values (5.6-6.1 μ_B) [39]. It is noted that the effective magnetic moment calculated by EQ 4-4 assumes negligible magnetic correlations. The higher-than-expected magnetic moment, compared to the spin only values, likely indicates the presence of magnetic correlation effects occurring in the MPILSDS Fe^{3+} complex, even at 300 K.

Regardless, the higher moments observed in the MPILSDS complexes compared to the MPIL copolymer with lower weight percentages of metal content suggests that the surfactant induced self-assembly enhances the coupling of metal centers, resulting in a larger effective moment. As seen in other MPIL systems containing long alkyl chains or microphase separated morphologies, this may be a result of restricted movement of the metal species in the self-assembled structures and improved coupling interactions[15, 18, 19]. Previously, drop-cast MPILSDS Co^{2+} complex films on silicon wafers demonstrated lamellar-like assembly behavior through AFM and GISAXS analysis[37]. Further, FTIR analysis of the MPILSDS Co^{2+} and MPILSDS Fe^{3+} complexes do show evidence of partially ordered alkyl chains in the CH_2 C-H str and CH_2 bending modes as discussed above (Figure C.17-Figure C.20). However, further structural studies, such as XRD or WAXS/SAXS, will likely be needed to confirm internal ordering structure of the freeze-dried flakes at the nano- and angstrom- scales. As the Co^{2+} and Fe^{3+} cations were found to coordinate with both the acrylamide monomer unit and the surfactant SO_4^- group in the FTIR studies above, the change in coordination structure of the metal species may also influence the resulting spin state of the metal species within the MPILSDS complexes.

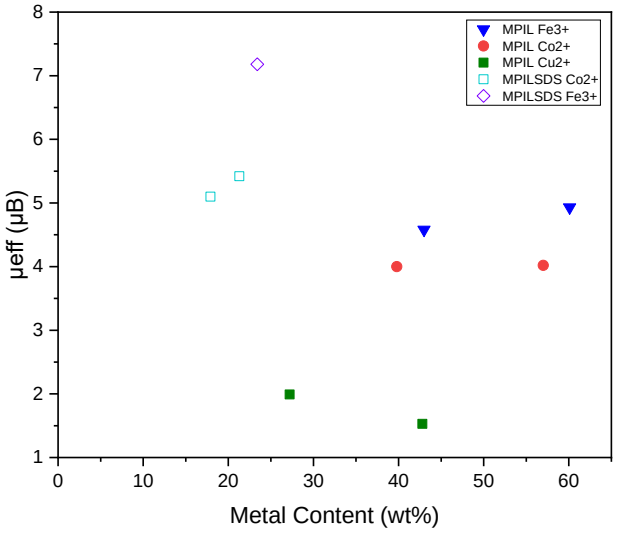

Figure 4.9 Effective moments estimated by (EQ 4) at 300 K for the MPIL copolymers and MPILSDS complexes as a function of metal content weight percentage.

4.4. Conclusions

Vibrating sample magnetometry studies performed on multi-component MPIL random copolymers with metal-coordinating acrylamide units and their corresponding self-assembled polyelectrolyte-surfactant complexes showed changes in magnetic behavior based on metal type, metal concentration, coordination structure, and self-assembled structure. The magnetometry studies were paired with further chemical, structural, and thermal characterizations. FTIR spectroscopies confirmed polymer-metal coordination with the acrylamide unit in the MPIL copolymers and with the surfactant SO_4^- group in the MPILSDS complexes for all transition metal cations studied. DLS, ZP, and SEM characterizations indicate a change in MPILSDS complex structure from self-assembled spherical particles in solution to flake-like morphology after freeze drying. MPIL copolymers were found to exhibit paramagnetic behavior in the temperature range measured with either antiferromagnetic or ferromagnetic correlations present depending on metal cation type, concentration, and resulting coordination structure. In particular [Pam-*co*-PDADMA][Co^{2+}] and [Pam-*co*-PDADMA][Cu^{2+}] copolymers displayed antiferromagnetic and

ferromagnetic correlations respectively, while the [Pam-*co*-PDADMA][Fe^{3+}] copolymers transitioned from ferromagnetic interactions at 1 eq to antiferromagnetic at 2eq with changing metal coordination structure. Lower than expected effective magnetic moments suggested a possible mixture of spin states in the MPIL copolymers as a result of a mixture of metal-acrylamide coordination species and $[FeCl_4]^-$/$[CoCl_4]^{2-}$ species, demonstrating the importance of understanding polymer-metal coordination interactions in multi-component MPILs.

Examination of the magnetic moment of the MPILSDS complexes as a function of magnetic field strength and temperature revealed characteristics of non-paramagnetic behavior. ZFC-FC experiments on the MPILSDS complexes indicated deviations from Curie Weiss paramagnetism below 190 K for the MPILSDS Co^{2+} complexes while the full temperature range for the MPILSDS Fe^{3+} complex did not comply with the Curie Weiss law. Strong antiferromagnetic interactions in the MPILSDS Co^{2+} complexes were indicated by the large decrease in $1/\chi$-T response below 190 K and large negative θ_{CW} values, suggesting long range antiferromagnetic ordering at temperatures below 50 K, which may be verified with further SQUID magnetometry studies between 2-50K. Corresponding DSC studies in the 300-110 K range indicate that the magnetic thermal transitions observed for the MPILSDS complexes and the MPIL copolymers are based solely on magnetic interaction changes and not physical changes. Higher effective magnetic moments were observed for the MPILSDS complexes compared to the MPIL copolymers, even with the lower weight percentages of metal content. This indicates that the self-assembled structure of the magnetically responsive polyelectrolyte-surfactant complexes or a change in metal-polymer-surfactant coordination state enhance magnetic coupling in the MPILSDS complexes compared to the MPIL random copolymers. Transition of the MPIL copolymers from paramagnetic materials with weak magnetic correlations to strongly antiferromagnetic interactions in the surfactant induced self-

assembled structures further demonstrates the importance of co-materials on MPIL magnetic behavior.

Acknowledgements

The authors would like to thank the Center for Integrated Nanotechnologies (CINT) and Sandia National Labs for access to the vibrating sample magnetometer instrument. The authors would also like to thank Dr. Tammy Lutz-Rechtin for her aid in the freeze-drying process of the polyelectrolyte-surfactant complex samples.

4.5. References

(1) Clark, K. D.; Nacham, O.; Purslow, J. A.; Pierson, S. A.; Anderson, J. L. Magnetic ionic liquids in analytical chemistry: A review. *Anal. Chim. Acta* **2016**, *934*, 9-21, 10.1016/j.aca.2016.06.011. DOI: 10.1016/j.aca.2016.06.011.

(2) Joseph, A.; Zyla, G.; Thomas, V. I.; Nair, P. R.; Padmanabhan, A. S.; Mathew, S. Paramagnetic ionic liquids for advanced applications: A review. *J. Mol. Liq.* **2016**, *218*, 319-331, 10.1016/j.molliq.2016.02.086. DOI: 10.1016/j.molliq.2016.02.086.

(3) Brown, P.; Alan Hatton, T.; Eastoe, J. Magnetic surfactants. *Curr. Opin. Colloid Interface Sci.* **2015**, *20* (3), 140-150, 10.1016/j.cocis.2015.08.002. DOI: 10.1016/j.cocis.2015.08.002.

(4) Wang, L.; Dong, S.; Hao, J. Recent progress of magnetic surfactants: Self-assembly, properties and functions. *Curr. Opin. Colloid Interface Sci.* **2018**, *35*, 81-90, 10.1016/j.cocis.2018.01.014. DOI: 10.1016/j.cocis.2018.01.014.

(5) Dobbelin, M.; Jovanovski, V.; Llarena, I.; Marfil, L. J. C.; Cabanero, G.; Rodriguez, J.; Mecerreyes, D. Synthesis of paramagnetic polymers using ionic liquid chemistry. *Polym. Chem.* **2011**, *2* (6), 1275-1278. DOI: 10.1039/c1py00044f.

(6) Sahiner, N.; Demir, S.; Yildiz, S. Magnetic colloidal polymeric ionic liquid synthesis and use in hydrogen production. *Colloids Surf., A* **2014**, *449*, 87-95, 10.1016/j.colsurfa.2014.02.046. DOI: 10.1016/j.colsurfa.2014.02.046.

(7) Hazell, G.; Hinojosa-Navarro, M.; McCoy, T. M.; Tabor, R. F.; Eastoe, J. Responsive materials based on magnetic polyelectrolytes and graphene oxide for water clean-up. *J. Colloid Interface Sci.* **2016**, *464*, 285-290, 10.1016/j.jcis.2015.11.029. DOI: 10.1016/j.jcis.2015.11.029.

(8) de la Fuente-Nunez, C.; Brown, P.; Torres, M. D. T.; Cao, J.; Lu, T. K. Magnetic Surfactant Ionic Liquids and Polymers With Tetrahaloferrate (III) Anions as Antimicrobial Agents With Low Cytotoxicity. *Colloid and Interface Science Communications* **2018**, *22*, 11-13. DOI: https://doi.org/10.1016/j.colcom.2017.11.002.

(9) Sun, J.-K.; Kochovski, Z.; Zhang, W.-Y.; Kirmse, H.; Lu, Y.; Antonietti, M.; Yuan, J. General Synthetic Route toward Highly Dispersed Metal Clusters Enabled by Poly(ionic liquid)s. *Journal of the American Chemical Society* **2017**, *139* (26), 8971-8976. DOI: 10.1021/jacs.7b03357.

(10) Chikh Alard, I.; Soubhye, J.; Berger, G.; Gelbcke, M.; Spassov, S.; Amighi, K.; Goole, J.; Meyer, F. Triple-stimuli responsive polymers with fine tuneable magnetic responses. *Polym. Chem.* **2017**, *8* (16), 2450-2456, 10.1039/C7PY00218A. DOI: 10.1039/C7PY00218A.

(11) Malecha, J. J.; Biller, J. R.; Lama, B.; Gin, D. L. System for Living ROMP of a Paramagnetic FeCl4–-Based Ionic Liquid Monomer: Direct Synthesis of Magnetically Responsive Block Copolymers. *ACS Macro Letters* **2020**, *9* (1), 140-145. DOI: 10.1021/acsmacrolett.9b00902.

(12) Ohara, Y.; Kawata, Y.; Hyde, A.; Phan, C.; Takeda, R.; Takemura, Y.; Yusa, S.-i. Preparation of a Magnetic-responsive Polycation with a Tetrachloroferrate Anion. *Chemistry Letters* **2017**, *46* (10), 1473-1475. DOI: 10.1246/cl.170621 (acccessed 2021/11/07).

(13) Rahman, M. T.; Barikbin, Z.; Badruddoza, A. Z. M.; Doyle, P. S.; Khan, S. A. Monodisperse Polymeric Ionic Liquid Microgel Beads with Multiple Chemically Switchable Functionalities. *Langmuir* **2013**, *29* (30), 9535-9543, 10.1021/la401613w. DOI: 10.1021/la401613w.

(14) Ji, S.; Yuan, X.; Guo, Q.; Ren, L. Self-assembly induced ferromagnetic interaction in magnetic polymers with terphenyl linkers. *Polymer Chemistry* **2023**, *14* (18), 2238-2245, 10.1039/D3PY00186E. DOI: 10.1039/D3PY00186E.

(15) Li, J.; Ji, S.; Yu, X.; Yuan, X.; Zhang, K.; Ren, L. Magnetic Poly(ionic liquid)s: Bottlebrush versus Linear Structures. *Macromolecules* **2022**, *55* (6), 2067-2074. DOI: 10.1021/acs.macromol.1c02457.

(16) Yu, X.; Xia, Z.; Zhao, T.; Yuan, X.; Ren, L. Pyrene-Enhanced Ferromagnetic Interaction in a FeCl4–-Based Poly(ionic liquid)s Organic Magnet. *Macromolecules* **2021**, *54* (9), 4227-4235. DOI: 10.1021/acs.macromol.1c00213.

(17) Yu, X.; Yuan, X.; Zhao, Y.; Ren, L. From Paramagnetic to Superparamagnetic Ionic Liquid/Poly(ionic liquid): The Effect of π–π Stacking Interaction. *ACS Macro Letters* **2019**, *8* (11), 1504-1510. DOI: 10.1021/acsmacrolett.9b00714.

(18) Xia, Z.; Yu, X.; Dai, D.; Yuan, X.; Ren, L. Magnetic monomers and polymers based on alkyl-imidazolium FeCl4: The effect of alkyl chain length. *Polymer* **2018**, *157*, 32-37. DOI: https://doi.org/10.1016/j.polymer.2018.10.015.

(19) Xia, Z.; Yu, X.; Zhang, T.; Yuan, X.; Ren, L. Inorganic/organic hybrid magnetic polymers based on POSS and pyridinium FeCl4: the effect of self-assembly. *Polymer Chemistry* **2019**, *10* (33), 4604-4610, 10.1039/C9PY00807A. DOI: 10.1039/C9PY00807A.

(20) Yu, X.; Mu, C.; Dai, D.; Yuan, X.; Zhang, K.; Ren, L. Well-Defined Magnetic Responsive Polymers Containing Ammonium FeCl4 from ROMP. *Macromolecular Chemistry and Physics* **2016**, *217* (24), 2700-2707. DOI: https://doi.org/10.1002/macp.201600435.

(21) Zhang, T.; Yu, X.; Yuan, X.; Zhao, Y.; Ren, L. Tadpole-shaped magnetic block copolymer: Self-assembly induced increase of magnetic susceptibility. *Polymer* **2018**, *135*, 9-15. DOI: https://doi.org/10.1016/j.polymer.2017.12.009.

(22) Bonnefond, A.; Ibarra, M.; Mecerreyes, D.; Leiza, J. R. Adding magnetic ionic liquid monomers to the emulsion polymerization tool-box: Towards polymer latexes and coatings with new properties. *J. Polym. Sci., Part A: Polym. Chem.* **2016**, *54* (8), 1145-1152, 10.1002/pola.27953. DOI: 10.1002/pola.27953.

(23) de Pedro, I.; Rojas, D. P.; Blanco, J. A.; Fernández, J. R. Antiferromagnetic ordering in magnetic ionic liquid Emim[FeCl4]. *Journal of Magnetism and Magnetic Materials* **2011**, *323* (10), 1254-1257. DOI: https://doi.org/10.1016/j.jmmm.2010.11.016.

(24) Del Sesto, R. E.; McCleskey, T. M.; Burrell, A. K.; Baker, G. A.; Thompson, J. D.; Scott, B. L.; Wilkes, J. S.; Williams, P. Structure and magnetic behavior of transition metal based ionic liquids. *Chemical Communications* **2008**, (4), 447-449, 10.1039/B711189D. DOI: 10.1039/B711189D.

(25) James, B. D.; Mrozinski, J.; Klak, J.; Skelton, B. W.; White, A. H. Tetrachloroferrate(III) Complexes Containing Some Heteroaromatic Organic Cations: Structures and Magnetic Properties. *Zeitschrift für anorganische und allgemeine Chemie* **2009**, *635* (2), 317-322, https://doi.org/10.1002/zaac.200800429. DOI: https://doi.org/10.1002/zaac.200800429 (acccessed 2023/06/07).

(26) Krieger, B. M.; Lee, H. Y.; Emge, T. J.; Wishart, J. F.; Castner, J. E. W. Ionic liquids and solids with paramagnetic anions. *Physical Chemistry Chemical Physics* **2010**, *12* (31), 8919-8925, 10.1039/B920652N. DOI: 10.1039/B920652N.

(27) Nacham, O.; Clark, K. D.; Yu, H.; Anderson, J. L. Synthetic Strategies for Tailoring the Physicochemical and Magnetic Properties of Hydrophobic Magnetic Ionic Liquids. *Chemistry of Materials* **2015**, *27* (3), 923-931. DOI: 10.1021/cm504202v.

(28) Wyrzykowski, D.; Kruszyński, R.; Kłak, J.; Mroziński, J.; Warnke, Z. Magnetic Characteristics of Tetrabutylammonium Tetrahalogenoferrates(III): X-ray Crystal Structure of Tetrabutylammonium Tetrabromoferrate(III). *Zeitschrift für anorganische und allgemeine Chemie* **2007**, *633* (11-12), 2071-2076, https://doi.org/10.1002/zaac.200700261. DOI: https://doi.org/10.1002/zaac.200700261 (acccessed 2023/06/07).

(29) Yoshida, Y.; Otsuka, A.; Saito, G.; Natsume, S.; Nishibori, E.; Takata, M.; Sakata, M.; Takahashi, M.; Yoko, T. Conducting and magnetic properties of 1-ethyl-3-methylimidazolium (EMI) salts containing paramagnetic irons: liquids [EMI][MIIICl4](M= Fe and Fe0. 5Ga0. 5) and solid [EMI] 2 [FeIICl4]. *Bulletin of the chemical society of Japan* **2005**, *78* (11), 1921-1928.

(30) Brown, P.; Butts, C. P.; Eastoe, J.; Glatzel, S.; Grillo, I.; Hall, S. H.; Rogers, S.; Trickett, K. Microemulsions as tunable nanomagnets. *Soft Matter* **2012**, *8* (46), 11609-11612, 10.1039/C2SM26827B. DOI: 10.1039/C2SM26827B.

(31) Carrasco, P. M.; Tzounis, L.; Mompean, F. J.; Strati, K.; Georgopanos, P.; Garcia-Hernandez, M.; Stamm, M.; Cabañero, G.; Odriozola, I.; Avgeropoulos, A.; et al. Thermoset Magnetic Materials Based on Poly(ionic liquid)s Block Copolymers. *Macromolecules* **2013**, *46* (5), 1860-1867. DOI: 10.1021/ma302261c.

(32) Cui, J.; Yang, S.; Zhang, J.; Zhao, S.; Yan, Y. A novel poly[(N-vinylimidazole)-co-(1-pyrenylmethyl methacrylate)] ferric complex with fluorescence and superparamagnetism. *RSC Advances* **2012**, *2* (32), 12224-12230, 10.1039/C2RA22395C. DOI: 10.1039/C2RA22395C.

(33) Carrasco, P. M.; Tzounis, L.; Mompean, F. J.; Strati, K.; Georgopanos, P.; Garcia-Hernandez, M.; Stamm, M.; Cabanero, G.; Odriozola, I.; Avgeropoulos, A.; et al. Thermoset Magnetic Materials Based on Poly(ionic liquid)s Block Copolymers. *Macromolecules (Washington, DC, U. S.)* **2013**, *46* (5), 1860-1867, 10.1021/ma302261c. DOI: 10.1021/ma302261c.

(34) Yang, J.; Sun, W.; Lin, W.; Shen, Z. Synthesis and magnetic properties of comb-like copolymeric complexes based on thiazole ring and ionic liquid. *Journal of Polymer Science Part A: Polymer Chemistry* **2008**, *46* (15), 5123-5132. DOI: https://doi.org/10.1002/pola.22840.

(35) Cui, J.; Nie, F.-M.; Yang, J.-X.; Pan, L.; Ma, Z.; Li, Y.-S. Novel imidazolium-based poly(ionic liquid)s with different counterions for self-healing. *Journal of Materials Chemistry A* **2017**, *5* (48), 25220-25229, 10.1039/C7TA06793C. DOI: 10.1039/C7TA06793C.

(36) Kayla Foley, L. C., Keisha B. Walters. Influence of metal-coordinating comonomers on the coordination structure and binding in magnetic poly(ionic liquid)s. *Molecular Systems Design and Engineering, Under Review (ME-ART-05-2023-000076, submitted 05-18-2023)* **2023**.

(37) Foley, K.; Walters, K. B. Development of Nano- and Micro-Fluids Using Magnetic Poly(Ionic Liquid)-Surfactant Complexes for Stimuli Response. In *ASME 2022 Fluids Engineering Division Summer Meeting*, 2022; V002T06A006, Vol. Volume 2: Multiphase Flow (MFTC); Computational Fluid Dynamics (CFDTC); Micro and Nano Fluid Dynamics (MNFDTC). DOI: 10.1115/fedsm2022-87758.

(38) Garcia, M. A.; Fernandez Pinel, E.; de la Venta, J.; Quesada, A.; Bouzas, V.; Fernández, J. F.; Romero, J. J.; Martín González, M. S.; Costa-Krämer, J. L. Sources of experimental errors in the observation of nanoscale magnetism. *Journal of Applied Physics* **2009**, *105* (1). DOI: 10.1063/1.3060808 (acccessed 6/10/2023).

(39) Mugiraneza, S.; Hallas, A. M. Tutorial: a beginner's guide to interpreting magnetic susceptibility data with the Curie-Weiss law. *Communications Physics* **2022**, *5* (1), 95. DOI: 10.1038/s42005-022-00853-y.

(40) Gosk, J. B.; Kulszewicz-Bajer, I.; Twardowski, A. Magnetic properties of polyaniline doped with FeCl3. *Synthetic Metals* **2006**, *156* (11), 773-778. DOI: https://doi.org/10.1016/j.synthmet.2006.02.003.

(41) Mozur, E. M.; Seshadri, R. Methods and Protocols: Practical Magnetic Measurement. *Chemistry of Materials* **2023**, *35* (9), 3450-3463. DOI: 10.1021/acs.chemmater.3c00297.

(42) Nag, A.; Ray, S. Misjudging frustrations in spin liquids from oversimplified use of Curie-Weiss law. *Journal of Magnetism and Magnetic Materials* **2017**, *424*, 93-98. DOI: https://doi.org/10.1016/j.jmmm.2016.10.014.

(43) Khan, N.; Brettmann, B. Intermolecular interactions in polyelectrolyte and surfactant complexes in solution. *Polymers (Basel, Switz.)* **2019**, *11* (1), 51/51. DOI: 10.3390/polym11010051.

(44) Ober, C. K.; Wegner, G. Polyelectrolyte-surfactant complexes in the solid state. Facile building blocks for self-organizing materials. *Adv. Mater. (Weinheim, Ger.)* **1997**, *9* (1), 17-31, 10.1002/adma.19970090104. DOI: 10.1002/adma.19970090104.

(45) Abraham, A.; Campbell, R. A.; Varga, I. New Method to Predict the Surface Tension of Complex Synthetic and Biological Polyelectrolyte/Surfactant Mixtures. *Langmuir* **2013**, *29* (37), 11554-11559. DOI: 10.1021/la402525w.

(46) Nizri, G.; Lagerge, S.; Kamyshny, A.; Major, D. T.; Magdassi, S. Polymer-surfactant interactions: Binding mechanism of sodium dodecyl sulfate to poly(diallyldimethylammonium chloride). *J. Colloid Interface Sci.* **2008**, *320* (1), 74-81, 10.1016/j.jcis.2008.01.016. DOI: 10.1016/j.jcis.2008.01.016.

(47) Nizri, G.; Magdassi, S.; Schmidt, J.; Cohen, Y.; Talmon, Y. Microstructural Characterization of Micro- and Nanoparticles Formed by Polymer-Surfactant Interactions. *Langmuir* **2004**, *20* (11), 4380-4385, 10.1021/la0364441. DOI: 10.1021/la0364441.

(48) Plazzotta, B.; Fegyver, E.; Mészáros, R.; Pedersen, J. S. Anisometric Polyelectrolyte/Mixed Surfactant Nanoassemblies Formed by the Association of Poly(diallyldimethylammonium chloride) with Sodium Dodecyl Sulfate and Dodecyl Maltoside. *Langmuir* **2015**, *31* (26), 7242-7250. DOI: 10.1021/acs.langmuir.5b01280.

(49) Girma, K. B.; Lorenz, V.; Blaurock, S.; Edelmann, F. T. Coordination chemistry of acrylamide. *Coordination Chemistry Reviews* **2005**, *249* (11), 1283-1293. DOI: https://doi.org/10.1016/j.ccr.2005.01.028.

(50) Girma, K. B.; Lorenz, V.; Blaurock, S.; Edelmann, F. T. Coordination Chemistry of Acrylamide 4. Crystal Structures and IR Spectroscopic Properties of Acrylamide Complexes with CoII, NiII, and ZnII nitrates. *Zeitschrift für anorganische und allgemeine Chemie* **2005**, *631* (10), 1843-1848, https://doi.org/10.1002/zaac.200500210. DOI: https://doi.org/10.1002/zaac.200500210 (acccessed 2022/05/11).

(51) Girma, K. B.; Lorenz, V.; Blaurock, S.; Edelmann, F. T. Coordination Chemistry of Acrylamide 2. Classical Complexes of Acrylamide with Manganese(II), Iron(II) and Nickel(II) Chlorides: Syntheses and Crystal Structures. *Zeitschrift für anorganische und allgemeine Chemie* **2005**, *631* (13-14), 2763-2769, https://doi.org/10.1002/zaac.200500132. DOI: https://doi.org/10.1002/zaac.200500132 (acccessed 2023/02/21).

(52) Pereira, R. F. P.; Valente, A. J. M.; Burrows, H. D.; de Zea Bermudez, V.; Carvalho, R. A.; Castro, R. A. E. Structural characterization of solid trivalent metal dodecyl sulfates: from aqueous solution to lamellar superstructures. *RSC Adv.* **2013**, *3* (5), 1420-1433. DOI: 10.1039/c2ra21906a.

(53) Scheuing, D. R.; Weers, J. G. A Fourier transform infrared spectroscopic study of dodecyltrimethylammonium chloride/sodium dodecyl sulfate surfactant mixtures. *Langmuir* **1990**, *6* (3), 665-671, 10.1021/la00093a023. DOI: 10.1021/la00093a023.

(54) Viana, R. B.; da Silva, A. B. F.; Pimentel, A. S. Infrared spectroscopy of anionic, cationic, and zwitterionic surfactants. *Adv. Phys. Chem.* **2012**. DOI: 10.1155/2012/903272.

(55) Shriver, D.; Weller, M.; Overton, T.; Armstrong, F.; Rourke, J. *Inorganic Chemistry*; W. H. Freeman, 2014.

(56) Blundell, S. *Magnetism in Condensed Matter*; Oxford University Press, 2001.

(57) Nacham, O.; Clark, K. D.; Anderson, J. L. Synthesis and characterization of the physicochemical and magnetic properties for perfluoroalkyl ester and Fe(iii) carboxylate-based

hydrophobic magnetic ionic liquids. *RSC Advances* **2016**, *6* (14), 11109-11117, 10.1039/C5RA25002A. DOI: 10.1039/C5RA25002A.

(58) Koch, W. O.; Schünemann, V.; Gerdan, M.; Trautwein, A. X.; Krüger, H.-J. Evidence for an Unusual Thermally Induced Low-Spin (S=1/2) ⇄ Intermediate-Spin (S=3/2) Transition in a Six-Coordinate Iron(III) Complex: Structure and Electronic Properties of a (1,2-Benzenedithiolato)iron(III) Complex Containing N,N′-Dimethyl-2,11-diaza[3.3](2,6)pyridinophane as Ligand. *Chemistry – A European Journal* **1998**, *4* (4), 686-691, https://doi.org/10.1002/(SICI)1521-3765(19980416)4:4<686::AID-CHEM686>3.0.CO;2-P. DOI: https://doi.org/10.1002/(SICI)1521-3765(19980416)4:4<686::AID-CHEM686>3.0.CO;2-P (acccessed 2023/06/08).

(59) Sahoo, D.; Quesne, M. G.; de Visser, S. P.; Rath, S. P. Hydrogen-Bonding Interactions Trigger a Spin-Flip in Iron(III) Porphyrin Complexes. *Angewandte Chemie International Edition* **2015**, *54* (16), 4796-4800, https://doi.org/10.1002/anie.201411399. DOI: https://doi.org/10.1002/anie.201411399 (acccessed 2023/06/08).

(60) Sinn, E.; Sim, G.; Dose, E. V.; Tweedle, M. F.; Wilson, L. J. Iron(III) chelates with hexadentate ligands from triethylenetetramine and .beta.-diketones or salicylaldehyde. Spin state dependent crystal and molecular structures of [Fe(acac)2trien]PF6(S = 5/2), [Fe(acacCl)2trien]PF6(S = 5/2), [Fe(sal)2trien]Cl.2H2O(S = 1/2), and [Fe(sal)2trien]NO3.H2O(S = 1/2). *Journal of the American Chemical Society* **1978**, *100* (11), 3375-3390. DOI: 10.1021/ja00479a021.

(61) Stuzhin, P. A.; Nefedov, S. E.; Kumeev, R. S.; Ul-Haq, A.; Minin, V. V.; Ivanova, S. S. Effects of Solvation on the Spin State of Iron(III) in 2,8,12,18-Tetrabutyl-3,7,13,17-tetramethyl-5,10-diazaporphyrinatoiron(III) Chloride. *Inorganic Chemistry* **2010**, *49* (11), 4802-4813. DOI: 10.1021/ic9012075.

(62) Walker, J. D.; Poli, R. Trichloroiron (FeCl3)-phosphine adducts with trigonal-bipyramidal geometry. Influence of the phosphine on the spin state. *Inorganic Chemistry* **1989**, *28* (10), 1793-1801.

(63) Zhao, Q.; Sun, J.; Chen, S.; Zhou, Q. Properties of a poly(acrylamide-co-diallyl dimethyl ammonium chloride) hydrogel synthesized in a water–ionic liquid binary system. *Journal of Applied Polymer Science* **2010**, *115* (5), 2940-2945, https://doi.org/10.1002/app.31368. DOI: https://doi.org/10.1002/app.31368 (acccessed 2023/06/08).

Chapter 5: Solution and film self-assembly behavior of a block copolymer comprised of a poly(ionic liquid) and a stimuli-responsive weak polyelectrolyte

***** This appendix contains the adapted supplemental information from the submitted journal article: **Kayla Foley**, Keisha B. Walters. "Poly(ionic liquid)s blocked with the stimuli responsive weak polyelectrolyte poly[2-(dimethylamino) ethyl methacrylate] and their solution and film assembly," Submitted May 2023, *ACS Omega.* [Under Review]

Abstract

Cu(0)-mediated atom transfer radical polymerization was used to synthesize the poly(ionic liquid), poly[4-vinylbenzyl-3butylimidazolium bis(trifluoromethylsulfonyl)imide] (PVBBImTf_2N), a stimuli-responsive polyelectrolyte, poly[2-(dimethylamino)ethyl methacrylate] (PDMAEMA), and a novel block copolymer formed from these two polymers. The synthesis of the block copolymer, poly[2-(dimethylamino) ethyl methacrylate]-*block*-[poly(4-vinylbenzyl-3-butylimidazolium bis(trifluoromethane)sulfonylimide] (PDMAEMA-*b*-PVBBImTf_2N) was examined for "livingness" polymerization control through molecular weight and degree of polymerization characterizations and ^{1}HNMR spectroscopy. 2D DOSY NMR measurements revealed successful block copolymerization and connectivity of the two polymer blocks. PDMAEMA-*b*-PVBBImTf_2N was further characterized for supramolecular interactions in both the bulk and solution states through FTIR and ^{1}H NMR spectroscopies. While the block copolymer demonstrated similar intermolecular behavior to the PIL homopolymer in the bulk state as indicated by FTIR, hydrogen bonding and counterion interactions in solution were observed in polar organic solvent through ^{1}H NMR measurements. The DLS characterization revealed that the PDMAEMA-*b*-PVBBImTf_2N block copolymer forms a network-like aggregated structure due to a combination of hydrogen bonding between the PDMAEMA and PIL group and electrostatic

repulsive interactions between PIL blocks. This structure was found to collapse upon KNO_3 addition while still maintaining hydrogen bonding interactions. AFM-IR reveals varied morphologies depending on film thicknesses, with spherical PDMAEMA in PVBBImTf_2N matrix morphology exhibited at thicker regions of the film. AFM-IR further revealed signals from silica nano-contaminates, which selectively interacted with the PDMAEMA spheres, demonstrating the potential for the PDMAEMA-*b*-PVBBImTf_2N PIL block copolymer in polymer-inorganic nanoparticle composite applications.

5.1. Introduction

Poly(ionic liquids) (PILs) are a special type of strong polyelectrolytes that combine the diverse functionality and unique properties of ionic liquids (ILs) with the mechanical stability, long-range ordering, and processability of polymers. In recent years, PILs have found application in a variety of fields including battery electrolytes, separations, nanomaterials, and more. In the past decade, PILs have been combined with highly incompatible neutral polymers to form block copolymers (BCPs) either in solution or as films. These systems have been used in forming polymer films and membranes with unique nanostructures such as lamellae, cylinders, spheroids, and bicontinuous structures[1-4]. In solution, they can form various structures (e.g., micellar spheres, vesicles, cubosomes) that are modulated by salt environment and PIL design[5-10]) in addition to traditional BCP assembly behaviors (e.g., solvent, polymer block length, concentration) [11]. Depending on the structure, these morphologies and supramolecular interactions can enhance the properties of PILs materials, such as ion conductivity in battery electrolytes[1, 2, 12, 13] or interfacial behavior in emulsions[14].

While neutral-poly(ionic liquid) block copolymers have been explored in some depth, there are only a few reports of all-PIL block copolymers[14-17] and of PILs blocked with weak

polyelectrolytes[10, 18, 19] . All-polyelectrolyte PILs block copolymers are of potential interest as it allows increasing the overall charge density and ion conductivity, improving overall electrochemical properties, and the providing multiple blocks that are both tunable by a simple ion exchange. Thus far, the all-PIL block copolymers systems examined have mainly consisted of polyvinylimidazolium-based PIL blocks where covalent alterations to the imidazolium pendant alkyl chain or the spacer chain between the polymer backbone and imidazolium group are the main drivers for self-assembly behavior in solution[14-17]. Further the self-assembled structures produced in these systems have been generally limited to spherical or rod like micelles in solution[15, 17]. Additionally, to the authors' knowledge, no study has examined the self-assembly behavior of all-PIL block copolymers in the bulk or as films.

Blocking PILs with weak polyelectrolytes instead offers additional design parameters for controlling self-assembly behavior including the ability to modulate the charge density based on degree of protonation. Such materials show conformational changes in response to environmental stimuli such as changes in pH and salt[20, 21]. The weak polyelectrolyte block may also be used to control the overall charge density of the block copolymer, which can aid in controlled solid electrolyte design or polyelectrolyte gels. However, only a few studies have investigated block copolymers composed of PILs and weak polyelectrolytes— either anionic[7, 10, 22] or cationic[19]— and of these, only the solution self-assembly behavior has been examined. Synthesizing and characterizing novel PIL-*b*-polyelectrolytes and expanding studies to include bulk phase self-assembly characterization of polyelectrolyte block copolymers will aid in the development of novel all polyelectrolyte materials for stimuli response, polymer battery electrolyte, and flexible electronics applications.

In this work, a novel cationic (PIL-*b*-polyelectrolyte) BCPs was synthesized through Cu(0)-mediated atom transfer radical polymerization (ATRP), a type of controlled "living" radical polymerization technique. Specifically, poly[4-vinylbenzyl-3-butyl imidazolium bis(trifluoromethanesulfonyl)imide] (PVBBImTf_2N) was polymerized utilizing a tertiary amine, weak polyelectrolyte macroinitiator. The synthesized polymers were characterized for their molecular weight and polymerization "livingness" using a combination of gel permeation chromatography (GPC) and nuclear magnetic resonance (NMR). The chemical structure and supramolecular behavior as a bulk polymer and in solution was also investigated using NMR and Fourier Transform Infrared (FTIR) spectroscopies, indicating a combination of hydrogen bonding and electrostatic interactions occurring in the block copolymer. The solubility and solution behavior of the block copolymer was investigated with dynamic light scattering (DLS) in polar organic solvent and in response to added salt. The block copolymer demonstrated an extended network-like aggregated state in pure polar organic solvent which could respond to salt addition. Self-assembly of the unique poly(ionic liquid)-block-(poly)tertiary amine with the stimuli-responsive weak polyelectrolyte block was further examined using solution-cast films and, for the first time in a PIL system, simultaneous infrared-atomic force microscopy (AFM-IR).

5.2. Results and Discussion

Cu(0)-mediated ATRP is a controlled polymerization technique that uses a zero-valence metal to *in situ* produce the Cu(I) activating species through comproportionation, which then mediates the monomer addition to the polymer chain backbone in a controlled manner[23-25]. ATRP is characterized by pseudo ^{1s}t order kinetics as determined by a linear $\ln[M]_o/[M]$ plot with time where M_o and M are the monomer concentration initially and at time, t, respectively. ATRP also allows for predicting the degree of polymerization (DP) and the number average molecular weight

(M_n) based on the starting monomer (M_o) and initiator (I_o) concentrations and conversion (χ), and monomer molecular weight ($MW_{monomer}$):

$$\textbf{EQ 5-1}\ DP^{theo} = \frac{[M]_o}{[I]_o} * \chi$$

$$\textbf{EQ 5-2}\ M_n^{theo} = DP * (MW_{monomer})$$

This method generally produces narrow polydispersity indices (ratio of weight, M_w, to number, M_n, average molecular weights, PDI=M_w/M_n) of less than ≤1.5 for polyelectrolytes[10, 26].

Here, the block copolymer poly[(2-(dimethylamino)ethyl methacrylate)] -*block*- poly[4-vinylbenzyl-3-butylimidazolium bis(trifluoromethylsulfonyl)imide] (PDMAEMA-*b*-PVBBImTf_2N) was synthesized using PDMAEMA as a macroinitiator to from an all-polyelectrolyte PIL block copolymer (Figure 5.1). PDMAEMA was selected as it has a weak tertiary amine pendant group that can be protonated at pH values lower than ~7.5 (pKa ~7-8) to form cationic charge groups[23, 27, 28]. Further, PDMAEMA has been previously found to display material property changes in response to pH and salt[29, 30]. An imidazolium-based PIL with a styrenic polymer backbone was selected as it has been successfully polymerized by ATRP methods previously[3, 31-33]. Additionally, the styrenic backbone will provide hydrophobic content to facilitate microphase separation behavior between the two blocks.

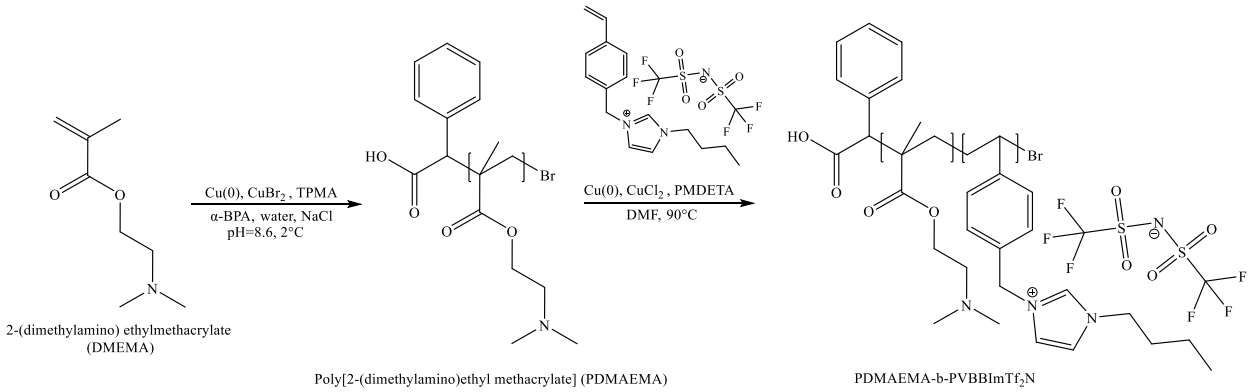

Figure 5.1 The PDMAEMA macroinitiator was first synthesized using Cu(0)-mediated ATRP in pH 8.6 aqueous conditions. Using PDMAEMA as a macroinitiator, the polymer was extended through the synthesis of a PVBBImTf_2N PIL block by Cu(0)-mediated ATRP in dimethylformamide.

5.2.1. Polymerization of the Tertiary Amine Macroinitiator PDMAEMA.

The macroinitiator was synthesized using an aqueous based Cu(0)-mediated ATRP procedure recently reported by the authors' group[23]. Figure 5.2 shows the kinetic results for the macroinitiator synthesis in aqueous solution. The PDMAEMA displayed pseudo 1st order kinetics as demonstrated by the linear increase in $\ln[M_o]/[M]$ with time (Figure 5.2a) with a final monomer conversion of ~70%. The final polymer had a degree of polymerization ($DP_{PDMAEMA,NMR}$) and number average molecular weight ($M_n^{PDMAEMA,NMR}$) of 45 units and 7074 g/mol respectively as calculated by NMR peak integral ratioing (Figure 5.2b). Aqueous gel permeation chromatography (GPC) results using PEG standards gave a slightly higher molecular weight and degree of polymerization ($M_n^{PDMAEMA,GPC}$ = 9323 g/mol and $DP_{PDMAEMA,GPC}$ = 59 units) with a polydispersity of 1.41. The difference in the NMR and GPC determined molecular weights may stem from several factors in the GPC measurement process such as polymer-column interactions and the difference between the hydrodynamic volume behavior of the PEG calibration standards and the PDMAEMA[34, 35]. The NMR calculated $M_n^{PDMAEMA,NMR}$ and $DP_{PDMAEMA,NMR}$ for the PDMAEMA macroinitiator will be used for comparisons with the PIL block copolymer.

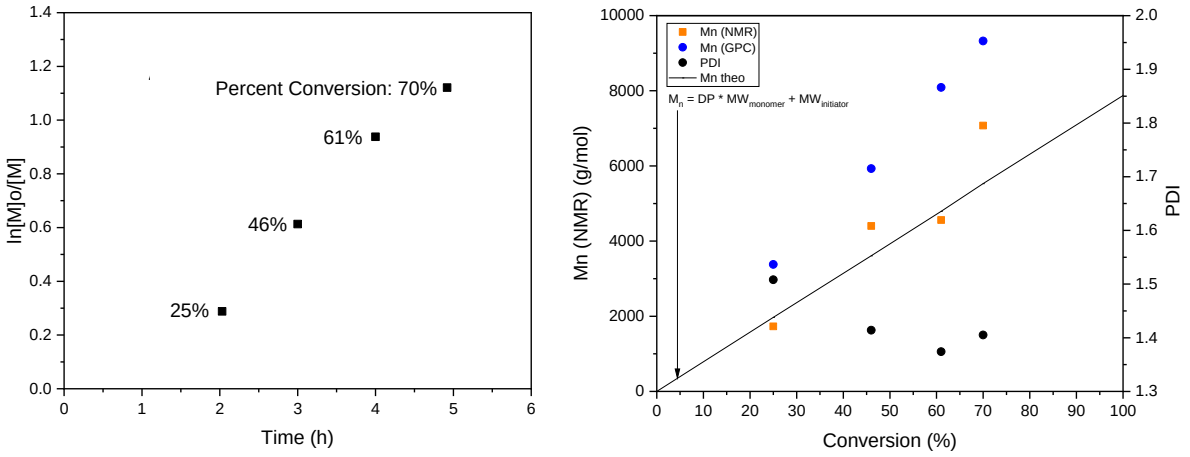

Figure 5.2 PDMAEMA shows (a) pseudo-first order kinetics are through a linear $\ln[M]_o/[M]$ response with time. (b) Relatively narrow PDI's of ~1.5 were observed for the macroinitiator (black circles). M_n increased linearly with time with slightly higher values observed for the GPC results (blue circles) (9,323 g/mol at 70% conversion) compared to the NMR (orange circles) (7,074 g/mol at 70% conversion) calculated values. Both M_n values were slightly higher than the theoretical M_n (5531 g/mol) calculated based on initial monomer and initiator concentration ($[M]_o/[I]_o = 50$).

5.2.2. Block Copolymerization of PDMAEMA-*b*-PVBBImTf$_2$N and Comparison to PVBBImTf$_2$N Homopolymerization.

Figure 5.3 shows the kinetic results for the PVBBImTf$_2$N homopolymer and the PDMAEMA-*b*-PVBBImTf$_2$N block copolymer. Due to solubility issues and column interactions, GPC measurements were not possible for the PIL-based polymers, even with the addition of 10 mM LiTf$_2$N salt to the mobile phase to reduce column interactions following the method used successfully by Matyjaszewski et al. [5] Instead NMR peak integral ratioing was used to determine monomer conversion and polymer $DP_{PVBBImTf2N,NMR}$ as has been done by other groups with similar issues[36-38]. The PVBBImTf$_2$N showed a linear increase in $\ln[M_o]/[M]$ (Figure 5.3a) and conversion (Figure 5.3b) with time, indicating controlled polymerization. The final conversion at 24 h was 76% for PVBBImTf$_2$N. Conversely, the PDMAEMA-*b*-PVBBImTf$_2$N block copolymer showed a large increase in conversion (from 0 to 58%) in 1 h, followed by a gradual increase to

67 % conversion at 24 h (Figure 5.3b). The $\ln[M]_o/[M]$ plot shows a similar sharp increase followed by a plateau between 1 h and 24 h. The sharp increase in conversion and $\ln[M]_o/[M]$ during the first hour of the PVBBImTf_2N block polymerization for the PDMAEMA-*b*-PVBBImTf_2N copolymer suggests faster kinetics in comparison to the homopolymerization. Due to these fast kinetics, time points were not collected in the first hour of the reaction, and so controlled polymerization for PDMAEMA-*b*-PVBBImTf_2N cannot be confirmed.

$DP_{PVBBImTf2N,\ NMR}$ was determined using NMR by ratioing the benzyl group peak integral in the PVBBImTf_2N block to the tertiary amine methyl group peak integral in the PDMAEMA block and assuming a 45-unit $DP_{PDMAEMA,\ NMR}$ for the PDMAEMA block. Here, the block copolymer showed a gradual increase in $DP_{PVBBImTf2N,\ NMR}$ from ~33 units at 1 h to 63 units at 5 h before plateauing to ~67 units at 24 h. This is close to the theoretically predicted $DP_{PVBBImTf2N,Theo}$ (67 units) and $M_n^{PVBBImTf2N,Theo}$ (42011 g/mol) for 67 % conversion for $[M]_o/[I]_o = 100$ as calculated by EQ 5-1 and :

$$\textbf{EQ 5-3}\ M_n = \left(\frac{[M_o]}{[I_o]} * conversion\right) MW_{monomer} + M_n^{PDMAEMA}$$

where $M_n^{PDMAEMA,NMR}$ (7074 g/mol) is the number average molecular weight the PDMAEMA block with a 45-unit $DP_{PDMAEMA,\ NMR}$. Overall, the block copolymer by NMR peak integral ratioing had a 45-unit PDMAEMA block, 67-unit PVBBImTf_2N block, and an overall $M_n^{PDMAEMA\text{-}b\text{-}PVBBImTf2N}$ of ~42 kDa. The degree of polymerization of the PIL block matches well with the theoretically predicted DP and overall molecular weight despite the uncaptured data in the 1st hour of the block copolymer polymerization.

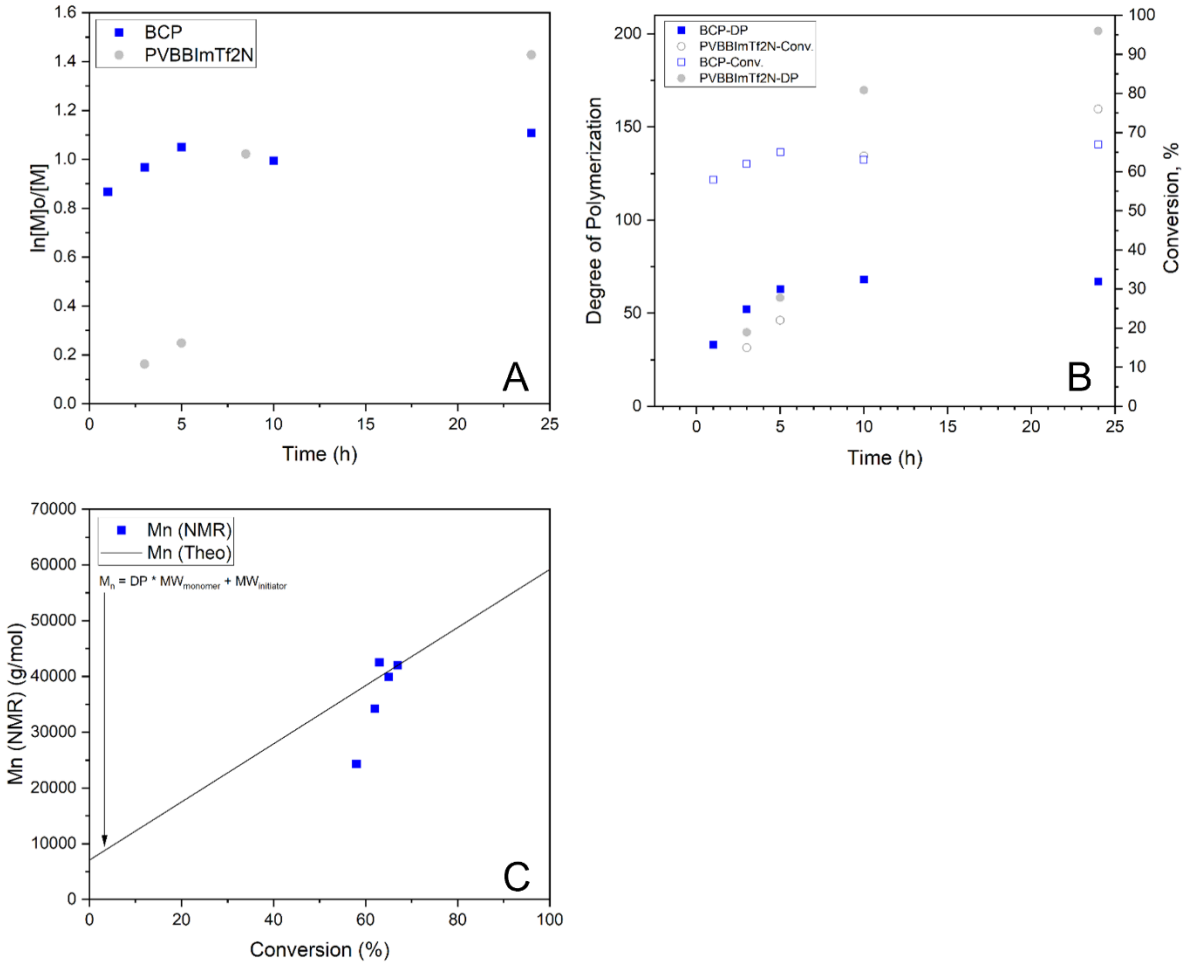

Figure 5.3 (a) Pseudo-1st order kinetics are observed for the PVBBImTf$_2$N homopolymer but not necessarily for the PDMAEMA-*b*-PVBBImTf$_2$N block copolymer. (b) Conversion increased linearly with time for the PVBBImTf$_2$N homopolymer to 76% (24 h) (grey) while the block copolymer (blue) increased sharply in the first hour to 58% conversion before gradually increasing to 67% conversion after 24 hrs. PDMAEMA-*b*-PVBBImTf$_2$N $DP_{PVBBImTf2N,\ NMR}$ increased gradually from ~33 units (1 h) to ~63 units in the first 5 h before increasing slightly to 67 units (24 h) at the end of the reaction. (c) NMR calculated M_n (42014 g/mol) corresponds closely to the theoretical M_n (42011 g/mol for $[M]_o/[I]_o$ =100)at 67 % conversion after 24 h.

In order to confirm successful polymerization and connectivity of the polymer blocks, FTIR and NMR spectroscopies were performed for the PDMAEMA MI, PVBBImTf$_2$N homopolymer, and PDMAEMA-*b*-PVBBImTf$_2$N block copolymer. These spectroscopic studies also provided

insight into supramolecular bonding interactions occurring in the bulk polymer and in solution conditions.

5.2.3. Chemical Structure and Bonding

Figure 5.4a and b show the ATR-FTIR spectra for the polymers and VBBImTf_2N monomer above 2200 cm^{-1} and below 1800 cm^{-1}, respectively. In the VBBImTf_2N monomer, PVBBImTf_2N homopolymer, and PDMAEMA-*b*-PVBBImTf_2N block copolymer samples, the peaks at 3147, 3113, and 3090 cm^{-1} are assigned to the C_2 and $C_{4,5}$ C-H stretches on the imidazolium ring. The first peak is typically attributed to the $C_{4,5}$-H stretches of the diene group and latter two peaks are typically attributed to the more acidic C_2-H proton[39, 40]. These imidazolium ring protons are sensitive to hydrogen bonding and intermolecular interactions and may show shifts in absorbances depending on the counterion type and other intermolecular interactions[41-43]. In this case, both the PIL homopolymer and the block copolymer have similar absorbances for the C_2-H and $C_{4,5}$-H protons as the VBBImTf_2N monomer, indicating a similar intermolecular environment of the imidazolium ring for both the dry homo- and block-copolymers. An emergence of a peak at 2850 cm^{-1} in the PVBBImTf_2N and PDMAEMA-*b*-PVBBImTf_2N samples is typically for the symmetrical CH_2 stretching modes of the polymer backbone[44, 45]. Several peaks in the 3000-2870 cm^{-1} region are due to various asymmetrical and symmetrical CH_2/CH_3 stretching modes from the methylene groups and alkyl chains present in both polymers[44, 46]. Several weak N^+-H stretch and combination modes in the 2800-2400 cm^{-1} region were also observed in the PDMAEMA-*b*-PVBBImTf_2N and PDMAEMA samples[47]. These peaks are typical for tertiary amine salts, which indicates at least partial protonation of the tertiary amine group in the block copolymer after synthesis. As the PDMAEMA was synthesized in pH~8.6 conditions, the protonation likely results

from a drop in pH to below the pKa of PDMAEMA (pKa ~7-8) [23, 28] during the purification step on precipitation with ammonium sulfate[48].

Below 1800 cm^{-1}, the C=O ester stretch at ~1728 cm^{-1} from the PDMAEMA block is observed in the block copolymer sample[49] (Figure 5.4b). A loss of the 920 cm^{-1} vinyl bending mode (R-C=CH_2) in the PVBBImTf_2N homopolymer and block copolymer further confirms polymerization and successful purification of the polymers[44, 46]. Also characteristic of the PIL are the imidazolium ring C=N/C=C stretches at 1563 cm^{-1} and the C-N stretch at 1515 cm^{-1} for the PVBBImTf_2N block[40, 50, 51], which are also at similar wavenumbers in both the homo- and block-copolymer PILs. This suggests the cation-anion interaction environment does not change on block copolymerization with PDMAEMA when in the bulk polymer state. Several intense peaks for the Tf_2N anion were also observed at 1346 cm^{-1} (SO_2 asym str), 1330 cm^{-1} (SO_2 asym str), 1178 cm^{-1} (SO_2 sym str), 1133 (SO_2 sym str), 1050 cm^{-1} (C-S str), 612 cm^{-1} (SNS bending), and 569 cm^{-1} (CF_3 bending) and compare well to the literature[40, 41, 50, 52].

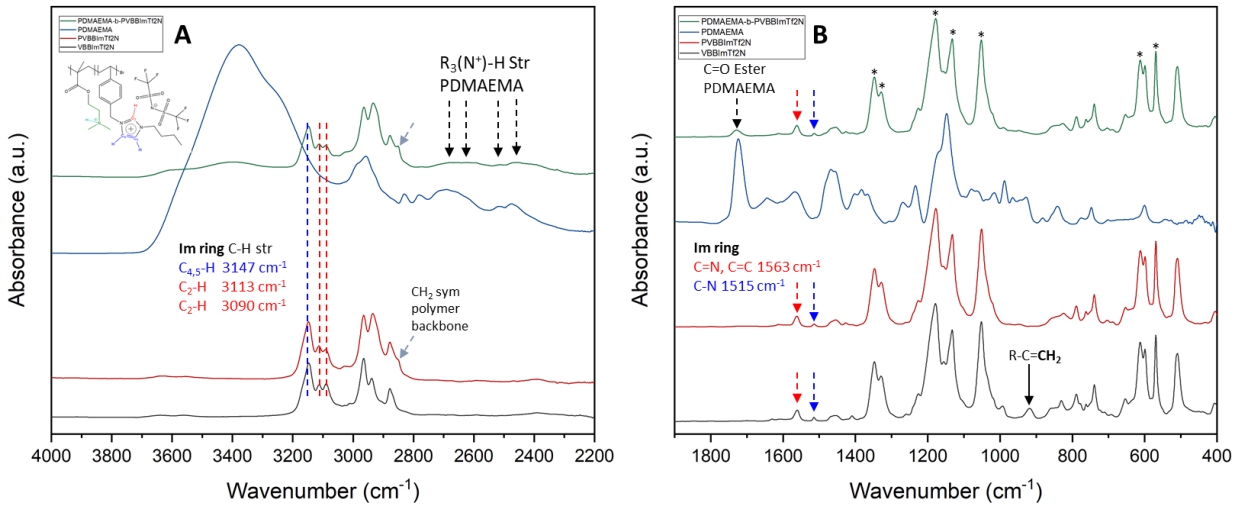

Figure 5.4 ATR-FTIR results for the VBBImTf_2N monomer (black), PVBBImTf_2N homopolymer (red), PDMAEMA macroinitiator (blue), and PDMAEMA-*b*-PVBBImTf_2N block copolymer in the (a) 4000-2200 cm^{-1} and (b) <1800 cm^{-1} regions. Red and blue arrows and dotted lines indicate the C_2-H and $C_{4,5}$- H imidazolium ring methylene stretches, respectively. The grey arrows mark the 2850 cm^{-1} peak corresponding to CH_2 sym str of the polymer backbone. Black dotted arrows

mark the N^+-H str and combinations modes of the protonated tertiary amine group and the ester C=O str in the PDMAEMA block. The solid black arrow indicates the vinyl group in the VBBImTf_2N IL monomer, and the black asterisks designate the Tf_2N^- anion modes.

FTIR results confirm the successful polymerization of the block copolymer. The spectra also indicate partial protonation of the PDMAEMA block and similar cation-anion interaction behavior in the PVBBImT_2N block as was also observed for the homopolymer PIL. NMR spectroscopy was performed to corroborate successful polymerization of the PDMAEMA-*b*-PVBBImTf_2N block copolymer. In addition to confirming chemical composition and connectivity of the polymer blocks, the NMR data provides insight into the supramolecular interactions (e.g., cation-anion electrostatic interactions, hydrogen bonding interactions) of the block copolymer in solution and subsequently a better understanding of the solution self-assembly behavior of PDMAEMA-*b*-PVBBImTf_2N.

NMR spectra were collected for the VBBImTf_2N monomer, PVBBImTf_2N homopolymer, PDMAEMA macroinitiator, and PDMAEMA-*b*-PVBBImTf_2N block copolymer samples in DMSO-d_6 solvent (Figure 5.5). Due to solubility issues, it was necessary to add 10 mM of KNO_3 salt to the PDMAEMA-*b*-PVBBImTf_2N solution to improve block copolymer solubility in DMSO and allow for NMR characterization. KNO_3 was selected as it has better solubility in DMSO versus other salts such as NaCl and KCl[53]. The block copolymer shows the tertiary amine methyl groups and methylene group peaks at 2.60 ppm and 3.07 ppm, respectively. These are slightly upshifted from 2.38 ppm and 2.78 ppm in PDMAEMA macroinitiator. The benzyl ring (7.23 and 6.32 ppm) and methylene connecting group (5.40 ppm) from the PVBBImTf_2N block are present and at approximately the same ppm as the PVBBImTf_2N homopolymer. The PVBBImTf_2N butyl chain CH_2 and CH_3 protons are present at ~ 0.78, 1.17, 1.70, and 4.16 ppm, and these peaks remain relatively constant in the homo- and block-copolymer samples. The imidazolium ring C_2-H and

$C_{4,5}$-H protons were observed in the PIL polymers between 9.75-9.25 ppm and 7.81-7.74 ppm, respectively. A 2D diffusion ordered (DOSY) NMR experiment (Figure 5.6; 1D DOSY array provided in the Figure D.1) shows the presences of both the PVBBImTf_2N and PDMAEMA peaks in the block copolymer with a diffusion coefficient of $4.9x10^{-8}$ cm^2/s, confirming successful block copolymerization. Some residual IL monomer and un-chain extended PDMAEMA macroinitiator signals—separate from those for the block copolymer—were also observed with a diffusion coefficient of ~5.4×10^{-6} cm^2/s.

In contrast to the IR results for the bulk polymer, differences in the imidazolium ring proton signals were observed between the PIL homopolymer and block copolymers in solution. The imidazolium ring C_2-H and $C_{4,5}$-H protons in the PDMAEMA-*b*-PVBBImTf_2N sample are located at 9.74 ppm and 7.81 ppm, respectively. These peaks are upshifted from their signal in the PVBBImTf_2N homopolymer (C_2-H 9.19 ppm and $C_{4,5}$-H 7.74 ppm) and monomer (C_2-H 9.25 ppm and $C_{4,5}$-H 7.77 ppm) with greater shifts observed for the C_2-H proton. While all the protons on the imidazolium ring are capable of hydrogen bonding interactions, the acidic C_2-H proton is particularly sensitive to hydrogen bonding interactions between the imidazolium cation and anions in solution[54]. Generally, the strength of hydrogen bonding interactions between C_2-H and the counterions increases with decreasing anion size and increasing coordinating ability of the anion[55, 56]. Imidazolium based-PILs containing multiple types of counterions also tend to display intermediate C_2-H ppm values between the ppm values observed if only one of the counterions was present[54, 57]. However, the PDMAEMA block is also capable of acting as a hydrogen bond acceptor at the amine nitrogen and carbonyl oxygen, allowing for potential hydrogen bonding interactions with the acidic imidazolium C_2-H proton[58, 59]. To determine if the C_2-H and $C_{4,5}$-H proton peak shifts in the block copolymer were due to partial ion exchange with the added KNO_3

salts or due to interactions between polymer blocks, the NMR spectra for the PVBBImTf_2N and PDMAEMA homopolymers without and with 10 mM KNO_3 salts were also measured.

PVBBImTf_2N homopolymer without added salts display C_2-H (9.19 ppm) and $C_{4,5}$-H (7.74 ppm) signals that are slightly shifted downfield in comparison to the VBBImTf_2N monomer (C_2-H 9.25 ppm and $C_{4,5}$-H 7.77 pm). Horne et al. reported a similar result that was attributed to a weakening of the cation-anion interactions from increased steric effects in the immobilized cation on the polymer backbone or increased anion dissociation from the PIL imidazolium cation in DMSO[60]. Adding 10 mM KNO_3 salt to the PVBBImTf_2N homopolymer increases the C_2-H signal to 9.46 ppm while the $C_{4,5}$-H signal remains approximately the same (7.75 ppm). The observed 9.46 ppm C_2-H peak compares well with other imidazolium-based ILs with nitrate counterions which have been found to have C_2-H ppm values between 9.3-9.5 ppm in DMSO-d_6 or pure IL[55, 61, 62]. This increase in the C_2-H signal indicates at least partial ion exchange of the NO_3^- anion with the Tf_2N^- anion in the PIL homopolymer. These same signals are shifted even further downfield in the PDMAEMA-*b*-PVBBImTf_2N block copolymer with C_2-H at 9.74 ppm and $C_{4,5}$-H at 7.81 ppm, indicating the shifts are likely due in part to interactions between the PDMAEMA and PVBBImTf_2N blocks in addition to the partial NO_3^- ion exchange. A slight increase in the PDMAEMA tertiary amine methyl and methylene groups in the block copolymer (2.60 and 3.07 ppm) compared to the macroinitiator (2.38 and 2.78 ppm) also support this. Further, no differences in the NMR spectra for the PDMAEMA macroinitiator in pure DMSO-d_6 and 10 mM KNO_3 DMSO-d_6 were observed, supporting that the downfield shifts in the macroinitiator methylene and

amine methyl groups are due to interactions in between the two polymer blocks and not the salt environment (Supporting Information, Figure D.2).

NMR results indicate that the intermolecular environment of the PDMAEMA-*b*-PVBBImTf$_2$N block copolymer is influenced by both hydrogen bonding interactions between the imidazolium group in the PIL block and the tertiary amine co-block in addition to the salt environment in solution. Such intermolecular interactions can significantly influence structural behavior of polymers in solution[63, 64]. Therefore, to further examine the influence of these supramolecular interactions on self-assembly behavior of the block copolymer, dynamic light scattering measurements were performed.

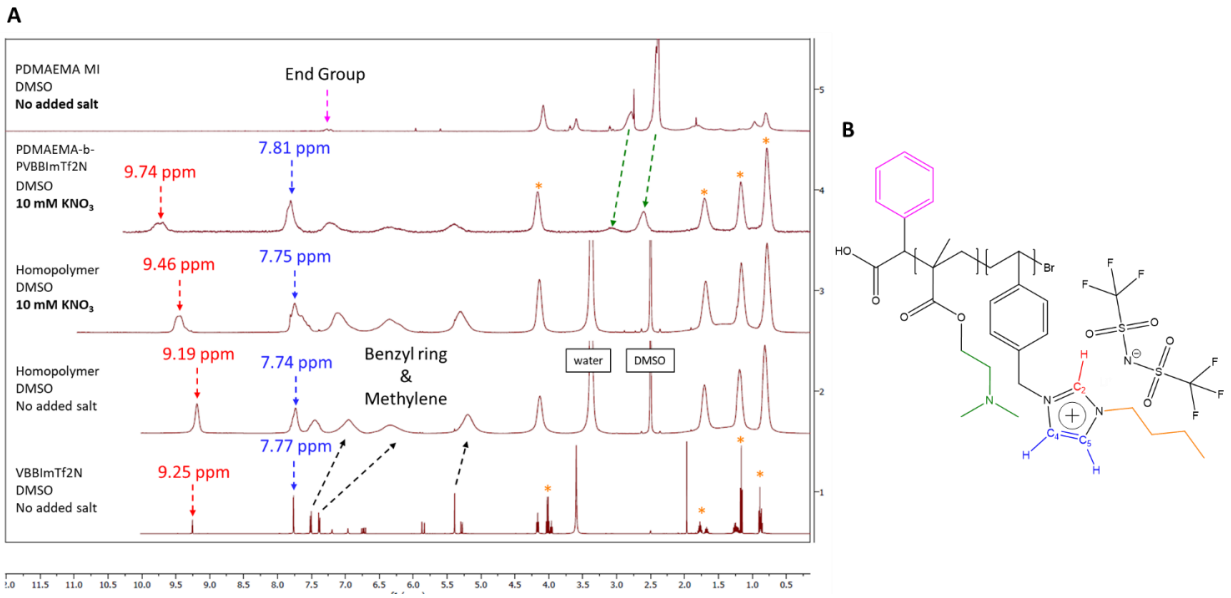

Figure 5.5 (a) NMR results (bottom to top) for the VBBImTf$_2$N monomer in DMSO-d$_6$, PVBBImTf$_2$N homopolymer in DMSO-d$_6$, PVBBImTf$_2$N homopolymer in 10 mM KNO$_3$ DMSO-d$_6$ solution, PDMAEMA-*b*-PVBBImTf$_2$N block copolymer in 10 mM KNO$_3$ DMSO-d$_6$ solution, and PDMAEMA macroinitiator in DMSO-d$_6$. Orange asterisks mark the imidazolium butyl chain CH$_2$/CH$_3$ protons. Green arrows mark the shift in the PDMAEMA tertiary amine and methylene groups. Red and blue arrows mark the shifts in the C$_2$-H and C$_{4,5}$-H protons, respectively, and (b) correspond to the colored portions of the PDMAEMA-*b*-PVBBImTf$_2$N chemical structure.

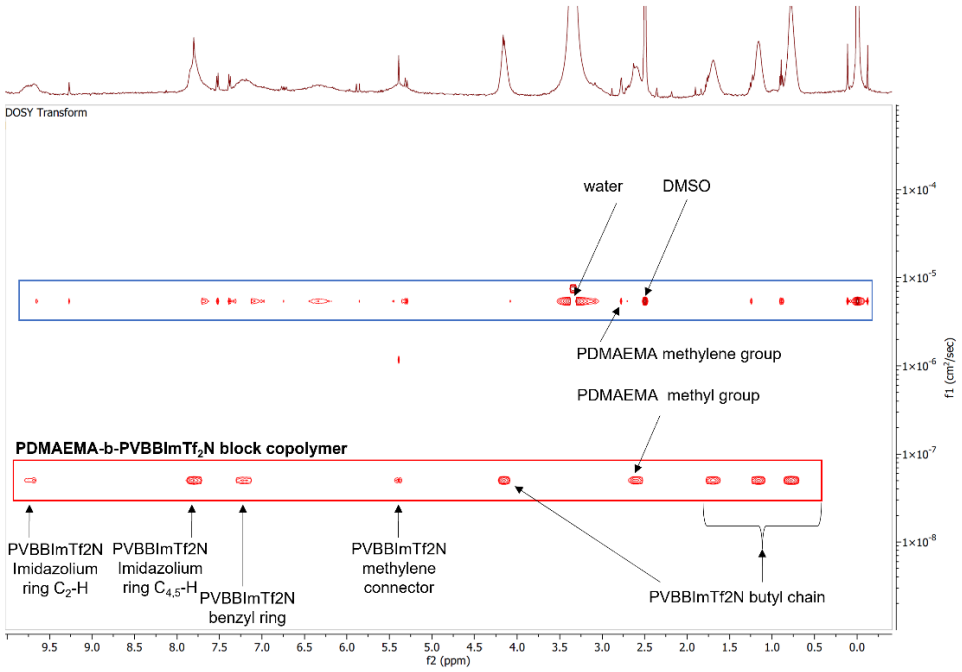

Figure 5.6 NMR 2D DOSY showing the diffusion separated PDMAEMA-*b*-PVBBImTf$_2$N proton signals (red box) with a lower diffusion coefficient at ~10^{-8} cm^2/s as compared to the residual VBBImTf2N monomer, PDMAEMA MI, water, and DMSO signals (blue box) at 10^{-5} cm^2/s.

5.2.4. Solution Behavior of PDMAEMA-*b*-PVBBImTf$_2$N Diblock Copolymer

Dynamic light scattering (DLS) measurements were obtained for the PDMAEMA-*b*-PVBBImTf$_2$N block copolymer in DMSO at 1 mg/mL concentration with and without 10 mM KNO_3. While the PDMAEMA-*b*-PVBBImTf$_2$N block copolymer was found to also swell in other polar organic solvents (Supplemental Table D.1), DMSO was selected to allow for a more direct comparison to the NMR results. Figure 5.7 shows the correlation curves and the hydrodynamic structural lengths for the PDMAEMA-*b*-PVBBImTf$_2$N block copolymer aggregates in pure DMSO (Figure 5.7a and b) and DMSO with 10 mM KNO_3 salt (Figure 5.7c and d). For the block copolymer in pure DMSO, the correlation function was best fit by a Dblexp model for bimodal distributions (see Supplemental Figure D.3). Two populations of large aggregate sizes are observed for the block copolymer in pure DMSO with the smaller population between ~570-1750 nm and the larger population greater than 17 μm. It should be noted that DLS is typically limited

to below ~10 μm, so while there indeed is a larger aggregate size population observed (17.1-53.6 μm), the quantitative value of the hydrodynamic diameter should be interpreted with caution. Addition of KNO_3 salt resulted in a collapse of the polymer structure producing several populations of diameters between 14 nm and 4.12 μm, and the resulting correlation function was best fit with a NNLS model (Figure D.4). This reduction of the overall range of hydrodynamic structural lengths from 572 nm to 53.6 μm in pure DMSO to ca. 14 nm to 4.12 μm upon addition of KNO_3 indicates the polyelectrolyte block copolymer structure can be modulated by salt addition as would be expected for polyelectrolyte systems. Generally, increasing the salt content in polyelectrolytes leads to screening of repulsive interactions between the pendant charge groups on the polymer chain, eventually leading to a collapse from a rod-like structure to a coiled structure similar to the solution behavior of neutral polymers[65-67].

However, a large portion of the hydrodynamic structural lengths in the 10 mM KNO_3 DMSO solution are still significantly larger than expected for a solubilized polymer, even upon addition of salt. For a block copolymer with degrees of polymerization of 45 units ($DP_{PDMAEMA,NMR}$) for the PDMAEMA block and 67 units for the PVBBImTf_2N block, the fully stretched contour length of a single polymer chain is theoretically 57 nm as calculated by[68]:

EQ 5-4 $Contour\ length = \left(2\ atoms * \left(N_{PDMAEMA} + N_{PVBBImTf2N}\right) - 1\right) * (0.154\ nm) * sin\left(\frac{111.5^{\circ}}{2}\right)$

where 0.154 nm is the length of a C-C bond, 111.5° is the bond angle, and $N_{PDMAEMA}$ and $N_{PVBBImTf2N}$ are the number of monomer units for each polymer block. The contour length would be 74 nm if the GPC determined $DP_{PDMAEMA,\ GPC}$ of 59 units is assumed instead. As the majority of hydrodynamic structural lengths are significantly larger than these theoretical single-polymer contour lengths, this is indicative of the block copolymers aggregating into a self-assembled network-like structure in both pure DMSO and 10 mM KNO_3 DMSO. An additional DLS study

as a function of KNO_3 concentration between 0 and 25 mM also demonstrates a collapse in structure with increasing salt concentration (Supporting Information, Figure D.5). The hydrodynamic structural lengths in Figure D.5 correspond well to the results as shown in Figure 6.

Based on the NMR and DLS characterization, the proposed solution behavior of the PDMAEMA-*b*-PVBBImTf_2N block copolymer in DMSO is depicted in Figure 5.8. In polar organic solvents, weakly coordinating counterions, such as Tf_2N^-, are often dissociated from the PIL in solution, resulting in unshielded pendant positive charges on the PIL backbone[54, 60]. In the PDMAEMA-*b*-PVBBImTf_2N block copolymer system, the dissociation would result in an increased repulsion between the PIL blocks in the polymer chains. As a result, the hydrogen bonding between the imidazolium C_2-H proton and the PDMAEMA block (Figure 5.8a) likely dominates the block copolymer chain-chain interactions. The combined hydrogen bonding between PDMAEMA/PVBBImTf_2N blocks and repulsive interactions between PIL blocks in the block copolymer system results in a long strand-like extended networks (Figure 5.8b). Additional images support these structures (Supporting Information, Figure D.6-Figure D.8).

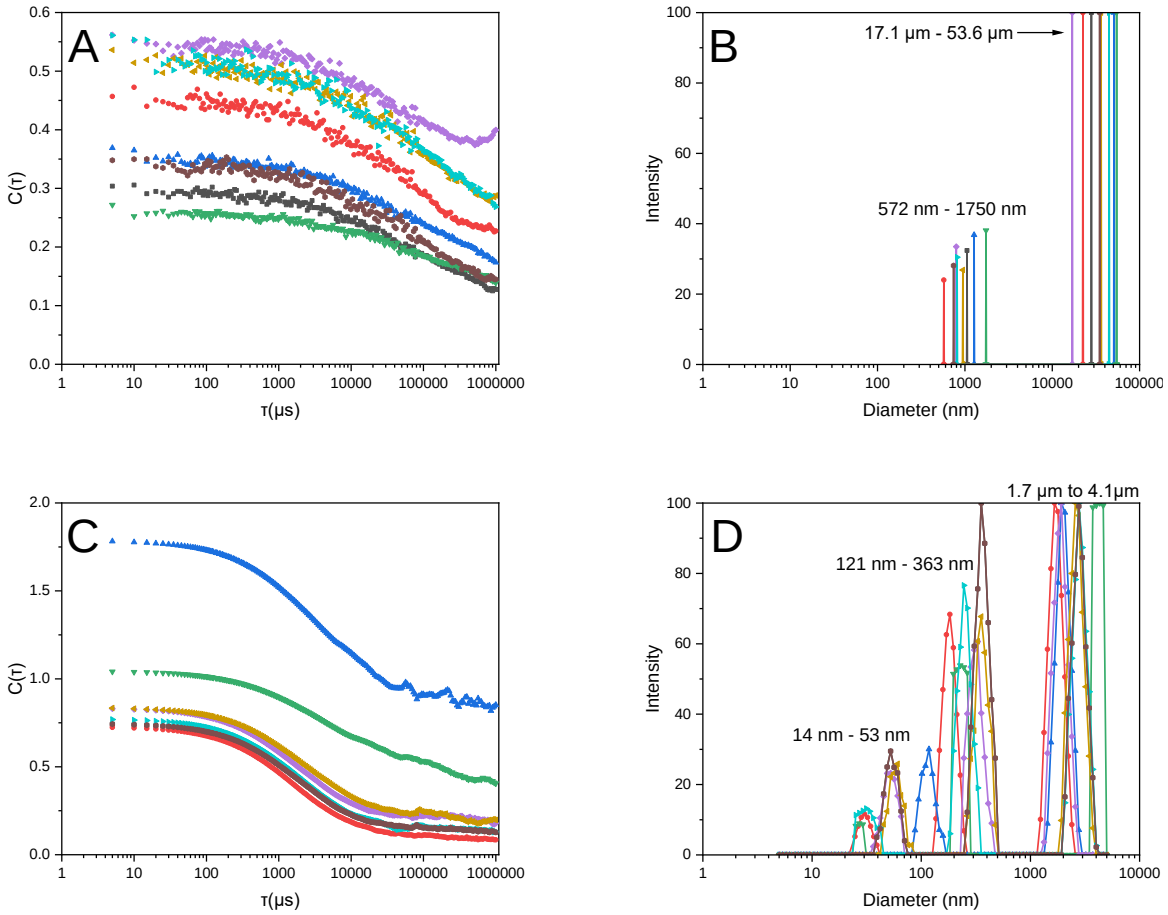

Figure 5.7 DLS correlation function and intensity-based hydrodynamic diameters for the PDMAEMA-*b*-PVBBImTf$_2$N block copolymer in (a and b) pure DMSO and (c and d) 10 mM KNO_3 DMSO solution are shown with 8 measurements each. (b) Particle sizes between 500 nm and 54 μm were observed for the block copolymer in pure DMSO. (d) Aggregate sizes overall decreased by more than an order of magnitude upon 10 mM KNO_3 addition resulting in hydrodynamic diameters between 14-4120 nm.

Upon addition of the KNO_3 salt into the solution, the NO_3^- anions more strongly coordinate with the imidazolium ring and screen the positive charges along the PIL block, allowing for PIL-PIL block interactions. While some decrease in hydrogen bonding may occur, as evidenced by NMR characterization of PDMAEMA-*b*-PVBBImTf$_2$N in 10 mM KNO_3 DMSO solution the hydrogen bonding interactions are largely maintained after salt addition. In this case, the reduction of PIL-PIL repulsive interactions causes the extended network to collapse while still maintaining

PDMAEMA/PVBBImTf$_2$N block interactions through hydrogen bonding forming overall smaller aggregated structures (Figure 5.8c) that are still larger than fully extended individual polymer chains. The population aggregates observed in the 14 – 50 nm range are likely due to collapsed polymer chains where hydrogen bonding was disrupted. Overall, the PDMAEMA-*b*-PVBBImTf$_2$N block copolymer demonstrates self-assembly behavior that can be triggered by addition of KNO_3 salt. Similar salt-triggered self-assembly has been observed for PIL and polyelectrolyte systems, where salt type and concentration influence intermolecular interactions between polyelectrolyte chain segments including charge screening repulsive interactions, solvophobic chain-chain interactions, and hydrogen bonding[6, 57, 69-74].

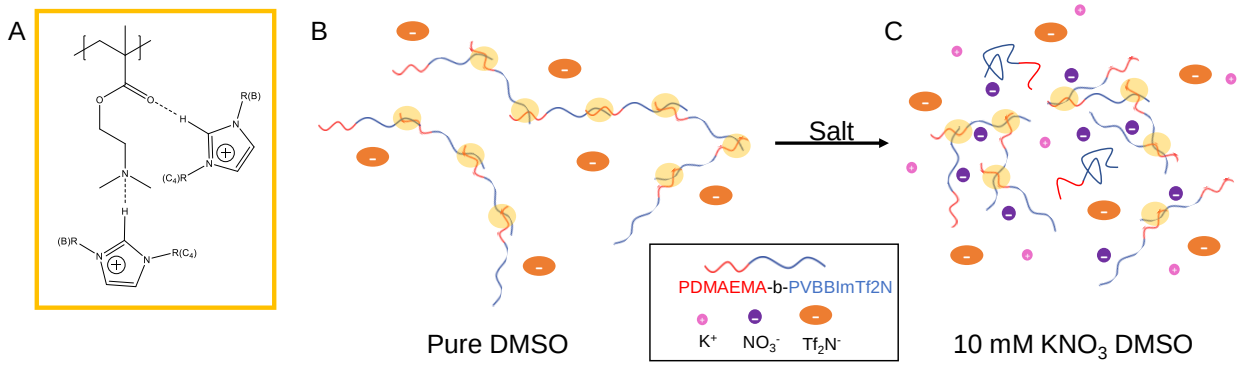

Figure 5.8 (a) Hydrogen bonding of the imidazolium C$_2$-H proton with the PDMAEMA block at the unprotonated tertiary amine or the ester carbonyl group. In solution the PDMAEMA-*b*-PVBBImTf$_2$N copolymer displays behavior of (b) an extended network structure mediated by hydrogen bonding and repulsive interactions between PIL-PIL blocks in pure DMSO to (c) a collapsed network-like structure with salt addition. Yellow circles indicate the hydrogen bonding between PDMAEMA and PVBBImTf$_2$N blocks.

5.2.5. Film Self-Assembly of PDMAEMA-*b*-PVBBImTf$_2$N Diblock Copolymer

To gather further data on the self-assembly behavior of the PDMAEMA-*b*-PVBBImTf$_2$N block copolymer, the system was also studied using AFM-IR, a coupled atomic force microscopy-infrared spectroscopic technique. During AFM-IR analysis, a pulsed IR laser illuminates the

sample at the AFM cantilever tip, producing a photothermal expansion response that is directly proportional to the IR absorption of the material. This allows for collecting simultaneous chemical images with nanoscale spatial resolution at specific wavenumbers or full spectra at specified points in the AFM image[75, 76]. While AFM-IR has previously been used to provide paired nano-structural and chemical composition characterization of different material systems including block copolymers[77], proteins[78, 79], and nanocomposites[80, 81], to the authors' knowledge this is the first reporting of a poly(ionic liquid) system being characterized with AFM-IR.

The film self-assembly of the PDMAEMA-*b*-PVBBImTf_2N block copolymer was observed by solution casting on silicon wafers. Due to low solubility and subsequent poor film formation for the block copolymer in pure DMSO solution, only the drop cast film for PDMAEMA-*b*-PVBBImTf_2N in 10 mM KNO_3 DMSO solution was characterized. Figure 5.9 shows the AFM height and IR chemical maps for a 20 by 10 μm section located at the edge of the block copolymer film displaying several different structural features. The height trace (Figure 5.9a) shows three regions: one on the far left with large, depressed deposits or irregular features (marked by a red arrow), a homogenous center section with few topographical features (green arrow), and a thicker section on the right with spherical morphology separation (pink arrow). The IR wavenumbers of 1730 cm^{-1} for the PDMAEMA block ester carbonyl stretch (C=O) (Figure 5.9b) and the Tf_2N^- anion SO_3^- asymmetrical stretch (Figure 5.9c) for the PVBBImTf_2N block were selected for chemical mapping to observe microphase separation between the two polymer blocks. The Tf_2N^- IR mode was selected over the imidazolium C=N/C-N bands at 1566 and 1513 cm^{-1} as the Tf_2N^- band had greater intensity and greater contrast compared to other IR modes for the chemical imaging. Lighter colors in the chemical map traces indicate the presence of the selected IR signal while dark blue colors indicate either their absence or lower concentration at the analysis

penetration depth. Figure 5.9e shows a 3D depiction of the 1730 cm^{-1} chemical map, indicating that the block copolymer film increases in thickness from the outer edge of the film towards the center (left to right in the AFM traces). Figure 1.9f displays the point spectra between 1800 and 800 cm^{-1} for each of the spots marked by arrows.

The bright signals produced in the left of Figure 5.9b (1730 cm^{-1} map) indicates that the ~1 μm x 1 μm irregular depressed deposits contain a large concentration of the C=O str ester band. Taking a point spectrum of one of these features marked by the red arrow and the corresponding red IR spectra trace (Figure 5.9f) shows an intense peak at 1728 cm^{-1} with no contributions at 1566 cm^{-1} from the imidazolium ring band or at 1350 cm^{-1} from the Tf_2N^- anion S=O str band. This suggests the depressed deposits are mainly composed of PDMAEMA. As indicated by the NMR 2D DOSY results, the depressed deposits are likely residual PDMAEMA macroinitiator that was not fully removed during purification of the block copolymer. The large crystalline feature near this section marked by the blue arrow yields an intense peak from excess precipitated KNO_3 (1356 cm^{-1}).

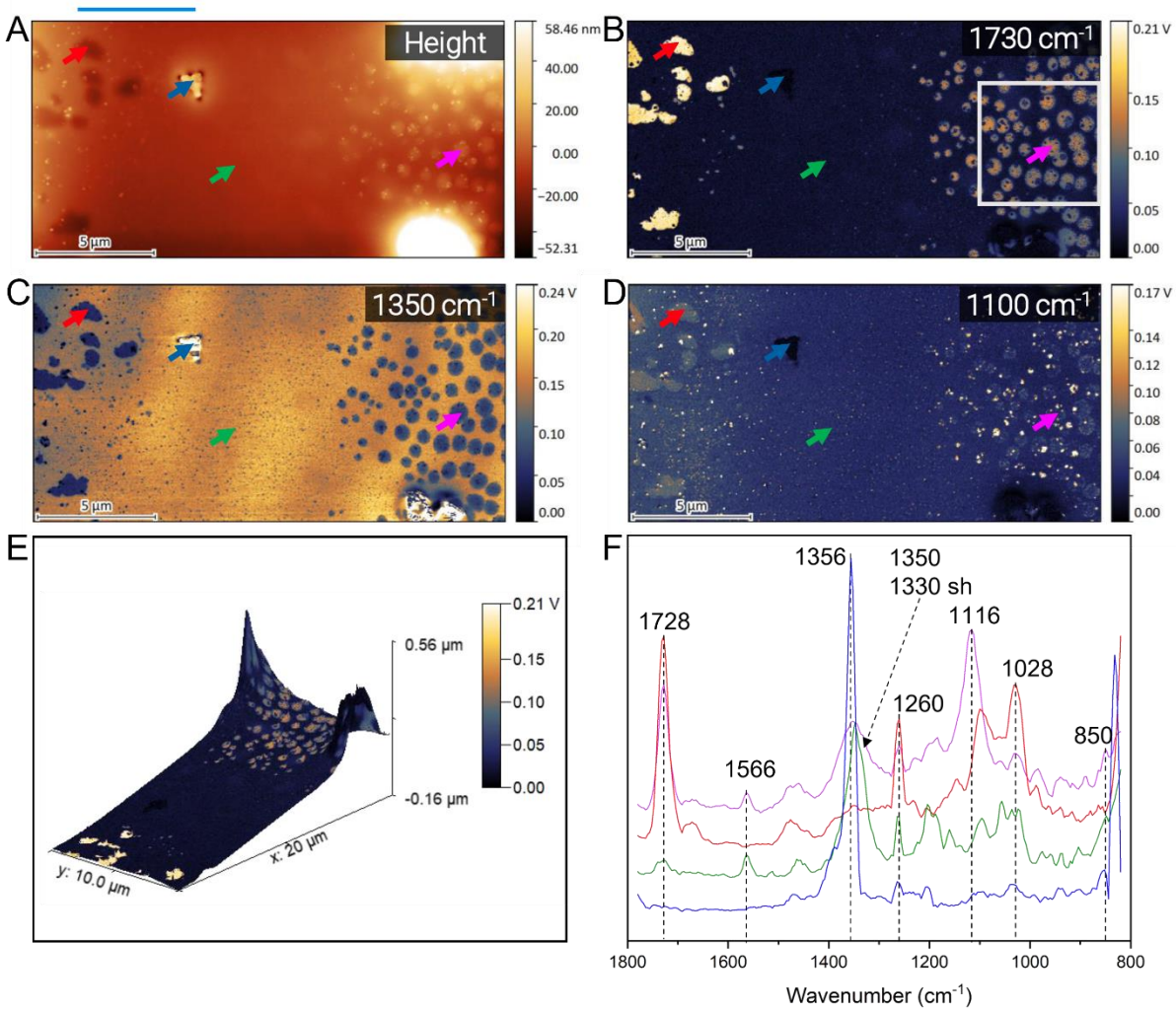

Figure 5.9 AFM-IR characterization of a 10 x 20 µm section of PDMAEMA-*b*-PVBBImTf_2N drop-cast onto a silicon wafer from 10 mM KNO_3 DMSO solution including (a) height and chemical IR map traces at (b) 1730 cm^{-1} (C=O str ester PDMAEMA), (c) 1350 cm^{-1} (SO_2 asym str of the Tf_2N anion), and (d) 1100 cm^{-1} (Si-O silica contaminate). The 10 by 20 µm section of film analyzed was located near the edge of the film. (e) 3D rendering shows spherical morphology inclusions present only at larger film thicknesses (>0.2 µm, right side of AFM images) whereas the thinner film section (left side) displays residual PDMAEMA macroinitiator deposits. f) Point IR spectra were collected at four film locations as indicated by the arrows with the arrow colors (a-d) corresponding to the spectra colors in (f).

The large homogenous center section is mainly composed of Tf_2N^- signals as indicated by the 1350 cm^{-1} chemical map (Figure 5.9c). Point spectra for the green arrow shows contributions from both the PDMAEMA and PVBBImTf_2N polymer blocks as indicated by a weaker intensity peak

for PDMAEMA C=O str (1730 cm^{-1}) as well as peaks for the imidazolium ring (1566 cm^{-1}) and the $Tf2N^-$ anion (1350cm^{-1}). This indicates that no phase separation of the polymer blocks occurs at this film thickness (~150 nm). For thicker film sections, such as the right side of the height and chemical image maps in Figure 5.9 (~300 nm), a phase separated spherical morphology emerged. The spheres displayed darker yellow color and lighter blue color signals in the 1730 cm^{-1} map (Figure 5.9b) and 1350 cm^{-1} (Figure 5.9c) chemical maps, respectively, suggesting that contributions from both polymer blocks are occurring with a higher signal from the PDMAEMA block. This is further corroborated by a point spectrum (Figure 5.9f) of one of the spheres marked by the pink arrow containing peaks for the PDMAEMA carbonyl band (1728 cm^{-1}), imidazolium ring (1566 cm^{-1}) and 1350 cm^{-1} anion. Compared to the homogenous center section, the PDMAEMA carbonyl peak (1728cm^{-1}) is more intense in the sphere's IR spectrum, suggesting that there is a higher concentration of the PDMAEMA block at the surface of the spheres. The height trace (Figure 5.9a) indicates that the spheres are slightly raised from the surrounding morphology, and the particle size was found to be on average ~ 930 nm (± 240 nm). These results would overall suggest that the spheres are predominately composed of the PDMAEMA block and surrounded by a PVBBImTf_2N matrix. Interestingly, the spheres appeared to contain another small particle-like feature that yielded dark blue colors in both the 1730 cm^{-1} (Figure 5.9b) and 1350 cm^{-1} (Figure 5.9c) maps but produced a bright yellow signal at 1100 cm^{-1} (Figure 5.9d). A smaller AFM scan marked by the white box in Figure 5.9b was taken of this region to allow for closer examination of these features.

Figure 5.10 shows the AFM-IR images (5 μm by 5 μm) collected for the spherical morphology region of the block copolymer film, including the height trace (Figure 5.10a) and the chemical maps (Figure 5.10b-d) at 1350 cm^{-1} (SO_2 asym str of the Tf_2N anion), 1100 cm^{-1} (particles), and

1730 cm^{-1} (C=O ester str in PDMAEMA). A composite image of all three traces is compiled in Figure 5.10e where the red, green, and blue colors are for the PDMAEMA (1730 cm^{-1}), PVBBImTf_2N anion (1350 cm^{-1}), and silica particle (1100 cm^{-1}) signals. A point spectrum of one of the particles in the PDMAEMA spheres gives a single strong peak at 1100 cm^{-1} (Figure 5.10f). Based on the spectra, these small particles located within the PDMAEMA spheres are attributed to silica particle contaminants from either the Si wafer piranha treatment or due to the solution conditions (nitrate and fluorinated species)[88], which corresponds well with the characteristic Si-O-Si stretch at ~1100 cm^{-1} [82] [83]. Interestingly, it appears the silica contaminates selectively interact with the PDMAEMA spheres. This is likely due to the ability of the more hydrophilic PDMAEMA block to form hydrogen bonding interactions between unprotonated tertiary amine groups and the silica -OH groups or through electrostatic binding of protonated amines with the partially negatively charged oxygen groups in silica. Similar behavior has been observed in other amine-silica blends and on silicon surfaces[84].

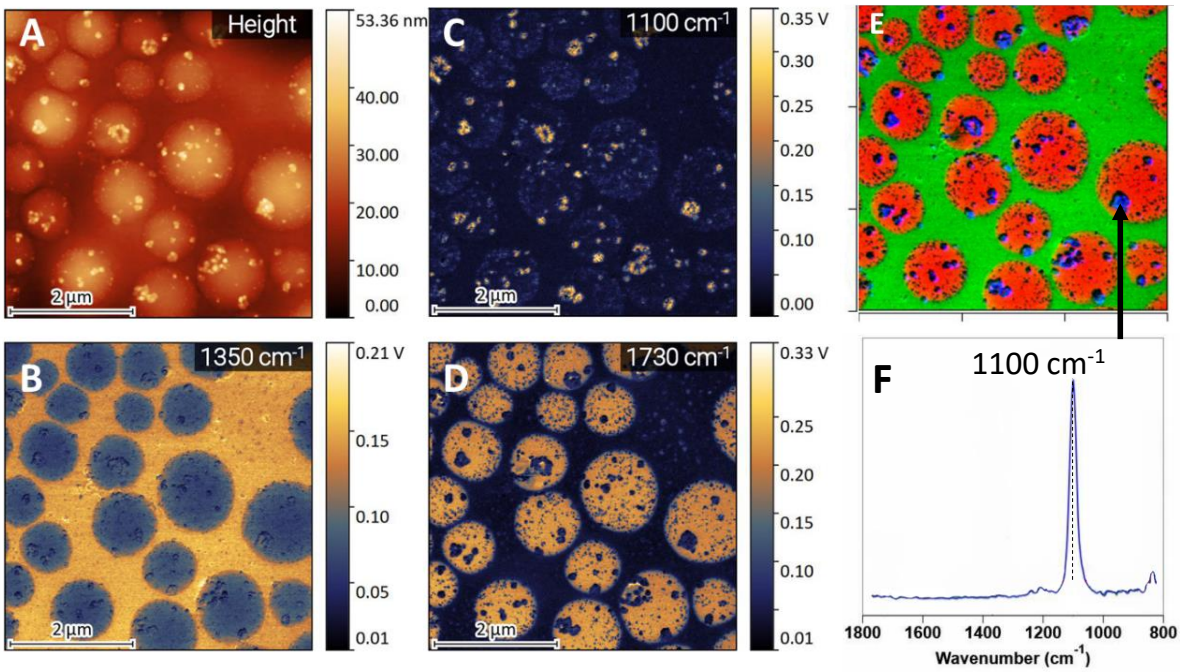

Figure 5.10 AFM-IR characterization of PDMAEMA-co-PVBBImTf_2N block copolymer drop-cast from 10 mM KNO_3 DMSO solution onto silicon wafers. The (a) height trace and several IR traces at (b) 1350 cm^{-1} (SO_2 asym str of the Tf_2N anion), (c) 1100 cm^{-1} (Si-O silica contaminate), and (d) 1730 cm^{-1} (C=O ester str PDMAEMA block) indicate microphase separation of the block copolymer. (e) a composite of the IR traces shows PDMAEMA spheres in a PVBBImTf_2N matrix with the silica particle contaminants in the hydrophilic PDMAEMA domains. (f) The point spectra trace of one of the silica particle contaminates (as indicated by the black arrow in the composite image) displays a strong peak at 1100 cm^{-1} typical for Si-O-Si networks.

The AFM-IR results of the self-assembled film structures indicate that the all-polyelectrolyte PDMAEMA-*b*-PVBBImTf_2N block copolymer is capable of microphase separation at thicknesses of ~300 nm, but only produced a single homogenous phase at lower thicknesses (~150 nm) at the used process conditions. As, processing parameters such as solvent and salt additives, annealing temperature and time, film thickness, and substrate surface properties greatly influence film morphology of block copolymers[85-87], further exploration of film and membrane processing parameters will be performed in a future work.

An interesting finding is that the more hydrophilic PDMAEMA phase can selectively interact with hydrophilic inclusions, such as silica nanoparticles. Potentially this could be leveraged to

develop self-assembled composites. For example, these all-polyelectrolyte block copolymers combined with inorganic nanomaterials could allow the weak polyelectrolyte block to selectively coordinate with the nanomaterials while the PIL block is free for application-based functionality, such as ion conductivity or property tunability through ion exchange. Such all-polyelectrolyte block copolymer systems can be useful for producing PILs-based composites for nanoparticle templates or for reinforcing the mechanical properties of solid electrolytes in a variety of electrochemical applications ranging from solid state battery electrolytes to ionic actuators and sensors.

5.3. Conclusions

A novel all-polyelectrolyte block copolymer composed of a poly(ionic liquid) block and a tertiary amine based weak polyelectrolyte was successfully synthesized using a Cu(0)-mediated atom transfer radical polymerization. Living control of a well-defined PDMAEMA macroinitiator was confirmed with a degree of polymerization of 45 units and PDI of ~1.41. While living control of the PIL block was not confirmed, FTIR, ^{1}HNMR, and NMR DOSY spectroscopies confirm successful synthesis and connectivity of the PDMAEMA-*b*-PVBBImTf_2N block copolymer with a ~67 PIL unit degree of polymerization. Differences in the supramolecular environment between the PIL homopolymer and block copolymer were examined with FTIR and 1HNMR spectroscopies in the bulk and in solution, respectively. While no differences were observed in the bulk, the block copolymer exhibited both hydrogen bonding and electrostatic interactions in DMSO and KNO_3 DMSO solutions, as demonstrated by shifts in the imidazolium C_2-H proton and the PDMAEMA block methyl and methylene groups. DLS measurements of the block copolymer indicate that an extended network-like structure is formed in pure DMSO as a result of combined hydrogen bonding between the PDMAEMA and PVBBIMTf_2N blocks and repulsive

interactions between positively charged groups on the polymer chain. The addition of 10 mM KNO_3 sufficiently screens these repulsive interactions, allowing for a collapse in the polymer network-like structure while still maintaining hydrogen bonding interactions as suggested by the imidazolium C_2-H and PDMAEMA methyl group NMR shifts in 10 mM KNO3 DMSO solution. The film assembly of the all-polyelectrolyte block copolymer film was interrogated for the first time by AFM-IR. The film morphology was found to be dependent on film thickness. At large thicknesses, the film morphology consisted of PDMAEMA spheres in a PVBBImTf_2N matrix while a homogenous morphology was observed at lower thicknesses. Silica nanoparticles were found to selectively interact with the PDMAEMA spheres, indicating the potential application of the PDMAEMA-*b*-PVBBImTf_2N block copolymer in inorganic nanoparticle-polymer composites.

5.4. Materials and Methods

5.4.1. Materials:

1-butylimidazole, 4-chloromethylsytrene, and lithium bis(trifluoromethylsulfonyl)imide (**$LiTf_2N$**) were purchased from TCI America. Acetonitrile, dimethylsulfoxide (**DMSO**), and ethyl acetate were purchased from VWR. Diethyl ether were purchased from Beantown Chemical. N,N-dimethylformamide (**DMF**) was purchased from Alfa Aesar. N,N,N',N",N"-Pentamethyl-diethylenetriamine (**PMDETA**), methyl 2-bromopropionate (**MBP**), copper (II) bromide (**$CuBr_2$**), 2-(dimethylamino) ethylmethacrylate (**DMAEMA**), tris (2-pyridylmethyl) amine (**TPMA**), hydrochloric acid, alpha-bromophenylacetic acid (**α-BPA**), and potassium nitrate (**KNO_3**) were purchased from Aldrich. DMSO-d6 was purchased from the University of Oklahoma Chemistry Stockroom. All purchased chemicals were used as received.

5.4.2. General 1-butyl-3-Vinylbenzylimidazolium Chloride Synthesis (VBBImCl):

1-butylimidazole (~ 11 mL) and 4-chloromethylstyrene (~10 mL) were dissolved in 40 mL of acetonitrile. The mixture was allowed to react at 40 °C for 24 h under stirring. The reaction was then allowed to cool to room temperature and then stirred for an additional 24 h at 20 °C. The product solution was concentrated with a rotary evaporator at 40 °C. The concentrated solution was poured into 100 mL of diethyl ether. A yellow transparent oil collected immediately at the bottom of the flask. The diethyl ether was decanted, and additional fresh diethyl ether (40 mL x 3 times) was added to wash the product. Finally, the IL was dried in the vacuum oven at room temperature overnight.

5.4.3. General 4-Vinylbenzyl-3-butylimidazolium bis(trifluoromethylsulfonyl)imide ($VBBImTf_2N$):

The VBBImCl product was dissolved in 150 mL of Millipore water under vigorous stirring. 20.1 g of $LiTf_2N$ was added to the reaction mixture under stirring. An immediate precipitation occurred with the product accumulating at the bottom of the flask. The solution was transferred to a 500 mL round bottom flask and the precipitated IL was dissolved in 250 mL of ethyl acetate under vigorous stirring. This ethyl acetate solution was added to the 500 mL round bottom flask and was then vigorously stirred to form a yellow-white emulsion. The biphasic reaction mixture was stirred for 24 h at room temperature, after which the stirring was stopped and allowed to separate into two phases. Product from the aqueous layer was extracted with 50 mL ethyl acetate (3x) and the organic phase was combined with the original ethyl acetate product phase. The total ethyl acetate product layer was then washed with 50 mL of Millipore water (3x). Ethyl acetate was removed by a rotary evaporator and dried in the vacuum oven at ~35 °C to remove trace ethyl acetate.

5.4.4. General Cu(0) Mediated ATRP Synthesis of Poly[4-vinylbenzyl-3-butylimidazolium bis(trifluoromethylsulfonyl)imide] (PVBBImTf_2N):

VBBImTf_2N monomer (2.32 g) was dissolved in (7 mL) DMF in a test tube for 30 min. $CuBr_2$ deactivator (0.002 g) was added to a separate dry test tube. The dissolved monomer, PMDETA ligand (12.4 μL), and MBP initiator (1.88 μL) was added to the test tube in that order. After adding the MBP, the test tube was quickly capped with a septum and frozen in liquid nitrogen. At least 4 freeze-pump-thaw cycles were performed to degas the solution. A 4 cm long Cu(0) wire was treated in a 6 M HCl/ methanol solution under nitrogen before removed the acid solution with a syringe and drying with nitrogen. On the last freeze cycle, the treated Cu(0) wire was added to the reaction test tube. Three cycles of vacuum and backfilling with nitrogen gas were performed while frozen. The test tube was then allowed to thaw to room temperature and was then added to an oil bath at 90 °C under nitrogen for 24 h. 100 μL samples were taken periodically to track monomer conversion. The polymerization was stopped by exposing the system to air. A 10 mL solution of a 4 to 1 volume ratio of methanol to water was used to precipitate out the polymer product.

5.4.5. Cu(0) Mediated ATRP Synthesis of Poly[2-(dimethylamino)ethyl methacrylate] (PDMAEMA) Macroinitiator:

The Cu(0) mediated ATRP synthesis of the PDMAEMA macroinitiator was performed similarly to a previous work by the authors' group and is briefly described here[23]. DMAEMA (2.5 mL), $CuBr_2$ (0.0168 g), TPMA (0.035 g), NaCl (0.248 g), α-BPA (~0.064 g), and 3 mL of water were added to a test tube. The pH of the solution was adjusted to ~8.6 by adding 2.5 mL of 1 M HCl solution. At least 4 freeze-pump thaw cycles were performed, and the 6.5 cm long Cu(0) wire and magnetic stirrer were added on the last free cycle. A 4-cm long Cu(0) wire had been pretreated in 1 M HCl/methanol solution as described previously. Three cycles of backfilling with nitrogen

and vacuuming were done. The solution was allowed to thaw and then was added to a water bath maintained at 2 °C. The reaction was allowed to proceed for ~ 5 h, and then the reaction was stopped by exposing the solution to air and adding ammonium sulfate directly to the reaction mixture to precipitate the product. The polymer was dissolved in methanol and separated from the ammonium sulfate through vacuum filtration before washing with methanol. The methanol was then evaporated, and the polymer was dried in the vacuum oven to remove trace solvent.

5.4.6. Cu (0) Mediated ATRP Synthesis of Poly(2-(dimethylamino) ethyl methacrylate]-*block*-[Poly(4-vinylbenzyl-3butylimidazolium bis(trifluoromethylsulfonyl)imide] block copolymer (PDMAEMA-*b*-PVBBImTf_2N):

VBBImTf_2N monomer (1.61 g) and PDMAEMA macroinitiator (0.24 g) were weighed out and dissolved separately in 4 mL and 2 mL of DMF, respectively. To a dry test tube, the $CuBr_2$ (0.0021 g) deactivator, PMDETA ligand (25 μL), and a magnetic stirrer were added. The monomer and macroinitiator solutions were then added to this test tube. Four FPT cycles were performed followed by addition of 4 cm length of Cu(0) copper wire after the last cycle. The system was backfilled and vacuumed (3x) before thawing the solution under nitrogen and adding it to the 90 °C oil bath and allowed to react for 24 h. Small 100 μL aliquots were collected periodically to track polymerization conversion and chain growth. The reaction was stopped by exposure to air. The product was precipitated in excess chloroform and washed (3x) with additional chloroform. The final product was dried in a vacuum oven to remove residual solvent.

5.4.7. Characterizations:

ATR FTIR was carried out on a Nicolet iS50R FT-IR Spectrometer with a DLaTGS detector at a resolution of $4cm^{-1}$ for 64 or 256 scans. ^{1}HNMR and Oneshot DOSY (DONESHOT) experiments were performed for the produced polymers on a Varian VNMRS 500 MHz NMR

Spectrometer at the (University of Oklahoma NMR Facility). Spectra were referenced at the DMSO-d_5 peak at 2.5 ppm. Polymerization conversion was determined by ratioing the monomer vinyl group peak integral to a select polymer peak integral. Degree of polymerization (DP) for the PDMAEMA macroinitiator was determined by ratioing the integral of one of the methylene peaks (~4.08 ppm) in the monomer unit to the benzyl chain end group (~7.18-7.18 ppm) integral. The degree of polymerization for the block copolymer was determined by ratioing the PVBBImTf_2N benzyl peak integral (5.98-6.71 ppm) to the macroinitiator PDMAEMA tertiary amine methyl group peak integral (2.52-2.35 ppm). Unfortunately, due to overlapping signals of the PVBBImTf_2N chain signals with the end group signals, the DP could not be determined for the PVBBImTf_2N homopolymer. One dimensional spectra collected in the DONESHOT experiment were converted to a 2D DOSY through a Bayesian transformation method using the MNova software package. A Shimadzu Prominence HPLC equipped with a Waters R410 differential refractometer and a Wyatt DAWN F light scattering detector was used to characterize the PDMAEMA macroinitiator molecular weight and polydispersity index (PDI) relative to poly(ethylene glycol) standards. The instrument used Aquagel-OH Mixed H and Aquagel-OH 30 columns, and the mobile phase was a 0.3 M sodium acetate solution at a pH of 4 containing 0.15 M triethylamine to suppress polymer-column interactions. Dynamic light scattering (DLS) was performed with a NanoBrook Omni using a 90° detector. Either double exponential (Dblexp) or non-negatively constrained least squares (NNLS) fitting models were used as appropriate for each sample. Example fittings using each model are provided in the supporting information (Figure D.3-Figure D.4). Eight measurements were performed per sample. Atomic force microscopy with an FTIR module (AFM-IR) of the PDMAEMA-*b*-PVBBImTf_2N block copolymer film was performed using a Bruker NanoIR3 System equipped with a Mircat-QT laser (Daylight Solutions).

The system was operated in tapping AFM-IR mode using a PR-EX-TNIR-A-10 probe (4 N/m, 60 kHz nominal resonance frequency), the pulse rate of the IR laser was chosen to be the difference frequency of the first 2 cantilever resonance frequencies (~300 kHz). PDMAEMA-*b*-PVBBImTf_2N block copolymer in 10 mM KNO_3 DMSO solution was drop casted on to a silicon wafer that had been pretreated with piranha solution and UV-ozone cleaning. The films were dried in the vacuum oven at 60 °C for ~ 2 h prior to AFM-IR analysis.

Acknowledgments

The authors would like to thank Dr. Cassandra Phillips and Bruker for assistance with the AFM-IR measurements and instrument access to the Bruker *Anasys NanoIR3* system. Also, the authors would like to thank Lucas Condes (University of Oklahoma) for aiding in the synthesis of the PIL homopolymer.

5.5. References

(1) Choi, J.-H.; Ye, Y.; Elabd, Y. A.; Winey, K. I. Network Structure and Strong Microphase Separation for High Ion Conductivity in Polymerized Ionic Liquid Block Copolymers. *Macromolecules* **2013**, *46* (13), 5290-5300. DOI: 10.1021/ma400562a.

(2) Margaretta, E.; Fahs, G. B.; Inglefield, D. L., Jr.; Jangu, C.; Wang, D.; Heflin, J. R.; Moore, R. B.; Long, T. E. Imidazolium-Containing ABA Triblock Copolymers as Electroactive Devices. *ACS Applied Materials & Interfaces* **2016**, *8* (2), 1280-1288. DOI: 10.1021/acsami.5b09965.

(3) Shi, Z.; Newell, B. S.; Bailey, T. S.; Gin, D. L. Ordered, microphase-separated, noncharged-charged diblock copolymers via the sequential ATRP of styrene and styrenic imidazolium monomers. *Polymer* **2014**, *55* (26), 6664-6671. DOI: https://doi.org/10.1016/j.polymer.2014.11.009.

(4) Wu, B.; Zhang, W.; Gao, N.; Zhou, M.; Liang, Y.; Wang, Y.; Li, F.; Li, G. Poly (ionic liquid)-Based Breath Figure Films: A New Kind of Honeycomb Porous Films with Great Extendable Capability. *Scientific Reports* **2017**, *7* (1), 13973. DOI: 10.1038/s41598-017-14563-x.

(5) He, H.; Zhong, M.; Adzima, B.; Luebke, D.; Nulwala, H.; Matyjaszewski, K. A Simple and Universal Gel Permeation Chromatography Technique for Precise Molecular Weight Characterization of Well-Defined Poly(ionic liquid)s. *Journal of the American Chemical Society* **2013**, *135* (11), 4227-4230. DOI: 10.1021/ja4012645.

(6) Luo, H.; Tang, Q.; Zhong, J.; Lei, Z.; Zhou, J.; Tong, Z. Interplay of Solvation and Size Effects Induced by the Counterions in Ionic Block Copolymers on the Basis of Hofmeister Series. *Macromolecular Chemistry and Physics* **2019**, *220* (4), 1800508, https://doi.org/10.1002/macp.201800508. DOI: https://doi.org/10.1002/macp.201800508 (acccessed 2023/03/16).

(7) Vijayakrishna, K.; Jewrajka, S. K.; Ruiz, A.; Marcilla, R.; Pomposo, J. A.; Mecerreyes, D.; Taton, D.; Gnanou, Y. Synthesis by RAFT and Ionic Responsiveness of Double Hydrophilic Block Copolymers Based on Ionic Liquid Monomer Units. *Macromolecules* **2008**, *41* (17), 6299-6308. DOI: 10.1021/ma800677h.

(8) Yang, Y.; Li, X.; Yan, Y.; Pan, R.; Liu, J.; Lian, M.; Luo, X.; Liu, G. RAFT polymerization-induced self-assembly of poly(ionic liquids) in ethanol. **2022**, *22* (1), 803-808. DOI: doi:10.1515/epoly-2022-0069 (acccessed 2023-03-17).

(9) Yang, Y.; Zheng, J.; Man, S.; Sun, X.; An, Z. Synthesis of poly(ionic liquid)-based nano-objects with morphological transitions via RAFT polymerization-induced self-assembly in ethanol. *Polymer Chemistry* **2018**, *9* (7), 824-827, 10.1039/C8PY00040A. DOI: 10.1039/C8PY00040A.

(10) He, H.; Rahimi, K.; Zhong, M.; Mourran, A.; Luebke, D. R.; Nulwala, H. B.; Möller, M.; Matyjaszewski, K. Cubosomes from hierarchical self-assembly of poly(ionic liquid) block copolymers. *Nature Communications* **2017**, *8* (1), 14057. DOI: 10.1038/ncomms14057.

(11) Mai, Y.; Eisenberg, A. Self-assembly of block copolymers. *Chemical Society Reviews* **2012**, *41* (18), 5969-5985, 10.1039/C2CS35115C. DOI: 10.1039/C2CS35115C.

(12) Green, M. D.; Wang, D.; Hemp, S. T.; Choi, J.-H.; Winey, K. I.; Heflin, J. R.; Long, T. E. Synthesis of imidazolium ABA triblock copolymers for electromechanical transducers. *Polymer* **2012**, *53* (17), 3677-3686. DOI: https://doi.org/10.1016/j.polymer.2012.06.023.

(13) Jangu, C.; Wang, J.-H. H.; Wang, D.; Sharick, S.; Heflin, J. R.; Winey, K. I.; Colby, R. H.; Long, T. E. Well-Defined Imidazolium ABA Triblock Copolymers as Ionic-Liquid-Containing Electroactive Membranes. *Macromolecular Chemistry and Physics* **2014**, *215* (13), 1319-1331, https://doi.org/10.1002/macp.201400121. DOI: https://doi.org/10.1002/macp.201400121 (acccessed 2022/08/10).

(14) Cordella, D.; Kermagoret, A.; Debuigne, A.; Jerome, C.; Mecerreyes, D.; Isik, M.; Taton, D.; Detrembleur, C. All Poly(ionic liquid)-Based Block Copolymers by Sequential Controlled Radical Copolymerization of Vinylimidazolium Monomers. *Macromolecules (Washington, DC, U. S.)* **2015**, *48* (15), 5230-5243, 10.1021/acs.macromol.5b01013. DOI: 10.1021/acs.macromol.5b01013.

(15) Cordella, D.; Debuigne, A.; Jérôme, C.; Kochovski, Z.; Taton, D.; Detrembleur, C. One-Pot Synthesis of Double Poly(Ionic Liquid) Block Copolymers by Cobalt-Mediated Radical Polymerization-Induced Self-Assembly (CMR-PISA) in Water. *Macromolecular Rapid Communications* **2016**, *37* (14), 1181-1187, https://doi.org/10.1002/marc.201600039. DOI: https://doi.org/10.1002/marc.201600039 (acccessed 2023/04/11).

(16) Cordella, D.; Ouhib, F.; Aqil, A.; Defize, T.; Jérôme, C.; Serghei, A.; Drockenmuller, E.; Aissou, K.; Taton, D.; Detrembleur, C. Fluorinated Poly(ionic liquid) Diblock Copolymers Obtained by Cobalt-Mediated Radical Polymerization-Induced Self-Assembly. *ACS Macro Letters* **2017**, *6* (2), 121-126. DOI: 10.1021/acsmacrolett.6b00899.

(17) Depoorter, J.; Yan, X.; Zhang, B.; Sudre, G.; Charlot, A.; Fleury, E.; Bernard, J. All poly(ionic liquid) block copolymer nanoparticles from antagonistic isomeric macromolecular blocks via aqueous RAFT polymerization-induced self-assembly. *Polymer Chemistry* **2021**, *12* (1), 82-91, 10.1039/D0PY00698J. DOI: 10.1039/D0PY00698J.

(18) Kawauchi, Y.; Kouka, A.; Guragain, S.; Bastakoti, B. P.; Yusa, S.-i.; Nakashima, K. Schizophrenic micelles of poly(3-(methacryloylamino)propyltrimethylammonium chloride-*b*-2-(dimethylamino)ethyl methacrylate) in aqueous solutions. *Colloids and Surfaces A: Physicochemical and Engineering Aspects* **2013**, *434*, 56-62. DOI: https://doi.org/10.1016/j.colsurfa.2013.05.033.

(19) Zhang, B.; Yan, X.; Alcouffe, P.; Charlot, A.; Fleury, E.; Bernard, J. Aqueous RAFT Polymerization of Imidazolium-Type Ionic Liquid Monomers: En Route to Poly(ionic liquid)-Based Nanoparticles through RAFT Polymerization-Induced Self-Assembly. *ACS Macro Letters* **2015**, *4* (9), 1008-1011. DOI: 10.1021/acsmacrolett.5b00534.

(20) Sanchez-Ballester, N. M.; Sciortino, F.; Mir, S. H.; Rydzek, G. Weak Polyelectrolytes as Nanoarchitectonic Design Tools for Functional Materials: A Review of Recent Achievements. *Molecules* **2022**, *27* (10), 3263.

(21) Lu, Y.; Zhuk, A.; Xu, L.; Liang, X.; Kharlampieva, E.; Sukhishvili, S. A. Tunable pH and temperature response of weak polyelectrolyte brushes: role of hydrogen bonding and monomer hydrophobicity. *Soft Matter* **2013**, *9* (22), 5464-5472, 10.1039/C3SM50268F. DOI: 10.1039/C3SM50268F.

(22) Vijayakrishna, K.; Mecerreyes, D.; Gnanou, Y.; Taton, D. Polymeric Vesicles and Micelles Obtained by Self-Assembly of Ionic Liquid-Based Block Copolymers Triggered by Anion or Solvent Exchange. *Macromolecules* **2009**, *42* (14), 5167-5174. DOI: 10.1021/ma900549k.

(23) Britten, C. N.; Lason, K.; Walters, K. B. Facile Synthesis of Tertiary Amine Pendant Polymers by Cu0-Mediated ATRP under Aqueous Conditions. *Macromolecules* **2021**, *54* (22), 10360-10369. DOI: 10.1021/acs.macromol.1c01234.

(24) Anastasaki, A.; Nikolaou, V.; Nurumbetov, G.; Wilson, P.; Kempe, K.; Quinn, J. F.; Davis, T. P.; Whittaker, M. R.; Haddleton, D. M. Cu(0)-Mediated Living Radical Polymerization: A Versatile Tool for Materials Synthesis. *Chemical Reviews* **2016**, *116* (3), 835-877. DOI: 10.1021/acs.chemrev.5b00191.

(25) Konkolewicz, D.; Wang, Y.; Krys, P.; Zhong, M.; Isse, A. A.; Gennaro, A.; Matyjaszewski, K. SARA ATRP or SET-LRP. End of controversy? *Polymer Chemistry* **2014**, *5* (15), 4396-4417, 10.1039/C4PY00149D. DOI: 10.1039/C4PY00149D.

(26) Mendonça, P. V.; Konkolewicz, D.; Averick, S. E.; Serra, A. C.; Popov, A. V.; Guliashvili, T.; Matyjaszewski, K.; Coelho, J. F. J. Synthesis of cationic poly((3-acrylamidopropyl)trimethylammonium chloride) by SARA ATRP in ecofriendly solvent mixtures. *Polymer Chemistry* **2014**, *5* (19), 5829-5836, 10.1039/C4PY00707G. DOI: 10.1039/C4PY00707G.

(27) Mohammadi, M.; Salami-Kalajahi, M.; Roghani-Mamaqani, H.; Golshan, M. Effect of molecular weight and polymer concentration on the triple temperature/pH/ionic strength-sensitive behavior of poly(2-(dimethylamino)ethyl methacrylate). *International Journal of Polymeric Materials and Polymeric Biomaterials* **2017**, *66* (9), 455-461. DOI: 10.1080/00914037.2016.1236340.

(28) Laaser, J. E.; Jiang, Y.; Sprouse, D.; Reineke, T. M.; Lodge, T. P. pH- and Ionic-Strength-Induced Contraction of Polybasic Micelles in Buffered Aqueous Solutions. *Macromolecules* **2015**, *48* (8), 2677-2685. DOI: 10.1021/acs.macromol.5b00360.

(29) Hunley, M. T.; England, J. P.; Long, T. E. Influence of Counteranion on the Thermal and Solution Behavior of Poly(2-(dimethylamino)ethyl methacrylate)-Based Polyelectrolytes. *Macromolecules* **2010**, *43* (23), 9998-10005. DOI: 10.1021/ma1017499.

(30) Karjalainen, E.; Aseyev, V.; Tenhu, H. Influence of Hydrophobic Anion on Solution Properties of PDMAEMA. *Macromolecules* **2014**, *47* (6), 2103-2111. DOI: 10.1021/ma5000706.

(31) Agudelo, N. A.; Elsen, A. M.; He, H.; López, B. L.; Matyjaszewski, K. ABA triblock copolymers from two mechanistic techniques: Polycondensation and atom transfer radical polymerization. *Journal of Polymer Science Part A: Polymer Chemistry* **2015**, *53* (2), 228-238, https://doi.org/10.1002/pola.27300. DOI: https://doi.org/10.1002/pola.27300 (acccessed 2023/05/18).

(32) Chi, W. S.; Hong, S. U.; Jung, B.; Kang, S. W.; Kang, Y. S.; Kim, J. H. Synthesis, structure and gas permeation of polymerized ionic liquid graft copolymer membranes. *Journal of Membrane Science* **2013**, *443*, 54-61. DOI: https://doi.org/10.1016/j.memsci.2013.04.049.

(33) He, H.; Luebke, D.; Nulwala, H.; Matyjaszewski, K. Synthesis of Poly(ionic liquid)s by Atom Transfer Radical Polymerization with ppm of Cu Catalyst. *Macromolecules* **2014**, *47* (19), 6601-6609. DOI: 10.1021/ma501487u.

(34) Izunobi, J. U.; Higginbotham, C. L. Polymer Molecular Weight Analysis by 1H NMR Spectroscopy. *Journal of Chemical Education* **2011**, *88* (8), 1098-1104. DOI: 10.1021/ed100461v.

(35) Abdelghafour, M. M.; Orbán, Á.; Deák, Á.; Lamch, Ł.; Frank, É.; Nagy, R.; Ádám, A.; Sipos, P.; Farkas, E.; Bari, F.; et al. The Effect of Molecular Weight on the Solubility Properties of Biocompatible Poly(ethylene succinate) Polyester. In *Polymers*, 2021; Vol. 13.

(36) Karjalainen, E.; Chenna, N.; Laurinmäki, P.; Butcher, S. J.; Tenhu, H. Diblock copolymers consisting of a polymerized ionic liquid and poly(N-isopropylacrylamide). Effects of PNIPAM block length and counter ion on self-assembling and thermal properties. *Polymer Chemistry* **2013**, *4* (4), 1014-1024, 10.1039/C2PY20815F. DOI: 10.1039/C2PY20815F.

(37) May, A. W.; Shi, Z.; Wijayasekara, D. B.; Gin, D. L.; Bailey, T. S. Self-assembly of highly asymmetric, poly(ionic liquid)-rich diblock copolymers and the effects of simple structural modification on phase behaviour. *Polymer Chemistry* **2019**, *10* (6), 751-765, 10.1039/C8PY01414K. DOI: 10.1039/C8PY01414K.

(38) Yuan, J.; Schlaad, H.; Giordano, C.; Antonietti, M. Double hydrophilic diblock copolymers containing a poly(ionic liquid) segment: Controlled synthesis, solution property, and application as carbon precursor. *European Polymer Journal* **2011**, *47* (4), 772-781. DOI: https://doi.org/10.1016/j.eurpolymj.2010.09.030.

(39) Roth, C.; Chatzipapadopoulos, S.; Kerlé, D.; Friedriszik, F.; Lütgens, M.; Lochbrunner, S.; Kühn, O.; Ludwig, R. Hydrogen bonding in ionic liquids probed by linear and nonlinear vibrational spectroscopy. *New Journal of Physics* **2012**, *14* (10), 105026. DOI: 10.1088/1367-2630/14/10/105026.

(40) Paschoal, V. H.; Faria, L. F. O.; Ribeiro, M. C. C. Vibrational Spectroscopy of Ionic Liquids. *Chemical Reviews* **2017**, *117* (10), 7053-7112. DOI: 10.1021/acs.chemrev.6b00461.

(41) Grondin, J.; Lassègues, J.-C.; Cavagnat, D.; Buffeteau, T.; Johansson, P.; Holomb, R. Revisited vibrational assignments of imidazolium-based ionic liquids. *Journal of Raman Spectroscopy* **2011**, *42* (4), 733-743. DOI: https://doi.org/10.1002/jrs.2754.

(42) Hunt, P. A.; Ashworth, C. R.; Matthews, R. P. Hydrogen bonding in ionic liquids. *Chemical Society Reviews* **2015**, *44* (5), 1257-1288, 10.1039/C4CS00278D. DOI: 10.1039/C4CS00278D.

(43) Katsyuba, S. A.; Dyson, P. J.; Vandyukova, E. E.; Chernova, A. V.; Vidiš, A. Molecular Structure, Vibrational Spectra, and Hydrogen Bonding of the Ionic Liquid 1-Ethyl-3-methyl-1H-imidazolium Tetrafluoroborate. *Helvetica Chimica Acta* **2004**, *87* (10), 2556-2565, https://doi.org/10.1002/hlca.200490228. DOI: https://doi.org/10.1002/hlca.200490228 (acccessed 2023/04/12).

(44) Larkin, P. J. Chapter 6 - IR and Raman Spectra–Structure Correlations: Characteristic Group Frequencies. In *Infrared and Raman Spectroscopy (Second Edition)*, Larkin, P. J. Ed.; Elsevier, 2018; pp 85-134.

(45) Coates, J. Interpretation of Infrared Spectra, A Practical Approach. In *Encyclopedia of Analytical Chemistry*.

(46) Socrates, G. *Infrared and Raman Characteristic Group Frequencies Tables and Charts*; John Wiley & Sons, LTD, 2001.

(47) Robert M. Silverstein, F. X. W., David J. Kiemle, David L. Bryce. *Spectrometric Identification of Organic Compounds*; Wiley, 2014.

(48) Mikol, V.; Rodeau, J.-L.; Giegé, R. Changes of pH during biomacromolecule crystallization by vapor diffusion using ammonium sulfate as the precipitant. *Journal of applied crystallography* **1989**, *22* (2), 155-161.

(49) Ni, P.; Zhang, M.; Ma, L.; Fu, S. Poly(dimethylamino)ethyl Methacrylate for Use as a Surfactant in the Miniemulsion Polymerization of Styrene. *Langmuir* **2006**, *22* (14), 6016-6023. DOI: 10.1021/la053276z.

(50) Kiefer, J.; Fries, J.; Leipertz, A. Experimental vibrational study of imidazolium-based ionic liquids: Raman and infrared spectra of 1-ethyl-3-methylimidazolium bis(trifluoromethylsulfonyl)imide and 1-ethyl-3-methylimidazolium ethylsulfate. *Appl Spectrosc* **2007**, *61* (12), 1306-1311. DOI: 10.1366/000370207783292000 From NLM.

(51) James, C.; Ravikumar, C.; Jayakumar, V. S.; Hubert Joe, I. Vibrational spectra and potential energy distributions for 1-benzyl-1H-imidazole by normal coordinate analysis. *Journal of Raman Spectroscopy* **2009**, *40* (5), 537-545, https://doi.org/10.1002/jrs.2160. DOI: https://doi.org/10.1002/jrs.2160 (acccessed 2022/10/12).

(52) Noack, K.; Schulz, P. S.; Paape, N.; Kiefer, J.; Wasserscheid, P.; Leipertz, A. The role of the C2 position in interionic interactions of imidazolium based ionic liquids: a vibrational and NMR spectroscopic study. *Physical Chemistry Chemical Physics* **2010**, *12* (42), 14153-14161, 10.1039/C0CP00486C. DOI: 10.1039/C0CP00486C.

(53) Long, B. Experimental Studies and Thermodynamic Modeling of the Solubilities of Potassium Nitrate, Potassium Chloride, Potassium Bromide, and Sodium Chloride in Dimethyl Sulfoxide. *Industrial & Engineering Chemistry Research* **2011**, *50* (11), 7019-7026. DOI: 10.1021/ie102134g.

(54) Cui, J.; Nie, F.-M.; Yang, J.-X.; Pan, L.; Ma, Z.; Li, Y.-S. Novel imidazolium-based poly(ionic liquid)s with different counterions for self-healing. *Journal of Materials Chemistry A* **2017**, *5* (48), 25220-25229, 10.1039/C7TA06793C. DOI: 10.1039/C7TA06793C.

(55) Cremer, T.; Kolbeck, C.; Lovelock, K. R. J.; Paape, N.; Woelfel, R.; Schulz, P. S.; Wasserscheid, P.; Weber, H.; Thar, J.; Kirchner, B.; et al. Towards a Molecular Understanding of Cation-Anion Interactions-Probing the Electronic Structure of Imidazolium Ionic Liquids by NMR Spectroscopy, X-ray Photoelectron Spectroscopy and Theoretical Calculations. *Chem. - Eur. J.* **2010**, *16* (30), 9018-9033, S9018/9011-S9018/9017, 10.1002/chem.201001032. DOI: 10.1002/chem.201001032.

(56) Matthews, R. P.; Villar-Garcia, I. J.; Weber, C. C.; Griffith, J.; Cameron, F.; Hallett, J. P.; Hunt, P. A.; Welton, T. A structural investigation of ionic liquid mixtures. *Physical Chemistry Chemical Physics* **2016**, *18* (12), 8608-8624, 10.1039/C6CP00156D. DOI: 10.1039/C6CP00156D.

(57) Guo, J.; Zhou, Y.; Qiu, L.; Yuan, C.; Yan, F. Self-assembly of amphiphilic random co-poly(ionic liquid)s: the effect of anions, molecular weight, and molecular weight distribution. *Polym. Chem.* **2013**, *4* (14), 4004-4009, 10.1039/c3py00460k. DOI: 10.1039/c3py00460k.

(58) Chen, S.-C.; Kuo, S.-W.; Liao, C.-S.; Chang, F.-C. Syntheses, Specific Interactions, and pH-Sensitive Micellization Behavior of Poly[vinylphenol-*b*-2-(dimethylamino)ethyl methacrylate] Diblock Copolymers. *Macromolecules* **2008**, *41* (22), 8865-8876. DOI: 10.1021/ma801546z.

(59) Yuk, S. H.; Cho, S. H.; Lee, S. H. pH/Temperature-Responsive Polymer Composed of Poly((N,N-dimethylamino)ethyl methacrylate-co-ethylacrylamide). *Macromolecules* **1997**, *30* (22), 6856-6859. DOI: 10.1021/ma970725w.

(60) Horne, W. J.; Andrews, M. A.; Terrill, K. L.; Hayward, S. S.; Marshall, J.; Belmore, K. A.; Shannon, M. S.; Bara, J. E. Poly(Ionic Liquid) Superabsorbent for Polar Organic Solvents. *ACS Applied Materials & Interfaces* **2015**, *7* (17), 8979-8983. DOI: 10.1021/acsami.5b01921.

(61) Wang, B.; Feng, Y.; Qi, X.; Deng, M.; Tian, J.; Zhang, Q. Designing Explosive Poly(Ionic Liquid)s as Novel Energetic Polymers. *Chemistry – A European Journal* **2018**, *24* (59), 15897-15902, https://doi.org/10.1002/chem.201803159. DOI: https://doi.org/10.1002/chem.201803159 (acccessed 2023/04/13).

(62) Zertal, Y.; Yong, M.; Levi, A.; Sevilia, S.; Tsoglin, A.; Parvari, G.; Gottlieb, L.; Eichen, Y. Alkyl Vinyl Imidazolium Ionic Liquids as Fuel Binders for Photo-curable Energetic Propellants. *ACS Applied Polymer Materials* **2022**, *4* (7), 4928-4939. DOI: 10.1021/acsapm.2c00499.

(63) Hsu, C.-H.; Kuo, S.-W.; Chen, J.-K.; Ko, F.-H.; Liao, C.-S.; Chang, F.-C. Self-Assembly Behavior of A-B Diblock and C-D Random Copolymer Mixtures in the Solution State through Mediated Hydrogen Bonding. *Langmuir* **2008**, *24* (15), 7727-7734. DOI: 10.1021/la703960g.

(64) Kuo, S.-W. Hydrogen bond-mediated self-assembly and supramolecular structures of diblock copolymer mixtures. *Polymer International* **2009**, *58* (5), 455-464, https://doi.org/10.1002/pi.2513. DOI: https://doi.org/10.1002/pi.2513 (acccessed 2023/04/13).

(65) Horkay, F. Polyelectrolyte Gels: A Unique Class of Soft Materials. In *Gels*, 2021; Vol. 7.

(66) Muthukumar, M. 50th Anniversary Perspective: A Perspective on Polyelectrolyte Solutions. *Macromolecules* **2017**, *50* (24), 9528-9560. DOI: 10.1021/acs.macromol.7b01929.

(67) Wanasingha, N.; Dorishetty, P.; Dutta, N. K.; Choudhury, N. R. Polyelectrolyte Gels: Fundamentals, Fabrication and Applications. In *Gels*, 2021; Vol. 7.

(68) Elias, H.-G. *An Introduction to Polymer Science*; Wiley, 1997.

(69) Borisov, O. V.; Zhulina, E. B. Effect of Salt on Self-Assembly in Charged Block Copolymer Micelles. *Macromolecules* **2002**, *35* (11), 4472-4480. DOI: 10.1021/ma010934n.

(70) Chavan, S. N.; Lee, H.-i. Random ionic polymers: Salt-triggered reversible vesicular self-assembly in water. *European Polymer Journal* **2023**, *193*, 112114. DOI: https://doi.org/10.1016/j.eurpolymj.2023.112114.

(71) Isik, M.; Fernandes, A. M.; Vijayakrishna, K.; Paulis, M.; Mecerreyes, D. Preparation of poly(ionic liquid) nanoparticles and their novel application as flocculants for water purification. *Polymer Chemistry* **2016**, *7* (8), 1668-1674, 10.1039/C5PY02001H. DOI: 10.1039/C5PY02001H.

(72) Korchagina, E. V.; Philippova, O. E. Ion-Specific Self-Assembly of Hydrophobically Modified Polycation of Natural Origin. *Macromolecules* **2015**, *48* (23), 8622-8628. DOI: 10.1021/acs.macromol.5b02213.

(73) Popescu, M.-T.; Liontos, G.; Avgeropoulos, A.; Tsitsilianis, C. Stimuli responsive fibrous hydrogels from hierarchical self-assembly of a triblock copolypeptide. *Soft Matter* **2015**, *11* (2), 331-342, 10.1039/C4SM02092H. DOI: 10.1039/C4SM02092H.

(74) Zhong, J.; Luo, H.; Tang, Q.; Lei, Z.; Tong, Z. Counterion-Mediated Self-Assembly of Ion-Containing Block Copolymers on the Basis of the Hofmeister Series. *Macromolecular Chemistry and Physics* **2019**, *220* (5), 1800554, https://doi.org/10.1002/macp.201800554. DOI: https://doi.org/10.1002/macp.201800554 (acccessed 2023/05/18).

(75) Dazzi, A.; Prater, C. B. AFM-IR: Technology and Applications in Nanoscale Infrared Spectroscopy and Chemical Imaging. *Chemical Reviews* **2017**, *117* (7), 5146-5173. DOI: 10.1021/acs.chemrev.6b00448.

(76) Mathurin, J.; Deniset-Besseau, A.; Bazin, D.; Dartois, E.; Wagner, M.; Dazzi, A. Photothermal AFM-IR spectroscopy and imaging: Status, challenges, and trends. *Journal of Applied Physics* **2022**, *131* (1), 010901. DOI: 10.1063/5.0063902 (acccessed 2023/04/13).

(77) Tseng, Y.-H.; Fan, Y.-C.; Chang, C.-T.; Lin, Y.-L.; Chang, C.-W.; Liao, C.-W.; Chen, J.-T. Photoinduced Alignment under Solvent Vapor Annealing (PA-SVA): Enhanced Ordering and Patterning in Block Copolymer Films. *ACS Applied Polymer Materials* **2022**, *4* (11), 8536-8542. DOI: 10.1021/acsapm.2c01453.

(78) Ramer, G.; Ruggeri, F. S.; Levin, A.; Knowles, T. P. J.; Centrone, A. Determination of Polypeptide Conformation with Nanoscale Resolution in Water. *ACS Nano* **2018**, *12* (7), 6612-6619. DOI: 10.1021/acsnano.8b01425.

(79) Ruggeri, F. S.; Habchi, J.; Chia, S.; Horne, R. I.; Vendruscolo, M.; Knowles, T. P. J. Infrared nanospectroscopy reveals the molecular interaction fingerprint of an aggregation inhibitor with single Aβ42 oligomers. *Nature Communications* **2021**, *12* (1), 688. DOI: 10.1038/s41467-020-20782-0.

(80) da Silva, P. M. M.; Camparotto, N. G.; Figueiredo Neves, T.; Mastelaro, V. R.; Nunes, B.; Siqueira Franco Picone, C.; Prediger, P. Instantaneous adsorption and synergic effect in simultaneous removal of complex dyes through nanocellulose/graphene oxide nanocomposites: Batch, fixed-bed experiments and mechanism. *Environmental Nanotechnology, Monitoring & Management* **2021**, *16*, 100584. DOI: https://doi.org/10.1016/j.enmm.2021.100584.

(81) Nguyen-Tri, P.; Nguyen, V. T.; Nguyen, T. A. Biological Activity and Nanostructuration of Fe3O4-Ag/High Density Polyethylene Nanocomposites. In *Journal of Composites Science*, 2019; Vol. 3.

(82) Almeida, R. M.; Guiton, T. A.; Pantano, C. G. Characterization of silica gels by infrared reflection spectroscopy. *Journal of Non-Crystalline Solids* **1990**, *121* (1), 193-197. DOI: https://doi.org/10.1016/0022-3093(90)90130-E.

(83) Osswald, J.; Fehr, K. T. FTIR spectroscopic study on liquid silica solutions and nanoscale particle size determination. *Journal of Materials Science* **2006**, *41* (5), 1335-1339. DOI: 10.1007/s10853-006-7327-8.

(84) De Cupere, V. M.; Gohy, J. F.; Jérome, R.; Rouxhet, P. G. Influence of substrate hydrophobicity on the adsorption of an amphiphilic diblock copolymer. *Journal of Colloid and Interface Science* **2004**, *271* (1), 60-68. DOI: https://doi.org/10.1016/j.jcis.2003.10.012.

(85) Albert, J. N. L.; Epps, T. H. Self-assembly of block copolymer thin films. *Materials Today* **2010**, *13* (6), 24-33. DOI: https://doi.org/10.1016/S1369-7021(10)70106-1.

(86) Cummins, C.; Lundy, R.; Walsh, J. J.; Ponsinet, V.; Fleury, G.; Morris, M. A. Enabling future nanomanufacturing through block copolymer self-assembly: A review. *Nano Today* **2020**, *35*, 100936. DOI: https://doi.org/10.1016/j.nantod.2020.100936.

(87) Majewski, P. W.; Yager, K. G. Rapid ordering of block copolymer thin films. *Journal of Physics: Condensed Matter* **2016**, *28* (40), 403002. DOI: 10.1088/0953-8984/28/40/403002.

(88) (1) Steinert, M.; Acker, J.; Oswald, S.; Wetzig, K. Study on the Mechanism of Silicon Etching in HNO3-Rich HF/HNO3 Mixtures. The Journal of Physical Chemistry C 2007, 111 (5), 2133-2140. DOI: 10.1021/jp066348j.

Chapter 6: Evaluation of novel poly(ionic liquid) block copolymer and homopolymer as electroactive polymer actuators.

***** This chapter is written in preparation for journal submission: Kayla Foley[1], Iwei Chu[2], Keisha B. Walters[1]. "Evaluation of novel poly(ionic liquid) block copolymer and homopolymer as electroactive polymer actuators."

[1] Ralph E. Martin Department of Chemical Engineering, University of Arkansas, Fayetteville, AR 72701, USA

[2] Institute for Imaging and Analytical Technologies, Mississippi State University, Starkville, MS 39759, USA

Abstract

A series of ionogels were prepared from a poly(ionic liquid) (PIL) block copolymer, poly[(2-dimethyl amino)ethyl methacrylate)]-*block*-poly[4-vinylbenzyl-3-butyl imidazolium bis(trifluoromethylsulfonyl)imide] (PDMAEMA-*b*-PVBBImTf_2N), and its corresponding homopolymer, poly[vinyl benzyl butyl imidazolium bis(trifluoromethane) sulfonyl imide] (PVBBImTf_2N), by combining the polymers with 1-butyl-3-methyl imidazolium tetrafluoroborate ($C_4C_1ImBF_4^-$) ionic liquid at weight percentages between 0 to 40 wt%. ATR-FTIR spectroscopy was performed to confirm successful incorporation of the ionic liquids into the PIL polymers. Shifts in the imidazolium ring IR modes and the BF_4^- and Tf_2N^- anion IR modes indicate a change in the electrostatic environment of immobilized and free ions depending on ionic liquid content. Thermal properties, including thermal stability and glass transition temperature, were determined through TGA and DSC analysis. Addition of the ionic liquid was found to increase the thermal stability of the PDMAEMA block in the block copolymer. The PVBBImTf_2N homopolymer showed a decrease in onset temperature with increasing ionic liquid content. DSC traces indicate

successful plasticization of the PDMAEMA-*b*-PVBBImTf_2N block copolymer and PVBBImTf_2N homopolymer ionogels through observed decreases in glass transition temperature with increasing ionic liquid content. Ion conductivity was increased from ~10^{-7} S/cm in the dry polymers to ~10^{-4} S/cm in the 40 wt% ionogels. AFM force curve analysis combined with a Derjaguin-Muller-Toporov (DMT) model indicated a reduction of Young's modulus with increasing ionic liquid content for both the homopolymer and block copolymer. The PDMAEMA-*b*-PVBBImTf_2N block copolymer and ionogels exhibited a spherical PDMAEMA particle morphology in a PIL-rich matrix, with a higher modulus observed for the spherical particles compared to the matrix. Gold leaf electrodes were successfully applied to dry polymer and 10 wt% ionogel films, and their electroactive actuator behavior was examined under an applied 4 V (DC). The PDMAEMA-*b*-PVBBImTf_2N block copolymer and 10 wt% ionogel exhibited micro-actuation abilities comparable to the literature and an in-house developed PVDF 40 wt% comparative control.

6.1. Introduction

Ionic electroactive polymers (IEAPs) are a class of polymer-electrolyte materials that exhibit a change in mechanical properties under an electrical potential stimulus[1-4]. Their electromechanical responsive behavior makes them excellent materials for soft robotics and flexible electronics applications, such as low voltage actuators and electromechanical sensors. A simple planar actuator may consist of an IEAP layer sandwiched between two electrode layers, typically noble metals (e.g., Au, Pt), forming an ionic polymer-metal layered composite (IPMC). The electromechanical behavior results from free cation migration and diffusion within the polymer IEAP layer in response to an applied voltage in the electrodes, which in turn induces localized swelling and bending stresses (Figure 6.1)[1, 3, 4]. This bending behavior depends on important electrolyte layer design parameters such as ion conductivity, glass transition

temperature, elastic modulus, and the plasticizing solvent. The most studied IPMC actuators are composed from anionic Nafion™ or Flemion™ hydrogels, which exhibit high ion conductivity (≥ 10^{-2} S/cm) and excellent mechanical properties (ca. 100 MPa modulus) for millimeter-scale actuation[1, 5-9]. However, their operation is limited to hydrated aqueous environments and low voltages (<1V) to maintain high ion conductivity and avoid electrolysis of water[10-12].

Ionogel-based IEAPs, where the actuating polymer matrix layer is swelled with an ionic liquid rather than water, are showing increasing interest in the ionic actuator community[11, 13]. In this case, the bending motion is a result of both ionic liquid cations and anions migrating under the electric potential (Figure 6.1). Ionogels exhibit many of the favorable properties of ionic liquids including high ion conductivity (10^{-3} to 10^{-2} S/cm), wide electrochemical windows (up to 7V), and practical nonvolatility at both high temperatures and low pressures. These properties make ionogels ideal materials for IEAP systems compared to current hydrogel-based IPMC layers as they do not suffer from water electrolysis limitations (~1 V) and the need to operate in aqueous environments. Currently, the majority of ionogel actuators are composed of ionic liquid swelled in commercial PVDF or Nafion polymers[14-16]. However, these polymers can suffer from IL leakage and compatibility issues which limits application potential and operational life [17, 18].

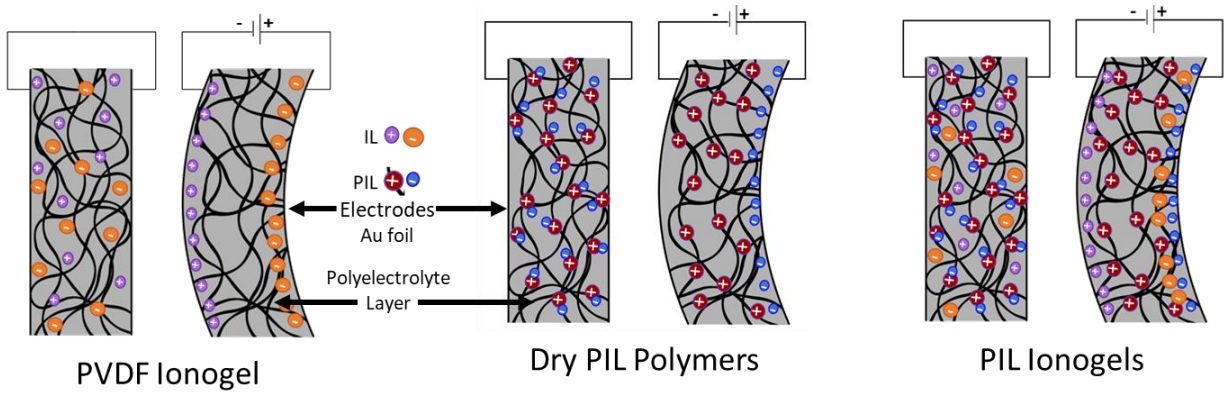

Figure 6.1 Ionic actuators consist of a solid polyelectrolyte layer sandwiched between two electrodes. The actuators exhibit a bending response under applied voltage as a result of free ion migration and interfacial swelling. For ionogels, both the ionic liquid cation and anion contribute to the actuation. Dry PIL actuators exhibit actuation behavior due to counterion mobility. Three types of polyelectrolyte layers were tested for actuation: (left) PVDF ionogel control containing 40 wt% $C_4C1ImBF_4$; (middle) dry PIL homopolymer and block copolymer with the mobile Tf_2N^- counterion; and (right) PIL-based ionogels with mobile imidazolium, BF_4^-, and Tf_2N^- ions.

In recent years, polymerized ionic liquids (PILs) have been evaluated as new candidates for the polymer matrix in actuator electrolyte layers to address these issues. PILs possess high compatibility with ionic liquids, resulting in gels with minimal IL leakage even at higher weight percentages and longer periods of operational stability[18]. They also are inherently conductive (~10^{-7}-10^{-5} S/cm) and have shown some limited micro-scale actuation in the dry state—without hydration or swelling with ILs—through single-ion migration[19, 20]. Ionogels formed from PIL systems with higher ionic conductivities (10^{-4}-10^{-2} S/cm) are expected to display suitable actuation on a millimeter scale, similar to their Nafion and PVDF counterparts. However, the use of PIL polymers in electroactive actuators is still in its infancy, with only a few examples of actuators developed involving dry[19, 20], hydrogel[21], and ionogel[22-25] PILs.

The vast majority of PIL actuator systems consist of ABA triblock copolymer[22-25] or penta-block copolymer[26] films. In these systems, a stiff, high-modulus block is copolymerized with the PIL block to improve overall actuator mechanical properties while maintaining reasonable ionic

conductivity with microphase separated conductive channels[22-25]. However, these studies were mainly limited to using styrenic polymer blocks. More investigation into non-styrenic PIL block copolymer chemistries is needed to expand the field of PIL-based IEAPs.

In the present effort, a novel PIL block copolymer and its corresponding homopolymer are evaluated as both dry and ionogel IEAP actuator layers. Specifically, an all-polyelectrolyte poly[(2-dimethyl amino)ethyl methacrylate)]-*block*-poly[4-vinyl-3-benzyl butyl imidazolium bis(trifluoromethylsulfonyl)imide], synthesized through Cu(0) mediated ATRP methods in the authors' previous work[27], and its homopolymer were combined with the ionic liquid 1-butyl-3-methyl-imidazolium tetrafluoroborate ($C_4C_1ImBF_4$) at weight percentages between 0 and 40 wt%. These PIL-based polymers and ionogels were characterized for important thermal, mechanical, and electrochemical polymer actuator design parameters. FTIR spectroscopy was performed to confirm successful formation of the ionogels and examine electrostatic interaction behavior of Tf_2N^- and BF_4^- anions with the imidazolium rings immobilized on the PIL polymer backbones and free in the ionic liquid phase. Thermal stability and glass transition temperature were evaluated with TGA and DSC, respectively. Addition of ionic liquid improved the stability of the PDMAEMA block in the block copolymer ionogels and a decrease in glass transition temperature was observed for all ionogel systems. EIS spectroscopy was utilized to measure room temperature ion conductivity of the dry polymers and ionogels, revealing similar or improved conductivity compared to other PIL-based actuator systems. PIL block copolymer and homopolymer morphology and nanomechanical properties were determined with AFM and force curve analysis. The novel PDMAEMA-*b*-PVBBImTf_2N block copolymer exhibited a PIL rich matrix-PDMAEMA particle morphology with greater Young's moduli compared to the porous PVBBImTf_2N homopolymer. IEAP actuators were developed using gold foil electrodes and their

actuation performance evaluated under an applied 4 V potential with comparison to a PVDF ionogel control. Micro-scale actuators were successfully developed from dry PIL homo- and block-copolymers and 10 wt% PDMAEMA-*b*-PVBBImTf_2N ionogel. The 10 wt% PVBBImTf_2N has displayed interesting compression behavior under electrical stimulus.

6.2. Materials and Methods

6.2.1. Materials

1-butylimidazole, 4-chloromethylsytrene, and lithium bis(trifluoromethylsulfonyl)imide (**$LiTf_2N$**) were purchased from TCI America. Acetonitrile, dimethylsulfoxide (**DMSO**), and ethyl acetate were purchased from VWR. Diethyl ether wase purchased from Beantown Chemical, and N,N-dimethylformamide (**DMF**) was purchased from Alfa Aesar. N,N,N',N",N"-Pentamethyl-diethylenetriamine (**PMDETA**), methyl 2-bromopropionate (**MBP**), copper (II) bromide (**$CuBr_2$**), 2-(dimethylamino) ethylmethacrylate (**DMAEMA**), tris(2-pyridylmethyl)amine (**TPMA**), hydrochloric acid, alpha-bromophenylacetic acid (**α-BPA**), and 1-butyl-3-methylimidazolium tetrafluoroborate (**$C_4C_1ImBF_4$**) were purchased from Sigma Aldrich. Isopropanol, sulfuric acid, hydrogen peroxide, and reagent alcohol were purchased from VWR Chemicals BDH. Gold leaf sheets (24K, ~100 nm thickness) were purchased from L.A. Gold Leaf Wholesaler. All purchased chemicals and materials were used as received.

6.2.2. Methods

6.2.2.1. Preparation of polymers and ionogels.

Both the poly[4-vinylbenzyl-3-butylimidazolium bis(trifluoromethylsulfonyl)imide] homopolymer (PVBBImTf_2N) and poly(2-(dimethylamino)ethyl methacrylate]-*block*-poly[4-vinylbenzyl-3-butylimidazolium bis(trifluoromethylsulfonyl)imide] (PDMAEMA-*b*-

PVBBIMTf$_2$N) block copolymer were synthesized through a Cu(0)-mediated atom-transfer radical polymerization (ATRP) as described previously[27]. Ionogels of PVBBImTf$_2$N and PDMAEMA-*b*-PVBBImTf$_2$N were formed through solution blending with an appropriate weight percentage of ionic liquid $C_4C_1ImBF_4$. As an example, the preparation of PVBBImTf$_2$N with 40 wt% $C_4C_1ImBF_4^-$ is described here. PVBBImTf$_2$N (0.06 g) was added to 2 mL of DMF and was allowed to dissolve fully overnight. Once dissolved, 0.04 g of $C_4C_1ImBF_4$ was added to the solution and gently shaken before allowing the solution to sit overnight. DMF was then evaporated in a vacuum oven at 65-70 °C for several days until the formed gel showed no DMF signatures in an ATR-FTIR spectra. Other PVBBImTf$_2$N ionogels with different weight percentages of ionic liquid and ionogels from PDMAEMA-*b*-PVBBImTf$_2$N were prepared in a similar manner. A poly(vinylidene fluoride) (PVDF) ionogel with 40 wt% IL was also prepared as a comparative control sample.

6.2.2.2. Attenuated Total Reflectance Fourier Transform Infrared Spectroscopy (ATR-FTIR).

ATR-FTIR spectra of the polymers and ionogels were collected using a ThermoFisher Scientific Nicolet iS50R spectrometer with an ATR diamond crystal accessory. Spectra were collected with 4 cm^{-1} resolution and a minimum of 256 scans over the 4000-400 cm^{-1} spectral range.

6.2.2.3. Thermal Characterization: Differential Scanning Calorimetry (DSC) and Thermogravimetric Analysis (TGA)

Differential scanning calorimetry (DSC) were performed for the polymers and ionogels on a TA Instruments Discovery DSC 250. Approximately ~15 mg of sample was added and sealed in DSC pans. In a typical DSC experiment, the sample was first cooled from room temperature to -70 °C at a cooling rate of 10 °C/min and then held at isothermally at -70° C for two minutes. The

sample was then heated to 150 °C at 10 °C/ minutes. Thermogravimetric analysis (TGA) was performed on a TA instruments Discovery 5500 TGA system. Thermal ramps on ~ 5-10 mg of sample were performed between 20 °C and 600 °C at a heating rate of 10 °C/ min. All thermal transitions were analyzed from the heating curve using TA Instruments Trios software.

6.2.2.4. Electrical Impedance Spectroscopy (EIS)

Ionic conductivity of the polymers and ionogels were determined through impedance measurements. A VSP-300 BioLogic potentiostat and a custom-made 2-electrode cell with stainless steel electrodes was used to collect EIS data. Impedance was measured in a frequency range of 7 MHz to 100 mHz. Ion conductivity was calculated from the measured bulk resistance (R_b) obtained from the Nyquist curve and polymer/gel cross-sectional area (A) and thickness (l) from the following relation:

$$\textbf{EQ 6-1}\ \sigma = \frac{l}{R_b A}$$

All EIS measurements were taken at room temperature (~20 °C) and ambient humidity.

6.2.2.5. Nanomechanical Atomic Force Microscopy (AFM)

AFM was used to determine the nanomechanical properties of the polymers and ionogels. Silicon wafers were first cleaned through sonication in reagent alcohol for 10 minutes followed by UV-Ozone treatment for 4 minutes (BioForce Nanociences UV/Ozone ProCleaner). The wafers were then added to a piranha solution (70:30 H_2SO_4:H_2O_2) for 45 minutes to remove any remaining organic material. The wafers were then removed from piranha solution and thoroughly rinsed with and stored in Millipore filtered water before further use. The polymers and their ionogels were dissolved in DMF and then drop-cast on the dried silicon wafers to form a thin film. DMF was removed by evaporation in a vacuum oven at 75 °C.

AFM measurements were performed with a Bruker Dimension Icon AFM using Peakforce QNM (quantitative nanomechanical property), a type of tapping mode offered by Bruker that maps several mechanical properties of probed samples, including modulus, dissipation, adhesion, and deformation, by measuring force-distance curves at each point on the sample surface. In this case, the Peakforce QNM mode was used to determine the reduced Young's modulus, of the polymer and ionogel films using the Derjaguin-Muller-Toporov (DMT) model[28, 29]:

$$\textbf{EQ 6-2}\ E^* = \frac{\left(\frac{3}{4}(F - F_{adh})\right)}{\sqrt{r(d-d_o)^3}}$$

where E^* is the reduced Young's modulus, F and F_{adh} are the applied tip and adhesion forces, $d-d_o$ is the sample deformation, and r is the tip radius. The reduced modulus is then related to the sample Young's modulus, E_s, by[29]:

$$\textbf{EQ 6-3}\ E^* = \left(\frac{1-\nu_s^2}{E_s} + \frac{1-\nu_{tip}}{E_{tip}}\right)^{-1}$$

where E_{tip} is the Young's modulus of the probe tip and ν_s and ν_{tip} are the Poisson ratios for the sample and probe tip, respectively. The Poisson ratio for each sample was assumed to be 0.5, which is in accordance with similar PIL systems[30]. The DMT model was selected over the Hertzian model as all sample moduli were found to be < 1 GPa and the DMT model accounts for adhesive interactions.[31] Due to the various range of Young's modulus observed, three Bruker probes with different nominal spring constants (k) were used to collect data: MPP-12120 probe (k=5 N/m) for the polymer (no IL added) samples, ScanAsyst - Air (k=0.4 N/m) for the 10-25 wt% ionogel samples, and SNL-C (k=0.32 N/m) for sample the 40 wt% ionogel samples. An absolute calibration method was employed to determine the probes' specific tip sensitivity (on sapphire), spring constant (on air), and tip radius (on titanium) before performing the Peakforce QNM study.

A 15 x 15 μm scan size was collected for each sample. The Young's modulus for each sample was determined from an average of at least 5 different spots within the DMT mapped image.

6.2.2.6. Preparation and Behavior of Ionic Electroactive Actuators

Poly(ionic liquids) polymer and corresponding ionogels were first formed into films through compression molding at 90 °C and 35 kN. The films were then sandwiched between two sheets of gold leaf and compression molded at 25 °C and 25 kN to ensure good contact. Actuation behavior of the polymers and ionogels were video recorded and tested under an applied voltage for at least 60 seconds using a DC power supply (Yescom DCP3010D). Initially, applied DC voltages of 1-3 V were attempted, but actuation only became visible on the camera system at 4 V. Actuator tip displacements were measured from the video using the motion-tracking software *Tracker 6.0.10* (Open Source Physics, https://physlets.org/tracker/).

Similar to the work of Margaretta et al., a conductive nanocomposite (CNC) layer was not included in actuator development[25]. Adding the CNC layer typically involves repeatedly dipping the ionogel film into an aqueous solution of poly(allyl amine) hydrochloride and gold nanoparticles through a layer-by-layer assembly process. To avoid trace water in the polymers (particularly the hydrophilic PDMAEMA block), leaching of the water miscible $C_4C_1ImBF_4$ ionic liquid, or degradation of the hydrolysis prone BF_4^- anion, the CNC layer was not added prior to applying the gold leaf electrodes. Initially, it was attempted to develop actuator films from the ionogels by first compression molding the ionogels into films and then applying gold leaf to those films. However, the ionogels for both the homopolymer and block copolymer with greater than 10 wt% IL would not maintain a film shape long enough to apply the gold leaf, instead reverting into a ball shape after a few seconds (Figure E.19). This behavior was attributed to a combination of low modulus and the adhesive nature of the PIL-based ionogels. 10 wt% gels were easier to handle, but they

exhibited significant adherence to the Teflon sheeting used in the compression molding process which led to deformed film shapes. This adhesive behavior for the 10 wt% IL and 25 wt% PDMAEMA-*b*-PVBBImTf_2N ionogels may be observed in the processing videos in the supplemental information (see Video S1-S2) and the measured low modulus values are discussed later on in this work.

6.3. Results and Discussion

6.3.1. Synthesis and chemical characterization of PIL-based polymer and ionogel electrolytes

In this work, a series of PIL-based homopolymer and block copolymer ionogels were developed to form the solid polymer electrolyte layer for the ionic actuators. The PIL-based solid polyelectrolyte layers were formed from the homopolymer PIL poly[4-vinylbenzyl-3-butyl imidazolium bis(trifluoromethylsulfonyl)imide] (PVBBImTf_2N) and its block copolymer with poly[2-(dimethylamino) ethyl methacrylate] (PDMAEMA-*b*-PVBBImTf_2N) (Figure 6.2). These polymers were synthesized through Cu(0)-mediated atom transfer radical polymerization (ATRP), as described previously[27]. Table 6.1 summarizes the degree of polymerization and molecular weight of the synthesized PIL-based polymers.

Table 6.1 Cu(0) ATRP polymer characterization results including conversion, degree of polymerization (DP), number average molecular weight (M_n), and polydispersity (PDI) determined from the authors' previous work Foley et al. [27]

Polymer	Conversion, χ	DP^{theo}	M_n^{theo}	DP^{NMR}	M_n^{NMR} [g/mol]	M_n^{GPC} [g/mol]	PDI
PDMAEMA MI	70%	35	5,531	45	7,074	9,323	1.41
PDMAEMA-*b*-PVBBImTf_2N	67%	67	42,011	67	42,014	N/A	N/A
PVBBImTf_2N	76%	228	118,788	228	N/A	N/A	N/A

(a) Conversion determined by NMR; (b) degree of polymerization of the PIL unit ; (c) theoretically determined based on [M]:[I] concentrations

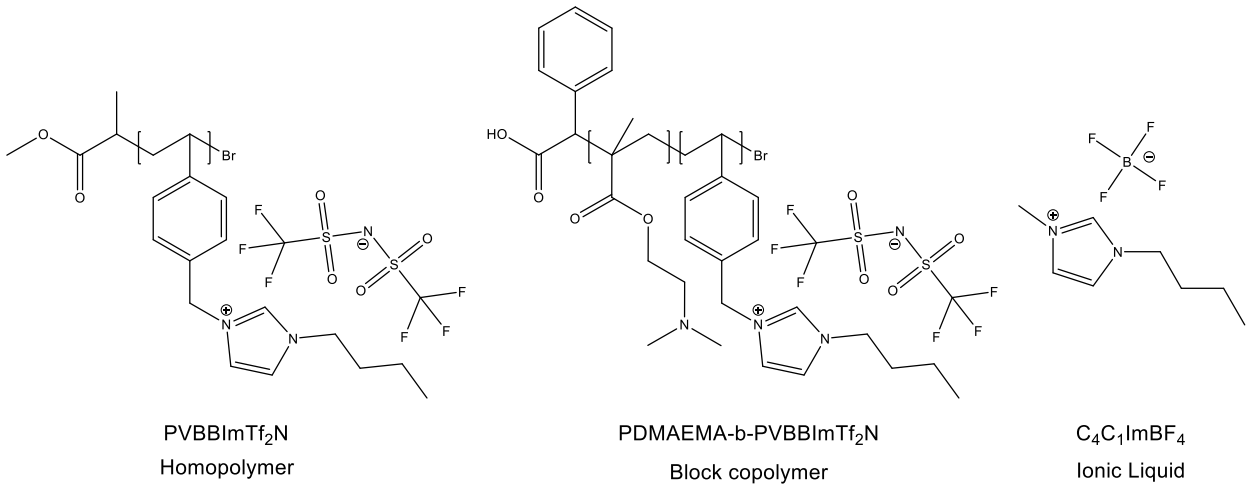

Figure 6.2 Chemical structures for the PIL homopolymer PVBBImTf_2N, PIL block copolymer PDMAEMA-*b*-PVBBImTf_2N, and the ionic liquid $C_4C_1ImBF_4$.

PVBBImTf_2N and PDMAEMA-*b*-PVBBImTf_2N were then combined with the ionic liquid 1-butyl-3-methylimidazolium tetrafluoroborate ($C_4C_1ImBF_4$) through solution blending to form the ionogels. $C_4C_1ImBF_4$ was selected as this ionic liquid has a low melting point (-71 °C), a wide electrochemical window (4.6-6 V), and good ionic conductivity ($1.7x10^{-3}$ S/cm) [32-34]. Ionogels were prepared with weight percentages between 10 and 40 wt% $C_4C_1ImBF_4$.

ATR-FTIR characterization was performed to confirm the incorporation of the IL into PVBBImTf_2N and PDMAEMA-*b*-PVBBImTf_2N and observe changes in electrostatic bonding in the ionogels. Figure 6.3a shows the ATR-FTIR spectra for the dry polymers and their ionogels at >2200 cm^{-1} wavenumbers. In this region, the imidazolium ring str modes (3150-3000 cm^{-1}) [35, 36], polymer and alkyl chain methyl and methylene C-H str (2965-2875 cm^{-1}) [37], and the typical polymer backbone symmetrical methylene C-H str 2850 cm^{-1} are clearly observed[37]. Below 1900 cm^{-1} (Figure 6.3b), the imidazolium ring C=C/C=N str modes are observed at ~1570 cm^{-1} [35, 36] and a set of bands attributed to the free IL imidazolium ring bending modes emerge at ~ 850 cm^{-1} and

~ 755 cm^{-1} [36, 38] in the ionogels. The presence of both the Tf_2N^- and BF_4^- anions are also noted in the ionogels. Specifically, the BF_4^- anion modes are observed as a set of three intense peaks at ~1050 cm^{-1}, 1035 cm^{-1}, and 1019 cm^{-1}, which overlaps with the 1050cm^{-1} (C-S str) Tf_2N^- anion peak. These peaks are slightly higher and display a different band shape from the pure IL BF_4^- modes at 1045, 1033, and 1016 cm^{-1}, but they correspond well with the literature[38, 39]. While the triplet peaks for BF_4^- are sensitive to cation-anion interactions and may show corresponding changes in splitting and band shape[38], it is unclear if the band shape change observed in the ionogels is a result of IR overlap with the Tf_2N^- modes or a change in electrostatic interactions. The Tf_2N^- anion also displays a series of intense bands related to the S=O str modes (~1346 cm^{-1}, ~1330 cm^{-1}, ~1178 cm^{-1}), SNS bending (~612 cm^{-1}) and CF_3 bending (~569 cm^{-1}) in the ~1400-500 cm^{-1} region[35, 36, 40, 41]. Some of the Tf_2N^- modes, particularly the S=O str modes, are slightly upshifted in the ionogels compared to the dry PIL polymers, suggesting a change in the electrostatic interactions of the Tf_2N^- anion. Overall, the combined observation of both PIL and IL bands in the ionogel samples indicate that the IL was successfully blended into the PIL homo- and block- copolymers.

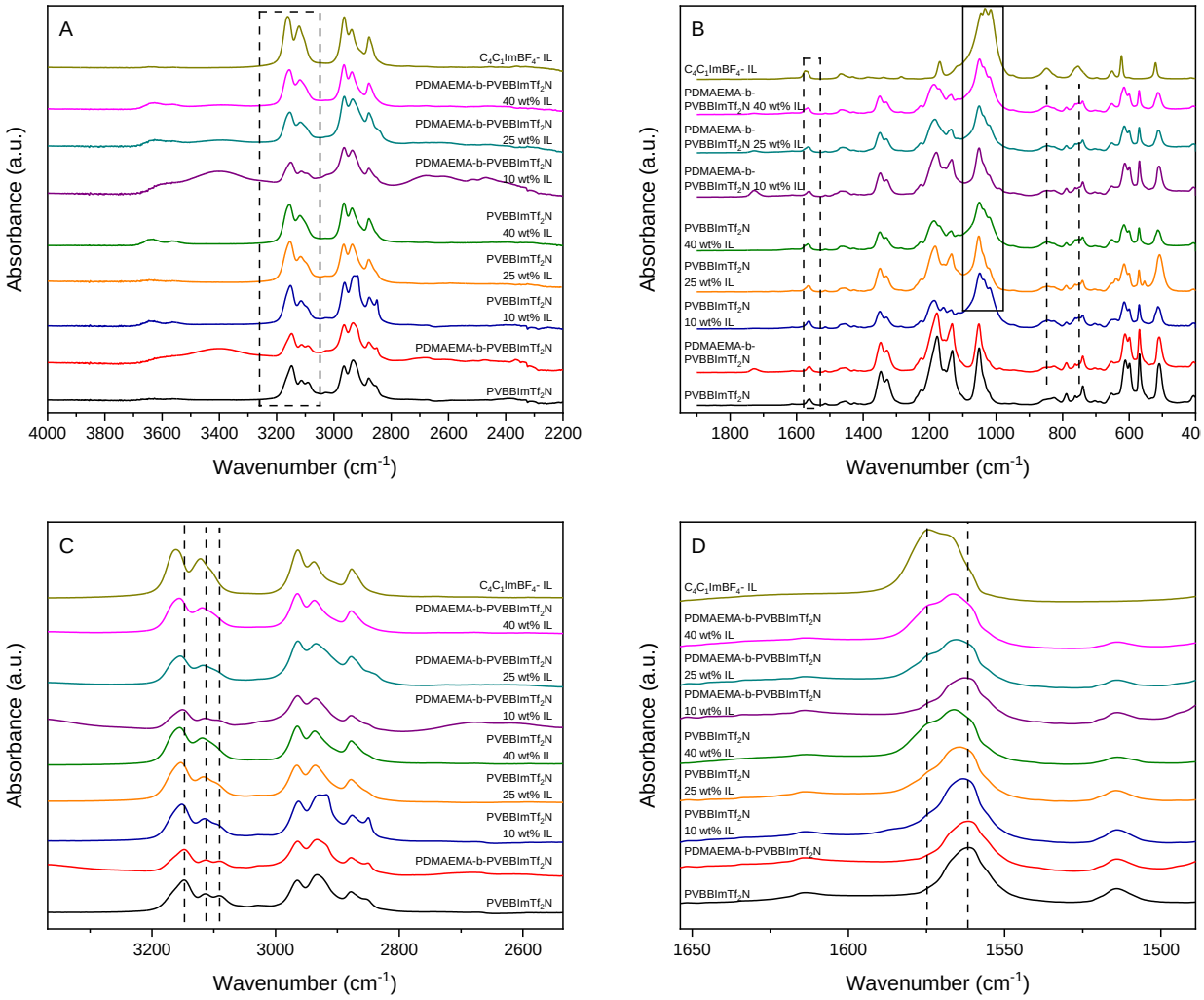

Figure 6.3 ATR-FTIR spectra for PVBBImTf$_2$N, PDMAEMA-*b*-PVBBImTf$_2$N, C$_4$C$_1$ImBF$_4$ IL and the ionogels in the IR regions (a) >2200 cm^{-1} and (b) <1900 cm^{-1}. (c) shows the imidazolium ring C$_2$-H and C$_{4,5}$-H str region marked by the dotted box in (a). The dotted box in (b) indicates the imidazolium ring C=C/C=N str and is shown expanded in (d). Dotted lines in (b) mark the imidazolium bending modes at ~ 850 and ~755 cm^{-1}. The solid box in (b) marks the BF4$^-$ triplet modes.

A closer look at the imidazolium ring C$_2$-H/C$_{4,5}$-H str and C=C/C=N str modes reveals interesting shifts and peak overlap upon addition of the ionic liquid. It is well known that the imidazolium ring IR modes are sensitive to cation-anion interactions and may display different wavenumbers depending on the anion type and strength of interaction[35, 36, 41, 42]. Figure 6.3c shows the 3150-3000 cm^{-1} region where the imidazolium ring C$_2$-H and C$_{4,5}$-H str modes present with

the $C_{4,5}$-H str typically attributed to one peak at higher wavenumbers and the C_2-H str mode to several peaks at lower wavenumbers[36, 42]. In both the dry homo- and block copolymer, the imidazolium ring C_2-H and $C_{4,5}$-H str modes are shown through three distinct peaks located at 3147 cm^{-1}, 3113 cm^{-1}, and 3090 cm^{-1} as reported previously[27]. In contrast, the pure $C_4C_1ImBF_4$ IL displays two distinct peaks at 3162 and 3120 cm^{-1} and a shoulder at 3104 cm^{-1}.The ionogels show intermediate wavenumbers for the imidazolium ring C-H stretching modes at ~3155 cm^{-1} ($C_{4,5}$-H str), 3117 cm^{-1} (C_2-H str), and 3090 cm^{-1} (C_2-H str) where the ~3090 cm^{-1} peak becomes less distinct with increasing IL weight percentage.

Similar behavior is also observed for the imidazolium ring C=C/C=N stretch modes below 1900 cm^{-1} (Figure 6.3d). A single peak at ~1562 cm^{-1} in PVBBImTf_2N and PDMAEMA-*b*-PVBBImTf_2N is observed. Upon addition of ionic liquid, this peak increases in wavenumber with increasing IL content to ~1566 cm^{-1} in the 40 wt% ionogels. A shoulder at ~1575 cm^{-1} also emerges and increases in intensity with increasing IL content. At higher IL weight percentages, the spectra more closely resemble the spectra for the pure $C_4C_1ImBF_4$ IL, with a doublet at 1575 and 1569 cm^{-1} and a possible shoulder noted at 1561 cm^{-1}. The intermediate peak shifts observed for the imidazolium ring C_2-H/$C_{4,5}$-H str and C=C/C=N str modes in the ionogel indicates that the electrostatic environment of the imidazolium ring is different from the dry PIL polymers and the pure $C_4C_1ImBF_4$ IL, suggesting that the BF_4^- and Tf_2N^- anions likely interact with both the pendant imidazolium ring on the polymer and with the free imidazolium ring to some extent. This is further corroborated by the shifts in the Tf_2N^- and BF_4^- modes observed above. Also, the extent of these interaction shifts is observed to be dependent on the amount of ionic liquid added.

6.3.2. Thermal Analysis of PIL Polymers and Ionogels

Characterization of the thermal properties of solid polymer electrolytes is important to inform electrolyte design as it provides insight into polymer chain dynamics and plasticization effects resulting in increased ion conductivity, and it also informs the thermal operating range of the polymer and ionogel based actuators[18, 43]. The thermal properties of the PIL-based polymers and ionogels were analyzed through TGA and DSC. Table 6.2 summarizes the glass transition temperatures (T_g), decomposition temperatures, and other thermal transitions for the polymers and ionogels.

Table 6.2 Thermal properties of the PVBBImTf_2N and PDMAEMA-*b*-PVBBImTf_2N and their ionogels. Glass transition temperatures, T_g, were determined from the second DSC heating curve, and decomposition temperatures, T_d, were determined by TGA.

Type	Sample	T_g (˚C)	T_{onset}^{1st} (˚C)	wt% loss 1st	T_{onset}^{2nd} (˚C)	wt% loss 2nd
Polymer	PVBBImTf_2N	0[b]	379[f], 337[g]	88.40%	--	--
	PDMAEMA-*b*-PVBBImTf_2N	-5[b], 134[b]	218[f], 202[g]	8.10%	383	73.80%
	PDMAEMA	-6[a]	229[e,f], 224[g]	51.20%	394	31%
Ionogels	PVBBImTf_2N 10 wt% IL	-25[b], -10[b]	337[f], 338[g]	37.30%	435	45.40%
	PVBBImTf_2N 25 wt% IL	14,-40[b], -23[c]	337[f], 331[g]	25.00%	430	65.60%
	PVBBImTf_2N 40 wt% IL	9, -52[b], -23[c]	332[f], 326[g]	22.00%	414	70.40%
	PDMAEMA-*b*-PVBBImTf_2N 10 wt%	-31[b]	257[f]	16.33%	390	73.78%
	PDMAEMA-*b*-PVBBImTf_2N 25 wt%	ND	277[f]	29.20%	425	60.50%
	PDMAEMA-*b*-PVBBImTf_2N 40 wt%	ND	322[f]	26.30%	424	62.10%
Ionic Liquid	$C_4C_1ImBF_4$	ND	423	99.80%	--	--
Literature	PVBBImTf_2N [44]	3				
	PVEBImTf_2N [22, 45]	29	343-345			
	PVHBImTf_2N [45]		345			
	PVBBImBF_4 [44]	78	315		437	
	PDMAEMA [46, 47]	19	290		400	
	PDMAEMA HCl H_2O[46] or H_2O[48]		230		300	
	$C_4C_1ImBF_4$ [49, 50]		360-437			

a) uncertain thermal transition; b) T_g midpoint analysis; c) peak minimum; ND) not determined; e) Small previous decomposition at 38 °C (11.10 wt%) attributed to water loss; f) onset determined by TGA; g) onset determined by DTG

The TGA and DTG traces for the PVBBImTf_2N polymer and its ionogels are shown in Figure 6.4a and Figure 6.4b. The dry PVBBImTf_2N homopolymer shows high stability with a single-step decomposition in the TGA trace with an onset temperature of ~379 °C (~337 °C by DTG), which is consistent with other alkyl benzyl imidazolium based PILs[22, 45]. The corresponding DTG trace for PVBBImTf_2N suggests four ranges of decomposition starting at 337 °C, 408 °C, 425 °C, and 470 °C. The decomposition method for alkyl benzyl imidazolium based PILs with fluorinated anions is believed to follow first decomposition of the styrenic backbone followed by degradation of the ionic liquid group[51]. The first DTG decomposition onset at 337 °C is slightly higher though in reasonable agreement with the decomposition onset for polystyrene at ~330 °C [25, 52]. The second DTG degradation onset beginning at 408 °C is attributed to the start of the ionic liquid group thermal decomposition and is consistent with the onset decomposition for the $C_4C_1Im Tf_2N$ ionic liquid[53-55]. $C_4C_1Im Tf_2N$ is believed to decompose mainly through degradation of the Tf_2N anion and SO_2 gas release[50, 56].

Addition of the ionic liquid to PVBBImTf_2N, resulted in two decompositions steps in the TGA traces. The first decomposition onset temperature ranged between 337-332 °C (338-326 °C by DTG) and the second decomposition between 414-435 °C for different IL weight percentages. The first decomposition step in the ionogels is lower than that observed in the dry PVBBImTf_2N polymer and in closer agreement with the ~330 °C polystyrene degradation onset temperature, while the second decomposition step moves to higher temperatures.

This latter step likely combines contributions from both the pendant imidazolium Tf_2N group and the free $C_4C_1ImBF_4$ ionic liquid as the onset temperatures match well with those reported for the $C_4C_1ImBF_4$ and $C_4C_1Im Tf_2N$ ionic liquids[56]. This suggests a possible cleavage of the IL group from the styrenic backbone, forming polystyrene and free IL[56,57]. Comparison of the DTG traces

for the dry PVBBImTf_2N polymer and its ionogel show an increasing separation of the styrenic backbone and IL group decomposition peaks with increasing $C_4C_1ImBF_4$ weight percentage, which possibly supports the loss of the immobilized imidazolium ring into the free IL phase. The pure $C_4C_1ImBF_4$ IL exhibits only one decomposition step with an onset temperature of 423 °C.

TGA and DTG traces for the PDMAEMA-*b*-PVBBImTf_2N polymer and its ionogels are shown in Figure 6.4c and Figure 6.4d. The dry PDMAEMA-*b*-PVBBImTf_2N block copolymer shows two main decomposition steps at 218 °C and 383 °C proceeded by a small initial decomposition attributed to absorbed water loss below 100 °C (~2 wt%). The first decomposition step is comparable with the 1st decomposition step for PDMAEMA which is typically attributed to loss of the pendant amine group[46,47]. The second decomposition is likely a combination of the PDMAEMA backbone and the PIL group thermal decomposition as described above. This is supported through comparison of the DTG trace for PVBBImTf_2N and PDMAEMA-*b*-PVBBImTf_2N, which indicates a similar decomposition step for the PIL group with an additional peak at ~414 °C likely related to the PDMAEMA backbone decomposition.

Adding ionic liquid to the block copolymer resulted in a 39 to 93 °C increase in the onset temperature of the 1st decomposition step. This is likely a result of the PDMAEMA block associating with the ionic liquid. The thermal stability of the PDMAEMA block has been previously found to increase when complexed with fluorinated anions such as BF_4^- and Tf_2N^-[46]. The second decomposition step also increased from 383 °C to ~425 °C, as seen above for the PVBBImTf_2N ionogels. The corresponding DTG traces for the PDMAEMA-*b*-PVBBImTf_2N ionogels show a more complex overlapping of decomposition peaks from the PDMAEMA backbone, polystyrene backbone, PIL group, and free ionic liquid. However, the larger decomposition peak associated with the ionic liquid group decomposition appears at ~445 °C in

both the PVBBImTf_2N and PDMAEMA-*b*-PVBBImTf_2N ionogels, suggesting a similar mechanism of decomposition for the PIL group in the block copolymer as was observed for the homopolymer PIL. Overall, the PVBBImTf_2N and its ionogels were found to have excellent thermal stability up to ~ 330 °C, though addition of the $C_4C_1ImBF_4^-$ ionic liquid possibly leads to loss of the immobilized imidazolium ring to the free ionic liquid phase and degradation of the styrenic backbone at earlier temperatures. The addition of the ionic liquid improves the overall thermal stability of the PDMAEMA-*b*-PVBBImTf_2N ionogels, increasing the initial onset temperature by ~60 to 100 °C at 25 and 40 wt% ionic liquid.

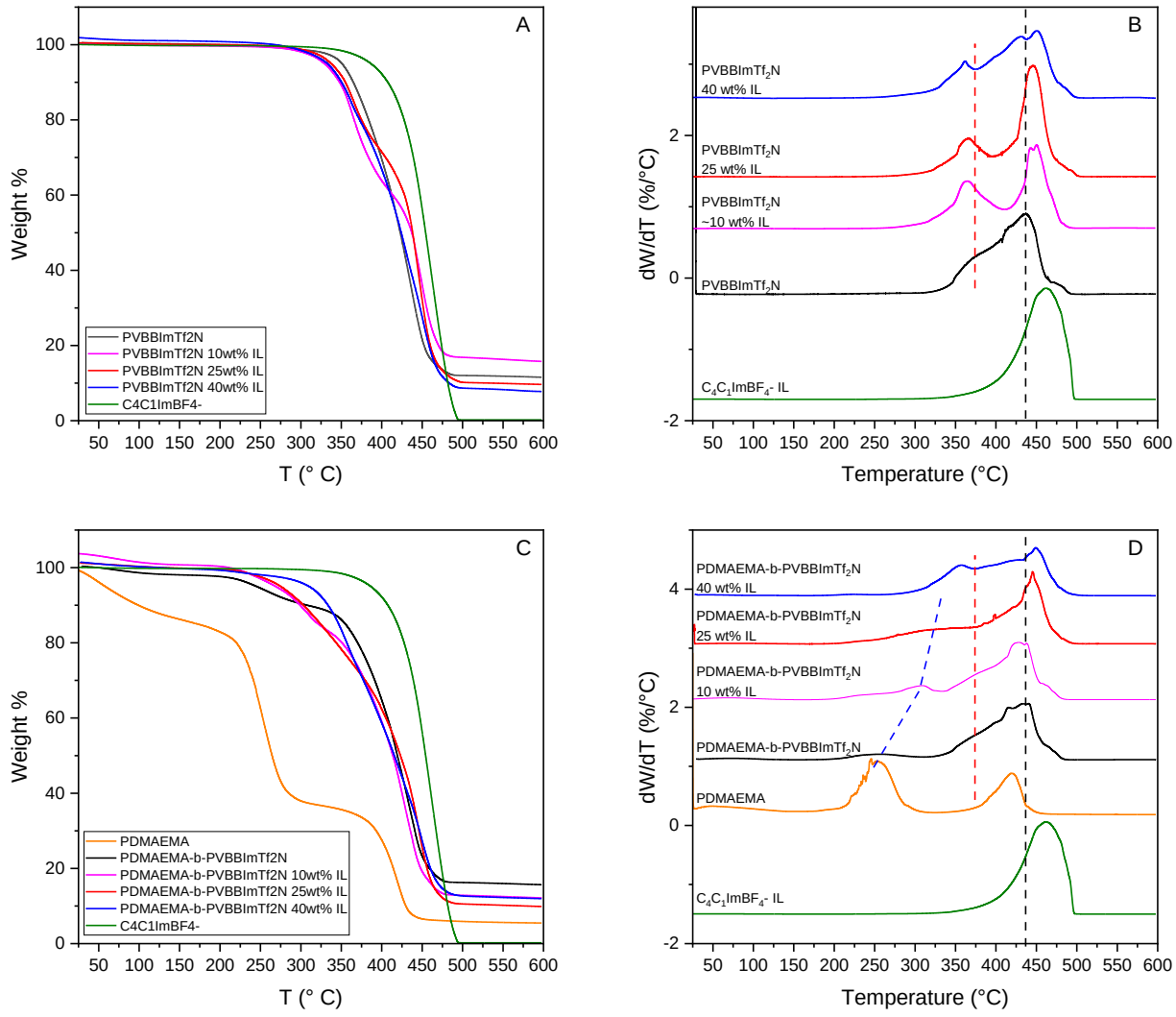

Figure 6.4 TGA and their corresponding DTG traces for the (a and b) PVBBImTf$_2$N and (c and d) PDMAEMA-*b*-PVBBImTf$_2$N polymers and ionogels. The dotted lines in (b and d) correspond to the PDMAEMA pendent group (blue), polystyrene backbone (red), and imidazolium Tf2N/BF4 IL group (black) decomposition peaks.

The DSC profiles for the PVBBImTf$_2$N and PDMAEMA-*b*-PVBBImTf$_2$N dry polymers are shown as the black trace in Figure 6.5a and Figure 6.5b, respectively. The T_g for the dry PVBBImTf$_2$N was ~ 0 °C which corresponds well to the 3 °C T_g obtained by Tang et al. for an ATRP synthesized PVBBImTf$_2$N polymer[44]. The PDMAEMA-*b*-PVBBImTf$_2$N block copolymer displayed two glass transition temperatures with a stronger T_g at ~ -5 °C and a weaker T_g at ~134

°C. The former is attributed to the PIL block, which was likely plasticized by the PDMAEMA block as the macroinitiator DSC trace shows a weak thermal transition at ~ -6 °C. The latter T_g for the block copolymer has a value similar to a small T_g observed at ~136 ° C in the PDMAEMA macroinitiator trace. It is likely that this smaller T_g in the block copolymer is related to a smaller portion of protonated PDMAEMA associated with either HCl or sulfate residue from the PDMAEMA synthesis and purification. The glass transition temperature of PDMAEMA has been found to be dependent on associated anions and can vary significantly from 20 to 160° C as observed by Hunley et al. for PDMAEMA protonated and complexed with various acids[46].

Figure 6.5a shows the DSC traces for the PVBBImTf_2N polymer and its corresponding ionogels. The PVBBImTf_2N-based ionogel showed a decrease in T_g upon addition of ~ 10 wt% IL to -25 °C as a result of plasticization from the IL. A possibly weak glass transition temperature at ~ -10° C is also observed (Figure E.6). At 25 and 40 wt% IL, the PVBBImTf_2N ionogels showed more clearly two thermal transitions (see supporting Figure E.3-Figure E.4 for expanded visualization). The small higher temperature transition appears to be a weak glass transition temperature with relaxation effects and is located at ~14 °C (25 wt% IL) and ~9 °C (40 wt% IL). This may be associated with regions of partial ion exchange of Tf_2N^- with BF_4^- on the polymer chains as PVBBImBF_4^- has been reported to have much higher T_g values of ~80-85 °C [44, 58]. It is unclear if the lower temperature transition is a glass transition with relaxation or a melting peak. The pure ionic liquid $C_4C_1ImBF_4$ has been reported to have a thermal transition at ca. -85 °C with a similarly shaped trace with some controversy as to its transition type and exact temperature as well[49, 55, 59-62]. Glass transition temperature midpoint analysis of the peaks yields glass transition temperatures of -40 °C (25 wt% IL) and -52 °C (40 wt% IL) while the temperature of the peak minimums was at -23 °C for both IL weight percentages. In either case, the lower thermal

transitions compared to the dry PVBBImTf$_2$N and 10 wt% PVBBImTf$_2$N ionogel indicate further plasticization of the ionogels with increasing ionic liquid content. The PDMAEMA-*b*-PVBBImTf$_2$N 10 wt% ionogel showed a decrease in glass transition temperature to -31 °C, indicating plasticization of the block copolymer on ionic liquid addition. Interestingly, no thermal transitions were observed for the PDMAEMA-*b*-PVBBImTf$_2$N based ionogels at 25 and 40 wt% IL content and showed a similar trace to the pure $C_4C_1ImBF_4$ ionic liquid (Figure 6.5b). As the melting point and glass transition temperature for the ionic liquid has been generally reported to range between -70 °C and -90 °C[49, 59, 60], it is expected that the block copolymer with higher ionic liquid contents was also plasticized with a thermal transition outside the temperature range of the DSC instrumentation.

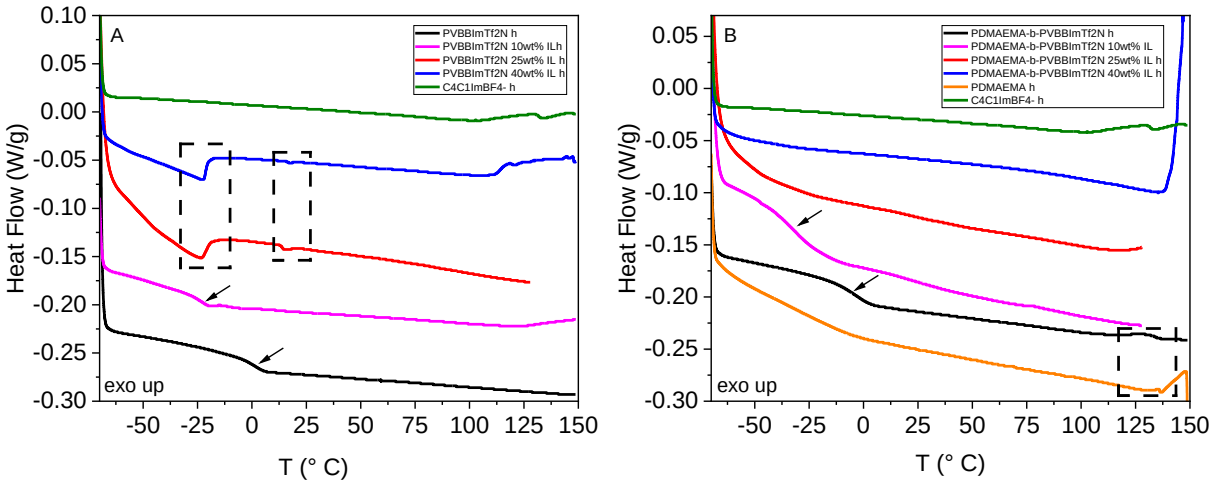

Figure 6.5 DSC traces (exo up) for (a) the PVBBImTf$_2$N-ionogels and (b) PDMAEMA-*b*-PVBBImTf$_2$N- ionogels. Arrows mark the glass transition temperatures, Tg. Supplemental Figures S1-S3 show the expanded views of the regions marked by the dotted boxes.

6.3.3. Ion Conductivity

Ionic material performance for electrochemical applications is highly dependent on the ionic conductivity of the electrolyte layer. In ionic-based electromechanical systems, the actuation

motion is dependent on the mobility of free ions in the electrolyte layer and the subsequent swelling behavior at the polymer-electrode interface[1, 11]. Ionic actuators based on commercially available Nafion and PVDF hydrogels and ionogels generally have ion conductivities in the 10^{-4} to 10^{-2} S/cm range and are considered the benchmark of comparison for many ionic actuator-based systems[14, 15, 63, 64].

Table 6.3 shows the resulting ion conductivity, σ, from electrical impedance measurements for each polymer and their ionogel as well as several literature comparisons to other PIL ionic actuator systems. Both the dry PVBBImTf_2N and PDMAEMA-*b*-PVBBImTf_2N polymers had room temperature ion conductivities on the order of 10^{-7} S/cm, which is representative for many dry PIL polymers and copolymers systems that typically range between 10^{-10} to 10^{-5} S/cm depending on ionic composition and morphology.[65-69] While the midrange ~10^{-7} S/cm is too low for millimeter-scale actuation, several PIL systems have achieved micrometer-scale actuation with ion conductivities in the range of 10^{-5} to 10^{-8} S/cm)[19, 20]. These results suggest that the PDMAEMA-*b*-PVBBImTf_2N block copolymer and PVBBImTf_2N have ion conductivities adequate for at least micro-actuation behavior without any added ionic liquid.

Table 6.3 Ion conductivities, σ (S/cm), and Young's Modulus, E (MPa) for the PVBBImTf_2N and PDMAEMA-*b*-PVBBImTf_2N polymers and ionogels and similar PIL block copolymer and crosslinked literature examples.

Type	Sample	σ (S/cm)	E (MPa)[c]	Ref.
Polymer	PVBBImTf_2N	4.4 x10^{-7} (± 7.2 x10^{-9}), ~20 °C	46.5 (± 1.2)	This work
	PDMAEMA-*b*-PVBBImTf_2N	7.9 x10^{-7} (± 4.8 x10^{-8}), ~20 °C	209.4 (± 4.8)[a], 295.0 (± 18.4)[b]	This work
	PDMAEMA	ND	214.2 (± 39.8)	This work
Ionogel	PVBBImTf_2N 10 wt% IL	3.5 x10^{-6} (± 2.4 x10^{-8}), ~20 °C	132.8 (±4.6)	This work
	PVBBImTf_2N 25 wt% IL	2.7 x10^{-5} (± 5.6 x 10^{-7}), ~20 °C	10.9 (±0.3)	This work
	PVBBImTf_2N 40 wt% IL	8.0 x10^{-4} (± 3.2 x10^{-6}), ~20 °C	1.3 (±0.02)	This work
	PDMAEMA-*b*-PVBBImTf_2N 10 wt%	3.4 x10^{-6} (± 8.2 x10^{-8}), ~20 ° C	148.2 (±11.1)[a]; 375.6 (±90.0)[b]	This work
	PDMAEMA-*b*-PVBBImTf_2N 25 wt%	9.5 x10^{-5} (± 4.7 x10^{-7}), ~20 °C	12.3 (±0.8)[a], 43.5 (±5.0)[b]	This work
	PDMAEMA-*b*-PVBBImTf_2N 40 wt%	2.3 x10^{-4} (± 1.9 x10^{-6}), ~20 °C	1.0 (±0.2)[a], 9.4 (±0.6)[b]	This work
	PVDF 40 wt% IL	2.3 x10^{-5} (± 1.3 x10^{-7}), ~20 °C	~100[d]	This work
Ionic Liquid	IL: $C_4C_1ImBF_4$	1.7 x 10^{-3}, ~20 °C	--	Palm et al. 2012[34]
Literature				
Polymer	Poly(Sty-*b*-PVBEImTf_2N-*b*-Sty)	~2 x10^{-7}, ~40 °C	~100[e] (45 °C) ~1000[e] (20 °C)	Green et al. 2012[22]
	Poly(Sty_{35}-*b*-($PVBMImTf_2N)_{80}$-*b*-Sty_{35})	~10^{-11} , ~20 °C	~500[e]	Jangu et al. 2014[24]
	Poly(Sty-b[$PVBMImTf_2N_{52}$-co-$DEGMEMA_{48}$]-*b*-Sty)	~10^{-11} , ~20 °C	~1000[e]	Jangu et al. 2015[23]
	Poly(C_3C_1Im-MA)(Tf_2N-)	10^{-6} to 10^{-7}, ~25 °C	~0.17-0.28[f]	Kokubo et al. 2018[20]
	Poly(Tf_2N-MA)(N_{0222})	10-6 to 10-7 , ~25 °C	~0.15-0.21[f]	Kokubo et al. 2018[20]
Ionogel	Poly(Sty-*b*-PVBEImTf_2N-*b*-Sty) + 20 wt% C_2C_1ImTfO	3.0 x10^{-5}, ~20 °C		Green et al. 2012[22]

Table 6.3 Cont.

Type	Sample	σ (S/cm)	E (MPa)[c]	Ref.
Ionogel	Poly(Sty-*b*-PVBEImTf$_2$N-*b*-Sty) + 40 wt% C_2C_1ImTfO	9.0 x10^{-4}, ~20 °C		Green et al. 2012[22]
	Poly(Sty-*b*-AA(MIm)-*b*-Sty) + 30 wt% C_2C_1ImTfO	~10^{-4}, ~80 °C	~200-300[d]	Margaretta et al. 2016[25]
	Poly(t-butyl Sty-*b*-Sty-*b*-isoprene-*b*-t-butyl Sty) Sulfonated Imidazolium cation		400[d]	Gao (2012) [26]
	Nafion hydrogel	1.1x10^{-1}, ~30 °C	120	Akle et al. [70]
	PVDF-C_2C_1ImBF$_4$ (PVDF/IL 3:1)	8 x10^{-4} , 20 °C	447[g]	Guo 2019[15]

(a) Young's modulus of the PDMAEMA-*b*-PVBBImTf$_2$N matrix, (b) Young's modulus of the PDMAEMA-*b*-PVBBImTf$_2$N stiff spheres, (c) Young's modulus determined by AFM DMT fitting, (d) estimated modulus based on the neat PVDF 1.19 GPa from the technical sheet and the 90% decrease in modulus observed by Correia et al. for PVDF with 40 wt% IL[13], (e) Storage modulus determined by dynamic mechanical analysis, (f) Young's modulus determined by tensile testing, (g) Young's modulus determined by nanoindentation.

In the ionogel systems, the ionic conductivity was found to significantly increase with even small amounts of ionic liquid content. In particular, the ionic conductivity increased by an order of magnitude upon the addition of only 10 wt% (~10^{-6} S/cm) ionic liquid with further increases in ion conductivity for 25 wt% (~10^{-5} S/cm) and 40 wt% (~10^{-4} S/cm) for the PVBBImTf_2N based ionogels. PDMAEMA-*b*-PVBBImTf_2N-based ionogels also had similar ion conductivities, increasing from 3.4x10^{-6} S/cm (10 wt%) to 8 x10^{-4} S/cm (40 wt%). The ion conductivity increase corresponds well with the decrease in glass transition temperature observed for the ionogels with increasing IL content as expected from increased plasticization. These room temperature conductivities are comparable or even better than several PIL ionic actuator systems at similar IL weight percentages. For instance, Green et al. produced several styrenic based PIL block copolymers with room temperature ion conductivities of 10^{-5} and 10^{-4} S/cm at 20 wt% IL and 40 wt% IL, respectively[22]. The anionic styrenic based PIL block copolymer ionogel produced by Margaretta et al. had an ion conductivity of 10^{-4} S/cm at 80 °C with 30 wt% IL[25]. The ion conductivity is also comparable to several PVDF-ionogels with ion conductivities on the order of 10^{-5} to 10^{-4} S/cm that exhibited actuation displacements between 1 and 6 mm[14, 15]. Overall, both the PIL homopolymer and block copolymer ionogels were found to have good conductivities for actuation performance.

6.3.4. Morphology and Nanomechanical Properties

Mechanical properties and morphology of the polyelectrolyte layer can also play an important role in the actuator performance. In particular, micro-phase separation may lead to an enhancement in ion conductivity depending on morphology type, as has been seen in PIL styrenic block copolymers [23, 25, 71] and Nafion™ actuators[72]. Favorable mechanical properties are required to provide solid matrix that can maintain its shape while still providing enough flexibility for bending

motion. The mechanical benchmark for comparison for ionic actuator performance is typically commercially available Nafion hydrogels or PVDF ionogels, which generally has been cited to have a modulus between ~50-500 MPa depending on hydration or IL weight percent[13, 15, 22, 73-75]. Therefore, a nanomechanical AFM analysis was performed for the dry polymers and ionogels as films on silicon wafers to evaluate the morphology and mechanical properties of the polymers and ionogels. Figure 6.6 shows AFM images mapping height and Young's modulus (based on DMT model fittings) for the PVBBImTf_2N (Figure 6.6a and b) and PDMAEMA-*b*-PVBBImTf_2N (Figure 6.6c and d) dry polymers. Similar AMF images for the ionogels are included in the supplemental information Figure E.7-Figure E.8.

The film from the dry PVBBImTf_2N homopolymer displayed a homogenous morphology with divots or depressions in the matrix that had an average diameter of ~2.5 μm. The PDMAEMA-*b*-PVBBImTf_2N block copolymer also contained these depressions with reduced diameters (~ 0.31 ±0.05 μm). Additionally, an irregular raised spherical morphology was also observed in the block copolymer film with an average size of ~0.14 ± 0.04 μm. These spheres are likely composed of primarily PDMAEMA within a porous PIL-rich matrix as similarly observed in the authors' previous work[27]. While the ion conductivity of the PDMAEMA-*b*-PVBBImTf_2N block copolymer (σ = 7.9x10^{-7} S/cm at 20 °C) was slightly higher than the PVBBImTf_2N homopolymer (σ = 4.4 x 10^{-7} S/cm), an order of magnitude enhancement in ion conductivity was not observed as has been seen in several other PIL block copolymer systems[23, 25, 71, 76]. Usually, block copolymers with lamellae or cylinders oriented perpendicular to the electrode and bicontinuous morphologies are required for ion conducting channel formation and enhanced ion conductivity[71]. In this case, an ion conductivity on the same order of magnitude as the homopolymer would be expected for a

block copolymer with morphology consisting of a PIL-rich matrix and spheres rich in the non-PIL block.

Changes in morphology for both the PVBBImTf_2N homopolymer and PDMAEMA-*b*-PVBBImTf_2N block copolymer with ionic liquid addition can be observed in the height and DMT traces in Figures S7 and S8. While the 10 wt% and 25 wt% PVBBImTf_2N ionogels still exhibit a matrix with depressions, the ionogel with 40 wt% resulted in a disordered film with possible phase separation or phase inversion as seen by the lighter network-like phase in the height and DMT modulus traces and small particles with higher moduli (Figure E.7 g,h). The 10 wt% and 25 wt% PVBBImTf_2N ionogels also showed some interesting additional phases. The PVBBImTf_2N 10 wt% ionogel (Figure S7 c,d), similarly had small particles with diameters primarily between 100-200 nm, mostly residing in the depressions. The PVBBImTf_2N 25 wt% ionogel (Figure E.7 e,f) appeared to contain shallower depressions with a gradient of stiffer moduli (~19-25 MPa). This suggests that, at least at the depression locations if not the full film, the internal modulus of the film is greater than the surface of the main matrix, possibly indicating a gradient of ionic liquid concentrations within the film.

PDMAEMA-*b*-PVBBImTf_2N ionogels were also composed of a PIL-rich matrix and PDMAEMA spheres for 25wt % IL (Figure E.8 e,f) and 40 wt% IL (Figure E.8 g,h) content with more irregularity of the spheres in the 40 wt% ionogel. This possibly indicates an upper limit for IL addition in the PVBBImTf_2N homopolymer. Interestingly, the size of the spheres seem to increase with increasing ionic liquid content, with sphere diameters of 0.38 μm (±0.09 μm) and 1.02 μm (± 0.15 μm) at 25 wt% (Figure E.8 e,f) and 40 wt% IL (Figure E.8 g,h), respectively. This would suggest either a change in compatibility between the two polymer blocks with IL addition or the PDMAEMA blocks are swelling with IL. It is noted that the 10 wt% ionogel presented with

an irregular particle morphology, possibly due to the greater thickness of the film compared to the other samples (Figure E.8 c,d) Additional, AFM-IR studies would provide further insight to the particle morphology and corresponding chemical composition.

Table 6.3 includes the Young's modulus, E, for the matrix of the dry polymers and ionogels. The modulus of the PVBBImTf_2N film without ionic liquid was found to be ~47 MPa and was consistent throughout the film (Figure 6.6b). Alternatively, the dry PDMAEMA-*b*-PVBBImTf_2N block copolymer had two different modulus values for the matrix (~209 MPa) and for the raised spheres (~295 MPa) as seen by the lighter spheres in the surrounding darker matrix of the PDMAEMA-*b*-PVBBImTf_2N DMT Modulus map (Figure 6.6d DMT). For comparison, the macroinitiator PDMAEMA homopolymer had a modulus of ~214 MPa. In the authors' previous work, AFM-IR analysis revealed homogenous regions in PDMAEMA-*b*-PVBBImTf_2N block copolymer films containing IR contributions from both the PIL and PDMAEMA blocks[27]. This information combined with the almost 4.5 times greater modulus of the PDMAEMA-*b*-PVBBImTf_2N matrix compared to the PVBBImTf_2N homopolymer suggests the block copolymer matrix contains a blend of the two polymer blocks.

Overall, incorporating ionic liquid into the polymers results in a significant reduction of Young's modulus for both systems with increasing ionic liquid content. As the major phase in the polymers, the matrix Young's modulus values for both PVBBImTf_2N and PDMAEMA-*b*-PVBBImTf_2N ionogels are shown in Figure 6.6e as a function of ionic liquid content, although the moduli for each observed phase as a function of ionic liquid content are also provided in supplemental Figure E.9. PVBBImTf_2N-based ionogels fall from ~47 MPa at 0 wt% IL to ~11 MPa (25 wt% IL), and ~1.3 MPa (40 wt% IL). Interestingly, the PVBBImTf_2N 10 wt% ionogel showed the highest Young's modulus at ~ 133 MPa. As DSC measurements indicated a decrease

in glass transition temperature for the 10 wt% ionogel compared to the dry PVBBImTf_2N polymer, a lower Young's modulus would have been expected. However, the higher modulus may be a result of another factor such as the solvent-casting method in preparing the films or the modulus of the film surface may also be different from the bulk of the ionogel.

The matrix of the block copolymer ionogels had matrix modulus values at of ~148 MPa (10 wt% IL), 12.3 MPa (25 wt% IL), and 1.0 MPa (40 wt% IL) while the corresponding spheres/particle morphology had modulus values of ~ 376 MPa (10 wt% IL), ~44 MPa (25 wt% IL), and ~9 MPa (40 wt% IL). The decrease in modulus for the sphere/particle morphology suggests that the PDMAEMA spheres help reinforce the overall PDMAEMA-*b*-PVBBImTf_2N matrix but were also plasticized with increasing ionic liquid content.

While the dry PIL-based polymers and 10 wt% ionogels have Young's modulus values significantly lower than the 500-1000 MPa reported for several styrenic based PIL ABA triblock copolymer actuator systems[22-24], the block copolymer and its 10 wt% ionogel have moduli that does fall within or near the range of the reported Nafion^{TM} actuator modulus values (50-500 MPa) [73-75]. Further, the PDMAEMA-*b*-PVBBImTf_2N block copolymer's matrix modulus of 209 MPa is also comparable to the modulus for a styrenic anionic PIL ABA triblock copolymer actuator film containing 30 wt% ionic liquid developed by Margaretta et al. [25]. Conversely, with the exception of the 10 wt% ionogel (~148 MPa PDMAEMA-*b*-PVBBImTf_2N and ~133 MPa PVBBImTf_2N), the modulus values for the other ionogels are likely too low for favorable actuation behavior. However, they are higher than the ~0.15-0.30 MPa Young's modulus reported by Kokubo et al. for micro-actuating crosslinked PIL films composed of either an imidazolium based PIL or a Tf_2N-based anionic PIL with methacrylate backbones[20].

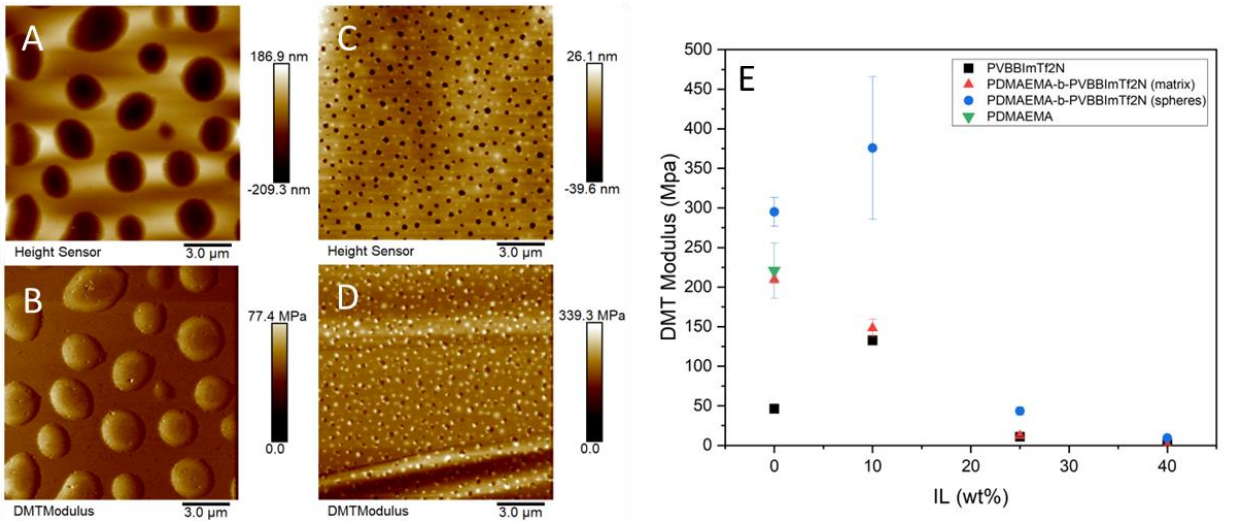

Figure 6.6 AFM images (15 µm x 15µm) for the PVBBImTf_2N and PDMAEMA-*b*-PVBBImTf_2N dry polymers including the (a and c) height trace and their corresponding Young's modulus map based on a DMT fitting (b and d) are shown. Similar AFM images for the ionogels are provided in the supplemental information (Figures S7-S8). (e) Average Young's moduli (collected at 5 different locations) as a function of ionic liquid weight percentage for the PVBBImTf_2N and PDMAEMA-*b*-PVBBImTf_2N matrix. Additional AFM scans for adhesion, dissipation, deformation, and peak force error are included in Figures S11-S18.

6.3.5. Actuation Behavior

The dry polymers and their 10 wt% ionogels were found to have sufficiently high ion conductivity (~10^{-7}-10^{-6} S/cm) and Young's modulus (~47 to 209 MPa) for examining actuation behavior. Actuator films were developed by sandwiching the dry polymers and their 10 wt% ionogel electrolyte layers between gold leaf foil. Video stills of the produced actuator films and their actuation behavior are shown in Figure 6.7 for PDMAEMA-*b*-PVBBImTf_2N (Figure 6.7a-b), PDMAEMA-*b*-PVBBImTf_2N 10 wt% ionogel (Figure 6.7c-d), PVBBImTf_2N (Figure 6.7e-f), and PVBBImTf_2N 10 wt% ionogel (Figure 7g-h). Figure 6.8a also shows the tip displacement measured for the actuator films in comparison to a prepared PVDF 40 wt% $C_4C_1ImBF_4$ control under an applied 4 V from a DC power source. Tip-displacements after 50 sec of applied voltage and other specified times are also provided in Table E.1.

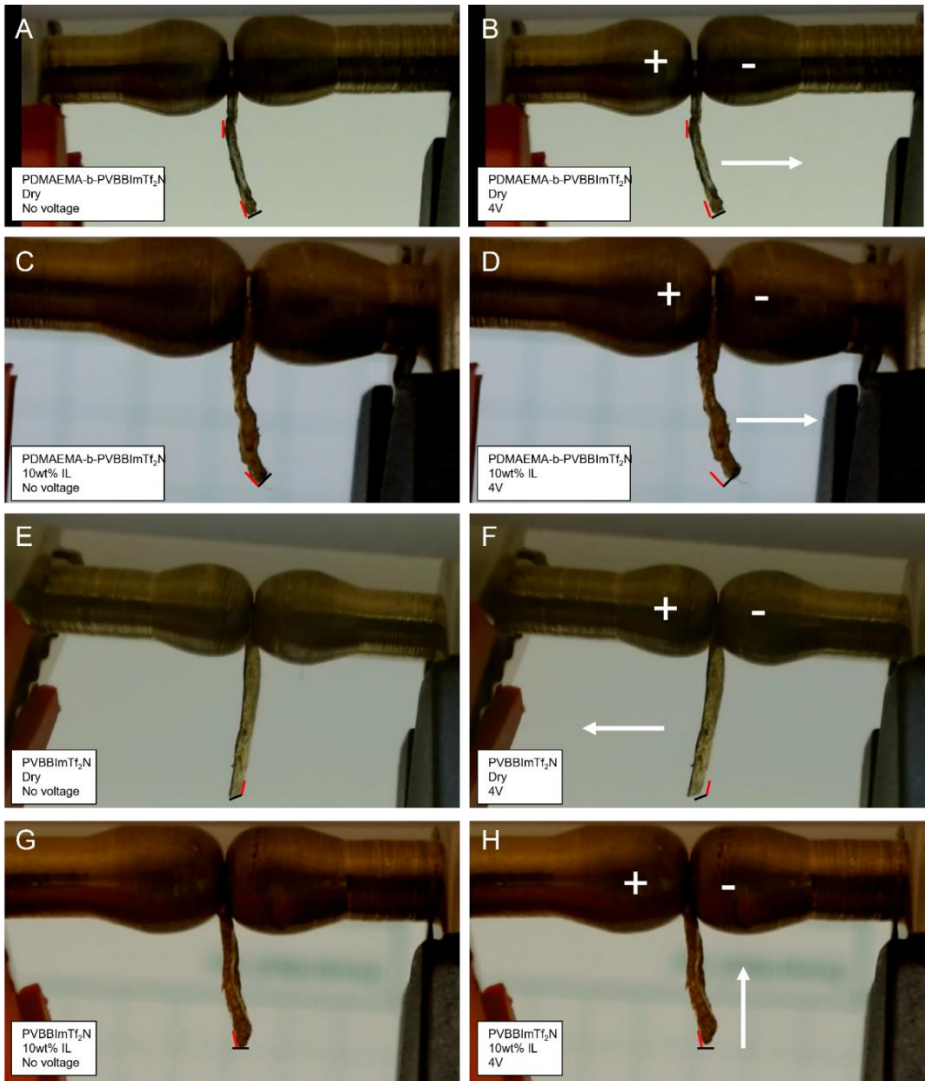

Figure 6.7 Video still images of the dry PIL polymers and ionogels before and after applying 4 V: (a,b) dry PDMAEMA-*b*-PVBBImTf_2N; (c,d) PDMAEMA-*b*-PVBBImTf_2N 10 wt% IL; (e,f) dry PVBBImTf_2N; and (g,h) PVBBImTf_2N 10 wt% IL. A more planar shape was achieved for the dry PIL polymers (a and e) while deformations in the actuator film are observed for the 10 wt% ionogels (c and g). The black and red lines mark the side and bottom of the actuator initial position (no voltage) to aid visualization of the actuator displacement. White arrows point the direction of actuation. Actuation video stills of the PVDF 40 wt% control can be found in the supplemental information (Figure S20).

After 50 sec of applied voltage, the PDMAEMA-*b*-PVBBImTf_2N block copolymer with only mobile Tf_2N^- anions displayed a ~110 μm x-tip displacement towards the negative electrode. This compares well to the expected bending direction for a single-ion cationic polyelectrolyte actuator. In this case, the bending motion results from the Tf_2N^- anions migrating towards the positive electrode which induces swelling at the polymer-electrode interface and results in tip displacement towards the negative electrode. As the PDMAEMA-*b*-PVBBImTf_2N copolymer has a favorable Young's modulus of ~223 MPa for the matrix, the micro-scale actuation behavior is likely due to relatively low ion conductivity ~10^{-7} S/cm. Despite the deformed shape of the 10 wt% PDMAEMA-*b*-PVBBImTf_2N ionogel, it displayed similar behavior to the dry block copolymer with tip displacements of ~90 μm in the same bending direction after 50s. After 195 sec, this actuator displaced ~279 μm, demonstrating micro-actuation behavior. The observed tip-displacements for the PDMAEMA-*b*-PVBBImTf_2N copolymer and its 10 wt% ionogel were lower than the comparative control PVDF 40 wt% $C_4C_1ImBF_4$ ionogel, which displaced 525 μm in the x-direction towards the negative electrode after 45 sec. While the actuation for these dry PIL-based films is lower than the PVDF ionogel, they are comparable to tip displacements observed by the crosslinked PIL actuators developed by Kokubo et al[20].

In ionogel based actuators, the bending direction is dependent on both the free ionic liquid cation and anion size as this affects their migration towards oppositely charged electrodes. Generally, the larger volume of ionic liquid cations, compared to the smaller Tf_2N^- or BF_4^- anions, leads to greater swelling at the negatively charged electrode and bending motion towards the positive electrode in PVDF ionogels[1, 15]. The tip-displacement towards the negative electrode for the PDMAEMA-*b*-PVBBImTf_2N 10 wt% ionogel suggests that swelling was predominately caused by the Tf_2N^- and BF_4^- anions at the positive electrode interface. This may be due to the

greater concentration of anions in the polymer layer compared to free imidazolium cations or possibly reduced mobility of the imidazolium ring with the longer butyl chain. The PVDF 40 wt% ionogel control exhibited similar tip displacement towards the negative electrode. In this case, bending towards the negative electrode likely indicates hindered migration of the free IL butylimidazolium cation in the PVDF matrix, resulting in swelling primarily occurring due to the BF_4^- anions instead.

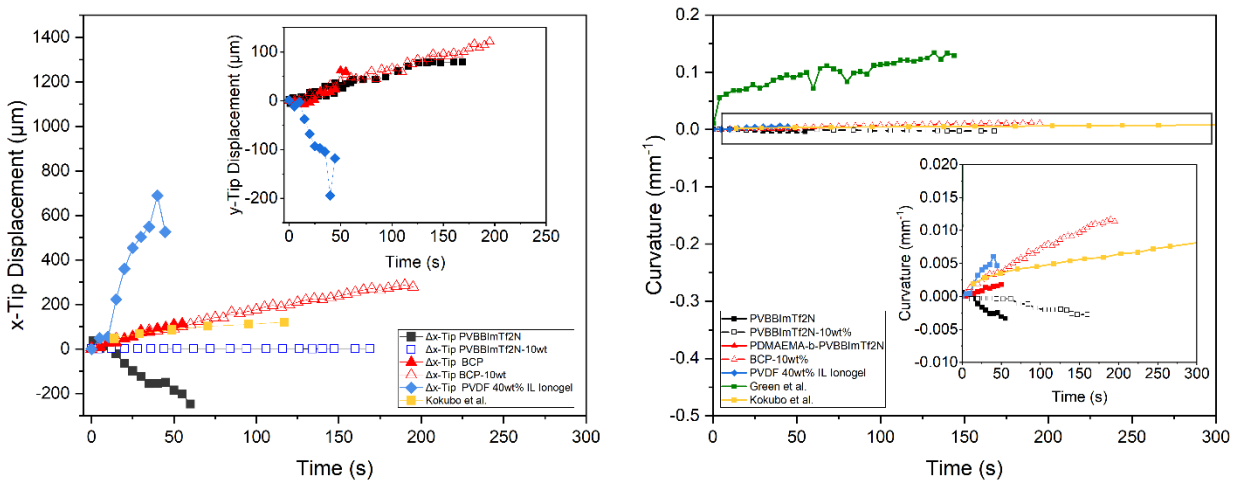

Figure 6.8 (a) Tip displacement in the x-direction (y-direction in insert) for PVBBImTf_2N (black squares), PVBBImTf2N 10 wt% ionogel (black open squares), PDMAEMA-*b*-PVBBImTf_2N (red triangles), PDMAEMA-*b*-PVBBImTf_2N (red open triangles), PVDF with 40 wt% IL (blue diamonds), and the crosslinked PIL micro-actuators developed by Kokubo et al.[20] (yellow squares). Positive displacements values indicate tip-displacement towards the negative electrode. (b) Curvature (inverse radius of curvature) for the actuators (same labels) are shown in comparison to the styrenic PIL ABA triblock copolymer actuator developed by Green et al.[22] and the crosslinked PIL micro-actuators by Kokubo et al. [20] The insert shows an expanded view of the section boxed in (b).

To allow for more direct comparisons to the styrenic ABA triblock copolymers developed in the literature, the curvature, k (mm^{-1}), was also calculated for the PDMAEMA-*b*-PVBBImTf_2N dry polymer and PDMAEMA-*b*-PVBBImTf_2N 10 wt% ionogel films in accordance with[4, 77]:

$$\textbf{EQ 6-4}\ k = \frac{2\delta}{\delta^2 + L^2}$$

where δ is the tip displacement in the x-direction and L is the free length of the actuator film, and is shown in Figure 8b. The absolute curvature for the PDMAEMA-*b*-PVBBImTf_2N polymer and ionogel actuators was found to be significantly lower than the actuation film developed by Green et al. (~0.1 mm^{-1} for a styrenic ABA PIL block copolymers without a CNC layer) [22], but comparable to the crosslinked PIL micro-actuator's developed by Kokubo et al. [20] The micro-scale ionic actuation performance of PDMAEMA-*b*-PVBBImTf_2N polymer and ionogel actuators is likely due to a combination of the low dry-state ion conductivity (~10^{-7} S/cm) and the lower Young's moduli compared to the styrenic ABA triblock copolymers. Nevertheless, the novel PDMAEMA-*b*-PVBBImTf_2N block copolymer was successfully able to produce micro-scale actuation behavior at low voltages (4 V).

Electroactive actuation behavior of the PVBBImTf_2N and PVBBImTf_2N 10 wt% ionogels was also examined, which similarly showed micro-actuation behavior, but with unexpected bending directions. After 50 sec of applied voltage the PVBBImTf_2N actuator exhibited x-tip displacement of ~185 μm and, interestingly, displaced towards the positive electrode. A replicate PVBBImTf_2N actuator film displayed similar displacement towards the positive electrode (Figure E.21). The 10 wt% PVBBImTf_2N ionogel did not displace in the x-direction. Rather it exhibited an out-of-plane (towards the camera) bending motion response resulting in a measurable y-tip displacement of ~26.4 μm.

Similar to the dry PDMAEMA-*b*-PVBBImTf_2N block copolymer above, PVBBImTf_2N would be expected to displace towards the negative electrode as a single-ion conducting polycation with only mobile anions. The opposite behavior observed for the PVBBImTf_2N dry copolymer film potentially indicates another underlying physical reason for the electromechanical bending motion

competing with ion migration and the resulting osmotic pressure. It is currently uncertain if the out-of-plan bending of the PVBBImTf_2N 10 wt% ionogel is following a similar underlying electromechanical mechanism as is dry PVBBImTf_2N counterpart or if the physical shape of the film (e.g., varying thickness) is directing the motion. Further examination and characterization of the electrochemical properties of the PVBBImTf_2N polymer and ionogel will provide further insight into their actuation behavior. It is also noted that attempts at re-testing both the polymer ionogel actuator films several weeks or months after their initial testing led to lower displacements, and in some cases, changes in bending motion direction compared to their initial testing behavior (Figure E.22). The loss of actuation behavior is tentatively attributed to potential changes in contact between the electroactive layer and the gold foil electrode or possible electrochemical degradation from the initial testing which may be further verified through cyclic voltammetry characterizations.

As to the potential underlying electrochemical mechanism broached above, one possibility involves the increased dominance of Maxwell stresses resulting from changes in electrostatic interactions at the polymer-electrode interface under the applied voltage. In their recent modeling work on back-relaxation often observed in Nafion-based IPMC actuators, Porfiri et al. indicated that Maxwell stress begin to dominate over osmotic pressure contributions as the electric double layers at the electrode interface becomes thicker with accumulating ions and thinner with depleted ions at the opposite electrode, leading to a change in the electric field at the electrode interfaces and the resulting bending moment[78]. Similar localized changes in the electric field at the polymer electrode-interface in the PVBBImTf_2N layer under the DC potential may also be occurring.

Similar maxwell stresses are also observed in the electroactive actuation behavior of dielectric elastomer actuators (DEAs). In DEAs, the applied voltage results in an electrostatic attraction of

the oppositely charged electrodes, producing a compressive stress within the polymer layer. DEA polymer systems typically display low Young's modulus values (~0.5-20 MPa) and dielectric constants between 3-7 V (a dimensionless quantity of the ratio of material permittivity to the permittivity of free space) [79]. A similar PIL, poly[vinylbenzyl butylimidazolium tetrafluoroborate] ($PVBBImBF_4^-$) developed by Tang et al., exhibited dielectric constants between 3-4, which falls within the lower end of this DEA dielectric constant range[80]. Calculation of the dielectric constant for $PVBBImTf_2N$ produced in this work from EIS measurements yielded a value of ~13.6 (see supplemental information Figure E.23), which is comparable to a recent PIL-acrylic tape DEA actuator composite developed by Wang et al. [81] In their work, a crosslinked polyvinylhexylimidazolium BF_4^- PIL was utilized as the filler in a DEA actuator due to its low Young's modulus and its ability to increase the overall dielectric constant for the actuator composite from ~5 for the acrylic-based tape to ~16 for the PIL-acrylic tape composite. Their actuator exhibited a bending behavior under an applied 6.3 V/μm electric field. Some DEA based actuators have included ionic liquids in the matrix to decrease Young's modulus and enhance the dielectric constant[82]. With similar moderate dielectric constants and low Young's modulus, crosslinked versions of the ionogels developed in this work, particularly for the 25 wt% and 40 wt% ionogels, may show similar potential for use in DEA actuator composites.

6.4. Conclusions

In this work, the novel all-polyelectrolyte block copolymer poly[(2-dimethyl amino)ethyl methacrylate)]-*block*-poly[4-vinylbenzyl-3-butyl imidazolium bis(trifluoromethylsulfonyl)imide)], its corresponding homopolymer, and their ionogels were thoroughly characterized for important IEAP actuator parameters and evaluated as ionic actuators. FTIR spectroscopy confirmed successful formation of the ionogels, which exhibited intermediate electrostatic interaction behavior between the pure IL and the dry polymers. Excellent thermal

stability was found for all PIL-based ionogels in the TGA analysis, with increased overall stability of the PDMAEMA-*b*-PVBBImTf_2N ionogels with increasing ionic liquid content. DSC analysis indicated successful plasticization of PVBBImTf_2N and PDMAEMA-*b*-PVBBImTf_2N with increasing ionic liquid content which corresponded well with the increase ion conductivities observed from ~10^{-7} S/cm in the dry polymers and up to 10^{-4} S/cm in the ionogels. AFM morphology and nanomechanical analysis of the PDMAEMA-*b*-PVBBImTf_2N block copolymer revealed spherical morphology consisting of PDMAEMA-rich spheres in a PIL-rich matrix with depressions. The high modulus of the matrix (223 MPa) compared to the PVBBImTf_2N homopolymer and the spherical PDMAEMA inclusions (294 MPa) indicate possible blending of the PDMAEMA and PVBBImTf_2N blocks, resulting in an overall stiffer polymer layer with improved mechanical properties. Addition of ionic liquid significantly reduced the modulus values for the ionogels; however, the PDMAEMA-*b*-PVBBImTf_2N 10 wt% ionogel still had a favorable modulus of ~145 MPa. Actuator films from the dry PDMAEMA-*b*-PVBBImTf_2N block copolymer and PVBBImTf_2N homopolymer were successfully sandwiched between gold foil electrodes and evaluated for actuation performance at 4 V. 10 wt% ionogel actuator films were produced, albeit with a deformed form, which displayed an out-of-plan bending motion behavior (PVBBImTf_2N 10 wt% ionogel) and bending behavior (PDMAEMA-*b*-PVBBImTf_2N 10 wt% ionogel). Micro-scale actuation was achieved for both of the dry-polymer systems, indicating their potential as single-ion micro actuators. While the majority of the ionogels had modulus values too low for actuation, important thermal and electrochemical information was determined that will aid in the design of future actuators with novel PIL materials. The authors are currently exploring other methods to improve the mechanical properties of the PVBBImTf_2N and PDMAEMA-*b*-

PVBBImTf_2N ionogels and expect improved actuation performance for the highly ion conductive ionogels.

Acknowledgements

The authors would like to acknowledge Josh Kasitz, Muhammad Ghufran, and their advisor Dr. David Huitink for aiding in DSC data collection.

6.5. References

(1) Martins, P.; Correia, D. M.; Correia, V.; Lanceros-Mendez, S. Polymer-based actuators: back to the future. *Physical Chemistry Chemical Physics* **2020**, *22* (27), 15163-15182, 10.1039/D0CP02436H. DOI: 10.1039/D0CP02436H.

(2) Rahman, M. H.; Werth, H.; Goldman, A.; Hida, Y.; Diesner, C.; Lane, L.; Menezes, P. L. Recent Progress on Electroactive Polymers: Synthesis, Properties and Applications. *Ceramics* **2021**, *4* (3), 516-541. DOI: 10.3390/ceramics4030038.

(3) White, B. T.; Long, T. E. Advances in Polymeric Materials for Electromechanical Devices. *Macromolecular Rapid Communications* **2019**, *40* (1), 1800521, https://doi.org/10.1002/marc.201800521. DOI: https://doi.org/10.1002/marc.201800521 (acccessed 2022/08/10).

(4) Yanjie, W.; Takushi, S. Ionic Polymer Actuators: Principle, Fabrication and Applications. In *Actuators*, Constantin, V. Ed.; IntechOpen, 2018.

(5) Nguyen, V. K.; Lee, J. W.; Yoo, Y. Characteristics and performance of ionic polymer–metal composite actuators based on Nafion/layered silicate and Nafion/silica nanocomposites. *Sensors and Actuators B: Chemical* **2007**, *120* (2), 529-537. DOI: https://doi.org/10.1016/j.snb.2006.03.015.

(6) Pugal, D.; Kim, K. J.; Aabloo, A. An explicit physics-based model of ionic polymer-metal composite actuators. *Journal of Applied Physics* **2011**, *110* (8), 084904. DOI: 10.1063/1.3650903 (acccessed 2022/08/10).

(7) Pugal, D.; Stalbaum, T.; Palmre, V.; Kim, K. J. Chapter 5 Modeling Ionic Polymer Metal Composites with COMSOL: Step-by-Step Guide. In *Ionic Polymer Metal Composites (IPMCs): Smart Multi-Functional Materials and Artificial Muscles, Volume 1*, Vol. 1; The Royal Society of Chemistry, 2016; pp 185-214.

(8) James Jungho, P.; Jihong, K.; Sang Woo, O.; Jee Hee, S.; Sung Hwan, C.; Seung-Ki, L.; Jong-Yeon, P.; Byungkyu, K. Fabrication of ionic-polymer-metal-composite (IPMC) micropump using a commercial Nafion. In *Proc.SPIE*, 2004; Vol. 5385, pp 272-280. DOI: 10.1117/12.539671.

(9) Bian, K.; Liu, H.; Tai, G.; Zhu, K.; Xiong, K. Enhanced Actuation Response of Nafion-Based Ionic Polymer Metal Composites by Doping BaTiO3 Nanoparticles. *The Journal of Physical Chemistry C* **2016**, *120* (23), 12377-12384. DOI: 10.1021/acs.jpcc.6b03273.

(10) Bashir, M.; Rajendran, P. A review on electroactive polymers development for aerospace applications. *Journal of Intelligent Material Systems and Structures* **2018**, *29* (19), 3681-3695. DOI: 10.1177/1045389X18798951 (acccessed 2022/10/12).

(11) Dong, Y.; Yeung, K.-W.; Tang, C.-Y.; Law, W.-C.; Tsui, G. C.-P.; Xie, X. Development of ionic liquid-based electroactive polymer composites using nanotechnology. *Nanotechnology Reviews* **2021**, *10* (1), 99-116. DOI: doi:10.1515/ntrev-2021-0009.

(12) Edgar, H.; Zane, Z.; Andres, P.; Urmas, J.; Alvo, A. Some electrochemical aspects of aqueous ionic polymer-composite actuators. In *Proc.SPIE*, 2016; Vol. 9798, p 979815. DOI: 10.1117/12.2219031.

(13) Correia, D. M.; Fernandes, L. C.; Martins, P. M.; García-Astrain, C.; Costa, C. M.; Reguera, J.; Lanceros-Méndez, S. Ionic Liquid–Polymer Composites: A New Platform for Multifunctional Applications. *Advanced Functional Materials* **2020**, *30* (24), 1909736, https://doi.org/10.1002/adfm.201909736. DOI: https://doi.org/10.1002/adfm.201909736 (acccessed 2022/08/10).

(14) Correia, D. M.; Barbosa, J. C.; Costa, C. M.; Reis, P. M.; Esperança, J. M. S. S.; de Zea Bermudez, V.; Lanceros-Méndez, S. Ionic Liquid Cation Size-Dependent Electromechanical Response of Ionic Liquid/Poly(vinylidene fluoride)-Based Soft Actuators. *The Journal of Physical Chemistry C* **2019**, *123* (20), 12744-12752. DOI: 10.1021/acs.jpcc.9b00868.

(15) Guo, D.; Han, Y.; Huang, J.; Meng, E.; Ma, L.; Zhang, H.; Ding, Y. Hydrophilic Poly(vinylidene Fluoride) Film with Enhanced Inner Channels for Both Water- and Ionic Liquid-Driven Ion-Exchange Polymer Metal Composite Actuators. *ACS Applied Materials & Interfaces* **2019**, *11* (2), 2386-2397. DOI: 10.1021/acsami.8b18098.

(16) Mejri, R.; Dias, J. C.; Hentati, S. B.; Martins, M. S.; Costa, C. M.; Lanceros-Mendez, S. Effect of anion type in the performance of ionic liquid/poly(vinylidene fluoride) electromechanical actuators. *Journal of Non-Crystalline Solids* **2016**, *453*, 8-15. DOI: https://doi.org/10.1016/j.jnoncrysol.2016.09.014.

(17) Alashkar, A.; Al-Othman, A.; Tawalbeh, M.; Qasim, M. A Critical Review on the Use of Ionic Liquids in Proton Exchange Membrane Fuel Cells. *Membranes* **2022**, *12* (2), 178.

(18) Eshetu, G. G.; Mecerreyes, D.; Forsyth, M.; Zhang, H.; Armand, M. Polymeric ionic liquids for lithium-based rechargeable batteries. *Mol. Syst. Des. Eng.* **2019**, *4* (2), 294-309, 10.1039/c8me00103k. DOI: 10.1039/c8me00103k.

(19) Frederic, B. R.; Cedric, P.; Giao, T. M. N.; Sofia, M. M.; Eric, D.; Alexander, S. S.; Frederic, V. All-solid state ionic actuators based on polymeric ionic liquids and electronic conducting polymers. In *Proc.SPIE*, 2018; Vol. 10594, p 105941H. DOI: 10.1117/12.2300774.

(20) Kokubo, H.; Sano, R.; Murai, K.; Ishii, S.; Watanabe, M. Ionic polymer actuators using poly(ionic liquid) electrolytes. *European Polymer Journal* **2018**, *106*, 266-272. DOI: https://doi.org/10.1016/j.eurpolymj.2018.07.026.

(21) Kanaan, A. F.; Piedade, A. P.; de Sousa, H. C.; Dias, A. M. A. Effect of mold assemblies-induced interfaces in the mechanical actuation of electro-responsive ionic liquid-based polycationic hydrogels. *Applied Materials Today* **2020**, *20*, 100711. DOI: https://doi.org/10.1016/j.apmt.2020.100711.

(22) Green, M. D.; Wang, D.; Hemp, S. T.; Choi, J.-H.; Winey, K. I.; Heflin, J. R.; Long, T. E. Synthesis of imidazolium ABA triblock copolymers for electromechanical transducers. *Polymer* **2012**, *53* (17), 3677-3686. DOI: https://doi.org/10.1016/j.polymer.2012.06.023.

(23) Jangu, C.; Wang, J.-H. H.; Wang, D.; Fahs, G.; Heflin, J. R.; Moore, R. B.; Colby, R. H.; Long, T. E. Imidazole-containing triblock copolymers with a synergy of ether and imidazolium sites. *Journal of Materials Chemistry C* **2015**, *3* (16), 3891-3901, 10.1039/C5TC00169B. DOI: 10.1039/C5TC00169B.

(24) Jangu, C.; Wang, J.-H. H.; Wang, D.; Sharick, S.; Heflin, J. R.; Winey, K. I.; Colby, R. H.; Long, T. E. Well-Defined Imidazolium ABA Triblock Copolymers as Ionic-Liquid-Containing Electroactive Membranes. *Macromolecular Chemistry and Physics* **2014**, *215* (13), 1319-1331, https://doi.org/10.1002/macp.201400121. DOI: https://doi.org/10.1002/macp.201400121 (acccessed 2022/08/10).

(25) Margaretta, E.; Fahs, G. B.; Inglefield, D. L.; Jangu, C.; Wang, D.; Heflin, J. R.; Moore, R. B.; Long, T. E. Imidazolium-Containing ABA Triblock Copolymers as Electroactive Devices. *ACS Applied Materials & Interfaces* **2016**, *8* (2), 1280-1288. DOI: 10.1021/acsami.5b09965.

(26) Gao, R.; Wang, D.; Heflin, J. R.; Long, T. E. Imidazolium sulfonate-containing pentablock copolymer–ionic liquid membranes for electroactive actuators. *Journal of Materials Chemistry* **2012**, *22* (27), 13473-13476, 10.1039/C2JM16117F. DOI: 10.1039/C2JM16117F.

(27) Kayla Foley, K. B. W. Solution and film self-assembly of a block copolymer comprised of a poly(ionic liquid) and a stimuli-responsive weak polyelectrolyte *ACS Omega, Under Review (AO-2023-039894, submitted 06-06-2023)* **2023**.

(28) Derjaguin, B. V.; Muller, V. M.; Toporov, Y. P. Effect of contact deformations on the adhesion of particles. *Journal of Colloid and Interface Science* **1975**, *53* (2), 314-326. DOI: https://doi.org/10.1016/0021-9797(75)90018-1.

(29) Eyiler, E.; Chu, I. W.; Walters, K. B. Toughening of poly(lactic acid) with the renewable bioplastic poly(trimethylene malonate). *Journal of Applied Polymer Science* **2014**, *131* (20), https://doi.org/10.1002/app.40888. DOI: https://doi.org/10.1002/app.40888 (acccessed 2023/06/09).

(30) Minamimoto, H.; Irie, H.; Uematsu, T.; Tsuda, T.; Imanishi, A.; Seki, S.; Kuwabata, S. Polymerization of Room-Temperature Ionic Liquid Monomers by Electron Beam Irradiation with

the Aim of Fabricating Three-Dimensional Micropolymer/Nanopolymer Structures. *Langmuir* **2015**, *31* (14), 4281-4289. DOI: 10.1021/la503252p.

(31) Cappella, B. *Mechanical properties of Polymers measured through AFM force-distance curves*; Springer, 2016.

(32) Kazemiabnavi, S.; Zhang, Z.; Thornton, K.; Banerjee, S. Electrochemical Stability Window of Imidazolium-Based Ionic Liquids as Electrolytes for Lithium Batteries. *The Journal of Physical Chemistry B* **2016**, *120* (25), 5691-5702. DOI: 10.1021/acs.jpcb.6b03433.

(33) Xue, Z.; Qin, L.; Jiang, J.; Mu, T.; Gao, G. Thermal, electrochemical and radiolytic stabilities of ionic liquids. *Physical Chemistry Chemical Physics* **2018**, *20* (13), 8382-8402, 10.1039/C7CP07483B. DOI: 10.1039/C7CP07483B.

(34) Palm, R.; Kurig, H.; Tõnurist, K.; Jänes, A.; Lust, E. Is the mixture of 1-ethyl-3-methylimidazolium tetrafluoroborate and 1-butyl-3-methylimidazolium tetrafluoroborate applicable as electrolyte in electrical double layer capacitors? *Electrochemistry Communications* **2012**, *22*, 203-206. DOI: https://doi.org/10.1016/j.elecom.2012.06.029.

(35) Kiefer, J.; Fries, J.; Leipertz, A. Experimental vibrational study of imidazolium-based ionic liquids: Raman and infrared spectra of 1-ethyl-3-methylimidazolium bis(trifluoromethylsulfonyl)imide and 1-ethyl-3-methylimidazolium ethylsulfate. *Appl Spectrosc* **2007**, *61* (12), 1306-1311. DOI: 10.1366/000370207783292000 From NLM.

(36) Paschoal, V. H.; Faria, L. F. O.; Ribeiro, M. C. C. Vibrational Spectroscopy of Ionic Liquids. *Chemical Reviews* **2017**, *117* (10), 7053-7112. DOI: 10.1021/acs.chemrev.6b00461.

(37) Coates, J. Interpretation of Infrared Spectra, A Practical Approach. In *Encyclopedia of Analytical Chemistry*.

(38) Yamada, T.; Mizuno, M. Infrared and Terahertz Spectroscopic Investigation of Imidazolium, Pyridinium, and Tetraalkylammonium Tetrafluoroborate Ionic Liquids. *ACS Omega* **2022**, *7* (34), 29804-29812. DOI: 10.1021/acsomega.2c02601.

(39) Heimer, N. E.; Del Sesto, R. E.; Meng, Z.; Wilkes, J. S.; Carper, W. R. Vibrational spectra of imidazolium tetrafluoroborate ionic liquids. *Journal of Molecular Liquids* **2006**, *124* (1), 84-95. DOI: https://doi.org/10.1016/j.molliq.2005.08.004.

(40) Grondin, J.; Lassègues, J.-C.; Cavagnat, D.; Buffeteau, T.; Johansson, P.; Holomb, R. Revisited vibrational assignments of imidazolium-based ionic liquids. *Journal of Raman Spectroscopy* **2011**, *42* (4), 733-743. DOI: https://doi.org/10.1002/jrs.2754.

(41) James, C.; Ravikumar, C.; Jayakumar, V. S.; Hubert Joe, I. Vibrational spectra and potential energy distributions for 1-benzyl-1H-imidazole by normal coordinate analysis. *Journal of Raman Spectroscopy* **2009**, *40* (5), 537-545, https://doi.org/10.1002/jrs.2160. DOI: https://doi.org/10.1002/jrs.2160 (acccessed 2022/10/12).

(42) Roth, C.; Chatzipapadopoulos, S.; Kerlé, D.; Friedriszik, F.; Lütgens, M.; Lochbrunner, S.; Kühn, O.; Ludwig, R. Hydrogen bonding in ionic liquids probed by linear and nonlinear vibrational spectroscopy. *New Journal of Physics* **2012**, *14* (10), 105026. DOI: 10.1088/1367-2630/14/10/105026.

(43) Bocharova, V.; Sokolov, A. P. Perspectives for Polymer Electrolytes: A View from Fundamentals of Ionic Conductivity. *Macromolecules (Washington, DC, U. S.)* **2020**, *53* (11), 4141-4157, 10.1021/acs.macromol.9b02742. DOI: 10.1021/acs.macromol.9b02742.

(44) Tang, J.; Tang, H.; Sun, W.; Radosz, M.; Shen, Y. Poly(ionic liquid)s as new materials for CO2 absorption. *Journal of Polymer Science Part A: Polymer Chemistry* **2005**, *43* (22), 5477-5489, https://doi.org/10.1002/pola.21031. DOI: https://doi.org/10.1002/pola.21031 (acccessed 2023/06/10).

(45) Weber, R. L.; Ye, Y.; Banik, S. M.; Elabd, Y. A.; Hickner, M. A.; Mahanthappa, M. K. Thermal and ion transport properties of hydrophilic and hydrophobic polymerized styrenic imidazolium ionic liquids. *Journal of Polymer Science Part B: Polymer Physics* **2011**, *49* (18), 1287-1296, https://doi.org/10.1002/polb.22319. DOI: https://doi.org/10.1002/polb.22319 (acccessed 2023/06/10).

(46) Hunley, M. T.; England, J. P.; Long, T. E. Influence of Counteranion on the Thermal and Solution Behavior of Poly(2-(dimethylamino)ethyl methacrylate)-Based Polyelectrolytes. *Macromolecules* **2010**, *43* (23), 9998-10005. DOI: 10.1021/ma1017499.

(47) Stawski, D.; Nowak, A. Thermal properties of poly(N,N-dimethylaminoethyl methacrylate). *PLOS ONE* **2019**, *14* (6), e0217441. DOI: 10.1371/journal.pone.0217441.

(48) Bonkovoski, L. C.; Martins, A. F.; Bellettini, I. C.; Garcia, F. P.; Nakamura, C. V.; Rubira, A. F.; Muniz, E. C. Polyelectrolyte complexes of poly[(2-dimethylamino) ethyl methacrylate]/chondroitin sulfate obtained at different pHs: I. Preparation, characterization, cytotoxicity and controlled release of chondroitin sulfate. *International Journal of Pharmaceutics* **2014**, *477* (1), 197-207. DOI: https://doi.org/10.1016/j.ijpharm.2014.10.017.

(49) Knorr, M.; Icker, M.; Efimova, A.; Schmidt, P. Reactivity of Ionic Liquids: Studies on Thermal Decomposition Behavior of 1-Butyl-3-methylimidazolium Tetrafluoroborate. *Thermochimica Acta* **2020**, *694*, 178786. DOI: https://doi.org/10.1016/j.tca.2020.178786.

(50) Kroon, M. C.; Buijs, W.; Peters, C. J.; Witkamp, G.-J. Quantum chemical aided prediction of the thermal decomposition mechanisms and temperatures of ionic liquids. *Thermochimica Acta* **2007**, *465* (1), 40-47. DOI: https://doi.org/10.1016/j.tca.2007.09.003.

(51) Tang, H.; Tang, J.; Ding, S.; Radosz, M.; Shen, Y. Atom transfer radical polymerization of styrenic ionic liquid monomers and carbon dioxide absorption of the polymerized ionic liquids. *Journal of Polymer Science Part A: Polymer Chemistry* **2005**, *43* (7), 1432-1443, https://doi.org/10.1002/pola.20600. DOI: https://doi.org/10.1002/pola.20600 (acccessed 2023/06/13).

(52) Krevelen†, D. W. v.; Nijenhuis, K. t. Properties of Polymers - Their Correlation with Chemical Structure; Their Numerical Estimation and Prediction from Additive Group Contributions (4th, Completely Revised Edition). Elsevier.

(53) Huddleston, J. G.; Visser, A. E.; Reichert, W. M.; Willauer, H. D.; Broker, G. A.; Rogers, R. D. Characterization and comparison of hydrophilic and hydrophobic room temperature ionic liquids incorporating the imidazolium cation. *Green Chemistry* **2001**, *3* (4), 156-164, 10.1039/B103275P. DOI: 10.1039/B103275P.

(54) Parajó, J. J.; Teijeira, T.; Fernández, J.; Salgado, J.; Villanueva, M. Thermal stability of some imidazolium [NTf2] ionic liquids: Isothermal and dynamic kinetic study through thermogravimetric procedures. *The Journal of Chemical Thermodynamics* **2017**, *112*, 105-113. DOI: https://doi.org/10.1016/j.jct.2017.04.016.

(55) Shirota, H.; Mandai, T.; Fukazawa, H.; Kato, T. Comparison between Dicationic and Monocationic Ionic Liquids: Liquid Density, Thermal Properties, Surface Tension, and Shear Viscosity. *Journal of Chemical & Engineering Data* **2011**, *56* (5), 2453-2459. DOI: 10.1021/je2000183.

(56) Maton, C.; De Vos, N.; Stevens, C. V. Ionic liquid thermal stabilities: decomposition mechanisms and analysis tools. *Chemical Society Reviews* **2013**, *42* (13), 5963-5977, 10.1039/C3CS60071H. DOI: 10.1039/C3CS60071H.

(57) Erdmenger, T.; Vitz, J.; Wiesbrock, F.; Schubert, U. S. Influence of different branched alkyl side chains on the properties of imidazolium-based ionic liquids. *Journal of Materials Chemistry* **2008**, *18* (43), 5267-5273, 10.1039/B807119E. DOI: 10.1039/B807119E.

(58) Tang, J.; Tang, H.; Sun, W.; Plancher, H.; Radosz, M.; Shen, Y. Poly(ionic liquid)s: a new material with enhanced and fast CO2 absorption. *Chemical Communications* **2005**, (26), 3325-3327, 10.1039/B501940K. DOI: 10.1039/B501940K.

(59) Valkenburg, M. E. V.; Vaughn, R. L.; Williams, M.; Wilkes, J. S. Thermochemistry of ionic liquid heat-transfer fluids. *Thermochimica Acta* **2005**, *425* (1), 181-188. DOI: https://doi.org/10.1016/j.tca.2004.11.013.

(60) Ohtani, H.; Ishimura, S.; Kumai, M. Thermal Decomposition Behaviors of Imidazolium-type Ionic Liquids Studied by Pyrolysis-Gas Chromatography. *Analytical Sciences* **2008**, *24* (10), 1335-1340. DOI: 10.2116/analsci.24.1335.

(61) Han, D.; Row, K. H. Recent Applications of Ionic Liquids in Separation Technology. In *Molecules*, 2010; Vol. 15, pp 2405-2426.

(62) Fredlake, C. P.; Crosthwaite, J. M.; Hert, D. G.; Aki, S. N. V. K.; Brennecke, J. F. Thermophysical Properties of Imidazolium-Based Ionic Liquids. *Journal of Chemical & Engineering Data* **2004**, *49* (4), 954-964. DOI: 10.1021/je034261a.

(63) Jung, J.-H.; Jeon, J.-H.; Sridhar, V.; Oh, I.-K. Electro-active graphene–Nafion actuators. *Carbon* **2011**, *49* (4), 1279-1289. DOI: https://doi.org/10.1016/j.carbon.2010.11.047.

(64) Surana, K.; Singh, P. K.; Bhattacharya, B.; Verma, C. S.; Mehra, R. M. Synthesis of graphene oxide coated Nafion membrane for actuator application. *Ceramics International* **2015**, *41* (3, Part B), 5093-5099. DOI: https://doi.org/10.1016/j.ceramint.2014.12.080.

(65) Weber, R. L.; Ye, Y.; Schmitt, A. L.; Banik, S. M.; Elabd, Y. A.; Mahanthappa, M. K. Effect of Nanoscale Morphology on the Conductivity of Polymerized Ionic Liquid Block Copolymers. *Macromolecules* **2011**, *44* (14), 5727-5735. DOI: 10.1021/ma201067h.

(66) Li, S.; Zhang, Z.; Yang, K.; Yang, L. Polymeric Ionic Liquid-poly(ethylene glycol) Composite Polymer Electrolytes for High-Temperature Lithium-Ion Batteries. *ChemElectroChem* **2018**, *5* (2), 328-334, https://doi.org/10.1002/celc.201700984. DOI: https://doi.org/10.1002/celc.201700984 (acccessed 2023/06/13).

(67) Fan, F.; Wang, W.; Holt, A. P.; Feng, H.; Uhrig, D.; Lu, X.; Hong, T.; Wang, Y.; Kang, N.-G.; Mays, J.; et al. Effect of Molecular Weight on the Ion Transport Mechanism in Polymerized Ionic Liquids. *Macromolecules* **2016**, *49* (12), 4557-4570. DOI: 10.1021/acs.macromol.6b00714.

(68) Choi, U. H.; Lee, M.; Wang, S.; Liu, W.; Winey, K. I.; Gibson, H. W.; Colby, R. H. Ionic Conduction and Dielectric Response of Poly(imidazolium acrylate) Ionomers. *Macromolecules* **2012**, *45* (9), 3974-3985. DOI: 10.1021/ma202784e.

(69) Biswas, Y.; Banerjee, P.; Mandal, T. K. From Polymerizable Ionic Liquids to Poly(ionic liquid)s: Structure-Dependent Thermal, Crystalline, Conductivity, and Solution Thermoresponsive Behaviors. *Macromolecules* **2019**, *52* (3), 945-958. DOI: 10.1021/acs.macromol.8b02351.

(70) Akle, B. J.; Leo, D. J.; Hickner, M. A.; McGrath, J. E. Correlation of capacitance and actuation in ionomeric polymer transducers. *Journal of Materials Science* **2005**, *40* (14), 3715-3724. DOI: 10.1007/s10853-005-3312-x.

(71) Meek, K. M.; Elabd, Y. A. Polymerized ionic liquid block copolymers for electrochemical energy. *Journal of Materials Chemistry A* **2015**, *3* (48), 24187-24194, 10.1039/C5TA07170D. DOI: 10.1039/C5TA07170D.

(72) Allen, F. I.; Comolli, L. R.; Kusoglu, A.; Modestino, M. A.; Minor, A. M.; Weber, A. Z. Morphology of Hydrated As-Cast Nafion Revealed through Cryo Electron Tomography. *ACS Macro Letters* **2015**, *4* (1), 1-5. DOI: 10.1021/mz500606h.

(73) Danyliv, O.; Martinelli, A. Nafion/Protic Ionic Liquid Blends: Nanoscale Organization and Transport Properties. *The Journal of Physical Chemistry C* **2019**, *123* (23), 14813-14824. DOI: 10.1021/acs.jpcc.9b02874.

(74) Liu, S.; Montazami, R.; Liu, Y.; Jain, V.; Lin, M.; Zhou, X.; Heflin, J. R.; Zhang, Q. M. Influence of the conductor network composites on the electromechanical performance of ionic polymer conductor network composite actuators. *Sensors and Actuators A: Physical* **2010**, *157* (2), 267-275. DOI: https://doi.org/10.1016/j.sna.2009.11.022.

(75) Stalbaum, T.; Pugal, D.; Nelson, S. E.; Palmre, V.; Kim, K. J. Physics-based modeling of mechano-electric transduction of tube-shaped ionic polymer-metal composite. *Journal of Applied Physics* **2015**, *117* (11). DOI: 10.1063/1.4914034 (acccessed 6/11/2023).

(76) Choi, J.-H.; Ye, Y.; Elabd, Y. A.; Winey, K. I. Network Structure and Strong Microphase Separation for High Ion Conductivity in Polymerized Ionic Liquid Block Copolymers. *Macromolecules* **2013**, *46* (13), 5290-5300. DOI: 10.1021/ma400562a.

(77) Fang, Y.; Pence, T. J.; Tan, X. Nonlinear elastic modeling of differential expansion in trilayer conjugated polymer actuators. *Smart Materials and Structures* **2008**, *17* (6), 065020. DOI: 10.1088/0964-1726/17/6/065020.

(78) Porfiri, M.; Leronni, A.; Bardella, L. An alternative explanation of back-relaxation in ionic polymer metal composites. *Extreme Mechanics Letters* **2017**, *13*, 78-83. DOI: https://doi.org/10.1016/j.eml.2017.01.009.

(79) Shankar, R.; Ghosh, T. K.; Spontak, R. J. Dielectric elastomers as next-generation polymeric actuators. *Soft Matter* **2007**, *3* (9), 1116-1129, 10.1039/B705737G. DOI: 10.1039/B705737G.

(80) Tang, J.; Radosz, M.; Shen, Y. Poly(ionic liquid)s as Optically Transparent Microwave-Absorbing Materials. *Macromolecules* **2008**, *41* (2), 493-496. DOI: 10.1021/ma071762i.

(81) Wang, H.; Ming Tan, M. W.; Poh, W. C.; Gao, D.; Wu, W.; Lee, P. S. A highly stretchable, self-healable, transparent and solid-state poly(ionic liquid) filler for high-performance dielectric elastomer actuators. *Journal of Materials Chemistry A* **2023**, 10.1039/D3TA01954C. DOI: 10.1039/D3TA01954C.

(82) Ankit; Tiwari, N.; Ho, F.; Krisnadi, F.; Kulkarni, M. R.; Nguyen, L. L.; Koh, S. J. A.; Mathews, N. High-k, Ultrastretchable Self-Enclosed Ionic Liquid-Elastomer Composites for Soft Robotics and Flexible Electronics. *ACS Applied Materials & Interfaces* **2020**, *12* (33), 37561-37570. DOI: 10.1021/acsami.0c08754.

Chapter 7: Conclusions

The overall focus of this dissertation was on the development and investigation of PIL materials. Specifically, the research studies were designed to study the magnetic (CH 2-4), (ii) ionic (CH 5), and (iii) electrical (CH 6) stimuli-responsive behavior of PIL homopolymers and random and block copolymers containing PILs. One of the primary goals was to further the understanding of multi-component magnetically responsive poly(ionic liquids) (MPILs), and this effort was supported by the following investigations:

- CH 2—influence of a metal-coordinating co-monomer on metal-ion coordination structure and polymer-metal binding interactions as a function of metal species and concentration;
- CH 3—development of self-assembled MPIL nanostructures from polyelectrolyte-surfactant complexes and the examination of their applied magnetic stimuli response in solution and film states; and
- CH 4—magnetic behavior of MPIL copolymers and their self-assembled polyelectrolyte-surfactant complexes as a function of magnetic field strength and temperature.

This dissertation also sought to explore other important PIL responsive behaviors including salt- and electrical stimuli response. In CH 5 the salt-responsive behavior of multi-cation PILs was investigated by synthesizing and characterizing a novel all-polyelectrolyte PIL blocked with a weak cationic polyelectrolyte and examining its solution response to salt addition and its film self-assembly behavior. This work was performed to advance the field of all-PIL and multi-cation-based PIL block copolymer systems and explore the potential of these materials for multiple-stimuli responsive capabilities. Electrical stimuli response was examined by converting this PIL block copolymer and its corresponding homopolymer into electroactive polymer actuator materials. In CH 6, important electrochemical and thermal properties were determined, and the

electromechanical responsiveness of these materials was assessed under an applied DC voltage. Major findings and opportunities to extend this research are described in the following sections.

7.1. Magnetic Stimuli Response:

7.1.1. Magnetic and Chemical Investigation of Metal Coordinating MPIL Copolymers (CH 2)

As the field of magnetic poly(ionic liquid)s (MPILs) continues to expand into developing new MPIL systems and exploring new applications, more MPIL systems that are multi-component and/or contain chemical functionalities capable of metal ion-coordination will be encountered. However, the influence of metal coordinating co-materials on the paramagnetic transition metal complex structure and its binding interactions within multi-component MPIL polymers is not well understood. In an attempt to further understand the role of metal-coordinating co-materials in MPIL systems, an MPIL random copolymer containing a metal-coordinating acrylamide comonomer was systematically complexed with different concentrations of Co^{2+}, Fe^{3+}, and 1:1 molar ratio of Fe^{3+}/Co^{2+} chloride salts. A comprehensive spectroscopic investigation revealed changes to both the structure of the paramagnetic transition metal complex and its binding interactions with the polymer that was dependent on the transition metal type and concentration. In particular, both Raman and UV-vis analysis of [Pam-*co*-PDADMA][Co^{2+}] copolymers indicated the presence of tetrahedral structured Co^{2+} for all mole equivalencies of added metal studied, with this structure likely due to a combination of $[CoCl_4]^{2-}$ and various Co^{2+}-acrylamide coordination complexes (e.g., $[CoCl_2L_2]$, $[CoCl_3L]^-$, $[CoL_4]^{2+}[Cl]_2^-$, where L is the acrylamide ligand). The presence of $[FeCl_4]^-$ and $[Fe_2Cl_7]^-$ species was verified only in the [Pam-*co*-PDADMA][Fe^{3+}] and [Pam-*co*-PDADMA][Fe^{3+}/Co^{2+}] copolymers containing 2 and 3 molar equivalecies, while the [Pam-*co*-PDADMA][Fe^{3+} (1eq)] was found to contain only various Fe^{3+}-acrylamide coordination

complexes. These results demonstrate the influence of a metal-coordinating comonomer on the coordination structure of the paramagnetic metal species, resulting in a mixture of polymer coordinated metal species and the traditional MPIL $[FeCl_4]^-$ and $[CoCl_4]^{2-}$ paramagnetic species with the mixture dependent on the metal type and concentration. FTIR and XPS spectroscopies confirm that the dominate polymer-metal binding interaction results from coordination with the acrylamide at both O- and N-binding sites rather than electrostatic interactions typically found in homopolymer MPIL systems, confirming that the metal-coordinating comonomer does impact polymer binding interactions in MPIL systems.

The MPIL copolymer magnetic response and properties were also examined. All dry copolymers demonstrated attraction to a magnetic field while only the iron-containing copolymers with sufficient hydrophobicity were responsive to a magnet while in an aqeous solution. AC magnetic susceptibility studies of the MPIL copolymers revealed room temperature magnetic susceptibilities—ranging between ~18 $x10^{-6}$ to 44 $x10^{-6}$ emu/g—which are comparable to values of other MPILs reported in the literature. However, estimation of the effective magnetic moment from the AC susceptibility data and $\mu_{eff} = \sqrt{8\chi T}$ (assuming no magnetic correlations) indicates lower than expected spin-only values for high spin Fe^{3+} and Co^{2+} and similar $[FeCl_4]^-$ and $[CoCl_4]^{2-}$ containing magnetic ionic liquids (MILs) and MPIL systems. This suggests that metal-acrylamide coordination does indeed influence the magnetic properties of the MPIL copolymers. These results support the value in investigating the magnetic properties further through magnetometry to determine the presence of magnetic correlations or changes in magnetic behavior with temperature; these studies were then performed at a national lab, with the findings presented in CH 4.

7.1.2. Magnetically Responsive MPIL-Surfactant Complexes and Applied Magnetic Stimuli Response (CH 3)

As MPIL self-assembled structures are known to influence magnetic properties, inducing self-assembly in the MPIL random copolymers was examined in CH 3 along with the impact of self-assembly on stimuli responsive behavior. While most MPIL studies have been focused on synthesis and characterization of magnetic properties, few have examined their application in applied magnetic stimuli response where a magnetic field is used to direct the motion of or influence self-assembly behavior of MPIL structures. In CH 3, in addition to inducing self-assembly of the random MPIL copolymer [Pam-*co*-PDADMA][Co^{2+}] through complexation with sodium dodecyl sulfate (SDS) surfactant, magnetically responsive polyelectrolyte-surfactant complexes (MPILSDS) were successfully utilized to direct ordered structure in drop-cast films.

A combination of structural (DLS, Cryo-TEM), charge (ZP), and chemical characterizations of the self-assembly of the [Pam-*co*-PDADMA][Co^{2+}] copolymer and the non-magnetic [Pam-*co*-PDADMA][Cl^-] as a function of surfactant concentration revealed that the Co^{2+} chloride salts created additional charged groups on the MPIL copolymer for surfactant binding in addition to electrostatic interactions between the surfactant and PIL immobilized cation. This allowed for the formation of solution stable micellular structures, which were not present in the non-magnetic [Pam-*co*-PDADMA][Cl^-]-surfactant (PILSDS) complexes. Preliminary analysis of the air-dried complexes yielded (AC) magnetic mass susceptibilities of ~7-9 x 10^{-6} emu/g for the MPILSDS complexes compared to the ~18 x 10^{-6} emu/g of the neat [Pam-*co*-PDADMA][Co^{2+}] copolymer, indicating dilution of the metal species with surfactant addition as expected. It was attempted to manipulate or direct the motion of the MPILSDS complexes in solution as observed by optical microscopy of a droplet of the complexes ~1.8 cm from the face of a ~0.7 T neodymium magnet.

Unfortunately, no magnetic stimuli response was observed, likely due to the magnetic field being too weak or other factors influencing the Co^{2+} species, including possible hydration, partial dissociation from the MPILSDS complex, or dilution within the MPILSDS complex. As observed through AFM and GISAXS characterizations, a magnetic field was successfully implemented for inducing order in MPILSDS films drop-cast onto silicon wafers. MPILSDS complexes drop-cast in the presence of a magnetic field formed more cohesive lamellae with preferential orientation parallel to the substrate compared to films drop-cast without a magnetic field present, which yielded randomly oriented lamellae.

This study demonstrated, for the first time in the MPIL field, the ability to direct the self-assembled structure of MPIL materials with a magnetic field, thus *applying* the magnetic stimuli-response capabilities of the MPIL beyond simple magnetic attraction. This study also further demonstrated the importance of understanding how co-materials interact and influence MPIL materials. In this case, the paramagnetic species synergistically coordinated with both co-materials—surfactant and acrylamide comonomer—to influence the solution self-assembly mechanism of the polyelectrolyte-surfactant complexes. Utilizing the paramagnetic species in more active roles beyond its magnetic properties presents the opportunity to free the immobilized PIL group for association with other ionic materials, as was observed here with electrostatic interaction between the surfactant and quaternary ammonium group. With the paramagnetic species now incorporated into a self-assembled structure, magnetometry studies were performed in CH 4 to evaluate the influence of both structure and coordination on the magnetic properties.

7.1.3. Vibrating Sample Magnetometry Study of MPIL Copolymers and their Polyelectrolyte-Surfactant Complexes (CH 4)

Examining the magnetic properties and behaviors of MPIL systems is essential for informing their design and application. In many multi-component MPIL systems, magnetic interactions other than paramagnetic have been observed—particularly in block copolymer systems, blends, or modified homopolymer structures—as a result of self-assembled structure or increased confinement of the paramagnetic species. Metal-coordination structure can also play an important role in magnetic properties. In CH 2 and CH 3, evidence of metal coordination with the co-materials in the MPIL copolymers was revealed, with a possible reduction in the effective magnetic moment indicated in CH2. Therefore, in CH 4, a thorough vibrating sample magnetometry (VSM) study as a function of magnetic field strength and temperature was performed for select MPIL copolymers (developed in CH 2), [Pam-*co*-PDADMA][Cu^{2+} (1 and 2 eq)], MPILSDS Co^{2+} complexes (developed in CH 3), and MPILSDS Fe^{3+} complexes to evaluate the influence of metal-coordination and self-assembled structure on the magnetic behavior of these MPIL materials. Magnetometry results were also paired with structural (DLS/ZP, SEM), chemical (ATR-FTIR), and thermal (DSC) characterizations to inform the findings.

MPIL copolymers were found to be paramagnetic in the 50-300 K temperature range measured with weak ferromagnetic or antiferromagnetic correlations depending on metal type, concentration, and coordination structure. Application of a modified Curie Weiss law confirmed a reduction in the effective magnetic moment compared to expected spin-only values for the transition metal cations and values typically cited for $[FeCl_4]^-$ and $[CoCl_4]^{2-}$ species in the magnetic ionic liquid (MIL) and MPIL literature. Calculation of the effective magnetic moments based on the calculated Curie constant for [Pam-*co*-PDADMA][Fe^{3+}] and [Pam-*co*-PDADMA][Co^{2+}]

copolymers were lower than the expected spin values for high spin Fe^{3+} (S=5/2, 5.9 μ_B) and Co^{2+} (S=3/2, 3.88 μ_B) but higher than their corresponding low spin state (S=1/2, 1.73 μ_B). This suggests a potential mix of spin states in the MPIL copolymers as a result of multiple metal-coordinated acrylamide species and anionic $[FeCl_4]^-$ and $[CoCl_4]^{2-}$ species. These results further demonstrate the role of coordinating co-materials on the coordination structure of added paramagnetic species and on the resulting magnetic properties.

Magnetization and zero-field cooling/field cooling (ZFC-FC) studies of the MPILSDS complexes reveal strong antiferromagnetic interactions with a strong decrease in then $1/\chi$-T between 50 K and 190 K. In the MPILSDS Co^{2+} complexes, antiferromagnetic correlations were further verified by the large negative Weiss constants obtained by Curie-Weiss fitting. Comparison of the MPIL copolymer and MPILSDS complex effective moments, estimated by $\mu_{eff} = \sqrt{\chi T}$ at 300 K, shows larger moments for MPLSDS complexes at lower metal weight percentages versus MPIL copolymers without surfactant, indicating that the self-assembled structure of the MPILSDS complexes enhance magnetic coupling interactions, as has been previously observed in other self-assembled MPIL systems.

7.1.4. Future Directions in MPILs

Continued research efforts for these magnetically responsive polyelectrolyte-surfactant complexes will involve conducting a DLS/ZP study for [Pam-*co*-PDADMA][Fe^{3+}] as a function of surfactant concentration to determine the shift in critical aggregation concentration due to the added Fe^{3+} salts. Since MPILSDS Fe^{3+} demonstrated higher magnetic susceptibilities and effective magnetic moments (CH 4), an expansion of GISAXS studies on the film assembly of MPILSDS Fe^{3+} complexes as a function of surfactant concentration will lead to a better understanding of stimuli-response from the application of a magnetic field for inducing self-assembled structures.

Efforts to improve stimuli response in solution can be expanded by studies utilizing more hydrophobic components in the MPIL systems that can coordinate with or confine the metal species within a hydrophobic core of micellular structures. This might be accomplished by synthesizing a PIL block copolymer with a metal-coordinating co-block that forms the core of the micellular structure with the PIL block forming the stabilizing corona in water. Incorporating the paramagnetic species into the hydrophobic core of other structures, such as multi-lamellae or vesicle structures, would also support directed design of magnetically responsive delivery vehicles or similar nanoobjects with magnetically directed motion.

To expand the magnetization work presented in CH 4, low temperature (2-50 K) SQUID magnetometry studies and either electron paramagnetic resonance spectroscopy or Mössbauer spectroscopy studies at select temperatures would be needed to confirm antiferromagnetic behavior (i.e., identification of the Neet temperature) and determine metal ion spin state of select MPIL copolymer and MPILSDS complexes. Further XRD or WAXS/SAXS studies of the freeze-dried MPILSDS complexes will also aid in identifying the internal ordering structure and the resulting metal species coupling interactions (such as those observed in the magnetometry studies, CH 4).

7.2. Synthesis of an All-Polyelectrolyte Block Copolymer from a PIL and Weak Tertiary Amine Polyelectrolyte and its Solution and Film Self-Assembly (CH 5)

Investigation of self-assembly in PIL block copolymers in solution and in the bulk state have mainly been limited to PILs blocked with neutral polymers, with very few studies involving PILs blocked with other PILs or weak polyelectrolytes. All-polyelectrolyte block copolymers present an opportunity to expand PIL design parameters into multi-ion block polymers similar to that of di- or tri-cationic ionic liquids. CH 5 describes an attempt to advance the field of all-polyelectrolyte

PIL block copolymers through synthesis of a novel PIL-block-[weak polyelectrolyte] copolymer and examine its solution behavior in response to added salt. For the first time, the film self-assembly of an all-polyelectrolyte PIL block copolymer was also studied through a combined atomic force microscopy-infrared spectroscopy technique (AFM-IR).

Specifically, the PIL block copolymer poly[2-(dimethylamino) ethyl methacrylate]-*block*-poly[4-vinylbenzyl-3- butylimidazolium bis(trifluoromethylsulfonyl)imide] (PDMAEMA-*b*-PVBBImTf_2N) was synthesized through Cu(0) mediated atom transfer radical polymerization (ATRP). The PIL block was grown from a well-defined PDMAEMA macroinitiator. While the living nature of the PIL block polymerization could not be confirmed, covalent boding between the PDMAEMA and PVBBImTf_2N blocks was confirmed by FTIR, ^{1}H NMR, and NMR DOSY spectroscopy studies indicating the successful synthesis of the block copolymer.

Solution behavior and assembly of the block copolymer was examined with ^{1}H NMR spectroscopy and DLS size characterization revealing a combination of electrostatic interactions and hydrogen bonding interactions between the PDMAEMA and PVBBImTf_2N blocks. The study demonstrated salt responsive behavior of the synthesized block compolymer as seen by a collapse in structure upon addition of 10 mM KNO_3 to DMSO solution. The collapse is likely a result of partial ion exchange of the initial Tf_2N^- ions with NO_3^- ions and charge shielding of the repulsive interactions between PIL block chains. As the DLS particle sizes of the block copolymer in 10 mM KNO_3 DMSO were larger than the calculated contour length based on its degree of polymerization, the block copolymer is assembled into aggregate structures likely mediated by hydrogen bonding between PVBBImTf_2N/PDMAEMA blocks in 10 mM KNO_3 DMSO solution as evidenced in the ^{1}H NMR spectrum. This investigation of the solution behavior of the PDMAEMA-*b*-

PVBBImTf_2N block copolymer demonstrated stimuli-responsive self-assembly behavior triggered by KNO_3 salt addition.

The film self-assembly behavior of the drop-cast block copolymer was also examined using a novel technique for PILs, coupled AFM-IR. A matrix of PVBBImTf_2N with PDMAEMA spherical inclusions was observed. IR analysis confirmed that the spherical morphology primarily consisted of the PDMAEMA block in a matrix of PVBBImTf_2N. Small silica particle contaminates due to leaching (from the silicon wafer and/or glassware) were identified, and these were selectively contained within the PDMAEMA spheres. This finding indicates the potential of developing all-polyelectrolyte composites with hydrophilic inclusions, such as silica or iron oxide nanoparticles, to form self-assembled inorganic nanoparticle-polymer composites.

7.2.1. Future Directions for PDMAEMA-*b*-PVBBImTf_2N All-Polyelectrolyte Block Copolymer

As the PDMAEMA-*b*-PVBBImTf_2N block copolymer has a weak tertiary amine block, it has the potential to respond to changes in environmental pH as well as different types and concentrations of salt. These studies would best be carried in aqueous environments. However, the PIL block copolymer with Tf_2N^- had limited solubility in a range of solvents and would quickly precipitate out of solution upon the addition of even small quantities of water. If a similar PDMAEMA-*b*-PVBBIm[X^-] block copolymer was synthesized with more hydrophilic counterions (e.g., X = Cl^-, Br^-, NO_3^-), the block copolymer may have improved solubility in water as a common solvent for both polymer blocks. Solution self-assembly could then be induced through either the addition of different salts (e.g., NO_3^-, PF_6^-, Tf_2N^-) or similar acids (e.g., HNO_3, HTf_2N^-) to examine salt and pH responsive behavior. Note, it may be possible to ion exchange most of the Tf_2N^- in the current block copolymer with more hydrophilic anions; however, it would require large excess of the salt to drive the ion exchange reaction followed by additional purification steps. To synthesize

the more hydrophilic PDMAEMA-*b*-PVBBIm[X^-] block copolymer, a synthesis technique less sensitive to coordinating counterions, such as reversible addition-fragmentation chain transfer (RAFT) living radical polymerization, would be more advantageous versus atom transfer radical polymerization (ATRP) which is sensitive to these counterions.

Further examination of the film self-assembly could involve drop-casting the film from DMSO with different concentrations of KNO_3 or other additives such as ionic liquids or inorganic nanoparticles. Annealing time and temperature would also provide further parameters for exploration. As the polymer self-assembly was found to be dependent on film thickness, methods to control film thickness and uniformity would aid in these studies.

7.3. Evaluation of Novel Poly(ionic liquid) Block Copolymer and Homopolymer as Electroactive Polymer Actuators.

As inherently conductive materials, PILs are responsive to electrical stimuli. Currently, a growing field for PILs in electrical stimuli response involves employing them as electroactive polymer layers in applications such as actuators, sensors, and flexible electronics. In CH6, the PDMAEMA-*b*-PVBBImTf_2N block copolymer developed in CH 5 and its corresponding PVBBImTf_2N homopolymer were combined with 1-butyl-3-methyl imidazolium tetrafluoroborate ($C_4C_1ImBF_4$) ionic liquid to form ionogels, which were then evaluated as electroactive polymer actuators. In particular, a series of ionogels were developed for both polymer systems and evaluated for important thermal, chemical, morphology, and electromechanical parameters including ion conductivity, glass transition temperature, thermal stability, electrostatic interactions, Young's modulus, and morphology.

Thermal analysis of the PIL-based ionogels revealed improved stability of the PDMAEMA block with ionic liquid content but a decrease in the onset temperature for the PVBBImTf_2N block

as a result of loss of the immobilized imidazolium ring on the styrenic backbone to the ionic liquid phase. DSC analysis indicated an overall decrease in glass transition temperature with increasing ionic liquid content for the PDMAEMA-*b*-PVBBImTf_2N block copolymer and PVBBImTf_2N homopolymer which corresponded well with the increased ion conductivity from ~10^{-7} S/cm in the dry polymers to ~10^{-4} S/cm in the 40 wt% ionogels. These values compare and/or exceed the ion conductivities observed in similar PIL actuator systems at room temperature, confirming favorable ion conductivity for electroactive polymer layers.

Morphology and nanomechanical analysis of the ionogels with AFM revealed phase and Young's modulus changes with increasing ionic liquid content for ionogels made from both PVBBImTf_2N and PDMAEMA-*b*-PVBBImTf_2N. In particular, ionogels began to show phase separation at 40 wt% IL content and ionogels with 25 wt% IL content yielded Young's modulus of the matrix phase below 25 MPa, so mechanical integrity that is generally too low at least for film applications. Out of the samples examined, the dry polymers and 10 wt% IL ionogels were found to have the best combination of ion conductivity and modulus for micro-actuation with ion conductivities of ~10^{-7} to 10^{-6} S/cm and Young's moduli in the ca. 50-500 MPa range that has been observed for other PIL-based, Nafion, and PVDF ionogel actuators. Although their modulus is too low for ionic actuation applications, the 25-40 wt% ionogels had favorable thermal properties and ion conductivity that will benefit other electrochemical applications, including potentially dielectric elastic actuators (DEAs).

Micro-scale actuation was successfully achieved for the dry PVBBImTf_2N and PDMAEMA-*b*-PVBBImTf_2N polymers and their corresponding 10 wt% ionogels under an applied 4 V (DC). In particular, the PDMAEMA-*b*-PVBBImTf_2N block copolymer demonstrated actuation behavior with expected bending direction as other micro-scale PIL actuators in the literature. Radius of

curvature calculations indicate smaller actuation behavior than the literature values for PIL-actuators formed from styrenic ABA triblock copolymers but the actuation is comparable to other PIL micro-actuators as well as the PVDF 40 wt% IL control. The PVBBImTf_2N polymer and its 10 wt% ionogel also exhibited micro-scale actuation behavior; however, with unexpected tip-deflection towards the positive electrode or out-of-plane. This result may be due to a competing underlying electomechanical phenomenon other than ion migration, but further investigation on these systems is needed to confirm this result.

Overall, the PDMAEMA-*b*-PVBBImTf_2N block copolymer and corresponding PVBBImTf_2N homopolymer formed ionogels with good thermal stability, increased chain dynamics (i.e., reduced glass transition temperature), and increased ion conductivity making them strong candidates as electroactive polymers for micro-scale actuation or other flexible electronic or electromechanical sensor applications. This work demonstrates a novel PIL material system, beyond styrenic ABA block copolymers, for use as electromechanical ionic actuators.

7.3.1. Future Directions for PIL Electroactive Polymer Actuators

Future efforts for improving the mechanical properties of these and similar PIL-based ionogels as ionic actuators includes introducing reinforcing agents into the PIL layer that would be a cheaper and faster development method in comparison to systematic block copolymerization. A preliminary investigation into reinforced ionogel composites was initiated and is described in Appendix F. Fibrous materials (e.g., Whatman cellulose filter paper, filtration membranes) and graphene oxide were combined with PILs, poly[4-vinylbenzyl-3-butylimidazolium bis(trifluoromethylsulfonyl)imide] (PVBBImTf_2N) or poly[1-vinyl-3-ethylimidazolium bis(trifluoromethylsulfonyl)imide] (PVC_2ImTf_2N), and an ionic liquid, C_4C_1ImBF_4. Initial results indicate that graphene oxide addition into the ionogel up to ~6 wt% improves the qualitative

mechanical properties of the ionogels while still maintaining high ion conductivities (~10^{-5} to 10^{-4} S/cm). Tip-displacements of up to ~1.8 mm was achieved for the PVC_2ImTf_2N reinforced ionogel composite containing 40 wt% IL and 6 wt% GO. However, adhesion of the gold foil electrodes was reduced in comparison to the neat polymers resulting in electrode buckling during actuation testing. Future implementation could evaluate other types of flexible organic electrodes, such as carbon black or carbon nanotubes.

The development of functional block copolymer-based PIL actuators will likely require block copolymerization with stiffer polymer blocks or grafting to other polymers to improve the overall mechanical properties. As the majority of PIL-actuator work in the literature has involved combining PILs with polystyrene, the focus on future efforts should be the evaluation of non-styrenic polymer blocks, such as poly(methyl methacrylate) or poly(tert-butyl acrylate), to advance the PIL ionic actuator field.

Appendix A: Supplemental Information for Chapter 2

* This appendix contains the adapted supplemental information from the submitted journal article: Kayla Foley., Lucas Condes, Keisha B. Walters. "Influence of metal-coordinating comonomers on the coordination structure and binding in magnetic poly(ionic liquid)s," Submitted and under review April 2023, Molecular Systems Design and Engineering (RSC)

A.1. Magnetic Video Characterization

Supplemental videos showing magnetic attraction are included as supplementary files (see link). In each video, a magnet with a calculated surface field strength of 0.62 T was held close to the dry polymers or the [Pam-*co*-PDADMA][Fe^{3+}] and [Pam-*co*-PDADMA][Mixed Fe^{3+}/Co^{2+}] suspensions. Clear magnetic attraction was observed in all cases.

A.2. UV-Vis Spectra

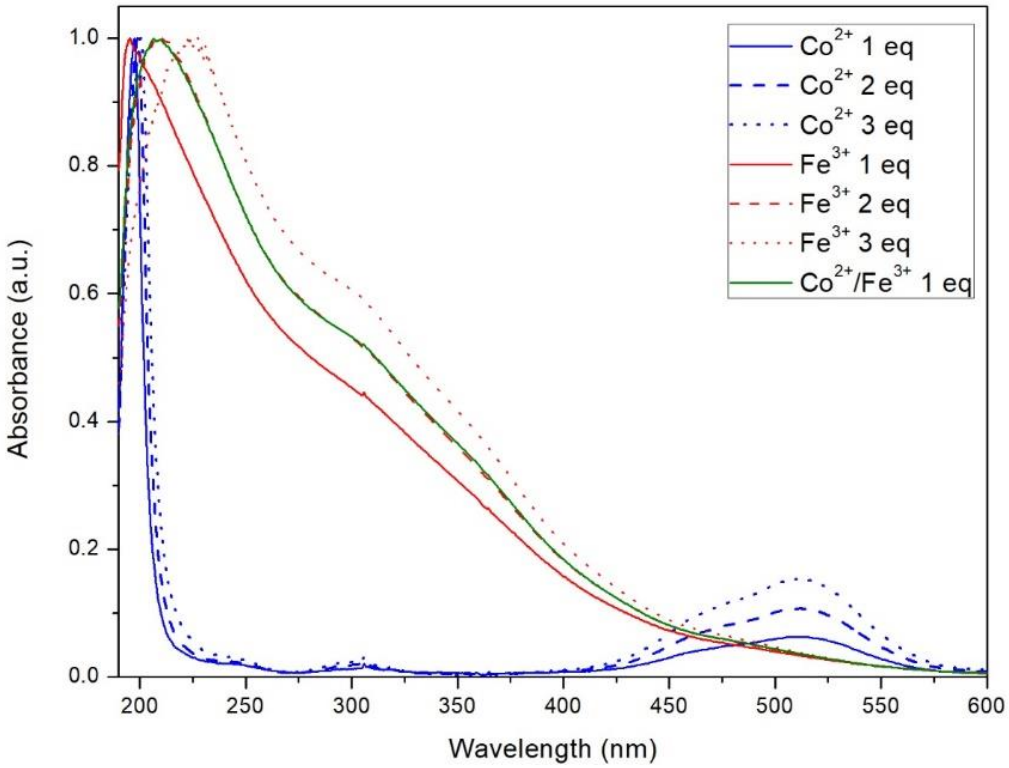

Figure A.1 UV-visible spectra of the salts $CoCl_2$ (blue), $FeCl_3$ (red), and their mixtures in aqueous solution without any added copolymer.

A.3. ATR-FTIR Spectra

Table A.1 ATR-FTIR frequencies of the amide N-H stretches, amide I, amide II, and metal hydroxide stretching and bending modes for the [Pam-*co*-PDADMA][X] copolymers where X indicates [Cl^-] anions or the transition metal salt complexes for each mole equivalence.

[Pam-*co*-PDADMA][X]	**Cl^-**	**Fe^{3+}**			**Co^{2+}**			**Mixed**		
Sample		**1eq**	**2eq**	**3eq**	**1eq**	**2eq**	**3eq**	**1eq**	**2eq**	**3eq**
N-H asym	3286	3330	3330	3330	3333	3333	3384[a]	3335	3335	3389[a]
N-H sym	3200	3190	3190	3190	3192	3196	3162[a]	3192	3192	3175[a]
Amide I (C=O str)	1662	1650	1643	1643	1656	1654	1648	1657	1650	1642
M-OH	--	--	--	1608	--	--	1620	--	--	--
Amide II (NH_2 wag)	1615	1574	1568	1565	1604	1599	1597	1607, 1572[b]	--	--
Amide III (N-C str)	1417	1417	1417	1417	1418	1417	1416	1418	1416	1416

a Peaks are related to the hydrated metal M-O-H stretch or bending modes overlapping with the amide modes.
b Peaks determined through peak deconvolution.

Table A.1 Cont.

[Pam-*co*-PDADMA][X]	**Metal Halide Salts**	
Sample	**$CoCl_2*6H_2O$**	**$FeCl_3*6H_2O$**
N-H asym	3522, 3383, 3163[a]	3526, 3386, 3217, 3005[a]
N-H sym	--	--
Amide I (C=O str)	--	--
M-OH	1618, 1643[a]	1595[a]
Amide II (NH_2 wag)	--	--
Amide III (N-C str)	--	--

a Peaks are related to the hydrated metal M-O-H stretch or bending modes overlapping with the amide modes.
b Peaks determined through peak deconvolution.

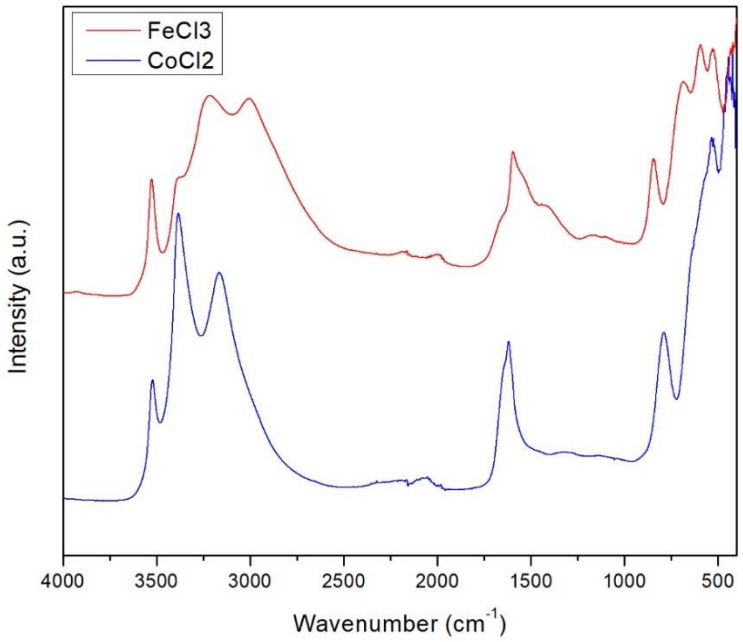

Figure A.2. ATR-FTIR spectra of the $CoCl_2$ and $FeCl_3$ salts with no added polymer

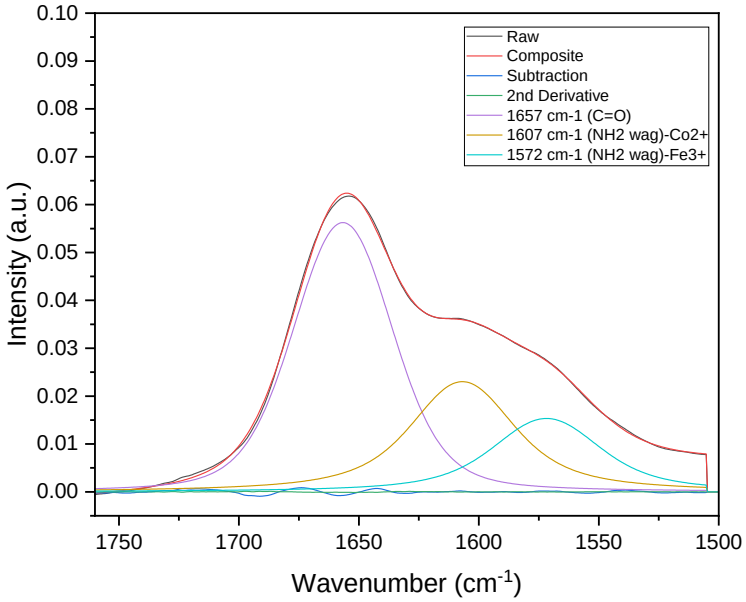

Figure A.3 Deconvolution result of the amide region for the [Pam-*co*-PDADMA][Mixed Fe^{3+}/Co^{2+} 1eq] ATR-FTIR spectra. The peak centers are located at 1657 cm^{-1} (amide I C=O), 1607 cm^{-1} (amide II-Co^{2+}), 1572 cm^{-1} (amide II-Fe^{3+}).

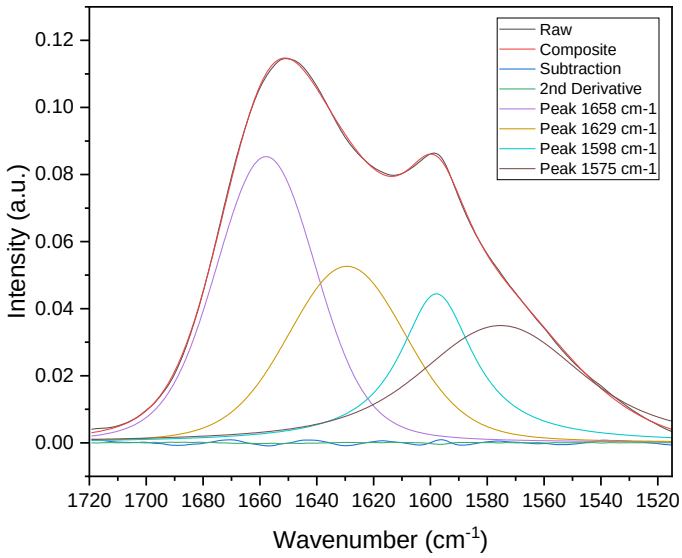

Figure A.4 Deconvolution result of the amide region for the [Pam-*co*-PDADMA][Mixed Fe^{3+}/Co^{2+} 2eq] ATR-FTIR spectra. Two peaks were observed for amide I C=O (1658 and 1629 cm^{-1}) and two peaks for amide II NH_2 wag (1598 and 1575 cm^{-1}).

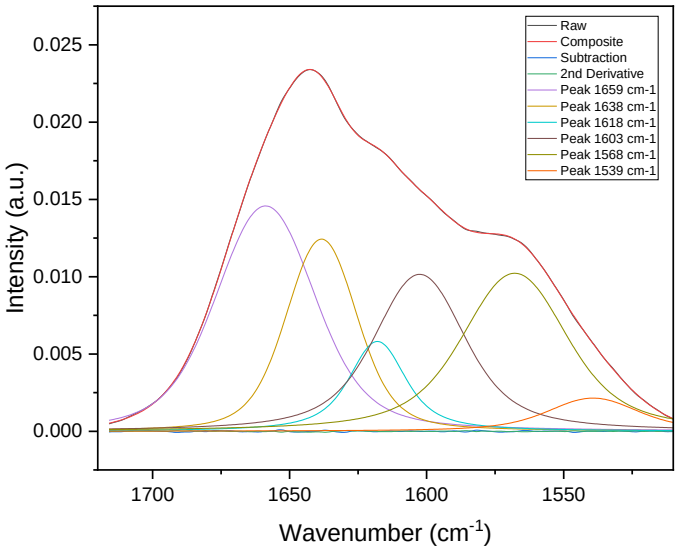

Figure A.5 Deconvolution result of the amide region for the [Pam-*co*-PDADMA][Mixed Fe^{3+}/Co^{2+} 3eq] ATR-FTIR spectra. Two peaks were observed for amide I C=O (1659 and 1638 cm^{-1}) and two peaks for amide II NH_2 wag (1603 and 1568 cm^{-1}). The peak at 1618 cm^{-1} is likely Co-OH from excess uncoordinated salt.

A.4. XPS Spectra

Table A.2 XPS peak positions (± 0.2 eV) and area percentages for collected high resolution spectra for the N1s, O1s, and C1s spectral ranges corresponding to the high resolution spectra shown in .

	N1s						**O1s**							
	PDADMA		*Pam*		*Pam-M*		*Pam*		*M-O*		*Water*		*Na KLL*	
Sample	Position	%	position	%	position	%	position	%	position	%	position	%	position	%
[Pam-*co*-PDADMA][Cl^-]	402.4	46.6	399.6	53.4	--	--	531.3	41.9	--	--	532.5	16.8	536.1, 538.0	41.4
[Pam-*co*-PDADMA][Co^{2+} 1eq]	402.4	45.0	400.0	55.0	--	--	531.9	94.5	--	--	533.6	2.0	536.1	3.5
[Pam-*co*-PDADMA][Co^{2+} 2eq]	402.6	44.8	400.2	27.6	402.1	27.6	532.3	83.7	--	--	533.5	12.2	536.3	4.0
[Pam-*co*-PDADMA][Fe^{3+} 1eq]	402.5	44.8	399.8	29.6	402.0	25.6	531.6	74.5	529.9	3.33	532.3	20.4	535.7	1.7
[Pam-*co*-PDADMA][Fe^{3+} 2eq]	402.5	44.8	400.0	37.4	402.3	17.9	531.8	88.3	530.1	9.96	533.3	1.8	--	--
[Pam-*co*-PDADMA][Mixed Fe^{3+}/Co^{2+} 1eq]	402.4	44.8	399.8	44.7	401.9	10.6	531.7	71.3	529.9	3.3	533.2	4.7	535.7	20.8

Table A.2 Cont.

		C1s					
		Aliphatic		*PDADMA*		*Pam*	
Sample		position	%	position	%	position	%
[Pam-*co*-PDADMA][Cl^-]		285.0	55.2	286.1	33.3	287.7	11.5
[Pam-*co*-PDADMA][Co^{2+} 1eq]		285.0	55.2	286.1	39.6	288.5	5.3
[Pam-*co*-PDADMA][Co^{2+} 2eq]		285.0	55.2	286.2	43.1	288.8	1.7
[Pam-*co*-PDADMA][Fe^{3+} 1eq]		285.0	47.7	286.2	45.0	288.1	7.3
[Pam-*co*-PDADMA][Fe^{3+} 2eq]		285.0	55.7	286.3	37.9	288.6	6.4
[Pam-*co*-PDADMA][Mixed 1eq]	Fe^{3+}/Co^{2+}	285.0	55.1	286.2	34.0	288.1	10.9

Table A.3 XPS peak positions (± 0.2eV) for the Fe $2p^{3/2}$, Co $2p^{3/2}$, and Cl $2p^{3/2}$ peaks in the respective 2p high resolution spectra shown in Figure 8 of the main text.

	Metals		Cl $2p^{3/2}$		
Sample	Fe $2p^{3/2}$	Co $2p^{3/2}$	Main Species	Minor Species	Ref.
[Pam-*co*-PDADMA][Cl^-]	--	--	198.8	--	This work
[Pam-*co*-PDADMA][Co^{2+} 1eq]	--	781.6	198.4	--	This work
[Pam-*co*-PDADMA][Co^{2+} 2eq]	--	781.9	198.8	200.1	This work
[Pam-*co*-PDADMA][Fe^{3+} 1eq]	710.9	--	198.4	200.2	This work
[Pam-*co*-PDADMA][Fe^{3+} 2eq]	711.4	--	198.7	200.2	This work
[Pam-*co*-PDADMA][Mixed Fe^{3+}/Co^{2+} 1eq]	710.9	781.3	198.4	200.0	This work
$FeCl_3$	711.5		199.7		Grosvenor et al. [1]
$FeCl_3$, Russo et al.	712.0		199.0		Russo et al. [2]
$[Et_4N^+][FeCl_4]^-$	711.2		198.6		Russo et al. [2]
$[C_8C_1Im^+][FeCl_4]^-$	711.9		199.4		Taylor et al. [3]
$[C_8C_1Im^+][CoCl_4]^{2-}$		780.6	198.2		Taylor et al. [3]
$CoCl_2$		782.1			Brown et al. [4]

XPS survey spectra for all samples are shown below.

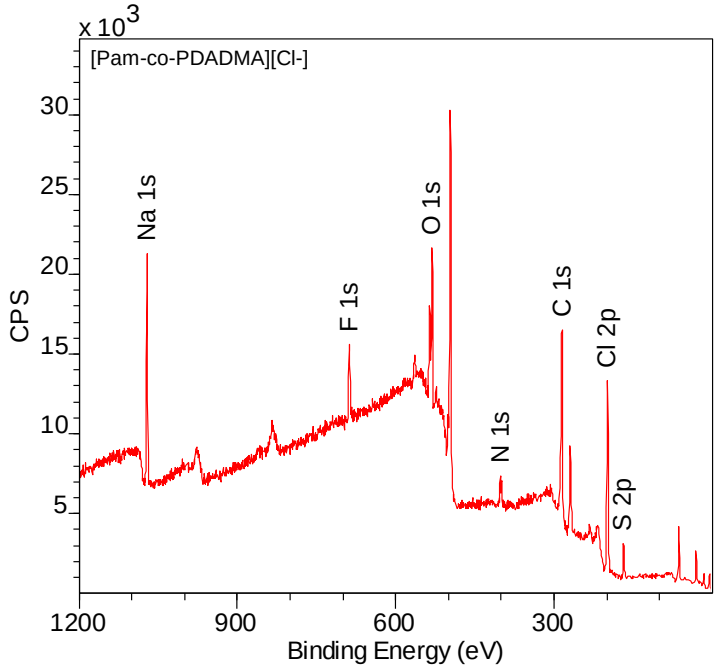

Figure A.6 XPS survey spectrum for [Pam-*co*-PDADMA][Cl^-].

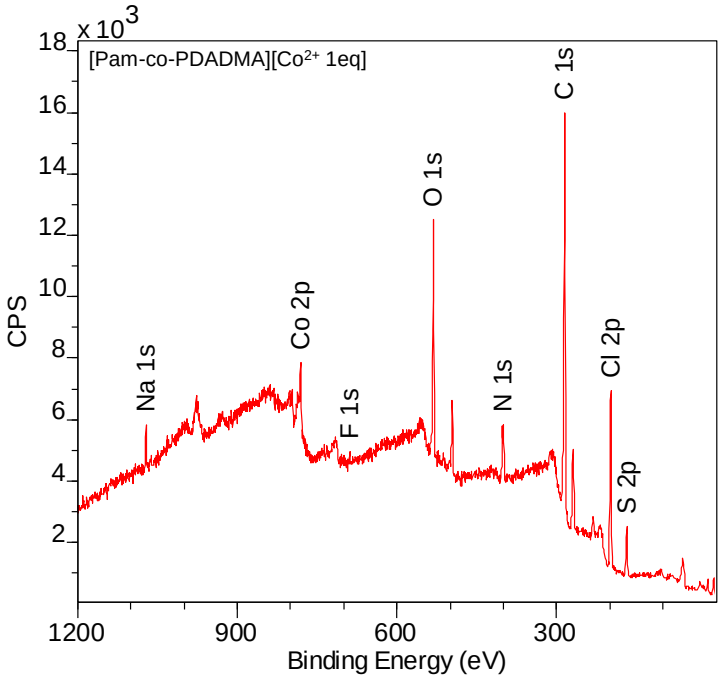

Figure A.7 XPS survey spectrum for [Pam-*co*-PDADMA][Co^{2+} 1eq].

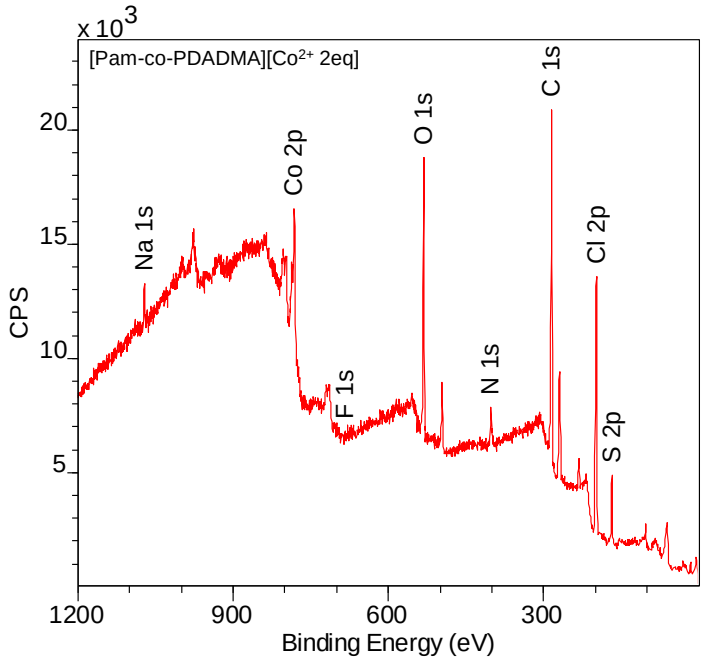

Figure A.8 XPS survey spectrum for [Pam-*co*-PDADMA][Co^{2+} 2eq].

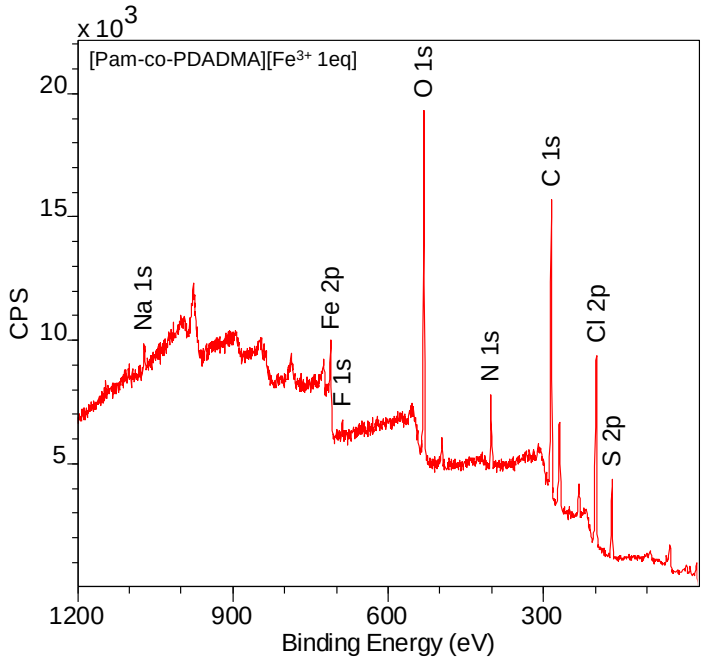

Figure A.9 XPS survey spectrum for [Pam-*co*-PDADMA][Fe^{3+} 1eq].

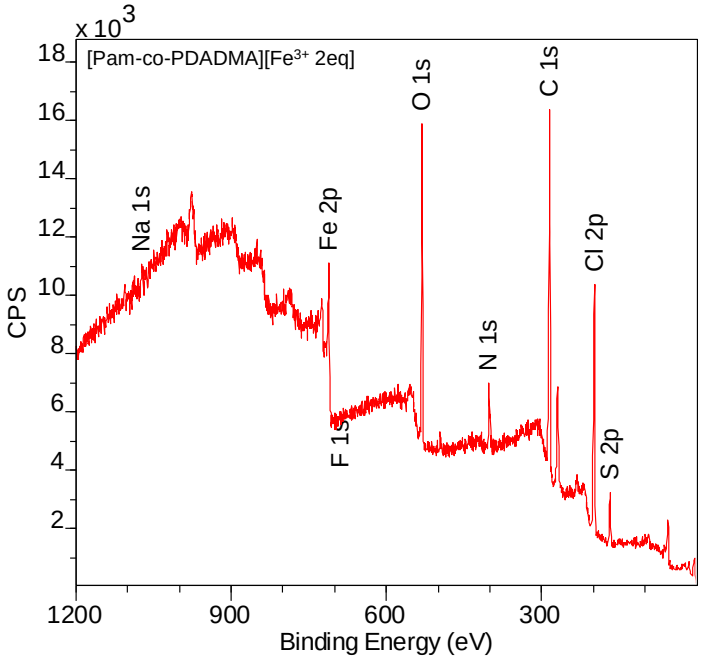

Figure A.10 XPS survey spectrum for [Pam-*co*-PDADMA][Fe^{3+} 2eq].

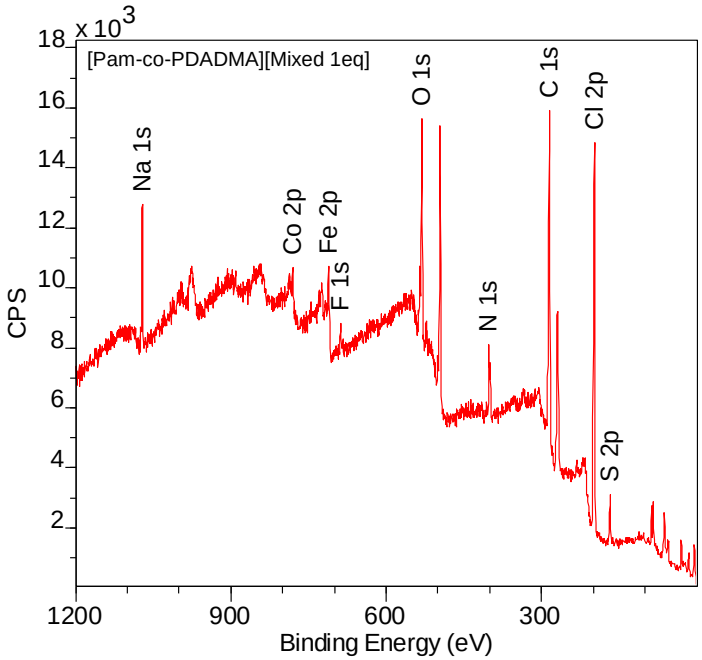

Figure A.11 XPS survey spectrum for [Pam-*co*-PDADMA][Mixed 1eq].

A.5. Comparison of Metal Coordination in Polyacrylamide Homopolymer

A.5.1. Synthesis of Polyacrylamide.

All materials and reagents were used as received from the vendor without any further purification. Ultrapure acrylamide monomer was purchased from VWR Life Science, potassium persulfate (radical initiator) was purchased from Fisher Scientific, and ultrapure type 1 water was prepared in-house by a Synergy® UV-R water purification system. Ultrapure acrylamide monomer (7.07 g, 99.5 mmol), ultrapure type 1 water (200 mL), and initiator potassium persulfate (69.6 mg, 0.259 mmol) were added to a three-necked round-bottom flask equipped with a reflux condenser. The reaction mixture was degassed by nitrogen sparge for 30 minutes before being heated to 45 °C in a water bath under stirring. The polymerization was performed for 2 h under stirring at temperature. The highly viscous reaction mixture was immediately precipitated into 500 mL of acetone, collected, redissolved into 200 mL of water, and then precipitated into a 400 mL of 3:1 acetone:water solution by volume, and then left under stirring for ten minutes. The isolated polyacrylamide product was collected and dried under vacuum at ambient temperature for 48 h.

A.5.2. ATR-FTIR Comparison of Polyacrylamide Homopolymer and the [Pam-*co*-PDADMA][Cl^-] Copolymer.

The neat homopolymer poly(acrylamide) synthesized *via* conventional free radical polymerization was characterized using ATR-FTIR (Figure A.2). A dried film of the neat poly(acrylamide) displayed amide I (C=O str) and amide II (NH_2 wag) bands at 1651 cm^{-1} and 1608 cm^{-1}, respectively. Compared to the unmodified commercial [Pam-*co*-PDADMA][Cl^-] copolymer used in the main study of this work, the amide I band was downshifted 11 cm^{-1} and the amide II band was downshifted 7 cm^{-1} in the poly(acrylamide) homopolymer.

The [Pam-*co*-PDADMA][Cl^-] copolymer is expected to have less intramolecular hydrogen bonding interactions occurring between the hydrogen bond donor (C=O) and acceptor (NH) in the amide groups occurring due to steric hinderance introduced by the diallyl dimethyl ammonium comonomer compared to the poly(acrylamide) homopolymer. The higher wavenumbers observed in the [Pam-*co*-PDADMA][Cl^-] copolymer for the amide I (C=O str) reflect this decrease in self-hydrogen bonding of the amide groups as a result of the shorter C=O bond compared to the longer C=O bond in hydrogen bonded -C=O···H_2N-. However, hydrogen bonding at the NH_2 group is expected to increase the frequency at which the Amide II (NH_2 wag) band occurs[5]. As the amide II band is found at a higher wavenumber in the copolymer compared to the neat poly(acrylamide) homopolymer, this suggests the NH_2 is receiving a hydrogen bond interaction from another other source. Tentatively, this hydrogen-bonding source is attributed to the Cl^- counterions associated to the quaternary ammonium groups in the copolymer (R-NH_2···Cl^-) acting as a proton acceptor group.

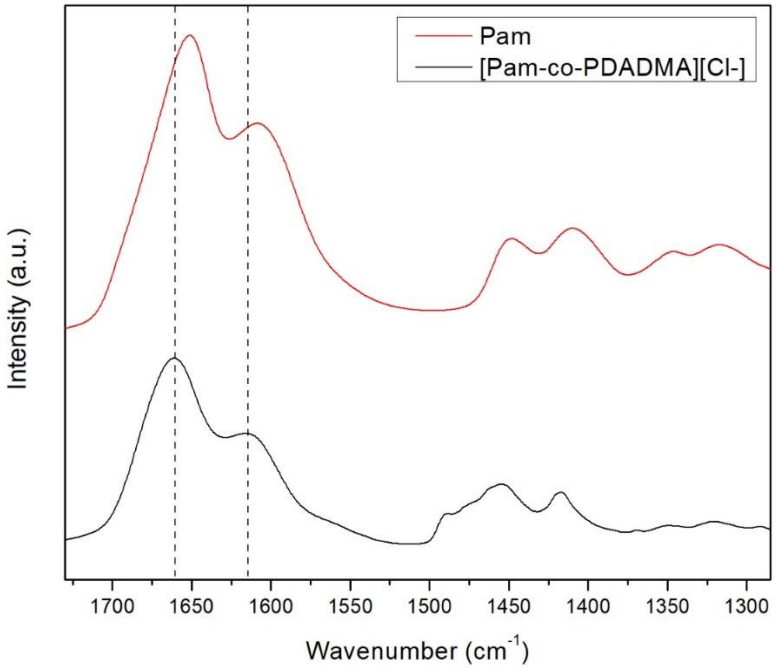

Figure A.12 ATR-FTIR spectra of the poly[acrylamide-*co*-diallyl dimethyl ammonium chloride] copolymer and poly(acrylamide) homopolymer. The dotted lines indicate the observed shifts in the amide I and amide II bands.

A.6. References

(1) A. P. Grosvenor, B. A. Kobe, M. C. Biesinger and N. S. McIntyre, *Surface and Interface Analysis*, 2004, **36**, 1564-1574.

(2) M. V. Russo, G. Polzonetti, A. Furlani, A. Bearzotti, I. Fratoddi and P. Altamura, *Journal of Vacuum Science & Technology A*, 1998, **16**, 35-44.

(3) A. W. Taylor, S. Men, C. J. Clarke and P. Licence, *RSC Advances*, 2013, **3**, 9436-9445.

(4) D. G. Brown and U. Weser, 1979, **34**, 1468-1470.

(5) R. M. Silverstein and G. C. Bassler, *Journal of Chemical Education*, 1962, **39**, 546.

Appendix B: Vibrating Sample Magnetometry of Magnetic Poly(ionic liquid) Copolymers and their Surfactant Complexed Nanostructures

* Kayla Foley, Keisha Walters. DOE Center for Integrated Nanotechnologies (CINT) User Proposal 2022AU0062 (June 28th, 2022 – Dec. 31st , 2023), Funded

What is(are) the main scientific questions(s) being addressed in this user project, including the connection to nanoscience?

The scientific question that needs to be answered is how polymer-metal ion coordination in magnetic poly(ionic liquid) (MPIL) multicomponent systems affects magnetism type and behavior. Our overall objective is to examine the magnetic properties of MPIL copolymers containing metal-coordinating pendant groups. Specifically, we will utilize magnetometry to examine the role of polymer-metal ion interactions on magnetic behavior as a function of metal-ion type and concentration. It is well known that metal ion coordination plays a significant role in the electron spin state and thus magnetic behavior of transition metal complexes. Investigating the role of polymer-metal coordination on the magnetic properties of these multicomponent MPIL systems is needed to guide the appropriate selection of co-materials or modifying functional groups in the design and nano-assembly of these materials. The relationship between magnetic properties and polymer chemistry examined in this study will direct the development of magnetically responsive nanomaterials, such as self-assembled MPIL block copolymers or MPIL composites with non-magnetic nanomaterials (e.g., silica particles, graphene, etc.) for applications in organic magnets, magnetic separations, stimuli-response, and more.

Briefly describe the state of research in this area and how your work is advancing the field.

MPIL systems that have displayed magnetism (other than paramagnetic)—including antiferromagnetic [1], ferromagnetic [2, 3], and superparamagnetic [4, 5]—have mainly consisted of multicomponent materials such as blends, copolymers, or homopolymers modified with functional groups. These efforts have primarily involved increasing magnetic coupling by reducing the distance between metal ions. Self-assembled block copolymers and blends induce nanophase confinement of metal content [2]. Integration of π-π functional groups into the polymer structure can reduce the distance between polymer chains and metal ions [4, 5]. In most cases, the co-materials and modified structures contain functional groups capable of metal ion coordination, such as N, O, or S atoms, which can alter the coordination of the paramagnetic complex and consequently the magnetic behavior of the multicomponent MPIL systems. The proposed study will advance the field by (1) determining the type of magnetism produced in metal coordinating MPIL systems in different temperature ranges and (2) providing data for a series of MPIL copolymers to allow for the development of models to guide the design of more complex MPIL multicomponent systems with ferromagnetic/superparamagnetic properties or enhanced paramagnetic susceptibilities.

What is (are) the expected impact(s) of this user project?

This user project will contribute to the completion of a PhD dissertation. Our findings will be published in 1+ peer-reviewed journal manuscript and presented as a conference paper at 1+ (inter)national conference, such as the American Chemical Society or Materials Research Society. The results obtained in this project will also provide preliminary data for proposals submitted to federal agencies, with the goal of developing new magnetically responsive nanomaterials for magnetic switches or magnetofluids. Specifically, the work will provide guidance to select appropriate co-block chemistries to form magnetically responsive block copolymer nanostructures. With regards to graduate student training, this project offers an excellent

opportunity for the PhD student to gain hands-on experience working alongside senior instrument scientists at a national laboratory and build their network in the scientific community.

What specific work will be performed at the user's institution in preparation for, or in support of, the proposed CINT work?

We have prepared MPIL copolymer samples through the complexation of different molar equivalents of $FeCl_3$ and $CoCl_2$ salts with a poly(acrylamide-co-diallyl dimethyl ammonium chloride) copolymer (Figure B1.1a). These metal-PIL materials have been thoroughly characterized for their metal-polymer interactions in dry and wet states using XPS, FTIR, and Raman and UV-Vis spectroscopies. We performed an initial AC magnetic mass susceptibility study at room temperature using an M1F1 Kappabridge instrument. The metal-PILs display magnetic mass susceptibilities of 17 to 44 x 10^{-6} emu/g, depending on the metal type and concentration of metal salts in the copolymer (Figure B1.1b). The samples ($\geq$ 100 mg) for this study are ready for shipment. We will focus the CINT magnetic characterization study on cobalt and iron MPIL samples with $\leq$ 2 equivalents of metal. Prior work has shown these materials can be induced to nano-assemble through surfactant addition, forming spherical and oblong nanostructures with diameters from 100 to 500 nm (determined by DLS and cryo-TEM) depending on surfactant concentration. The MPIL/surfactant systems are also magnetically responsive as dried powders and films[6]. Self-assembled structure has the potential to increase magnetic coupling of the metal ions through nanoconfinement, leading to non-paramagnetic behavior, such as ferromagnetism. Therefore, magnetometry data for select MPIL/surfactant samples will support future studies for these self-assembled nanostructures and their resultant magnetic properties. As

low temperatures strengthen magnetic response, we will also perform DSC studies on MPIL copolymers in the 185-300 K range.

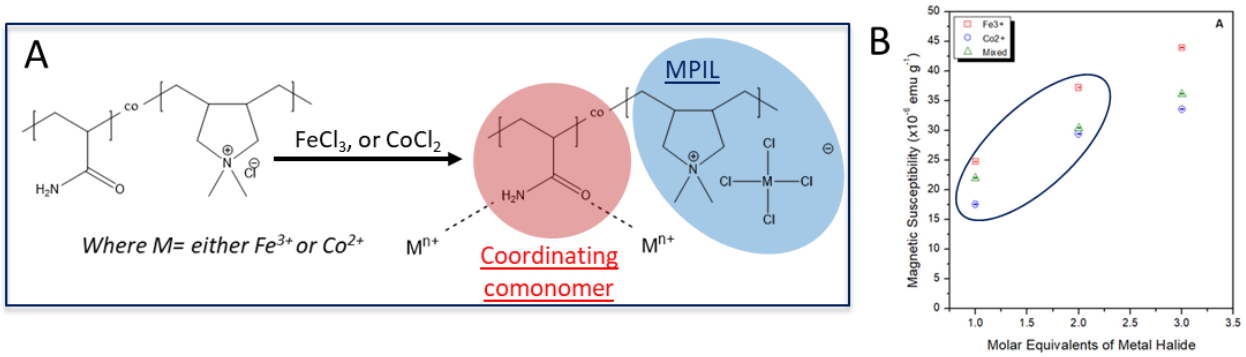

Figure B.1 (a) MPIL copolymer synthesis through metal halide complexation. (b) AC magnetic mass susceptibility data for dry powders. Circled samples are the focus of this study.

What specific tasks will be performed by the user(s) in conjunction with CINT?

We are proposing two experimental schemes. First, we will investigate the magnetic properties of a series of MPIL copolymers as a function of metal type and concentration using the PPMS Versalab instrument in collaboration with CINT staff scientist Dr. Dale Huber at Sandia National Laboratories (SNL). Specifically, we will measure the magnetization of each sample over the full magnetic field strength range of ± 3 Telsa at three temperatures (50, 150, and 300 K). The magnetization curves vs. field strength will be examined for any hysteresis or deviations from paramagnetic behavior as a function of temperature which will provide the type of magnetism for these materials. We will also calculate the magnetic susceptibility from these results through curve fitting in the linear region to compare to our previous AC magnetic susceptibility measurements. Each experiment is expected to take ~3.5-4 hours/sample, including sample preparation and analysis time. Six samples in total will be analyzed: the iron and cobalt MPILs at 1 and 2 metal equivalents (data circled in Fig. 1b) and two MPIL-surfactant samples at different surfactant concentrations. All samples will be prepared by placing the solid powders in straw-holders for analysis. The diamagnetic contribution of the sample holder will be subtracted out prior to analysis.

The full experimental setup is expected to take 3-4 days to complete. If necessary, the analyzed sample set can be reduced to four samples, namely the cobalt 1 and 2 equivalent samples and MPIL-surfactant samples system, where the focus would be on metal concentration, temperature, and surfactant induced self-assembled structure. One PhD student, and possibly a postdoc, will travel to SNL to perform the experiments onsite after initial training. While our previous AC susceptibility measurements can provide an idea of magnetic strength for the material, it cannot discern the type of material magnetism. Magnetometry, with either SQUID or a Vibrating Sample Magnetometer (VSM), is required to determine the magnetism type and is the traditional method to evaluate MPIL magnetic properties. The PPMS Versalab instrument will allow us to evaluate the magnetic behavior of weakly magnetic material in the low-temperature range of interest. Our university does not have access to a SQUID or VSM magnetometer capable of these temperatures of interest. Further, Dr. Huber's expertise in magnetometry and background in polymer science is ideal for guiding the graduate student in appropriate sample preparation for the instrument, data collection, and analysis of these particular magnetic polymer systems.

Key References:

(1) A. Bonnefond,et al. *J Polym Sci Part A: Polym Chem* 2016, **54**:1145-1152.

(2) P. M. Carrasco, et al. *Macromol* 2013, **46**:1860-1867.

(3) X. Yu, et al., *Macromol* 2021, **54**:4227-4235.

(4) J. Cui, et al. *RSC Adv* 2012, **2**:12224-12230.

(5) X. Yu, et al. *ACS Macro Lett* 2019, **8**:1504-1510.

(6) K. Foley and K.B Walters, *FEDSM2022*, 2022 (in print).

Appendix C: Magnetometry Studies of Magnetic Poly(ionic liquids) Using Surfactant Complexation to Direct Self Assembly and Increase the Effective Moment

***** This chapter is written in preparation for journal submission: Kayla Foley[1], Charles P. Easterling[2], Dale Huber[2], Keisha B. Walters[1]. "Magnetometry Studies of Poly(ionic liquid)s Using Surfactant Complexation to Direct Self Assembly and Increase the Effective Moment."

[1] Ralph E. Martin Department of Chemical Engineering, University of Arkansas, Fayetteville, AR 72701, USA

[2] Center for Integrated Nanotechnologies, Sandia National Laboratories, Albuquerque, NM 87123, USA

C.1. Data Processing for the Magnetization vs Temperature (MVT) Measurements:

The ZFC-FC curve moment data was examined normalized by mass (M-T and χT-T curves) and converted to molar susceptibility to allow for fitting to the Curie Weiss law (1/χ-T curve). Moment data was converted to molar susceptibility using the following equation[1]:

$$\textbf{EQ C-1}\quad \chi_{mol}[emu\,mol^{-1}Oe^{-1}] = \left(\frac{M[emu]}{H[Oe]}\right)\left(\frac{MW[g\,mol^{-1}]}{m[g]}\right)$$

where χ_{mol} is the molar susceptibility, M is the measured magnetic moment, H is the applied magnetic field strength, m is the sample mass, and MW is the molecular weight of the sample. The molar susceptibility was determined in two ways, (1) based on only metal salts contribution and (2) based on the full polymer molecular weight.

For the former case, using only the metal salts contribution to mass and molecular weight allowed for a more direct comparison of the calculated effective magnetic moments with the Fe^{3+}

and Co^{2+} species' spin-only effective magnetic moments and with other small molecule paramagnetic materials such as magnetic ionic liquids (MILs) and magnetic surfactants (Mag-Surf). Alternatively, the latter case based on the polymer's full molar mass allows for comparison with other MPIL systems such as the MPIL homo- and copolymers produced by Alard et al. 2017[2]. The authors provide an example calculation of both cases in the following sections.

C.1.1. Converting to molar susceptibility based only on metals content:

The [Pam-*co*-PDADMA][Co^{2+} 1eq] MPIL copolymer was synthesized by combining 1.11 g of copolymer [Pam-*co*-PDADMA][Cl^-] with 0.736 g of $CoCl_2$, resulting in a copolymer consisting of 39.8 wt% $CoCl_2$. The total amount of sample added to the polycarbonate capsule was 0.1041 g, resulting in a metals content mass, m, of 0.041483 g of $CoCl_2$. The MW of $CoCl_2$ is 129.839 g/mol. For a magnetic field strength of 100 Oe and a measured moment of 0.00139 emu, the molar susceptibility is calculated to be 0.0279 emu/mol utilizing equation EQ C-1. A similar calculation determining the molar susceptibility based on per mole of Co^{2+} resulted in the same effective moment.

C.1.2. Converting to molar susceptibility based only on metals content:

The molecular weight for the MPIL was derived similarly as the method done by Alard et al. [2] GPC results indicate the base copolymer [Pam-*co*-PDADMA[Cl-] has a M^n of 142,874 g/mol (PDI 1.941). As the copolymer consists of 55 wt% Pam (unit MW 71.087 g/mol) and 45 wt% PDADMA (unit MW 161.671 g/mol), it was determined the polymer consists of ~398 units of PDADMA and ~1105 units of Pam. The $CoCl_2$ was added at n=1 or 2 mole equivalent with respect to the PDADMA group. Therefore, the total molecular weight of the MPIL copolymer was determined to be $M_n^{MPIL} = M_n^{PIL} + DP_{Pam}(MW_{CoCl_2} * n)$. In the case of [Pam-*co*-PDADMA][Co^{2+} 1eq], the total molecular weight was determined to be $M_n^{MPIL} = 194{,}549$ g/mol. For a magnetic field

strength of 100 Oe and a measured moment of 0.00139 emu, the molar susceptibility is calculated to be 30.1 emu/mol utilizing equation EQ C-1 and the polymer molecular weight.

C.1.3. Applying Curie-Weiss Law

The molar susceptibility was converted to a $1/\chi$-T plot and fitted to both the Curie-Weiss (CW) equation:

$$\textbf{EQ C-2}\ \chi = \frac{C}{T-\theta_{CW}}$$

and to a modified version of the Curie Weiss (MCW) equation:

$$\textbf{EQ C-3}\ \chi = \frac{C}{T-\theta_{CW}} + \chi_o$$

where χ is molar susceptibility, C is the material dependent Curie constant, T is the temperature in Kelvin, θ_{CW} is the Curie-Weiss temperature, and χ_o is a temperature independent susceptibility contribution. OriginPro 2022 was used to perform all fittings. Figure C.2 - Figure C.7 below show the $1/\chi$-T curve for the fittings for the CW and MCW laws for all MPIL copolymers.

Figure C.1, shows several different fittings of the Curie-Weiss law attempted initially. A full linear fitting of the data was first performed to visualize any deviations from the linearity required for the Curie-Weiss law (Figure C.1a). In the case of [Pam-*co*-PDADMA][Co^{2+} 1eq], a positive small curvature was observed leading to deviations from linearity at the low and high temperature ends as well as a center section.

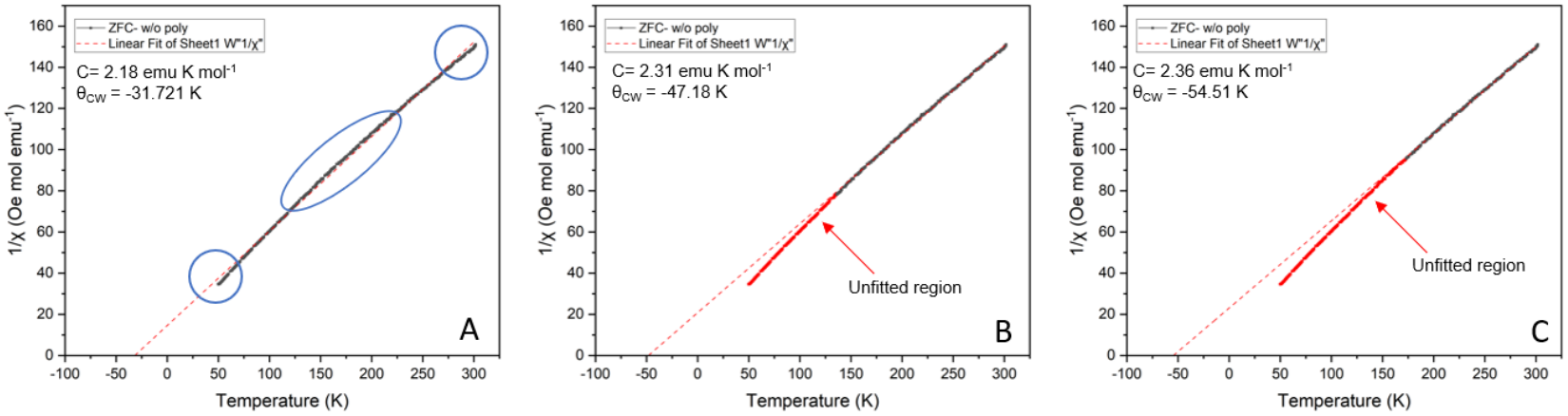

Figure C.1 Initial Curie-Weiss law fitting attempts for the for [Pam-*co*-PDADMA][Co^{2+} 1eq] $1/\chi$-T data (a) over the full data range and over (b and c) temperature ranges where no visual deviations from linearity were observed.

When the data was then refitted in the higher temperature range to avoid deviations from linearity as done by other MPIL literature[3, 4], it was found (as expected) the choice of where the linearity ends significantly influences the slope and intercept determined, leading to different μ_{eff} and significantly different θ_{CW} values (Figure C.1 b and c).

The data was then refitted to the modified Curie-Weiss law, which accounts for temperature independent contributions to the susceptibility. OriginPro 2022 was used to perform the fitting using a Levenberg Marquardt iteration algorithm and initial parameters determined from the linear fitting results. As shown in Figure C.2, the $1/\chi$-T curve for [Pam-*co*-PDADMA][Co^{2+} 1eq] was well fitted by the modified Curie-Weiss law and resulted in C= 1.70 emu K mol^{-1}, θ_{CW} = -10.88 K , and μ_{eff} = 3.69 μ_B. The χ_o = 0.00123 emu/mol is a temperature independent contribution to susceptibility. See the main text for further discussion.

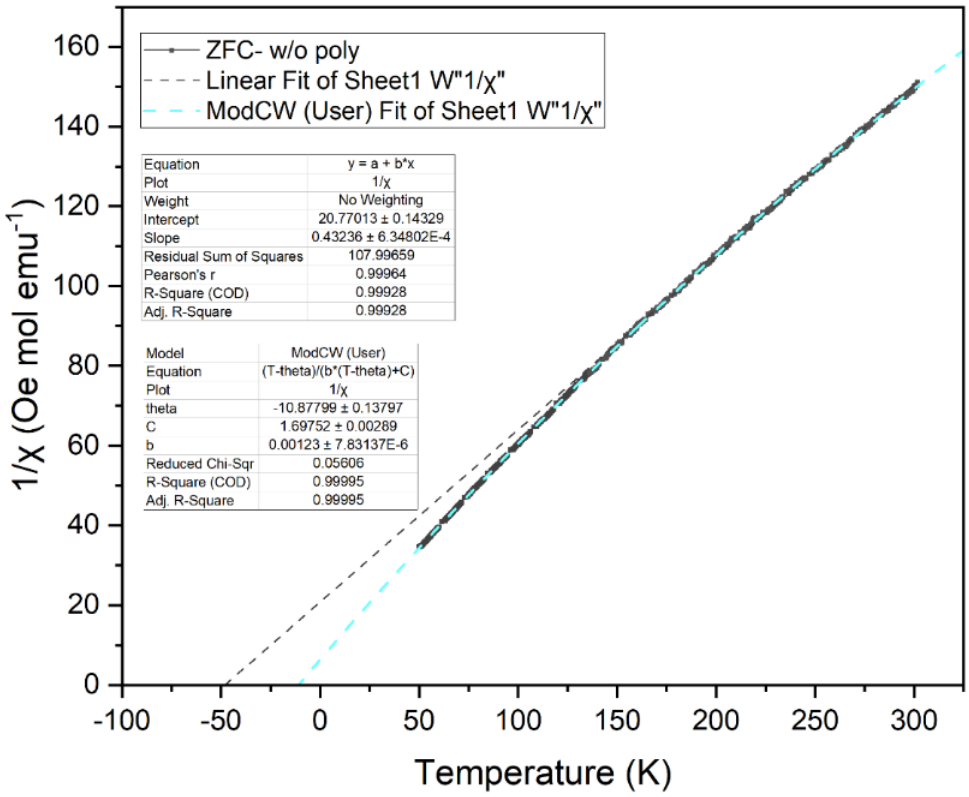

Figure C.2 1/χ -T plot for [Pam-*co*-PDADMA][Co^{2+} 1eq]. The grey and blue dotted lines show the Curie-Weiss and Modified Curie-Weiss fittings, respectively. The Curie-Weiss fitting results in C= 2.31 emu K mol^{-1} , θ_{CW} = -48.04 K, and μ_{eff} = 4.30 μ_B. The modified Curie-Weiss fitting results in C= 1.70 emu K mol^{-1}, θ_{CW} =-10.88 K , χ_o = 0.00123 emu/mol, and μ_{eff} = 3.69 μ_B.

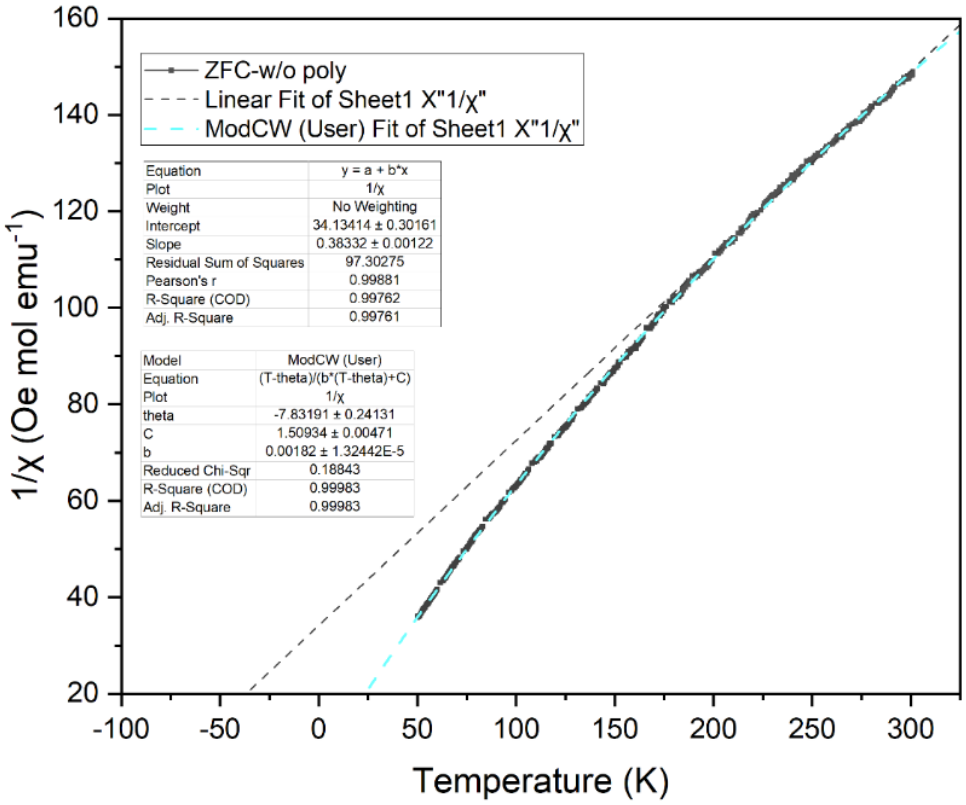

Figure C.3 1/χ -T plot for [Pam-*co*-PDADMA][Co^{2+} 2eq]. The grey and blue dotted lines show the Curie-Weiss and Modified Curie-Weiss fittings, respectively. The Curie-Weiss fitting results in C= 2.61 emu K mol^{-1}, θ_{CW} = -89.05 K, and μ_{eff} = 4.57 μ_B. The modified Curie-Weiss fitting results in C= 1.51 emu K mol^{-1}, θ_{CW} = -7.83 K , χ_o = 0.0018 emu/mol, and μ_{eff} = 3.47 μ_B.

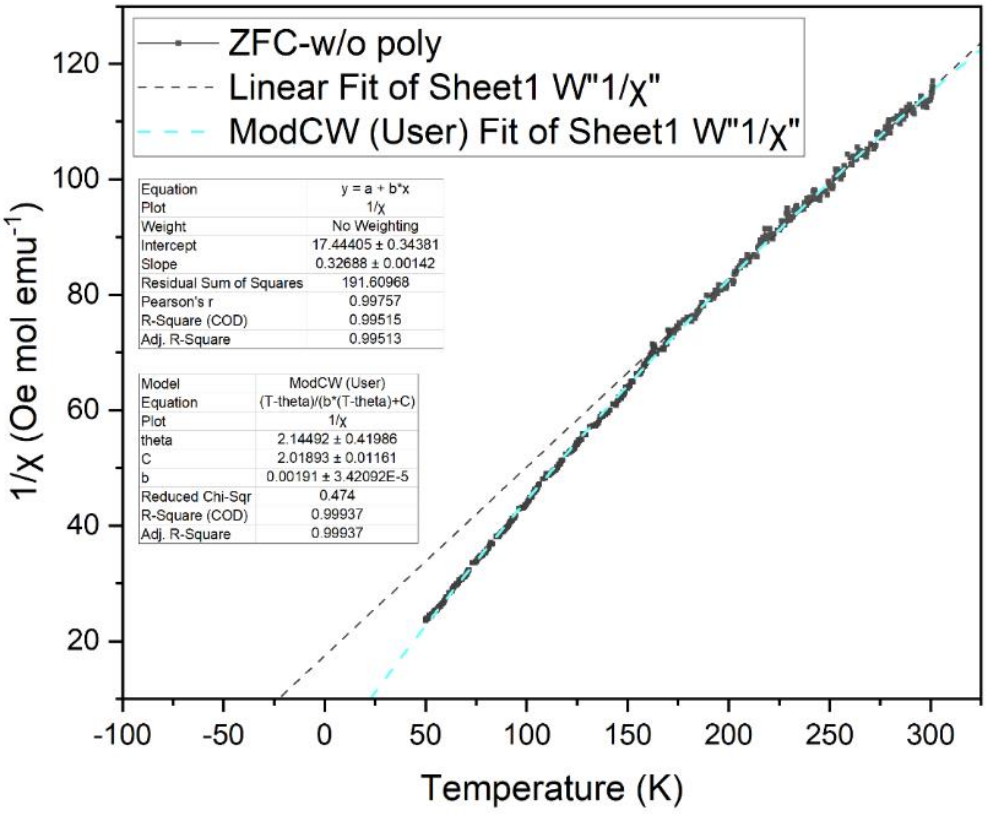

Figure C.4 $1/\chi$ -T plot for [Pam-*co*-PDADMA][Fe^{3+} 1eq]. The grey and blue dotted lines show the Curie-Weiss and Modified Curie-Weiss fittings, respectively. The Curie-Weiss fitting results in C= 3.06 emu K mol^{-1}, θ_{CW} = -53.37 K, and μ_{eff} = 4.95 μ_B. The modified Curie-Weiss fitting results in C= 2.02 emu K mol^{-1}, θ_{CW} = 2.14 K, χ_o = 0.0019 emu/mol, and μ_{eff} = 4.02 μ_B.

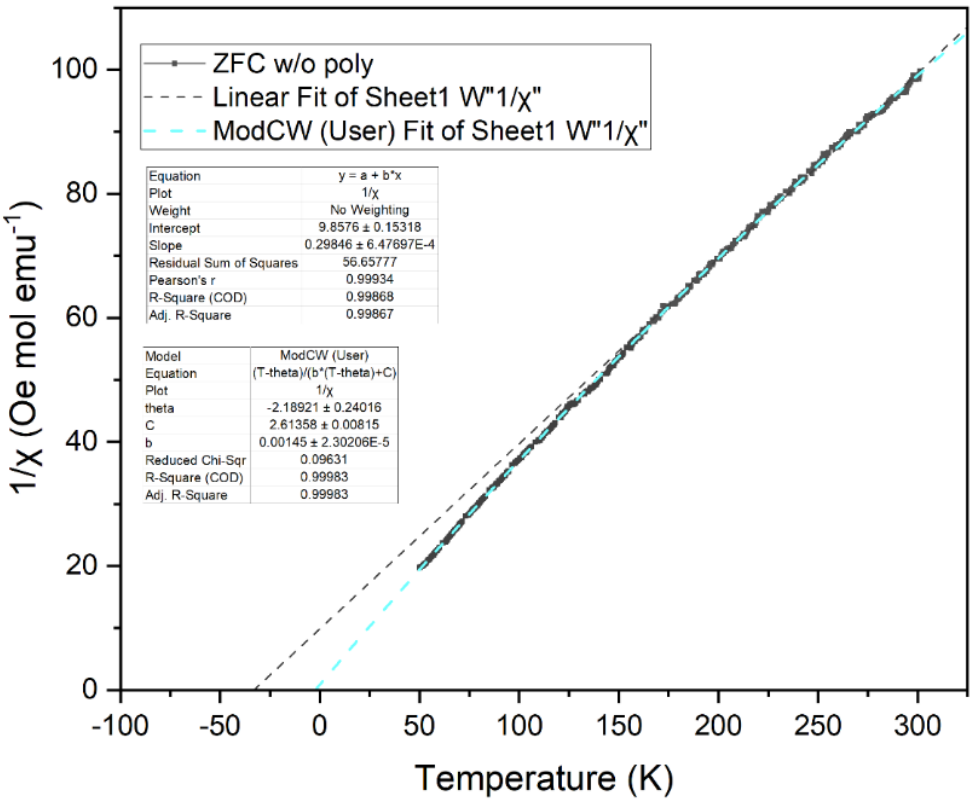

Figure C.5 $1/\chi$ -T plot for [Pam-*co*-PDADMA][Fe^{3+} 2eq]. The grey and blue dotted lines show the Curie-Weiss and Modified Curie-Weiss fittings, respectively. The Curie-Weiss fitting results in C= 3.35 emu K mol^{-1}, θ_{CW} = -33.03 K, and μ_{eff} = 5.18 μ_B. The modified Curie-Weiss fitting results in C= 2.61 emu K mol^{-1}, θ_{CW} = -2.19 K , χ_o = 0.0015 emu/mol, and μ_{eff} = 4.57 μ_B.

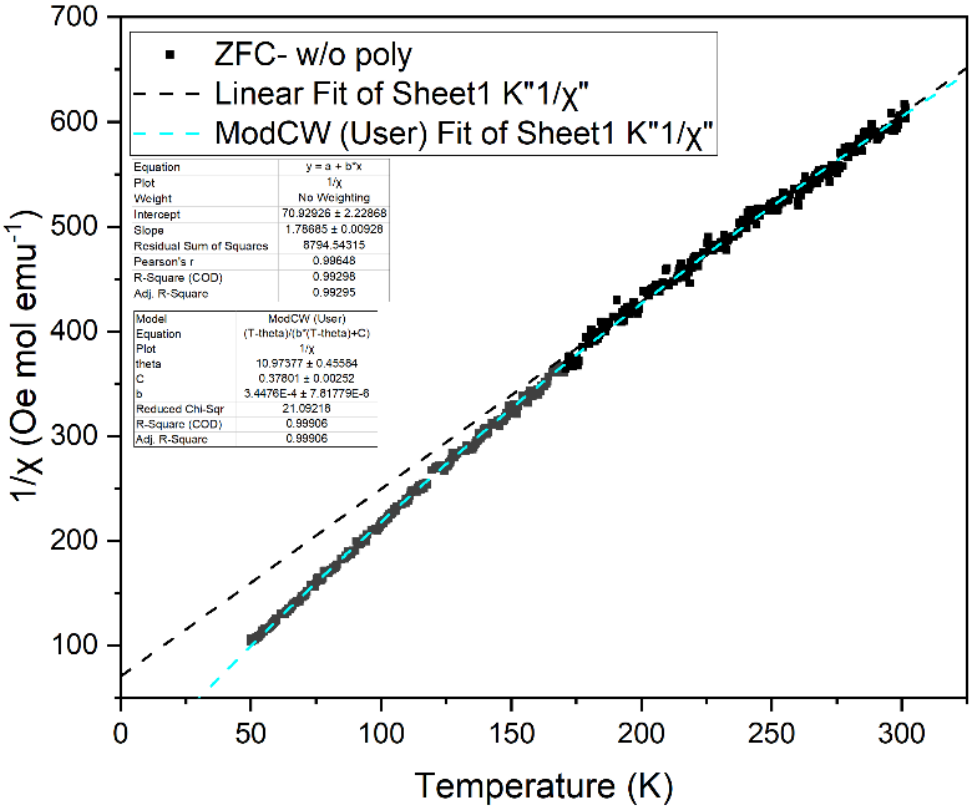

Figure C.6 1/χ -T plot for [Pam-*co*-PDADMA][Cu^{2+} 1eq]. The grey and blue dotted lines show the Curie-Weiss and Modified Curie-Weiss fittings, respectively. The Curie-Weiss fitting results in C=0.57 emu K mol^{-1}, θ_{CW} =-40.37 K, and μ_{eff} =2.13μ_B. The modified Curie-Weiss fitting results in C=0.378 emu K mol^{-1}, θ_{CW} =10.97 K , χ_o=0.00035 emu/mol, and μ_{eff} =1.74 μ_B.

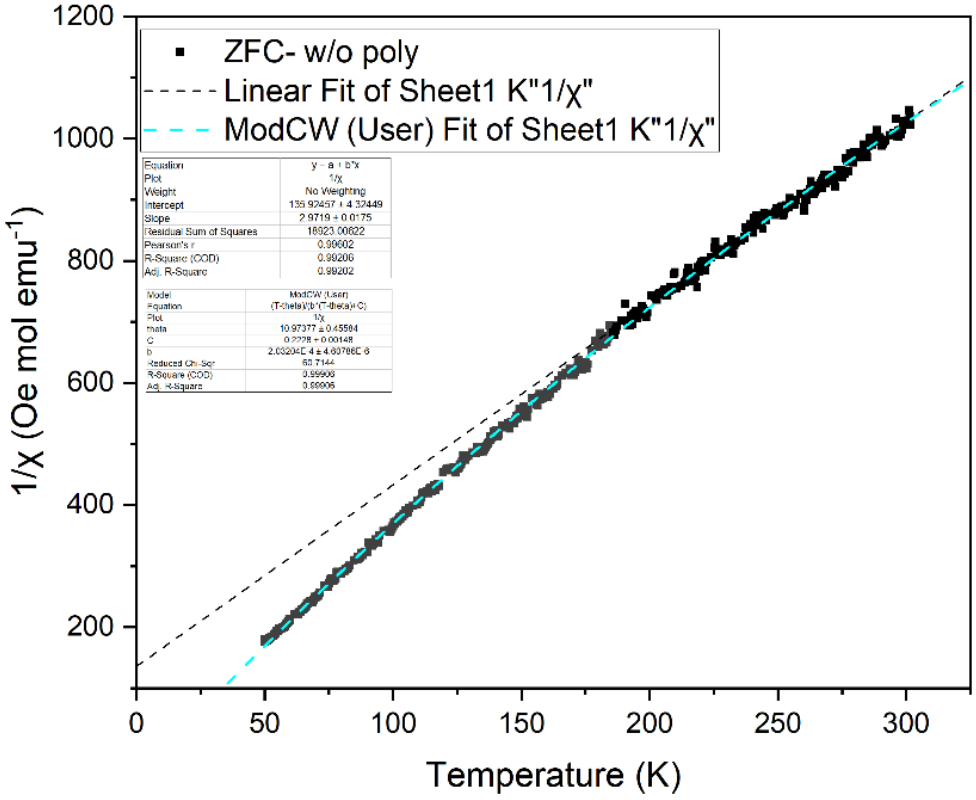

Figure C.7 1/χ -T plot for [Pam-*co*-PDADMA][Cu^{2+} 2eq]. The grey and blue dotted lines show the Curie-Weiss and Modified Curie-Weiss fittings, respectively. The Curie-Weiss fitting results in C=0.34 emu K mol^{-1}, θ_{CW} =-45.74 K, and μ_{eff} =1.64 μ_B. The modified Curie-Weiss fitting results in C=0.2228 emu K mol^{-1}, θ_{CW} =10.974K , χ_o =0.00020 emu/mol, and μ_{eff} =1.34 μ_B.

C.1.4. Moment and χT of the MPIL Copolymers

The Zero-Field Cooling and Field Cooling (ZFC-FC) curves for the MPIL copolymers show no significant hysteresis in the [Pam-*co*-PDADMA][Co^{2+}] and [Pam-*co*-PDADMA][Fe^{3+}] copolymer samples (Figure C.8). A possible small hysteresis is noted in the [Pam-co-PDADMA][Cu^{2+}] samples at ~120 K where the separation for the ZFC and FC curves is 3.0 $x10^{-6}$ emu/g and 6.9 $x10^{-7}$ emu/g for the 1eq and 2eq copolymers, respectively. The χT response for the [Pam-*co*-PDADMA][Co^{2+}] and [Pam-*co*-PDADMA][Fe^{3+}] copolymer samples decrease

slightly with decreasing temperature, suggesting antiferromagnetic interactions. The [Pam-*co*-PDADMA][Cu^{2+}] copolymer χT response is relatively constant over the 225 to 300 K temperature range indicating paramagnetic behavior. Below 75K, there is a possible slight upturn in χT at ~75K suggesting weak ferromagnetic interactions occurring.

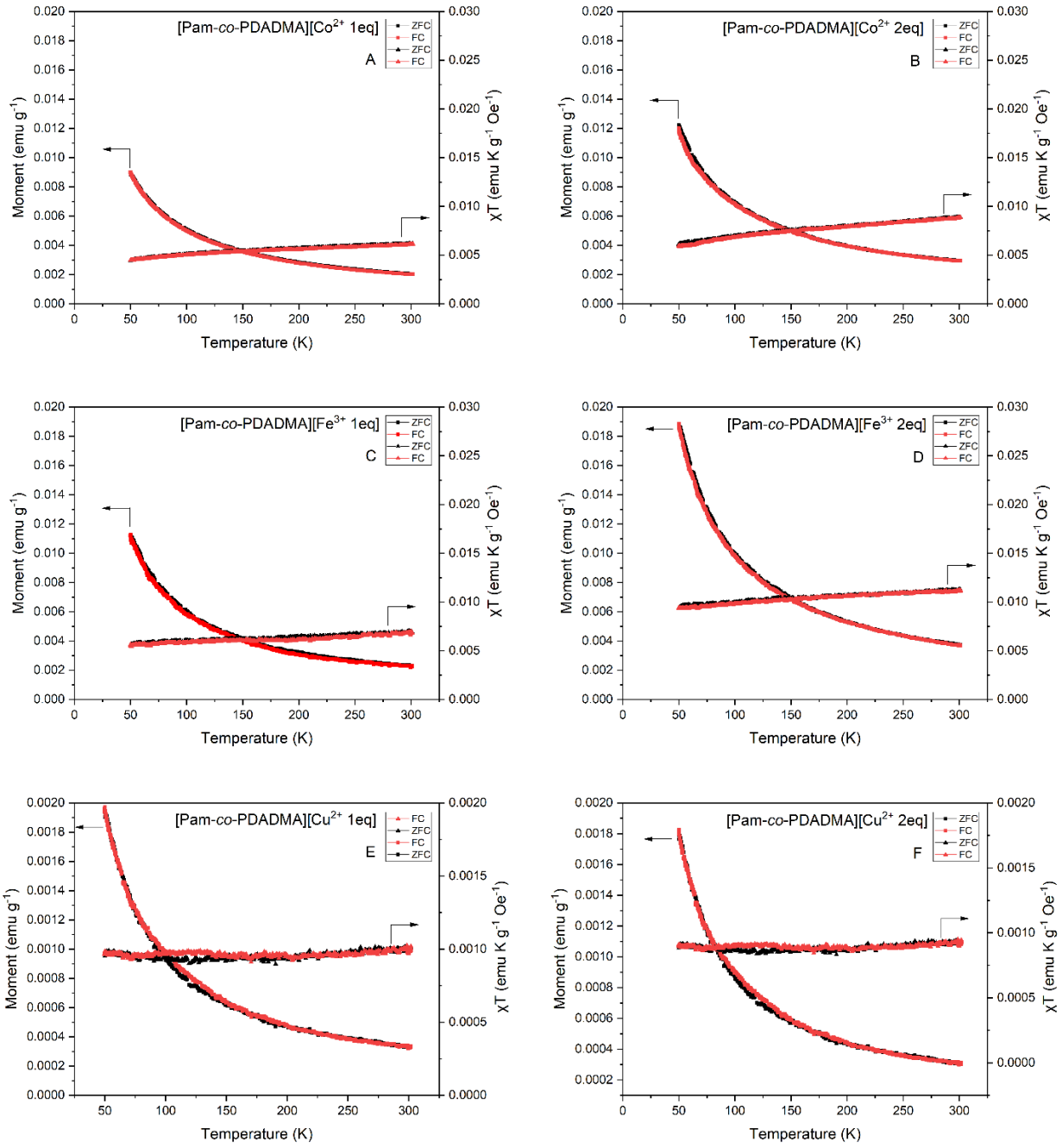

Figure C.8 Temperature dependence of magnetic moment (emu/g) and χT-T for the MPIL copolymers, [Pam-*co*-PDADMA][M^{n+} Xeq] where [M^{n+} Xeq] is (a) [Co^{2+} 1eq], (b) [Co^{2+} 2eq], (c) [Fe^{3+} 1eq], (d) [Fe^{3+} 2eq], (e) [Cu^{2+} 1eq], (f) [Cu^{2+} 2eq].

C.2. Processing Data for Magnetic Moment vs Magnetic Field Curves (MVH):

Figure C.9-Figure C.14 display the magnetic moment response to magnetic field from ± 30 kOe for a series of temperatures between 50 and 300 K. All MPIL copolymers exhibited a linear response indicative of paramagnetic behavior. Linear fittings were applied, and the magnetic mass susceptibility was extracted from the slope. The magnetic mass susceptibilities are summarized in Table C.1.

Table C.1 Magnetic mass susceptibilities determined from fitting the magnetic moment vs. field curves for the MPIL copolymers are displayed with the standard deviation in emu/g.

	[Fe^{3+} 1eq]		**[Fe^{3+} 2eq]**		**[Co^{2+} 1eq]**		**[Co^{2+} 2eq]**	
T [K]	**χ (emu/g)**	**Error (emu/g)**	**χ (emu/g)**	**Error (emu/g)**	**χ (emu/g)**	**Error (emu/g)**	**χ (emu/g)**	**Error (emu/g)**
300	1.88E-05	4.10E-08	3.89E-05	3.23E-07	1.90E-05	1.64E-07	2.44E-05	1.16E-07
250	2.26E-05	4.88E-08	3.89E-05	3.23E-07	1.95E-05	4.22E-08	2.62E-05	1.14E-07
200	2.78E-05	4.17E-08	4.75E-05	4.98E-08	2.46E-05	4.06E-08	3.39E-05	5.40E-08
150	3.66E-05	3.84E-08	6.31E-05	4.74E-08	3.20E-05	4.09E-08	4.40E-05	5.36E-08
100	5.41E-05	4.75E-08	9.29E-05	5.53E-08	4.58E-05	4.15E-08	6.04E-05	5.93E-08
50	1.04E-04	1.15E-07	1.76E-04	8.12E-08	8.34E-05	4.90E-08	1.08E-04	9.80E-08

Table C.1 Cont.

	[Cu^{2+} 1eq]		**[Cu^{2+} 2eq]**	
T	**χ (emu/g)**	**Error (emu/g)**	**χ (emu/g)**	**Error (emu/g)**
300	2.86E-06	6.36E-08	4.05E-06	6.34E-08
250	3.33E-06	5.90E-09	3.08E-06	5.58E-09
200	4.22E-06	5.11E-09	3.91E-06	4.73E-09
150	5.68E-06	8.88E-09	5.26E-06	8.23E-09
100	8.80E-06	7.71E-09	8.15E-06	7.14E-09
50	1.84E-05	1.41E-08	1.71E-05	1.31E-08

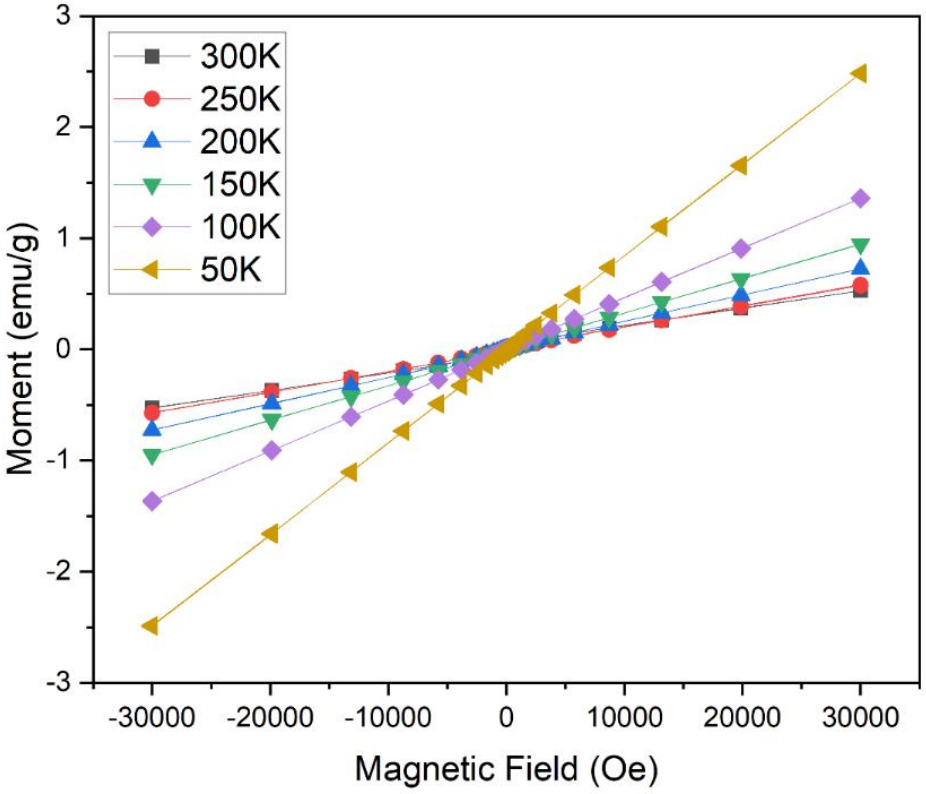

Figure C.9 Magnetic moment as a function of magnetic field strength (±30 kOe) for the [Pam-*co*-PDADMA][Co^{2+} 1eq] copolymer at different temperatures ranging from 50 to 300 K.

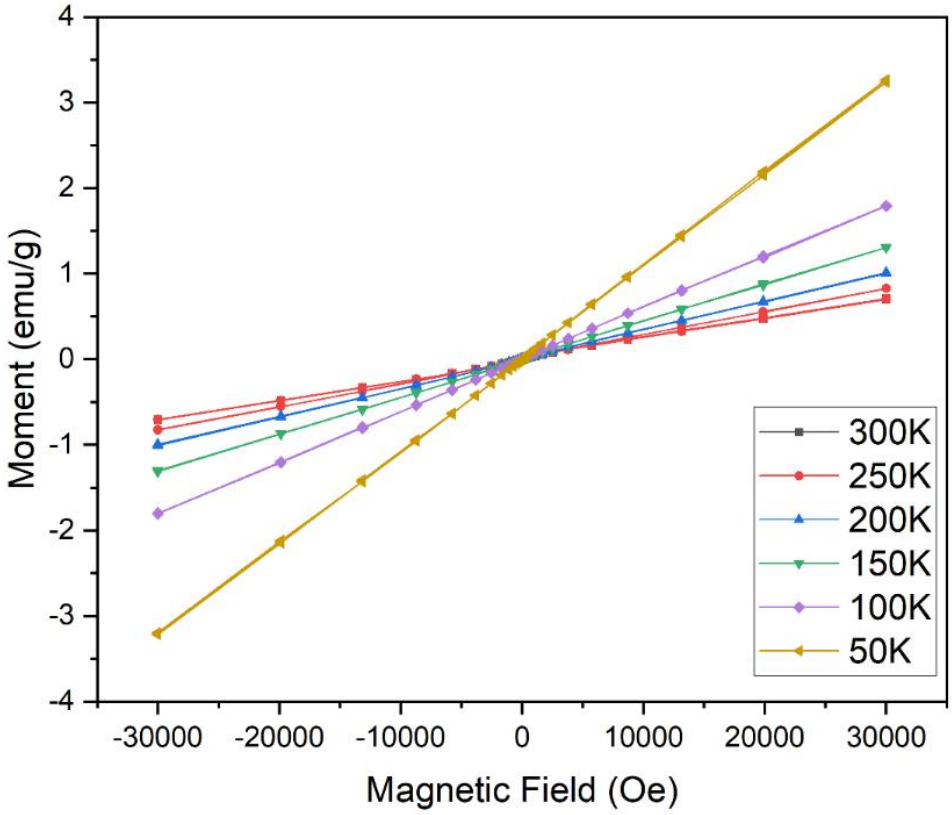

Figure C.10 Magnetic moment as a function of magnetic field strength (±30 kOe) for the [Pam-*co*-PDADMA][Co^{2+} 2eq] copolymer at different temperatures ranging from 50 to 300 K.

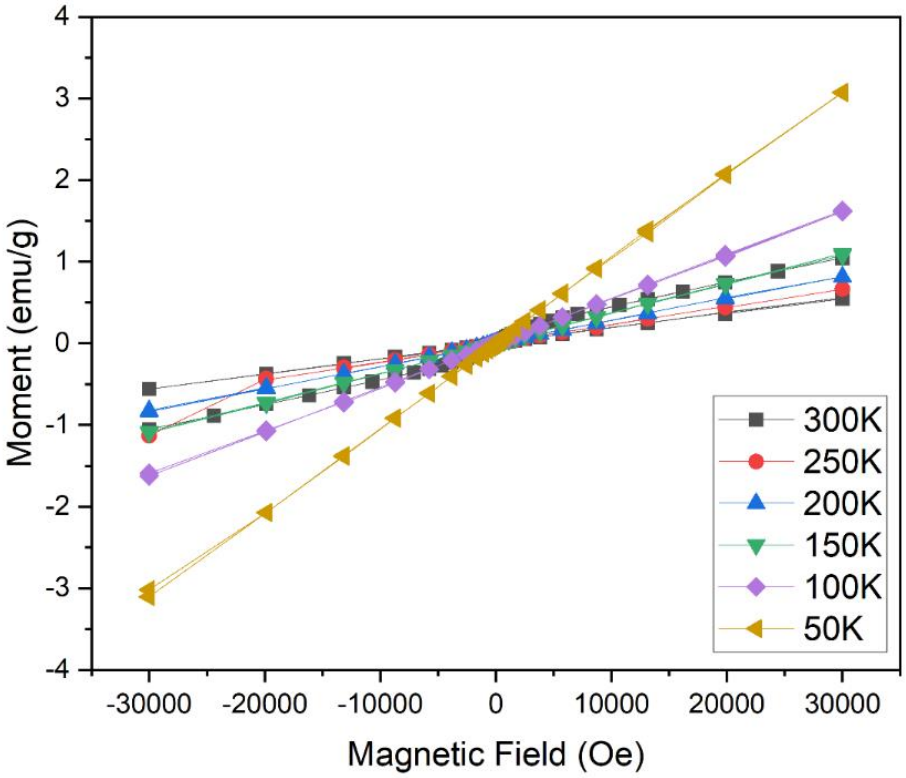

Figure C.11 Magnetic moment as a function of magnetic field strength (±30 kOe) for the [Pam-*co*-PDADMA][Fe^{3+} 1eq] copolymer at different temperatures ranging from 50 to 300 K.

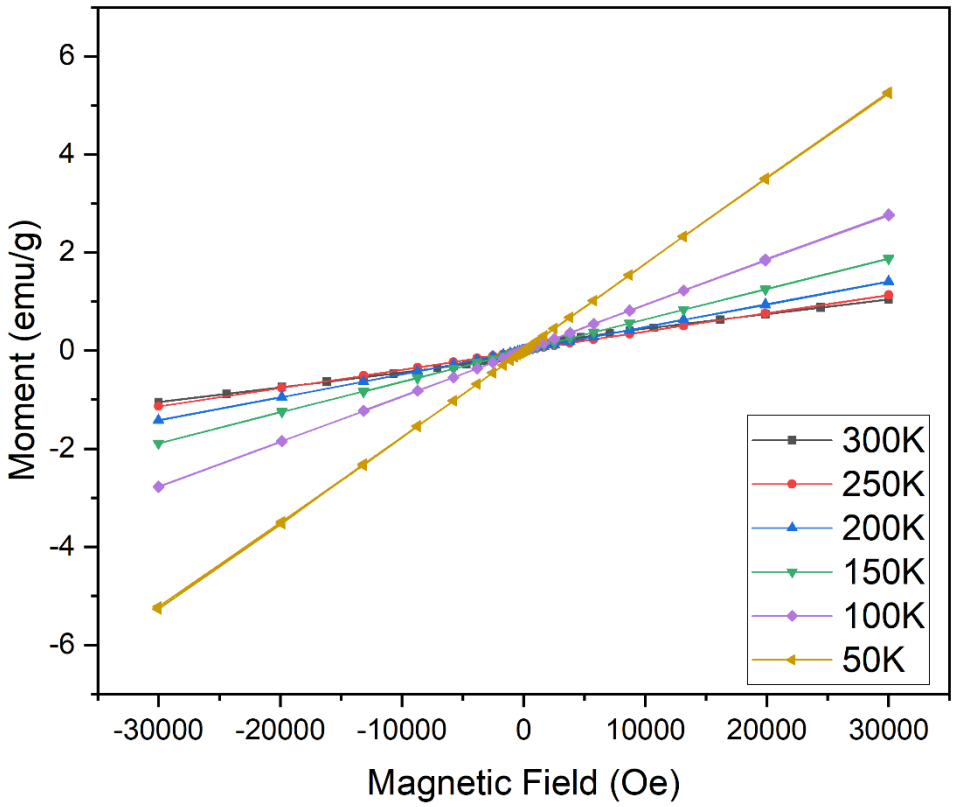

Figure C.12 Magnetic moment as a function of magnetic field strength (±30 kOe) for the [Pam-*co*-PDADMA][Fe^{3+} 2eq] copolymer at different temperatures ranging from 50 to 300 K.

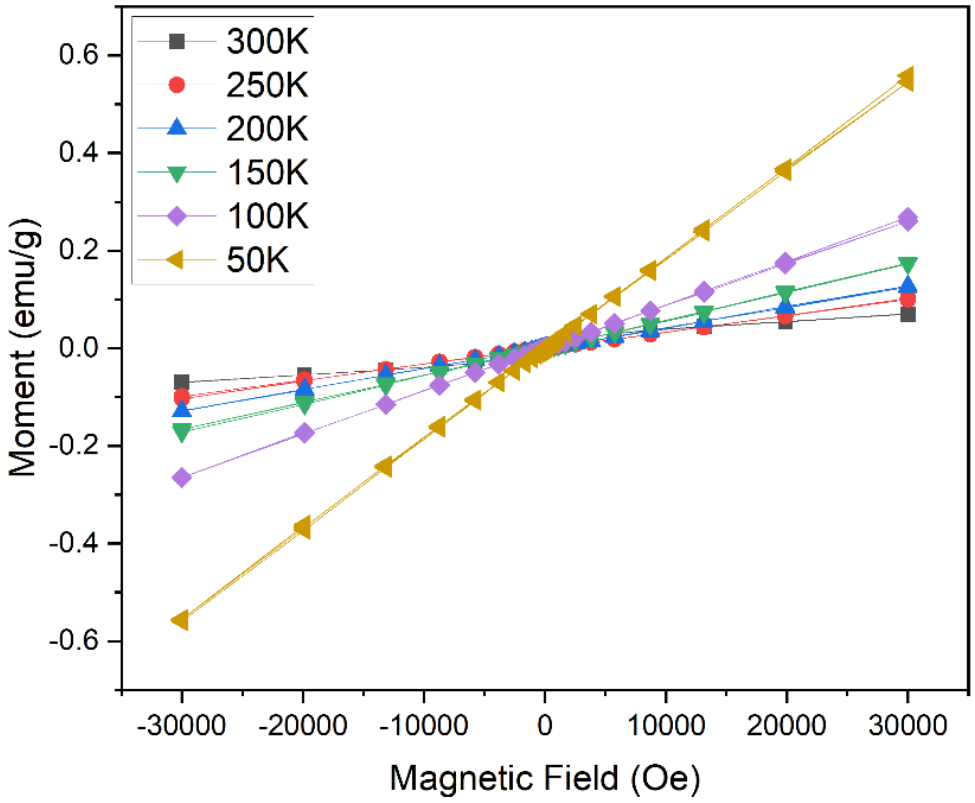

Figure C.13 Magnetic moment as a function of magnetic field strength (±30 kOe) for the [Pam-*co*-PDADMA][Cu^{2+} 1eq] copolymer at different temperatures ranging from 50 to 300 K.

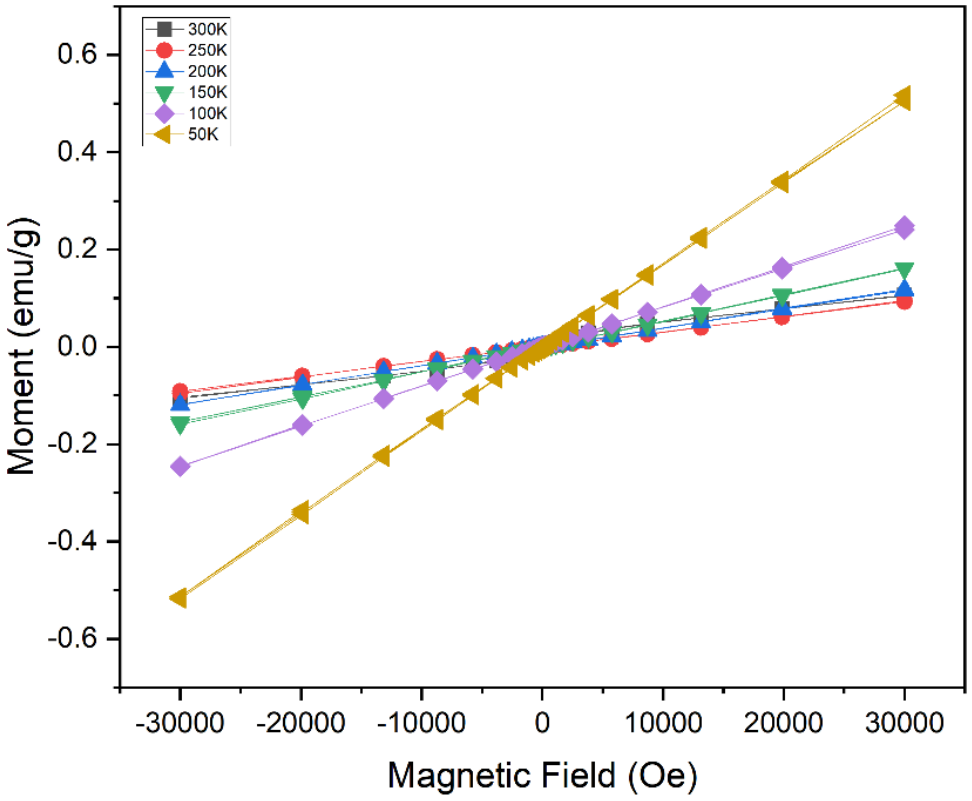

Figure C.14 Magnetic moment as a function of magnetic field strength (±30 kOe) for the [Pam-*co*-PDADMA][Cu^{2+} 2eq] copolymer at different temperatures ranging from 50 to 300 K.

C.3. MVH Curves for the [Pam-*co*-PDADMA][Cl-] and [SDS] Controls:

Magnetization curves for the non-magnetic copolymer and the surfactant were also collected at 300 K. SDS showed a diamagnetic response. The first run of the [Pam-*co*-PDADMA][Cl-] copolymer produced a diamagnetic response at higher magnetic fields and a paramagnetic response with no hysteresis between ±5000 Oe. The paramagnetic susceptibility measured was 1.4 x 10^{-6} emu/g through a linear fit of the paramagnetic region. Interestingly, on a re-run of the same sample, only a diamagnetic response was observed. Except for the [Pam-*co*-PDADMA][Cu^{2+} 1eq] and [Pam-*co*-PDADMA][Cu^{2+} 2eq] samples, which had magnetic mass susceptibilities of 2.86

x10^{-6} and 4.05 x10^{-6} emu/g, the mass susceptibilities measured for the [Pam-*co*-PDADMA][Co^{2+}] and [Pam-*co*-PDADMA][Fe^{3+}] were significantly higher (between 18.85 x10^{-6} and 38.9 x 10^{-6} emu/g) compared to the potential paramagnetic impurity in the [Pam-*co*-PDADMA][Cl-] copolymer.

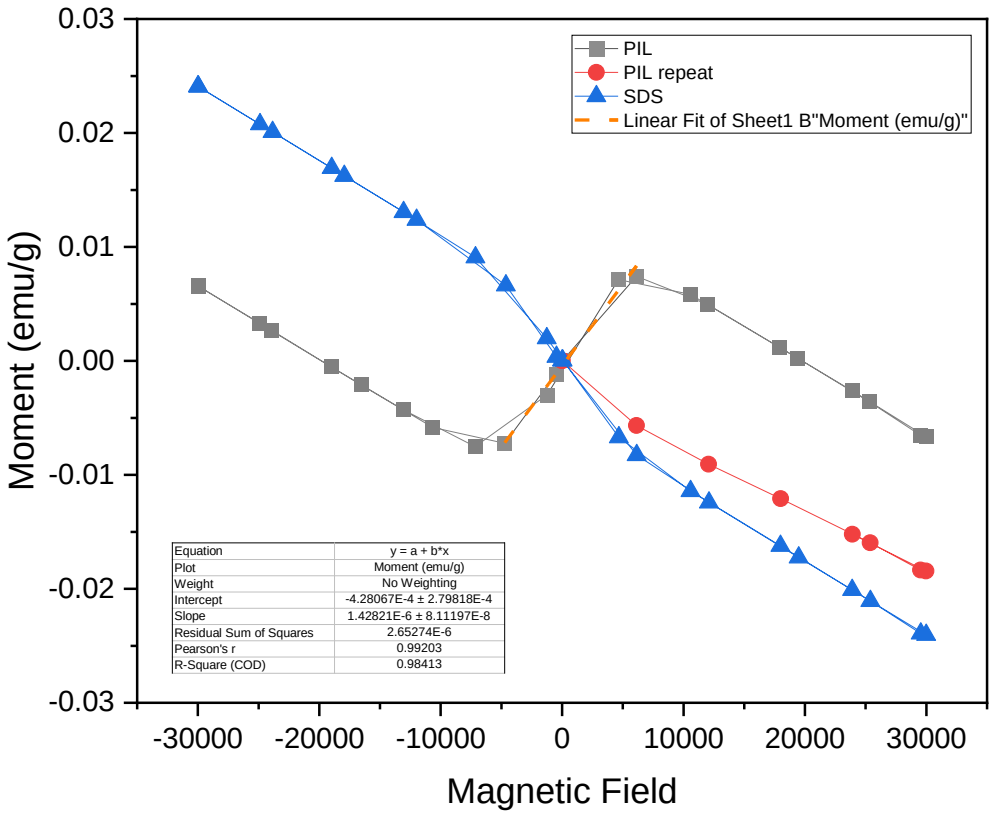

Figure C.15 Magnetic moment as a function of magnetic field strength (±30 kOe) for the [Pam-*co*-PDADMA][Cl^-] copolymer and SDS surfactant at 300 K.

C.4. DSC Supplemental Information:

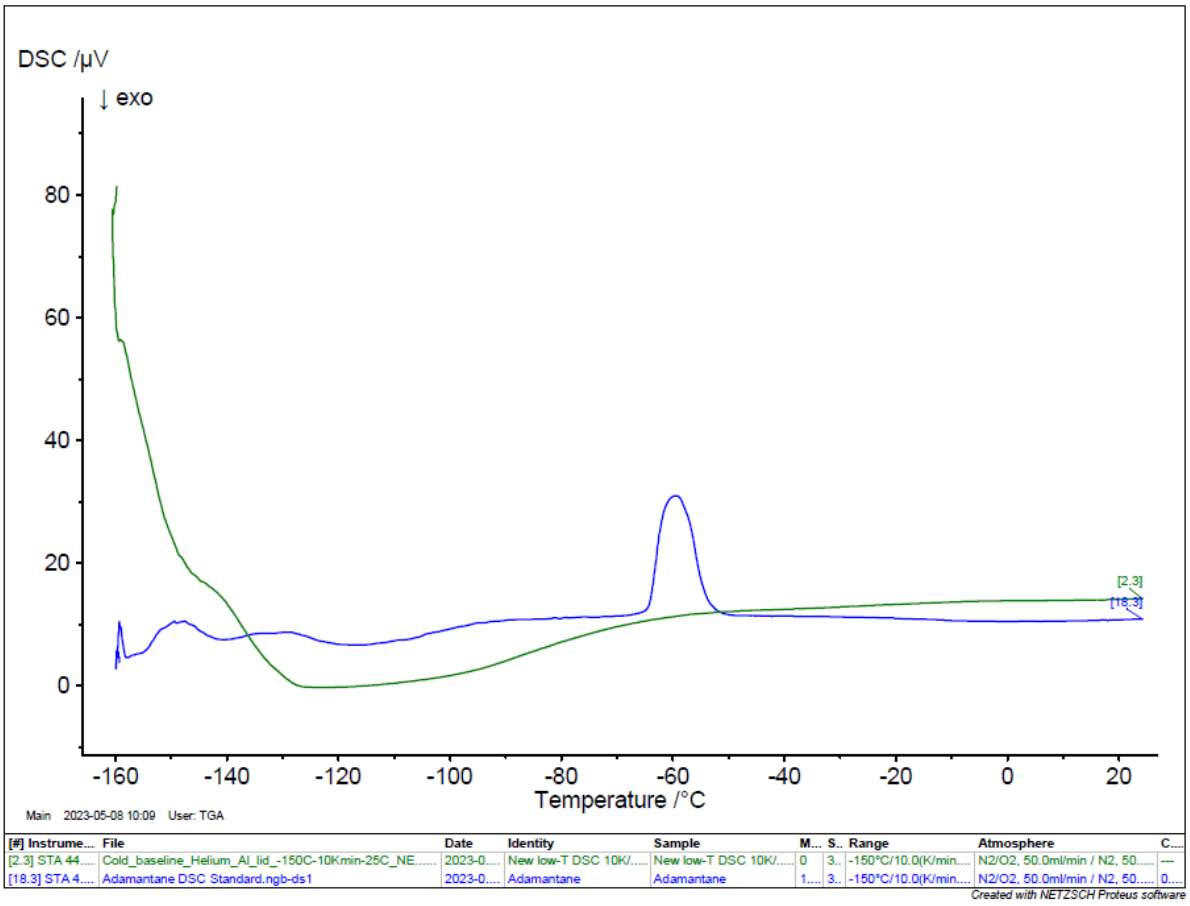

Figure C.16 DSC trace for an adamantane control sample. The peaks and exothermic dips observed below -100 °C are related to instrumental baseline drift and not physical transitions. The endothermic peak at approximately -60 °C is related to a solid-solid phase transition of the lattice structure[5].

C.5. DLS-ZP Measurements of MPILSDS Complexes:

Dynamic light scattering (DLS) and zeta potential (ZP) measurements were performed on an Anton Paar Litesizer 500 instrument with side scatter (90 °) detection. The hydrodynamic diameters of the complexes were determined with the Anton Paar Kaliope software "General" analysis model. ZP was determined using the Smoluchowski model.

Table C.2 DLS and ZP results for the MPILSDS polyelectrolyte surfactant complexes form from the [Pam-*co*-PDADMA][Co^{2+} 1eq] and [Pam-co-PDADMA][Fe^{3+} 1eq] magnetic copolymers and sodium dodecyl sulfate in water.

Sample	**Fe^{3+} 5mM**	**Co^{2+} 5mM**	**Co^{2+} 7mM**
D_H (nm)	235.8 (± 5.1)	400.4 (± 27.7)	374.8 (± 12.8)
Peak 1 (nm)	232.6 (± 65.4)	409.2 (± 148.1)	402.9 (± 145.7)
Peak 2 (nm)	N/A	20.3 (± 5.2)	20.0 (± 3.7)
ZP (mV)	11.3 (± 0.2)	-9.0 (± 0.2)	-23.2 (± 0.7)

C.6. FTIR Spectra of MPILSDS Complexes at Wavenumbers from 2700 to 3050 cm^{-1}:

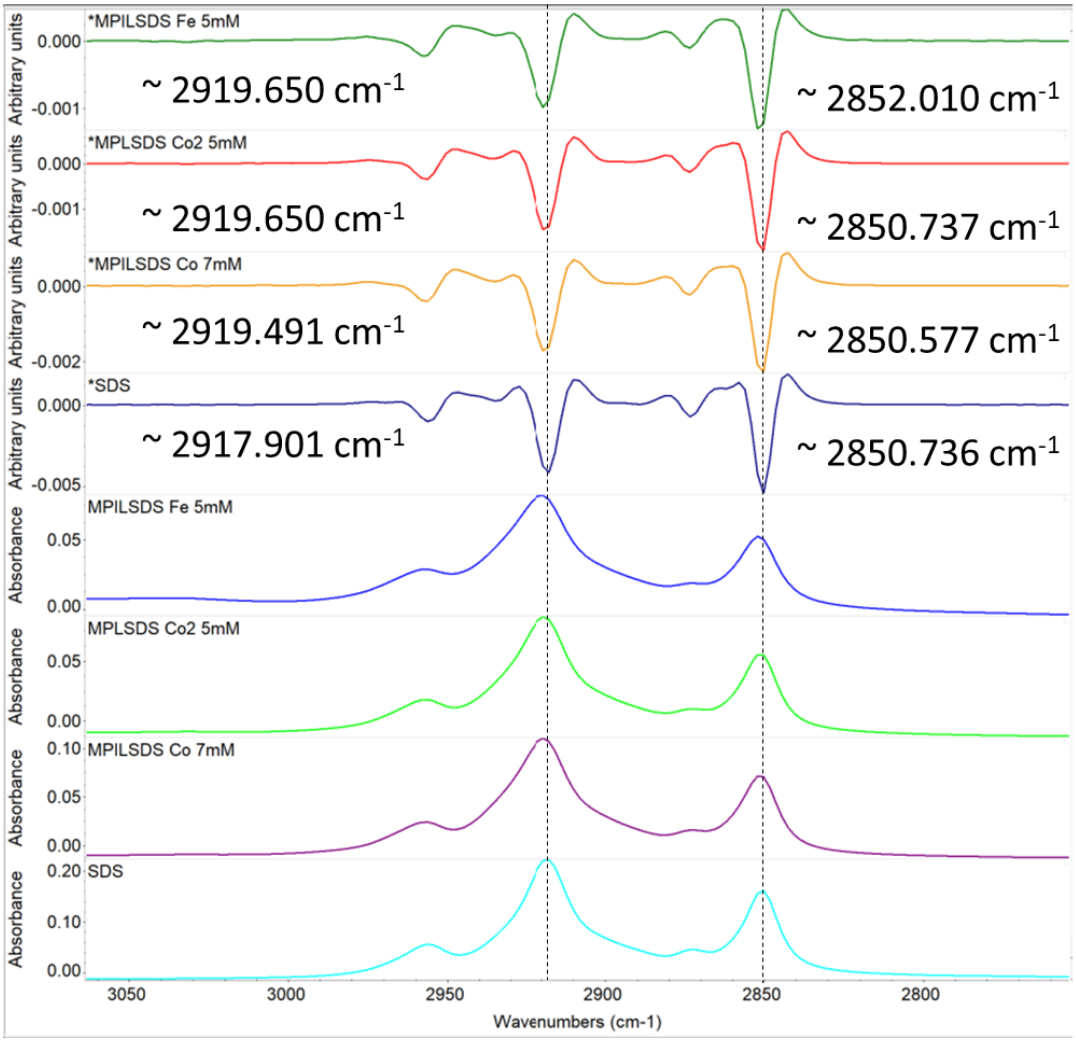

Figure C.17 ATR-FTIR trace and their second derivatives (marked by *) of the freeze-dried MPILSDS complexes in the C-H str mode region showing the shifts in the dodecyl sulfate CH_2 asym and sym str modes. A slight increase in the CH_2 asym str at ~ 2918 cm^{-1} in neat SDS and ~2919-2920 cm^{-1} in the MPILSDS complexes as well as the presence of the CH_2 sym mode at ~2851-2852 cm^{-1} are indicative at least partial crystalline ordering of the surfactant alkyl chains in an all-trans conformation[6, 7]. The dotted line marks the center of the neat SDS peaks.

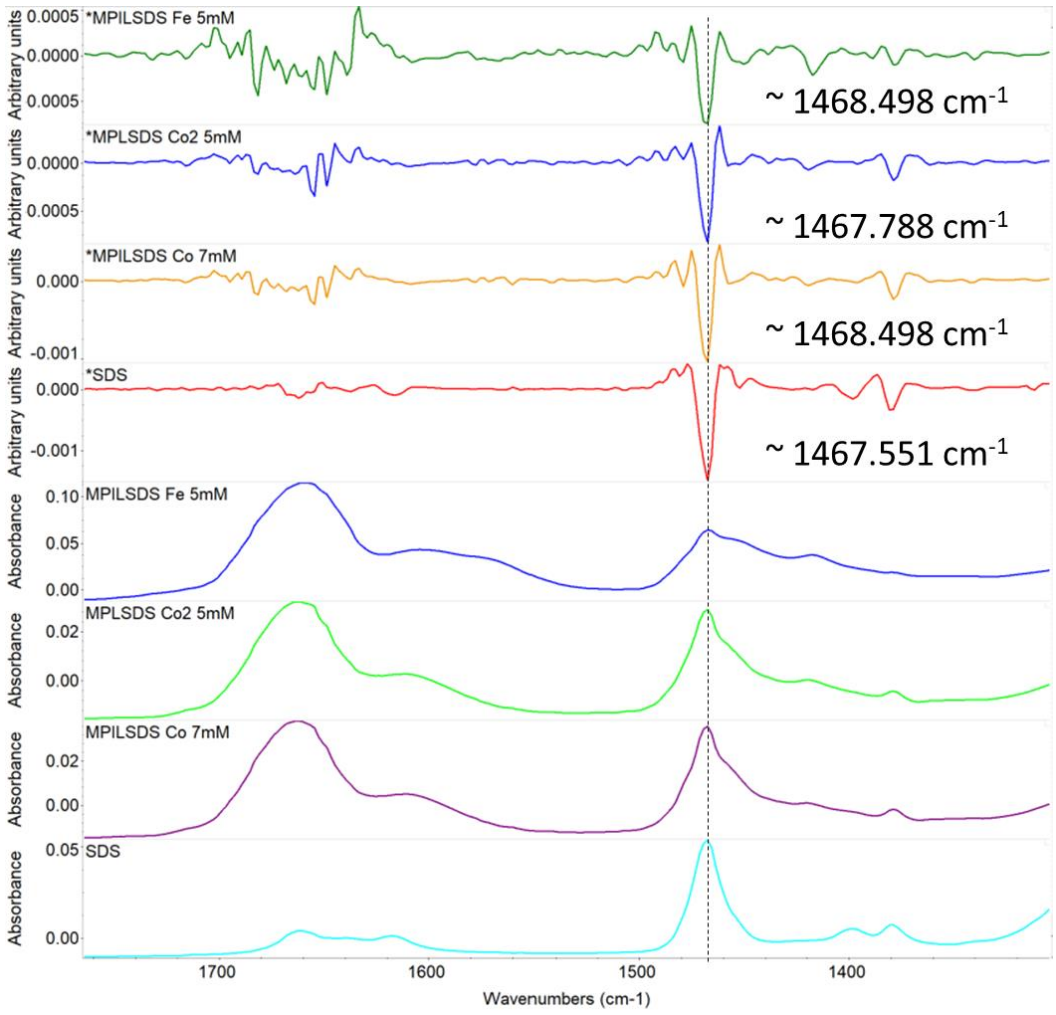

Figure C.18 ATR-FTIR trace and their second derivatives (marked by *) of the freeze-dried MPILSDS complexes showing the CH_2 bending mode at ~1468 cm^{-1}, which is consistent with partially ordered surfactant alkyl chains[6, 7]. The dotted line marks the center of the neat SDS peaks.

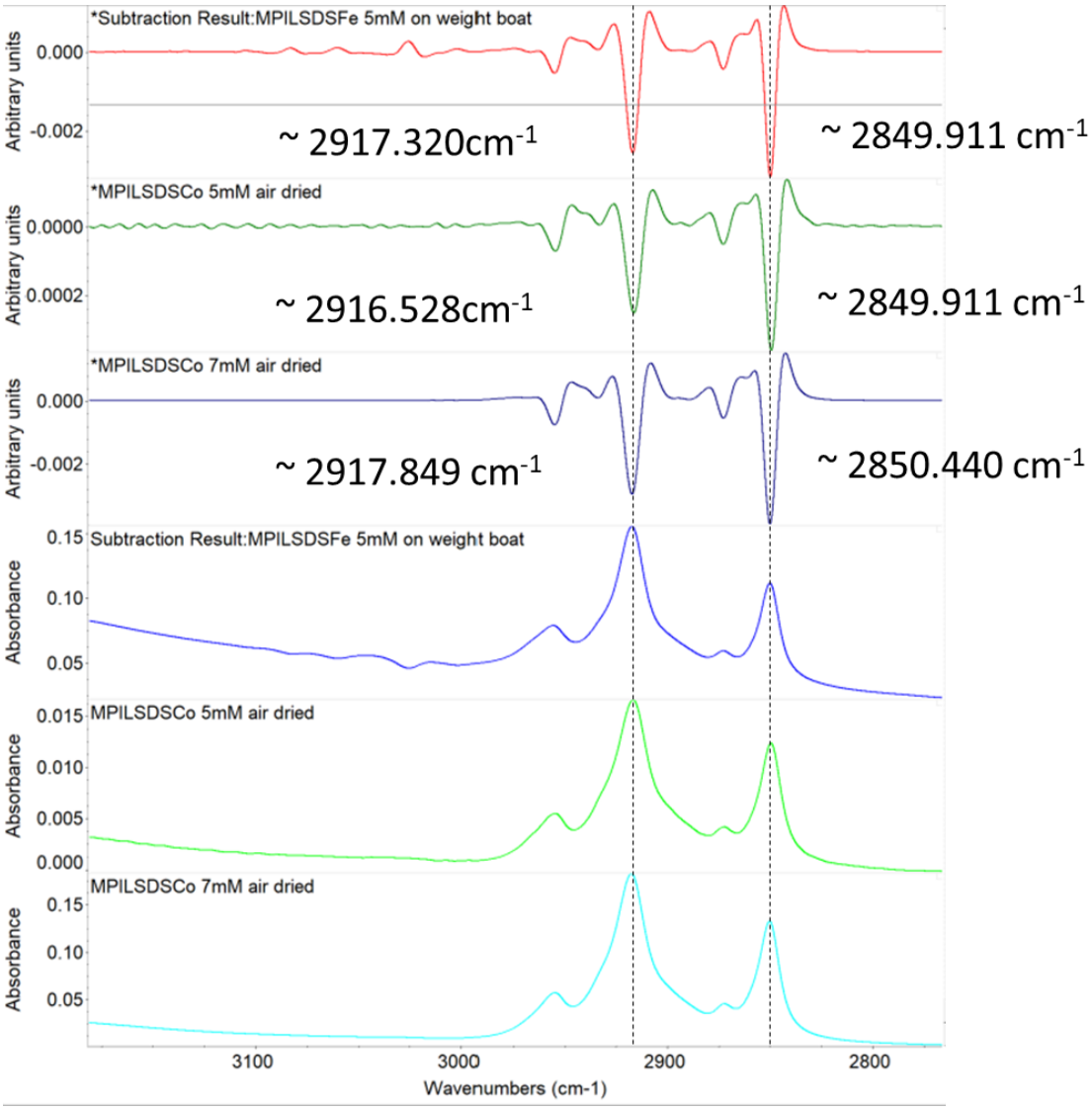

Figure C.19 ATR-FTIR spectra and their second derivatives (marked by *) of the air dried MPILSDS complexes displaying similar wavenumbers for the CH_2 asym and sym str modes for the dodecyl sulfate as was observed for the freeze-dried MPILSDS (Figure C.17).

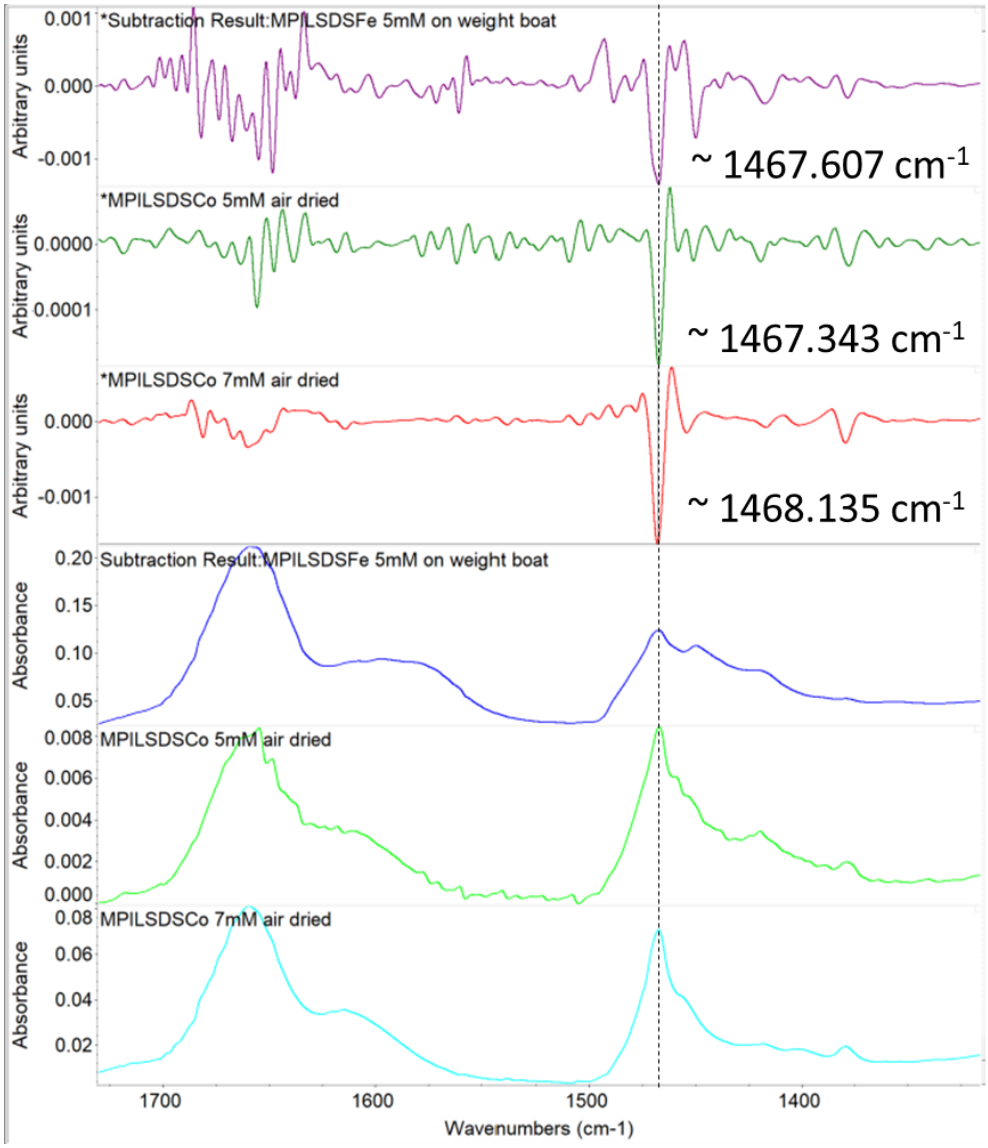

Figure C.20 ATR-FTIR spectra and their second derivatives (marked by *) of the air dried MPILSDS complexes showing the CH_2 bending mode at ~1468 cm^{-1}, similar to the freeze-dried MPILSDS complexes (Figure C.18).

C.7. Optical Images Supplement

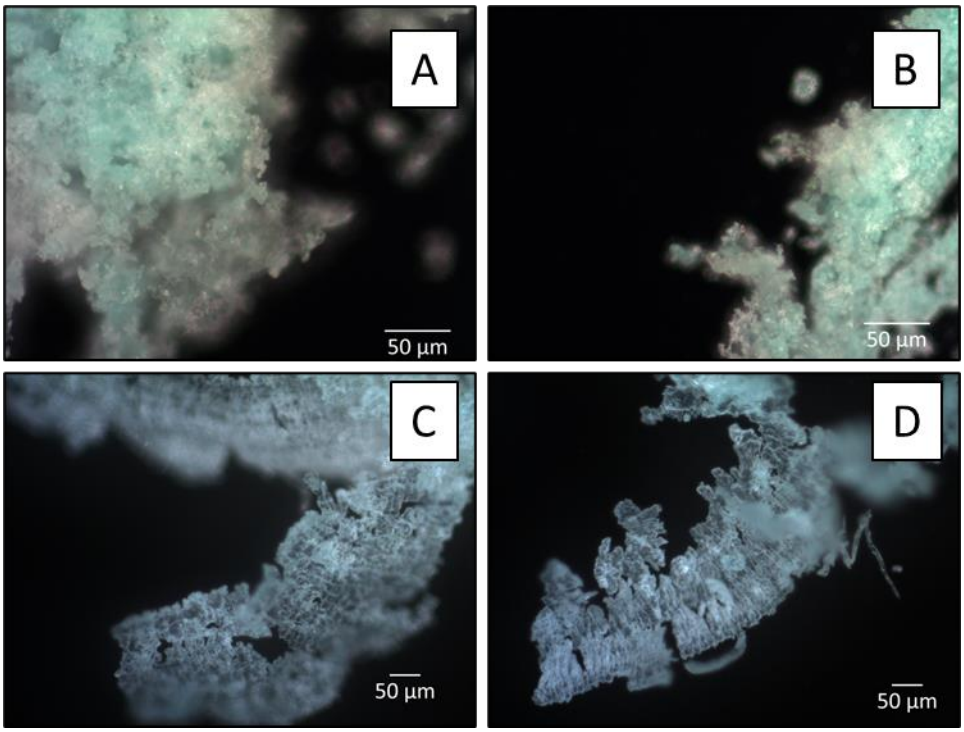

Figure C.21 Dark field optical microscopy images of the MPILSDS Co^{2+} 7mM complexes after (a and b) freeze drying or (c and d) air drying. For the air-dried samples, the MPILSDS Co^{2+} 7mM complex solution was poured into a petri dish and the water was allowed to evaporate. A thin film resulted and was subsequently scrapped off the glass to produce the powders. No further changes were made to the freeze-dried samples after the freeze-drying procedure.

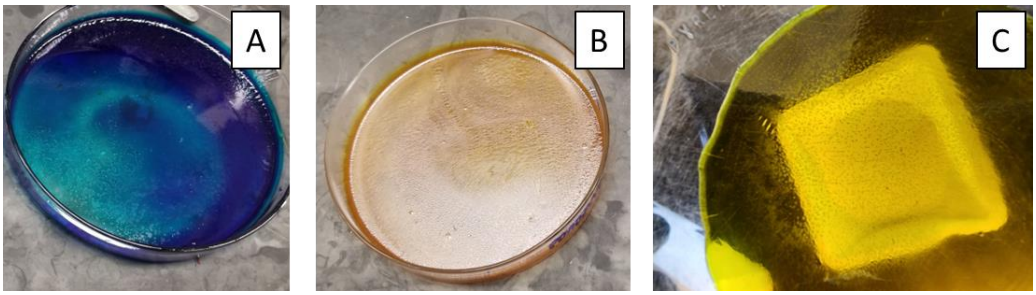

Figure C.22 MPIL 1eq copolymer films after pouring the synthesis solution into petri dishes and allowing the water to evaporate. A deep blue color, yellow-brown, and yellow-green color was produced for the MPIL Co^{2+} , MPIL Fe^{3+}, and MPIL Cu^{2+} copolymer films, respectively.

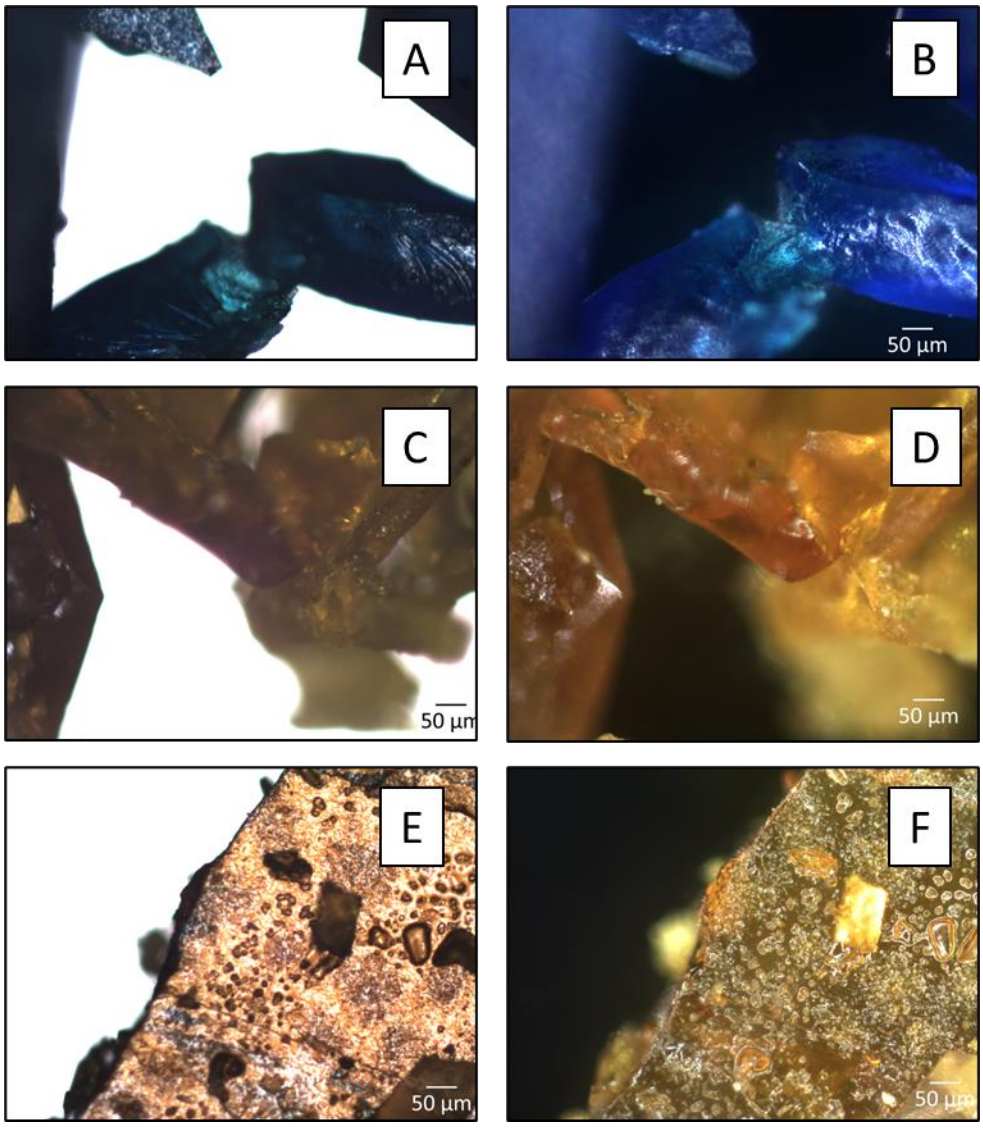

Figure C.23 Bright field and dark field optical microscopy images for the MPIL Co^{2+} 1eq (a and b) and MPIL Fe^{3+} 1eq (c-f) coarse powders produced after air drying and grinding in a mortar and pestle.

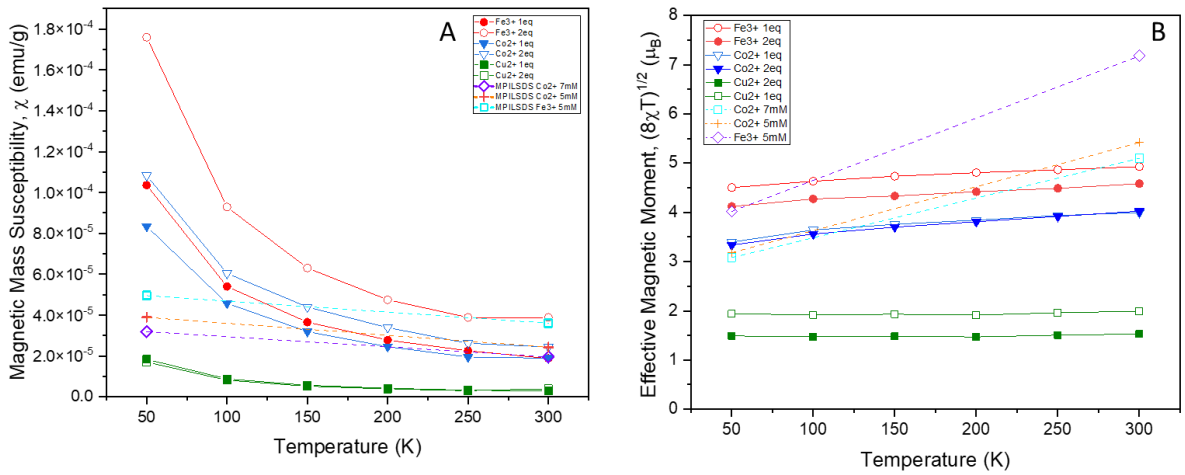

Figure C.24 Magnetic mass susceptibilities (a) and the effective magnetic moment (b) as a function of temperature for the MPIL copolymers and MPILSDS complexes are shown. Susceptibilities were determined from the slope of the linear region of the magnetic moment vs field curves (Figure C.9-Figure C.14 MPIL copolymers; Figure 4.6 MPILSDS complexes). The effective magnetic moments, μ_{eff}, were calculated from EQ 4-4, where magnetic correlations are assumed negligible.

Table C.3 Masses of each MPIL copolymer and MPILSDS complexes used to normalize the measured magnetic moment.

Sample	Sample (g)	Sample (mg)
[Pam-*co*-PDADMA][Fe^{3+} 1eq]	0.119	119
[Pam-*co*-PDADMA][Fe^{3+} 2eq]	0.105	105
[Pam-*co*-PDADMA][Co^{2+} 1eq]	0.1041	104.1
[Pam-*co*-PDADMA][Co^{2+} 2eq]	0.1134	113.4
[Pam-*co*-PDADMA][Cu^{2+} 1eq]	0.1185	118.5
[Pam-*co*-PDADMA][Cu^{2+} 2eq]	0.1279	127.9
MPILSDS Co^{2+} 7mM	0.0378	37.8
MPILSDS Co^{2+} 5mM	0.0286	28.6
MPILSDS Fe^{3+} 5mM	0.0157	15.7
Pam-*co*-PDADMA[Cl^-]	0.0973	97.3
SDS	0.0651	65.1

C.8. References

(1) Mugiraneza, S.; Hallas, A. M. Tutorial: a beginner's guide to interpreting magnetic susceptibility data with the Curie-Weiss law. *Communications Physics* **2022**, *5* (1), 95. DOI: 10.1038/s42005-022-00853-y.

(2) Chikh Alard, I.; Soubhye, J.; Berger, G.; Gelbcke, M.; Spassov, S.; Amighi, K.; Goole, J.; Meyer, F. Triple-stimuli responsive polymers with fine tuneable magnetic responses. *Polym. Chem.* **2017**, *8* (16), 2450-2456, 10.1039/C7PY00218A. DOI: 10.1039/C7PY00218A.

(3) Yu, X.; Xia, Z.; Zhao, T.; Yuan, X.; Ren, L. Pyrene-Enhanced Ferromagnetic Interaction in a FeCl4–-Based Poly(ionic liquid)s Organic Magnet. *Macromolecules* **2021**, *54* (9), 4227-4235. DOI: 10.1021/acs.macromol.1c00213.

(4) Yu, X.; Yuan, X.; Zhao, Y.; Ren, L. From Paramagnetic to Superparamagnetic Ionic Liquid/Poly(ionic liquid): The Effect of π–π Stacking Interaction. *ACS Macro Letters* **2019**, *8* (11), 1504-1510. DOI: 10.1021/acsmacrolett.9b00714.

(5) Blaine, R. L. Adamantane- A New Certified and Traceable Reference Material for Subambient DSC Temperature and Enthalpy Calibration on Heating and Cooling. *TA372*, Technical Note.

(6) Pereira, R. F. P.; Valente, A. J. M.; Burrows, H. D.; de Zea Bermudez, V.; Carvalho, R. A.; Castro, R. A. E. Structural characterization of solid trivalent metal dodecyl sulfates: from aqueous solution to lamellar superstructures. *RSC Adv.* **2013**, *3* (5), 1420-1433. DOI: 10.1039/c2ra21906a.

(7) Viana, R. B.; da Silva, A. B. F.; Pimentel, A. S. Infrared spectroscopy of anionic, cationic, and zwitterionic surfactants. *Adv. Phys. Chem.* **2012**. DOI: 10.1155/2012/903272.

Appendix D: Supplemental Information for Chapter 5

***** This appendix contains the adapted supplemental information from the submitted journal article: Kayla Foley, Keisha B. Walters. "Poly(ionic liquids) blocked with the stimuli responsive weak polyelectrolyte poly[2-(dimethylamino)ethyl methacrylate] and their solution and film assembly," Submitted May 2023, *ACS Omega.* [Under Review]

D.1. Supplemental NMR Characterization

A Varian 1D diffusion ordered pulse sequence NMR experiment, DONESHOT, was collected for the purified PDMAEMA-*b*-PVBBImTf_2N block copolymer utilizing the following parameters: 150 ms diffusion decay; 2 s relaxation delay time; 8 scans per increment; and 30 increments (Figure D.1). 1H NMR was also collected for the PDMAEMA macroinitiator in pure DMSO and 10 mM KNO3 DMSO solution, displaying no shifts in the methylene peaks between 2 and 3 ppm upon salt addition (Figure D.2).

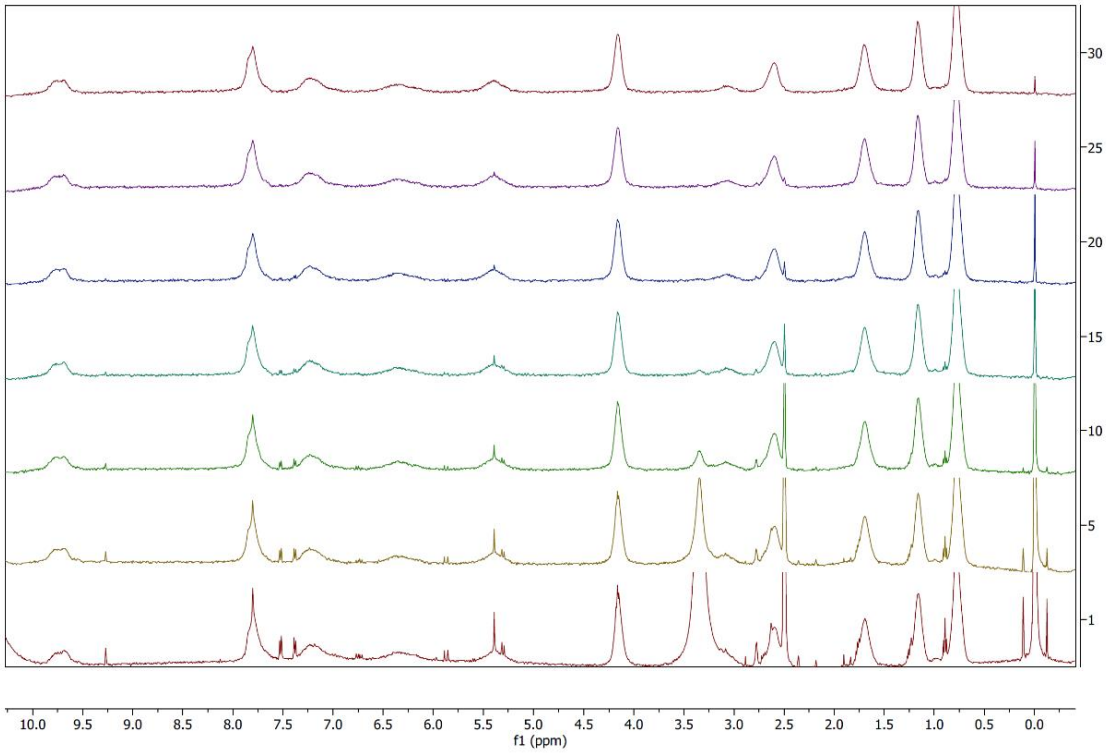

Figure D.1 1D DONESHOT DOSY array displaying 7 of the 30 proton spectra collected in the 30 increments. This data was converted to a 2D DOSY using a Bayesian transformation method.

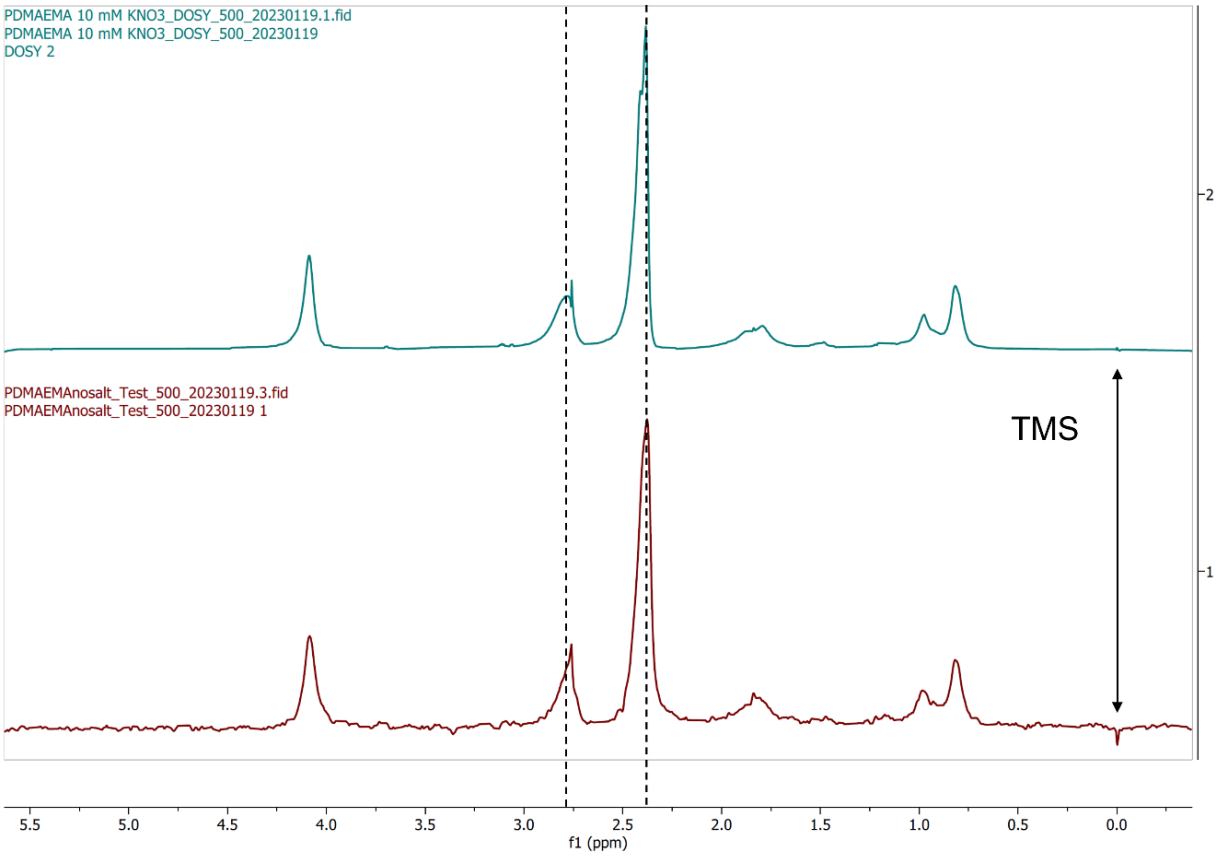

Figure D.2 ^{1}H NMR spectra of the PDMAEMA macroinitiator in pure DMSO-d6 (bottom) and 10 mM KNO_3 DMSO-d6 (top) solvent displaying no significant shifts in peaks. Dotted lines mark the methyl and methylene groups on the PDMAEMA macroinitiator. Both spectra were referenced to the trimethyl siloxane (TMS) internal reference at 0 ppm.

D.2. Additional Solubility Characterization

Solubilities of the PVBBImTf_2N homopolymer and PDMAEMA-*b*-PVBBImTf_2N block copolymer were examined in various solvents by placing the polymer in a given solvent at target concentrations of 1 mg/mL at room temperature. After 24 hours, the polymers solubilities were examined and are reported in Table D.1. The PVBBImTf_2N homopolymer was found to be well solubilized in DMSO, DMF, ACN, and THF with some partial solubility in MeOH. The PVBBImTf_2N homopolymer was insoluble in EtOAc, Acetone, EtOH, IPA, and water. The

PDMAEMA-*b*-PVBBImTf_2N block copolymer was not fully soluble in any of the tested solvents, but did swell in polar organic solvents, including DMSO, NMP, DMF, and DAm.

Table D.1 Solubilities of the PVBBImTf_2N homopolymer and PDMAEMA-*b*-PVBBImTf_2N block copolymer in a series of solvents where their solubility behavior is denoted as: Soluble (S), Swelled (SW), Partially Soluble (PS), Not Soluble (NS), or Not Tested (N/A). Solubility was determined by attempting to dissolve the polymers in the appropriate solvent at concentrations of 1 mg/mL.

	DMSO	NMP	DMF	DAm	ACN	MeOH	Acetone	EtOAc	Water	THF	EtOH	IPA
PVBBImTf_2N	S	N/A	S	N/A	S	PS	NS	NS	NS	S	NS	NS
PDMAEMA-*b*-PVBBImTf_2N	SW	SW	SW	SW	NS	NS	NS	NS	NS	NS	NS	NS

D.3. Supplemental DLS Data

D.3.1. DLS Model Fittings

Dblexp (red),Non-Negative Least Squares NNLS (dotted blue), and CONTIN (dash green) fittings of the correlation functions for the block copolymer in pure DMSO and 10 mM KNO3 are shown in Figure D.3 and Figure D.4, respectively.

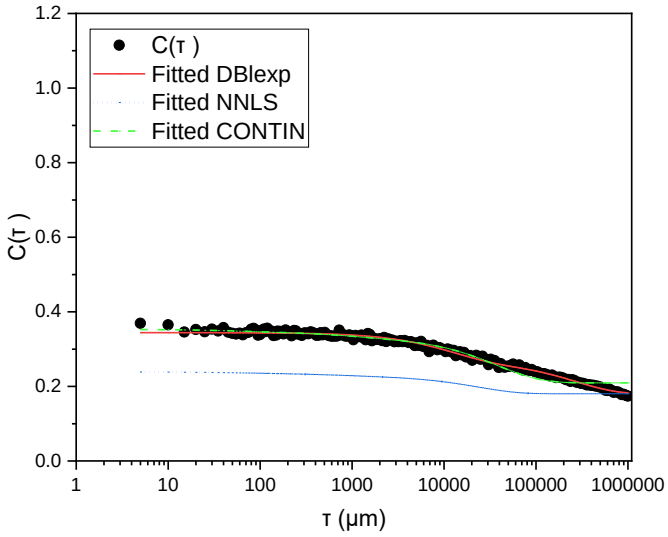

Figure D.3 DLS correlation function for the PDMAEMA-*b*-PVBBImTf_2N in pure DMSO displaying the double exponential fitting Dblexp (red), Non-Negative Least Squares NNLS (dotted blue), and CONTIN (dash green) fitting models.

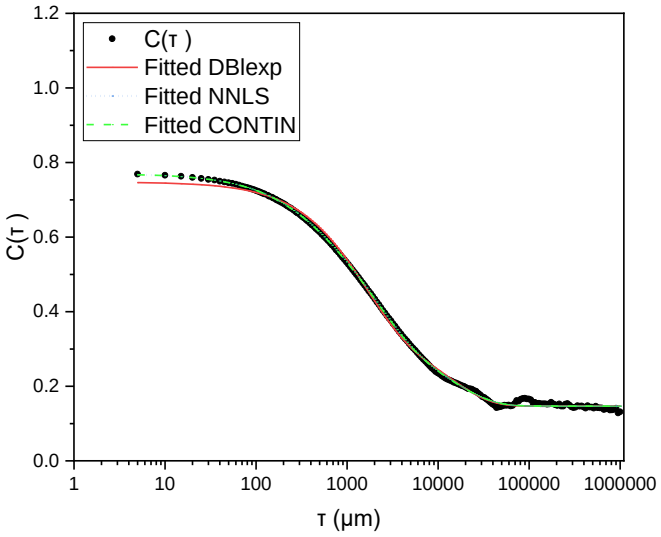

Figure D.4 Correlation function for the PDMAEMA-*b*-PVBBImTf_2N in 10 mM KNO_3 DMSO displaying the double exponential fitting Dblexp (red),Non-Negative Least Squares NNLS (dotted blue), and CONTIN (dash green) fitting models.

D.3.2. DLS Salt Study

Additional DLS measurements were performed on the block copolymers in DMSO/KNO_3 solutions as a function of KNO_3 concentration. These measurements were collected with an Anton Paar *Litesizer 500*, and the data was analyzed with Anton Paar *Kalliope* software. A minimum of 10 measurements were collected per salt condition at a 90° scattering angle. The software's Advanced model was used for fitting the correlation functions and cumulant analysis.

Figure D.5a shows one of the 10 DLS correlation functions measured for the block copolymer in each salt condition (0, 5, 10, 15, and 25 mM KNO_3 in DMSO). In pure DMSO, the correlation function does not form a clear baseline at longer delay times, which is indicative of large population sizes. This is similar to the correlation function obtained for the block copolymer in pure DMSO with the Brookhaven *Nanobrook Omni* instrument. At 5 mM, two steps in the correlation function are observed with the latter step also not forming a clear baseline. Multiple steps in DLS correlation functions are indicative of multiple distinct population sizes. In this case, a smaller population size is produced as the KNO_3 salts begin screening the positive charges from the PIL block and any protonated PDMAEMA groups. At 10 mM KNO_3 and higher, a typical correlation function is obtained with a clear baseline.

Unfortunately, the Kalliope software does not allow for fittings with a double exponential relationship, nor did the software allow for extending the delay time fitting range to fully encompass the correlation function. The red trace in Figure D.5a shows the cumulant fitting result with the Advanced model in Kalliope based on the average of 10 measurements. While the correlation functions for the block copolymer in 10-25 mM KNO_3 solutions showed a reasonable fit, the data set over the full delay time for the block copolymer in pure DMSO and 5 mM KNO_3 DMSO solution was not completely fitted. Therefore, the hydrodynamic structural lengths

calculated based on the cumulant fittings shown in Figure D.5b are considered with caution, especially for the 0 and 5 mM KNO_3 DMSO solutions.

For 15 and 25 mM KNO_3 solutions, the block copolymer showed structures ranging between ~10 and ~300 nm with a peak maximum at ~ 60 nm for the main population. A slightly broader population was observed for the 10 mMKNO_3 solution, with two main peaks at ~65 nm and 2720 nm. At 5 mM KNO_3, only the first correlation function step was fitted and is related to the smaller population sizes, with two main peaks found at 13 and 270 nm and a possible minor peak at 4550 nm. The resulting structure size distribution for the block copolymer in DMSO produced several peaks that are likely artifacts in the 0 to 300 nm range. The main peaks are located at ~810 nm, 1340 nm, and 4930 nm.

Overall, the combined analysis of the correlation functions and the structural lengths, at least qualitatively, indicate the block copolymer in pure DMSO has an expanded structure with large structural lengths which begin to collapse with increasing KNO_3 concentration, likely as a result of charge screening. Additional images of the block copolymer solvation in DMSO and KNO3 DMSO solutions are shown in Figure D.6-Figure D.8.

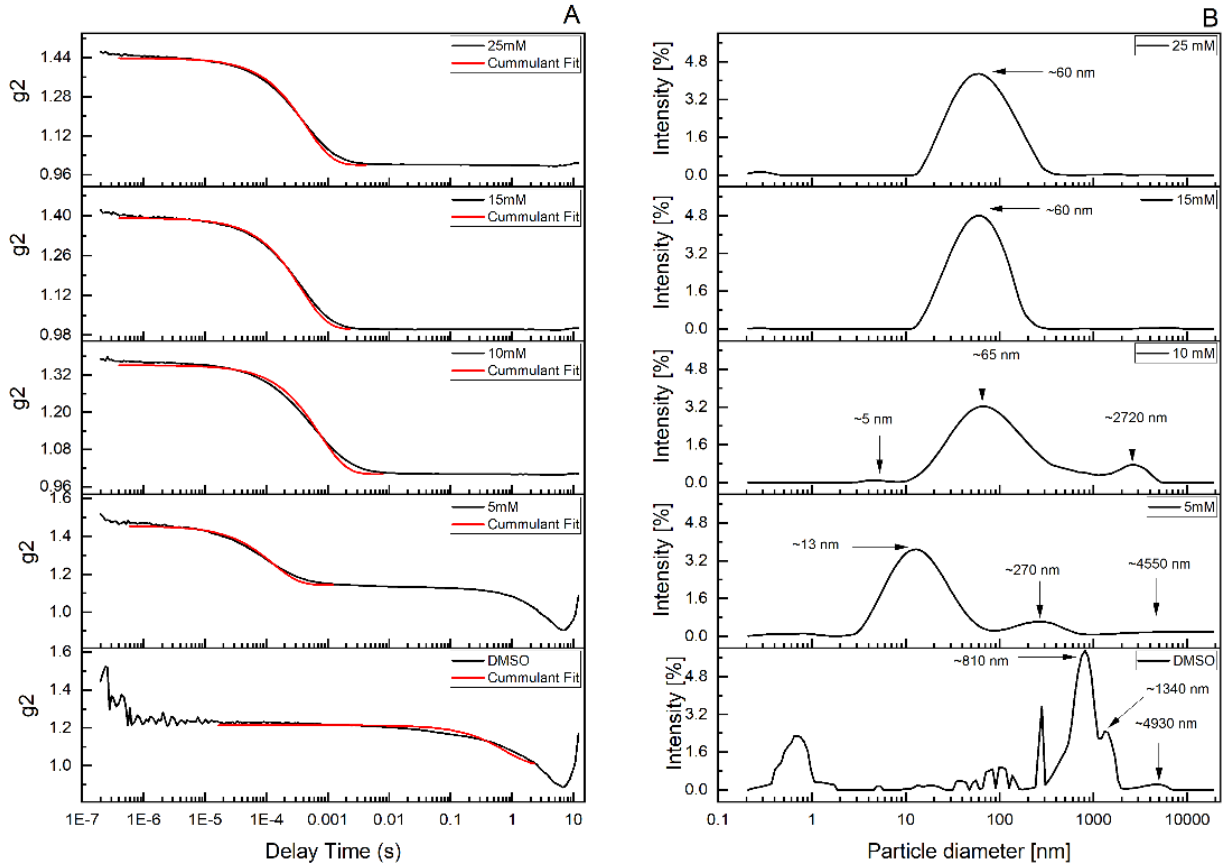

Figure D.5 DLS (a) representative correlation functions (black) with cumulant fittings (red) for one of 10 DLS measurements and (b) average particle distributions based on the Kalliope Advanced cumulant fitting model.

D.3.3. Block copolymer solvation in DMSO

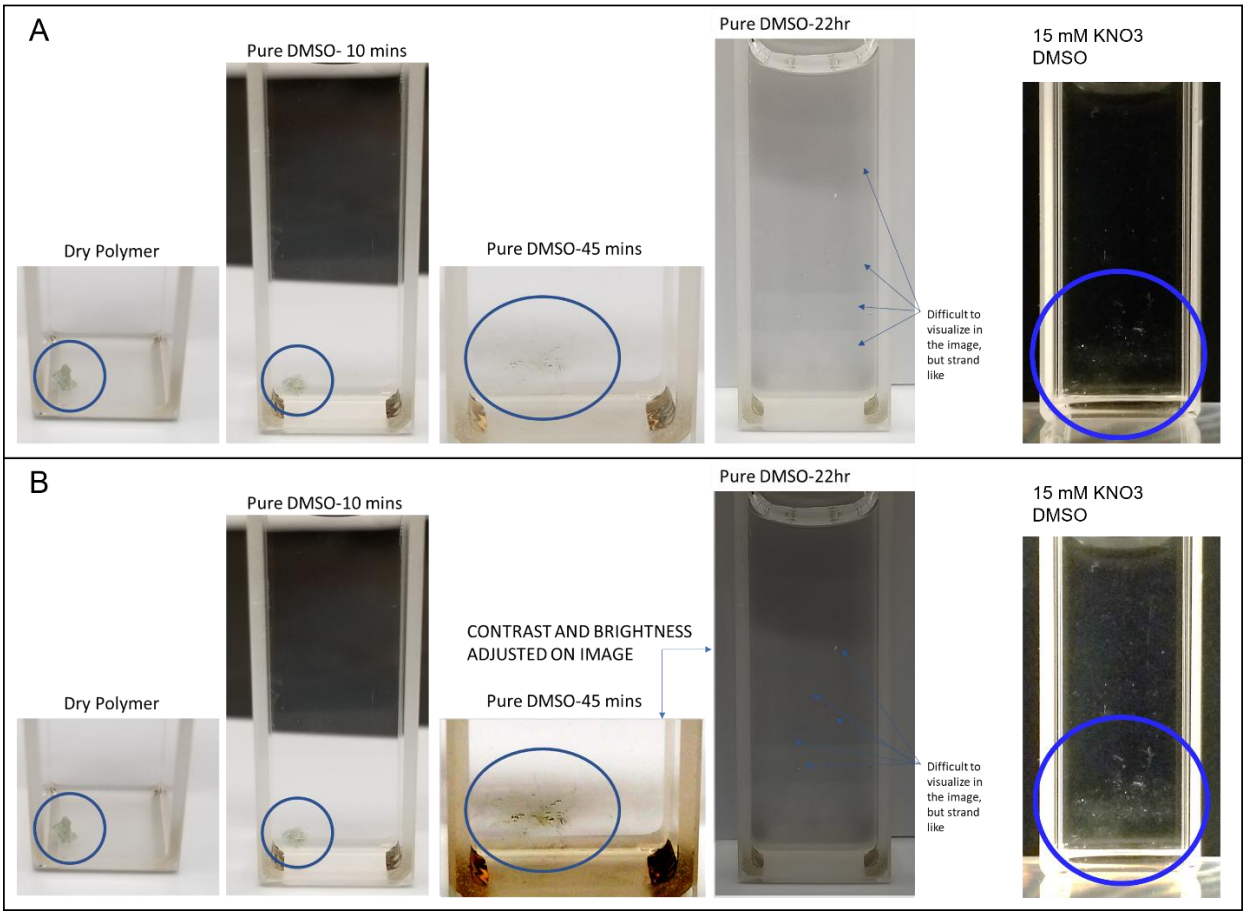

Figure D.6 (a) Optical images of the block copolymer solvating in pure DMSO for 22 h and after addition of 15 mM KNO_3. (b) The same images with the contrast and brightness adjusted to aid visualization of the partially solvated block copolymer (45 min), strand like structures (22 h), and the collapsed block copolymer in 15 mM KNO_3 solution.

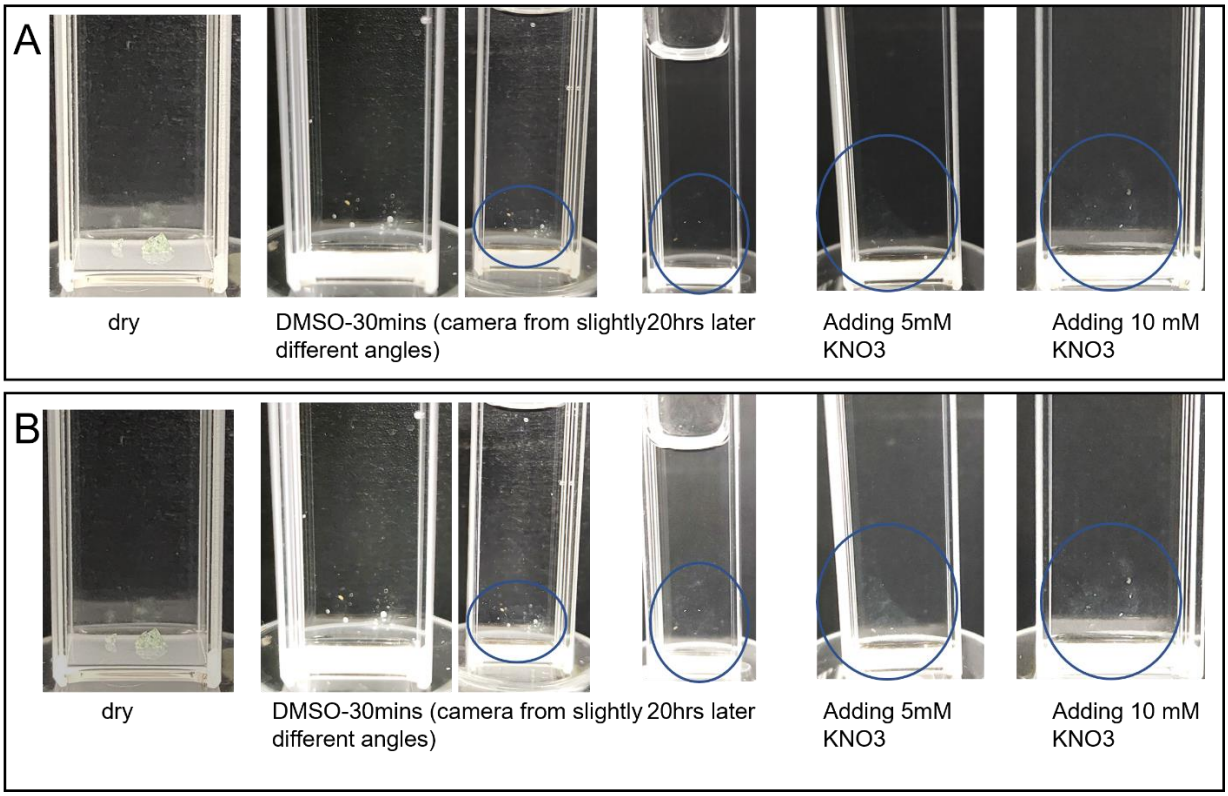

Figure D.7 (a) Optical images showing a second sample of the block copolymer solvating in pure DMSO over 20 h and after the addition of 5 and 15 mM KNO_3. (b) The same images with the contrast and brightness adjusted to aid visualization of the partially solvated block copolymer (30 min), expanded structures (20 h), and the collapsed block copolymer in 5 and 10 mM KNO_3 solution. Also included in the supplemental information is Video S1 which also shows the block copolymer in 15 mM KNO_3 DMSO and provides another view of the collapsed structure.

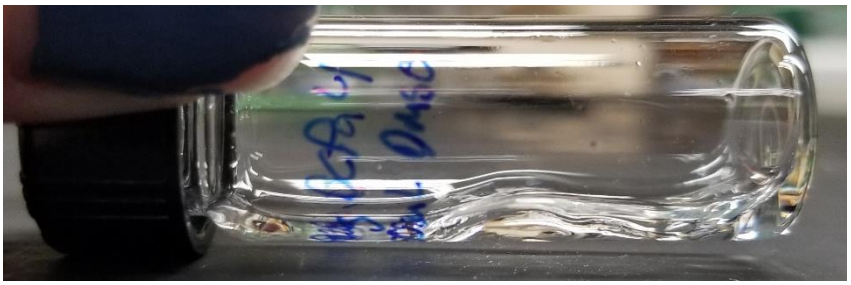

Figure D.8 Gel-like behavior of the block copolymer in small quantities of pure DMSO (~0.0029 g in 250 μL DMSO).

Appendix E: Evaluation of a novel poly(ionic liquid) block copolymer and homopolymer as ionic electroactive polymer actuators

Included in this document are additional spectroscopic, thermal DSC traces, and AFM images to support the main text. Additional ATR-FTIR spectra of the PDMAEMA macroinitiator, VBBImTf_2N monomer, and the PVDF 40 wt% IL control are provided in Figure E.1 and Figure E.2. Expanded DSC traces of the the regions discussed in the main text are provided in Figure E.3-Figure E.6. AFM section traces, in addition to the height and DMT modulus scans provided in the main text, are presented as a function of ionic liquid content (Figure E.7-Figure E.8) and each individual sample AFM scan is shown in Figure E.11-Figure E.18. The AFM scans include height, DMT modulus, adhesion, dissipation, deformation, and peak force error.

E.1. ATR-FTIR

Additional ATR-FTIR spectra for the PDMAEMA macroinitiator and the VBBImTf_2N monomer reported in the author's previous work is provided for comparison in Figure E.1[1]. Figure E.2 shows the neat PVDF and the PVDF with 40 wt% C_4C1ImBF_4 ionic liquid. The emergence of peaks corresponding to the imidazolium ring $C_{4,5}$-H (3163 cm^{-1}) and C_2-H (3123 cm^{-1}) str, C=C/C=N str (~1571 cm^{-1}), and BF_4^- triplet (1051, 1037, 1020 cm^{-1}) confirm the incorporation of the ionic liquid into PVDF.

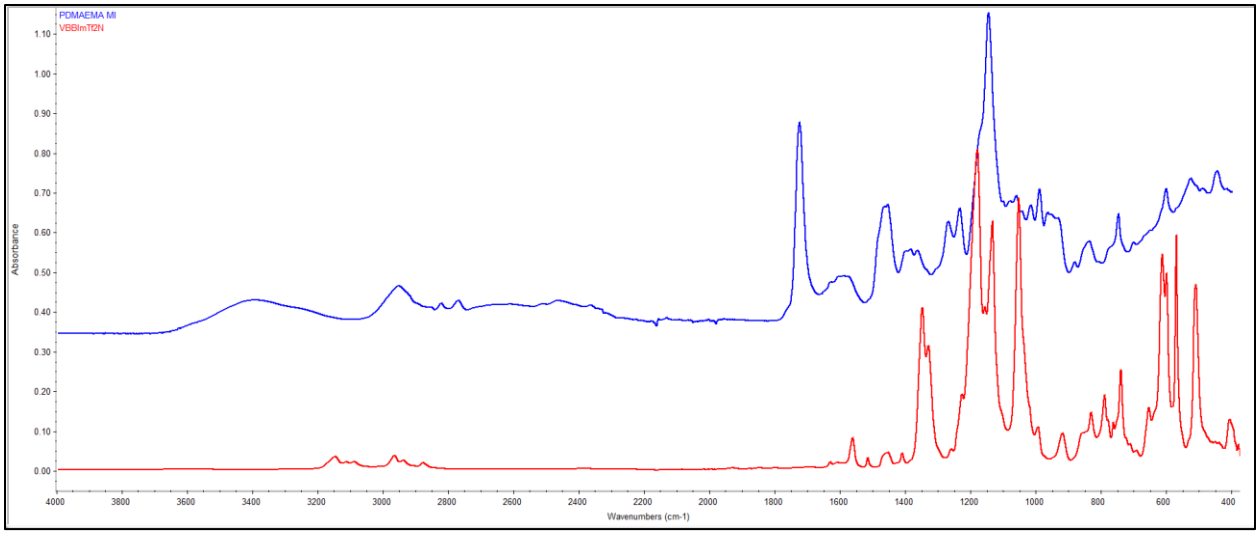

Figure E.1 ATR-FTIR spectra of the PDMAEMA macroinitiator (blue) and $VBBImTf_2N$ monomer (red) [1].

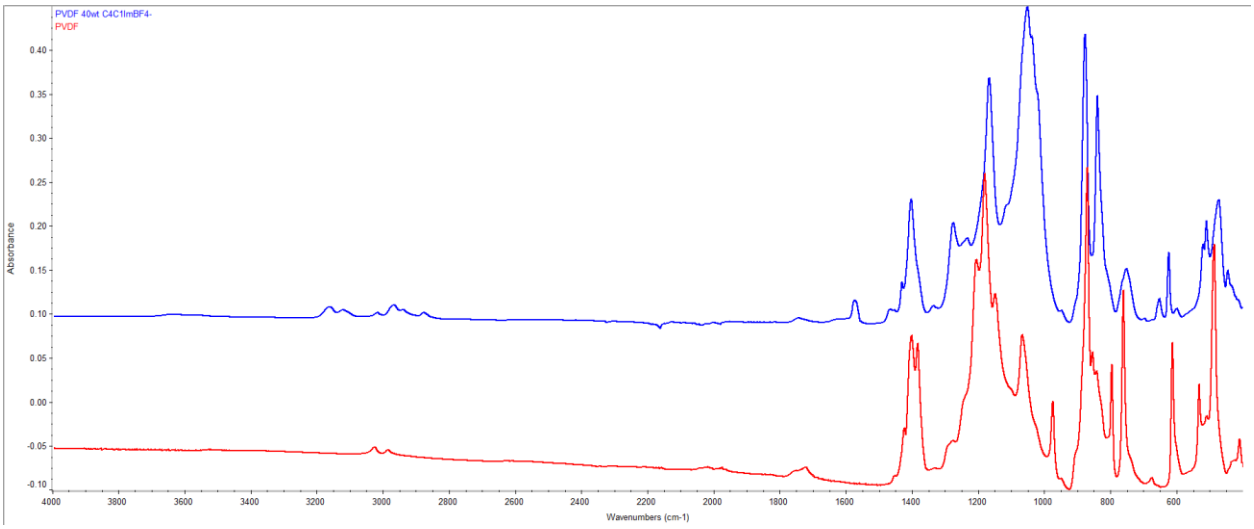

Figure E.2 ATR-FTIR spectra of PVDF (red) and the corresponding PVDF 40 wt% $C_4C_1ImBF_4^-$ ionogel (blue).

E.2. DSC

Zoomed in portions of the DSC profiles marked in the dashed boxes of Figure 5 (main text) are provided in Figure E.3-Figure E.6.

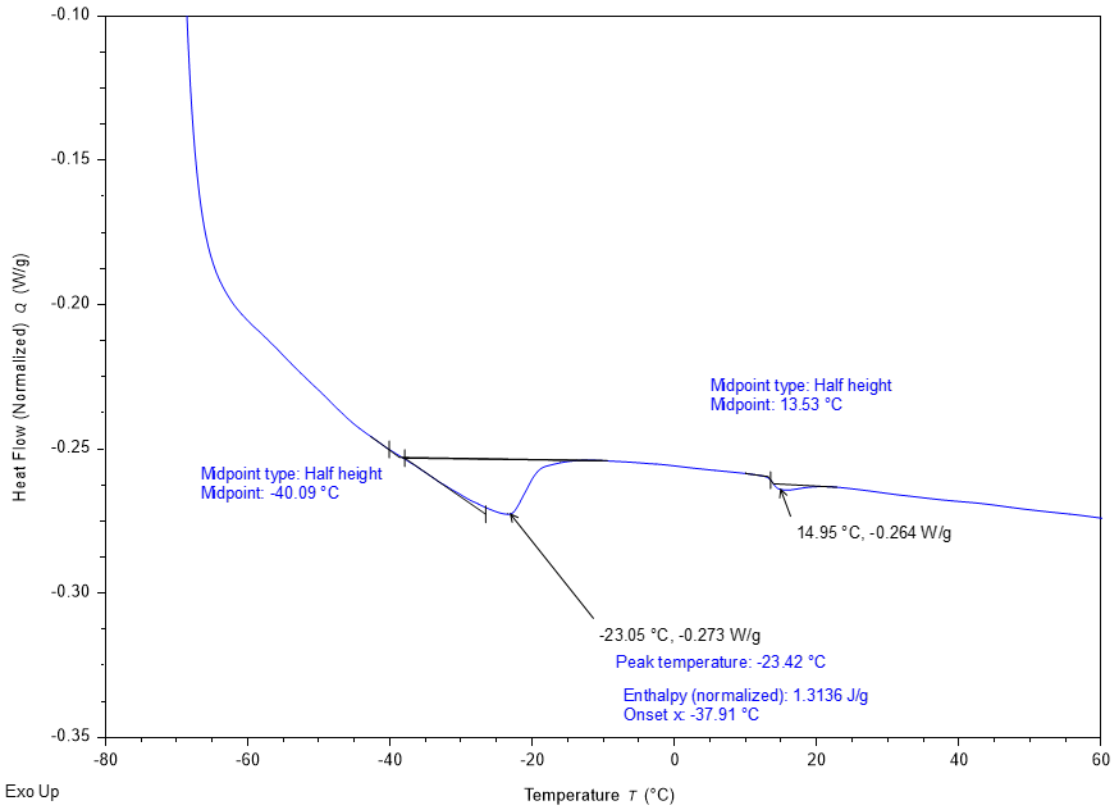

Figure E.3 PVBBImTf$_2$N 25 wt% IL DSC trace highlighting the thermal transitions with the glass transition analysis midpoint (-40 °C) and the peak minimum temperature (-23 °C) shown.

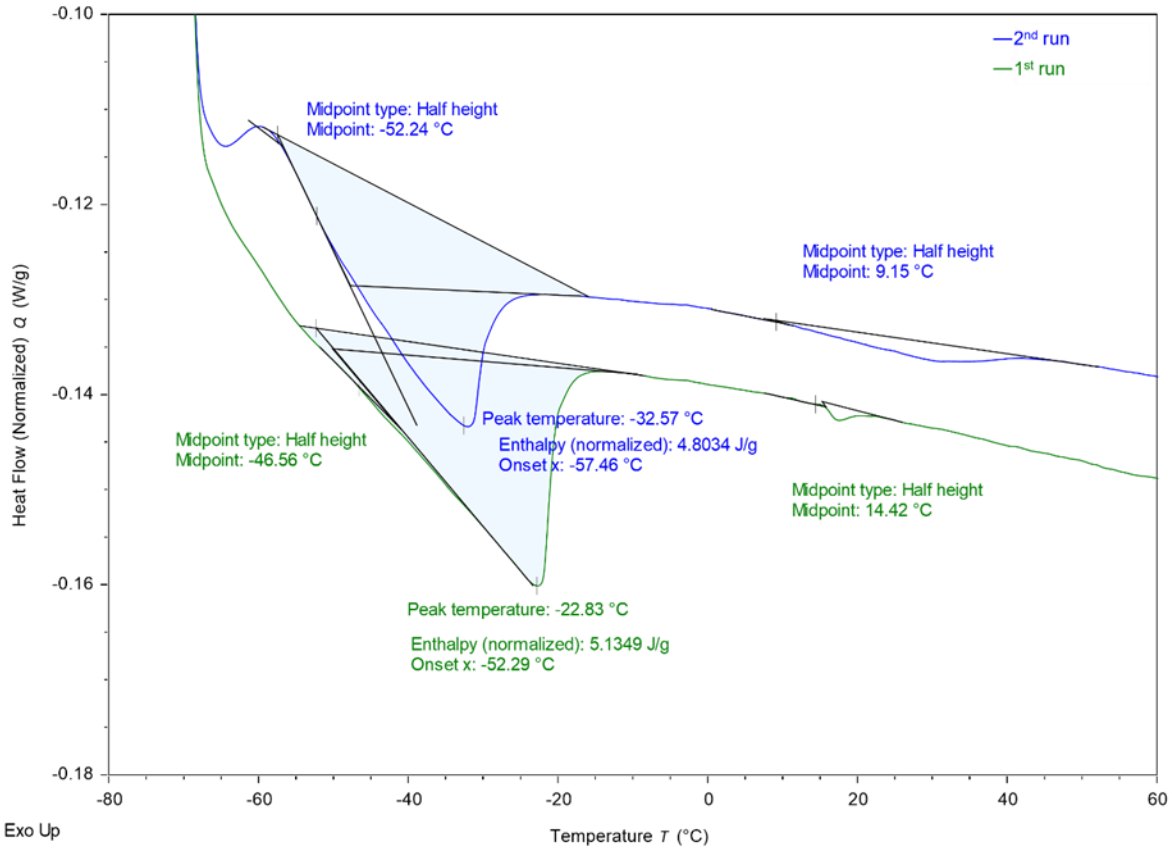

Figure E.4 DSC profiles from two heating and cooling cycles for PVBBImTf_2N 40 wt% IL. The green trace shows the first run and the blue trace shows the second run on the same sample (but performed on a separate day). Both the glass transition analysis midpoint and the peak minimum temperature are shown.

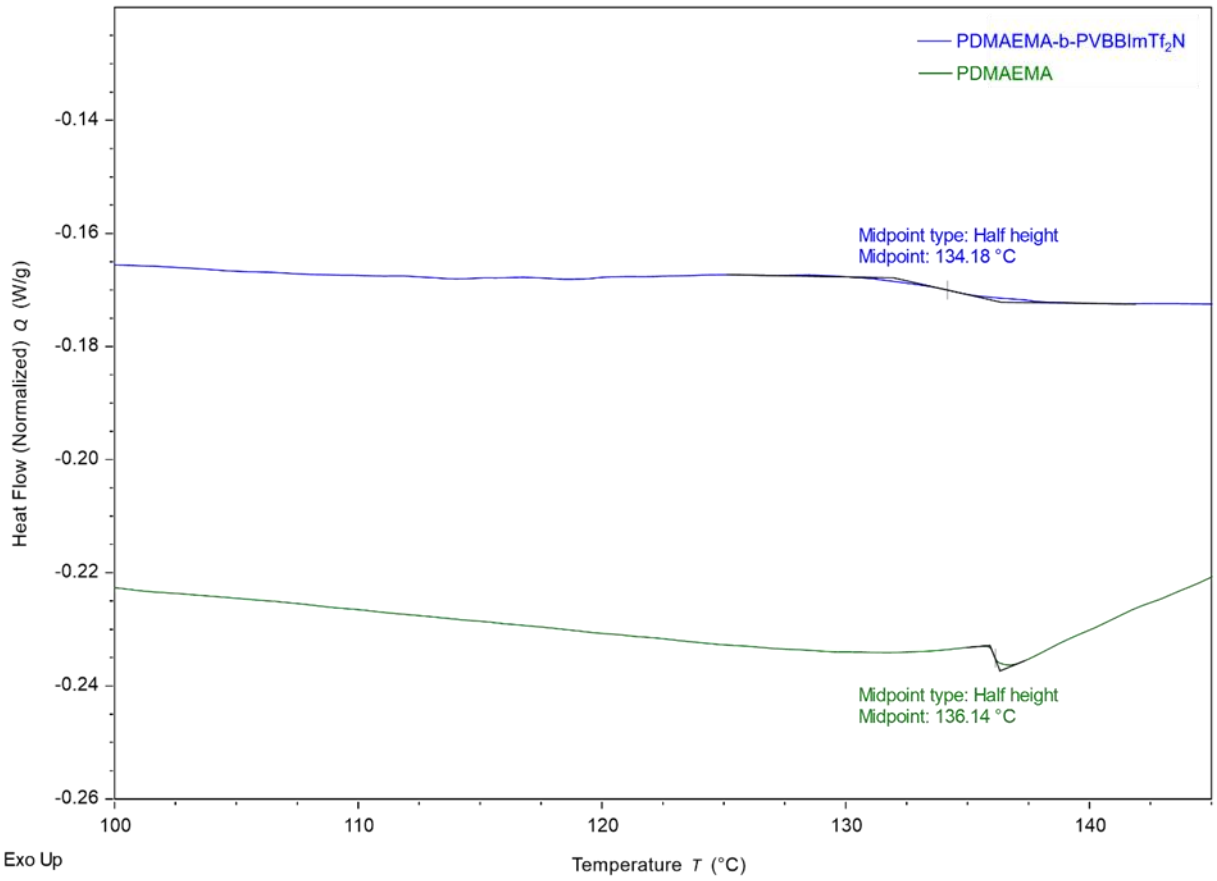

Figure E.5 DSC traces for PDMAEMA (green) and PDMAEMA-*b*-PVBBImTf$_2$N (blue) between 100 and 145 °C showing the weak glass transition temperature at ca. 136 °C and 134 °C for the macroinitiator and block copolymer, respectively.

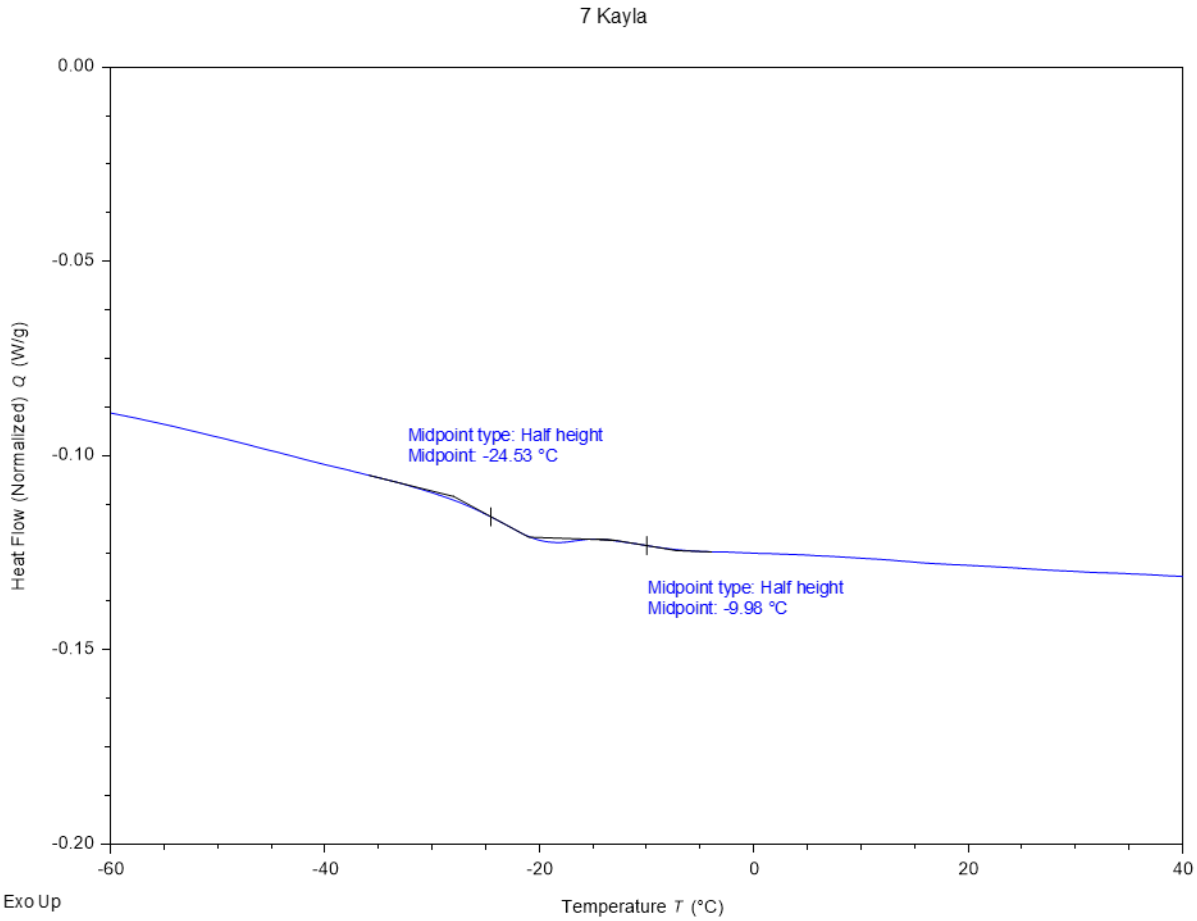

Figure E.6 DSC trace of PVBBImTf2N 10 wt% ionogel showing the primary glass transition temperature at approx. -25 °C and a possible week glass transition temperature at approx. -10 °C.

E.3. Nanomechanical Analysis Using AFM

Figure E.7-Figure E.8 show the AFM height and DMT modulus traces for the PVBBImTf_2N homopolymer and PDMAEMA-*b*-PVBBImTf_2N block copolymer ionogels for 0, 10, 25, and 40 wt% ionic liquid content. (Weight percentages are calculated with respect to total polymer mass.)

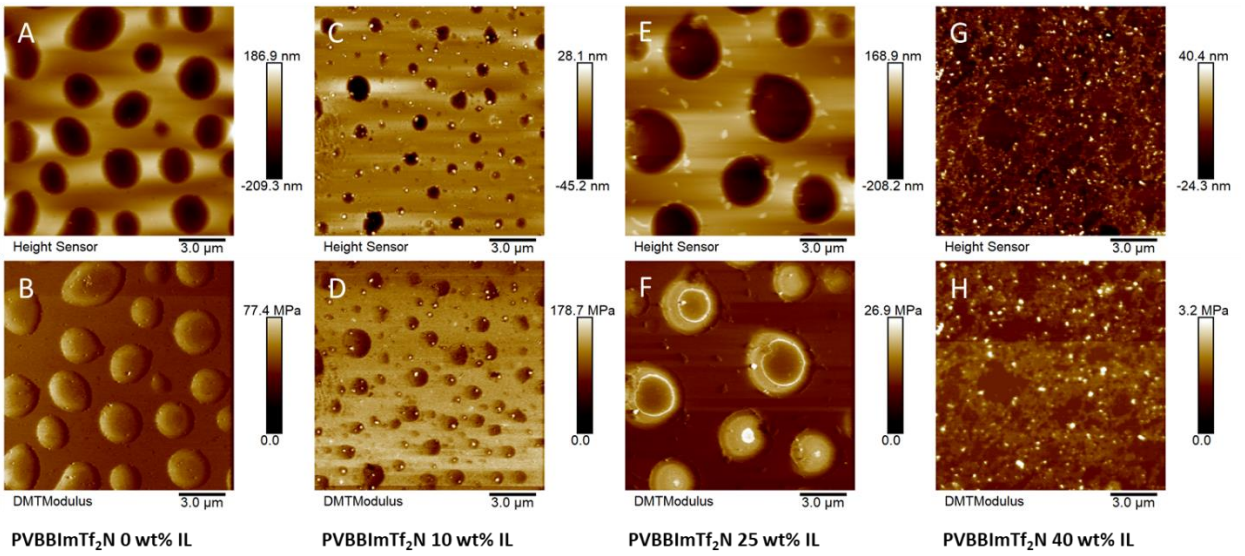

Figure E.7 AFM height and DMT modulus maps for (left to right) PVBBImTf_2N with 0 wt% IL, 10 wt% IL, 25 wt% IL, and 40 wt% IL.

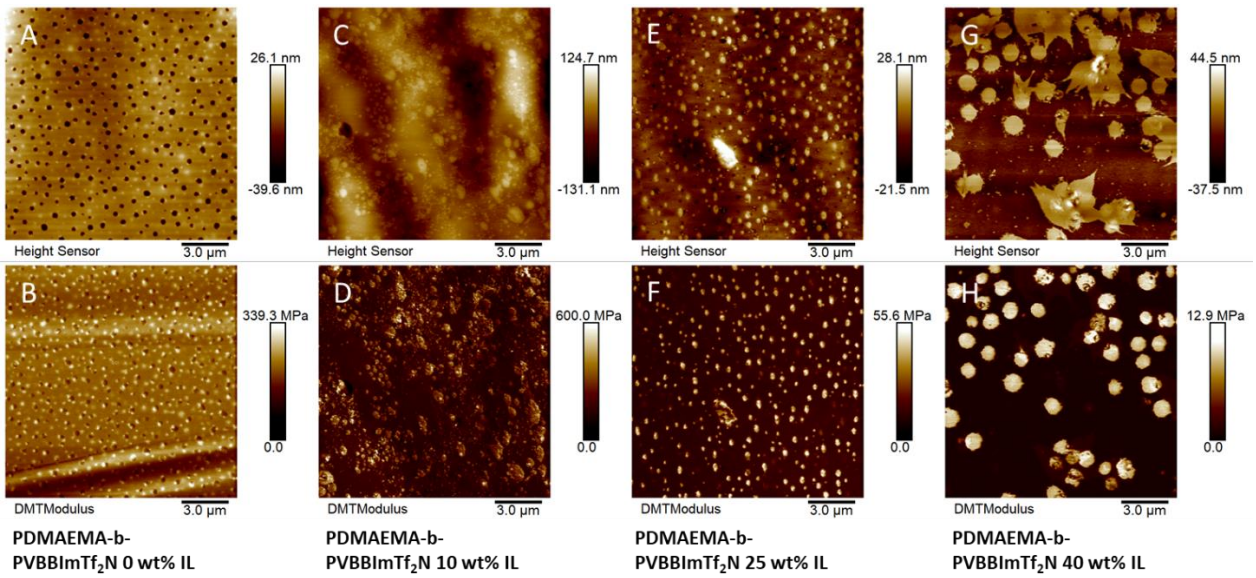

Figure E.8 AFM height and DMT modulus maps for (left to right) PDMAEMA-*b*-PVBBImTf$_2$N block copolymer with 0 wt% IL, 10 wt%, 25 wt% IL, and 40 wt% IL.

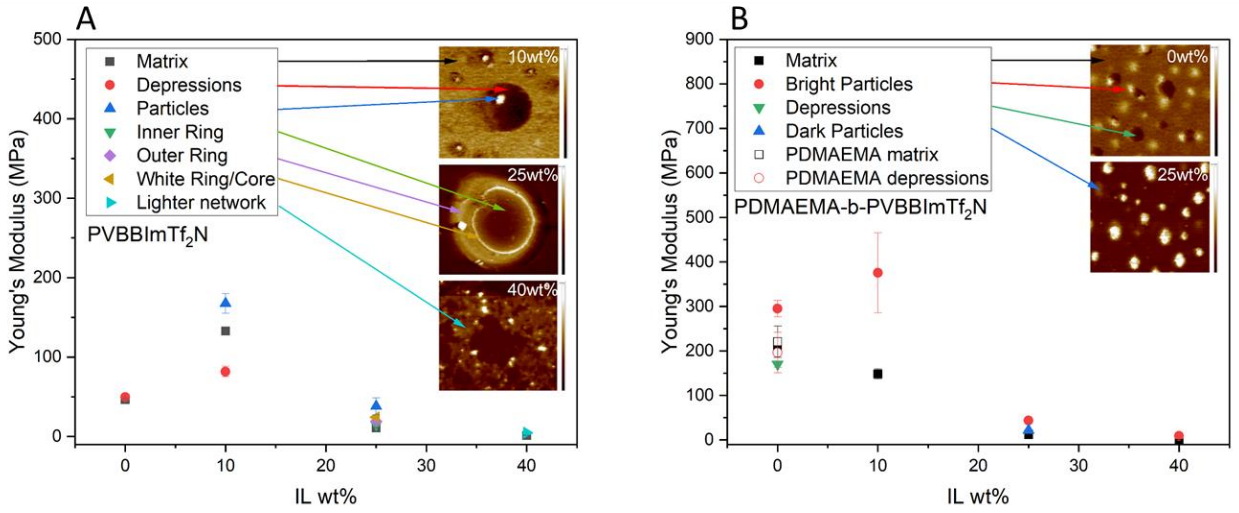

Figure E.9 Young's modulus as a function of ionic liquid content for the different phases in the (a) PVBBImTf$_2$N ionogels and the (b) PDMAEMA-*b*-PVBBImTf$_2$N ionogels. Inserts in each plot are zoomed in portions of the DMT modulus traces for each ionogel, which can be seen in full in Figure E.7-Figure E.8.

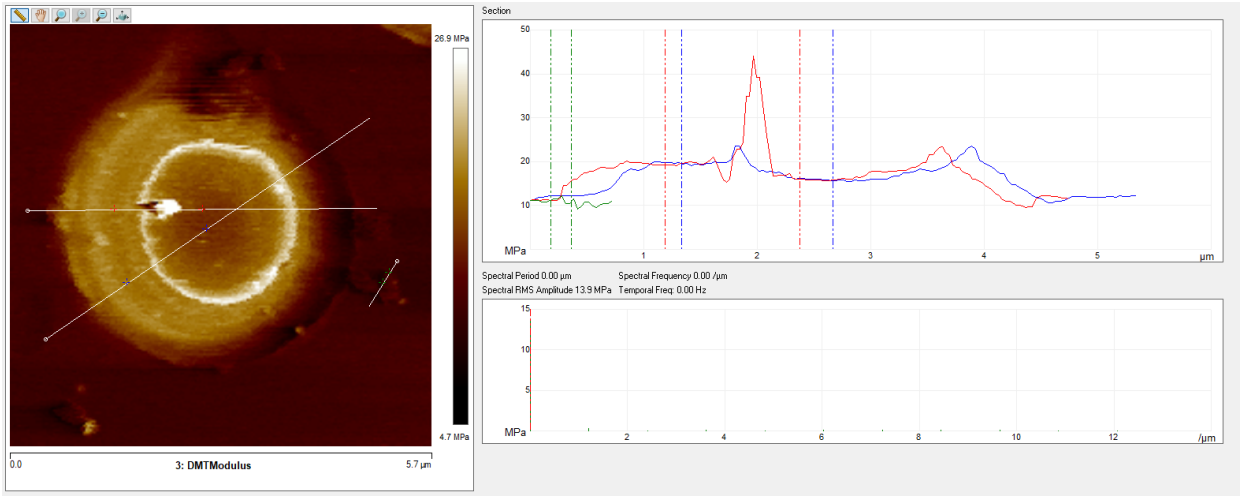

Figure E.10 DMT modulus scan with line traces for one of the depressions in PVBBImTf$_2$N 10 wt% ionogel showing a gradient of moduli. Starting from the matrix, the modulus increases from ~10 MPa to ~19 MPa in the outer ring, ~24 MPa for the sharp white ring, and ~15 MPa in the inner ring. The small particle on the perimeter of the depression has a modulus of ~45 MPa.

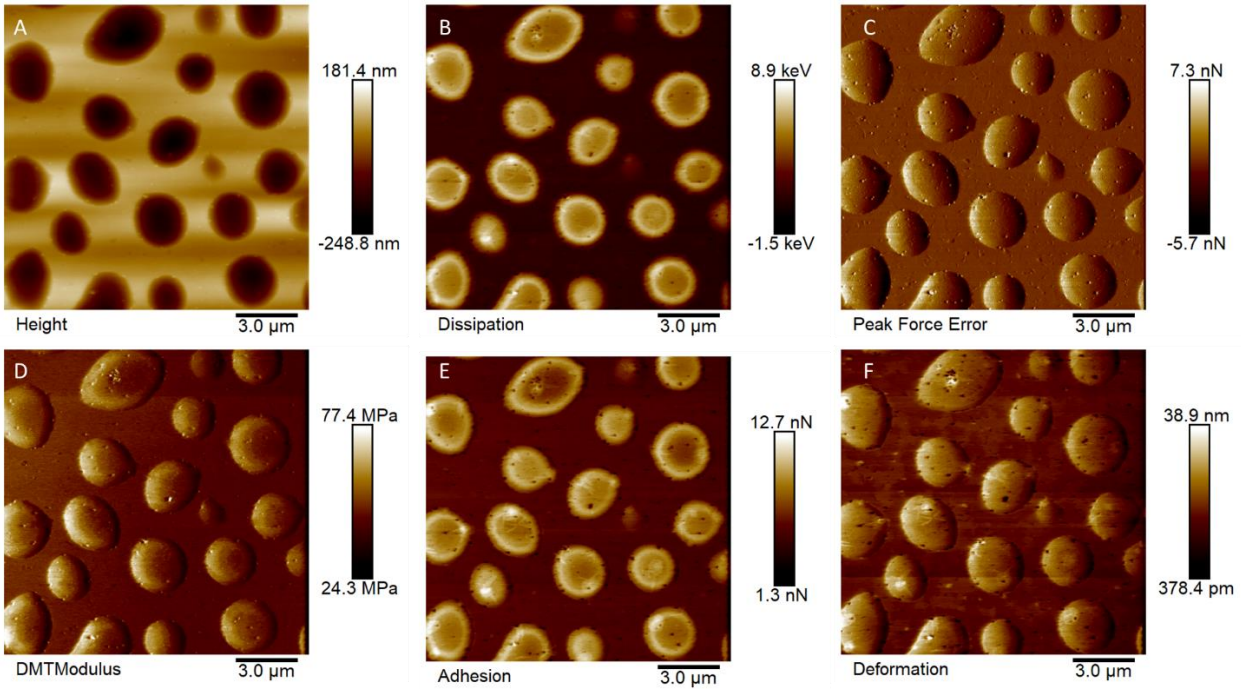

Figure E.11 AFM images for dry PVBBImTf$_2$N including: (a) height; (b) dissipation; (c) peak force error; (d) DMT modulus; (e) adhesion; and (f) deformation.

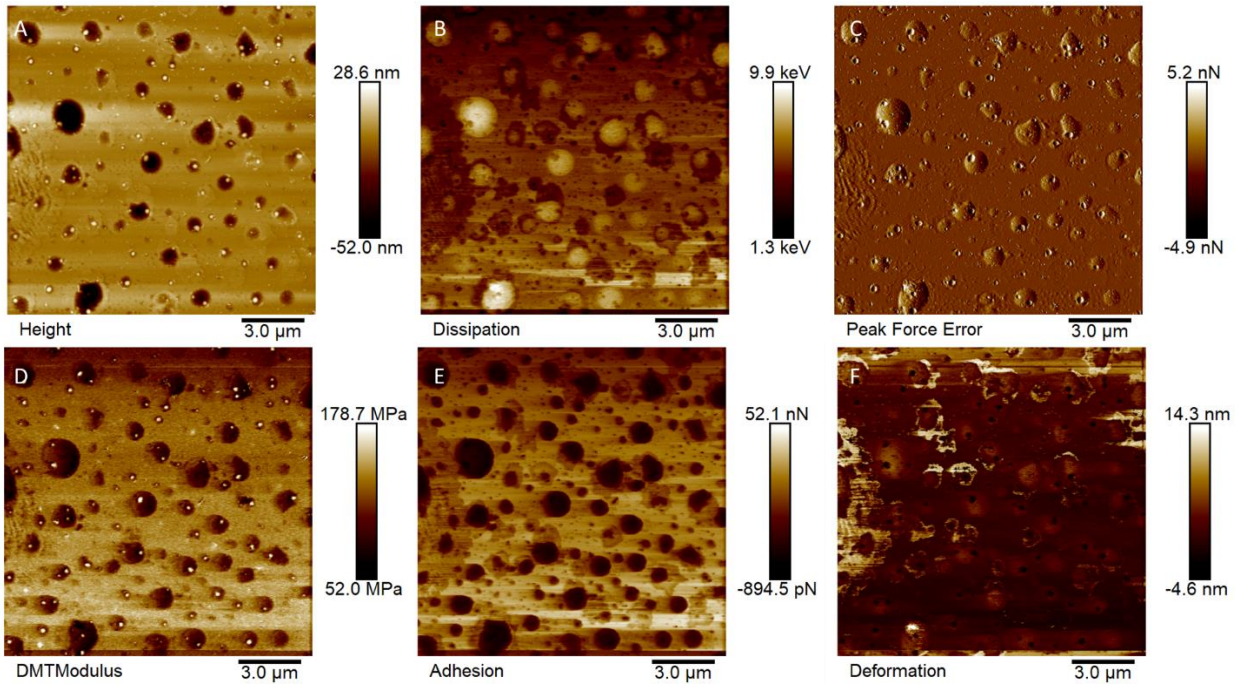

Figure E.12 AFM images for PVBBImTf_2N 10 wt% ionogel including the following data: (a) height; (b) dissipation; (c) peak force error; (d) DMT modulus; (e) adhesion; and (f) deformation.

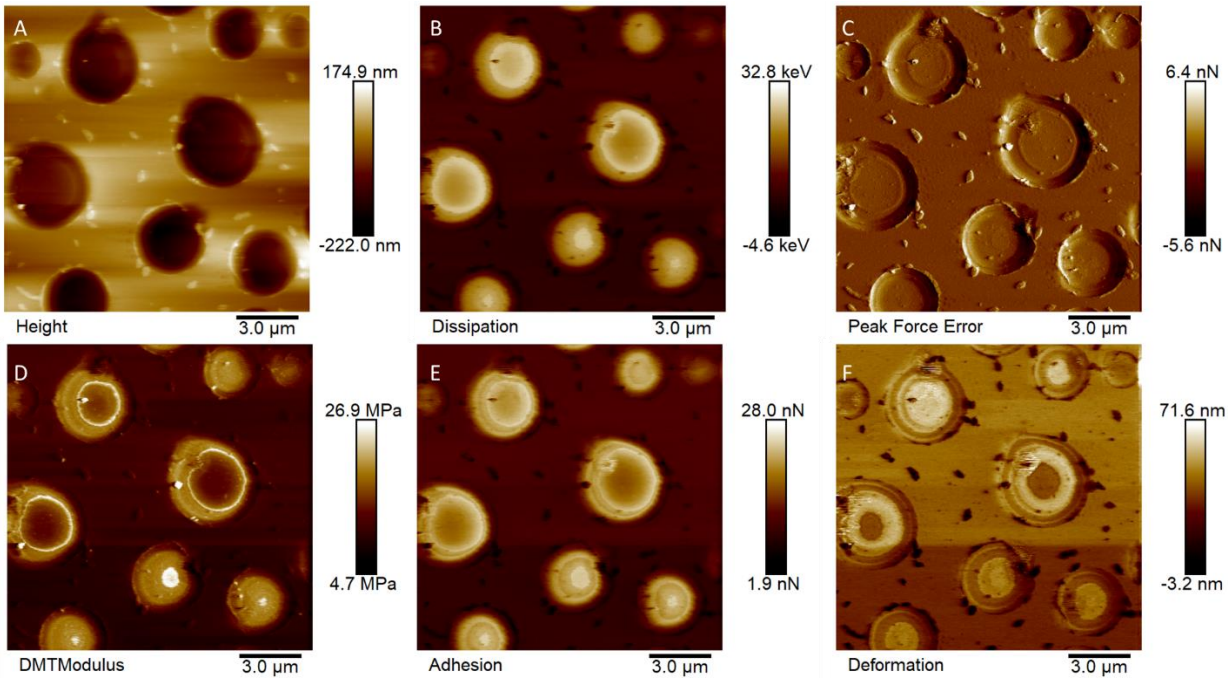

Figure E.13 AFM images for PVBBImTf_2N 25 wt% ionogel including: (a) height; (b) dissipation; (c) peak force error; (d) DMT modulus; (e) adhesion; and (f) deformation.

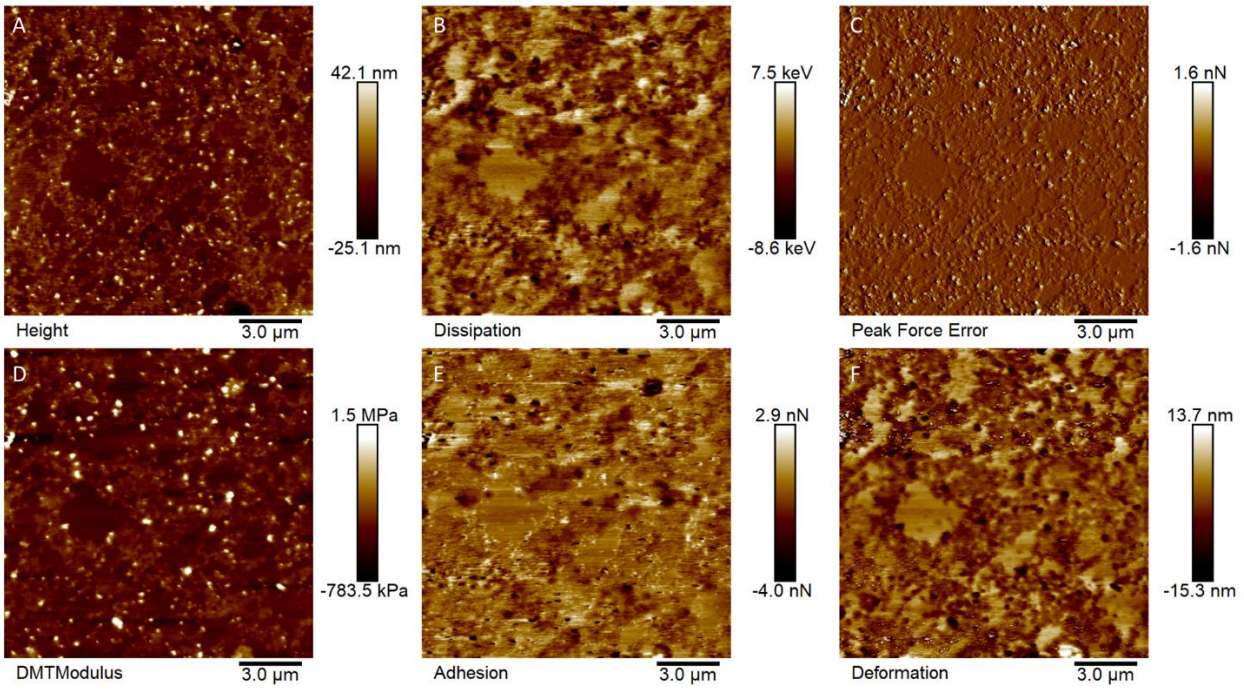

Figure E.14 AFM images for PVBBImTf_2N 40 wt% ionogel including: (a) height; (b) dissipation; (c) peak force error; (d) DMT modulus; (e) adhesion; and (f) deformation.

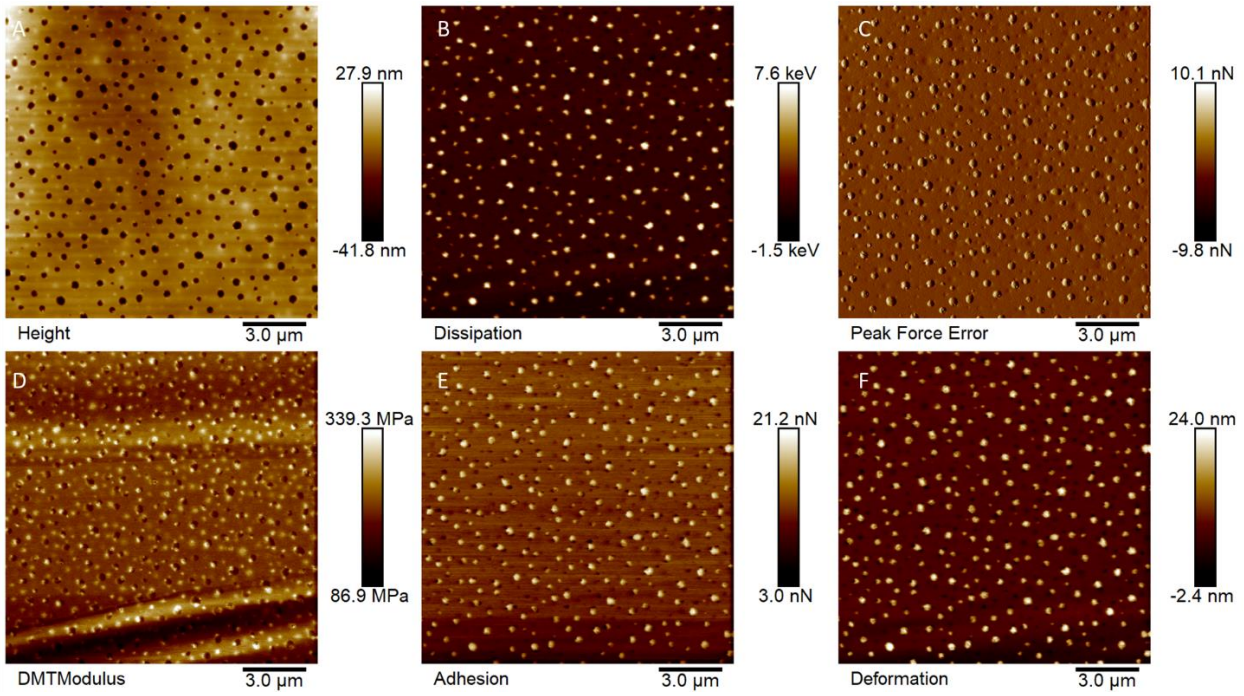

Figure E.15 AFM images for dry PDMAEMA-*b*-PVBBImTf_2N including: (a) height; (b) dissipation; (c) peak force error; (d) DMT modulus; (e) adhesion; and (f) deformation.

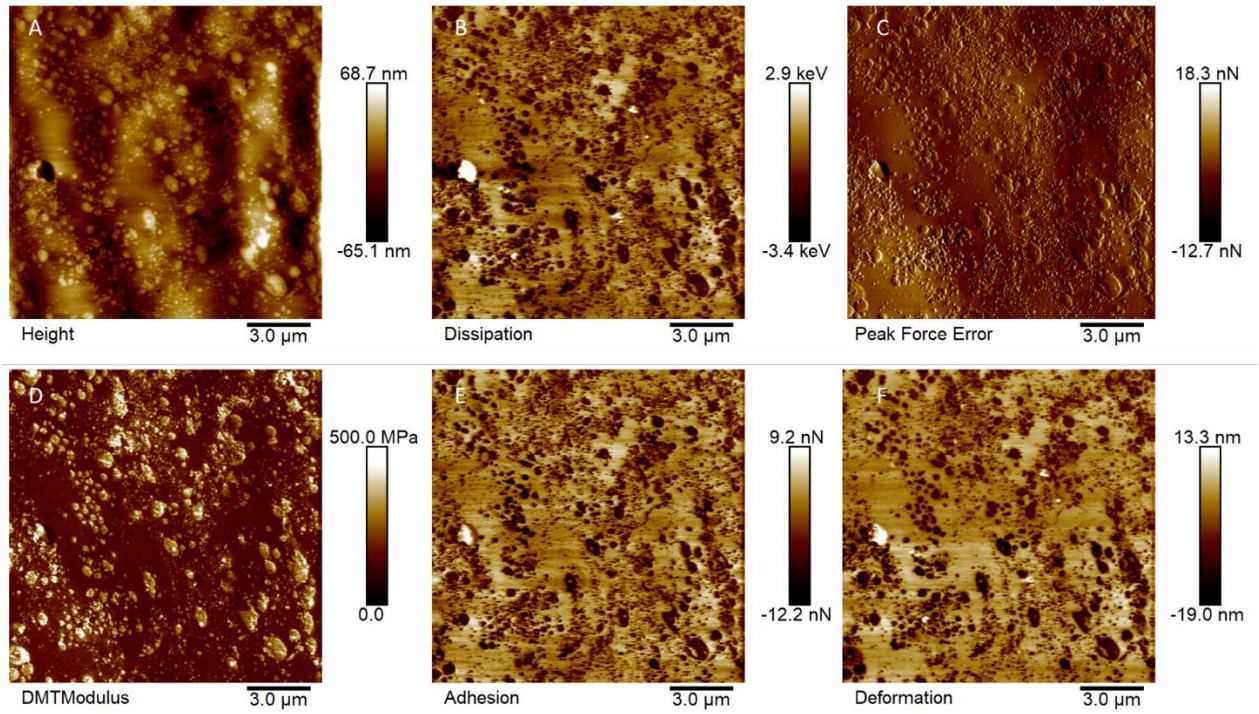

Figure E.16 AFM images for PDMAEMA-*b*-PVBBImTf_2N 10 wt% ionogel including: (a) height; (b) dissipation; (c) peak force error; (d) DMT modulus; (e) adhesion; and (f) deformation.

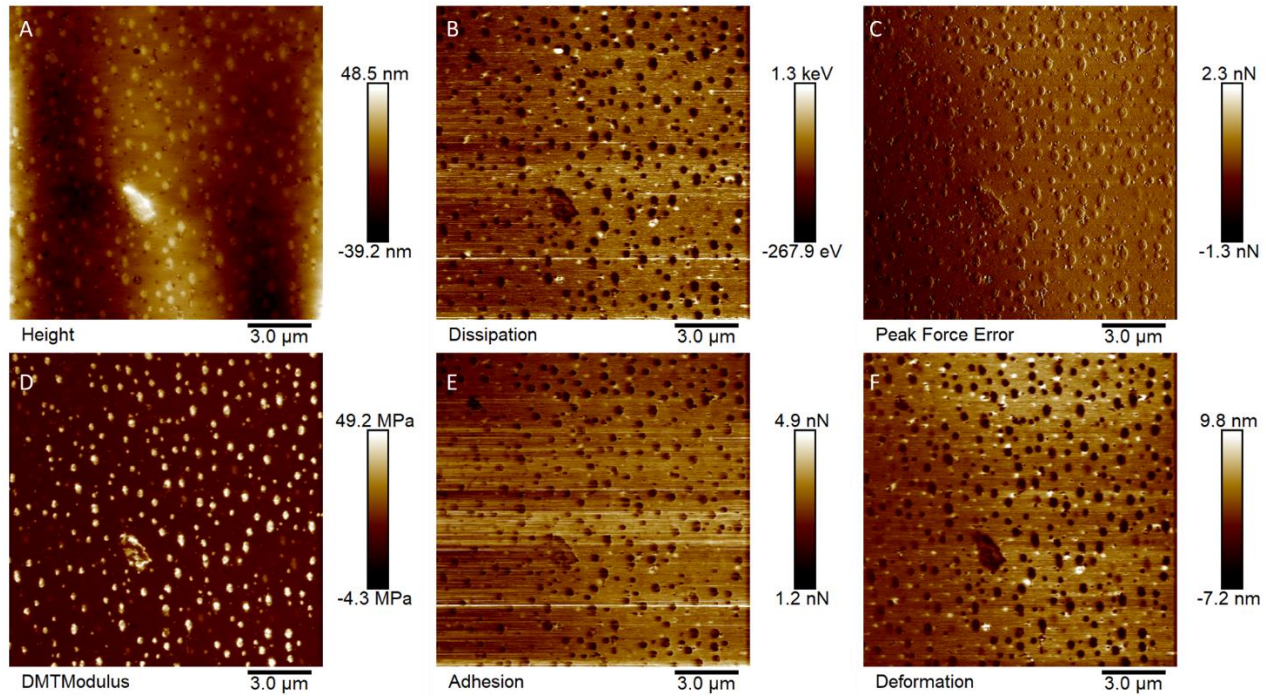

Figure E.17 AFM images for PDMAEMA-*b*-PVBBImTf_2N 25 wt% ionogel including: (a) height; (b) dissipation; (c) peak force error; (d) DMT modulus; (e) adhesion; and (f) deformation.

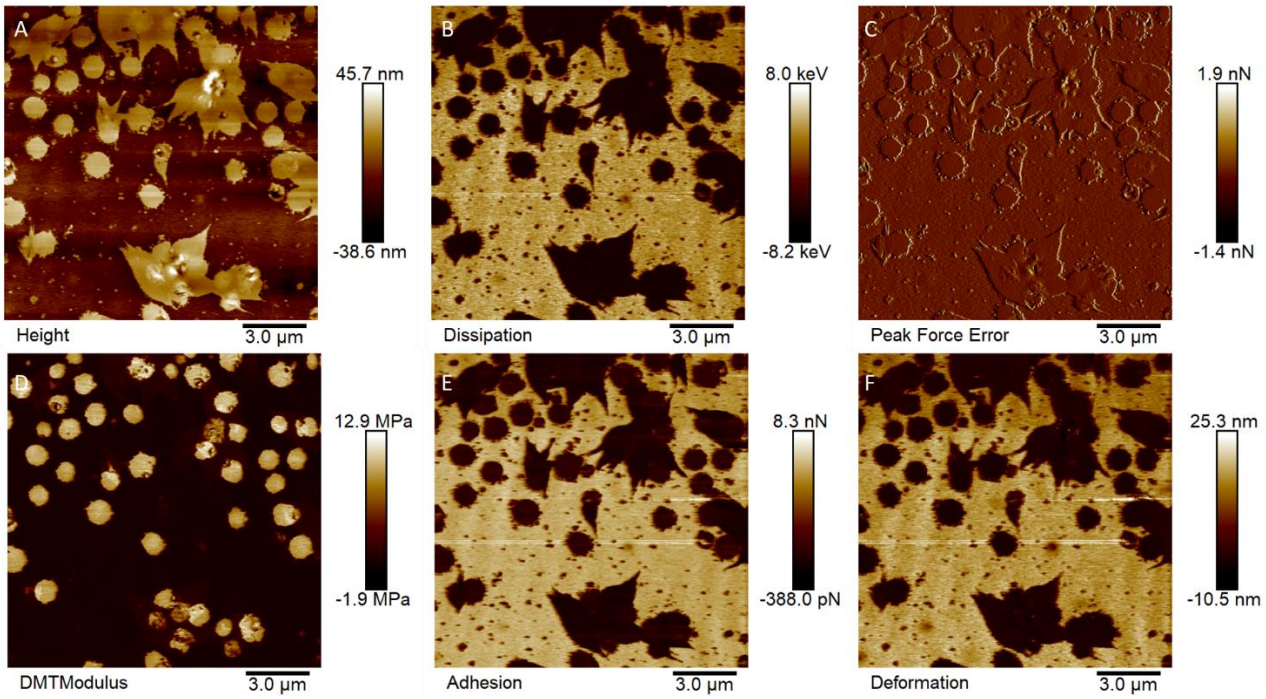

Figure E.18 AFM images for PDMAEMA-*b*-PVBBImTf$_2$N 40 wt% ionogel including: (a) height; (b) dissipation; (c) peak force error; (d) DMT modulus; (e) adhesion; and (f) deformation.

E.4. Actuator Film Development Images

Figure E.19 PDMAEMA-*b*-PVBBImTf$_2$N 25 wt% IL attempt at developing an actuator film with gold foil electrodes. After peeling from the Teflon sheeting, the film rolled up into a ball.

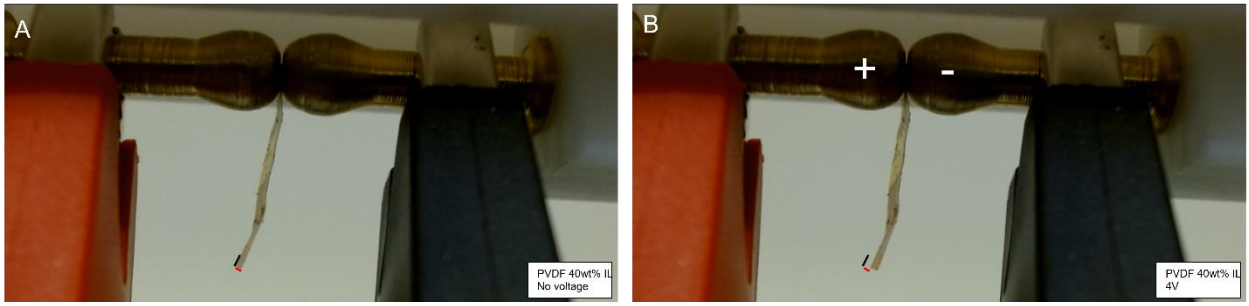

Figure E.20 PVDF 40 wt% IL actuator video still frames (a) before voltage application and (b) after applying 4 V. The black and red lines mark the side and bottom of the actuator initial position to aid visualization of the actuator displacement.

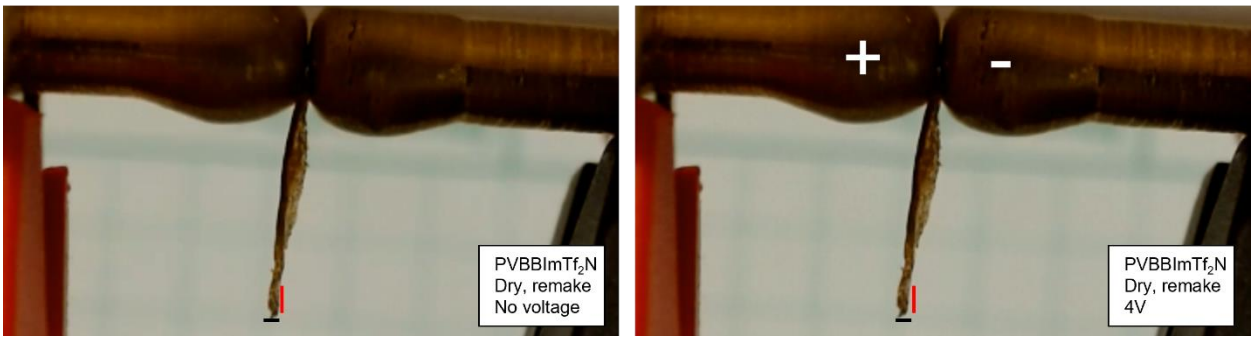

Figure E.21 PVBBImTf$_2$N dry replicate actuator video still frames (a) before voltage application and (b) after applying 4 V. The black and red lines mark the side and bottom of the actuator initial position to aid visualization of the actuator displacement.

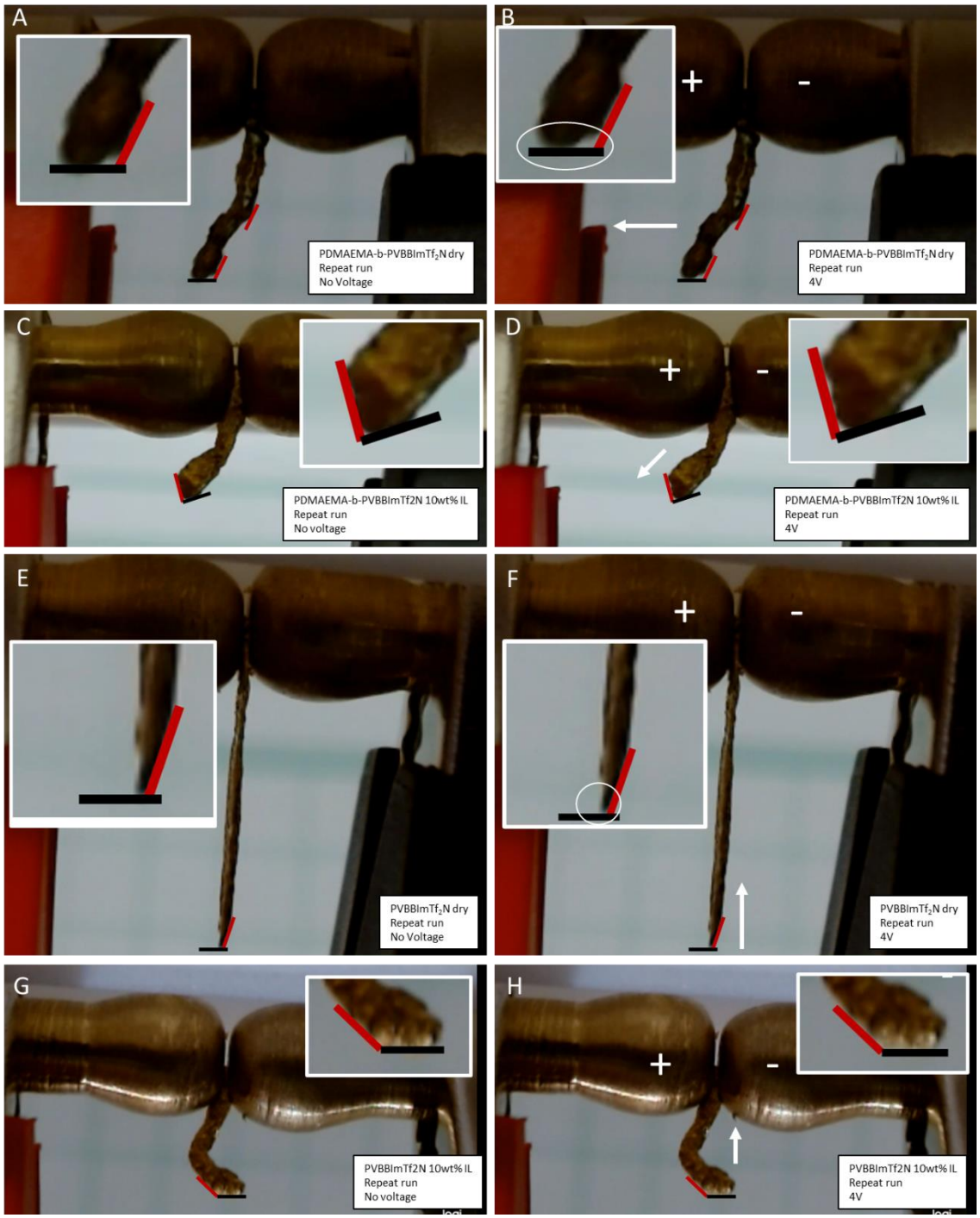

Figure E.22 Re-testing of the PDMAEMA-*b*-PVBBImTf$_2$N dry polymer (a,b), PDMAEMA-*b*-PVBBImTf$_2$N 10 wt% ionogel (c,d), PVBBImTf$_2$N polymer (e,f), and PVBBImTf$_2$N 10 wt% ionogel are shown. Smaller displacements and, in some cases, changes in bending direction from the original testing of the films are observed.

Table E.1 Tip displacements for the actuators developed at 50 sec of applied 4 V and at specified times. Tip displacements observed by Kokubo et al. are included for comparison[2]. Positive numbers indicate displacement towards the anode (negatively charged electrode) and negative displacements indicate displacement towards the cathode (positively charged electrode).

	Tip Displacement at 50 sec		**Tip Displacement at Specified Times**		
Sample	**x (µm)**	**y (µm)**	**Time (s)**	**x (µm)**	**y (µm)**
PVBBImTf_2N	-184.5	30.5	60	-184.5	30.5
PVBBImTf_2N 10 wt% IL	1.6	26.4	60	1.8	41.6
			169	1.5	79.6
PDMAEMA-*b*-PVBBImTf_2N	110.0	62.0	55	113.8	59.3
PDMAEMA-*b*-PVBBImTf_2N 10 wt%	89.4	40.2	60	110.9	48.2
			195	278.9	121.4
PVDF 40 wt% IL (45s)			45	525.9	-117.7
Kokubo et al.			202	-163.0	NA
			1933	-517.0	NA

Supplemental actuation videos and sample preparation videos are also provided and are described as follows:

Video S1. Processing of the PDMAEMA-*b*-PVBBImTf2N 25 wt% ionogel after compression molding, demonstrating the adhesion of the polymer to the Teflon sheeting. An attempt at a stretchability test is also included. (link).

Video S2. Processing of the PDMAEMA-*b*-PVBBImTf2N 10 wt% ionogel after compression molding. This film exhibited less adhesion to the Teflon™ sheeting compared to the 25 wt% ionogel sample (link). An attempt at a stretchability test is also included (link).

Video S3. Actuation video for the PVBBImTf_2N dry actuator film at 64x speed. (link).

Video S4. Actuation video for the PDMAEMA-*b*-PVBBImTf_2N film at 64x speed. (link).

Video S5. Actuation video for the PVBBImTf_2N 10 wt% ionogel actuator film at 64x speed. (link).

Video S6. Actuation video for the PDMAEMA-*b*-PVBBImTf_2N 10 wt% ionogel actuator film at 64x speed. (link).

E.5. Dielectric Constant

The dielectric constant for the PVBBImTf$_2$N polymer was calculated by:

$$\textbf{EQ E-1}\ \epsilon_r = \frac{CL}{\epsilon_o A}$$

where C is the capacitance determined from EIS measurements, L is the film thickness (L= 0.6 mm), ϵ_o is the dielectric constant of a vacuum (8.85 x 10^{-12} F/m), and A is the cross-sectional area of the polymer film (A=0.309 cm^2). C was determined by fitting the impedance data to an equivalent circuit for a polymer layer sandwiched between two blocking electrodes (see Halim et al.)[3] in EC-Labs software (BioLogic).

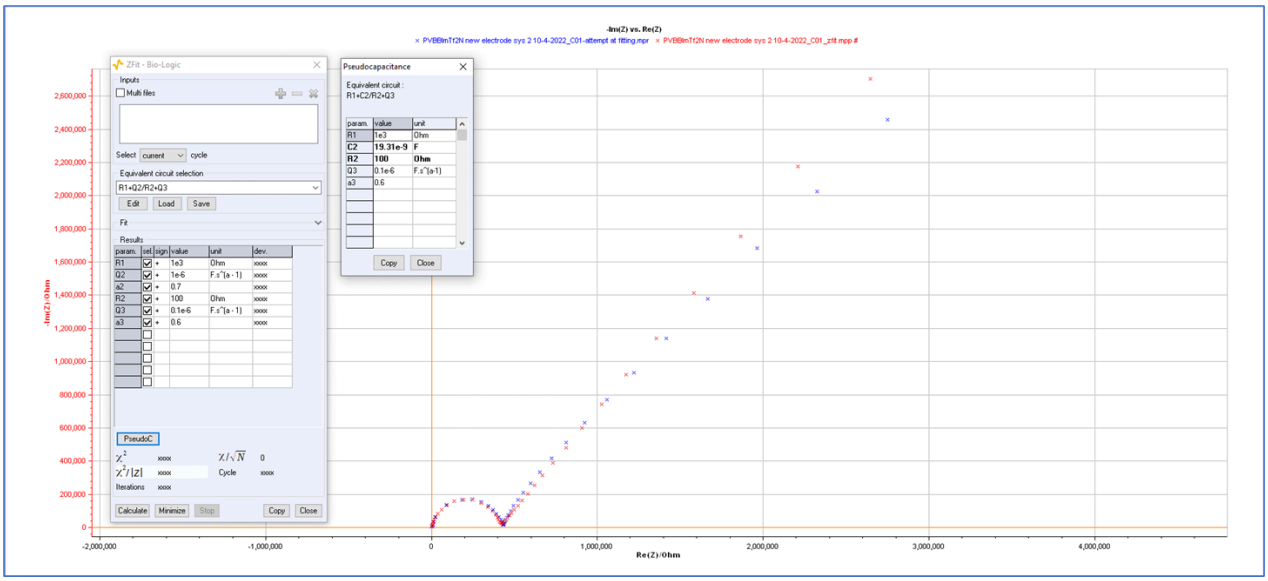

Figure E.23 EIS Nyquist plot and equivalent circuit fitting for the PVBBImTf$_2$N dry polymer yielding a capacitance of 19.3 x 10^{-9} F.

E.6. References

(1) Kayla Foley, K. B. W. Solution and film self-assembly of a block copolymer comprised of a poly(ionic liquid) and a stimuli-responsive weak polyelectrolyte *ACS Omega, Under Review (AO-2023-039894, submitted 06-06-2023)* **2023**.

(2) Kokubo, H.; Sano, R.; Murai, K.; Ishii, S.; Watanabe, M. Ionic polymer actuators using poly(ionic liquid) electrolytes. *European Polymer Journal* **2018**, *106*, 266-272. DOI: https://doi.org/10.1016/j.eurpolymj.2018.07.026.

(3) Abdul Halim, S. I.; Chan, C. H.; Apotheker, J. Basics of teaching electrochemical impedance spectroscopy of electrolytes for ion-rechargeable batteries – part 1: a good practice on estimation of bulk resistance of solid polymer electrolytes. **2021**, *3* (2), 105-115. DOI: doi:10.1515/cti-2020-0011 (acccessed 2023-06-26).

Appendix F: Preliminary survey of reinforces poly(ionic liquid) composites for ionic actuators

F.1. Introduction

Poly(ionic liquid)s (PILs) have recently been evaluated as promising ionic electroactive polymer electrolytes (iEAP) as they are inherently ion conductive, have good compatibility with ionic liquids, and possess favorable thermal and electrochemical properties[1, 2]. These material features have led to the development of PIL-based electomechanical sensors and ionic actuators[3-8]. The majority of the PIL-based actuators developed have been ionic polymer metal composites (IPMCs) where the PIL electrolyte layer is sandwiched between two gold electrodes making an actuator film. With one end of the film clamped between leads of a power supply, a bending response is produced under applied voltage as a result of ion migration and subsequent swelling within the polyelectrolyte layer. However, to achieve a favorable bending response on the millimeter scale, the actuators need to have both high ion conductivity and good mechanical properties. Having these two characteristics together is somewhat contradictory as polyelectrolyte ion conductivity increases as glass transition temperature, and consequently mechanical properties, decreases. Therefore, a sensitive balance between conductivity and mechanical properties is needed for a single material system. In the case of the actuators developed in Chapter 6 of this dissertation, only limited actuation behavior was produced due to the low mechanical properties of the ionogels, but they had favorably high ~10^{-4} S/cm room temperature ion conductivities. Further efforts to improve the mechanical properties and still maintain good ion conductivities are needed to further PIL actuator design.

Current efforts to address poor mechanical properties in PILs without significantly sacrificing favorable ion conductivity have typically involved block copolymerization with stiffer co-blocks[3-

[5, 9]. However, this method suffers from lengthy and costly living radical polymerizations and requires specific self-assembled morphologies to provide improved mechanical properties while retaining favorable ion conductivity. An alternate approach, utilizing reinforcing agents such as fibrous materials or nanoparticles agents, has not been examined in PIL iEAP-based actuator systems, although they have been successfully utilized in other PIL applications[10-12]. Developing reinforced PIL composites will provide an alternative way to improve the mechanical properties of the PIL ionogel composites without lengthy and costly synthesis procedures.

In this appendix, a preliminary investigation of reinforced PIL ionogel composites is performed. Tested reinforcing agents included fibrous materials, specifically Whatman cellulose filter paper and graphene oxide (GO). These materials were selected as they were readily available in the laboratory and may provide insight into future research interests and applications such as paper batteries and high thermal and electrical conductivity GO composites [11, 13, 14]. The two reinforcing materials investigated, filter paper and GO, were individually combined with one of two PIL polymers and an ionic liquid, 1-butyl-3-methylimidazolium tetrafluoroborate ($C_4C_1ImBF_4^-$), through solution blending or coating methods. The two PILs examined in this study were poly[4-vinylbenzyl-3butyl imidazolium bis(trifluoromethylsulfonyl)imide] ($PVBBImTf_2N$) and poly[1-vinyl-3-ethylimidazolium bis(trifluoromethylsulfonyl)imide] (PVC_2ImTf_2N), which were synthesized through conventional free radical polymerization. ATR-FTIR spectroscopy was used to confirm the composite composition. EIS was used to measure the ion conductivity of the composites. Ionogels with ion conductivity values that met or exceeds those for the polymer actuators developed in Chapter 6 were considered for further reinforced actuator development. A qualitative assessment of film structure, cohesion, and overall physical state was also included in the preliminary assessment of the ionogels for actuation potential. One basic criterion was that the

composite film had to maintain its physical integrity and not break during the gold foil application process. Ionogel composites meeting these ion conductivity and structural criteria were converted to actuator films and further tested by applying gold leaf to the composite film surfaces and then observing the actuation behavior using an applied DC voltage of 4 V.

F.2. Methods and Materials

F.2.1. Materials:

1-butylimidazole, 4-chloromethylsytrene, and lithium bis(trifluoromethylsulfonyl)imide (**$LiTf_2N$**) were purchased from TCI America. Acetonitrile and ethyl acetate were purchased from VWR. Diethyl ether was purchased from Beantown Chemical, and N,N-dimethylformamide (**DMF**) was purchased from Alfa Aesar. 1-butyl-3-methylimidazolium tetrafluoroborate (**$C_4C_1ImBF_4$**) was purchased from Sigma Aldrich. Gold leaf sheets (24K, ~100 nm thickness) were purchased from L.A. Gold Leaf Wholesaler. All purchased chemicals and materials were used as received.

F.2.2. 1-Vinyl-3-ethyl-imidazolium bromide (VC_2ImBr) synthesis:

20 g of 1-vinylimidazolium was added to a round bottom flask and heated to ~75 °C. A dropping funnel was used to add 22 g of bromoethane slowly dropwise to the round bottom flask over a period of 1.5 hours. During this time, the solution first became cloudy and then gradually more viscous until a solidified product was obtained. The solid white product was then washed 5 times with 20 mL of ethyl acetate before drying under a nitrogen stream for 48 hours. 37.7 g of VC_2ImBr was produced giving a 92% yield.

F.2.3. Poly(1-vinyl-3-ethyl-imidazolium bis(trifluoromethylsulfonyl)imide) (PVC_2ImTf_2N) synthesis:

The VC_2ImBr monomer (~4.9 g) was dissolved in 50 mL of DMF with 0.2 g AIBN initiator. The system was degassed with bubbling nitrogen for 2 hours before starting the reaction by placing the vessel in an oil bath heated to 65-70 °C. The reaction was allowed to react at this temperature overnight. After cooling to room temperature, the polymer product was dialyzed against water (3500 MWCO Snake Skin tubing) for 48 hours. The water was allowed to evaporate in the fume hood and the final product was then dried in a vacuum oven overnight. A 57% yield was achieved with 2.8 g of polymer recovered.

The entire PVC_2ImBr product was then dissolved in 65 mL of Millipore water. In a separate containing 16.2 g of $LiTf_2N$ was dissolved in 20 mL of water. The $LiTf_2N$ solution was then added dropwise to the polymer solution to perform the ion exchange, which resulted in a cloudy white suspension, and this suspension was stirred for one hour. The white product was then separated from solution through centrifugation and subsequently washed with water to remove residual $LiTf_2N$. 4.8 g of PVC_2ImTf_2N product was recovered.

F.2.4. 4-Vinylbenzyl-3-butyl imidazolium bis(trifluoromethylsulfonyl)imide ($VBBImTf_2N$) synthesis:

The $VBBImTf_2N$ monomer was similarly synthesized as reported in Chapter 6 of this dissertation. Briefly, a ~1:1 mole ratio mixture of 1-butylimidazolium (7.6 g) and 4-chloromethylstyrene (9.7 g) were dissolved in 40 mL of acetonitrile and reacted at 40 °C for 24 hours. Rotary evaporation was performed to reduce the solution volume and the concentrated product was then precipitated into excess diethyl ether. The resulting yellow oil was separated

from the diethyl ether and further washed with diethyl ether. The final product was dried under vacuum to remove residual solvents. 16.1 g of product was produced for a yield of 95.8%.

The 9 g of VBBImCl product was then dissolved into 125 mL Millipore filtered water. Approximately 17 g of $LiTf_2N$ was separately dissolved in 50 mL of water and then added dropwise to the VBBImCl solution. Immediate precipitation was observed. Then 50 mL of ethyl acetate was added to redissolve the precipitant. The biphasic solution was then stirred at room temperature for 24 hours. Afterwards, the stirring was stopped and the water and ethyl acetate phases were allowed to separate. The water layer was removed then a liquid extraction was performed with 50 mL of ethyl acetate 3 times to recover product from the water layer. The extracted ethyl acetate layer was then combined with the original reaction ethyl acetate layer. This organic layer was then washed with 50 mL of water 4 times. Ethyl acetate was removed with rotor evaporation, producing a viscous yellow layer. Residual ethyl acetate was evaporated under a nitrogen flow in the fume hood. A 62.3 % yield was achieved with 19.2 g of $VBBImTf_2N$ recovered.

F.2.5. Poly(4-vinylbenzyl-3-butyl imidazolium bis(trifluoromethylsulfonyl)imide ($PVBBImTf_2N$) synthesis:

The $PVBBImTf_2N$ polymer was also synthesized through conventional free radical polymerization. The $VBBImTf_2N$ monomer (10 g) and 0.1 g of AIBN initiator was dissolved in 30 mL of DMF. The solution was allowed to degas under nitrogen bubbling for 2 hours. The reaction vessel was then heated to 65-70 °C with an oil bath and was allowed to react under nitrogen for 30 hours. The reaction was then exposed to air and allowed to cool to room temperature before purification. The polymer was precipitated by adding the reaction solution dropwise to a 4:1 methanol:water solution. The polymer would immediately precipitate out as a

white cloudy sticky solid suspended in solution. Centrifugation at 5000 rcf for 3 minutes separated the white solid from the solution. The polymer product was then redissolved in methanol and dialyzed against water (3500 MWCO Snake Skin tubing) for 24 hours. Methanol was then evaporated, and the polymer produced was dried further in the vacuum oven at 45 °C overnight. 4.3 g of product was recovered (43% yield).

F.2.6. Preparation of PIL or ionogel composites with no reinforcing agents:

The appropriate amount each PIL polymer and ionic liquid $C_4C_1ImBF_4$- for 40 and 60 wt% ionogel composites was allowed to dissolve in ~2-3 mL of DMF overnight. The solution was then poured into a petri dish coated with a Teflon sheet, and the DMF was evaporated in a vacuum oven at 75-80 °C for 48 hours. ATR-FTIR was used to confirm the removal of DMF solvent through the loss of the ~1660 cm^{-1} C=O amide peak in the composite IR spectra.

F.2.7. Preparation of PIL- or ionogel-coated cellulose paper:

Each PIL polymer was dissolved in 5 mL of DMF at a concentration of 100 mg/mL. The polymers were allowed to fully dissolve in the solvent overnight. To select solutions, ~40 wt% (275 μL) of $C_4C_1ImBF_4^-$ was then added to the polymer solution. Whatman cellulose filter paper was cut into 3-inch x 1-inch strips. Each paper strip was then coated with 1 mL of the appropriate polymer solution by pipetting solution across the film until the entire paper cutting was visually wetted. The coated paper strips were then dried in a vacuum oven for 24 hours at 75 °C. The dried coated polymer strips were stored in sealed bags until characterized.

F.2.8. Preparation of PIL or Ionogel graphene oxide composites:

The appropriate amount of ionic liquid $C_4C1ImBF_4^-$ was massed in a glass vial. PIL polymer was then added to the ionic liquid before dissolving both materials in ~2-3 mL of DMF overnight. In a separate vial, the appropriate amount of graphene oxide was dispersed in ~1 mL of DMF under

sonication. Once dispersed, the graphene oxide solution was added to the PIL-IL solution. After 10 mins of sonication to ensure good mixing, the combined solution was poured on to a petri dish lined with Teflon sheeting. DMF was then evaporated in a vacuum oven at 75-85 °C for 48 hours. ATR-FTIR was performed on the resulting black film composites to ensure full removal of the DMF solvent as signaled by absence of the amide carbonyl peak at ~1660 cm^{-1}.

F.2.9. Characterizations:

Attenuated total reflectance Fourier transform infrared spectroscopy (ATR-FTIR) spectra were collected with a ThermoFisher Scientific Nicolet iS50R spectrometer. A minimum of 64 scans at a resolution of 4 cm^{-1} was performed for each sample over the 4000-400 cm^{-1} wavenumber range. Impedance measurements were performed with a VSP-300 BioLogic potentiostat and a custom-made 2-electrode cell with stainless steel electrodes to determine ion conductivity of the polymers and ionogel composites. EIS spectra were collected at frequencies between 7 MHz to 100 mHz. The following relationship was used to calculate ion conductivity mased on the impedance measured bulk resistance (R_b) and polymer/gel cross-sectional area (A) and thickness (l):

$$\textbf{EQ F-1 } \sigma = \frac{l}{R_b A}$$

All measurements were performed at room temperature and ambient humidity conditions. For the Whatman filter paper composites, a biopsy punch was used to create small circular sections to analyze. Polymers, ionogels, and graphene oxide composites were solution cast on Teflon sheeting and similarly sectioned into disks for analysis.

F.2.10. Preparation and behavior of ionic electroactive actuators:

Actuators were developed by applying gold leaf to both sides of the solution-cast composite ionogel films. Actuation was tested with a DC power supply (Yescom DCP3010D) at 4 V. A

Logitech camera was used to record the actuation, and motion-tracking software *Tracker 6.0.10* (Open Source Physics, https://physlets.org/tracker/) was used to evaluate actuation behavior.

F.3. Results and Discussion

For this preliminary investigation, fibrous materials and graphene oxide were used to reinforce PIL ionogels. Specifically, Whatman cellulose paper, polypropylene 0.45 μm filtration membrane, and graphene oxide powders were used to develop the reinforced ionogel composites. Two different PILs were synthesized through conventional free radical polymerization, including poly[4-vinylbenzyl-3- butyl imidazolium bis(trifluoromethylsulfonyl)imide] ($PVBBImTf_2N$) and poly[1-vinyl-3ethylimidazolium bis(trifluoromethylsulfonyl)imide] (PVC_2ImTf_2N). $PVBBImTf_2N$ was selected to provide direct comparison to the ATRP synthesized $PVBBImTf_2N$ in Chapter 6 of this dissertation. PVC_2ImTf_2N was selected as it is a commonly synthesized PIL with readily available thermal, solubility, electrochemical characterization information in the literature. The ionic liquid butyl methyl imidazolium tetrafluoroborate ($C_4C_1ImBF_4^-$) was also used for this study for direct comparison to Chapter 6. The chemical structures for the PIL polymers and the IL are shown in Figure F.1.

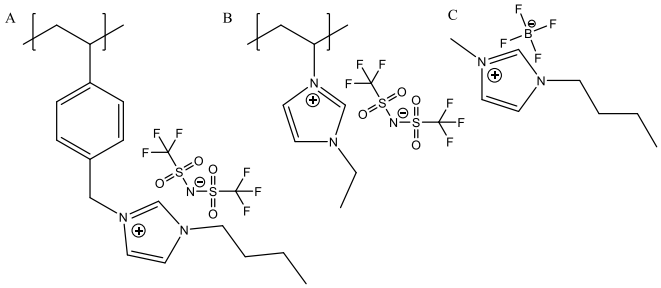

Figure F.1 Chemical structures for the (a) $PVBBImTf_2N$ and (b) $PVC_2ImTf2N$ PIL polymers as well as the (c) $C_4C_1ImBF_4$- ionic liquid.

Table F.1 Ion conductivity and qualitative mechanical properties of the reinforced ionogels.

Type	Sample	σ (S/cm) at 20° C	Qualitative Film Structure	Ref.
Polymer	$PVBBImTf_2N$	2.2×10^{-6} ($\pm 1.8 \times 10^{-8}$)	Solid adhesive film	This work
	PVC_2ImTf_2N	4.9×10^{-7} ($\pm 5.0 \times 10^{-8}$)	Solid adhesive film	This work
Ionogels	$PVBBImTf_2N$-40 wt% $C_4C_1ImBF_4$	5.2×10^{-4} ($\pm 9.8 \times 10^{-5}$)	Gooey gel	This work
	$PVBBImTf_2N$ 60 wt% $C_4C_1ImBF_4$	5.7×10^{-4} ($\pm 2.4 \times 10^{-5}$)	Phase separated	This work
	PVC_2ImTf_2N 40 wt% $C_4C_1ImBF_4$	6.5×10^{-4} ($\pm 1.2 \times 10^{-4}$)	Gooey gel	This work
	PVC_2ImTf_2N 60 wt% $C_4C_1ImBF_4$	1.9×10^{-3} ($\pm 8.0 \times 10^{-5}$)	Phase separated	This work
Whatman Paper composites	$PVBBImTf_2N$	2.7×10^{-9} ($\pm 1.5 \times 10^{-9}$)	paper film	This work
	$PVBBImTf_2N$ 40 wt% $C_4C_1ImBF_4$	2.2×10^{-6} ($\pm 3.2 \times 10^{-6}$)	paper film	This work
	PVC_2ImTf_2N	2.3×10^{-9} ($\pm 1.1 \times 10^{-9}$)	paper film	This work
	PVC_2ImTf_2N 40 wt% $C_4C_1ImBF_4$	6.1×10^{-7} ($\pm 5.3 \times 10^{-7}$)	paper film	This work
PP Syringe filter	$PVBBImTf_2N$ 40 wt% $C_4C_1ImBF_4$	1.3×10^{-6} ($\pm 8.9 \times 10^{-9}$)	paper film	This work
Graphene Oxide composites				This work
2wt% GO	$PVBBImTf_2N$ 40 wt% $C_4C_1ImBF_4$	N/A	Unstable gooey gel	This work
	PVC_2ImTf_2N 40 wt% $C_4C_1ImBF_4$	1.9×10^{-4} ($\pm 1.4 \times 10^{-5}$)	Tacky film	This work
6wt% GO	$PVBBImTf_2N$ 40 wt% $C_4C_1ImBF_4$	7.6×10^{-4} ($\pm 1.8 \times 10^{-5}$)	Stable gooey gel	This work
	PVC2ImTf_2N 40 wt% $C_4C_1ImBF_4$	7.9×10^{-5} ($\pm 1.2 \times 10^{-6}$)	Film	This work
10 wt% GO	$PVBBImTf_2N$ 40 wt% $C_4C_1ImBF_4$	1.5×10^{-5} (1.0×10^{-6})	Brittle Film	This work
	PVC_2ImTf_2N 40 wt% $C_4C_1ImBF_4$	9.7×10^{-6} ($\pm 2.6 \times 10^{-6}$)	Brittle Film	This work
Ionic Liquid	IL: $C_4C_1ImBF_4$	1.7×10^{-3}	Liquid	Palm et al. 2012[15]

Ionogels were evaluated for their ion conductivity and qualitative mechanical properties for their potential use as solid electrolytes for actuation performance. Specifically, the ionogels had to display at least comparable ion conductivity as the ionogels produced in Chapter 6 ($\geq 10^{-6}$ S/cm) and had to create a solid film. Table F.1 shows the measured ion conductivities and qualitative

film structure or physical state (e.g., solid film, gooey gel, liquid) of all developed ionogels. For convenience, similar results for the Chapter 6 ionogels are also provided in Table F.2 for comparison. Discussion on ionogel development, ion conductivity, film structure, and actuation for each system is presented separately in the following sections.

Table F.2 Ion conductivity and qualitative mechanical properties of the ionogels produced in evaluated in Chapter 6.

Type	Sample	σ (S/cm) at 20° C	Qualitative Film Structure	Ref.
Polymer	PVBBImTf_2N	4.4 x10^{-7} (± 7.2 x10^{-9})	Adhesive Film	CH6
	PDMAEMA-*b*-PVBBImTf_2N	7.9 x10^{-7} (± 4.8 x10^{-8})	Adhesive Film	CH6
Ionogel	PVBBImTf_2N 10 wt% IL	3.5 x10^{-6} (± 2.4 x10^{-8})	Adhesive Film	CH6
	PVBBImTf_2N 25 wt% IL	2.7 x10^{-5} (± 5.6 x 10^{-7})	Sticky Gel	CH6
	PVBBImTf_2N 40 wt% IL	8.0 x10^{-4} (± 3.2 x10^{-6})	Sticky Gel	CH6
	PDMAEMA-*b*-PVBBImTf_2N 10 wt%	3.4 x10^{-6} (± 8.2 x10^{-8})	Adhesive Film	CH6
	PDMAEMA-*b*-PVBBImTf_2N 25 wt%	9.5 x10^{-5} (± 4.7 x10^{-7})	Sticky gel	CH6
	PDMAEMA-*b*-PVBBImTf_2N 40 wt%	2.3 x10^{-4} (± 1.9 x10^{-6})	Sticky gel	CH6
	PVDF 40 wt% IL	2.3 x10^{-5} (± 1.3 x10^{-7})	Film	CH6

F.3.1. Characterization of PIL ionogels without reinforcement

Ionogels with no reinforcing materials were developed first at 40 and 60 wt% ionic liquid content through solution blending in DMF and subsequent drying in a petri dish lined with Teflon sheeting. ATR-FTIR of the ionogels demonstrates successful addition of the ionic liquid through shifts and changes in band shape for the imidazolium ring (C_2-H and $C_{4,5}$-H C-H str bands between 3200-3050 cm^{-1}, C=C/C-N str between 1550-1575 cm^{-1}) [16, 17] and BF_4^- modes (typically three peaks between 1050-1000 cm^{-1}) [18, 19]. Specifically, in Figure F.2a, the imidazolium C_2-H and $C_{4,5}$-H C-H str bands between 3200-3050 cm^{-1} showed small increases in wavenumber for both polymer systems with increasing ionic liquid content as marked by the blue dashed lines. Below 1800 cm^{-}

[1] (Figure F.2b), the imidazolium ring C=N/C-N str emerges as a single peak at ~1562 cm^{-1} in $PVBBImTf_2N^-$ which shifts up to ~1566 cm^{-1} with a shoulder at 1574 cm^{-1} upon ionic liquid addition. The PVC_2ImTf_2N polymer shows two separate peaks for the C=N/C-N modes at 1550 and 1571 cm^{-1}. Adding ionic liquid increases the intensity of the ~1572 cm^{-1} peak with increasing ionic liquid content, which corresponds with the single C=N/C-N ring str peak at 1572 cm^{-1} in the pure ionic liquid. In all polymer systems, the BF_4^- modes emerge as a set of triplet bands in the 1056-1020 cm^{-1} range, though they exhibited slightly different band shapes based on the polymer system and ionic liquid content.

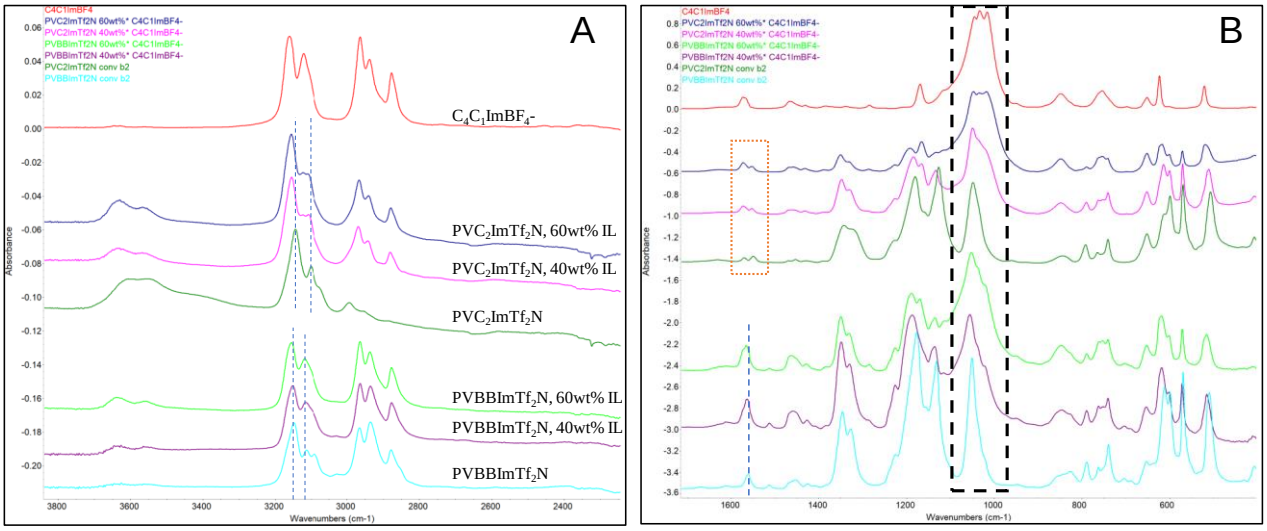

Figure F.2 ATR-FTIR of the $PVBBImTf_2N$ and PVC_2ImTf_2N polymers, their corresponding ionogels, and the $C_4C_1ImBF_4^-$ ionic liquid in the (a) >2200 cm^{-1} and (b) <1800 cm^{-1} wavenumber regions. Dotted blue dashed lines in (a) show the shifts in the imidazolium ring C_2-H and $C_{4,5}$-H stretching modes. In (b) the orange box and the dotted blue line mark the imidazolium ring C=N/C-N stretching modes for the PVC_2ImTf_2N and $PVBBImTf_2N$ polymers and ionogel, respectively. The black dashed box indicates the characteristic BF_4^- anion triplet modes between 1056-1020 cm^{-1}.

The physical state of the 40 wt% IL ionogels for both polymer systems was a loose gel that did not maintain a film format after being peeled off the Teflon sheeting. At 60 wt%, a mixture of

liquid and solid polymer was present on the Teflon film, likely indicating phase separation. These ionogels were considered inadequate for actuation due to their physical state. Nevertheless, their ion conductivity was still characterized.

The ion conductivity of the dry PVBBImTf_2N and PVC_2ImTf_2N polymers were found to be $2.2x10^{-6}$ and $4.9x10^{-7}$ S/cm, respectively. The ion conductivity measured here for the PVBBImTf_2N polymer was an order of magnitude higher than the PVBBImTf_2N produced by living radical polymerization in Chapter 6 ($4.4x10^{-7}$ S/cm). This higher ion conductivity observed is tentatively attributed to plasticization via the low molecular chains produced in the conventional free radical polymerization, as compared to the low polydispersity expected for the polymer produced through living radical polymerizations. The PVBBImTf_2N ionogels both had ion conductivities of ~10^{-4} S/cm, which is similar to the PVBBImTf_2N ionogels developed in Chapter 6. PVC_2ImTf_2N 40 wt% ionogel also had an ion conductivity of 10^{-4} S/cm, although the PVC_2ImTf_2N 60 wt% ionogel had a ~10^{-3} S/cm conductivity. The higher ion conductivity is likely due to coating of the solid phase separated polymer with free ionic liquid on the surface due to phase separation and not a realistic conductivity of a composite ionogel. From this point forth, only reinforcement of the 40 wt% PIL ionogels is examined.

F.3.2. Whatman filter paper

For the fibrous materials, the PIL copolymers and ionic liquid were first dissolved in DMF at the appropriate weights for a 40 wt% IL ionogel. Cuttings of the cellulose filter paper were coated with the ionogel solution and then were allowed to dry. As the PILs and ionogels are only coating the paper, all composites structure and mechanical properties qualitatively matched the neat cellulose filter paper.

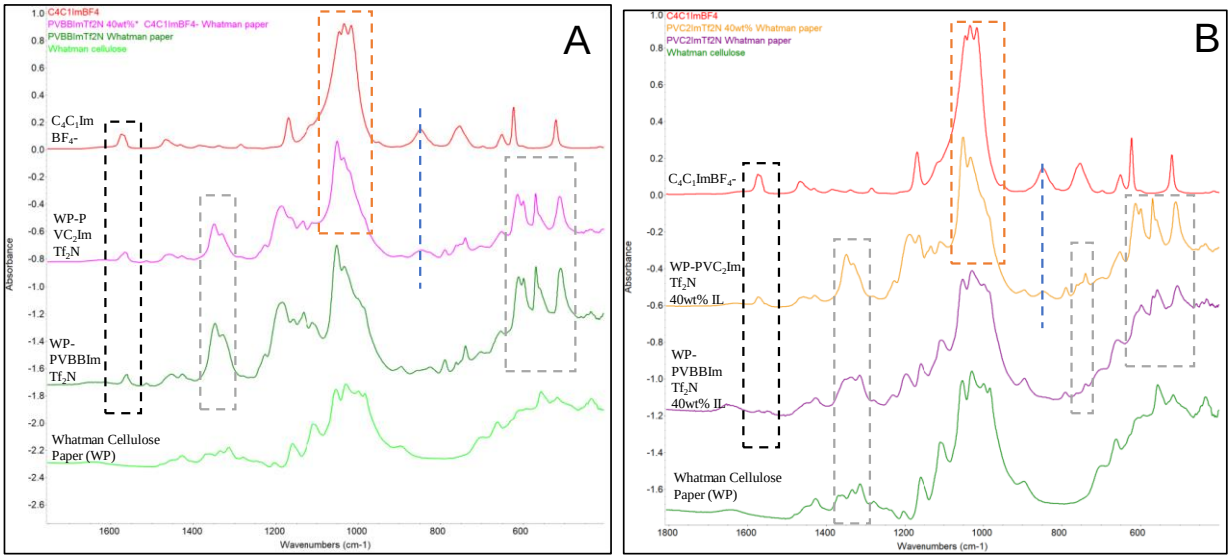

Figure F.3 ATR-FTIR of the (a) $PVBBImTf_2N$-based polymer and ionogel coated Whatman papers and (b) PVC_2ImTf_2N-based polymer and ionogel coated Whatman papers. Included in both a and b are the $C_4C_1ImBF_4^-$ ionic liquid and neat Whatman cellulose paper for comparison. The black dashed box marked the imidazolium ring C=N/C-N str modes. The grey dashed boxes mark characteristic Tf_2N^- anion modes. The orange dashed boxes mark the expected location of the triplet BF_4^- anion modes. The blue dashed line marks the imidazolium ring bending mode at ~850 cm^{-1}.

ATR-FTIR of the $PVBBImTf_2N$ and ionogel coated filter paper (Figure F.3a) showed the emergence of the imidazolium C=N/C-N ring str modes at ~1563 cm^{-1} with a slight increase in wavenumber (~1566 cm^{-1}) for the ionogel coated paper. Tf_2N- anion modes were clearly observed in both the polymer and ionogel coated papers as marked by the IR signals in the grey dashed boxes. The BF_4^- IR modes were difficult to distinguish from the overlapping cellulose and Tf_2N^- modes (a series of typically intense bands between ~1400-500 cm^{-1}) [17], however a broadening at 850 cm^{-1} attributed to the ionic liquid imidazolium ring bending mode confirms the addition of the ionic liquid[17, 19].

ATR-FTIR of the PVC_2ImTf_2N polymer and ionogel coated Whatman papers (Figure F.3b), does show the presence of the two peaks for the imidazolium ring C=N/C-N stretches (1572 cm^{-1} and 1547 cm^{-1}) with the 1572 cm^{-1} peak being more intense in the ionogel as seen for the non-

reinforced ionogels above. The Tf_2N^- anion modes (marked by grey dashed boxes) were only weakly present in the PVC_2ImTf_2N coated paper but were more clearly observed in the PVC_2ImTf_2N 40 wt% ionogel coated paper. The triplet BF_4^- peaks in the PVC_2ImTf_2N 40 wt% coated paper were also not clearly distinguishable due to overlap with the cellulose and the Tf_2N^- IR signal, although an increase in intensity of the 1050 cm^{-1} peak compared to the PVC_2ImTf_2N coated paper suggests its presence. The addition of the ionic liquid was also verified for PVC_2ImTf_2N 40 wt% ionogel coated paper through the emergence of the imidazolium ring bending mode ~850 cm^{-1} IR mode.

EIS measurements of the coated Whatman paper composites indicated a significant reduction in ion conductivity. $PVBBImTf_2N$ and $PVBBImTf_2N$ 40 wt% IL coated Whatman papers had conductivities of ~10^{-9} S/cm and ~10^{-6} S/cm – almost two orders of magnitude lower compared to the non-reinforced ionogels. Similar reductions were observed for the PVC_2ImTf_2N and PVC_2ImTf_2N 60 wt% IL coated Whatman papers with conductivities of ~10^{-9} and 10^{-7} S/cm, respectively. The SEM images shown in Figure F.4 of the polymer and ionogel coated Whatman papers provide insight into the reduction of ion conductivity. For the dry polymers, both the $PVBBImTf_2N^-$ and PVC_2ImTf_2N-coated Whatman paper appear to have a coating of polymer at the surface of the Whatman paper that does not penetrate into the paper, which would explain the significant reduction in ion conductivity compared to the neat dry PIL polymers. The ionogel-based papers do appear to contain additional ionogel material within the pores of the Whatman paper which corresponds with the higher 10^{-7} to 10^{-6} S/cm ion conductivities compared to the dry-polymer coated papers.

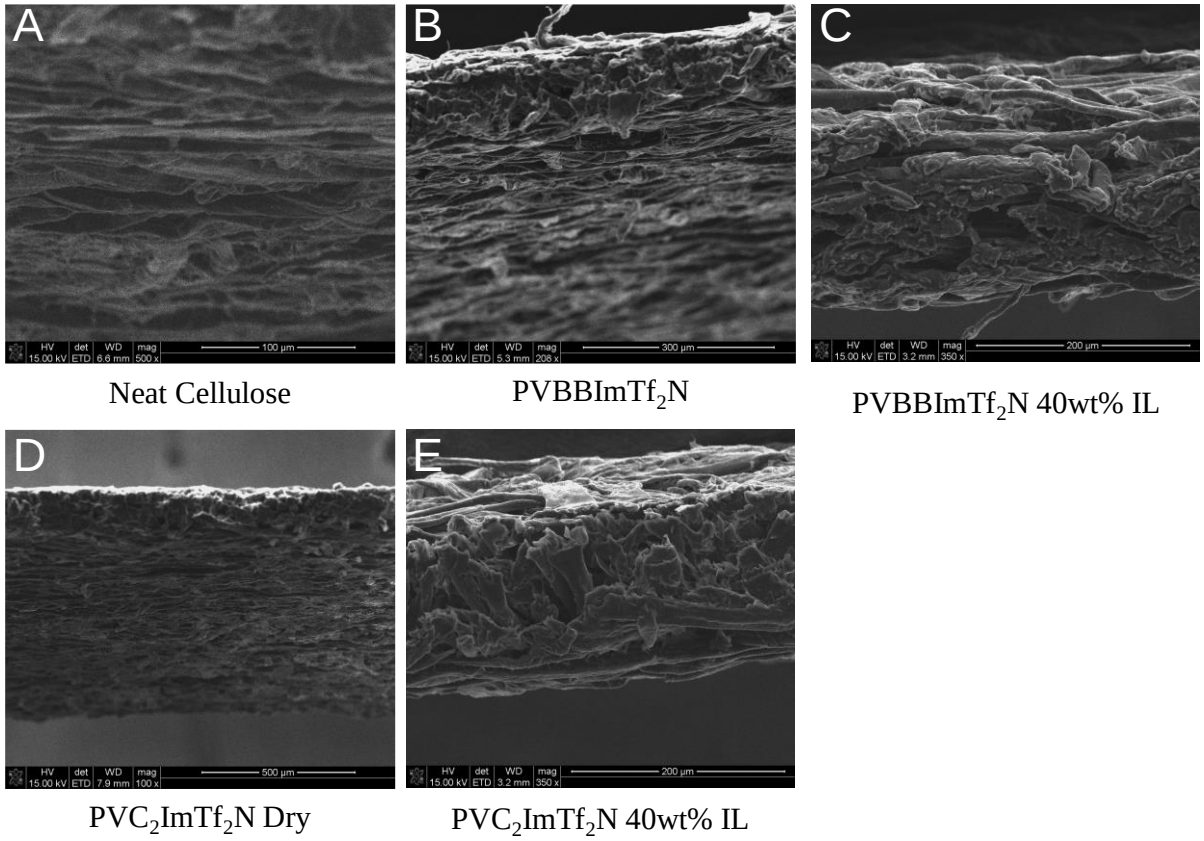

Figure F.4 SEM images of the (a) neat cellulose Whatman paper, (b) $PVBBImTf_2N$ coated paper, (c) $PVBBImTf_2N$ 40 wt% IL ionogel coated paper, (d) PVC_2ImTf_2N coated paper, and (e) PVC_2ImTf_2N 40 wt% IL ionogel coated paper. The top of the films in (b) and (d) show a thicker polymer coating at the top surface while the center of the film resembles the neat cellulose. The ionogel coated papers (c and e) appear to have polymer incorporated into the pores.

While the ion conductivities are lower than would be favorable for actuation behavior (~10^{-4} to 10^{-2} S/cm) [20-23], the ionogel coated Whatman papers have ion conductivities similar to the dry polymers developed in Chapter 6 and to other PILs that showed micron-scale actuation behavior[24, 25]. Therefore, actuation behavior of the $PVBBImTf_2N$-40 wt% IL and PVC_2ImTf_2N 40 wt% IL ionogel coated Whatman papers was tested. While a very small bending motion can be visual observed for the PVC_2ImTf_2N 40 wt% IL ionogel coated Whatman paper composite in the video (Figure F.5b and insert), the extent of tip displacement was smaller than observed for the actuators

developed in Chapter 6 and could not be easily tracked with the motion tracking software. The PVBBImTf_2N 40 wt% IL ionogel coated Whatman paper did not show any actuation behavior. While the paper does provide good qualitative film and mechanical properties, the ion conductivity was likely too low for good actuation behavior. Future use of fibrous materials will likely need fiber mats with larger porosity and surface area to allow for adequate ion conductivity, such as electrospun fiber mats.

It is also noted that these composites were formed by pipetting ionogel solution on to the papers until wetted. Future efforts will examine having the paper immersed in the ionogel solution for longer time periods and then dried; this method modification may allow more time for the polymers to penetrate into the films before solvent evaporation.

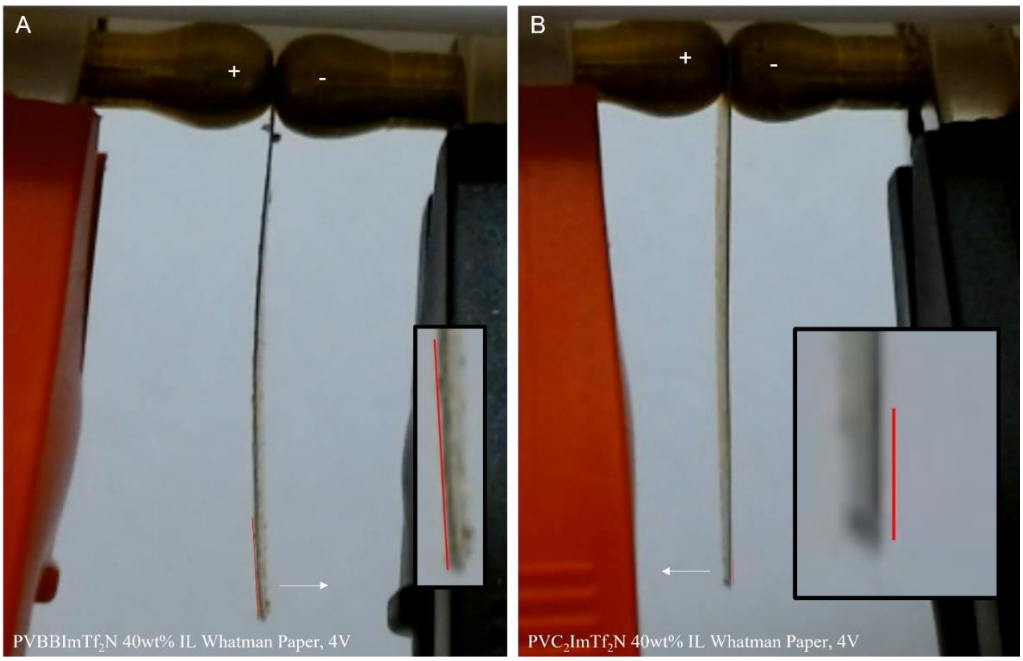

Figure F.5 Video frame stills of the bending behavior for the Whatman paper actuators coated with (a) PVBBImTf_2N 40 wt% IL and (b) PVC_2ImTf_2N 40 wt% IL after 3 minutes of applied 4 V. The red line on each image shows the initial position of the actuator film before voltage application. The white arrow shows the direction of tip displacement.

It was also attempted to combine the PVBBImTf_2N 40 wt% IL ionogel with polypropylene filter membrane (0.2 μm pore) and electrospun polycaprolactone fibers that were in stock. The ionogel coated polypropylene membrane showed an ion conductivity of ~10^{-6} S/cm, similar to the tested Whatman composites above; however, the membranes were too small to form the actuator. Due to solubility issues of the $C_4C_1ImBF_4^-$ ionic liquid with non-solvents for the polycaprolactone fibers, the ionic liquid 1-ethyl-3-methylimidazolium bis(trifluoromethanesulfonyl)imide ($C_2C_1ImTf_2N^-$) was selected as an alternative. While the polycaprolactone fiber mat was stable in acetonitrile, adding the $C_2C_1ImTf_2N^-$ ionic liquid dissolved the polycaprolactone. Future attempts at using electrospun fibers should be composed of polymers that are insoluble and stable in DMF or acetonitrile and the selected ionic liquid.

F.3.3. Graphene oxide (GO)

Graphene oxide (GO) was selected as a potential reinforcement agent as it has been similarly used in Nafion-[26] (Lian 2010) PVDF-[27] based hydrogels and ionogels and also provides other interesting properties to the polymers such as improved thermal conductivity[14] and electrical conductivity[11]. Reinforcement of the PIL ionogels was examined at 2, 6, and 10 wt% graphene oxide (GO) and at 40 wt% IL. Graphene oxide was combined with the PILs and ionogels through solution bending and subsequent removal of DMF solvent, producing black colored films or gels. Figure F.6 shows the ATR-FTIR of the PIL and ionogel GO composites. Signals from the graphene oxide were too weak to discern in the FTIR spectra for both polymer systems; however, the black color of the films confirms the incorporation of the graphene oxide into the composites. Signals from both the polymer and the ionic liquid imidazolium rings are observed as marked by the blue dashed boxes. Further, the presence of the three BF_4^- modes are present in the 1050-1000 cm^{-1} region marked by the orange dashed box.

At 2 wt% GO, the PVBBImTf_2N-based ionogel was still a loose gel; in fact, the ion conductivity of the 2 wt% GO film could not be measured as the gel would seep out between the electrodes during measurement. Increasing the GO weight percentage to 6 wt% produced a firmer gel with an ion conductivity on the order of ~10^{-4} S/cm, similar to the non-reinforced PVBBImTf_2N 40 wt% ionogel. At 10 wt% GO, the film became brittle, and broke and crumbled easily when handling. The ion conductivity was also reduced to 10^{-5} S/cm at 10 wt% GO.

PVC_2ImTf_2N 40 wt% ionogel with 2 wt% GO produced a tacky film with an ion conductivity of ~10^{-4} S/cm. While gel-like, this composite could maintain a film shape when removed from the Teflon sheeting. Increasing the weight percentage of GO resulted in a stable film at 6 wt% GO and a brittle film at 10 wt%. The corresponding ion conductivities were ~10^{-5} S/cm and ~10^{-6} S/cm at 6 and 10 wt% GO, respectively.

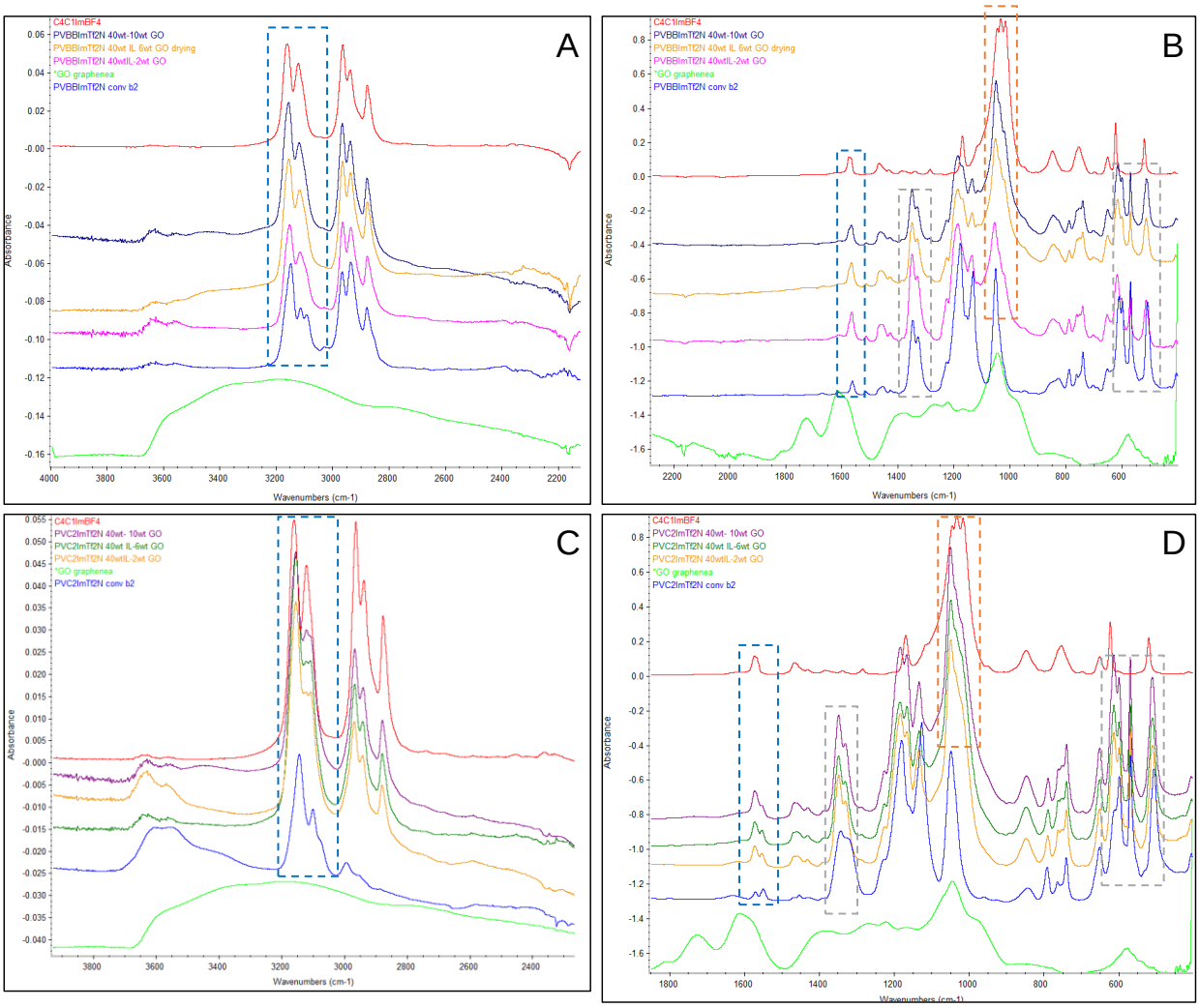

Figure F.6 ATR-FTIR of the PIL and ionogel GO composites for PVBBImTf_2N-based composites (a and b) and PVC_2ImTf_2N-based composites (c and d). All gels contain 40 wt% IL and GO at 2, 6, or 10 wt%.

Attempts to produce actuators from the ionogels reinforced with GO resulted in four stable film compositions: PVBBImTf_2N 10 wt% GO; PVC_2ImTf_2N 2 wt% GO; PVC_2ImTf_2N 6 wt% GO; and PVC_2ImTf_2N 10 wt% GO. For both polymer systems, the 10 wt% GO composites cracked due to the brittle nature of the films while applying the gold foil to the film surfaces, so actuation behavior was not tested. Actuator films from PVC_2ImTf_2N 2 wt% GO and PVC_2ImTf_2N 6 wt% GO were successfully produced and tested. Figure F.7 shows video frames of the actuator film

bending motion before and after application of 4 V, and Figure F.8 and Figure F.9 show their corresponding tip displacement and curvature overtime. The curvature was calculated similar to Fang et al. and Wang et al. through the equation[28, 29]:

$$\textbf{EQ F-2}\ k = \frac{2\delta}{\delta^2 + L^2}$$

where δ is the tip displacement in the x-direction and L is the free length of the actuator film. Curvature measurements from several of the PIL triblock copolymer systems[3, 5, 6] were digitized and also plotted in Figure F.9 for comparison.

The PVC_2ImTf_2N 40 wt% IL with 2 wt% GO demonstrated a twisting behavior rather than actual bending (Figure F.7b), with the planar side of the actuator starting to face the camera on the negative electrode side. The twisting behavior is likely due to the modulus of the polymer gel being too low, although it presents an interesting opportunity for electrically responsive motion. The composite with 6 wt% GO demonstrated a clear bending response after 3 minutes of applied voltage (Figure F.7d), with a final x-tip displacement of ~1.8 mm towards the positive electrode. However, while the actuator was bending, it had appeared that the gold foil on the sides of the film were buckling off the composite surface. When it was attempted to apply -4 V by flipping the electrodes, the actuator did begin to bend towards the opposite direction, but sparking occurred, possibly indicating an electrical short due to the disfigurement of the gold foil. Future implementation of the composite actuators will likely need to have non-metal-based electrodes. Typically, all-organic electrodes formed from nanocarbon (e.g., carbon nanotube and/or carbon black blends) or electrically conductive polymers (e.g., polypyrrole, polyaniline) show significant potential compared to noble metal-based electrodes as they are more flexible, typically adhere better to the polyelectrolyte layer, are not as prone to cracking as noble metal electrodes, and are relatively inexpensive[30, 31].

Compared to the actuators developed in Chapter 6, the PVC_2ImTf_2N 40 wt% 6 wt% GO composite showed significantly improved actuation behavior. After ~45 sec of applied voltage, the tip displacement for this GO ionogel composite actuator was 336 μm towards the positive electrode while the living radical synthesized polymers $PVBBImTf_2N$ and PDMAEMA-*b*-$PVBBImTf_2N$ (CH6) displaced only ~150 μm (towards the positive electrode) and ~97 μm (towards the negative electrode), respectively. However, the GO ionogel composite tip displacement was still only half that compared to the PVDF 40 wt% control (525 μm at 45 sec) developed in Chapter 6. Qualitatively, the PVC_2ImTf_2N 40 wt% 6 wt% GO was stiffer than the PVDF 40 wt% ionogel composite; however, tensile testing or dynamic mechanical analysis characterization will be needed to compare the modulus and other mechanical properties of each actuator film.

Curvature of the PVC_2ImTf_2N 40 wt% 6 wt% GO composite actuator was found to be comparable to the PVDF 40 wt% IL control and higher than the Chapter 6 actuator films and the micro-actuators developed by Kokubo et al, consisting of crosslinked methacrylate based PILs (Kokubo et al.). However, the curvatures were still significantly lower than those observed for the styrenic block copolymer PIL actuators in the literature[3, 5, 6]. As the ion conductivity of this composite (~10^{-5} S/cm) is higher than the conductivity measured by Green et al. for their dry polymer actuator but the curvature is smaller, the difference in actuation behavior is likely related to the mechanical properties of the films. In this case, it is likely that the PVC_2ImTf_2N 40 wt% 6 wt% GO composite actuator was stiffer than the styrenic block copolymer PIL developed by Green et al.[3]; however, further mechanical characterizations will be needed to confirm this.

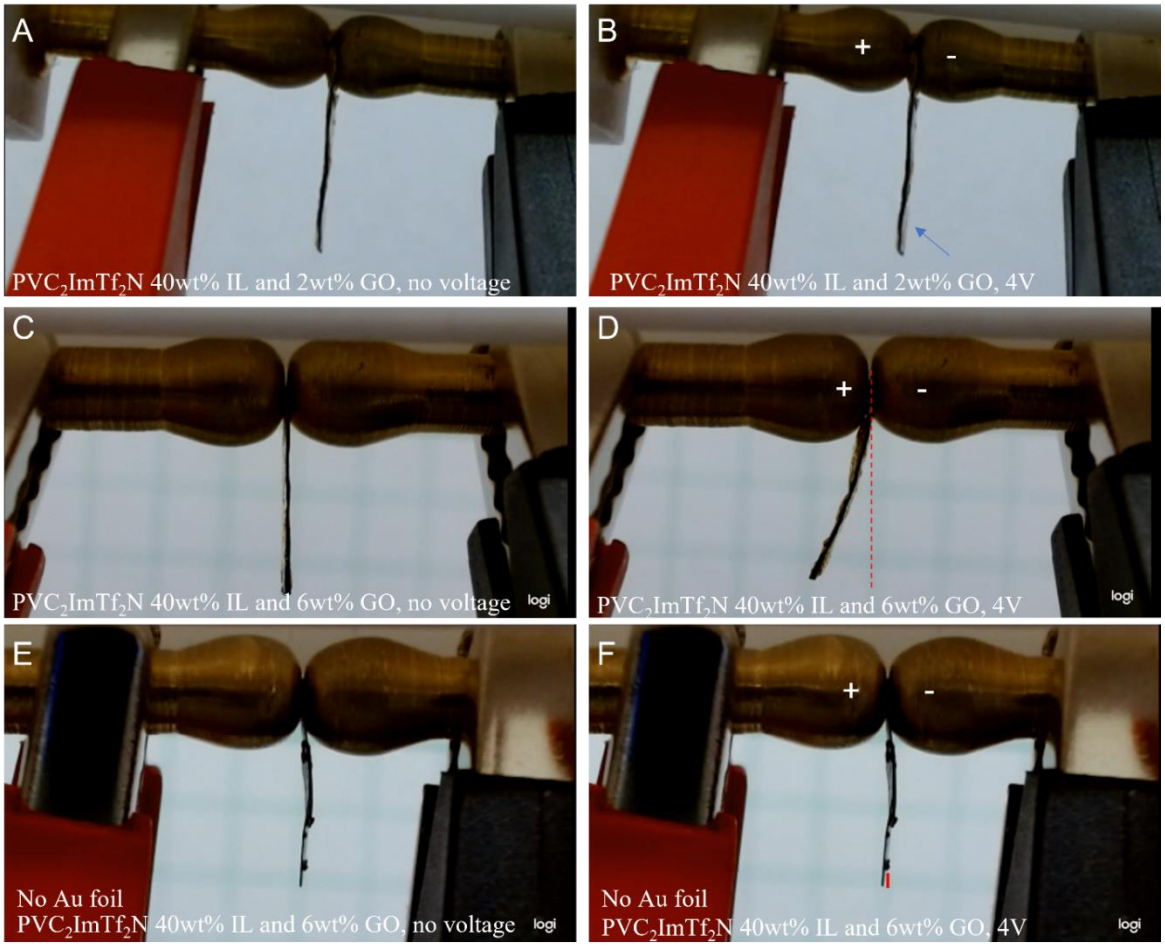

Figure F.7 Video frame stills are shown of the PVC_2ImTf_2N 40 wt% IL GO composite ionogel actuators for (a and b) 2 wt% GO, (c and d) 6 wt% GO, and (e and f) 6 wt% GO with no applied gold electrodes. Frames a, c, and e show the actuator films before voltage application. Frames b, d, and f show the final bending behavior under 4 V application after approximately 3 minutes of applied voltage.

Due to the interface issues of the gold foil with the actuator film during actuation mentioned above, it was attempted to observe the behavior of the PVC_2ImTf_2N 40 wt% 6 wt% GO composite under similarly applied voltage (4 V) without the gold foil applied. Interestingly, a small bending motion was observed with a tip displacement of approximately 85 μm towards the positive electrode after 3 minutes. While the ~1.8 mm actuation observed for the composite with gold foil electrodes indicates that the primary actuation mechanism is related to the ion migration of the

ionic liquid within the film under an applied voltage between the electrodes, this small displacement (~ 85 μm, 3 min) for the composite without the gold electrodes indicates another contribution to the actuation motion. This is tentatively ascribed to the electrical properties of the GO within the composite, though the electrical conductivity will need to be measured in future work[32, 33].

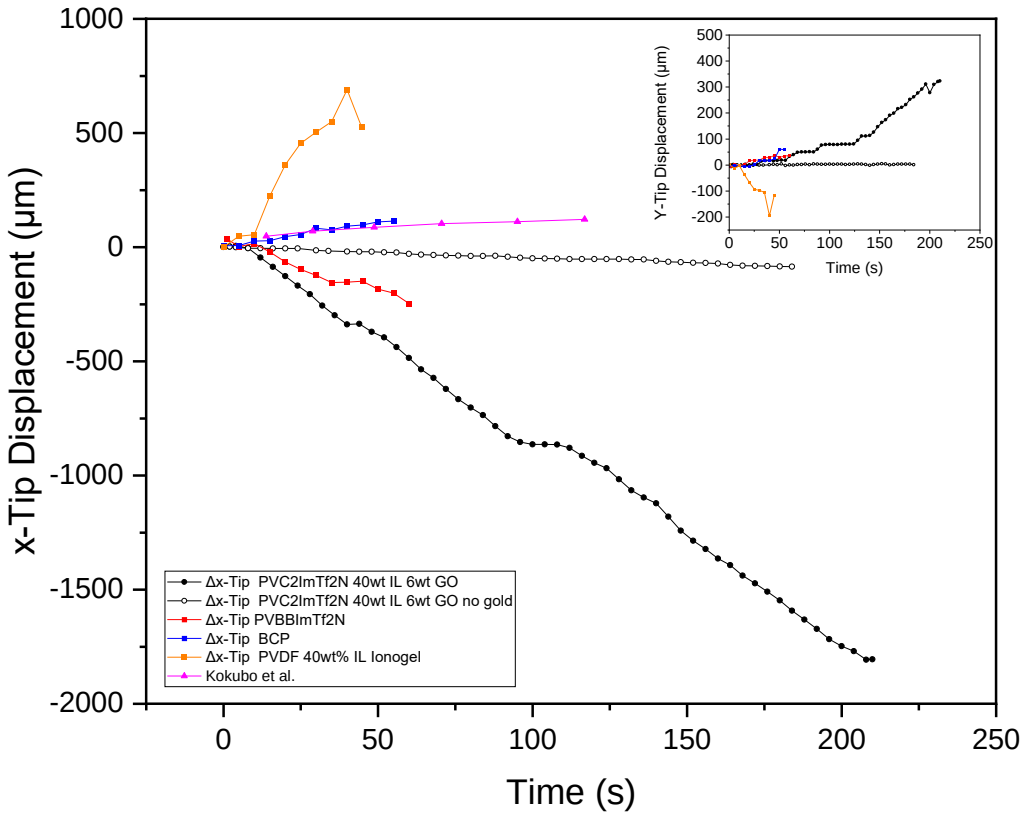

Figure F.8 Tip displacement of the PVC_2ImTf_2N 40 wt% IL 6wt% GO ionogel composite with and without the applied gold foil, the actuators developed in Chapter 6, and a literature comparison to Kokubo et al. [25]

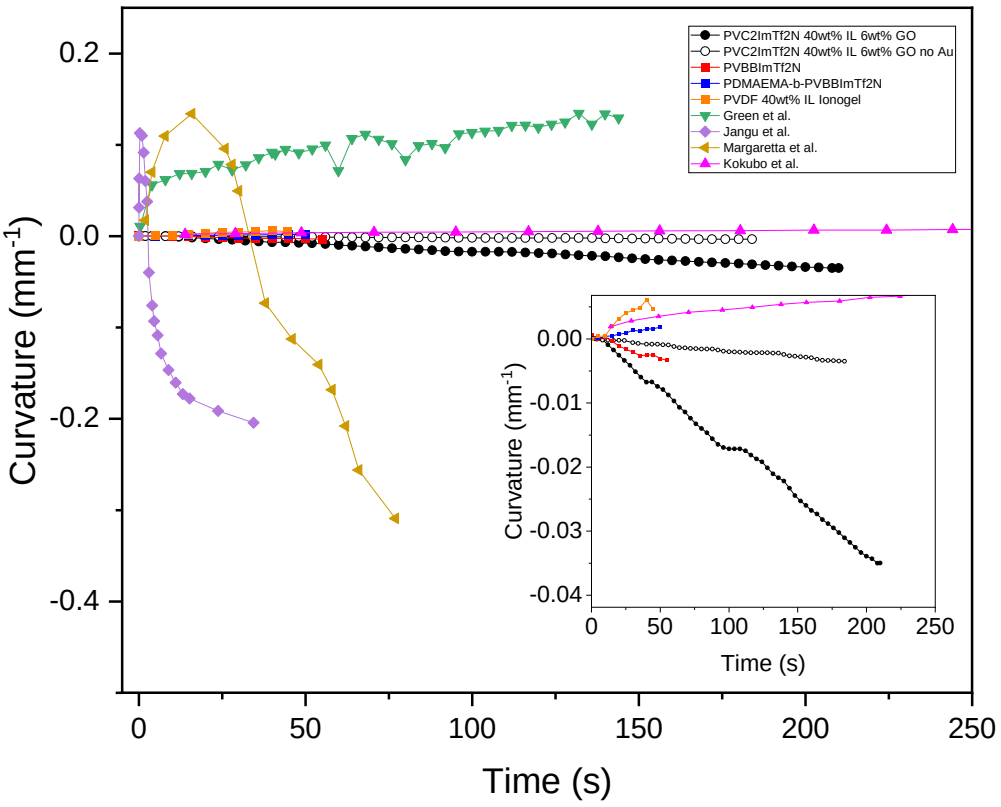

Figure F.9 Curvature of the PVC_2ImTf_2N 40 wt% IL-6wt% GO composite with and without gold foil applied along with the actuators developed in Chapter 6 and several literature comparison. [3, 5, 25]

F.4. Conclusions and Future Work

In this work, two types of PIL polymers, namely poly[4-vinylbenzyl-3-butyl imidazolium bis (trifluoromethylsulfonyl)imide] ($PVBBImTf_2N$) and poly[1-vinyl-3-ethylimidazolium bis(trifluoromethylsulfonyl)imide] (PVC_2ImTf_2N) and their ionogels with 1-butyl-3-methylimidazolium tetrafluoroborate ($C_4C_1ImBF_4$-) were reinforced with cellulose paper and graphene oxide. The chemical composition, ionic conductivity, and film structure properties of the reinforced ionogel composites were determined through FTIR spectroscopy, EIS spectroscopy,

and qualitative assessment. Without reinforcement, the PVBBImTf_2N and PVC_2ImTf_2N ionogels with 40 wt% IL content displayed excellent room temperature ion conductivity of ~10^{-4} S/cm; however, they presented gooey gels with poor mechanical properties. Increasing the ionic liquid content to 60 wt% indicated phase separation; therefore, only reinforce composites with 40 wt% IL were developed. Whatman cellulose filter papers coated with ionogel exhibited reduced ion conductivities of ~10^{-6} and 10^{-7} S/cm for the PVBBImTf_2N 40 wt% and PVC_2ImTf2N 40 wt% ionogels. ATR-FTIR and SEM analysis of the coated papers suggests the lower ion conductivity is likely due to issues with the ionogel penetrating into the cellulose filter paper. Attempted actuation of the composites resulted in no measurable actuation for the PVBBImTf_2N 40 wt% composite and a small visual actuation for the PVC_2ImTf2N 40 wt% composite. Utilizing fibrous materials with larger porosities, such as electrospun nanofibers, and implementing an immersion processing method rather than a wetting procedure may help improve the ionogel penetration and ion conductivity of the fibrous composites.

PIL ionogel composites reinforced with graphene oxide were developed and examined as a function of graphene oxide weight percentage (2, 6, and 10 wt%). Ion conductivity was found to decrease with increasing graphene oxide content (~10^{-4} at 2 wt% and ~10^{-5} to 10^{-6} S/cm at 10 wt%). Similarly, the GO composites converted from a gooey gel or sticky film at 2 wt% GO to brittle films at 10 wt% GO. The 6 wt% GO composite composed from PVC_2ImTf_2N 40 wt% IL ionogel was found to have a good balance between ion conductivity (~10^{-5} S/cm) and a stable film structure. Investigation of the actuation behavior of this composite resulted in improved bending behavior compared to the polymer actuators and ionogels developed in Chapter 6. In particular, a tip displacement of ~1.8 mm was achieved under an applied voltage of 4 V for 3 minutes. Although significant deformation of the gold electrodes was observed during actuation. Future

implementation of the GO composites will likely require applying more flexible electrodes such nanocarbon or carbon nanotubes. Interestingly, a small bending behavior (~85 μm tip displacement) was also observed for the PVC_2ImTf_2N 40 wt% IL 6 wt% GO composite without gold leaf electrodes applied to the surface, indicating a possible contribution from the electrical conductivity of graphene oxide. Future experiments will need to include electrical conductivity measurements and mechanical characterizations for modulus and other mechanical properties.

Acknowledgements

The author would like to thank undergraduate researcher Stephen Cockman for his aid in collecting some of the impedance data.

F.5. References

(1) Eshetu, G. G.; Mecerreyes, D.; Forsyth, M.; Zhang, H.; Armand, M. Polymeric ionic liquids for lithium-based rechargeable batteries. *Mol. Syst. Des. Eng.* **2019**, *4* (2), 294-309, 10.1039/c8me00103k. DOI: 10.1039/c8me00103k.

(2) Qian, W.; Texter, J.; Yan, F. Frontiers in poly(ionic liquid)s: synthesis and applications. *Chem. Soc. Rev.* **2017**, *46* (4), 1124-1159, 10.1039/C6CS00620E. DOI: 10.1039/C6CS00620E.

(3) Green, M. D.; Wang, D.; Hemp, S. T.; Choi, J.-H.; Winey, K. I.; Heflin, J. R.; Long, T. E. Synthesis of imidazolium ABA triblock copolymers for electromechanical transducers. *Polymer* **2012**, *53* (17), 3677-3686. DOI: https://doi.org/10.1016/j.polymer.2012.06.023.

(4) Jangu, C.; Wang, J.-H. H.; Wang, D.; Fahs, G.; Heflin, J. R.; Moore, R. B.; Colby, R. H.; Long, T. E. Imidazole-containing triblock copolymers with a synergy of ether and imidazolium sites. *Journal of Materials Chemistry C* **2015**, *3* (16), 3891-3901, 10.1039/C5TC00169B. DOI: 10.1039/C5TC00169B.

(5) Jangu, C.; Wang, J.-H. H.; Wang, D.; Sharick, S.; Heflin, J. R.; Winey, K. I.; Colby, R. H.; Long, T. E. Well-Defined Imidazolium ABA Triblock Copolymers as Ionic-Liquid-Containing Electroactive Membranes. *Macromolecular Chemistry and Physics* **2014**, *215* (13), 1319-1331, https://doi.org/10.1002/macp.201400121. DOI: https://doi.org/10.1002/macp.201400121 (acccessed 2022/08/10).

(6) Margaretta, E.; Fahs, G. B.; Inglefield, D. L.; Jangu, C.; Wang, D.; Heflin, J. R.; Moore, R. B.; Long, T. E. Imidazolium-Containing ABA Triblock Copolymers as Electroactive Devices. *ACS Applied Materials & Interfaces* **2016**, *8* (2), 1280-1288. DOI: 10.1021/acsami.5b09965.

(7) Wang, F.; Jeon, J.-H.; Kim, S.-J.; Park, J.-O.; Park, S. An eco-friendly ultra-high performance ionic artificial muscle based on poly(2-acrylamido-2-methyl-1-propanesulfonic acid) and

carboxylated bacterial cellulose. *Journal of Materials Chemistry B* **2016**, *4* (29), 5015-5024, 10.1039/C6TB01084A. DOI: 10.1039/C6TB01084A.

(8) Zhang, Y.; Chang, L.; Sun, P.; Cao, Z.; Chen, Y.; Liu, H. High-performance double-network ionogels enabled by electrostatic interaction. *RSC Advances* **2020**, *10* (13), 7424-7431, 10.1039/C9RA09632A. DOI: 10.1039/C9RA09632A.

(9) Gao, R.; Wang, D.; Heflin, J. R.; Long, T. E. Imidazolium sulfonate-containing pentablock copolymer–ionic liquid membranes for electroactive actuators. *Journal of Materials Chemistry* **2012**, *22* (27), 13473-13476, 10.1039/C2JM16117F. DOI: 10.1039/C2JM16117F.

(10) Lin, H.; Gong, J.; Miao, H.; Guterman, R.; Song, H.; Zhao, Q.; Dunlop, J. W. C.; Yuan, J. Flexible and Actuating Nanoporous Poly(Ionic Liquid)–Paper-Based Hybrid Membranes. *ACS Applied Materials & Interfaces* **2017**, *9* (17), 15148-15155. DOI: 10.1021/acsami.7b02920.

(11) Chang, J.; Zhou, X.; Zhao, Q.; Cao, W.; Zhang, M.; Yuan, J. Reduced Graphene Oxide-Poly (Ionic Liquid) Composite Films of High Mechanical Performance. *Frontiers in Materials* **2021**, *8*, Original Research. DOI: 10.3389/fmats.2021.635987.

(12) Qu, X.; Zhao, Y.; Chen, Z. a.; Wang, S.; Ren, Y.; Wang, Q.; Shao, J.; Wang, W.; Dong, X. Thermoresponsive Lignin-Reinforced Poly(Ionic Liquid) Hydrogel Wireless Strain Sensor. *Research 2021*. DOI: 10.34133/2021/9845482 (acccessed 2023/06/12).

(13) Veach, A. Battery Desin, Construction, and Characterization for Small Motor Use Focusing on Anodic Zinc for Electron Flow. Chemical Engineering Undergraduate Honors Thesis, University of Arkansas, 2023. https://scholarworks.uark.edu/cheguht/192

(14) Tarannum, F.; Muthaiah, R.; Danayat, S.; Foley, K.; Annam, R. S.; Walters, K. B.; Garg, J. Chemically Edge-Carboxylated Graphene Enhances the Thermal Conductivity of Polyetherimide–Graphene Nanocomposites. *ACS Applied Materials & Interfaces* **2022**, *14* (12), 14753-14763. DOI: 10.1021/acsami.1c25279.

(15) Palm, R.; Kurig, H.; Tõnurist, K.; Jänes, A.; Lust, E. Is the mixture of 1-ethyl-3-methylimidazolium tetrafluoroborate and 1-butyl-3-methylimidazolium tetrafluoroborate applicable as electrolyte in electrical double layer capacitors? *Electrochemistry Communications* **2012**, *22*, 203-206. DOI: https://doi.org/10.1016/j.elecom.2012.06.029.

(16) Kiefer, J.; Fries, J.; Leipertz, A. Experimental vibrational study of imidazolium-based ionic liquids: Raman and infrared spectra of 1-ethyl-3-methylimidazolium bis(trifluoromethylsulfonyl)imide and 1-ethyl-3-methylimidazolium ethylsulfate. *Appl Spectrosc* **2007**, *61* (12), 1306-1311. DOI: 10.1366/000370207783292000 From NLM.

(17) Paschoal, V. H.; Faria, L. F. O.; Ribeiro, M. C. C. Vibrational Spectroscopy of Ionic Liquids. *Chemical Reviews* **2017**, *117* (10), 7053-7112. DOI: 10.1021/acs.chemrev.6b00461.

(18) Heimer, N. E.; Del Sesto, R. E.; Meng, Z.; Wilkes, J. S.; Carper, W. R. Vibrational spectra of imidazolium tetrafluoroborate ionic liquids. *Journal of Molecular Liquids* **2006**, *124* (1), 84-95. DOI: https://doi.org/10.1016/j.molliq.2005.08.004.

(19) Yamada, T.; Mizuno, M. Infrared and Terahertz Spectroscopic Investigation of Imidazolium, Pyridinium, and Tetraalkylammonium Tetrafluoroborate Ionic Liquids. *ACS Omega* **2022**, *7* (34), 29804-29812. DOI: 10.1021/acsomega.2c02601.

(20) Correia, D. M.; Fernandes, L. C.; Martins, P. M.; García-Astrain, C.; Costa, C. M.; Reguera, J.; Lanceros-Méndez, S. Ionic Liquid–Polymer Composites: A New Platform for Multifunctional Applications. *Advanced Functional Materials* **2020**, *30* (24), 1909736, https://doi.org/10.1002/adfm.201909736. DOI: https://doi.org/10.1002/adfm.201909736 (acccessed 2022/08/10).

(21) Guo, D.; Han, Y.; Huang, J.; Meng, E.; Ma, L.; Zhang, H.; Ding, Y. Hydrophilic Poly(vinylidene Fluoride) Film with Enhanced Inner Channels for Both Water- and Ionic Liquid-Driven Ion-Exchange Polymer Metal Composite Actuators. *ACS Applied Materials & Interfaces* **2019**, *11* (2), 2386-2397. DOI: 10.1021/acsami.8b18098.

(22) Correia, D. M.; Barbosa, J. C.; Costa, C. M.; Reis, P. M.; Esperança, J. M. S. S.; de Zea Bermudez, V.; Lanceros-Méndez, S. Ionic Liquid Cation Size-Dependent Electromechanical Response of Ionic Liquid/Poly(vinylidene fluoride)-Based Soft Actuators. *The Journal of Physical Chemistry C* **2019**, *123* (20), 12744-12752. DOI: 10.1021/acs.jpcc.9b00868.

(23) Ding, Y.; Zhang, J.; Chang, L.; Zhang, X.; Liu, H.; Jiang, L. Preparation of High-Performance Ionogels with Excellent Transparency, Good Mechanical Strength, and High Conductivity. *Advanced Materials* **2017**, *29* (47), 1704253. DOI: https://doi.org/10.1002/adma.201704253.

(24) Frederic, B. R.; Cedric, P.; Giao, T. M. N.; Sofia, M. M.; Eric, D.; Alexander, S. S.; Frederic, V. All-solid state ionic actuators based on polymeric ionic liquids and electronic conducting polymers. In *Proc.SPIE*, 2018; Vol. 10594, p 105941H. DOI: 10.1117/12.2300774.

(25) Kokubo, H.; Sano, R.; Murai, K.; Ishii, S.; Watanabe, M. Ionic polymer actuators using poly(ionic liquid) electrolytes. *European Polymer Journal* **2018**, *106*, 266-272. DOI: https://doi.org/10.1016/j.eurpolymj.2018.07.026.

(26) Lian, Y.; Liu, Y.; Jiang, T.; Shu, J.; Lian, H.; Cao, M. Enhanced Electromechanical Performance of Graphite Oxide-Nafion Nanocomposite Actuator. *The Journal of Physical Chemistry C* **2010**, *114* (21), 9659-9663. DOI: 10.1021/jp101337h.

(27) Maity, N.; Mandal, A.; Nandi, A. K. Interface engineering of ionic liquid integrated graphene in poly(vinylidene fluoride) matrix yielding magnificent improvement in mechanical, electrical and dielectric properties. *Polymer* **2015**, *65*, 154-167. DOI: https://doi.org/10.1016/j.polymer.2015.03.066.

(28) Fang, Y.; Pence, T. J.; Tan, X. Nonlinear elastic modeling of differential expansion in trilayer conjugated polymer actuators. *Smart Materials and Structures* **2008**, *17* (6), 065020. DOI: 10.1088/0964-1726/17/6/065020.

(29) Yanjie, W.; Takushi, S. Ionic Polymer Actuators: Principle, Fabrication and Applications. In *Actuators*, Constantin, V. Ed.; IntechOpen, 2018.

(30) Rasouli, H.; Naji, L.; Hosseini, M. G. Electrochemical and Electromechanical Study of Carbon-Electrode-Based Ionic Soft Actuators. *Industrial & Engineering Chemistry Research* **2018**, *57* (3), 795-806. DOI: 10.1021/acs.iecr.7b03030.

(31) Dong, Y.; Yeung, K.-W.; Tang, C.-Y.; Law, W.-C.; Tsui, G. C.-P.; Xie, X. Development of ionic liquid-based electroactive polymer composites using nanotechnology. *Nanotechnology Reviews* **2021**, *10* (1), 99-116. DOI: doi:10.1515/ntrev-2021-0009.

(32) Feng, C.; Zhu, D.; Wang, Y.; Jin, S. Electromechanical Behaviors of Graphene Reinforced Polymer Composites: A Review. In *Materials*, 2020; Vol. 13.

(33) Sigamani, N.; Ounaies, Z.; Ehlert, G.; Sodano, H. Electromechanical response of reduced graphene oxide–polyvinylidene fluoride nanocomposites prepared through in-situ thermal reduction. *Journal of Applied Physics* **2015**, *117* (15). DOI: 10.1063/1.4915116 (acccessed 6/13/2023).

Appendix G: List of Published Papers and Presentations

G.1. List of Published Papers

Publications from Ph.D. Dissertation Efforts

First Author

3. **Kayla Foley**, Keisha B. Walters. "Development of Nano- and Micro- Fluids Using Magnetic Poly(ionic liquid)-Surfactant Complexes for Stimuli Response." Proceedings of the ASME 2022 Fluids Engineering Division Summer Meeting. Volume 2: Multiphase Flow (MFTC); Computational Fluid Dynamics (CFDTC); Micro and Nano Fluid Dynamics (MNFDTC). Toronto, Canada. August 3-5, 2022. V002T06A006. In Print. ASME. https://doi.org/10.1115/FEDSM2022-87758. This text was used in Chapter 3.
4. **Kayla Foley**, Lucas Condes, Keisha B. Walters. Influence of metal-coordinating comonomers on the coordination structure and binding in magnetic poly(ionic liquid)s. [Accepted July 9th, 2023. ID ME-ART-05-2023-000076, Pre-publication] Journal: *RSC Molecular Systems Design and Engineering.* This text was used in Chapter 2.

Co-Author

1. Fatema Tarannum, Rajmohan Muthaiah, Swapneel S. Danayat, **Kayla Foley**, Roshan Sameer Annam, Keisha Walters, Jivtesh Garg. "Chemically edge-carboxylated graphene enhances thermal conductivity of polyetherimide-graphene nanocomposites," *ACS Applied Materials & Interfaces.* 2022, 14, 12, 14753-14763. In Print. https://doi.org/10.1021/acsami.1c25279. Contribution: FTIR characterization

Submitted and Under Review or In Revision

First Author

2. **Kayla Foley**, Keisha B. Walters. Solution and film self-assembly behavior of a block copolymer comprised of a poly(ionic liquid) and a stimuli-responsive weak polyelectrolyte. [Submitted June 6th, 2023. ID ao-2023-039894, In Revision] Journal: *ACS Omega.* This text was used in Chapter 5.

Co-Author

1. Syed Ashik Ali, **Kayla Foley**, Keisha B. Walters, Musharraf Zaman. "Micro-structural evaluation of the effects of aggregate type, aging, and additives on the moisture susceptibility of binder-aggregate systems using chemical and thermodynamic approaches." [Submitted May 22nd, 2023. ID MTENG-17006, Under Review] Journal: *Journal of Materials in Civil Engineering*. Contribution: FTIR characterization

In Preparation

3. **Kayla Foley**, Iwei Chu, Keisha B. Walters. Evaluation of novel poly(ionic liquid) block copolymer and homopolymer as electroactive polymer actuators. [In Preparation]. This text was used in Chapter 6.
4. **Kayla Foley,** Charles P. Easterling, Dale L. Huber. Keisha B. Walters. Magnetometry studies of magnetic poly(ionic liquids) using surfactant complexation to direct self-assembly and increase the effective moment. [In Preparation]. This text was used in Chapter 4.

Publications from Master's Thesis Efforts

1. **Foley, K. A.**, & Shambaugh, R. L. (2018). Fiber spinning with airfields enhanced by airfoil louvers. *Textile Research Journal*. In Print. https://doi.org/10.1177/0040517518807444

Awarded Proposals and Grants

1. Vibrating Sample Magnetometry of Magnetic Poly(ionic liquid) Copolymers and their Surfactant Complexed Nanostructures. DOE Center for Integrated Nanotechnologies (CINT) User Proposal. 2022AU0062 (June 28th, 2022 – Dec. 31st , 2023). Chapter 4 was a outcome for this proposal.

G.2. List of Presentations Related to Dissertation

Oral Presentations

1. **Kayla Foley,** Keisha B. Walters. " Development of poly(ionic liquid) ionogels for electroactive polymer applications." AIChE 2022 Annual Meeting. Polymers Section: Charged and Ion Containing Polymers II. Phoenix, AZ. (Nov. 14, 2022).
2. **Kayla Foley,** Keisha B. Walters. "Synthesis, Characterization, and assembly of all polyelectrolyte diblock copolymers from Poly(ionic liquid) and weak polyelectrolyte blocks." AIChE 2022 Annual Meeting. Polymers Section: Ionic Liquids: Novel Separation, Catalytic reaction and Electrochemical Processes. Phoenix, AZ. (Nov. 14, 2022)
3. **Kayla Foley**, Keisha B. Walters. "Development of Nano- and Micro-Fluids Using Magnetic Poly(ionic liquid)-Surfactant Complexes for Stimuli Response." 2022 Fluids Engineering Division's (FED) Summer Meeting. Toronto, Canada (Aug. 3rd, 2022)
4. **Kayla Foley**, Keisha B. Walters. "SARA ATRP Synthesis of Poly(ionic liquid)-*b*-Weak Polyelectrolytes and an Initial Look at its Solution Behavior in DMSO." MC15 15th International Conference on Materials Chemistry Royal Society of Chemistry. Digital, (July 14th , 2021).

Poster Presentations

1. **Kayla Foley** "Poly(ionic liquids) for Magnetic and Electrical Response Stimuli Response" AIChE 2022 Annual Meeting: Women in Chemical Engineering (WIC) Keynote Breakfast & Poster Session. Phoenix, AZ. Nov. 15, 2022
2. **Kayla Foley**; Lucas Condes, Keisha B. Walters. "Chemical and Magnetic Study of Metal-ion Poly(ionic liquid) Copolymers." Poster Presentation at SPE ANTEC 2021. Digital, (May 7th, 2021).
3. **Kayla Foley,** Natalie Berryman, Lucas Condes, Keisha B. Walters, "Development of Metal-containing Poly(Ionic liquid)-Surfactant Complexes for Biomedical Applications," Poster Presentation at the Great Plains Biomaterials Day 2021, The University of Kansas Society for Biomaterials Student Chapter/Digital. (April 17th, 2021).